

Metals in 3D: A Cosmic View from Integral Field Spectroscopy

Guest Editor: Jorge Iglesias-Páramo, José Manuel Vílchez Medina, Polychronis Papaderos, and Martin M. Roth





Metals in 3D: A Cosmic View from Integral Field Spectroscopy

Advances in Astronomy

Metals in 3D: A Cosmic View from Integral Field Spectroscopy

Guest Editors: Jorge Iglesias-Páramo,
José Manuel Vílchez Medina, Polychronis Papaderos,
and Martin M. Roth



Copyright © 2014 Hindawi Publishing Corporation. All rights reserved.

This is a special issue published in “Advances in Astronomy.” All articles are open access articles distributed under the Creative Commons Attribution License, which permits unrestricted use, distribution, and reproduction in any medium, provided the original work is properly cited.

Editorial Board

Michael Brotherton, USA
Alberto J. Castro-Tirado, Spain
Michael Disney, UK
Elmetwally Elabbasy, Egypt
Nye Evans, UK
Maurizio Falanga, Switzerland
Duncan Forbes, Australia
Andrew Fruchter, USA
Boris T. Gänsicke, UK
Paul Goldsmith, USA
Dean Hines, USA
Dieter Horns, Germany

Ivan Hubeny, USA
John Hughes, USA
Wing Huen Ip, Taiwan
Valentina Klochkova, Russia
Gregory Laughlin, USA
Myung G. Lee, Republic of Korea
Karen Leighly, USA
Jeffrey Linsky, USA
Ronald Mennickent, Chile
Zdzislaw E. Musielak, USA
Valery Nakariakov, UK
Jerome Orosz, USA

George Pavlov, USA
Juri Poutanen, Finland
Somak Raychaudhury, India
William Reach, USA
Peter Roming, USA
Regina Schulte-Ladbeck, USA
Ravi Sheth, USA
Josep M. Trigo-Rodríguez, Spain
Roberto Turolla, Italy
Gary Wegner, USA
Glenn J. White, UK
Paul J. Wiita, USA

Contents

Metals in 3D: A Cosmic View from Integral Field Spectroscopy, Jorge Iglesias-Páramo
Volume 2014, Article ID 753034, 1 page

Chemical and Photometric Evolution Models for Disk, Irregular, and Low Mass Galaxies, Mercedes Mollá
Volume 2014, Article ID 162949, 26 pages

Imaging FTS: A Different Approach to Integral Field Spectroscopy, Laurent Drissen, Laurie Rousseau-Nepton, Sébastien Lavoie, Carmelle Robert, Thomas Martin, Pierre Martin, Julie Mandar, and Frédéric Grandmont
Volume 2014, Article ID 293856, 15 pages

The Integral Field View of the Orion Nebula, Adal Mesa-Delgado
Volume 2014, Article ID 279320, 14 pages

Chemodynamical Simulations of Dwarf Galaxy Evolution, Simone Recchi
Volume 2014, Article ID 750754, 30 pages

Observing and Reducing IFUs: INTEGRAL and PMAS Properties of the Ionized Gas in HH 202, Luis López-Martín
Volume 2014, Article ID 290458, 8 pages

Properties of the H II REGIONS DERIVED USING INTEGRAL FIELD SPECTROSCOPY, Sebastian F. Sánchez
Volume 2013, Article ID 596501, 14 pages

The Mitchell Spectrograph: Studying Nearby Galaxies with the VIRUS Prototype, Guillermo A. Blanc
Volume 2013, Article ID 641612, 16 pages

Studying the Interstellar Medium of H II/BCD GALAXIES USING IFU SPECTROSCOPY, Patricio Lagos and Polychronis Papaderos
Volume 2013, Article ID 631943, 9 pages

The Study of Nebular Emission on Nearby Spiral Galaxies in the IFU Era, Fernando Fabián Rosales-Ortega
Volume 2013, Article ID 627867, 14 pages

Are Wolf-Rayet Stars Able to Pollute the Interstellar Medium of Galaxies? Results from Integral Field Spectroscopy, Enrique Pérez-Montero, Carolina Kehrig, Jarle Brinchmann, José M. Vílchez, Daniel Kunth, and Florence Durret
Volume 2013, Article ID 837392, 15 pages

Editorial

Metals in 3D: A Cosmic View from Integral Field Spectroscopy

Jorge Iglesias-Páramo

Instituto de Astrofísica de Andalucía, CSIC, 18008 Granada, Spain

Correspondence should be addressed to Jorge Iglesias-Páramo; jglesia@iaa.es

Received 8 April 2014; Accepted 8 April 2014; Published 21 May 2014

Copyright © 2014 Jorge Iglesias-Páramo. This is an open access article distributed under the Creative Commons Attribution License, which permits unrestricted use, distribution, and reproduction in any medium, provided the original work is properly cited.

Integral field spectroscopy (IFS) is an observational technique that has revolutionized our understanding of extended objects in the Universe since the last decade. IFS provides unique contributions to the study of Galactic ionized nebulae, extragalactic HII regions, and galaxies in the local and in the early Universe, which in some aspects are complementary to the high precision performance of existing wide area photometric and single-aperture spectroscopic surveys. The power of this technique is the possibility of gathering complete spectroscopic information across the spatial extension of astrophysical objects, thus allowing the study of physical spatial variations of their properties, this being specially significant for those properties related to their metal content and star formation activity. With this special issue we want to cover the most relevant aspects related to IFS, in order to illustrate to the reader the wide scope opened by this observational technique.

In what follows we present the main contents of this special issue split by subject. Two papers of this issue are devoted to modeling the chemical evolution of spiral and dwarf galaxies by M. Mollá and S. Recchi. Theoretical models are a key ingredient in order to be compared with the observational data since either their predictions open new observational avenues or they are constrained by new observational results. Both aspects must walk hand in hand to make progress in the field.

Two papers follow, dealing with the study of Galactic objects. The one by L. López-Martín mostly addresses some aspects of the particular technical problems of IFS data handling. A paper by A. Mesa-Delgado faces the chemical abundance discrepancy problem applied to Galactic Herbig Haro objects in the Orion nebula, illustrating how IFS can help to shed light on this issue.

A set of four papers follows focused on extragalactic studies with fiber-fed spectrographs: the first two papers, by E. Pérez-Montero et al. and P. Lagos and P. Papaderos, deal with the chemical properties of star-forming (HII/BCD) dwarf galaxies and with the interplay of the WR stellar population on the metal enrichment of the interstellar medium. The remaining two papers of this block, by F. F. Rosales-Ortega and S. F. Sánchez, are focused on the properties of the HII regions in spiral galaxies and review most recent results on chemical abundance gradients obtained from IFS observations.

Last but not least, a set of two papers of this issue are devoted to the description and main properties of two ongoing experiments/instruments. One is a wide-field integral field spectrograph, by G. A. Blanc, with applications in several astrophysical fields, in particular in the study of the properties of nearby galaxies. The second one, by L. Drissen et al., explains the basics of the operation of imaging Fourier transform spectrometers (IFTS), an interesting alternative to the traditional dispersive spectrographs due to their wide field of view, and it shows the main goals that can be achieved using them in the study of the chemical evolution of astrophysical objects.

Jorge Iglesias-Páramo

Research Article

Chemical and Photometric Evolution Models for Disk, Irregular, and Low Mass Galaxies

Mercedes Mollá^{1,2}

¹ *Departamento de Investigación Básica, CIEMAT, Avenida Complutense 40, 28040 Madrid, Spain*

² *IAG, University of São Paulo, 05508-900 São Paulo, SP, Brazil*

Correspondence should be addressed to Mercedes Mollá; mercedes.molla@ciemat.es

Received 18 October 2013; Revised 30 December 2013; Accepted 1 January 2014; Published 20 May 2014

Academic Editor: Jorge Iglesias Páramo

Copyright © 2014 Mercedes Mollá. This is an open access article distributed under the Creative Commons Attribution License, which permits unrestricted use, distribution, and reproduction in any medium, provided the original work is properly cited.

We summarize the updated set of multiphase chemical evolution models performed with 44 theoretical radial mass initial distributions and 10 possible values of efficiencies to form molecular clouds and stars. We present the results about the infall rate histories, the formation of the disk, and the evolution of the radial distributions of diffuse and molecular gas surface density, stellar profile, star formation rate surface density, and elemental abundances of C, N, O, and Fe, finding that the radial gradients for these elements begin steeper and flatten with increasing time or decreasing redshift, although the outer disks always show a certain flattening for all times. With the resulting star formation and enrichment histories, we calculate the spectral energy distributions (SEDs) for each radial region by using the ones for single stellar populations resulting from the evolutive synthesis model POPSTAR. With these SEDs we may compute finally the broad band magnitudes and colors radial distributions in the Johnson and in the SLOAN/SDSS systems which are the main result of this work. We present the evolution of these brightness and color profiles with the redshift.

1. Introduction

Chemical evolution models to study the evolution of spiral galaxies have been the subject of a high number of works for the last decades. From the works by Lynden-Bell [1], Tinsley [2], Clayton [3, 4], and Sommer-Larsen and Yoshii [5], many other models have been developed to analyze the evolution of a disk galaxy. The first attempts were performed to interpret the G-dwarf metallicity distribution and the radial gradient of abundances [6–16] observed in our Milky Way galaxy (MWG). A radial decrease of abundances was soon observed in most of external spiral galaxies, too (see Henry and Worthey [17] and references therein), although the shape of the radial distribution changes from galaxy to galaxy, at least when it is measured in dex kpc^{-1} (recent results seem to indicate that the radial gradient may be universal for all galaxies when it is measured in $\text{dex } r_{\text{eff}}^{-1}$ [18], r_{eff} being the radius enclosing the half of the total luminosity of a disk galaxy, or with any other normalization radius, something already suggested some years ago by Garnett [19] although the statistics was not large enough to reach accurate conclusions).

It was early evident that it was impossible to reproduce these observations by using the classical closed box model [20] which relates the metallicity Z of a region with its fraction of gas over the total mass, (stars, s , plus gas, g), $\mu_g = g/(g + s)$. Therefore infall or outflows of gas in MWG and other nearby spirals were soon considered necessary to fit the data. In fact, such as it was established theoretically by Goetz and Koeppen [21] and Koeppen [22] a radial gradient of abundances may be created only by 4 possible ways: (1) a radial variation of the initial mass function (IMF), (2) a variation of the stellar yields along the galactocentric radius, (3) a star formation rate (SFR) changing with the radius, and (4) a gas infall rate variable, f , with radius. The first possibility is not usually considered as probable, while the second one is already included in modern models, since the stellar yields are in fact dependent on metallicity. Thus, from the seminal works from Lacey and Fall [23], Güsten and Mezger [24], and Clayton [3] most of the models in the literature [25–32], including the multiphase model used in this work, explain the existence of this radial gradient by the combined effects of

a SFR and an infall of gas which vary with the galactocentric radius in the galaxy.

Most of the chemical evolution models of the literature, included some of the recently published, are, however, only devoted to the MWG, (totally or only for a region of it, halo or bulge) [33–38] or to any other individual local galaxy as M 31, M 33 or other local dwarf galaxies [35, 39–50]. These works perform the models in a *Tailor-Made Models* way, done by hand for each galaxy or region. There are not models applicable to any galaxy, except our grid of models shown in Mollá and Diaz ([51], hereinafter MD05) and these ones from Boissier and Prantzos [32, 52], who presented a wide set of models with two parameters, the total mass or rotation velocity, and the efficiency to form molecular clouds and stars in MD05 and a angular momentum parameter in the last authors grid.

Besides that, these classical numerical chemical evolution models only compute the masses in the different phases of a region (gas, stars, elements, etc.) or the different proportions among them. They do not give the corresponding photometric evolution, preventing the comparison of chemical information with the corresponding stellar one. There exist a few consistent models which calculate both things simultaneously in a consistent way, as those from Vazquez et al. [40], Boissier and Prantzos [52] or those from Fritze-Von Alvensleben et al. [53], Bicker et al. [54], and Kotulla et al. ([55], hereafter GALEV). The latter, GALEV evolutionary synthesis models, describe the evolution of stellar populations including a simultaneous treatment of the chemical evolution of the gas and of the spectral evolution of the stellar content. These authors, however, treat each galaxy as a whole for only some typical galaxies along the Hubble sequence and do not perform the study of radial profiles of mass, abundances, and light simultaneously. The series of works by Boissier and Prantzos [32, 52], Prantzos and Boissier [56], and Boissier et al. [57] seems one of few that give models allowing an analysis of the chemical and photometric evolution of disk galaxies.

Given the advances in the instrumentation, it is now possible to study high redshift galaxies as the local ones with spatial resolution are good enough to obtain radial distributions of abundances and of colors or magnitudes and thus to perform careful studies of the possible evolution of the different regions of disk galaxies. For instance to check the existence of radial gradients at other evolutionary times different than the present [58–61] and their evolution with time or redshift is now possible. It is also possible to compare these gradients with the radial distributions from the stellar populations to study possible migration effects. It is therefore important to have a grid of consistent chemo-spectro-photometric models which allows the analysis of both types of data simultaneously.

The main objective of this work is to give the spectrophotometric evolution of the theoretical galaxies presented in MD05, for which we have updated the chemical evolution models. In that work we presented a grid of chemical evolution models for 440 theoretical galaxies, with 44 different total mass, as defined by its maximum rotation velocity and radial mass distributions, and 10 possible values of efficiencies

to form molecular clouds and stars. Now we have updated these models by including a bulge region and by using a different relation mass-life-meantime for stars now following the Padova stellar tracks. These models do not consider radial flows nor stars migration since no dynamical model is included. The possible outflows by supernova explosions are not included, too. We check that with the continuous star formation histories resulting of these models, the supernova explosions do not appear in sufficient number as to produce the energy injection necessary to have outflows of mass. With these chemical evolution model results, we calculate the spectrophotometric evolution by using each time step of the evolutionary model as a single stellar populations at which we assign a spectrum taken from the POPSTAR evolutionary synthesis models [62]. Our purpose in to give as a catalogue the evolution of each radial region of a disk and this way the radial distributions of elemental abundances, star formation rate, gas, and stars will be available along with the radial profiles of broad band magnitudes for any time of the calculated evolution.

The work is divided as follows: we summarize the updated chemical evolution models in Section 2. Results related to the surface densities and abundances are given in Section 3. We describe our method to calculate the SEDs of these theoretical galaxies and the corresponding broad band magnitudes and colors in Section 4. The corresponding spectrophotometric results are shown in Section 5 where we give a catalog of the evolution of these magnitudes in the rest-frame of the galaxies. Some important predictions arise from these models which are given in the conclusions.

2. The Chemical Evolution Model Description

The models shown here are the ones from MD05 and therefore a more detailed explanation about the computation is given in that work. We started with a mass of primordial gas in a spherical region representing a protogalaxy or halo. The initial mass within the protogalaxy is the dynamical mass calculated by means of the rotation velocity, $V(\text{Radius})$, through the expression [63]:

$$M(\text{Radius}) = M_{H,0} = 2.32 \times 10^5 \text{ Radius } V^2(\text{Radius}) \quad (1)$$

with M in M_{\odot} , Radius in kpc, and V in km s^{-1} . We used the universal rotation curve from (URC) from Persic et al. [64] to calculate a set of rotation velocity curves $V(\text{Radius})$ and from these velocity distributions we obtained the mass radial distributions $M(\text{Radius})$ (see MD for details and Figure 2 showing these distributions). It was also possible to use those equations to obtain the scale length of the disk R_D , the optical radius, defined as the one where the surface brightness profile is $25 \text{ mag arcsec}^{-2}$, which, if disks follow the Freeman's [65] law, is $R_{\text{opt}} = 3.2R_D$ and the virial radius, which we take as the galaxy radius R_{gal} . The total mass of the galaxy M_{gal} is taken as the mass enclosed in this radius R_{gal} . The expression for the URC was given by means of the parameter $\lambda = L/L_*$, the ratio between the galaxy luminosity, L , and the one of the MWG, L_* , in band I. This parameter defines the maximum rotation velocity, V_{max} , and the radii described

TABLE 1: Theoretical galaxy models selected to represent a simulated Hubble sequence.

dis	V_{\max} Km s ⁻¹	M_{gal} 10 ¹¹ M _⊙	Ropt kpc	τ_c Gyr	nt	ϵ_η	ϵ_δ
3	48	0.3	2.3	31.6	8	0.037	2.6 10 ⁻⁴
10	78	1.3	4.1	15.5	7	0.075	1.5 10 ⁻³
21	122	4.3	7.1	8.1	6	0.15	1.0 10 ⁻²
24	163	9.8	10.1	5.4	5	0.30	5.0 10 ⁻²
28	200	17.9	13.0	4.0	4	0.45	1.4 10 ⁻¹
35	250	33.5	16.9	2.9	3	0.65	3.4 10 ⁻¹
39	290	52.7	20.6	2.3	1	0.95	8.8 10 ⁻¹

above. Thus, we obtained the values of the maximum rotation velocities and the corresponding parameters and mass radial distributions for a set of λ values such as it may be seen in Table 1 from MD05.

To the radial distributions of disks calculated by means of (1) described above, we have added a region located at the center ($R = 0$) to represent a bulge. The total mass of the bulge is assumed as a 10% of the total mass of the disk. The radius of this bulge is taken as $R_D/5$. Both quantities are estimated from the correlations found by Balcells et al. [66] among the disk and the bulges data.

2.1. The Infall Rate: Its Dependence on the Dynamical Mass and on the Galactocentric Radius. We assume that the gas falls from the halo to the equatorial plane forming out the disk in a scenario ELS [67]. The time-scale of this process, or collapse-time scale $\tau_{\text{gal},c}$, characteristic of every galaxy, changes with its total dynamical mass M_{gal} , following the expression from Gallagher III et al. [68]:

$$\tau_{\text{gal},c} \propto M_{\text{gal}}^{-1/2} T, \quad (2)$$

where M_{gal} is the total mass of the galaxy and T is its age. We assume that all galaxies begin to form at the same time and evolve for a time of $T = 13.2$ Gyr. We use the value of 13.8 Gyr, given by the Planck experiment [69] for the age of the Universe and therefore galaxies start to form at a time $t_{\text{start}} = 0.6$ Gyr.

Normalizing to MWG, we obtain

$$\tau_{\text{gal},c} = \tau_{\text{MWG},c} \sqrt{\frac{M_{\text{MWG}}}{M_{\text{gal}}}}, \quad (3)$$

where $M_{\text{MWG}} \sim 1.8 \times 10^{12} M_{\odot}$ is the total mass of MWG and $\tau_{\text{MWG},c} = 4$ Gyr (see details in the next paragraph) is the assumed characteristic collapse-time scale for our galaxy.

The above expression implies that galaxies more massive than MWG form in a shorter time-scale, that is more rapidly, than the least massive galaxies which will need more time to form their disks. This assumption is in agreement with the observations from Jimenez et al. [70], Heavens et al. [71], and Pérez et al. [72] which find that the most massive galaxies have their stellar populations in place at very early times while the less massive ones form most of their stars at $z < 1$. This is also

in agreement with self-consistent cosmological simulations which show that a large proportion of massive objects are formed at early times (high redshift), while the formation of less massive ones is more extended in time, thus simulating a modern version of the monolithic collapse scenario ELS.

The calculated collapse-time scale $\tau_{\text{gal},c}$ is assumed that corresponds to a radial region located in a characteristic radius, which is $R_c = R_{\text{opt}}/2 \sim 6.5$ kpc for the MWG model which uses the distribution with $\lambda = 1.00$ and number 28, with a maximum rotation velocity $V_{\max} = 200$ km s⁻¹. The value $\tau_{\text{MWG},c} = 4$ Gyr was determined by a detailed study of models for MWG. We performed a large number of chemical evolution models changing the inputs free-parameters and comparing the results with many observational data [27, 28] to estimate the best value. Similar characteristic radii (all these radii and values are related to the stellar light and not to the mass, but we clear that we do not use them in our models except to define the characteristic radius R_c for each theoretical mass radial distribution. The free parameters are selected for the region defined by this R_c but taking into account that we normalize the values after a calibration with the solar neighborhood model, a change of this radius would not modify our model results) for our grid of models were given in Table 1 from MD05 too, with the characteristic τ_c (from now we will use the expression τ_c for $\tau_{\text{gal},c}$ for the sake of simplicity) obtained for each galaxy total mass M_{gal} .

By taking into account that the collapse time scale depends on the dynamical mass and that spiral disks show a clear profile of density with higher values inside than in the outside regions, we may assume that the infall rate, and therefore the collapse time scale τ_{coll} , has a radial dependence, too. Since the mass density seems to be an exponential in most of cases, we then assumed a similar expression:

$$\tau_{\text{coll}}(\text{Radius}) = \tau_c \exp\left(\frac{\text{Radius} - R_c}{\lambda_D}\right), \quad (4)$$

where λ_D is the scale-length of the collapse time-scale, taken as around half of the scale-length of surface density brightness distribution, R_D ; that is $\lambda_D = 0.15R_{\text{opt}} \sim 0.5R_D$.

Obviously the collapse time scale for the bulge region is obtained naturally from the above equation with Radius = 0. We show in Figure 1(a) the collapse time scale τ_{coll} , in natural logarithmic scale, as a function of the galactocentric radius, for seven radial distributions of total mass, as defined by their maximum rotation velocity, V_{\max} , and plotted with different colors, as labeled. These seven theoretical galaxies are used as examples and their characteristics are summarized in Table 1, where we have the number of the distribution, dis, corresponding to column 2 from Table 1 in MD05 in column 1, the maximum rotation velocity, V_{\max} , in km s⁻¹, in column 2, the total mass, M_{gal} , in 10¹¹ M_⊙ units, in column 3, the theoretical optical radius R_{opt} , following Persic et al. [64] equations, in kpc, in column 4, the collapse time scale in the characteristic radius, τ_c , in Gyr in column 5, the value nt which defines the efficiencies (see Equation (7) in Section 2.2) in column 6, and the values for these efficiencies in columns 7 and 8.

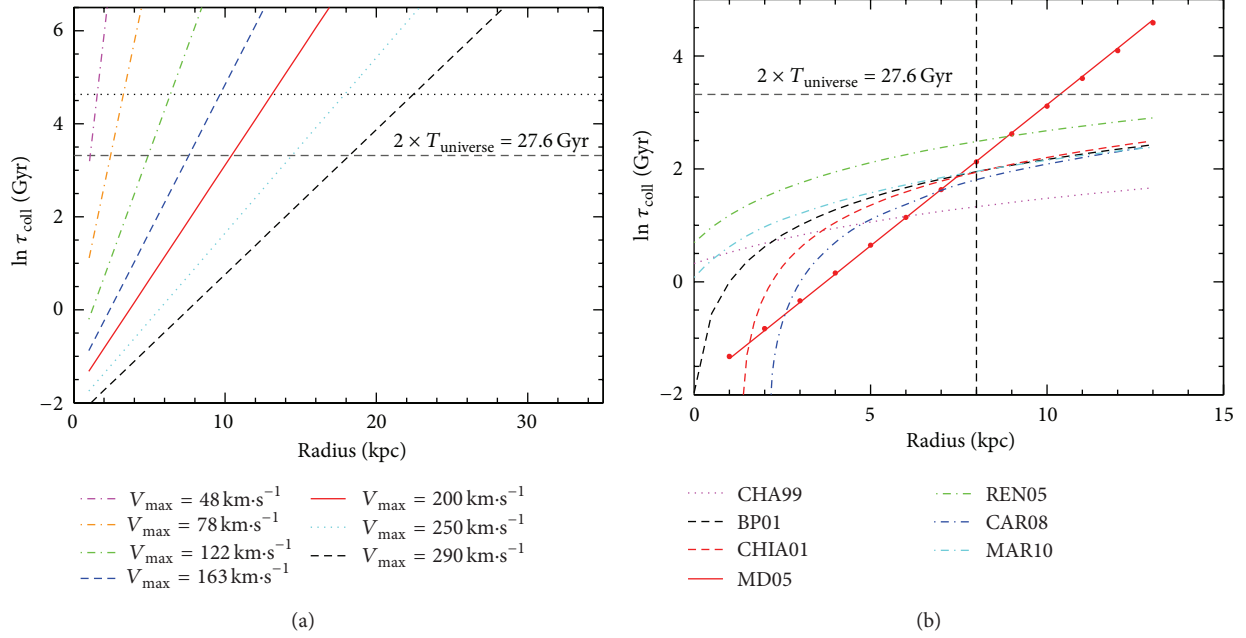


FIGURE 1: (a) Dependence of the collapse time scale, τ_{coll} , in natural logarithmic scale, (in Gyr) on the galactocentric radius, Radius, in kpc. Each line represents a given maximum rotation velocity, V_{max} , or radial mass distribution as labeled. The dashed (gray) and dotted (black) lines show the time corresponding to 2 and 5 times, respectively, the age of the Universe, $T_{\text{UNIVERSE}} = 13.8$ Gyr. (b) Comparison of the radial dependence of the collapse time scale, τ_{coll} , in natural logarithmic scale, for our MWG model, corresponding to $V_{\text{max}} = 200$ km s $^{-1}$, shown by the solid red line, with the radial functions used by Chang et al. [73], Boissier and Prantzos [32], Chiappini et al. [74], Renda et al. [75], Carigi and Peimbert [76], and Marcon-Uchida et al. [35] labeled CHA99, BP99, CHIA01, REN05, CAR08, and MAR10, respectively.

The red line corresponds to a MWG-like radial distribution. The long-dashed black line shows the time corresponding to 2 times the age of the Universe. Such as we may see, the most massive galaxies would have the most extended disks, since the collapse timescale is smaller than the age of the universe for longer radii, thus allowing the formation of the disk until radii as larger as 20 kpc, while the least massive ones would only have time to form the central region, smaller than 1-2 kpc, as observed. The dashed (gray) lines show the time corresponding to 2 times the age of the Universe, $T_{\text{UNIVERSE}} = 13.8$ Gyr. The dotted black line defines the collapse time scale for which the maximum radius for the disk of the MWG model would be 13 kpc, the optical radius, and it corresponds to a collapse time scale of 5 times the age of the Universe.

Other authors have also included a radial dependence for the infall rate in their models [23, 26, 27, 52, 80] with different expressions. In fact this dependence, which produces an in-out formation of the disk, is essential to obtain the observed density profiles and the radial gradient of abundances, such as it has been stated before [26, 28, 52]. In Figure 1(b) we show the collapse time scale τ_{coll} , in natural logarithmic scale, assumed in different chemical evolution models of MWG, as a function of the galactocentric radius. The red solid line corresponds to our MWG model ($\lambda = 1.00$ and number 28 of the mass distributions of Table 1) from MD05. The other functions, straight lines, are those used by Chang et al. [73], Boissier and Prantzos [32], Chiappini et al. [74], Renda et al. [75], Carigi and Peimbert [76], and Marcon-Uchida et al. [35], as labeled. Since they use straight lines the collapse time

scale for our model results shorter for the inner disk regions (except for the bulge region $R < 3$ -4 kpc) and longer for the outer ones, than the ones used by the other works. This will have consequences in the radial distributions of stars and elemental abundances as we will see.

2.2. The Star Formation Law in Two-Steps: The Formation of Molecular Gas Phase. The star formation is assumed different in the halo than in the disk. In the halo the star formation follows a Kennicutt-Schmidt law. In the disk, however, we assume a more complicated star formation law, by creating molecular gas from the diffuse gas in a first step, again by a Kennicutt-Schmidt law. And then stars from the cloud-cloud collisions. There is a second way to create stars from the interaction of massive stars with the surrounding molecular clouds.

Therefore the equation system of our model is

$$\frac{dg_H}{dt} = -(\kappa_1 + \kappa_2) g_H^n - fg_H + W_H$$

$$\frac{ds_{1,H}}{dt} = \kappa_1 g_H^n - D_{1,H}$$

$$\frac{ds_{2,H}}{dt} = \kappa_2 g_H^n - D_{2,H}$$

$$\frac{dg_D}{dt} = -\eta g_D^n + \alpha' c_D s_{2,D} + \delta' c_D^2 + fg_H + W_D$$

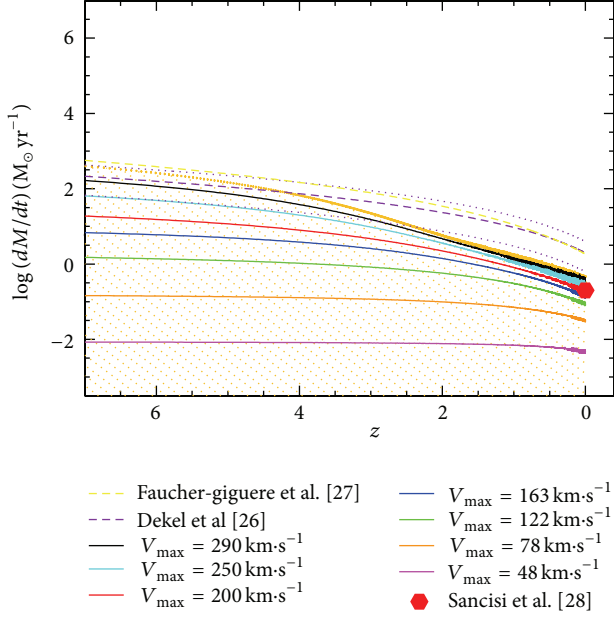


FIGURE 2: The evolution of the infall gas rate along the redshift z for all radial regions of our 44 galaxy mass values represented by the shaded zone. The solid lines show the evolution of the whole infall rate of the same 7 theoretical galaxies shown in Figure 1 with the same color coding. The higher the total mass, the higher the infall rate. Dashed purple and yellow lines represent the prescriptions from Dekel et al. [77] and Faucher-Giguère et al. [78], respectively. The dotted purple lines are the Dekel et al. [77] prescriptions for masses $2 \times 10^{12} M_{\odot}$ and $3 \times 10^{11} M_{\odot}$, while the red hexagon in the present time is the estimated value given by Sancisi et al. [79].

$$\frac{dc_D}{dt} = \eta g_D^n - (\alpha_1 + \alpha_2 + \alpha') c_D s_{2D} - (\delta_1 + \delta_2 + \delta') c_D^2$$

$$\frac{ds_{1,D}}{dt} = \delta_1 c_D^2 + \alpha_1 c_D s_{2D} - D_{1,D}$$

$$\frac{ds_{2,D}}{dt} = \delta_2 c_D^2 + \alpha_2 c_D s_{2D} - D_{2,D}$$

$$\frac{dr_H}{dt} = D_{1,H} + D_{2,H} - W_H$$

$$\frac{dr_D}{dt} = D_{1,D} + D_{2,D} - W_D$$

$$\frac{X_{i,H}}{dt} = \frac{(W_{i,H} - X_{i,H} W_H)}{g_H}$$

$$\frac{X_{i,D}}{dt} = \frac{[W_{i,D} - X_{i,D} W_D + f g_H (X_{i,H} - X_{i,D})]}{g_D + c_D} \quad (5)$$

These equations predict the time evolution of the different phases of the model: diffuse gas, g , molecular gas, c , low mass stars, s_1 , and intermediate mass and massive stars, s_2 , and stellar remnants, r , (where letters D and H correspond to disk and halo, resp.). Stars are divided in 2 ranges, s_1 being the low mass stars and s_2 the intermediate and massive ones,

considering the limit between both ranges stellar a mass $m = 4 M_{\odot}$. X_i are the mass fractions of the 15 elements considered by the model: ^1H , D , ^3He , ^4He , ^{12}C , ^{16}O , ^{14}N , ^{13}C , ^{20}Ne , ^{24}Mg , ^{28}Si , ^{32}S , ^{40}Ca , and ^{56}Fe and the rich neutron isotopes created from ^{12}C , ^{16}O , ^{14}N , and ^{13}C .

Therefore we have different processes defined in the galaxy as follows,

- (i) Star formation by spontaneous fragmentation of gas in the halo: $\propto \kappa_{1,2} g_D^n$, where we use $n = 1.5$.
- (ii) Clouds formation by diffuse gas: $\propto \eta g_D^n$ with $n = 1.5$ too.
- (iii) Star formation due to cloud collision: $\propto \delta_{1,2} c_D^2$.
- (iv) Diffuse gas restitution due to cloud collision: $\propto \delta' c_D^2$.
- (v) Induced star formation due to the interaction between clouds and massive stars: $\propto \alpha_{1,2} c_D s_{2,D}$.
- (vi) Diffuse gas restitution due to the induced star formation: $\propto \alpha' c_D s_{2,D}$.
- (vii) Galaxy formation by gas accretion from the halo or protogalaxy: $f g_H$,

where α , δ , η , and κ are the proportionality factors of the stars and cloud formation and are free input parameters (since stars are divided in two groups: those with s_1 and s_2 , the parameters are divided in the two groups too; thus, $\kappa = \kappa_1 + \kappa_2$, $\delta = \delta_1 + \delta_2$, $\alpha = \alpha_1 + \alpha_2$).

Thus, the star formation law in halo and disk is

$$\Psi_H(t) = (\kappa_1 + \kappa_2) g_H^n \quad (6)$$

$$\Psi_D(t) = (\eta_1 + \eta_2) c_D^2 + (\alpha_1 + \alpha_2) c_D s_{2D}$$

Although the number of parameters seems to be large, actually not all of them are free. For example, the infall rate, f , is the inverse of the collapse time τ_{coll} , as we described in the above section. Proportionality factors κ , η , δ , and α have a radial dependence, as we show in the study of MWG Ferrini et al. [28], which may be used in all disks galaxies through the volume of each radial region and some proportionality factors called *efficiencies*. These efficiencies or proportionality factors of these equations have a probability meaning and therefore their values are in the range $[0, 1]$. The efficiencies are then the probability of star formation in the halo, ϵ_{κ} , the probability of cloud formation, ϵ_{η} , cloud collision, ϵ_{δ} , and the interaction between massive stars ϵ_{α} . This last one has a constant value since it corresponds to a local process. The efficiency to form stars in the halo is also assumed constant for all of them. Thus, the number of free parameters is reduced to ϵ_{η} and ϵ_{δ} .

The efficiency to form stars in the halo, ϵ_{κ} , is obtained through the selection of the best value κ to reproduce the SFR and abundances of the Galactic halo (see Ferrini et al. [28], for details). We assumed that it is approximately constant for all halos with a value $\epsilon_{\kappa} \sim 1.5 - 6 \times 10^{-3}$. The value for ϵ_{α} is also obtained from the best value α for MWG and assumed as constant for all galaxies since these interactions massive stars-clouds are local processes. The other efficiencies ϵ_{η} and ϵ_{δ} may take any value in the range $[0, 1]$. From our previous models calculated for external galaxies of different types [81],

we found that both efficiencies must change simultaneously in order to reproduce the observations, with higher values for the earlier morphological types and smaller for the later ones. In MD05 there is a clear description about the selection of values and the relation $\epsilon_\eta - \epsilon_\delta$. As a summary, we have calculated these efficiencies with the expressions:

$$\begin{aligned}\epsilon_\eta &= \exp \frac{nt}{20}, \\ \epsilon_\delta &= \exp \frac{nt}{8},\end{aligned}\tag{7}$$

selecting 10 values nt between 1 and 10 (we suggest to select a value nt similar to the Hubble type index to obtain model results fitting the observations). The efficiencies values computed for the grid from MD05 are shown in Table 2 from that work.

2.3. Stellar Yields, Initial Mass Function, and Supernova Ia Rates. The selection of the stellar yields and the IMF needs to be done simultaneously since the integrated stellar yield for any element, which defines the absolute level of abundances for a given model, depends on both ingredients. In this work we used the IMF from Ferrini et al. [82] with limits $m_{\text{low}} = 0.15$ and $m_{\text{up}} = 100 M_\odot$. The stellar yields are from Woosley and Weaver [83] for massive stars ($m \geq 8 M_\odot$) and from Gavilán et al. [84, 85] for low and intermediate mass stars ($0.8 M_\odot < m \leq 8 M_\odot$). Stars in the range $0.15 M_\odot < m < 0.8 M_\odot$ have no time to die, so they still live today and do not eject any element to the interstellar medium. The mean stellar lifetimes are taken from the isochrones from the Padova group [86–89] instead of using those from the Geneva group Schaller et al. [90]. This change is done for consistency since we use the Padova isochrones on the POPSTAR code that we will use for the spectrophotometric models. The supernova Ia yields are taken from Iwamoto et al. [91]. The combination of these stellar yields with this IMF produces the adequate level of CNO abundances, which is able to reproduce most of observational data in the MWG galaxy [84, 85], in particular the relative abundances of C/O, N/O, and C/Fe, O/Fe, N/Fe. The study of other combinations of IMF and stellar yields will be analyzed in Mollá et al. [92]. The supernova type Ia rates are calculated by using prescriptions from Ruiz-Lapuente et al. [93].

3. Results: Evolution of Disks with Redshift

The chemical evolution models are given in Tables 2 and 3. We show as an example some lines corresponding to the model $nt = 4$ and $\text{dis} = 28$, the whole set of results will be given in electronic format as a catalogue. In Table 2 we give the type of efficiencies nt and the distribution number dis in columns 1 and 2, the time in Gyr in column 3, the corresponding redshift in column 4, the radius of each disk region in kpc in column 5, and the star formation rate in the halo and in the disk, in $M_\odot \text{yr}^{-1}$, in columns 6 and 7. In next columns 8 and 9 we have the total mass in the halo and in the disk. In columns 10 to 16 we show the mass in each phase of the halo, diffuse gas, low-mass stars, massive stars, and mass in remnants (columns 10

to 13) and of the disk, diffuse and molecular gas, low-mass stars, massive stars, and mass in remnants (columns 14 to 18).

We will give the results obtained for our grid of models by showing the corresponding ones to the galaxies from Table 1 as a function of the redshift or of the galactocentric radius. When the radial distributions are plotted, we do that for several times or values of redshifts. We assume that each time in the evolution of a galaxy corresponds to a redshift. To calculate this redshift, we use the relation redshift-evolutionary time given by MacDonald [94] with the cosmological parameters from the same PLANK experiment [69] ($\Omega_\lambda = 0.685$, $H_0 = 67.3$), and this way the time assumed for the beginning of the galaxy formation, $t_{\text{start}} = 0.6$ Gyr, corresponds to a redshift $z = 7$.

3.1. The Formation of the Disk. The process of infall of gas from the protogalaxy to the equatorial plane depends on time since the mass remaining in the protogalaxy or halo is decreasing with time. In Figure 2 we represent the resulting total infall of mass for our 44 radial distributions of mass as a function of the redshift z . Since this process is defined by the collapse time-scale, the total infall rate for the whole galaxy only depends on the total mass, and therefore there would be only 44 possible results, one for each maximum rotation velocity or mass of the theoretical galaxy. However, since we have assumed an infall rate variable with the radius, each radial region of a galaxy has a different infall rate. We show as a shaded region the locus where our results for all radial regions of the whole set of models fall. Over this region we show as solid lines the results for the whole infall of the same 7 theoretical galaxies as in the previous Figure 1, and with the same color coding, as labeled. The dashed purple and yellow lines correspond to the prescriptions given by Dekel et al. [77] and Faucher-Giguère Maciel et al. [78] for the infall of gas as obtained by their cosmological simulations to form massive galaxies. In both cases these expressions depend on the dynamical halo mass, so we have shown both lines for $M_{\text{dyn}} = 10^{12} M_\odot$ which will be compared to our most massive model which is on the top (black line) and which has a similar total mass. There are some differences with the results from cosmological simulations for the lowest redshifts, for which our models have lower infall rates than these cosmological simulations. However we remind that these simulations prescriptions are valid for spheroidal galaxies. We show as dotted purple lines 2 other lines following Dekel et al. [77] prescriptions but for masses $2 \times 10^{12} M_\odot$ and $3 \times 10^{11} M_\odot$, above and below the standard dashed line, checking that this last one is very similar to our cyan line. Therefore to decrease the infall rate for the most recent times is probably a good solution to obtain disks. In fact all our models for $V_{\text{max}} > 120 \text{ km s}^{-1}$ —the green line—(i.e., all lines except the orange and magenta ones) coincide in the same locus for the present time and reproduce well the observed value given by Sancisi et al. [79] and represented by the red full hexagon.

As a consequence of this infall of gas scenario, the disk is formed. The proportion of mass in the disk compared with the total dynamical mass of the galaxy is, as expected,

TABLE 2: Evolution of different phases along the time/redshift for the grid of models. We show as an example the results for the present time of a MWG-like model ($nt = 4$, $dis = 28$). The complete table will be available in electronic format.

(a)								
nt	dis	t Gyr	z	Radius kpc	Ψ_H $M_\odot \text{ yr}^{-1}$	Ψ_D $M_\odot \text{ yr}^{-1}$	M_H $10^9 M_\odot$	M_D $10^9 M_\odot$
4	28	1.3201e + 01	0.00	0	1.5431e - 05	4.9526e - 02	1.0337e + 00	8.4818e + 00
4	28	1.3201e + 01	0.00	2	2.5875e - 10	2.1748e - 02	9.7257e - 03	4.2363e + 00
4	28	1.3201e + 01	0.00	4	2.9111e - 08	5.7276e - 02	6.4913e - 02	9.7481e + 00
4	28	1.3201e + 01	0.00	6	2.1827e - 04	1.8737e - 01	3.7799e - 01	1.2042e + 01
4	28	1.3201e + 01	0.00	8	9.6978e - 03	4.7546e - 01	2.8732e + 00	9.6868e + 00
4	28	1.3201e + 01	0.00	10	3.4321e - 02	3.8606e - 01	6.6828e + 00	5.0472e + 00
4	28	1.3201e + 01	0.00	12	4.9261e - 02	1.8346e - 01	8.7949e + 00	2.0751e + 00
4	28	1.3201e + 01	0.00	14	5.2833e - 02	7.0495e - 02	9.5228e + 00	7.8723e - 01
4	28	1.3201e + 01	0.00	16	5.2396e - 02	2.2987e - 02	9.7360e + 00	2.9398e - 01
4	28	1.3201e + 01	0.00	18	5.1446e - 02	5.7661e - 03	9.8290e + 00	1.1004e - 01
4	28	1.3201e + 01	0.00	20	5.0964e - 02	9.0888e - 04	9.9186e + 00	4.1360e - 02
4	28	1.3201e + 01	0.00	22	5.1061e - 02	7.9634e - 05	1.0014e + 01	1.5583e - 02
4	28	1.3201e + 01	0.00	24	5.1747e - 02	4.7257e - 06	1.0104e + 01	5.8713e - 03

(b)								
g_H $10^9 M_\odot$	$s_{1,H}$ $10^9 M_\odot$	$s_{2,H}$ $10^9 M_\odot$	rem_H $10^9 M_\odot$	g_D $10^9 M_\odot$	c_D $10^9 M_\odot$	$s_{1,D}$ $10^9 M_\odot$	$s_{2,D}$ $10^9 M_\odot$	rem_D $10^9 M_\odot$
2.9016e - 03	8.6815e - 01	1.2048e - 05	1.6259e - 01	2.7416e - 02	1.4705e + 00	7.1689e + 00	3.3978e - 04	1.2371e + 00
1.3879e - 05	8.1686e - 03	1.7090e - 07	1.5430e - 03	1.4016e - 02	1.4705e + 00	3.5667e + 00	1.5015e - 04	6.2852e - 01
4.0674e - 04	5.4436e - 02	4.7128e - 07	1.0070e - 02	4.1804e - 02	1.4705e + 00	8.2575e + 00	3.9145e - 04	1.3868e + 00
1.7779e - 01	1.7061e - 01	2.0974e - 06	2.9597e - 02	1.3955e - 01	1.4705e + 00	1.0242e + 01	1.2864e - 03	1.5234e + 00
2.4434e + 00	3.7340e - 01	6.7054e - 05	5.6303e - 02	3.5938e - 01	1.4705e + 00	8.0530e + 00	3.2457e - 03	1.0218e + 00
6.0752e + 00	5.3545e - 01	2.3428e - 04	7.1939e - 02	3.9304e - 01	1.4705e + 00	3.9522e + 00	2.6251e - 03	4.4801e - 01
8.1503e + 00	5.7161e - 01	3.3513e - 04	7.2706e - 02	2.8478e - 01	1.4705e + 00	1.4482e + 00	1.2453e - 03	1.5079e - 01
8.9024e + 00	5.5139e - 01	3.5900e - 04	6.8586e - 02	1.7444e - 01	1.4705e + 00	4.4266e - 01	4.7796e - 04	4.2150e - 02
9.1454e + 00	5.2546e - 01	3.5588e - 04	6.4789e - 02	9.5622e - 02	1.4705e + 00	1.1078e - 01	1.5556e - 04	9.4763e - 03
9.2582e + 00	5.0801e - 01	3.4936e - 04	6.2419e - 02	4.6570e - 02	1.4705e + 00	2.0439e - 02	3.8890e - 05	1.5411e - 03
9.3567e + 00	5.0019e - 01	3.4607e - 04	6.1374e - 02	2.1461e - 02	1.4705e + 00	2.3765e - 03	6.0946e - 06	1.5895e - 04
9.4528e + 00	4.9999e - 01	3.4672e - 04	6.1317e - 02	1.0009e - 02	1.4705e + 00	1.7210e - 04	5.3111e - 07	1.0686e - 05
9.5352e + 00	5.0643e - 01	3.5137e - 04	6.2099e - 02	4.4897e - 03	1.4705e + 00	9.3097e - 06	3.1422e - 08	5.5691e - 07

dependent on this total mass. In Figure 3 we show the fraction M_{gal}/M_D , where M_D is the mass in the disk resulting from the applied collapse time scale prescriptions, as a function of the final mass in the disk. These results, shown as red points, are compared with the line obtained by Mateo [95] for galaxies in the local group, solid cyan line, and with the ratio by Shankar et al. [96] calculated through the halo and the stellar mass distributions in galaxies, solid black line. We also plot the results obtained by Leauthaud et al. [97] from cosmological simulations for three different ranges in redshift, such as those labeled in the figure. Our results have a similar slope to the one from Mateo [95], but the absolute value given by this author is slightly lower, which is probably due to a different value M_*/L to transform the observations (luminosities) in stellar masses. Our results are close to the ones predicted by Shankar et al. [96] and Leauthaud et al. [97] obtained with different techniques. These authors find in both cases an increase for high disk masses which, obviously, is not

apparent in our models, since we have assumed a continuous dependence of the collapse time scale with the dynamical mass. Shankar et al. [96] analyzed the luminosity function of halos and determine the relation with the mass formed there, while Leauthaud et al. [97] compute cosmological simulations and obtain the relation between the dynamical mass and the final mass in their disks. As we say before, disks obtained in simulations are smaller than observed what increases the ratio M_{gal}/M_D . Moreover the change of slope in these curves defines the limit in which the elliptical galaxies begin to appear, shown by the dotted black line as given by González Delgado et al. [98]. Therefore it is possible that these authors include some spheroids and galaxies SO in their calculations which are not computed in our models. It is necessary say, however, that the MWG value in this plot is slightly above this limit, and just where the Shankar et al. [96] line change the slope. Taking into account that spirals more massive than MWG there exist, maybe this limits is not totally

TABLE 3: Evolution of elemental abundances along the time/redshift for the grid of models. We show as an example the results for the present time of a MWG-like model ($nt = 4$, $dis = 28$). The complete table will be available in electronic format.

(a)										(b)									
nt	dis	t Gyr	z	Radius kpc	H	D	^3He	^4He		^{12}C	^{13}C	N	O	Ne	Mg	Si	S	Ca	Fe
4	28	1.3201e+01	0.00	0	7.1000e-01	7.4918e-08	5.2929e-04	2.7149e-01		3.1109e-03	5.6767e-05	1.3390e-03	6.9834e-03	1.1736e-03	3.2207e-04	1.2311e-03	6.2757e-04	8.8136e-05	2.8875e-03
4	28	1.3201e+01	0.00	2	7.1020e-01	3.7168e-08	5.2559e-04	2.7085e-01		3.1888e-03	5.8285e-05	1.3916e-03	7.1115e-03	1.1987e-03	3.3036e-04	1.2594e-03	6.4239e-04	9.0264e-05	2.9750e-03
4	28	1.3201e+01	0.00	4	7.0751e-01	1.4105e-06	4.9819e-04	2.7373e-01		3.1561e-03	5.3970e-05	1.2723e-03	7.0513e-03	1.1641e-03	3.1662e-04	1.2872e-03	6.5643e-04	9.1892e-05	3.0407e-03
4	28	1.3201e+01	0.00	6	7.2710e-01	2.9584e-05	2.3378e-04	2.5935e-01		2.4417e-03	2.8054e-05	7.2097e-04	5.4124e-03	8.6307e-04	2.2721e-04	9.2775e-04	4.7042e-04	6.5617e-05	2.0596e-03
4	28	1.3201e+01	0.00	8	7.4243e-01	4.6899e-05	1.0063e-04	2.4818e-01		1.7736e-03	1.3776e-05	4.0653e-04	4.0741e-03	6.4323e-04	1.6486e-04	6.0974e-04	3.0600e-04	4.2665e-05	1.2016e-03
4	28	1.3201e+01	0.00	10	7.4664e-01	5.1180e-05	7.1091e-05	2.4520e-01		1.5606e-03	1.0075e-05	3.1545e-04	3.6797e-03	5.7863e-04	1.4650e-04	5.1733e-04	2.5795e-04	3.5927e-05	9.5008e-04
4	28	1.3201e+01	0.00	12	7.4958e-01	5.3626e-05	5.6599e-05	2.4321e-01		1.3936e-03	7.4918e-06	2.3852e-04	3.3407e-03	5.2112e-04	1.3070e-04	4.5084e-04	2.2362e-04	3.1087e-05	7.8546e-04
4	28	1.3201e+01	0.00	14	7.5423e-01	5.7213e-05	4.2096e-05	2.4017e-01		1.0958e-03	4.5570e-06	1.4171e-04	2.6790e-03	4.1288e-04	1.0266e-04	3.4491e-04	1.7020e-04	2.3619e-05	5.6743e-04
4	28	1.3201e+01	0.00	16	7.6037e-01	6.2123e-05	2.7653e-05	2.3619e-01		6.7707e-04	2.1410e-06	6.2137e-05	1.6978e-03	2.5908e-04	6.4119e-05	2.0782e-04	1.0209e-04	1.4164e-05	3.2295e-04
4	28	1.3201e+01	0.00	18	7.6558e-01	6.6386e-05	1.7397e-05	2.3283e-01		3.1234e-04	8.0794e-07	2.2182e-05	8.0723e-04	1.2299e-04	3.0589e-05	9.4069e-05	4.6086e-05	6.4103e-06	1.4037e-04
4	28	1.3201e+01	0.00	20	7.6841e-01	6.8681e-05	1.2615e-05	2.3100e-01		1.1295e-04	2.7003e-07	8.2285e-06	2.9966e-04	4.6226e-05	1.1834e-05	3.3587e-05	1.6495e-05	2.3115e-06	5.1772e-05
4	28	1.3201e+01	0.00	22	7.6931e-01	6.9386e-05	1.1281e-05	2.3043e-01		5.0752e-05	1.2185e-07	4.7315e-06	1.3420e-04	2.1235e-05	5.7565e-06	1.4834e-05	7.3585e-06	1.0446e-06	2.6329e-05
4	28	1.3201e+01	0.00	24	7.6947e-01	6.9516e-05	1.1048e-05	2.3032e-01		3.9167e-05	9.4973e-08	4.1239e-06	1.0244e-04	1.6438e-05	4.5963e-06	1.1325e-05	5.6530e-06	8.0808e-07	2.1822e-05

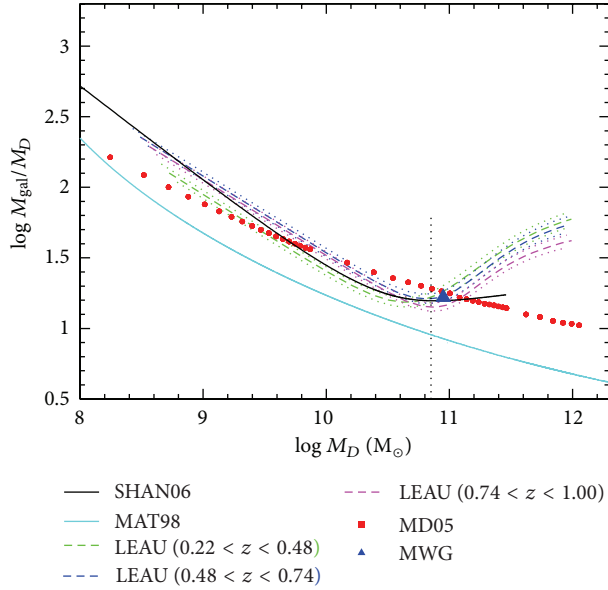


FIGURE 3: The ratio M_{gal}/M_D as a function of the mass in the disk M_D . Our models results are the solid red dots. The cyan and black lines are the results obtained by Mateo [95] and Shankar et al. [96] from observations of the local group of galaxies and from halo data, respectively. Magenta, blue, and green dashed lines are results from Leauthaud et al. [97] for different ranges of redshift as labeled. The MWG point is represented by a blue full triangle and the dotted black line marks the limit between disk and spheroidal galaxies from González Delgado et al. [98].

correct, and that, instead a sharp cut, there is a mix of galaxies in this zone of the plot.

3.2. The Relation of the SFR with the Molecular Gas. Since the formation of molecular gas is a characteristic which differentiates our model from other chemical evolution models in the literature, we would like to check if our resulting star formation is in agreement with observations. We compare the efficiency to form stars from the gas in phase H_2 , measured as $\text{SFR}/M_{\text{H}_2}$, with data in Figure 4. In Figure 4(a) we show the results for a galaxy like MWG, where each colored line represents a different radial region: solid red, yellow, magenta, blue, green, and cyan lines, correspond to radial regions located at 2, 4, 6, 8, 10, and 12 kpc of the Galactic center in the MWG model. In Figure 4(b) solid black, cyan, red, blue, green, orange, and magenta lines correspond to the galaxies of different dynamical masses and efficiencies (see Table 1). In (a) and (b) observations at intermediate-high redshift from Daddi et al. [99] and Genzel et al. [100] are shown as cyan dots and blue triangles, respectively, while the green squares refer to the local Universe data obtained by Leroy et al. [101]. The red star marks the average given by Sancisi et al. [79].

3.3. Evolution with Redshift of the Radial Distributions in Disks. In the next figures we show the results corresponding to the seven theoretical galaxies used as examples and whose characteristics are given in Table 1. We have selected 7 galaxies

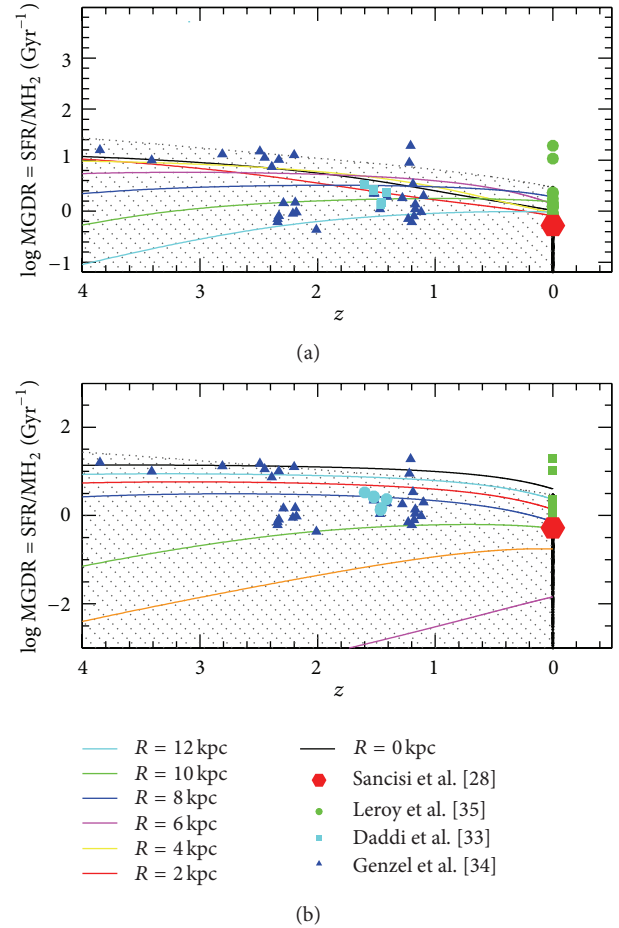


FIGURE 4: The efficiency to form stars from molecular gas, $\text{SFR}/M_{\text{H}_2}$, in logarithmic scale, as a function of redshift z for our grid of models. The evolution with redshift for all radial regions and galaxies is shown by the shaded zone, while solid black points represent the grid results for $z = 0$. (a) Solid black, red, yellow, magenta, blue, green, and cyan lines, correspond to radial regions located at 0, 2, 4, 6, 8, 10, and 12 kpc of the Galactic center in the MWG model. In (b) solid black, cyan, blue, red, green, orange, and magenta lines correspond to the galaxies of different dynamical masses and efficiencies (see Table 1). In (a) and (b) observations at intermediate-high redshift from Daddi et al. [99] and Genzel et al. [100] are shown as cyan dots and blue triangles, respectively, while the green squares refer to the local Universe data obtained by Leroy et al. [101]. The red star marks the average given by Sancisi et al. [79].

which simulate galaxies along the Hubble sequence. They have different masses and sizes and we have also selected different efficiencies to form stars in order to compare with real galaxies. In the next figures we will show our results for 7 values of evolutionary times or redshifts: $z = 5, 4, 3, 2, 1, 0.4$, and 0, with colors purple, blue, cyan, green, magenta, orange, and red, respectively. The resulting radial distributions in disks for diffuse and molecular gas, stellar mass, and star formation rate for the galaxies from Table 1 are shown in Figure 5. In this figure we show a galaxy in each column and a different quantity in each row. Thus top, top-middle, and bottom-middle panels show the diffuse gas, the molecular gas, and the stellar surface densities, respectively,

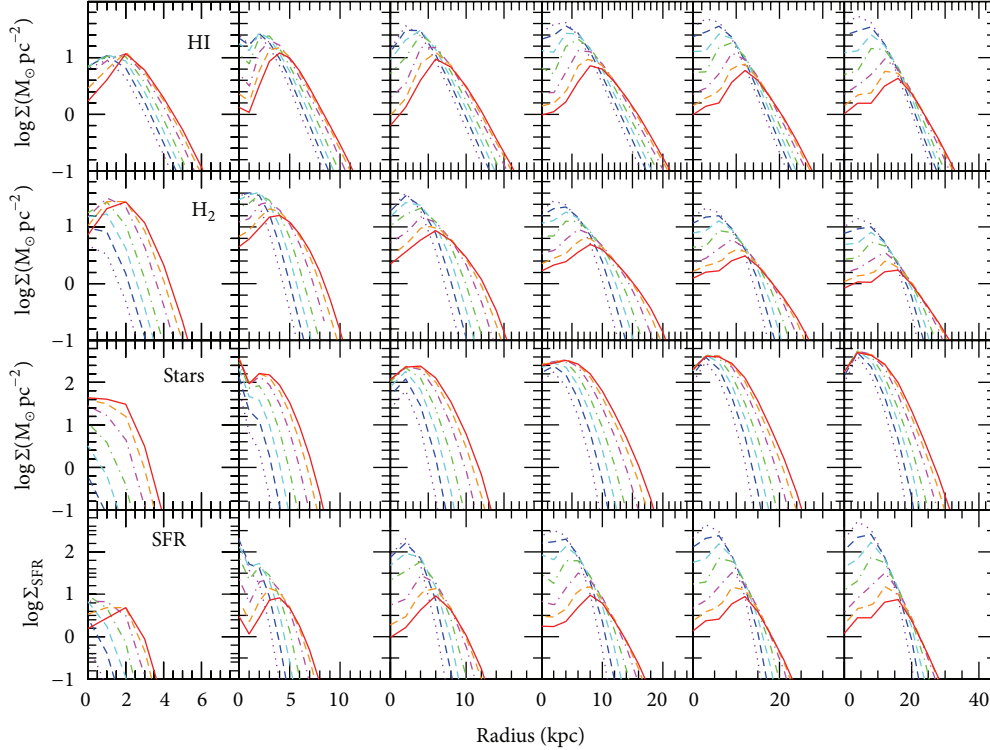


FIGURE 5: Evolution with redshift of the surface density of diffuse gas, Σ_{HI} , molecular gas, Σ_{H_2} , and stellar mass, Σ_* , in $M_\odot \text{pc}^{-2}$, in top, middle-top, and middle-bottom rows, and the star formation rate, Ψ , in $M_\odot \text{Gyr}^{-1} \text{pc}^{-2}$, in the bottom one. All in logarithmic scale. Each column shows the results for a theoretical galaxy of the Table 1, from the galaxy, with $V_{\text{max}} = 78 \text{ km s}^{-1}$, to the most massive one for $V_{\text{max}} = 290 \text{ km s}^{-1}$. Each line corresponds to a different redshift: purple, blue, cyan, green, magenta, orange, and red for $z = 5, 4, 3, 2, 1, 0.4$, and 0 , respectively.

all in $M_\odot \text{pc}^{-2}$ units and in logarithmic scale, while the bottom panel corresponds to the surface density of the star formation rate in $M_\odot \text{Gyr}^{-1} \text{pc}^{-2}$.

The radial distributions of diffuse gas density Σ_{HI} show a maximum in the disk. The radius of the maximum is near the center of the galaxy for $z = 5$ and move outwards with the evolution, reaching a radius $\sim 2/3 R_{\text{opt}}$ kpc for the present, that is, 1.3 times R_c , and ~ 2 the effective radius in mass or radius enclosed the half of the stellar mass of the disk (see next section). The density Σ_{HI} in this maximum reaches values $\sim 50 M_\odot \text{pc}^{-2}$ in early times or high redshift. For the present, the maximum density is $\sim 10 M_\odot \text{pc}^{-2}$, very similar in most of theoretical galaxies. These radial distributions reproduce very well the observations of HI. The radial distribution for regions beyond this point shows an exponential decrease but flatter now than that in the high-redshift distributions.

The radial distributions of molecular gas density Σ_{H_2} show basically the same behavior, with a maximum in the disks too. In each galaxy, however, this maximum is located slightly closer to the center than the one from the HI distribution. They show an exponential function too, after this maximum. These radial distributions seem more to be an exponential shape with a flattening at the center than the ones from HI which show a clearer maximum, mainly for the least massive galaxies.

The stellar profiles, Σ_* , show the classical exponential disks. The size of these stellar disks and the scale length of

these exponential functions are in agreement with observations. However they present a decreasing or flattening in the inner regions in most cases, although some of them have an abrupt increase just in the center. It is necessary to take into account that these models are calculated to model spiral disks, and the bulges are added by hand without any density radial profile. Probably this produces a behavior not totally consistent with observations at the center of galaxies.

In these three panels we show the results only for densities higher than $0.1 M_\odot \text{pc}^{-2}$, which corresponds to an atomic density $n \sim 0.1 \text{ cm}^{-2}$ which we consider as a lower limit for observations.

The star formation radial distributions show similar shapes as Σ_{H_2} and Σ_* , a similar decreasing in the inner regions of disks, too. Although these decreases have been observed in a large number of spiral disks for Σ_{H_2} and SFR distributions [102–104], we think, however, that they are stronger than observed.

From all panels we may say that spiral disks would have a more compact appearance at high redshift with higher values maximum and smaller physical sizes, as correspond to an inside-out disk formation as assumed. The present radial distributions show flatter shapes, with smaller values in the maximum and in the inner disks and higher densities in the outer regions.

The star formation is around 2 orders of magnitude larger at $z = 5$ than now for the massive galaxies, in agreement with

that estimated of the star formation in the Universe [105], while for the smaller galaxies the maximum value is low and very similar then than now.

In Figure 8 panel (a), we show the same four radial distributions for the lowest mass galaxy in our grid with a maximum rotation velocity of $V_{\max} \sim 50 \text{ km s}^{-1}$. In this case and taking into account the limit of the observational techniques, we see that the galaxy will be only detected in the region around 1 kpc and only for redshift $z < 2$ since for earlier times than this the galaxy will be undetected.

3.4. The Half Mass Radii. Since we know the mass of the disk and the corresponding one to each phase we may follow the increase of the stellar mass in each radial region and calculate for each evolutionary time of redshift the radius for which the stellar mass is the half of the total of the mass in stars in the galaxy, $Reff_{\text{mass}}$. This radius obviously will evolve with time and since we have assumed an in-out scenario of disk formation, it must increase with it. We show this evolution in Figure 6, where we plot with different colors the evolution of different efficiencies models: black, gray, green, red, orange, magenta, purple, cyan, and blue for sets $nt = 1$ to 9, respectively, for mass distributions from number 10 to 44, which correspond to maximum rotation velocities in the range $V_{\max} \sim 80$ to 400 km s^{-1} . The lowest mass galaxies, with $V_{\max} < 78 \text{ km s}^{-1}$ (or those for which efficiencies correspond to $nt = 10$) are not shown since, as we will show in Figure 8, they only would have a visible central region. It is evident that the effective radius increases, being smaller to high redshift, this increase begins later for the later types of smaller efficiencies than for the earlier ones or with high efficiencies. Blue and cyan points are below 1 kpc for redshifts higher than 1, while the others begin to increase already at $z = 5-6$. Moreover a change of slope with an abrupt increase in the size occurs at $z \sim 3$ until $z \sim 2$, for $nt < 5$, when the star formation suffers its maximum value in most of these galaxies which is in agreement with the data. Intermediate galaxies, as magenta and purple dots, which correspond to irregular galaxies show this change of the slope at $z < 2$.

3.5. Evolution of Elemental Abundances. The resulting elemental abundances are given in Table 3. For each type of efficiencies nt and mass distribution dis and columns 1 and 2, we give the time t in Gyr in column 3, the corresponding redshift z in column 4, and the Radius in Kpc in column 5. The elemental abundances for H, D, ^3He , ^4He , ^{12}C , ^{13}C , N, O, Ne, Mg, Si, S, Ca, and Fe are in columns 6 to 19 as fraction in mass.

The radial distributions of elemental abundances are shown in Figure 7. There we have for the same 6 galaxies of Figure 5 from the left to the right column, the abundance evolution for C, N, O, and Fe, as $12 + \log(X/H)$ from top to bottom panels. In each panel, as before, we represent the radial distributions for 7 different redshifts, $z = 5, 4, 3, 2, 1, 0.4$, and 0, with the same color coding. The well-known decrease from the inner to the outer regions, called the radial gradients of abundances, appear in the final radial distributions for the

present time in agreement with data. However the slope is not unique in most of cases. The radial distribution for any element, $12 + \log(X/H)$, is not a straight line but a curve which is flatter in the central region and also in the outer disk in agreement with the most recent observations [18].

The distributions of abundances change with the level of evolution of a galaxy. A very evolved galaxy, that is, as the one for the most massive ones, and/or those with the highest efficiencies to form stars show flatter radial gradients than those which evolve slowly, which have steeper distributions. There exists a saturation level of abundances, defined by the true yield and given by the combination of stars of a certain range of mass and the production of elements of these stars. For our combination of stellar yields from Woosley and Weaver [83], Gavilán et al. [84], and Gavilán et al. [85] and IMF from Ferrini et al. [82], this level is $12 + \log(X/H) \sim 8.8, 8.0, 9.0$ and 8.2 dex for C, N, O, and Fe, respectively. As the galaxy evolves the saturation level is reached in the outer regions of galaxy, thus flattening the gradient.

The radial gradient flattens with the evolutionary time or redshift, mainly in the most massive galaxies, although it maintains a similar value for the smallest galaxies. The extension in which the radial gradient appears, changes, however, with time. At the earliest time the radial gradient appears only for the central regions, until 1 kpc in the left column galaxy, while it does until 22 kpc in the right one with a change of slope at around 8 kpc. For the radial regions out of this limit, it shows a flat distribution. At the present, this gradient appears until a extended radius, 28 kpc, in our most massive galaxy, while it is only in the inner 4 kpc in the smallest one. If we analyze the results for the lowest mass galaxy in Figure 8, we see that abundances show a very uniform distribution along the galactocentric radius for all elements, with a slight increase at the center for all redshifts that may be considered as a nonexistent radial gradient, within the usual errors bars.

The flat radial gradient in the lowest mass galaxies, as shown in Figure 8, as this one of the most distant regions of the disk in the massive galaxies at the highest redshifts, must be considered as a product of the infall of a gas more rich than this one of the disk. It is necessary to take into account that the halo is forming stars too. When the collapse time is longer, as occurs in the outer regions of disks, there is more time and more gas in the halo to form stars and increase its abundances. Thus, the gas infalling is, even at a very low level ($12 + \log(X/H) \sim 4-5$), more enriched than the gas of the disk.

4. The Photometric Model Description

It is well known that galaxies have SEDs depending on their morphological type [106]. These SEDs and other data related to the stellar phase are usually analyzed through (evolutionary) synthesis models (see [107], for a recent and updated review about these models), based on SSPs created by an instantaneous burst of star formation (SF). The synthesis models began calculating the luminosity (in a broad band filter or as a SED, $F_{\lambda}(\lambda)$) or by using the spectral absorption

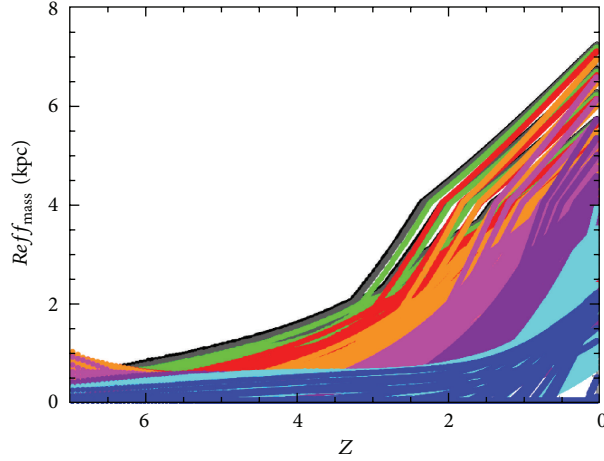


FIGURE 6: The evolution of the half mass radii, $Reff_{\text{mass}}$, as a function of the redshift z for models with efficiencies sets from $nt = 1$ to 9 and for mass distribution numbers from 10 to 44 (see Tables 1 and 2 from MD) corresponding to maximum rotation velocities in the range $[80\text{--}400]$ km s^{-1} . Black, gray, green, red, orange, magenta, purple, cyan, and blue dots correspond to $nt = 1, 2, 3, 4, 5, 6, 7, 8,$ and 9, respectively.

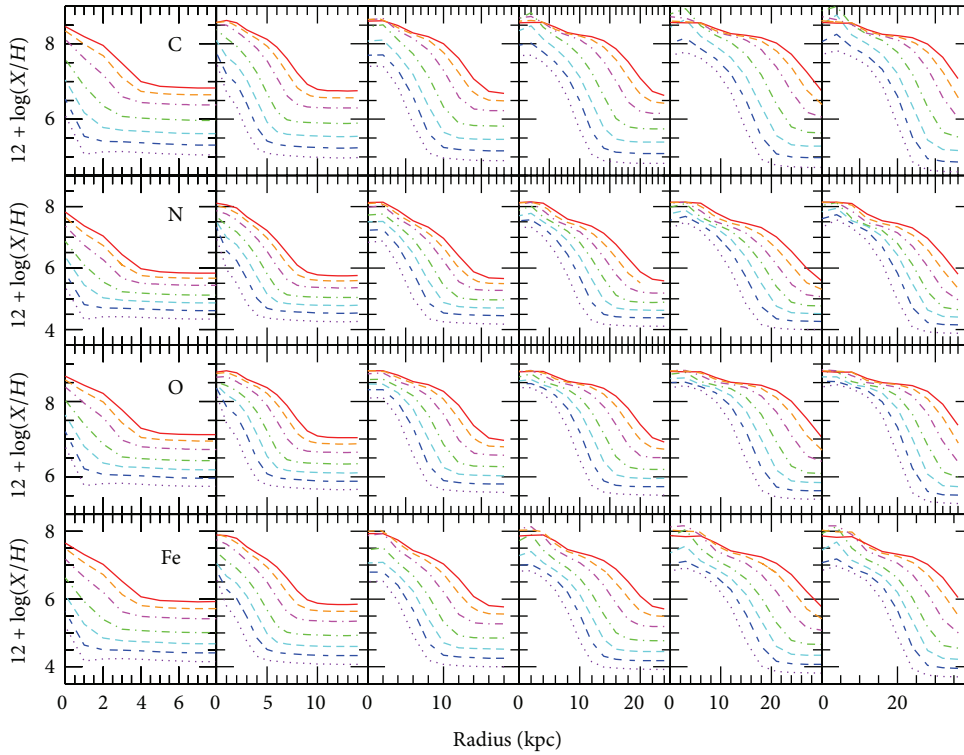


FIGURE 7: Evolution with redshift of radial distributions of elemental abundances, C, N, O, and Fe from top to bottom. Each column shows the results for a theoretical galaxy of Table 1, from the galaxy, with $V_{\text{max}} = 78 \text{ km s}^{-1}$, at left to the most massive one with $V_{\text{max}} = 290 \text{ km s}^{-1}$ at the right. In each panel distributions for 7 redshifts are shown, with the same color coding as in Figure 5.

indices) for a generation of stars created simultaneously, (therefore, with a same age, τ , and with a same metallicity, Z), that is, the so-called single stellar population (SSP). The evolutionary codes compute the corresponding colors, surface brightness, and/or spectral absorption indices emitted by a SSP from the sum of spectra of all stars created and distributed along a Hertzsprung Russell diagram, weighted with an IMF. This SED, given τ and Z , is characteristic of each

SSP. This way it is possible to extract some information of the evolution of galaxies by using evolutionary synthesis models in comparison with spectrophotometric observations. This method has been very useful for the study of elliptical galaxies, for which it was developed, with the hypothesis that they are practically SSPs and allowed to advance very much in the knowledge of these objects, determining their age and metallicity with good accurate [86, 108–113].

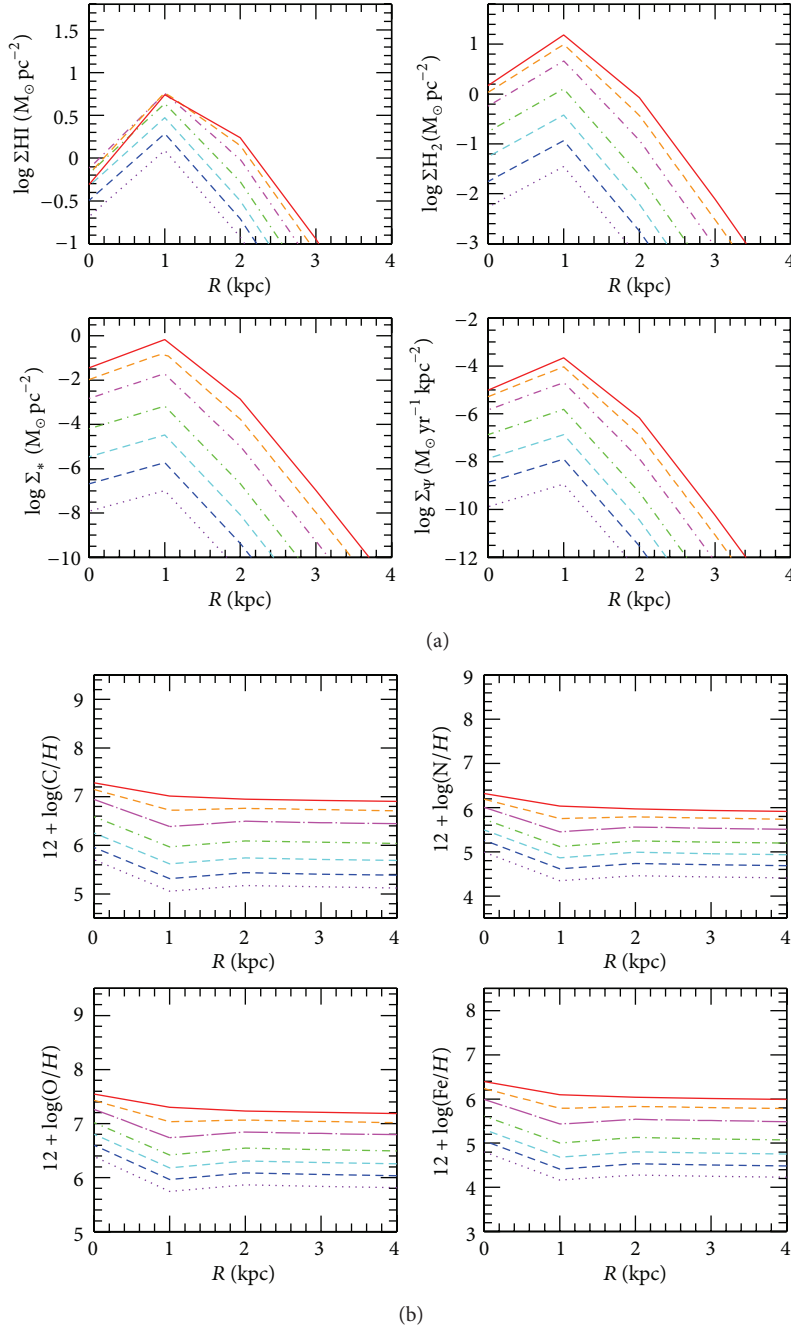


FIGURE 8: (a) Radial distributions of the surface density of diffuse gas, Σ_{HI} , molecular gas, Σ_{H_2} , and stellar mass, Σ_{*} , in $M_{\odot} \text{pc}^{-2}$, and the star formation rate surface density, Σ_{SFR} , in $M_{\odot} \text{yr}^{-1} \text{pc}^{-2}$, all in logarithmic scale, for the least massive galaxy of our example table, with $V_{\text{max}} = 48 \text{ km s}^{-1}$. (b) Evolution with redshift of radial distributions of elemental abundances, C, N, O, and Fe of the same galaxy.

Star formation history, however, does not always take place in a single burst, as occurs in spiral and irregular galaxies where star formation is continuous or in successive bursts. Since in these galaxies the star formation does not occur in a single burst the SSP SEDs are not good representative of their luminosity. In this case it is necessary to perform a convolution of these SEDs with the star formation history (SFH) of the galaxy, $\Psi(t)$. Thus, spectral evolution models of galaxies predict colors and luminosities of a galaxy

as a function of time, as for example Bruzual and Charlot ([114, 115], hereafter GALAXEV), or the ones from Fioc and Rocca-Volmerange [111], and Le Borgne et al. ([116], hereafter PEGASE 1.0 and 2.0, resp.), from the SEDs calculated for the SSPs and also for some possible combinations of them by following a given SFH. Usually some hypotheses about the shape and the intensity of the SFH are assumed; for example, an exponentially decreasing function of time is normally used. However an important point, usually forgotten when

this technique is applied is that $S_\lambda(\tau, Z(R)) = S_\lambda(\tau, Z(R, t'))$; that is, the metallicity changes with time since stars form and die continuously. It is not clear which Z must be selected at each time step without knowing this function $Z(t)$. Usually, only one Z is used for the whole integration which may be an oversimplification.

Besides the fact that most of these models do not compute the chemical evolution that occurs along the time (or do it in a very simple way), the star formation histories are assumed as inputs. In our approach we may take advantage from the results of the chemical evolution models section, which give us as outputs the SFH and the AMR, and use them as inputs to compute the SED of each galaxy or radial region. For each stellar generation created in the time step t' , a SSP-SED, $S(\tau, Z(R, t))$, from this set, is chosen taking into account its age, $\tau = t - t'$, from the time t' in which it was created until the present t and the metallicity $Z(R, t')$ reached by the gas. After convolution with the SFH, $\Psi(R, t)$, the final SED, $F_\lambda(\lambda, R, t)$, is obtained for each region. This way in a region of each galaxy, the final SED, F_λ , corresponds to the light emitted by the successive generations of stars. It may be calculated as the sum of several SSP SEDs, S_λ , being weighted by the created stellar mass in each time step, $\Psi(R, t)$. Thus, for each radial region:

$$F_\lambda(R, t) = \int_0^t S_\lambda(\tau, Z(R, t')) \Psi(R, t') dt', \quad (8)$$

where $\tau = t - t'$.

The set of SSP's SEDs, $S_\lambda(\tau, Z)$ used are those from the POPSTAR evolutionary synthesis code [62]. The isochrones used in that work are those from Bressan et al. [117] for six different metallicities: $Z = 0.0001, 0.0004, 0.004, 0.008, 0.02$, and 0.05 , updated and computed for that particular piece of work. The age coverage is from $\log \tau = 5.00$ to 10.30 with a variable time resolution which is $\Delta(\log \tau) = 0.01$ in the youngest stellar ages, doing a total of 106 ages. The WC and WN stars are identified in each isochrone according to their surface abundances. The grid is computed for six different IMFs. Here we have used the set calculated with the IMF from Ferrini et al. [82] to be consistent with the one used in the chemical evolution models grid. To each star in the HR diagram a stellar model is assigned based on the effective temperature and gravity. Stellar atmosphere models are taken from Lejeune et al. [118], due to their expansive coverage in effective temperature, gravity, and metallicities, for stars with $T_{\text{eff}} \leq 25000$ K. For O, B, and WR stars, the NLTE blanketed models of Smith et al. [119] (for metallicities $Z = 0.001, 0.004, 0.008, 0.02$, and 0.04) are used. There are 110 models for O-B stars, calculated by Pauldrach et al. [120], with $25000 \text{ K} < T_{\text{eff}} \leq 51500 \text{ K}$ and $2.95 \leq \log g \leq 4.00$, and 120 models for WR stars (60 WN and 60 WC), from Hillier and Miller [121], with $30000 \text{ K} \leq T^* \leq 120000 \text{ K}$ and $1.3 R_\odot \leq R^* \leq 20.3 R_\odot$ for WN, and with $40000 \text{ K} \leq T^* \leq 140000 \text{ K}$ and $0.8 R_\odot \leq R^* \leq 9.3 R_\odot$ for WC. T^* and R^* are the temperature and the radius at a Roseland optical depth of 10. The assignment of the appropriate WR model is consistently made by using the relationships between opacity, mass loss,

and velocity wind, as described in Mollá et al. [62]. For post-AGB and planetary nebulae (PN) with T_{eff} between 50000 K and 220000 K, the NLTE models from Rauch [122] are taken. For higher temperatures, POPSTAR uses black-bodies. The use of these latter models modifies the resulting intermediate age SEDs. The range of wavelengths are the same as the one from Lejeune et al. [118], from 91 Å to 160 μm.

5. Spectrophotometric Results

5.1. Spectral Energy Distributions. As an example of the technique described in the above section, we show the star formation history $\Psi(t)$ and the age metallicity distributions $Z(t)$, as $[\text{Fe}/H](t)$, for the characteristic radius, R_c , regions of the galaxies of Table 1 in Figure 9. By using these histories we obtain the resulting $F_\lambda(\lambda, t)$ for these regions which reproduce reasonably well the SEDs of the sampled galaxies. We have compared our resulting spectra after a time 13.2 Gyr of evolution for the models for galaxies from Table 1 with the known templates for the different morphological types from Coleman et al. [106], Buzzoni et al. [124], and Boselli et al. [125], such as can be seen in Figure 9 where we compared our results with Buzzoni [124]. We have represented galaxies ordered by the galactic mass, with the most massive in the top of the graph and each SED is shifted 2 dex compared with the previous one for the sake of clarity of the figure. There are some differences that probably are related to the fact that we are comparing a whole galaxy SED with the one modeled for a given radial region. With this we try to check that our resulting SEDs are in reasonable agreement with observations. A more detailed comparison with data for different radial regions of disks using both types of information, this one proceeding from the gas, the present state of disks, and the one coming from the stellar populations and represented by the brightness profiles in different broad bands are beyond the scope of this work and will be the objects of the next publication.

In order to use our model grid, we may therefore select the best model able to fit a given observed SED and then see if the corresponding SFH and the AMR of this model are also able to reproduce the present time observational data of SFR and metallicity of the galaxy or of the radial region. We have a SED for each radial region, so we may compare the information coming from different radial regions with our models. When only a spectrum is observed for one galaxy, it is possible to compare with the characteristic radius region or to add all spectra of a galaxy. For dwarf galaxies both methods give equivalent results since only central regions have suffered star formation enough to create visible stellar populations. We show an example of this method in Figure 10(a), where three SEDs from Hunt et al. [123] of BCD galaxies are compared with the characteristic region spectrum of the best model chosen for each one of them. In (b) of the same figure we show the corresponding SFH, $\Psi(t)$, and AMR, $[\text{Fe}/H](t)$, with which the modeled SEDs were computed. The final values are within the error bars of observations for these galaxies, compiled by the same authors. Since each SED is well fitted and, simultaneously, the corresponding present-time

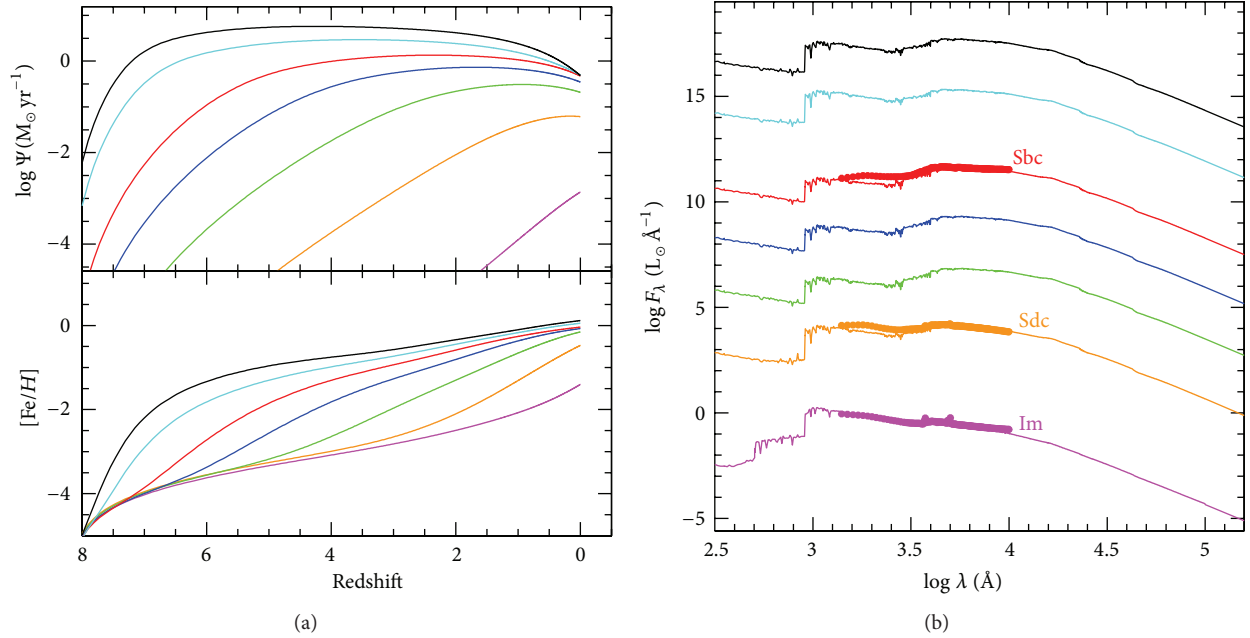


FIGURE 9: (a) The star formation $\Psi(t)$ and iron enrichment $[\text{Fe}/\text{H}](t)$ evolution with redshift z for the radial regions located at R_c of models of Table 1. (b) The resulting spectral energy distributions, $F_{\lambda}(\lambda, t = 13.2 \text{ Gyr})$ obtained for the same radial region and galaxy model compared with the fiducial templates from Coleman et al. [106].

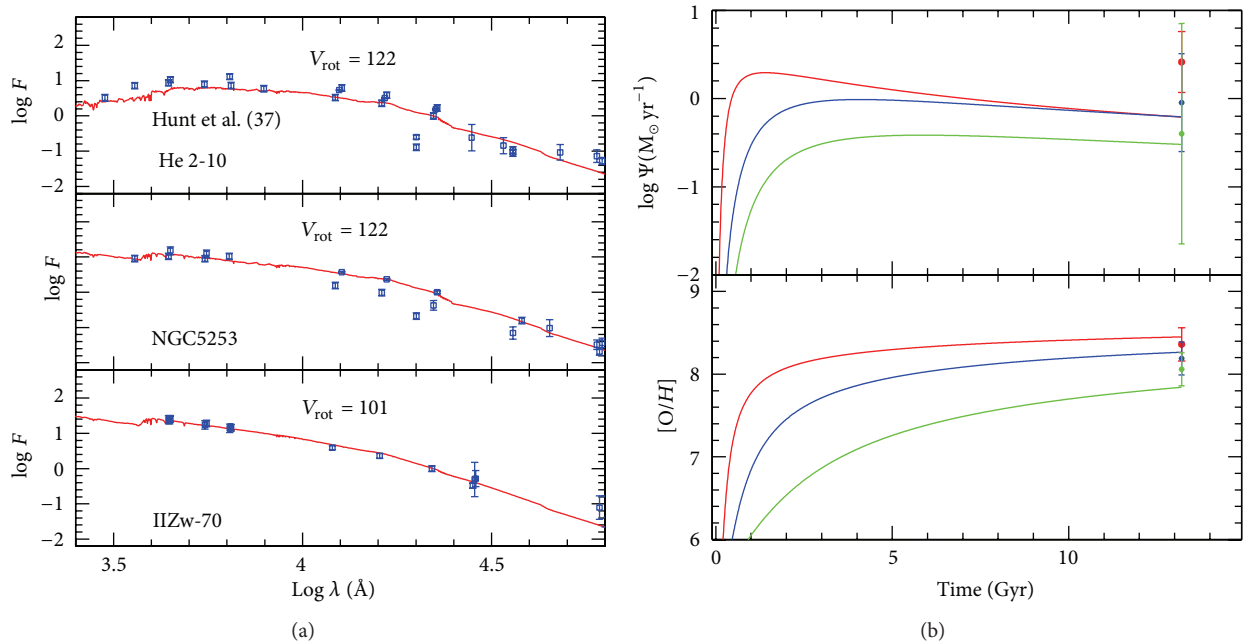


FIGURE 10: (a) The resulting spectral energy distributions—red solid lines—obtained to reproduce the observations from Hunt et al. [123]—blue open squares—for three BCD galaxies. (b) The star formation history and age-metallicity relation with which we obtain the SEDs which best fit observed spectra.

data of the galaxy by the same chemical evolution model, we may be confident that these SFH and AMR give us a reliable characterization of the evolutionary history of each galaxy.

It is clear that spiral and irregular galaxies are systems more complex than those represented by SSP's, and that,

in particular, their chemical evolution must be taken into account for a precise interpretation of the spectrophotometric data. On the plus side for these objects the gas phase data are also available and may be used as constraint. What is required then is to determine the possible evolutionary paths followed

by a galaxy that arrive at the observed present state, while, simultaneously, reproducing the average photometric properties defined by the possible underlying stellar populations.

5.2. Broad-Band Magnitudes and Color-Color Diagrams. Once the SEDs are obtained for all times/redshifts and radial regions of our whole grid of models, we may calculate the magnitudes in the usual broad-band filters. In this case we have computed these ones in the Johnson and SDSS/SLOAN systems by following the prescriptions given in Girardi et al. [126, 127]. For Johnson-Cousins-Glass magnitudes UV_1 , UV_2 , U , B , V , R , I , J , H , K , and L are computed using the definition suitable for photon counting devices [126]. Absolute magnitudes in the AB-SDSS photometric system have been calculated following Girardi et al. [127] and Smith et al. [128]. See more details about this in the refereed works or in Mollá et al. [62] where the magnitudes were obtained for the SSP-SEDs.

The results are absolute magnitudes in the rest-frame of an observed located at distance $d = 10$ pc. Therefore we have not used the distance at which a galaxy given redshift must be nor. The results are absolute magnitudes of the wavelength. These effects must be taken into account when observational apparent magnitudes are calculated. In that case it is necessary to calculate the decreasing of the flux due to the distance, to include the K -correction and the wavelength redshift.

These absolute magnitudes are given in Table 4, where for each set of efficiencies, defined by nt in column 1, and for each radial mass distribution, defined by the number given in Table 1 from MD05, dis, in column 2, we have the evolutionary time, t in Gyr, in column 3, and the associated redshift z , in column 4, the radius of each radial region, Radius in kpc, in column 5, and the corresponding disk area, Area, in kpc^2 , in column 6. Then, we have two ultraviolet from the Hubble telescope, and the classical Johnson system magnitudes, UV_1 , UV_2 , U , B , V , R , I , J , H , K , and L , and the SLOAN/SDSS magnitudes in the AB system, named u_{sdss} , g_{sdss} , r_{sdss} , i_{sdss} , and z_{sdss} .

We may check that our results for the whole grid are reasonable when comparing them with color-color diagrams as is shown in Figure 11. Colors $U-B$ versus $B-V$, $U-B$ versus $B-R$, $V-R$ versus $V-I$, $B-K$ versus $B-R$, $B-I$ versus $V-R$, and $V-K$ versus $B-V$ are represented as blue dots for all regions and galaxies modeled in this works and compared with observational data from Buta and Williams [129] in panel $V-R$ versus $V-I$, from Peletier and Balcells [130] in panel $B-K$ versus $B-R$, and from de Jong [131] in $B-I$ versus $V-R$ and $V-K$ versus $B-V$. The standard values for typical galaxies along the Hubble sequence as Sa, Sb, Sc, and Sd taken from Poggianti [132] are also shown, labeled in magenta. In panel $U-B$ versus $B-V$ the yellow line corresponds to data from Vitores et al. [133]. Green squares are from Buzzoni [124]. The cyan ones are the results corresponding to the galaxies from Table 1. In fact the dispersion of data is quite large, in particular in the two bottom panels. Probably due to the contribution of the emission lines, which move the points of the standard locus for galaxies in a orthogonal way, such

as we have demonstrated in Martín-Manjón et al. [134] and García-Vargas et al. [135], where we added the contribution of the emission lines to the broad band colors in single stellar populations and in star-forming galaxies models.

5.3. Brightness and Color Radial Profiles of Disks. As we know the luminosity of each radial region, we may compute the surface brightness as mag arcsec^{-2} . By assuming that our theoretical galaxies are located at 10 pc, the brightness is

$$\mu = M + 21.57 + \log \text{Area}, \quad (9)$$

where Area is the area of each radial region in pc^2 and the constant value 21.57 is $2.5 \times \log F_{\text{con}}$, where F_{con} is the factor to convert pc to arcsec.

As said before, we have not computed apparent magnitudes in each redshift and then the relation luminosity distance-redshift is not necessary and the redshift of the wavelength is not taken into account.

Brightness radial profiles are shown in Figure 12 for the same 6 galaxies of Table 1 as shown in Figures 6 and 8. Each column represents a galaxy, from the smallest one ($V_{\text{max}} = 78 \text{ km s}^{-1}$) at the left, to the most massive ($V_{\text{max}} = 290 \text{ km s}^{-1}$) at the right. Brightness in bands U , B , V , R , I , J , H , and K of the Johnson system are given from top to bottom. In Figure 13 we show similar radial profiles brightness radial profiles for bands u_{sdss} , g_{sdss} , r_{sdss} , i_{sdss} , and z_{sdss} in the SDSS/SLOAN system. In each panel the same 7 redshifts as in previous Figures 6 and 8 are shown with the same color coding. The profiles show the usual exponential shapes except for the central/inner regions where a flattening is evident. The results for the disks at $z = 0$ are similar to the observed ones. The value of $\mu = 21-22 \text{ mag arcsec}^{-2}$ observed as a common value in the center of most galaxies [65] is found with our models. Profiles are steeper for the highest redshifts, being galaxies less luminous, and disks smaller. As the galaxy evolves, more stellar mass appears and more extended in the disk, doing the profiles more luminous and extended. Thus, in K -band, the radius R_{25} , defined as this one where $\mu = 25 \text{ mag arcsec}^{-2}$, is in the most massive galaxy, $\sim 18 \text{ kpc}$ for $z = 5$, and is $> 30 \text{ kpc}$ for the present time. While for the left column galaxy, $R_{25} \sim 1 \text{ kpc}$ for $z = 3$ and $R_{25} \sim 4 \text{ kpc}$ for $z = 0$ but the brightness do not reach this level at higher redshifts than 3.

Again we show separately in Figure 14 the surface brightness profiles for the lowest mass galaxy of our Table 1. It has a very low luminosity in all bands and surface brightness that are difficult to observe even in the local Universe. Only the region around 1 kpc of distance might be observed for $z < 2$.

The radial profiles for some colors are shown in Figures 15 and 16 with similar columns for the same 6 galaxies from table examples as before, the lowest mass at left and the most massive one to the right. These radial distributions do not show uniform evolution doing evident that not all bands evolve equally. Thus, colors $V-R$, $B-K$ in Figure 15 or $r_{\text{sdss}}-i_{\text{sdss}}$ and $i_{\text{sdss}}-z_{\text{sdss}}$ in Figure 16 show at $z = 2-3$ an increase their radial distributions located in some place along the disk which varies with the redshift.

TABLE 4: Absolute magnitudes evolution along the time/redshift for the grid of models in Johnson and SDSS/SLOAN system.

(a)

nt	dis	t	z	Radius	Area	UV_1	UV_2	U	B	V
4	28	13.201	0.00	0.0	19	-18.920	-18.115	-17.796	-18.015	-18.827
4	28	13.201	0.00	2.0	13	-18.151	-17.351	-17.130	-17.322	-18.112
4	28	13.201	0.00	4.0	25	-19.109	-18.301	-18.021	-18.228	-19.034
4	28	13.201	0.00	6.0	38	-19.953	-18.920	-18.602	-18.749	-19.491
4	28	13.201	0.00	8.0	50	-20.669	-19.358	-18.983	-19.016	-19.618
4	28	13.201	0.00	10.0	63	-20.368	-18.970	-18.578	-18.561	-19.092
4	28	13.201	0.00	12.0	75	-19.554	-18.117	-17.733	-17.691	-18.183
4	28	13.201	0.00	14.0	88	-18.561	-17.088	-16.727	-16.661	-17.112
4	28	13.201	0.00	16.0	100	-17.443	-15.922	-15.580	-15.495	-15.894
4	28	13.201	0.00	18.0	110	-16.149	-14.502	-14.091	-13.969	-14.354
4	28	13.201	0.00	20.0	139	-14.297	-12.508	-11.986	-11.827	-12.212
4	28	13.201	0.00	22.0	140	-11.665	-9.836	-9.223	-9.054	-9.435
4	28	13.201	0.00	24.0	150E	-8.545	-6.786	-6.154	-5.971	-6.321

(b)

R	I	J	H	K	L	u_{sdss}	g_{sdss}	r_{sdss}	i_{sdss}	z_{sdss}
19.476	-20.100	-20.726	-21.295	-21.526	-21.673	-16.963	-18.537	-19.135	-19.486	-19.720
18.748	-19.353	-19.959	-20.516	-20.741	-20.885	-16.292	-17.832	-18.412	-18.749	-18.969
19.679	-20.295	-20.911	-21.476	-21.704	-21.849	-17.188	-18.747	-19.340	-19.686	-19.914
20.103	-20.700	-21.307	-21.867	-22.095	-22.241	-17.776	-19.235	-19.775	-20.097	-20.316
20.155	-20.701	-21.277	-21.819	-22.041	-22.187	-18.161	-19.429	-19.852	-20.117	-20.310
19.585	-20.096	-20.647	-21.174	-21.392	-21.536	-17.757	-18.938	-19.296	-19.526	-19.700
18.650	-19.136	-19.664	-20.175	-20.386	-20.528	-16.912	-18.050	-18.371	-18.577	-18.734
17.548	-18.005	-18.507	-19.000	-19.204	-19.342	-15.901	-17.000	-17.278	-17.460	-17.598
16.294	-16.718	-17.186	-17.647	-17.836	-17.969	-14.745	-15.807	-16.036	-16.188	-16.304
14.753	-15.151	-15.582	-15.990	-16.151	-16.270	-13.254	-14.269	-14.498	-14.638	-14.728
12.623	-13.018	-13.442	-13.834	-13.985	-14.096	-11.157	-12.122	-12.364	-12.511	-12.592
-9.872	10.303	-10.750	-11.184	-11.358	-11.478	-8.399	-9.346	-9.600	-9.781	-9.884
-6.757	-7.202	-7.658	-8.119	-8.308	-8.435	-5.333	-6.247	-6.482	-6.674	-6.786

6. Discussion

One of the things which arises from these models is that elemental abundances do not show exponential radial distributions and therefore it is not easy to fit a straight line in the logarithmic scale and to obtain a radial gradient. The distributions are always flatter on the inner regions than in the disk. It is in the disk region between the bulge and the optical radius (around 2 times the effective radius) where a radial gradient may actually be well defined. In the outer regions of the disk the distributions are flatter again, which is in agreement with recent observations from the CALIFA survey [18]. This flattening is more evident, at shorter radii, for early times or highest redshifts. By taking into account that at these same time/redshifts the stellar profiles continue being steep; it is evident that the abundances do not proceed from the stellar production in the disk. Since the radial gradient is created by the ratio Ψ/f , one possibility is that the infall causes an enrichment in the outer parts of the disks. We must remember that in our models the halos create stars too, with an efficiency $\epsilon_\kappa = 0.003$. With this value it is possible to

reproduce the star formation history and the age-metallicity relation of the Galactic halo. Since the infall rate is very high in the inner regions of the disk, the star formation in the inner halo occurs during a very short time, and then the gas falls towards the disk, and the star formation in the halo stops. Thus, stars in the halo will be old and with low metallicities, as observed. On the contrary, the infall of gas takes place during a longer time in the outer disk, and therefore the corresponding halo maintains a quantity of gas which allows us to have a star formation rate at a certain level along the galaxy life. Thus the gas infalling in the outer disk may be enriched, in a relative term, compared with the extremely low abundances of the outer disk. In order to check this possibility we have computed a model for a theoretical galaxy similar to MWG, which would be the same as the number 5 in Table 1, without star formation rate, that is, with $\epsilon_\kappa = 0$. Resulting radial distributions for both cases may be compared in Figure 17. In (a) we show the standard results, already shown in Figure 8 with the other galaxy examples. In (b) we have the same model with $\epsilon_\kappa = 0$. In the first case the flattening of the radial distributions for the outer disk is

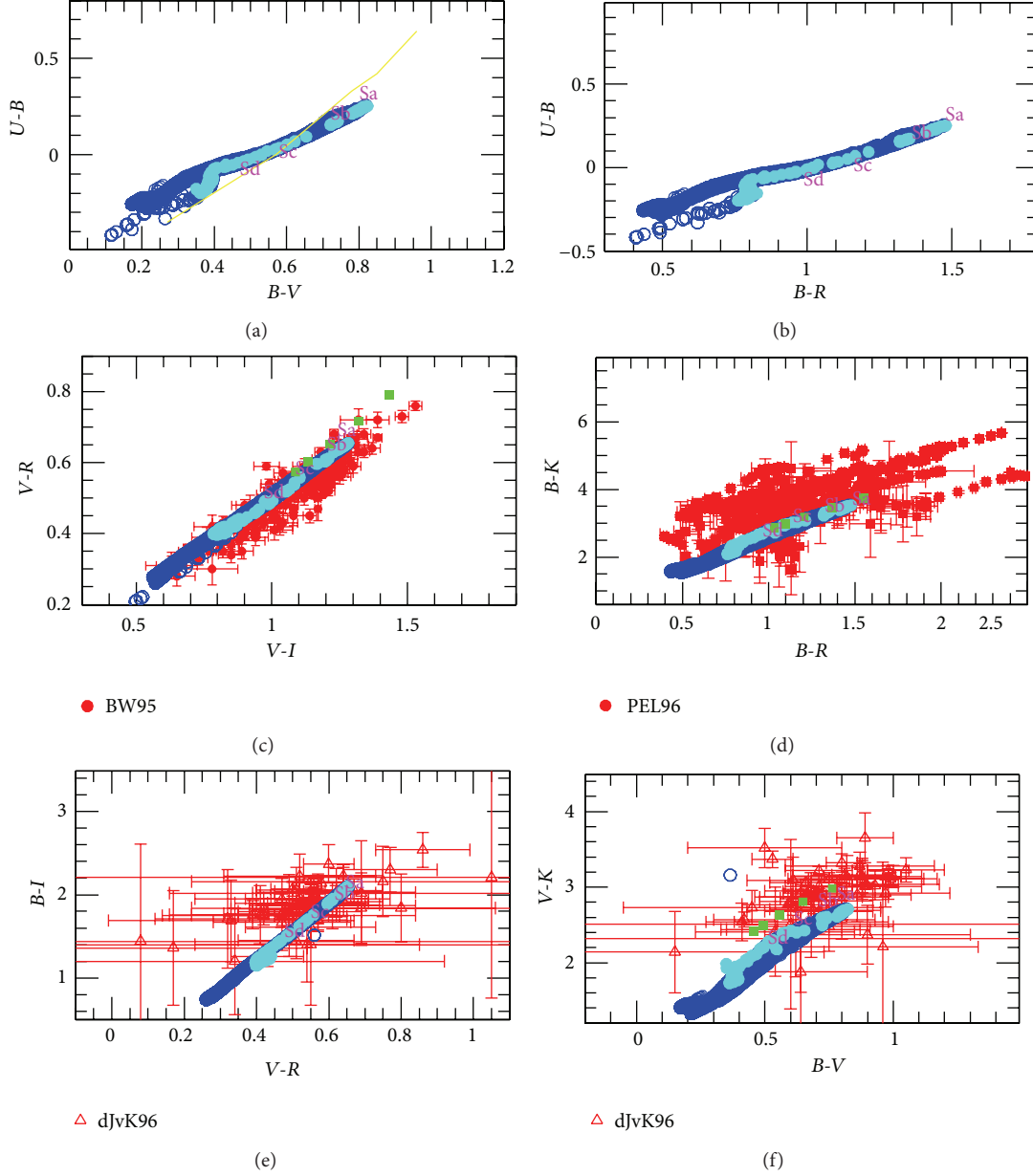


FIGURE 11: Color-color diagrams. Colors $U-B$ versus $B-V$, $U-B$ versus $B-R$, $V-R$ versus $V-I$, $B-K$ versus $B-R$, $B-I$ versus $V-R$, and $V-K$ versus $B-V$ are represented as blue dots and compared with observational data. The standard values for typical galaxies along the Hubble sequence as Sa, Sb, Sc, and Sd are taken from Poggianti [132] and shown as in magenta letters. In the panel $U-B$ versus $B-V$, the yellow line corresponds to data from Vitores et al. [133], the red dots are from Buta and Williams ([129], BW95) in $V-R$ versus $V-I$, from Peletier and Balcells ([130], PEL96) in panel $B-K$ versus $B-R$, and from de Jong ([131], dJvK96) in $B-I$ versus $V-R$ and $V-K$ versus $B-V$ panels. The green full squares are from [124].

evident for all redshifts, although more clearly in the highest ones, while in the bottom panel no flattening in this region appears. The flattening in the inner disk is similar in both cases.

The second result is that radial gradient flattens with the evolution for all galaxies. However the rate with which this occurs is not the same for all of them. Massive galaxies evolve more rapidly flattening very quickly their radial distributions of abundances. Low mass galaxies on the contrary maintain a steep radial gradient for a longer time. On the other hand,

this is a generic result when all radial range of the disk is used to compute the radial gradient. By taking into account that the distributions of abundances do not have a unique slope, as we have explained above, we might select different ranges to compute this gradient. That is if we calculate the gradient for all the spatial range, we obtain the red dashed line in Figure 18 for a MWG-like model, similar to our results in Mollá and Diaz [51]. The radial gradient decreases with the evolution. The radial gradient decreases with the evolution. If we select a restricted radial range, computing it only for $\text{Radius} < R_{\text{opt}}$

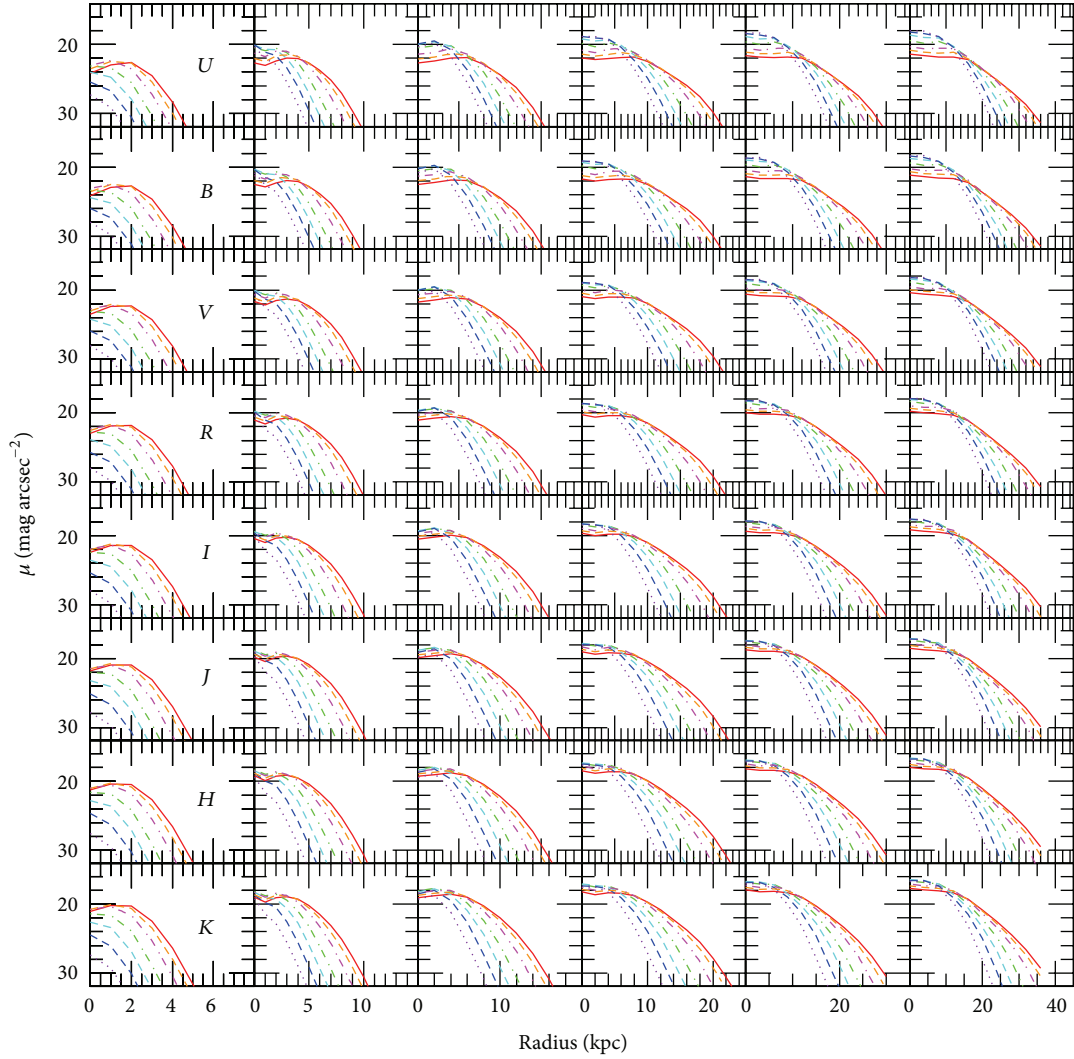


FIGURE 12: Evolution with redshift of surface brightness profiles in $U, B, V, R, I, J, H,$ and K bands. Each row shows the results for a theoretical galaxy of the Table 1, from the galaxy, with $V_{\max} = 78 \text{ km s}^{-1}$, to the most massive on the bottom for $V_{\max} = 290 \text{ km s}^{-1}$. Lines purple, blue, cyan, green, magenta, orange, and red are for $z = 5, 4, 3, 2, 1, 0.4,$ and $0,$ respectively.

(which increases with redshift decreasing), then we obtain the solid line results which show a smaller absolute value and less evolution along redshift. It is necessary to remember that other galaxies will have their own radial gradient evolution since each galaxy may evolve in a different way.

We may compare these results with observational data which are now being published. We do that in Figure 18 where data from Maciel et al. [136], Rupke et al. [137], Stanghellini et al. [138], Cresci et al. [58], Yuan et al. [59], Queyrel et al. [60], Jones et al. [61], and Maciel and Costa [139] are shown. It is evident that not all of them give the same result. Some authors claim that the radial gradient is steeper for early evolutionary times, while others found flat or even positive radial gradient and try to interpret these results with generic scenarios about the formation of galaxies. It is necessary to say again that not all galaxies evolve in the same way, and, furthermore, not all the observations measure the same thing. The radial range of the measurements is important as we

have shown before. There are other important observational effects, such as the angular resolution, the signal to noise, or the annular binning that may change the obtained radial gradient, such as it is demonstrated in Yuan et al. [143]. It is necessary to take care of how using these high redshift observations before to extract conclusions. Maybe a method more sure than to estimate oxygen abundance for high redshift is to study planetary nebula (PN), such as Maciel et al. [136], Maciel and Costa [139], and their group do, since PN give to us the radial gradient that a galaxy had some time ago.

7. Conclusions

We have shown a complete grid of chemo-spectro-photometric evolution models calculated for spiral and irregular galaxies. The evolution with redshift is given in the rest-frame of galaxies. We obtain the evolution of the radial gradient of abundances with higher abundances in the inner regions of

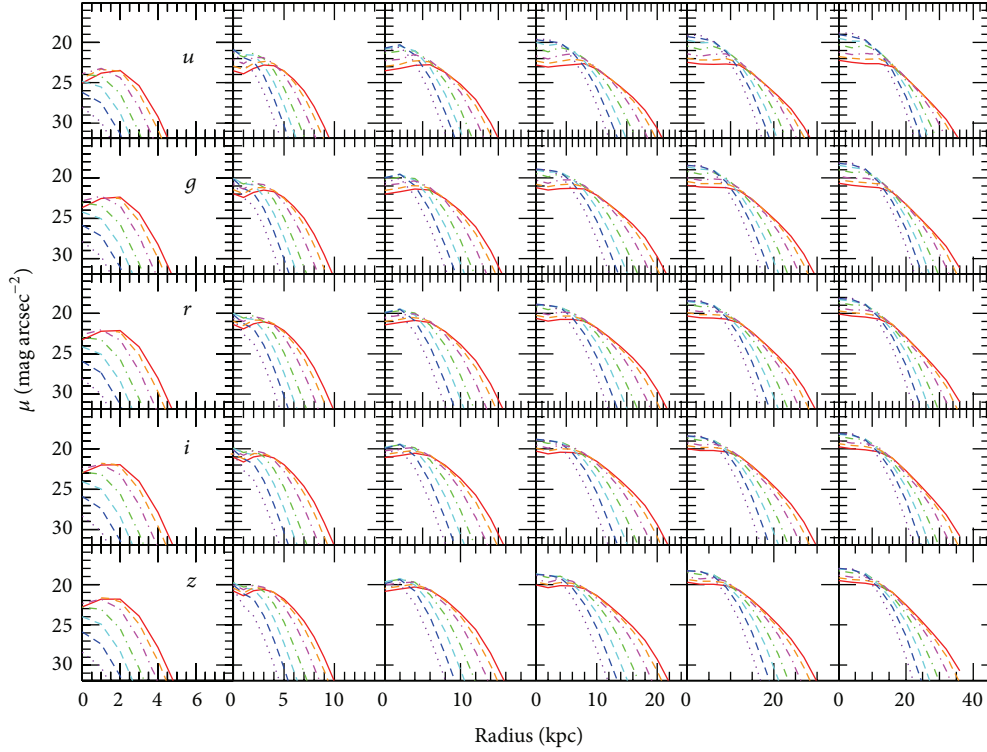


FIGURE 13: Evolution with redshift of surface brightness profiles for SDSS/SLOAN magnitudes u_{sdss} , g_{sdss} , r_{sdss} , i_{sdss} , and z_{sdss} . Each row shows the results for a theoretical galaxy of Table 1, from the galaxy, with $V_{\text{max}} = 78 \text{ km s}^{-1}$, to the most massive on the bottom for $V_{\text{max}} = 290 \text{ km s}^{-1}$. Lines purple, blue, cyan, green, magenta, orange, and red are for $z = 5, 4, 3, 2, 1, 0.4,$ and 0 , respectively.

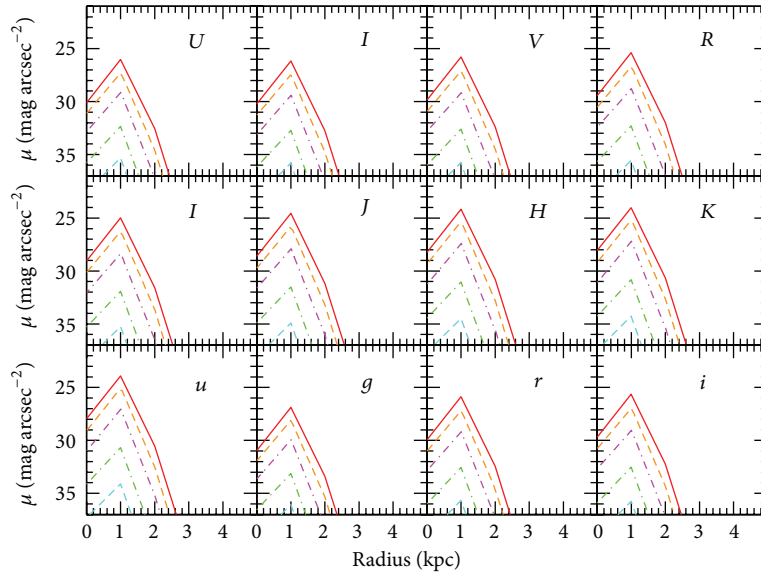


FIGURE 14: Evolution of surface brightness profiles for Johnson ($U, B, V, R, I, J, H,$ and K) and SDSS/SLOAN ($u_{\text{sdss}}, g_{\text{sdss}}, r_{\text{sdss}},$ and i_{sdss}) magnitudes radial distributions for the least massive galaxy of Table 1 with $V_{\text{max}} = 48 \text{ km s}^{-1}$.

disks than in the outer ones. These radial gradients flatten with decreasing redshifts, but always there are some outer regions that show no radial gradient, or it is flatter than in the inner disk. These regions are located increasingly far from the center as the evolution takes place. We have also presented the photometric evolution for this same set of theoretical

galaxies, given the surface brightness profiles at different evolutionary times or redshifts. Using the surface density of atomic, molecular, or stellar masses, and these surface brightness profiles we may predict observational limits for these quantities for different redshifts. We may also check that the flat radial gradients of abundances in the outer

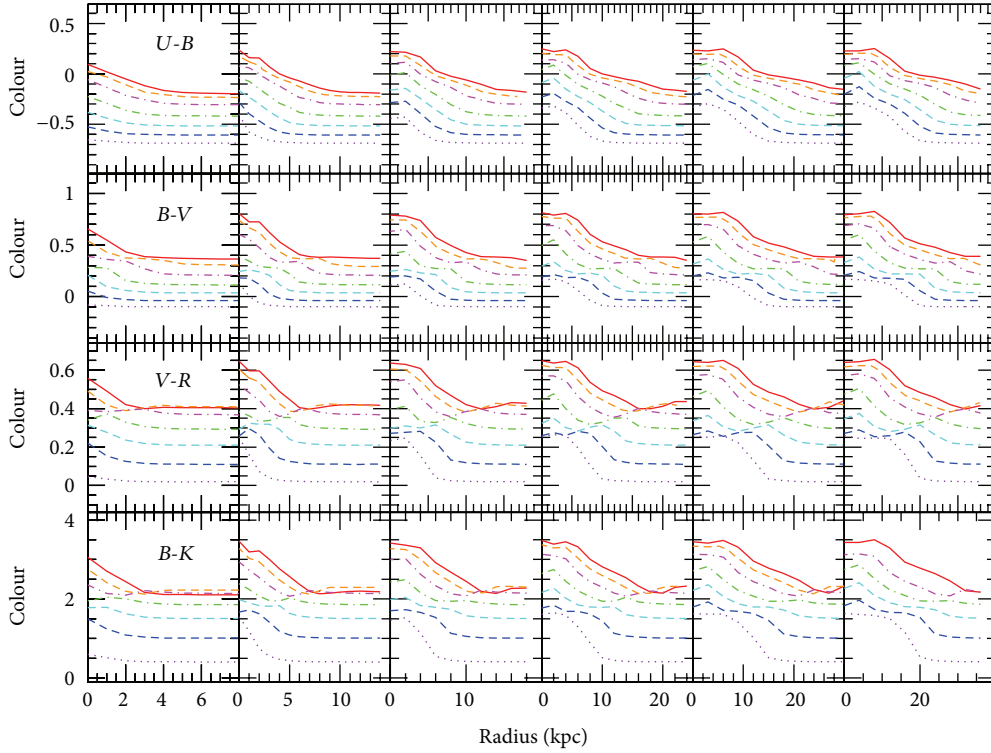


FIGURE 15: Evolution of colors radial profiles for $U-B$, $B-V$, $V-R$, and $R-I$. As in previous figures each color represents a redshift while each column is a different theoretical galaxy of Table 1, from the galaxy, with $V_{\max} = 78 \text{ km s}^{-1}$, to the most massive at the right for $V_{\max} = 290 \text{ km s}^{-1}$.

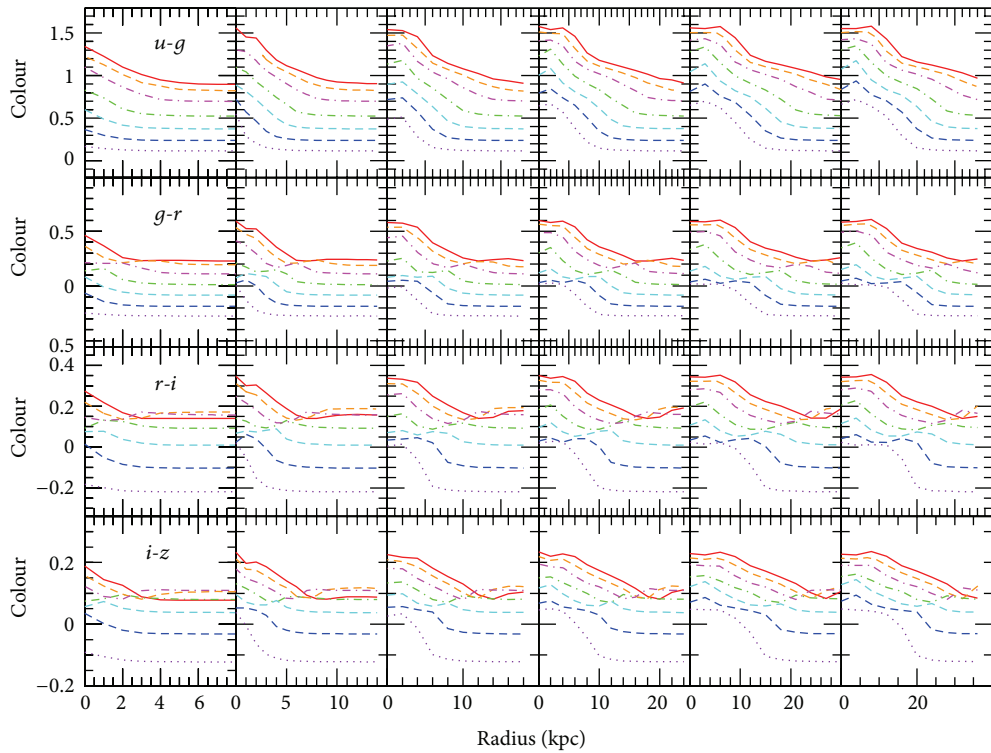


FIGURE 16: Evolution of colors radial profiles for $u_{\text{sdds}}-g_{\text{sdds}}$, $g_{\text{sdds}}-r_{\text{sdds}}$, $r_{\text{sdds}}-i_{\text{sdds}}$, and $i_{\text{sdds}}-z_{\text{sdds}}$. As in previous figures each color represents a redshift while each column is a different theoretical galaxy of Table 1, from the galaxy, with $V_{\max} = 78 \text{ km s}^{-1}$, to the most massive at the right for $V_{\max} = 290 \text{ km s}^{-1}$.

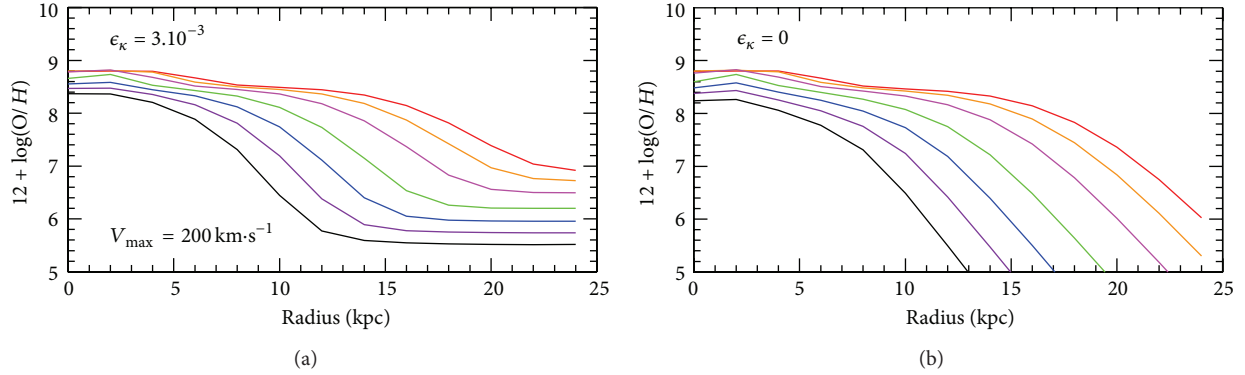


FIGURE 17: Evolution of the radial distributions of oxygen abundance for a MWG-like galaxy (number 5 from Table 1). (a) With a star formation efficiency in the halo, $\epsilon_\kappa = 0.003$. (b) Without star formation in the halo $\epsilon_\kappa = 0$.

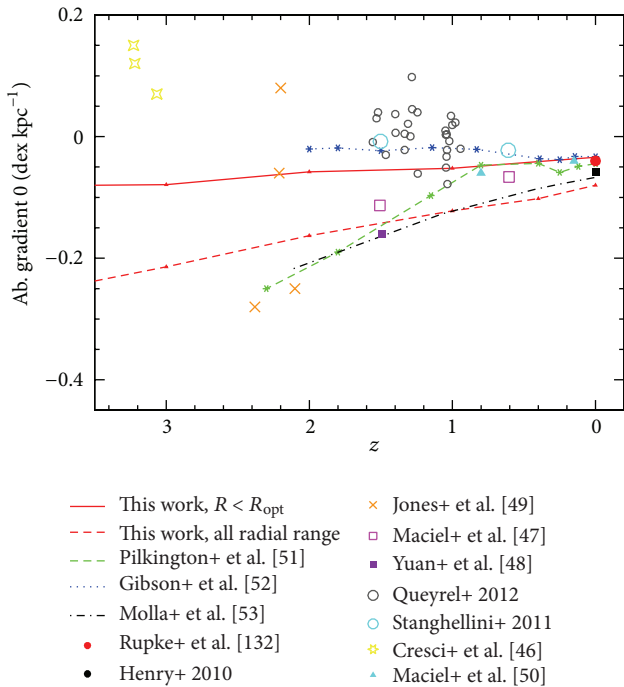


FIGURE 18: Evolution of the radial gradient of oxygen abundance for a MWG-like galaxy (number 5 from Table 1) along the redshift compared with observations. Dots are data from Maciel et al. [136], Rupke et al. [137], Stanghellini et al. [138], Cresci et al. [58], Yuan et al. [59], Queyrel et al. [60], Jones et al. [61], and Maciel et al. [139] as labeled, while lines are simulations from Pilkington et al. [140], Gibson et al. [141], and our old model results for MWG [142], as given in the plot. For this work we have two lines, one obtained by using all the radial range and the other only for disk within the optical radius, that are shown by the short-dashed and solid lines, respectively.

disks do not correspond to a similar flattening of the surface brightness profiles, and therefore the abundances in these regions do not arise by the stellar populations in the disk. We suggest that they are the result of the infall of gas coming from a halo that is in that moment more enriched than the one in the disk. This indicates that the infall law of

gas which forms-out the disk has important consequences in the predicted observational characteristics of galaxies at high redshift. Therefore analyzing other possible infall laws is essential and we will do that in the future.

Conflict of Interests

The author declares that there is no conflict of interests regarding the publication of this paper.

Acknowledgments

This work has been supported by DGICYT Grants AYA2010-21887-C04-02 and 04. Also, partial support from the Comunidad de Madrid under Grant CAM S2009/ESP-1496 (Astro-Madrid) is grateful. Mercedes Mollá thanks the kind hospitality and wonderful welcome of the Instituto de Astronomia, Geofísica e Ciências Atmosféricas in Sao Paulo, where this work was finished. The author thanks an anonymous referee for many useful comments and suggestions that have greatly improved this paper. The author also acknowledges to B. K. Gibson his kind help with the english version of the paper.

References

- [1] D. Lynden-Bell, “The chemical evolution of galaxies,” *Vistas in Astronomy*, vol. 19, no. 3, pp. 299–316, 1975.
- [2] B. M. Tinsley, “Evolution of the stars and gas in galaxies,” *Fundamentals of Cosmic Physics*, vol. 5, pp. 287–388, 1980.
- [3] D. D. Clayton, “Galactic chemical evolution—Z versus $\ln(1/\mu)$ relationship,” *The Astrophysical Journal*, vol. 315, pp. 451–459, 1987.
- [4] D. D. Clayton, “Nuclear cosmochronology within analytic models of the chemical evolution of the solar neighbourhood,” *Monthly Notices of the Royal Astronomical Society*, vol. 234, pp. 1–36, 1988.
- [5] J. Sommer-Larsen and Y. Yoshii, “The chemical evolution of star-forming viscous discs,” *Monthly Notices of the Royal Astronomical Society*, vol. 238, pp. 133–144, 1989.
- [6] M. Peimbert, “Chemical evolution of the galactic interstellar medium: abundance gradients,” in *IAU Symposium No. 84, The Large-Scale Characteristics of the Galaxy*, p. 307, 1979.

- [7] P. A. Shaver, R. X. McGee, L. Newton, A. C. Danks, and S. R. Pottasch, *Monthly Notices of the Royal Astronomical Society*, vol. 204, p. 53, 1983.
- [8] M. Fich and M. Silkey, "Abundances in H II regions at the edge of the galaxy," *Astrophysical Journal Letters*, vol. 366, no. 1, pp. 107–114, 1991.
- [9] A. Fitzsimmons, P. L. Dufton, and W. R. J. Rolleston, "A comparison of oxygen and nitrogen abundances in young clusters and associations and in the interstellar gas," *Monthly Notices of the Royal Astronomical Society*, vol. 259, no. 3, pp. 489–493, 1992.
- [10] J. M. Vílchez and C. Esteban, "The chemical composition of H II regions in the outer Galaxy," *Monthly Notices of the Royal Astronomical Society*, vol. 280, no. 3, pp. 720–734, 1996.
- [11] S. J. Smartt and W. R. J. Rolleston, "The Galactic oxygen abundance gradient," *Astrophysical Journal Letters*, vol. 481, no. 1, pp. L47–L50, 1997.
- [12] A. Afflerbach, E. Churchwell, and M. W. Werner, "Galactic abundance gradients from infrared fine-structure lines in compact H II regions," *Astrophysical Journal Letters*, vol. 478, no. 1, pp. 190–205, 1997.
- [13] C. Esteban, M. Peimbert, S. Torres-Peimbert, J. García-Rojas, and M. Rodríguez, "Faint emission lines and temperature fluctuations in M8," *Astrophysical Journal, Supplement Series*, vol. 120, no. 1, pp. 113–129, 1999.
- [14] C. Esteban, M. Peimbert, and S. Torres-Peimbert, "Physical conditions in the partially ionized zone of the Orion nebula," *Astronomy & Astrophysics*, vol. 342, no. 3, pp. L37–L40, 1999.
- [15] C. Esteban, M. Peimbert, S. Torres-Peimbert, and J. García-Rojas, "Chemical composition and temperature fluctuations in M17," *Revista Mexicana de Astronomía y Astrofísica*, vol. 35, no. 1, pp. 65–83, 1999.
- [16] S. J. Smartt, K. A. Venn, P. L. Dufton, D. J. Lennon, W. R. J. Rolleston, and F. P. Keenan, "Chemical abundances in the inner 5 kpc of the Galactic disk," *Astronomy & Astrophysics*, vol. 367, no. 1, pp. 86–105, 2001.
- [17] R. B. C. Henry and G. Worthey, "The distribution of heavy elements in spiral and elliptical galaxies," *Publications of the Astronomical Society of the Pacific*, vol. 111, no. 762, pp. 919–945, 1999.
- [18] S. F. Sánchez, F. F. Rosales-Ortega, J. Iglesias-Páramo et al., "A characteristic oxygen abundance gradient in galaxy disks unveiled with CALIFA," *Astronomy & Astrophysics*, vol. 563, pp. 49–74, 2014.
- [19] D. R. Garnett, "Abundances in spiral galaxies: spatial profiles and global correlations," *Revista Mexicana de Astronomía y Astrofísica*, vol. 7, p. 58, 1998.
- [20] B. E. J. Pagel, "The G-dwarf problem and radio-active cosmochronology," in *Evolutionary Phenomena in Galaxies*, p. 201, Cambridge University Press, Cambridge, UK, 1989.
- [21] M. Goetz and J. Koeppen, "On abundance gradients in spiral galaxies," *Astronomy & Astrophysics*, vol. 262, pp. 455–467, 1992.
- [22] J. Koeppen, "The evolution of abundance gradients in spiral galaxies," *Astronomy & Astrophysics*, vol. 281, no. 1, pp. 26–34, 1994.
- [23] C. G. Lacey and S. M. Fall, "Chemical evolution of the galactic disk with radial gas flows," *The Astrophysical Journal*, vol. 290, pp. 154–170, 1985.
- [24] R. Güsten and P. G. Mezger, "Star formation and abundance gradients in the galaxy," *Vistas in Astronomy*, vol. 26, no. 3, pp. 159–224, 1982.
- [25] A. I. Diaz and M. Tosi, "The chemical evolution of spiral galaxies—the Galaxy, M 31, M 33, M 83 and M 101," *Monthly Notices of the Royal Astronomical Society*, vol. 208, pp. 365–377, 1984.
- [26] F. Matteucci and P. Francois, "Galactic chemical evolution—abundance gradients of individual elements," *Monthly Notices of the Royal Astronomical Society*, vol. 239, pp. 885–904, 1989.
- [27] F. Ferrini, F. Matteucci, C. Pardi, and U. Penco, "Evolution of spiral galaxies. I. Halo-disk connection for the evolution of the solar neighborhood," *Astrophysical Journal Letters*, vol. 387, no. 1, pp. 138–151, 1992.
- [28] F. Ferrini, M. Mollá, M. C. Pardi, and A. I. Díaz, "Evolution of spiral galaxies. III. Application of the multiphase model to the galactic disk," *Astrophysical Journal Letters*, vol. 427, no. 2, pp. 745–758, 1994.
- [29] L. Carigi, "Chemical evolution of the solar neighborhood with yields dependent on metallicity," *Astrophysical Journal Letters*, vol. 424, no. 1, pp. 181–188, 1994.
- [30] N. Prantzos and O. Aubert, "On the chemical evolution of the galactic disk," *Astronomy & Astrophysics*, vol. 302, p. 69, 1995.
- [31] C. Chiappini, F. Matteucci, and R. Gratton, "The chemical evolution of the galaxy: the two-infall model," *Astrophysical Journal Letters*, vol. 477, no. 2, pp. 765–780, 1997.
- [32] S. Boissier and N. Prantzos, "Chemo-spectrophotometric evolution of spiral galaxies—I. The model and the Milky Way," *Monthly Notices of the Royal Astronomical Society*, vol. 307, no. 4, pp. 857–876, 1999.
- [33] R. D. D. Costa, W. J. Maciel, and A. V. Escudero, "Chemical evolution of the Galactic bulge: single and double infall models," *Baltic Astronomy*, vol. 17, no. 3–4, pp. 321–335, 2008.
- [34] J. Tumlinson, "Chemical evolution in hierarchical models of cosmic structure. II. the formation of the Milky Way stellar halo and the distribution of the oldest stars," *Astrophysical Journal Letters*, vol. 708, no. 2, pp. 1398–1418, 2010.
- [35] M. M. Marcon-Uchida, F. Matteucci, and R. D. D. Costa, "Chemical evolution models for spiral disks: the Milky Way, M 31, and M 33," *Astronomy & Astrophysics*, vol. 520, no. 20, article A35, 2010.
- [36] R. Caimmi, "Simple MCBR models of chemical evolution: an application to the thin and the thick disk," *Serbian Astronomical Journal*, vol. 185, pp. 35–51, 2012.
- [37] T. Tsujimoto and K. Bekki, "Two-component galactic bulge probed with renewed galactic chemical evolution model," *Astrophysical Journal*, vol. 747, no. 2, article 125, 2012.
- [38] A. Micali, F. Matteucci, and D. Romano, "The chemical evolution of the milky way: the three infall model," *Monthly Notices of the Royal Astronomical Society*, vol. 436, pp. 1648–1658, 2013.
- [39] L. Carigi, X. Hernandez, and G. Gilmore, "Chemical evolution models of local dwarf spheroidal galaxies," *Monthly Notices of the Royal Astronomical Society*, vol. 334, no. 1, pp. 117–128, 2002.
- [40] G. A. Vazquez, L. Carigi, and J. J. Gonzalez, "SPECTRAL: a new evolutionary synthesis code. Application to the irregular Galaxy NGC 1560," *Astronomy & Astrophysics*, vol. 400, pp. 31–40, 2003.
- [41] L. Carigi, P. Colín, and M. Peimbert, "Chemical and photometric evolution of the local group galaxy NGC 6822 in a cosmological context," *Astrophysical Journal Letters*, vol. 644, no. 2, pp. 924–939, 2006.
- [42] L. Magrini, J. M. Vílchez, A. Mampaso, R. L. M. Corradi, and P. Leisy, "The metallicity gradient of M 33: chemical abundances of H II regions," *Astronomy & Astrophysics*, vol. 470, no. 3, pp. 865–874, 2007.

- [43] M. K. Barker and A. Sarajedini, “The stellar populations of M33’s outer regions—IV. Inflow history and chemical evolution,” *Monthly Notices of the Royal Astronomical Society*, vol. 390, no. 2, pp. 863–880, 2008.
- [44] L. Magrini, L. Stanghellini, E. Corbelli, D. Galli, and E. Villaver, “Metal production in M 33: space and time variations,” *Astronomy & Astrophysics*, vol. 512, article A63, 15 pages, 2010.
- [45] G. A. Lanfranchi and F. Matteucci, “Chemical evolution models for the dwarf spheroidal galaxies Leo 1 and Leo 2,” *Astronomy & Astrophysics*, vol. 512, article A85, 12 pages, 2010.
- [46] L. Hernández-Martínez, L. Carigi, M. Peña, and M. Peimbert, “Planetary nebulae as observational constraints in chemical evolution models for NGC 6822,” *Astronomy & Astrophysics*, vol. 535, article A118, 14 pages, 2011.
- [47] X. Kang, R. Chang, J. Yin et al., “The evolution and star-formation history of M33,” *Monthly Notices of the Royal Astronomical Society*, vol. 426, pp. 1455–1464, 2012.
- [48] D. Romano and E. Starckenburg, “Chemical evolution of Local Group dwarf galaxies in a cosmological context—I. A new modelling approach and its application to the Sculptor dwarf spheroidal galaxy,” *Monthly Notices of the Royal Astronomical Society*, vol. 434, no. 1, pp. 471–487, 2013.
- [49] F. Robles-Valdez, L. Carigi, and M. Peimbert, “Outside-in stellar formation in the spiral galaxy M33?” *Monthly Notices of the Royal Astronomical Society*, vol. 429, pp. 2351–2360, 2013.
- [50] F. Robles-Valdez, L. Carigi, and M. Peimbert, “Star formation efficiency and flatten gradients in M31,” <http://arxiv.org/abs/1310.1420>.
- [51] M. Mollá and A. I. Diaz, “A grid of chemical evolution models as a tool to interpret spiral and irregular galaxies data,” *Monthly Notices of the Royal Astronomical Society*, vol. 358, pp. 521–543, 2005.
- [52] S. Boissier and N. Prantzos, “Chemo-spectrophotometric evolution of spiral galaxies—II. Main properties of present-day disc galaxies,” *Monthly Notices of the Royal Astronomical Society*, vol. 312, no. 2, pp. 398–416, 2000.
- [53] U. Fritze-Von Alvensleben, P. Weilbacher, and J. Bicker, “Chemically consistent evolutionary synthesis,” *Astrophysics and Space Science*, vol. 284, no. 2, pp. 893–896, 2003.
- [54] J. Bicker, U. F.-V. Alvensleben, C. S. Möller, and K. J. Fricke, “Chemically consistent evolution of galaxies. II. Spectrophotometric evolution from zero to high redshift,” *Astronomy & Astrophysics*, vol. 413, no. 1, pp. 37–48, 2004.
- [55] R. Kotulla, U. Fritze, P. Weilbacher, and P. Anders, “Galev evolutionary synthesis models—I. Code, input physics and web interface,” *Monthly Notices of the Royal Astronomical Society*, vol. 396, no. 1, pp. 462–484, 2009.
- [56] N. Prantzos and S. Boissier, “Chemo-spectrophotometric evolution of spiral galaxies—III. Abundance and colour gradients in discs,” *Monthly Notices of the Royal Astronomical Society*, vol. 313, no. 2, pp. 338–346, 2000.
- [57] S. Boissier, A. Boselli, N. Prantzos, and G. Gavazzi, “Chemo-spectrophotometric evolution of spiral galaxies—IV. Star formation efficiency and effective ages of spirals,” *Monthly Notices of the Royal Astronomical Society*, vol. 321, no. 4, pp. 733–742, 2001.
- [58] G. Cresci, F. Mannucci, R. Maiolino, A. Marconi, A. Gnerucci, and L. Magrini, “Gas accretion as the origin of chemical abundance gradients in distant galaxies,” *Nature*, vol. 467, no. 7317, pp. 811–813, 2010.
- [59] T.-T. Yuan, L. J. Kewley, A. M. Swinbank, J. Richard, and R. C. Livermore, “Metallicity gradient of a lensed face-on spiral galaxy at redshift 1.49,” *Astrophysical Journal Letters*, vol. 732, no. 1, article L14, 2011.
- [60] J. Queyrel, T. Contini, M. Kissler-Patig et al., “MASSIV: Mass Assembly Survey with SINFONI in VVDS III. Evidence for positive metallicity gradients in $z \sim 1.2$ star-forming galaxies,” *Astronomy & Astrophysics*, vol. 539, article A93, 12 pages, 2012.
- [61] T. Jones, R. S. Ellis, J. Richard, and E. Jullo, “The origin and evolution of metallicity gradients: probing the mode of mass assembly at $z \approx 2$,” *The Astrophysical Journal*, vol. 765, p. 48, 2013.
- [62] M. Mollá, M. L. García-Vargas, and A. Bressan, “PopStar I: evolutionary synthesis model description,” *Monthly Notices of the Royal Astronomical Society*, vol. 398, no. 1, pp. 451–470, 2009.
- [63] J. Lequeux, “Rotation curves and masses of galaxies,” *Astronomy & Astrophysics*, vol. 125, no. 2, p. 394, 1983.
- [64] M. Persic, P. Salucci, and F. Stel, “The universal rotation curve of spiral galaxies—I. the dark matter connection,” *Monthly Notices of the Royal Astronomical Society*, vol. 281, no. 1, pp. 27–47, 1996.
- [65] K. C. Freeman, “On the disks of spiral and so galaxies,” *The Astrophysical Journal*, vol. 160, p. 811, 1970.
- [66] M. Balcells, A. W. Graham, and R. F. Peletier, “Galactic bulges from hubble space telescope NICMOS observations: global scaling relations,” *Astrophysical Journal Letters*, vol. 665, no. 2, pp. 1104–1114, 2007.
- [67] O. J. Eggen, D. Lynden-Bell, and A. R. Sandage, “Evidence from the motions of old stars that the galaxy collapsed,” *Astrophysical Journal Letters*, vol. 525, no. 1, pp. 962–982, 1999.
- [68] J. S. Gallagher III, D. A. Hunter, and A. V. Tutukov, “Star formation histories of irregular galaxies,” *The Astrophysical Journal*, vol. 284, pp. 544–556, 1984.
- [69] P. A. R. Ade, N. Aghanim, C. Armitage-Caplan et al., “Planck 2013 results. XVI. Cosmological parameters,” *Astronomy & Astrophysics*. In press, <http://arxiv.org/abs/1303.5076>.
- [70] R. Jimenez, B. Panter, A. F. Heavens, and L. Verde, “Baryonic conversion tree: the global assembly of stars and dark matter in galaxies from the Sloan Digital Sky Survey,” *Monthly Notices of the Royal Astronomical Society*, vol. 356, no. 2, pp. 495–501, 2005.
- [71] A. Heavens, B. Panter, R. Jimenez, and J. Dunlop, “The star-formation history of the Universe from the stellar populations of nearby galaxies,” *Nature*, vol. 428, no. 6983, pp. 625–627, 2004.
- [72] E. Pérez, R. Cid Fernandes, R. M. González Delgado et al., “The evolution of galaxies resolved in space and time: a view of inside-out growth from the CALIFA survey,” *The Astrophysical Journal*, vol. 764, p. L1, 2013.
- [73] R. X. Chang, J. L. Hou, C. G. Shu, and C. Q. Fu, “Two-component model for the chemical evolution of the Galactic disk,” *Astronomy & Astrophysics*, vol. 350, no. 1, pp. 38–48, 1999.
- [74] C. Chiappini, F. Matteucci, and D. Romano, “Abundance gradients and the formation of the milky way,” *Astrophysical Journal Letters*, vol. 554, no. 2, pp. 1044–1058, 2001.
- [75] A. Renda, D. Kawata, Y. Fenner, and B. K. Gibson, “Contrasting the chemical evolution of the Milky way and Andromeda,” *Monthly Notices of the Royal Astronomical Society*, vol. 356, no. 3, pp. 1071–1078, 2005.
- [76] L. Carigi and M. Peimbert, “The helium and heavy elements enrichment of the Galactic disk,” *Revista Mexicana de Astronomía y Astrofísica*, vol. 44, no. 2, pp. 341–354, 2008.

- [77] A. Dekel, R. Sari, and D. Ceverino, "Formation of massive galaxies at high redshift: cold streams, clumpy disks, and compact spheroids," *Astrophysical Journal Letters*, vol. 703, no. 1, pp. 785–801, 2009.
- [78] C.-A. Faucher-Giguère, D. Kereš, and C.-P. Ma, "The baryonic assembly of dark matter haloes," *Monthly Notices of the Royal Astronomical Society*, vol. 417, pp. 2982–2999, 2011.
- [79] R. Sancisi, F. Fraternali, T. Oosterloo, and T. Van Der Hulst, "Cold gas accretion in galaxies," *Astronomy and Astrophysics Review*, vol. 15, no. 3, pp. 189–223, 2008.
- [80] L. Portinari, C. Chiosi, and A. Bressan, "Galactic chemical enrichment with new metallicity dependent stellar yields," *Astronomy & Astrophysics*, vol. 334, no. 2, pp. 505–539, 1998.
- [81] M. Mollá, F. Ferrini, and A. I. Díaz, "Evolution of spiral galaxies. VI. Radial distributions of abundances in external galaxies," *Astrophysical Journal Letters*, vol. 466, no. 2, pp. 668–685, 1996.
- [82] F. Ferrini, F. Palla, and U. Penco, "Bimodality versus multimodality—do fragmentation theories support a bimodal IMF?" *Astronomy & Astrophysics*, vol. 213, pp. 391–403, 1990.
- [83] S. E. Woosley and T. A. Weaver, "The evolution and explosion of massive stars. II. Explosive hydrodynamics and nucleosynthesis," *Astrophysical Journal, Supplement Series*, vol. 101, no. 1, pp. 181–235, 1995.
- [84] M. Gavilán, J. F. Buell, and M. Mollá, "Low and intermediate mass star yields: the evolution of carbon abundances," *Astronomy & Astrophysics*, vol. 432, pp. 861–877, 2005.
- [85] M. Gavilán, M. Mollá, and J. F. Buell, "Low and intermediate mass star yields II. The evolution of nitrogen abundances," *Astronomy & Astrophysics*, vol. 450, pp. 509–521, 2006.
- [86] A. Bressan, C. Chiosi, and F. Fagotto, "Spectrophotometric evolution of elliptical galaxies. I. Ultraviolet excess and color-magnitude-redshift relations," *Astrophysical Journal, Supplement Series*, vol. 94, no. 1, pp. 63–115, 1994.
- [87] F. Fagotto, A. Bressan, G. Bertelli, and C. Chiosi, "Evolutionary sequences of stellar models with new radiative opacities. IV. $Z = 0.004$ and $Z = 0.008$," *Astronomy & Astrophysics*, vol. 105, pp. 29–38, 1994.
- [88] F. Fagotto, A. Bressan, G. Bertelli, and C. Chiosi, "Evolutionary sequences of stellar models with new radiative opacities. III. $Z = 0.0004$ and $Z = 0.05$," *Astronomy & Astrophysics*, vol. 104, pp. 365–376, 1994.
- [89] L. Girardi, A. Bressan, C. Chiosi, G. Bertelli, and E. Nasi, "Evolutionary sequences of stellar models with new radiative opacities. VI. $Z = 0.0001$," *Astronomy and Astrophysics Supplement Series*, vol. 117, no. 1, pp. 113–125, 1996.
- [90] G. Schaller, D. Schaerer, G. Meynet, and A. Maeder, "New grids of stellar models from 0.8 to 120 solar masses at $Z = 0.020$ and $Z = 0.001$," *Astronomy and Astrophysics Supplement Series*, vol. 96, no. 2, pp. 269–331, 1992.
- [91] K. Iwamoto, F. Brachwitz, K. Nomoto et al., "Nucleosynthesis in chandrasekhar mass models for type Ia supernovae and constraints on progenitor systems and burning-front propagation," *The Astrophysical Journal Supplement Series*, vol. 125, no. 2, p. 439, 1999.
- [92] M. Mollá, O. Cavichia, M. Gavilán, and B. K. Gibson, "Chemical evolution models: stellar yields, initial mass function and true integrated yields," *Monthly Notices of the Royal Astronomical Society*. to be submitted.
- [93] P. Ruiz-Lapuente, S. Blinnikov, R. Canal et al., "Type IA supernova progenitors," *Memorie della Societa Astronomica Italiana*, vol. 71, pp. 435–447, 2000.
- [94] A. MacDonald, "Comment on the cosmic time in terms of the redshift," *Foundations of Physics Letters*, vol. 19, pp. 631–632, 2006.
- [95] M. Mateo, "Dwarf galaxies of the Local Group," *Annual Review of Astronomy and Astrophysics*, vol. 36, no. 1, pp. 435–506, 1998.
- [96] F. Shankar, A. Lapi, P. Salucci, G. De Zotti, and L. Danese, "New relationships between galaxy properties and host halo mass, and the role of feedbacks in galaxy formation," *Astrophysical Journal Letters*, vol. 643, no. 1, pp. 14–25, 2006.
- [97] A. Leauthaud et al., "A weak lensing study of X-ray groups in the cosmos survey: form and evolution of the mass-luminosity relation," *The Astrophysical Journal*, vol. 709, no. 1, p. 97, 2010.
- [98] R. M. González Delgado, E. Pérez, R. Cid Fernandes et al., "The star formation history of CALIFA galaxies: radial structures," *Astronomy & Astrophysics*, vol. 562, pp. 47–72, 2014.
- [99] E. Daddi, F. Bournaud, F. Walter et al., "Very high gas fractions and extended gas reservoirs in $z = 1.5$ Disk galaxies," *Astrophysical Journal Letters*, vol. 713, no. 1, pp. 686–707, 2010.
- [100] R. Genzel, L. J. Tacconi, J. Gracia-Carpio et al., "A study of the gas-star formation relation over cosmic time," *Monthly Notices of the Royal Astronomical Society*, vol. 407, no. 4, pp. 2091–2108, 2010.
- [101] A. K. Leroy, F. Walter, E. Brinks et al., "The star formation efficiency in nearby galaxies: measuring where gas forms stars effectively," *Astronomical Journal*, vol. 136, no. 6, pp. 2782–2845, 2008.
- [102] C. L. Martin and R. C. Kennicutt Jr., "Star formation thresholds in galactic disks," *Astrophysical Journal Letters*, vol. 555, no. 1, pp. 301–321, 2001.
- [103] K. Nishiyama and N. Nakai, "CO survey of nearby spiral galaxies with the Nobeyama 45-m telescope: I. The data," *Publications of the Astronomical Society of Japan*, vol. 53, no. 5, pp. 713–756, 2001.
- [104] M. W. Regan, M. D. Thornley, T. T. Helfer et al., "The BIMA survey of nearby galaxies. I. The radial distribution of CO emission in spiral galaxies," *Astrophysical Journal Letters*, vol. 561, no. 1, pp. 218–237, 2001.
- [105] K. Glazebrook, C. Blake, F. Economou, S. Lilly, and M. Colless, "Measurement of the star formation rate from $H\alpha$ in field galaxies at $z = 1$," *Monthly Notices of the Royal Astronomical Society*, vol. 306, no. 4, pp. 843–856, 1999.
- [106] G. D. Coleman, C.-C. Wu, and D. W. Weedman, "Colors and magnitudes predicted for high redshift galaxies," *The Astrophysical Journal Supplement Series*, vol. 43, pp. 393–416, 1980.
- [107] C. Conroy, "Modeling the panchromatic spectral energy distributions of galaxies," *Astronomy & Astrophysics*, vol. 51, pp. 393–455, 2013.
- [108] S. Charlot and A. G. Bruzual, "Stellar population synthesis revisited," *The Astrophysical Journal*, vol. 367, pp. 126–140, 1991.
- [109] A. G. Bruzual and S. Charlot, "Spectral evolution of stellar populations using isochrone synthesis," *Astrophysical Journal Letters*, vol. 405, no. 2, pp. 538–553, 1993.
- [110] G. Worthey, "Comprehensive stellar population models and the disentanglement of age and metallicity effects," *Astrophysical Journal, Supplement Series*, vol. 95, no. 1, pp. 107–149, 1994.
- [111] M. Fioc and B. Rocca-Volmerange, "PEGASE: a UV to NIR spectral evolution model of galaxies: application to the calibration of bright galaxy counts," *Astronomy & Astrophysics*, vol. 326, no. 3, pp. 950–962, 1997.
- [112] R. M. González Delgado and C. Leitherer, "Synthetic spectra of H Balmer and He I absorption lines. I. Stellar library,"

- Astrophysical Journal, Supplement Series*, vol. 125, no. 2, pp. 479–488, 1999.
- [113] A. Vazdekis, “Evolutionary stellar population synthesis at 2 Å spectral resolution,” *Astrophysical Journal Letters*, vol. 513, no. 1, pp. 224–241, 1999.
- [114] A. G. Bruzual and S. Charlot, “Stellar population synthesis at the resolution of 2003,” *Monthly Notices of the Royal Astronomical Society*, vol. 344, no. 4, pp. 1000–1028, 2003.
- [115] G. Bruzual and S. Charlot, “GALAXEV: evolutionary stellar population synthesis models,” Astrophysics Source Code Library, record ascl:1104.005, <http://arxiv.org/abs/1010.4376>, 2011.
- [116] D. Le Borgne, B. Rocca-Volmerange, P. Prugniel, A. Lançon, M. Fioc, and C. Soubiran, “Evolutionary synthesis of galaxies at high spectral resolution with the code PEGASE-HR metallicity and age tracers,” *Astronomy & Astrophysics*, vol. 425, no. 3, pp. 881–897, 2004.
- [117] A. Bressan, G. L. Granato, and L. Silva, “Modelling intermediate age and old stellar populations in the infrared,” *Astronomy & Astrophysics*, vol. 332, no. 1, pp. 135–148, 1998.
- [118] Th. Lejeune, F. Cuisinier, and R. Buser, “A standard stellar library for evolutionary synthesis—I. Calibration of theoretical spectra,” *Astronomy and Astrophysics Supplement Series*, vol. 125, p. 229, 1997.
- [119] L. J. Smith, R. P. F. Norris, and P. A. Crowther, “Realistic ionizing fluxes for young stellar populations from 0.05 to $2 Z_{\odot}$,” *Monthly Notices of the Royal Astronomical Society*, vol. 337, no. 4, pp. 1309–1328, 2002.
- [120] A. W. A. Pauldrach, T. L. Hoffmann, and M. Lennon, “Radiation-driven winds of hot luminous stars. XIII. A description of NLTE line blocking and blanketing towards realistic models for expanding atmospheres,” *Astronomy & Astrophysics*, vol. 375, no. 1, pp. 161–195, 2001.
- [121] D. J. Hillier and D. L. Miller, “The treatment of non-LTE line blanketing in spherically expanding outflows,” *Astrophysical Journal Letters*, vol. 496, no. 1, pp. 407–427, 1998.
- [122] T. Rauch, “A grid of synthetic ionizing spectra for very hot compact stars from NLTE model atmospheres,” *Astronomy & Astrophysics*, vol. 403, no. 2, pp. 709–714, 2003.
- [123] L. Hunt, S. Bianchi, and R. Maiolino, “The optical-to-radio spectral energy distributions of low-metallicity blue compact dwarf galaxies,” *Astronomy & Astrophysics*, vol. 434, no. 3, pp. 849–866, 2005.
- [124] A. Buzzoni, “Broad-band colours and overall photometric properties of template galaxy models from stellar population synthesis,” *Monthly Notices of the Royal Astronomical Society*, vol. 361, no. 2, pp. 725–742, 2005.
- [125] A. Boselli, G. Gavazzi, and G. Sanvito, “UV to radio centimetric spectral energy distributions of optically-selected late-type galaxies in the Virgo cluster,” *Astronomy & Astrophysics*, vol. 402, no. 1, pp. 37–51, 2003.
- [126] L. Girardi, G. Bertelli, A. Bressan et al., “Theoretical isochrones in several photometric systems I. Johnson-Cousins-Glass, HST/WFPC2, HST/NICMOS, Washington, and ESO imaging survey filter sets,” *Astronomy & Astrophysics*, vol. 391, no. 1, pp. 195–212, 2002.
- [127] L. Girardi, E. K. Grebel, M. Odenkirchen, and C. Chiosi, “Theoretical isochrones in several photometric systems II. The sloan digital sky survey ugriz system,” *Astronomy & Astrophysics*, vol. 422, no. 1, pp. 205–215, 2004.
- [128] J. A. Smith, D. L. Tucker, S. Kent et al., “The *ugriz* standard-star system,” *The Astronomical Journal*, vol. 123, no. 4, pp. 2121–2144, 2002.
- [129] R. Buta and K. L. Williams, “Total and effective colors of 501 galaxies in the cousins VRI photometric system,” *Astronomical Journal*, vol. 109, no. 2, pp. 543–557, 1995.
- [130] R. F. Peletier and M. Balcells, “Ages of galaxy bulges and disks from optical and near-infrared colors,” *Astronomical Journal*, vol. 111, no. 6, pp. 2238–2242, 1996.
- [131] R. S. De Jong, “Near-infrared and optical broadband surface photometry of 86 face-on disk dominated galaxies. IV. Using color profiles to study stellar and dust content of galaxies,” *Astronomy & Astrophysics*, vol. 313, no. 2, pp. 377–395, 1996.
- [132] B. M. Poggianti, “K and evolutionary corrections from UV to IR,” *Astronomy and Astrophysics Supplement Series*, vol. 122, no. 3, pp. 399–407, 1997.
- [133] A. G. Vitores, J. Zamorano, M. Rego, O. Alonso, and J. Gallego, “Photometric and morphological analysis of UCM galaxies I. Observations and reductions. Morphological classifications,” *Astronomy and Astrophysics Supplement Series*, vol. 118, no. 1, pp. 7–34, 1996.
- [134] M. L. Martín-Manjón, M. Mollá, A. I. Díaz, and R. Terlevich, “Evolution of star-forming dwarf galaxies: characterizing the star formation scenarios,” *Monthly Notices of the Royal Astronomical Society*, vol. 420, no. 2, pp. 1294–1308, 2012.
- [135] M. L. García-Vargas, M. Mollá, and M. L. Martín-Manjón, “popstar evolutionary synthesis models—III. Photometric properties of young star clusters and mixed populations,” *Monthly Notices of the Royal Astronomical Society*, vol. 432, pp. 2746–2772, 2013.
- [136] W. J. Maciel, R. D. D. Costa, and M. M. M. Uchida, “An estimate of the time variation of the O/H radial gradient from planetary nebulae,” *Astronomy & Astrophysics*, vol. 397, no. 2, pp. 667–674, 2003.
- [137] D. S. N. Rupke, L. J. Kewley, and L.-H. Chien, “Gas-phase oxygen gradients in strongly interacting galaxies. I. Early-stage interactions,” *Astrophysical Journal Letters*, vol. 723, no. 2, pp. 1255–1271, 2010.
- [138] L. Stanghellini, L. Magrini, E. Villaver, and D. Galli, “The population of planetary nebulae and H II regions in M 81,” *Astronomy & Astrophysics*, vol. 521, article A3, 12 pages, 2010.
- [139] W. J. Maciel and R. D. D. Costa, “Time variation of the O/H radial gradient in the galactic disk based on planetary nebulae,” *Revista Mexicana de Astronomía y Astrofísica*, vol. 49, pp. 333–343, 2013.
- [140] K. Pilkington, B. K. Gibson, C. B. Brook et al., “The distribution of metals in cosmological hydrodynamical simulations of dwarf disc galaxies,” *Monthly Notices of the Royal Astronomical Society*, vol. 425, no. 2, pp. 969–978, 2012.
- [141] B. K. Gibson, K. Pilkington, C. B. Brook, G. S. Stinson, and J. Bailin, “Constraining sub-grid physics with high-redshift spatially-resolved metallicity distributions,” *Astronomy & Astrophysics*, vol. 554, article A47, 5 pages, 2013.
- [142] M. Mollá, F. Ferrini, and A. I. Díaz, “Evolution of spiral galaxies. VII. Time evolution of the radial distributions of abundances,” *The Astrophysical Journal*, vol. 475, p. 519, 1997.
- [143] T.-T. Yuan, L. J. Kewley, and J. Rich, “Systematics in metallicity gradient measurements. I. Angular resolution, signal to noise, and annular binning,” *The Astrophysical Journal*, vol. 767, p. 106, 2013.

Research Article

Imaging FTS: A Different Approach to Integral Field Spectroscopy

Laurent Drissen,¹ Laurie Rousseau-Nepton,¹ Sébastien Lavoie,¹ Carmelle Robert,¹ Thomas Martin,¹ Pierre Martin,² Julie Mandar,³ and Frédéric Grandmont³

¹ *Département de Physique, de Génie Physique et d'Optique, Université Laval and Centre de Recherche en Astrophysique du Québec (CRAQ), 1045 Avenue de la Médecine, Québec, QC, Canada G1V 0A6*

² *Department of Physics and Astronomy, University of Hawaii at Hilo, 200 W. Kawili Street, Hilo, HI 96720-4091, USA*

³ *ABB Analytical, 585 Boulevard Charest Est, Suite 300, Québec, QC, Canada G1K 9H4*

Correspondence should be addressed to Laurent Drissen; ldrissen@phy.ulaval.ca

Received 15 November 2013; Accepted 24 February 2014; Published 22 April 2014

Academic Editor: Polychronis Papaderos

Copyright © 2014 Laurent Drissen et al. This is an open access article distributed under the Creative Commons Attribution License, which permits unrestricted use, distribution, and reproduction in any medium, provided the original work is properly cited.

Imaging Fourier transform spectroscopy (iFTS) is a promising, although technically very challenging, option for wide-field hyperspectral imagery. We present in this paper an introduction to the iFTS concept and its advantages and drawbacks, as well as examples of data obtained with a prototype iFTS, SpIOMM, attached to the 1.6 m telescope of the Observatoire du Mont-Mégantic: emission line ratios in the spiral galaxy NGC 628 and absorption line indices in the giant elliptical M87. We conclude by introducing SpIOMM's successor, SITELLE, which will be installed at the Canada-France-Hawaii Telescope in 2014.

1. Introduction

The vast majority of astronomical imaging spectrometers (or integral field spectrographs) are based on dispersive approaches. We present in this paper the most recent technical developments and some scientific results based on another approach, imaging Fourier transform spectroscopy (iFTS), which has been given a strong boost during the past decade, mostly because of enormous improvements in digital imaging capabilities, computer power, and servo control systems. A large number of research programs will certainly benefit from an instrument capable of simultaneously obtaining spatially resolved spectra on extended areas (~ 10 arcminutes) with a 100% filling factor, seeing-limited spatial resolution, and a flexible spectral resolution up to $R \sim 10^4$, and iFTS is very promising in that regard. Single-pixel FTS has been in regular use in commercial applications, remote sensing of the Earth's atmosphere, and astronomy, mostly in the infrared and sub-mm domain. However, by using appropriate optical configurations, fast readout CCD detectors, and especially improved metrology and servo systems, it is possible to

transform the traditional one-pixel infrared FTS into a truly integral field spectrometer for the visible range.

The most noteworthy scientific result from the use of the FTS approach in astronomy is the accurate measurement of the cosmic microwave background radiation spectral distribution, by the FIRAS instrument on the COBE satellite [1] and the COBRA rocket experiment [2]. On a completely different field, high resolution spectra of late-type stars were obtained on a regular basis with the FTS at Kitt Peak's Mayall telescope [3, 4]. A high-resolution FTS was one of the first instruments to be attached to the Canada-France-Hawaii Telescope and was widely used on a large variety of planetary and stellar programs [5, 6]. Combined with an imaging system in the early 1990s, it was renamed BEAR [7] and provided integral field spectra of a variety of objects such as planetary nebulae, massive star clusters, and star-forming regions in a 24-arcsecond field of view [8]. More recent examples include SPIRE-FTS, one of three instruments to fly on ESA's Herschel Space Observatory [9], a far-infrared FTS on the Japanese satellite AKARI, a mid-IR FTS (CIRS) on the Cassini spacecraft, and, for the near IR, PFS on Mars

Express with a copy on Venus Express. The development of imaging FTS in astronomy was given a strong incentive during the early definition phases of the NGST (now known as the James Webb Space Telescope): astronomers supported by the three participating space agencies (NASA, ESA, and the Canadian Space Agency) presented studies of imaging FTS at the NGST Instrumentation meeting in Hyannis in 1999 [10–12]. None of these concepts however was included in the final instrument suite of the telescope. Our involvement in the iFTS endeavour is a direct consequence of this meeting. More recently, Boulanger et al. [13] proposed the design of a 1.2 m space telescope, H2EX, equipped with a wide-field imaging FTS specifically aimed at studying molecular hydrogen in the Universe. The advantages and disadvantages of the imaging FTS technique, as well as the relative merit of different approaches to 3D imagery, are discussed by Bennett [14]. An earlier version of the present paper, more complete in terms of technical explanations, is presented by Drissen et al. [15]. A recent review of the imaging FTS concept, with some historical perspective, a detailed comparison between the various imaging spectroscopy concepts and technical details not discussed in the present paper, is presented by Maillard et al. [16].

2. The iFTS Concept

An astronomical imaging Fourier transform spectrometer is basically a Michelson interferometer inserted into the collimated beam of an astronomical camera system, equipped with two detectors. The Michelson interferometer consists of a beamsplitter used to separate the incoming beam into two equal parts, two mirrors on which the halves of the original beam are reflected back, a moving mechanism to adjust the position and orientation of one of the mirrors (the other mirror is fixed), and a metrology system (IR laser and detector) to monitor the mirror alignment. All wavelengths from the field are simultaneously transmitted to either one or both of the interferometer outputs in which the array detectors sit. By moving one of its two mirrors, the interferometer thus configured therefore modulates the scene intensity between the two outputs instead of spectrally filtering it. This configuration results in a large light gathering power since no light is lost except through items common to any optical design: substrate transmission, coatings efficiency, and quantum efficiency of the detectors. All photons from the source can hence be recorded at each exposure provided that both complementary outputs of the interferometer are recorded. This requires a modification to the “standard” Michelson configuration in which half the light goes back to the source: the incoming light enters the interferometer at an angle allowing the two output beams to be physically separated. A CCD detector is then attached to each of the two output optics collecting the light from the interferometer (see Figure 6 in [15]).

While in most FTSs targeting very bright sources the interferometer’s mirror is moved at a regular, servoed speed, the weak signal from astronomical sources requires a step-scan approach. The interferogram cube is obtained through

the acquisition of a series of short exposure images with the two CCDs. At each step, one of the two mirrors in the interferometer is moved by a very short distance (between 175 nm and $\sim 5 \mu\text{m}$, depending on the spectral resolution and waveband chosen). The signal at each pixel is modulated, as a function of the mirror position, by a pattern which depends on the spectral content of the source; each of the detectors’ pixels is recording at each step a signal complementary to the corresponding pixel on the other detector. The vector composed of such a pixel recording is called an interferogram and is uniquely determined by the spectral content of the incoming light. The sum of the two images acquired at each step by the two detectors is then identical to a single image obtained with a “normal” camera. Spectral information for every pixel is recovered through a Discrete Fourier Transform (DFT or FFT) through the interferogram cube which can at any time during acquisition be turned into a spectral cube since each image contains information covering the whole waveband. The inclusion of additional exposures to an interferogram cube simply refines the meshing of the output spectra (spectral resolution). Thus, with an iFTS, spectral resolution is proportional to the total optical path difference (OPD) between the two arms of the interferometer scanned between the first and the last image of the data cube; this OPD needs to be properly sampled through a series of mirror displacements at predetermined sequential interference positions. Once the data cube has been obtained and its individual images corrected for instrumental artifacts (bias, Flatfield, like for any imager), the Fourier transform of each pixel’s interferogram produces a wavelength-calibrated data cube. A by-product of the spectral data cubes is therefore a deep panchromatic image (within the limits of the filter used—see below) of the targets. Figure 1 summarizes the data acquisition with an iFTS and Figure 2 shows a tangible example.

2.1. Technical Challenges. Like every imager, an iFTS must include high transmission optics producing high quality panchromatic images across the entire waveband covered by the instrument. But this does not translate alone into a good spectroscopic performance. In order to perform well on this aspect, a good modulation efficiency is also required. The performance of an FTS is thus characterized by its modulation efficiency (ME), that is, the capability of the interferometer to modulate the incident light:

$$\text{ME} = \frac{I(\text{modulated light})}{I(\text{incoming light})}. \quad (1)$$

The modulation efficiency can be viewed as an analog to the grating efficiency in dispersive spectrographs. In the worst case scenario, where the modulation efficiency is zero, the light from the source is recorded on the detector but the interferogram is a straight line and no spectral information can be extracted from it.

This efficiency depends on a multitude of factors, the most technically challenging being the following.

- (1) The surface quality of the optical components in the interferometer (mirrors and beamsplitter): at a given

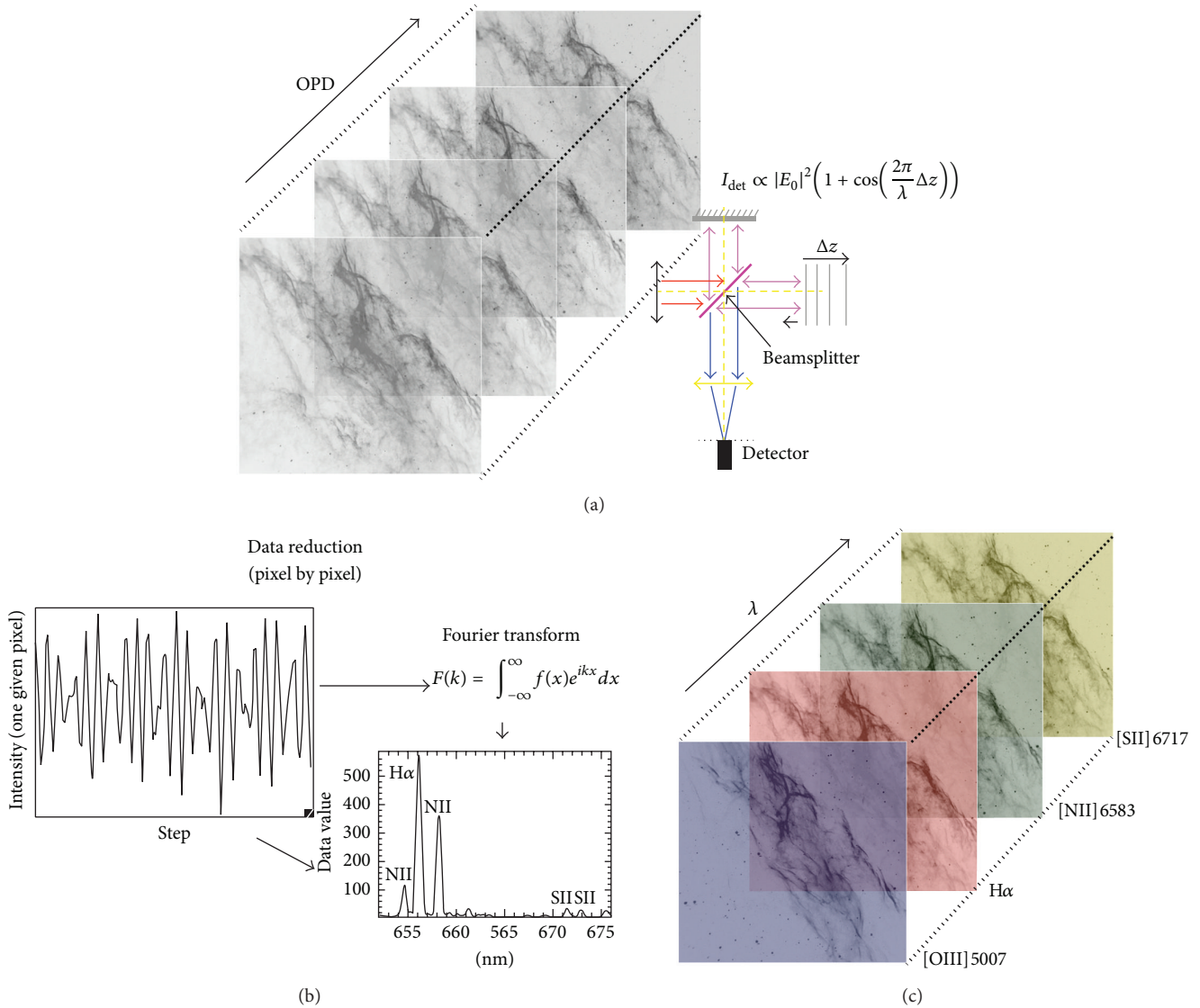


FIGURE 1: Data acquisition with an imaging FTS. (a) By scanning the Optical Path Difference (OPD) of the interferometer and taking images at every step, one gets a datacube composed of one interferogram for every pixel. (b) For a given pixel, the recorded intensity varies as a function of the OPD with a pattern that depends on the spectral content of the source; for example, a monochromatic laser beam would produce a sinusoidal pattern. A Fourier transform of the signal produces a spectrum for every pixel in the image. (c) After Fourier transforming every interferogram, one gets a spectral datacube from which monochromatic images corresponding to the emission lines of interest are extracted.

wavelength, ME is lowered by a decreased surface quality; it is therefore more and more difficult to obtain a good ME as we move from the infrared to the ultraviolet (most FTSs available today indeed work at infrared and sub-mm wavelengths); the number of reflections within the interferometer plays a major role in the global ME. Mirrors with a surface quality of $\lambda/20$ (peak-to-valley) are commercially available for a reasonable price, but large $\lambda/30$ mirrors must be custom made and are therefore much more expensive. In the case of a flat mirror design such as SpIOMM (see below), the ME at 350 nm doubles (from 35% to 70%) as the mirror and beamsplitter surface quality improves from $\lambda/20$ to $\lambda/30$; at 800 nm,

the improvement is not as large (from 85% to 92%). Moreover, even if the mirror substrate is of high enough quality, any error in the coating deposit or any tension caused by the mechanical parts used to maintain the mirror within the interferometer can ruin the initial surface figure and dramatically reduce the modulation efficiency, especially in the blue part of the spectral range.

- (2) The mirror alignment and the stability of the OPD during an exposure: both crucially depend on the quality of the metrology and the servo system, which represents the highest technical challenge a visible-band iFTS faces. In order for the beams from the two

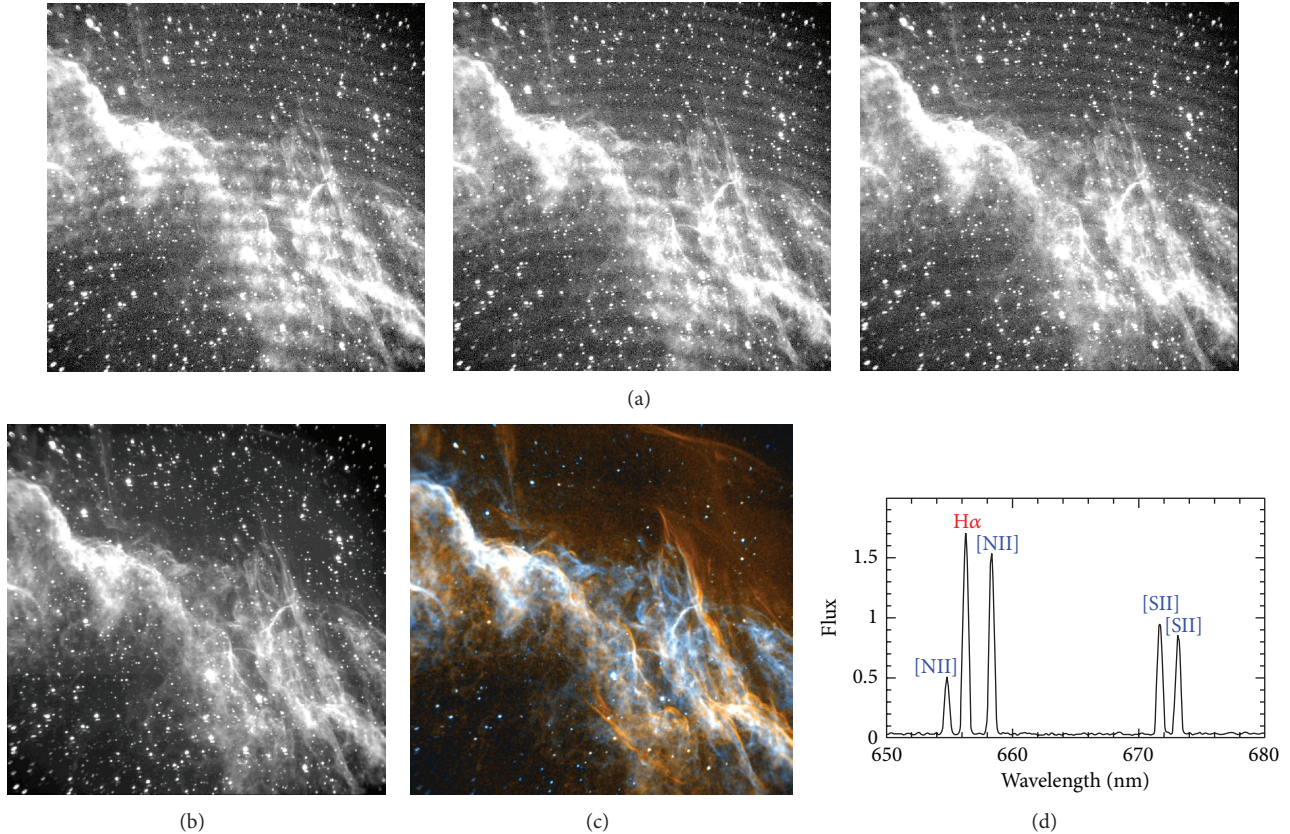


FIGURE 2: (a) Series of $12' \times 12'$ images from a raw data cube (only one camera is shown). The target is a section of NGC 6992 (Cygnus Loop), obtained through a 650–680 nm filter with SpIOMM (Section 2.3). Notice the fringes, moving from one frame to the next, caused by a combination of night sky (OH) and nebular ($H\alpha$, [NII], [SII]) emission lines. (b) Images from the raw data cube can be co-added to provide a deep, panchromatic image (within the limits of the filter). (c) This image is obtained after Fourier transforming the original data cube and extracting the $H\alpha$ (red) and [NII] 6584 (blue) images. (d) Spectrum from a group of 2×2 pixels in the same cube. Doppler maps of the field can also be extracted for each line from the ~ 400000 spectra in this cube.

arms to interfere properly, the two mirrors need to be very well aligned. The smallest deviation, in any direction, from the correct angle between the two mirrors reduces the spatial coherence (interference) of the two beams as they recombine. Again, this effect is more obvious at short wavelengths. A deviation of only 1.5 microradian from perfect alignment can decrease the ME by up to 25% at 350 nm. The DFT assumes that all data points of the interferogram vector are acquired at equidistant OPD intervals. Deviations from this assumption result in an increased noise level or artifacts in the resulting spectra. Even if the mirror steps are perfectly equidistant, a jitter of the OPD during an exposure, with a standard deviation as low as 10 nm (caused, e.g., by telescope vibrations transmitted through the structure of the instrument and uncompensated by the servo system) also decreases the ME by a significant amount, especially in the near UV. Therefore, monitoring the distance between the two mirrors as well as their alignment many thousand times per second, combined with a fast correction of

any deviation, is required to ensure a constant, high modulation efficiency.

Another factor that must be taken into account is the dead time due to the CCD readout. Since an interferogram is acquired through a series of a few hundred short exposure images, the time required to read the CCD (typically 10 s in the case of SpIOMM) lowers the global efficiency of the instrument. Recent improvement in CCD technology reduces this dead time to a minimum, ~ 2 s. Typical exposure times vary between 15 s for bright Galactic targets in the red to 120 s for galaxies in the blue. CCD readout noise (~ 3 –10 e) is usually unimportant as the photon noise from the source or the night sky background dominates.

2.2. Use of Filters with an iFTS. A spectrum of an extended source covering the entire visible range (say, 350–700 nm) could be obtained with an iFTS without the use of a filter, the only constraints being the optics transmission and the detector's quantum efficiency (which, in this wavelength range, are both excellent). However, two properties of this

instrument favor the use of filters: the need to properly sample the interferogram to reach the required spectral resolution, and the distributed photon noise.

As mentioned above, the spectral resolution of a data cube is set by the maximum distance travelled by the moving mirror of the interferometer between the first and the last image of the cube. But one cannot simply take an image at a given mirror position and then move the mirror far from its initial position and hope to get a good resolution. The total optical path difference needs to be properly sampled, the step size being determined by the shortest wavelength and the total wavelength range to be covered by the cube. Using filters to restrict the total wavelength range and spectral folding (or aliasing) techniques allows increasing the mirror step length and thus the number of mirror steps for a given spectral resolution, at the expense of the total wavelength coverage. A simplistic example will help clarify this: say that we would like to use the bright lines $H\beta$, [OIII] 4959, 5007, $H\alpha$, [NII] 6548, 6584 and [SII] 6717, and 6731 to characterise an HII region. The minimum spectral resolution required in the red ($R \sim 1200$) is set by the need to separate the [SII] doublet and in the blue ($R \sim 200$) to separate $H\beta$ from [OIII]. Getting $R = 1200$ with an unfiltered cube covering the entire range allowed by a visible-band iFTS would require ~ 1500 mirror steps, which would limit the individual exposures to ~ 6 seconds for a 4-hour integration (taking the CCD readout time into account). Using two filters to isolate the blue and red line groups with the same spectral resolution requires only 120 steps and therefore allows much deeper individual images at each step for the same total time spent on the target.

The second reason to use filters is to reduce photon noise, caused by the well-known multiplex disadvantage of the FTS [16], which, in some cases, counterbalances its clear multiplex advantage. With a dispersive spectrograph, photon noise at a given wavelength is only due to the total number of photons (from the source and the sky) at this particular wavelength. But with an iFTS (this is also the case for traditional, single-pixel FTS), photons from the entire wavelength range allowed by the optics are detected at each step (wavelengths are not filtered, but modulated) and distributed equally amongst all wavelengths after the Fourier transform. In an iFTS cube of an HII region, photon noise from a bright [OI] 5577 night-sky line affects the much fainter nebular [NII] 5755 or HeI 6678 lines, which is not the case for a spectrum of the same object obtained with a dispersive spectrograph. This also explains why an iFTS is at its best targeting emission-line objects, for which the continuum is rather low compared to the strengths of the emission lines. In some cases (very low surface brightness features such as the ionized stripping tails in galaxy clusters, distant $Ly\alpha$ galaxies), the night sky continuum sets the detection limit.

Within the limits imposed by the compromise between spectral coverage and resolution, once a filter has been selected the user can choose its preferred spectral resolution, from $R = 1$ (panchromatic image, which is anyway a by-product of all data cubes) to the maximum limit imposed by the interferometer's architecture (typically a few times 10^4), and tailor it for each object.

2.3. SpIOMM, an iFTS Prototype. In order to demonstrate the capabilities of a wide-field iFTS working in the visible band, our group has designed and built SpIOMM (Spectromètre Imageur de l'Observatoire du Mont Mégantic) at Université Laval [18] in close collaboration with ABB-Analytical (formerly Bomem), a Québec City-based company, and the Institut National d'Optique (INO). The primary objective of any astronomical instrument development being to address a science case, the design of SpIOMM was optimized to feed our science projects on the interstellar medium, late stages of stellar evolution, star formation, and galaxy evolution and which could not be obtained by existing instruments. This instrument, attached to the 1.6 m telescope of the Observatoire du Mont-Mégantic, is capable of obtaining seeing-limited, spatially resolved spectra of extended sources in filter-selected bandbases of the visible (350–900 nm) in a $12' \times 12'$ field of view with a spectral resolution $R \sim 10\text{--}25000$. It offers a very large contiguous field of view with 100% filling factor, resulting in millions of spectra per data cube. During its first few years of operations, only one output port was recorded, with a 1340×1300 , $0.55''$ -pixel LN-cooled CCD, with a readout time of 8 seconds. We recently added a $2k \times 2k$ CCD to its second output port.

SpIOMM's modulation efficiency is very good (85%) in the red, as measured with nightly observations of a He-Ne laser data cube, also used to spectrally calibrate the science cubes. The optical quality of its mirror and beamsplitter ($\lambda/20$, peak-to-valley), as well as the prototype metrology system implemented, does not allow us to obtain exquisite modulation efficiency in the near UV ($\sim 25\%$), so most of our data cubes are obtained in the 450–700 nm range. Nevertheless, some cubes were obtained in the U band, as shown in Figure 3.

Over the course of the past few years, we have obtained data cubes of HII regions [19], planetary nebulae [20], Wolf-Rayet bubbles, and unique 3D views of young supernova remnants [21, 22], as well as a sample of nearby spiral galaxies (next section). Exposure times vary from 7 seconds per step for the observations of bright nebulae in the red filter to 90 seconds per step for the observations of galaxies in the blue filter. A typical data cube therefore requires a total exposure time between one and five hours. The technical and scientific progress of SpIOMM have been described in a series of SPIE papers to which the reader is referred for more details [23–26]. Applications of SpIOMM to the field of nearby galaxies are presented in the next sections.

3. Nearby Spiral Galaxies: Emission Lines

The new possibilities offered by iFTS to observe extragalactic HII regions will greatly improve our understanding of galaxy evolution. With a high spatial resolution, SpIOMM allows us to observe several hundred star forming regions simultaneously over all the structural components of a galaxy. The excellence of the statistics and the systematic characterization achieved for the HII regions will help to derive metallicity gradients and gain knowledge about the different mechanisms that drive star formation. In this paper, NGC628 data

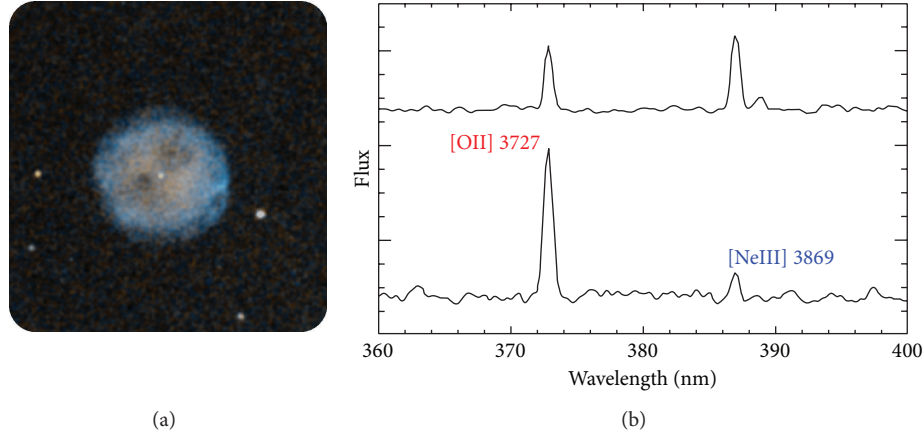


FIGURE 3: (a) Color-coded ([OII] 3727 in red, [NeIII] in blue) image of the planetary nebula M97, extracted from an SpIOMM data cube. (b) Spectra of selected pixels (binned 3×3) in the same cube with different [OII]/[NeIII] ratios.

cubes are going to be used as a typical example of SpIOMM's capabilities.

3.1. Observations and Data Reduction. Two filters have been used, a blue filter covering the wavelength domain from 475 to 515 nm and a red one from 650 to 680 nm. They include several useful emission lines: $H\beta$, [OIII] $\lambda\lambda$ 4959, 5007, [NIII] $\lambda\lambda$ 6548, 6584, $H\alpha$, HeI λ 6678, and [SII] $\lambda\lambda$ 6717, 6731. The spectral resolution ($R = \lambda/\Delta\lambda$) of the data cubes is ~ 700 in the blue and ~ 1600 in the red. A binning of the pixels was performed to achieve a pixel size of $1.07''$. We applied the basic CCD corrections (bias, darks, and flats) to the data cubes before correcting for sky transparency variations. A He-Ne laser was used for the wavelength calibration. The flux calibration was performed using data cubes of the standard star HD74721 in both filters. Finally, the average spectrum of the night sky was obtained from thousands of pixels around the galaxy and subtracted from the galaxy spectra (see Figure 4(a)).

3.2. Spectral Analysis. The ionized gas emission lines are fitted with two different techniques. One is based on a pixel-by-pixel Gaussian fit of spectral lines using the *fithi* routine from the IDL MAMDLIB library, available from the following web site: <http://www.cita.utoronto.ca/~mamd/mamdlib.html>. Figure 4(b) shows an example of the result for one pixel in an HII region.

The other method consists in using the *HIIphot* code [27] to define the HII regions contours and then fit the global spectrum (sum of the pixels in the same region) of each HII region using the *fithi* routine. Figure 4(c) shows an example of an HII region contours identified with *HIIphot* over the $H\alpha$ image. The parameters specified within *HIIphot* make sure that all the $H\alpha$ flux is included in the HII region contour map.

At the time of writing, no correction has been applied yet for Balmer absorption lines. Long slit spectra obtained along the galactic radius are going to be used to correct for the impact of the absorption on $H\beta$ and $H\alpha$ lines. In the case of NGC628, absorption in $H\beta$ and $H\alpha$ is not negligible only

in the very center of the galaxy (inner 1 kpc). For the moment with no correction for the absorption, the derived parameters using $H\alpha$ line are really close to reality and for the parameters using $H\beta$ line, we are only taking into account regions with radial position higher than 1 kpc. Detection limit for one pixel within an HII region is $\sim 6 \times 10^{-17} \text{ erg s}^{-1} \text{ cm}^{-2}$ in the $H\alpha$ line. Figure 4(d) shows an example of a faint pixel spectrum.

3.3. Results. The internal dust extinction is calculated using the theoretical ratio $H\alpha/H\beta \approx 2.87$ for HII regions at 10000 K with $R_V = 3.1$ (the Milky Way extinction on the line of sight was first taken into account). The internal $E(B - V)$ map of NGC628 is shown in Figure 5(a) using the pixel-by-pixel analysis. The total $H\alpha$ flux derived with SpIOMM for NGC 628 is $1.39 \times 10^{-11} \text{ erg s}^{-1} \text{ cm}^{-2}$. This value is in good agreement with other studies. For example, with a smaller field of view, Sánchez et al. ([28]; $6' \times 6'$) and Kennicutt et al. ([29]; $6.4' \times 6.4'$) found a value of $1.13 \times 10^{-11} \text{ erg s}^{-1} \text{ cm}^{-2}$ and $1.04 \times 10^{-11} \text{ erg s}^{-1} \text{ cm}^{-2}$, respectively, and with a larger field of view, Hoopes et al. ([30]; $29' \times 29'$) obtained a value of $1.51 \times 10^{-11} \text{ erg s}^{-1} \text{ cm}^{-2}$.

The dust-corrected pixel-by-pixel $H\alpha$ flux map of NGC628 is shown in Figure 5(b). Its total dust-corrected $H\alpha$ luminosity is then $3.56 \times 10^{41} \text{ erg s}^{-1}$ (assuming a distance of 9.7 Mpc). The global star formation rate of NGC628, using Kennicutt's [31] formula ($\text{SFR} [M_\odot \text{ yr}^{-1}] = 7.9 \times 10^{-42} L_{H\alpha} [\text{erg s}^{-1}]$), is then $\text{SFR} = 2.8 M_\odot \text{ yr}^{-1}$. This is somewhat higher than the $2.4 M_\odot \text{ yr}^{-1}$ estimated by Sánchez et al. [28] but the difference is explained by the larger number of HII regions revealed by SpIOMM in the external regions of the galaxy.

Using the N2 and the O3N2 metallicity indicators defined in [32] (PP04), we derived the metallicity of the HII regions identified with *HIIphot* as described above. As shown in Figure 6(a), a linear fit using the N2 indicator and all the HII regions identified gives the relation $12 + \log(O/H) = 8.687 - 0.020 r[\text{kpc}]$. A very similar relation, $12 + \log(O/H) = 8.689 - 0.022 r[\text{kpc}]$, is obtained using the N2 indicator for a subsample of HII regions also characterized with the O3N2 indicator (the 4σ detections of the OIII λ [5007]

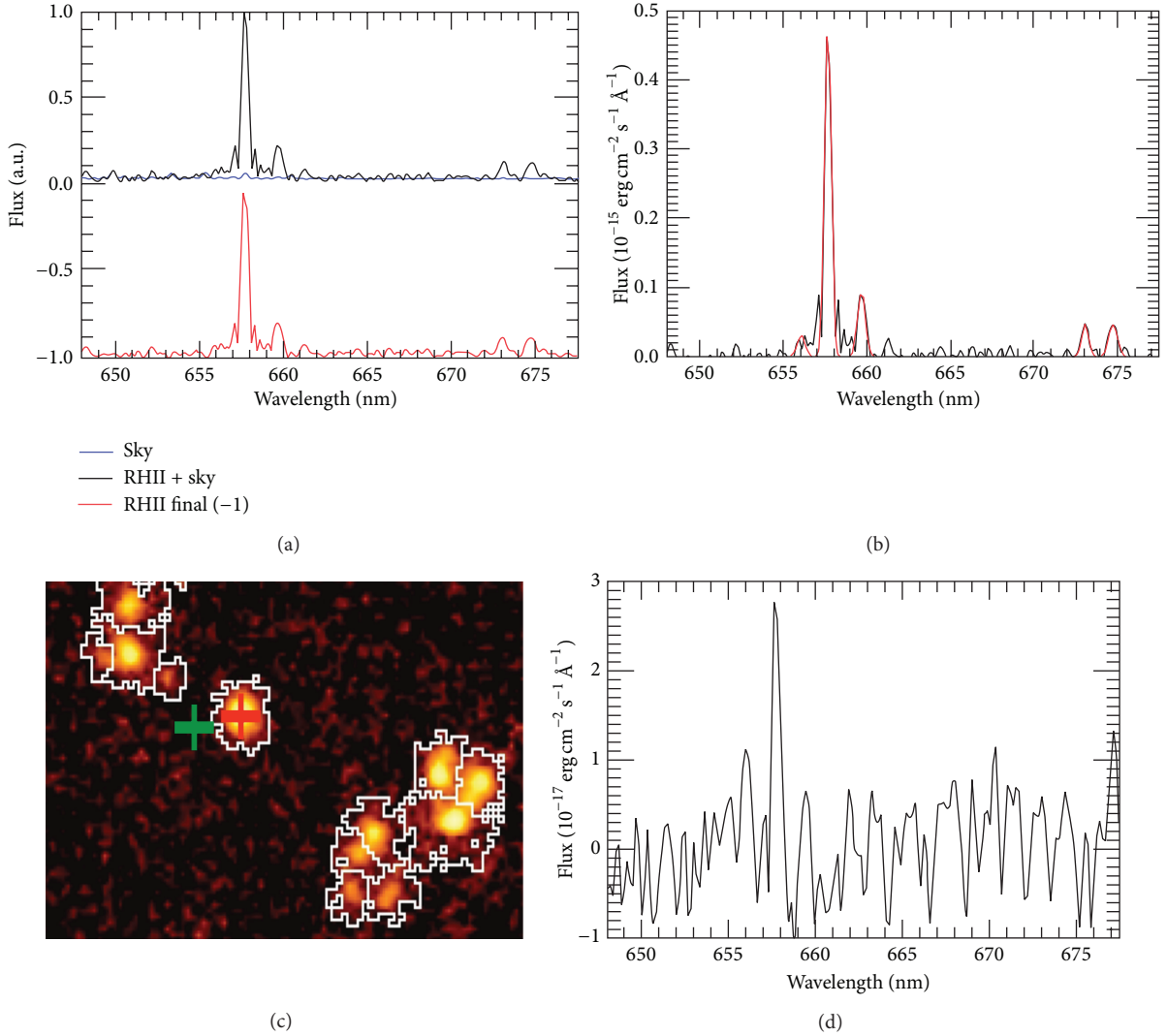


FIGURE 4: (a) Example of the sky subtraction for the spectrum of a bright pixel (1 h 36 m 54.1 s; $+15^{\circ} 46' 10.8''$). (b) Example of a Gaussian fit on the spectrum of a bright pixel. (c) Close-up on the contours map of NGC 628 selected by HIIphot; the field of view is $1.5' \times 1'$. The red cross identifies the position of the bright pixel used for the previous sky subtraction and Gaussian fit examples. The green cross identifies the pixel with $H\alpha$ in emission at $\sim 2\sigma$ limit of detection. (d) Example of the spectrum of a 1.1 arcsec^2 pixel with $H\alpha$ in emission at $\sim 2\sigma$ limit of detection.

lines have been successful for only 134 regions). As shown in Figure 6(b), if the O3N2 indicator is used, we find a steeper gradient, $12 + \log(O/H) = 8.780 - 0.033 r[\text{kpc}]$. Contrary to the O3N2 indicator, the N2 indicator has a local maximum in its metallicity distribution [33] that, we suspect, may introduce more dispersion and uncertainty in the N2 gradient.

A big advantage of an instrument like SpIOMM is the possibility to perform a detailed spatial analysis of the emission lines. The emission lines studied are affected by changes in the ionization parameter and the electron temperature [33] as we move away from the HII regions. Furthermore, a component in emission may come from the galaxy diffuse ionized gas (DIG; [34]). The origin for the DIG is still complex (background ionization from older stellar populations, stellar winds, AGN, shocks). Among others, the DIG can contribute

to low ionization species, like NII, SII, $H\alpha$, $H\beta$, and OII [35, 36]. In NGC628, we see systematic changes in line ratios as a function of the distance from an $H\alpha$ emission peak: in the case of a relatively low metallicity (~ 8.4) region we find an increasing $[NII]\lambda 6584/H\alpha$ ratio and a decreasing $[OIII]\lambda 5007/H\beta$ ratio (see the examples in Figure 7 for NGC 628), while for a relatively high metallicity (~ 8.8) region, these line ratio variations are inverted (see the examples in Figure 8 for NGC 628). These behaviors are to be discussed in terms of the DIG contribution and variation in the HII region conditions, but they clearly point out here to the importance of the spatial resolution when defining and characterizing HII regions and observing accurate metallicity gradient. As shown by the pixel-by-pixel O3N2 metallicity map of NGC 628 (Figure 9), if one uses a larger aperture to study the HII regions, it will have an impact on the abundance estimate for

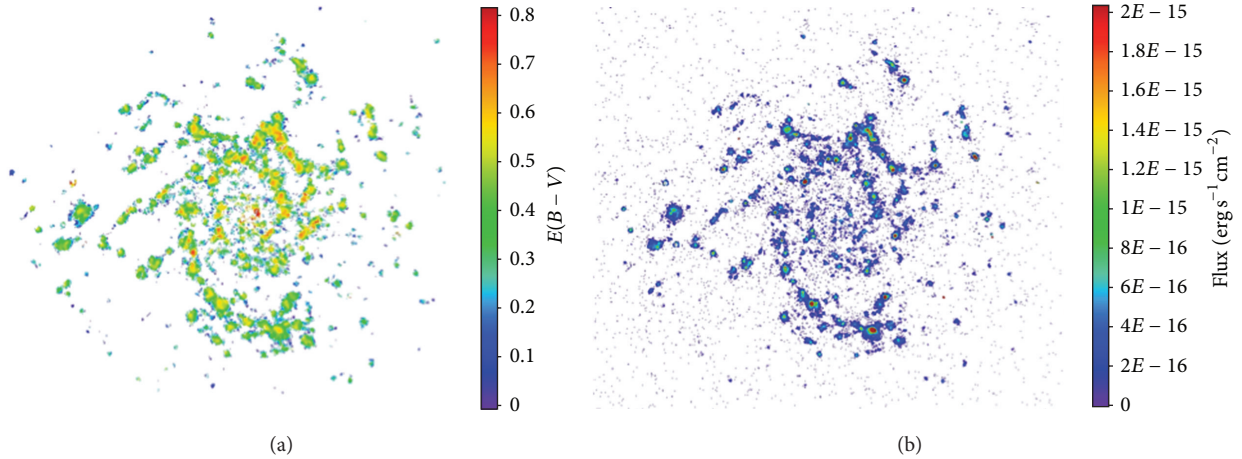


FIGURE 5: (a) NGC 628 dust extinction map from the $H\alpha/H\beta$ ratio. (b) NGC 628 dust-corrected $H\alpha$ flux map. Pixel size is 50.5 parsec^2 for a distance of 9.7 Mpc. The field of one CALIFA pointing is shown in the top right corner.

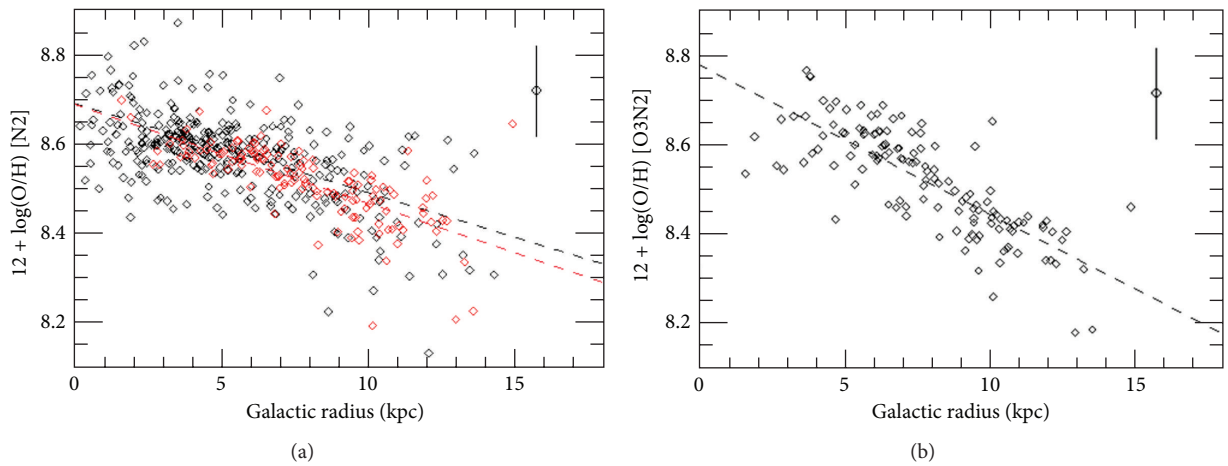


FIGURE 6: (a) Metallicity gradient of NGC628 derived using the N2 indicator from PP04 and the HII regions defined with HIIphot. The black diamonds (and their corresponding linear fit given by the black dash curve) is obtained using all the HII regions identified. The red diamonds (and corresponding dash red linear fit) are for the 134 regions that can also be characterized with the O3N2 indicator. (b) Metallicity gradient derived using the O3N2 indicator from PP04 and 134 HII regions defined with HII phot. Typical error bars are shown on the plot.

each region and also on the galaxy metallicity gradient. DIG effects on the characterization of extragalactic HII regions are going to be discussed in future publications.

4. Elliptical Galaxies: Absorption Lines

4.1. Absorption Lines Extraction. The vast majority of commercially available FTS use this technique to measure the strength of absorption lines in their target spectra. So nothing in the iFTS concept prevents it from obtaining spectra of continuum sources with absorption features. However, the multiplex disadvantage discussed above increases the noise level for a given spectral element compared to dispersive spectroscopy. This distributed noise recorded in the interferogram (photon noise from the entire bandpass contributes to the recorded signal at each mirror step) is transferred to the spectrum after the FFT.

Figure 10 shows a simplified example of distributed noise. Given two sources of equal total flux, one with emission and one with absorption, it is clear that the interferograms are utterly different even if the mean value is the same. The emission line shows large variation in its interferogram while they fade quickly for the absorption line. In this example, only a \sqrt{N} photon noise is applied and, since the mean flux is the same for both lines, the average level of noise is about the same. This in turn produces a level of noise in the spectra that is also about the same for both. It is then easy to see that if one were to extract the profile of both lines, the level of noise compared to the flux in the line would be much higher for the absorption feature. For the same mean flux in the bandwidth covered by the filter, spectra dominated by emission lines will show a greater SNR than spectra of continuum sources with absorption lines. Stellar spectra have been nevertheless obtained on a regular basis with SpIOMM; some are shown

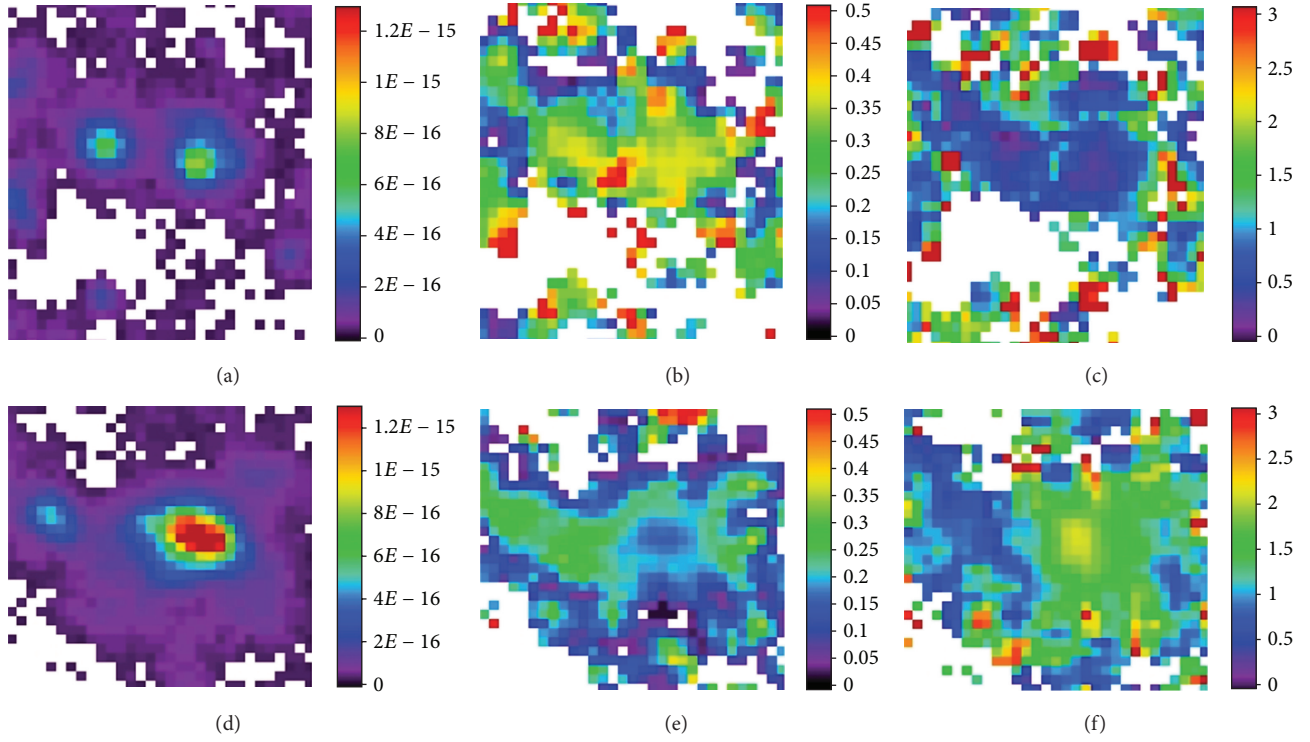


FIGURE 7: Images of HII regions located at RA = 1 h 36 m 38.9 s, DEC = 15 d 44 m 24.8 s with $12 + \log(O/H) \sim 8.4$ ((a), (b), and (c)), and at RA = 1 h 36 m 38.4 s, DEC = 15 d 47 m 00.9 s with $12 + \log(O/H) \sim 8.8$ ((d), (e), and (f)). In both cases, the image on the left shows the H α maximum intensity [$\text{erg s}^{-1} \text{cm}^{-2}$], center: [NII] λ 6584/H α , right: [OIII] λ 5007/H β . FOV is $33'' \times 33''$, North at the top, East to the left.

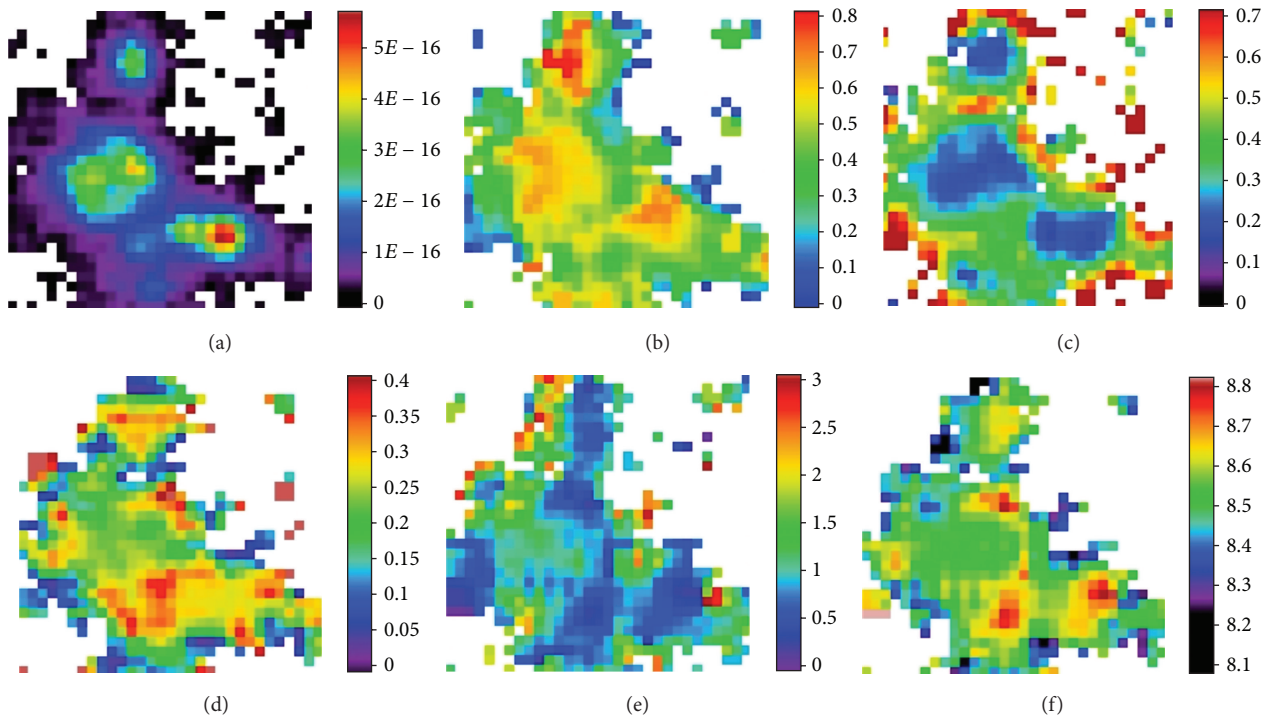


FIGURE 8: Images centered on HII regions located around RA = 1 h 36 m 46.5 s, DEC = 15 d 48 m 56.8 s. Top left: H α maximum intensity [$\text{erg s}^{-1} \text{cm}^{-2}$], top center: $E(B-V)$, top right: [SII] λ 6717+6731/H α , bottom left: [NII] λ 6584/H α , bottom center: [OIII] λ 5007/H β , and bottom right: O3N2 indicator from PP04. FOV is $33'' \times 33''$, North at the top, East to the left.

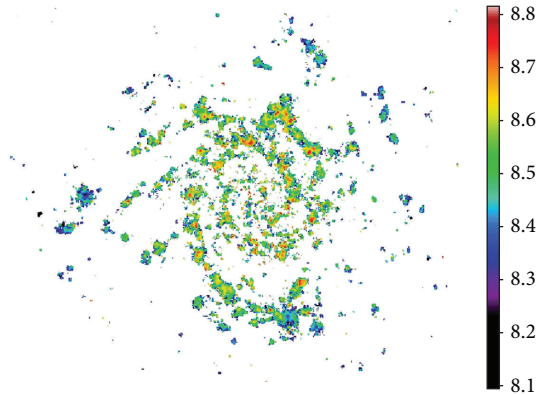


FIGURE 9: Pixel-by-pixel metallicity map using O3N2 indicator from PP04. FOV is $12' \times 12'$.

in Figure 11. In fact, all SpIOMM data cubes include stars for which spectra can be extracted.

It is then obvious that an iFTS is not the ideal instrument to observe individual stars. However, the wide field of view provided by SpIOMM allows observations of hundreds of stars simultaneously, as well as extended absorption line sources, which compensates for the multiplex disadvantage. Cubes of open clusters were obtained, and a technique was developed to optimize the extraction of the stellar interferograms, taking into account seeing variations during the cube acquisition; results will be presented elsewhere.

4.2. The Case of M87. To quantify SpIOMM's ability to provide scientifically useful absorption spectra of an extended source, we targeted the giant elliptical galaxy M87 using SpIOMM's custom V filter (538–649 nm). Our primary goal was to compare SpIOMM's data with those obtained from direct imagery and long-slit spectroscopy. Using IRAF's STSDAS package, we first extracted luminosity profiles and isophotes from the panchromatic image obtained by combining all slices from the spectral cube (see Figure 12(a)). Our data being in excellent agreement with multiband imagery from Liu et al. [37], we then extracted spectra along isophotal lines at different galactocentric radii, shown in Figure 12(b). The spectra show many interesting features, the two most important being a molecular TiO band on the red side and the sodium doublet line (NaD) in the center near 5900 Å.

In order to compare our data with those obtained by Davidge [17] with a long-slit spectrograph at the Canada-France-Hawaii 3.6 m Telescope, we extracted the NaD index as defined by Worthey and Ottaviani [38] as well as this line's equivalent width determined from a fitted Gaussian profile. These values are compared in Figure 13, which shows a clear negative gradient with increasing galactocentric radius. Our Lick NaD index values are slightly lower than Davidge's, on average, but this is mostly due to our lower spectral resolution (1.2 nm compared to 0.6 nm). Correction suggested by Vazdekis et al. [39] to compensate for this would add about 0.4 Å to our values which would bring them closer to Davidge's but would not affect the slope of the gradient which is similar.

The extraction of scientific data from absorption features in an extended object like a galaxy is proving to be feasible. Both visual and spectral data obtained on the source with the imaging FTS SpIOMM are in good agreement with the literature. Stability is of the essence during the observation to ensure the best possible SNR on the absorption features. This is particularly important for SITELLE, which should enable much more detailed and precise study of absorption features due to its more stable design compared with SpIOMM.

5. Next Steps: SITELLE and SNAGS

5.1. SITELLE. SpIOMM has been a wonderful prototype to work with and to learn from, special thanks to our privileged access to the well-equipped 1.6 m telescope at the Observatoire du Mont Mégantic, where observing conditions can be harsh, especially in winter when temperatures can drop to -30°C . But the full advantages of the iFTS technology can only be attained with a more robust instrument installed on a large telescope with excellent sky conditions. Our team therefore designed and built SITELLE, an iFTS accepted as a guest instrument by the Canada-France-Hawaii Telescope (CFHT). All the lessons learned from our regular use of SpIOMM have been implemented in the design of SITELLE [40, 41] and its data reduction software, ORBS [42]. SITELLE's field of view and maximum spectral resolution (resp., $11' \times 11'$ and $R \sim 25000$) are very similar to SpIOMM's, but its performance will be greatly enhanced, especially in the near UV, thanks to very high quality optics within the interferometer cavity ($\lambda/30$), more robust metrology, servo mechanism, and structural stiffness leading to very low mirror jitter (~ 10 nm RMS), as well as high QE, and low read noise $2k \times 2k$ CCDs by e2v. Thanks to four readout amplifiers on each CCD, readout time is ~ 3 s, thereby increasing the overall efficiency of the instrument. The overall throughput of SITELLE, including modulation efficiency and detectors' quantum efficiency, is shown in Figure 14. Spatial sampling is also improved ($0.32''$ pixels) to match the excellent seeing provided by the CFHT. Sky brightness on Mauna Kea is also remarkably low, significantly improving the detectability of faint sources. If all these factors are taken into account, we estimate that SITELLE at the CFHT will be about 15 times more sensitive at 350 nm and 6 times more at 700 nm than SpIOMM at OMM.

At the time of writing, SITELLE is in the final phases of integration and testing, for a planned delivery at the CFHT in early 2014. First light, commissioning, and science verification will occur soon after. As a guest instrument, SITELLE will be accessible to all CFHT partners. The long list of projects presented at a workshop organized in May 2013 (<http://www.craq-astro.ca/sitelles/talk.php>) has demonstrated the interest of the CFHT community (and beyond) for this instrument in areas as diverse as comets, star clusters, nearby galaxies, and high redshift Lyman- emitters. As demonstrated by Graham et al. [43] in a paper describing the rationale for equipping a space-based IR telescope with an iFTS, such an instrument is a very powerful tool to study distant galaxies in a relatively unbiased way. At very low flux levels, sky background sets the detection limits of emission-line

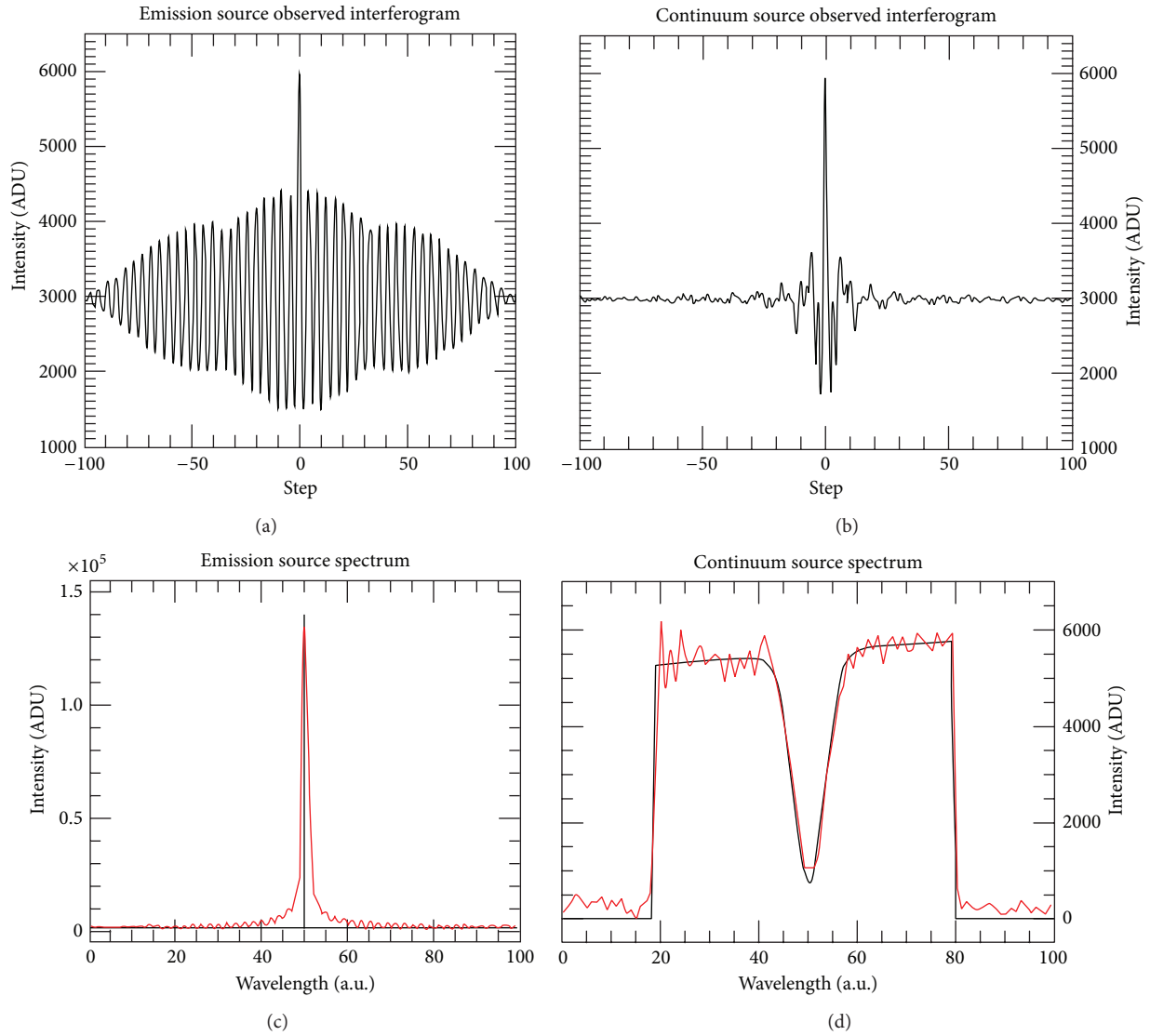


FIGURE 10: Comparison between simulated emission and absorption lines spectra.

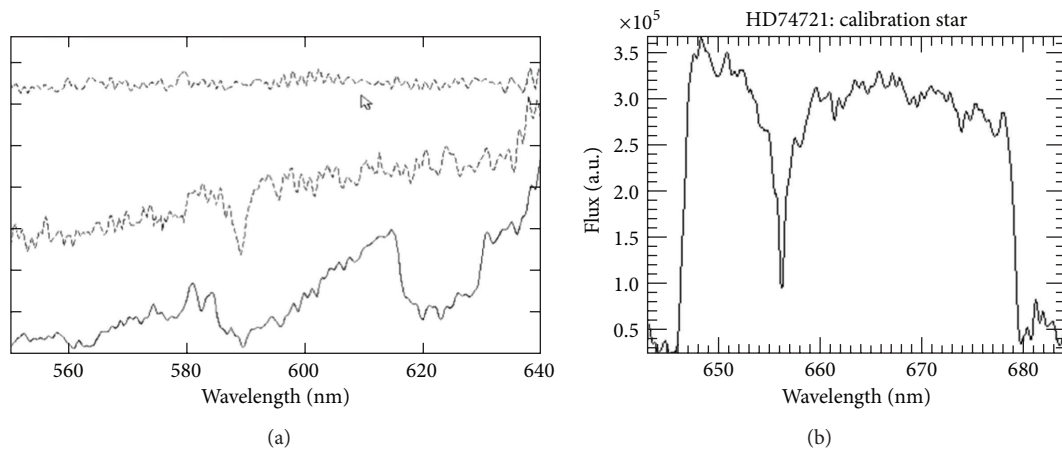


FIGURE 11: (a) Spectra of the 15th magnitude stars in the field of the planetary nebula M27; from top to bottom: the central white dwarf (featureless, as expected, in this wavelength range), a solar-type star with the NaD 5890, 96 lines, and an M star showing TiO bands. (b) Spectrum of the standard horizontal branch A-star HD 74721 used to flux-calibrate the NGC 628 data cube (see above).

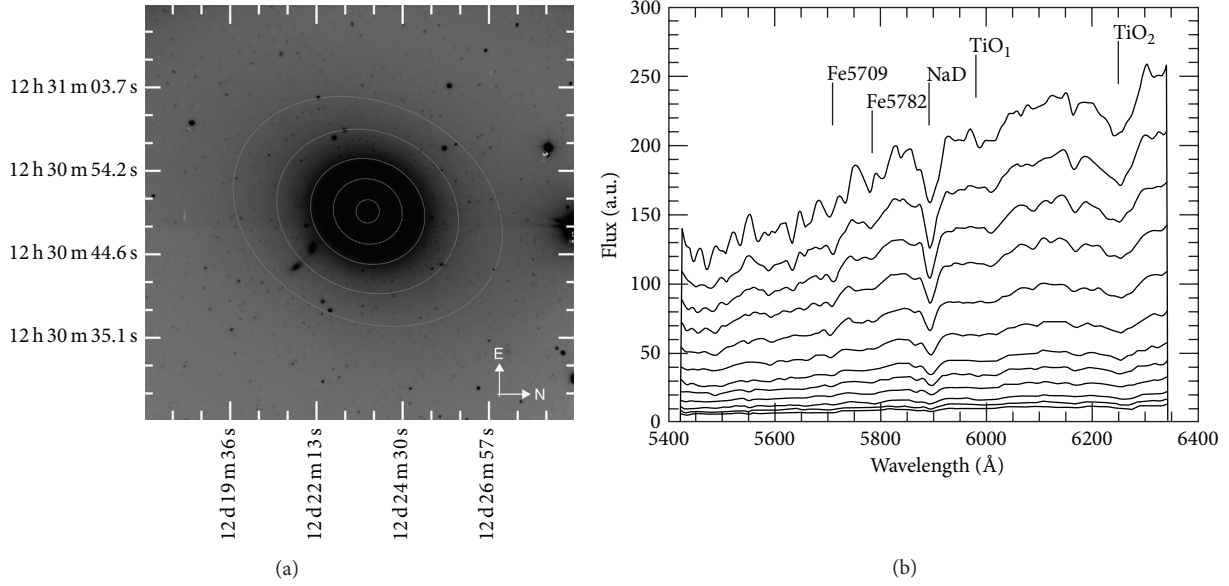


FIGURE 12: (a) Deep panchromatic V-band image of M87 extracted from the data cube showing some isophotes used to extract spectra. (b) Deredshifted radial spectra of M87. From top to bottom, $\log r$ (arcsec) = 0.79, 0.93, 1.06, 1.17, 1.25, 1.35, 1.46, 1.54, and 1.61.

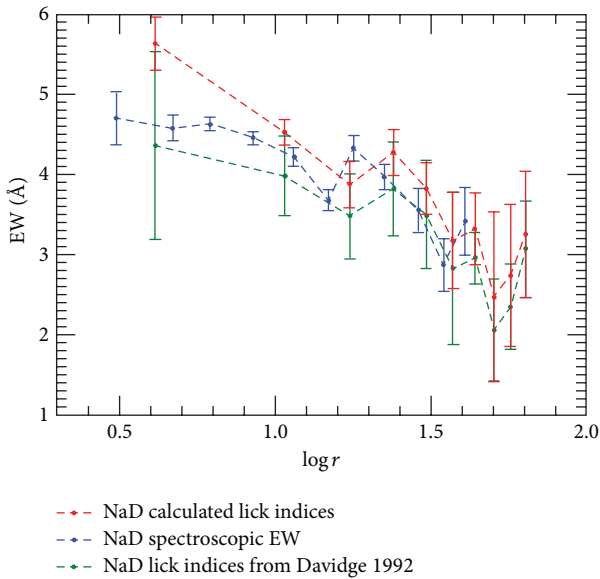


FIGURE 13: Strength of the NaD absorption line in the spectra of M87 at different galactocentric radii obtained from the SpIOMM data cube with two different methods and compared with Davidge [17].

sources; visible-band sky background on Mauna Kea being very similar to that of IR background in space, SITELLE can be seen as the ground-based version of Graham’s proposed iFTS. The power of SITELLE in this type of study is that it will sample the redshift space uniformly on a wide field, allowing unbiased spectroscopic redshift determination and line profile analysis on several galaxies per cube. In order to follow up on the SpIOMM work presented in this paper,

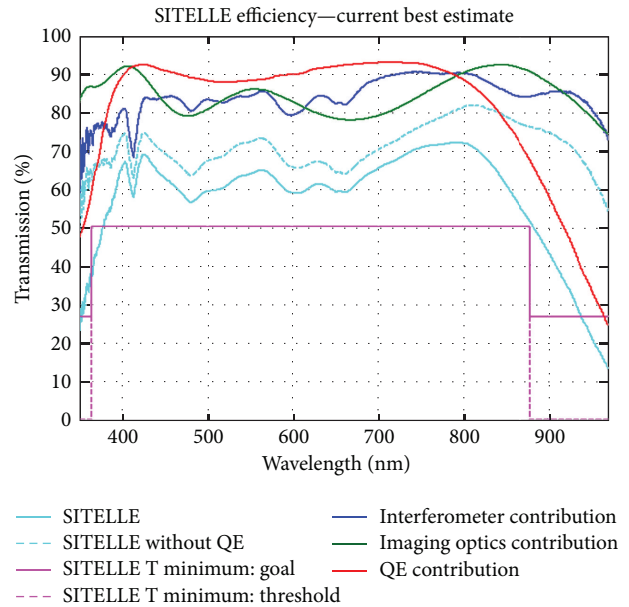


FIGURE 14: SITELLE’s expected combined throughput, including modulation efficiency.

the next section summarizes the plans for a survey of nearby galaxies, SNAGS.

5.2. SNAGS. Powerful constraints on models of galactic evolution and the dynamical processes that transform galaxies are derived from homogeneous determinations of chemical abundances in individual gaseous nebulae, the distribution of their stellar populations in terms of age and metallicity,

and the gaseous and stellar kinematics. With its efficient and versatile 3D spectroscopic capabilities over a large field-of-view, SITELLE offers an opportunity to study these evolution constraints in a significant number of large, nearby disk galaxies. Recent examples of using integral field capabilities to study nearby disk galaxies show the full potential of this technique to assess nebular abundances and stellar metallicity [28]. We are currently planning to conduct a survey (SNAGS) of a sample of ~ 75 large ($D > 3'$), nearby spirals with SITELLE at CFHT. Our main objectives are (1) to determine the spatial distribution of nebular abundances across their disk and assess radial, azimuthal, and local variations within different galaxy components (i.e., bars, arm and interarm regions, and outer disk), (2) to reconstruct their star formation history through stellar populations, and (3) to map the gaseous and stellar kinematics and study the diverse dynamical processes governing large-scale star formation and mixing within their disks.

As demonstrated by other papers in this volume, SNAGS is not the first project aiming at integral field spectroscopy of a large sample of nearby galaxies. One of the earliest and most successful is the SAURON survey, mostly concentrating on early-type galaxies [44, 45]. But by far the most similar programs are CALIFA [46–48] and VENGA [49, 50]. The science objectives of SNAGS will be distinguished from those of the other two projects by the main advantages of its instrumental setting: significantly higher spatial resolution (limited only by CFHT's exceptional image quality and SITELLE's pixel size of $0.32''$) with 100% filling factor; higher spectral resolution ($R \sim 2000$) which, combined with a very precise wavelength calibration inherent to the iFIS concept, will allow detailed kinematics studies on very small scales; very wide field of view which, combined with SITELLE's high throughput from the near UV across the visible range and Mauna Kea's dark sky, will allow us to probe the outermost regions of galaxies.

Our preliminary sample of galaxies includes objects of different morphologies, masses, and environment. For instance, several objects with bars will be observed to investigate the potential role of nonasymmetrical components in triggering/quenching star formation and in mixing chemical elements in galaxy disks. Other objects with star formation in their very outer disks (e.g., identified from GALEX observations) were selected to evaluate large-scale breaks in radial abundance gradients and to study chemical processes at the periphery of these disks [51]. SNAGS will obtain spectrophotometrically calibrated data cubes within three spectral ranges to cover the strong lines from $[\text{OII}]\lambda 3727$ to $[\text{SII}]\lambda\lambda 6717, 6731$. Nebular abundances will be determined using several line-ratio methods and calibrations (e.g., R_{23} , $N2\text{Ha}$, and O3N2 , see Kewley and Zahid [52] for a review); complementary observations on larger telescopes will be obtained for a smaller sample of galaxies to derive the abundances through “direct” auroral line measurements in order to evaluate the “indirect” methods. Gas kinematics on a small-scale will be studied using moderate resolution ($R \sim 4000$) for all three spectral ranges. Current studies so far (e.g., CALIFA and VENGA) have concentrated on global properties (abundance gradients) in galaxies. SNAGS

will also assess small-scale variations caused by multiphase stellar winds, enrichment by starburst clusters in peculiar evolutionary stages, and dynamical processes. SITELLE is an ideal instrument to concentrate on these small-scale (< 100 pc) variations and establish conditions under which they take place. A pilot study for SNAGS will be carried out during the science verification phase for the instrument planned for early 2014, with the survey itself starting later on after final commissioning.

6. Conclusions

We have presented in this paper the iFIS as a viable approach to integral field spectroscopy. The regular use of SpIOMM and preliminary tests performed with SITELLE have demonstrated that the technical challenges imposed by the very stringent requirements on the optical quality of an iFIS components as well as its metrology and servo system have been overcome and now they allow us to reach a high modulation efficiency in the visible and the near UV.

The science niche for the iFIS approach must take into account its main advantages (very wide field of view, high throughput, seeing-limited image quality, and flexible spectral resolution) and disadvantages (spectrally distributed noise, and necessary compromise between spectral coverage and resolution) compared with standard integral field spectrographs. Although the original, single-pixel FIS was classically known for its ability to obtain very high spectral resolution (R up to 10^5), the “sweet-spot” of the astronomical iFIS clearly sits in the observations of extended emission-line sources at low-to-moderate values of R . One can however still exploit the high spectral resolution capability of an iFIS by using narrow-band filters and use it for absorption line studies as well.

The arrival of SITELLE on a 4 m class telescope (CFHT) under exceptional skies, where it will be used for a wide variety of science projects, will better define the iFIS niche and its capabilities.

Conflict of Interests

The authors declare that there is no conflict of interests regarding the publication of this paper.

Acknowledgments

We would like to acknowledge financial contributions from the Canadian Foundation for Innovation, the Canadian Space Agency, the Natural Sciences and Engineering Council of Canada, the Fonds Québécois de la Recherche sur la Nature et les Technologies, the Canada-France-Hawaii Telescope, and Université Laval. We also thank Ghislain Turcotte, Bernard Malenfant, and Pierre-Luc Lévesque for their help at the telescope and the CFHT team led by Marc Baril for their exquisite work on the detector system for SITELLE and its implementation at the telescope.

References

- [1] J. C. Mather, E. S. Cheng, R. E. Eplee Jr. et al., "A preliminary measurement of the cosmic microwave background spectrum by the cosmic background explorer (COBE) satellite," *The Astrophysical Journal*, vol. 354, pp. L37–L40, 1990.
- [2] H. P. Gush, M. Halpern, and E. H. Wishnow, "Rocket measurement of the cosmic-background-radiation mm-wave spectrum," *Physical Review Letters*, vol. 65, no. 5, pp. 537–540, 1990.
- [3] N. Scoville, D. N. B. Hall, S. G. Kleinmann, and S. F. Ridgway, "Detection of CO band emission in the Becklin-Neugebauer object," *The Astrophysical Journal*, vol. 232, pp. L121–L124, 1979.
- [4] S. T. Ridgway, D. F. Carbon, D. N. B. Hall, and J. Jewell, "An atlas of late-type stellar spectra, 2400–2778 inverse centimeters," *The Astrophysical Journal, Supplement Series*, vol. 54, pp. 177–209, 1984.
- [5] A. A. Chalabaev and J. P. Maillard, "Near-infrared spectroscopy of gamma cassiopeiae—constraints on the velocity field in the envelope," *The Astrophysical Journal*, vol. 294, pp. 640–645, 1985.
- [6] J. P. Maillard, J. Crovisier, T. Encrenaz, and M. Combes, "The spectrum of comet p/Halley between 0.9-MICRONS and 2.5-MICRONS," *Astronomy and Astrophysics*, vol. 187, p. 398, 1987.
- [7] J. P. Maillard and D. Simons, "Progress in telescope and instrumentation technologies," in *Proceedings of the ESO Conference Workshop*, p. 733, 1992.
- [8] T. Paumard, J.-P. Maillard, and M. Morris, "Kinematic and structural analysis of the minispiral in the galactic center from BEAR spectro-imagery," *Astronomy and Astrophysics*, vol. 426, no. 1, pp. 81–96, 2004.
- [9] R. Wu, E. T. Polehampton, M. Etxaluze et al., "Observing extended sources with the Herschel SPIRE fourier transform spectrometer," *Astronomy and Astrophysics*, vol. 556, article A116, 11 pages, 2013.
- [10] W. Posselt, J.-P. Maillard, and G. Wright, "NIRCAM-IFTS: imaging fourier transform spectrometer for NGST," in *NGST Science and Technology Exposition*, vol. 207 of *Astronomical Society of the Pacific Conference Series*, p. 303, 2000.
- [11] J. R. Graham, "IFIRS: an imaging Fourier transform spectrometer for the next generation space telescope," in *NGST Science and Technology Exposition*, vol. 207 of *Astronomical Society of the Pacific Conference Series*, p. 240, 2000.
- [12] S. L. Morris, J. Ouellette, A. Villemaire, F. Grandmont, and L. Moreau, "A Canadian IFTS for the NGST," in *NGST Science and Technology Exposition*, vol. 207 of *Astronomical Society of the Pacific Conference Series*, p. 276, 2000.
- [13] F. Boulanger, J. P. Maillard, P. Appleton et al., "The molecular hydrogen explorer H2EX," *Experimental Astronomy*, vol. 23, no. 1, pp. 277–302, 2008.
- [14] C. L. Bennett, "Critical comparison of 3-D imaging approaches (review)," in *Imaging the Universe in Three Dimensions: Astrophysics with Advanced Multi-Wavelength Imaging Devices*, vol. 195 of *Astronomical Society of the Pacific Conference Series*, p. 58, 2000.
- [15] L. Drissen, A. P. Bernier, M. Charlebois, A. Alarie, F. Grandmont, and J. Mandar, "Imaging Fourier transform spectroscopy for astronomy," in *Fourier Transforms—New Analytical Approaches and FTIR Strategies*, G. Nikolic, Ed., chapter 23, InTech, Rijeka, Croatia, 2011.
- [16] J. P. Maillard, L. Drissen, F. Grandmont, and S. Thibault, "Integral wide-field spectroscopy in astronomy: the imaging FTS solution," *Experimental Astronomy*, vol. 35, no. 3, pp. 527–559, 2013.
- [17] T. J. Davidge, "Spectroscopic gradients in bright elliptical galaxies," *The Astronomical Journal*, vol. 103, no. 5, pp. 1512–1525, 1992.
- [18] F. Grandmont, *Développement d'un spectromètre imageur à transformée de Fourier pour l'astronomie [Ph.D. thesis]*, Université Laval, 2007.
- [19] D. Lagrois, G. Joncas, and L. Drissen, "Diagnostic line ratios in the IC1805 optical gas complex," *Monthly Notices of the Royal Astronomical Society*, vol. 420, no. 3, pp. 2280–2299, 2012.
- [20] D. Lagrois, L. Drissen, and G. Joncas, Submitted to *Monthly Notices of the Royal Astronomical Society*.
- [21] M. Charlebois, L. Drissen, A.-P. Bernier, F. Grandmont, and L. Binette, "A hyperspectral view of the crab nebula," *The Astronomical Journal*, vol. 139, no. 5, pp. 2083–2096, 2010.
- [22] A. Alarie, A. Bilodeau, and L. Drissen, *Monthly Notices of the Royal Astronomical Society*. In press.
- [23] F. Grandmont, L. Drissen, and G. Joncas, "Development of an imaging Fourier transform spectrometer for astronomy," in *Specialized Optical Developments in Astronomy*, vol. 4842 of *Proceedings of SPIE*, pp. 392–401, Waikoloa, Hawaii, USA, August 2002.
- [24] A.-P. Bernier, F. Grandmont, J.-F. Rochon, M. Charlebois, and L. Drissen, "First results and current development of SpIOMM: an imaging Fourier transform spectrometer for astronomy," in *Ground-Based and Airborne Instrumentation for Astronomy*, vol. 6269 of *Proceedings of SPIE*, p. 135, Orlando, Fla, USA, May 2006.
- [25] A.-P. Bernier, L. Drissen, P. Charlebois et al., "Science results from the imaging Fourier transform spectrometer SpIOMM," in *2nd Ground-Based and Airborne Instrumentation for Astronomy*, vol. 7014 of *Proceedings of SPIE*, Marseille, France, June 2008.
- [26] L. Drissen, A. Alarie, T. Martin et al., "New scientific results with SpIOMM: a testbed for CFHT's imaging Fourier transform spectrometer SITELLE," in *4th Ground-Based and Airborne Instrumentation for Astronomy*, vol. 8446 of *Proceedings of SPIE*, Amsterdam, The Netherlands, July 2012.
- [27] D. A. Thilker, R. Braun, and R. A. M. Walterbos, "HIphot: automated photometry of H II regions applied to M51," *The Astronomical Journal*, vol. 120, no. 6, pp. 3070–3087, 2000.
- [28] S. F. Sánchez, F. F. Rosales-Ortega, R. C. Kennicutt et al., "PPAK wide-field integral field spectroscopy of NGC 628—I. The largest spectroscopic mosaic on a single galaxy," *Monthly Notices of the Royal Astronomical Society*, vol. 410, no. 1, pp. 313–340, 2011.
- [29] R. C. Kennicutt, J. C. Lee, J. G. Funes, S. Sakai, and S. Akiyama, "An H α imaging survey of galaxies in the local 11 Mpc volume," *The Astrophysical Journal, Supplement Series*, vol. 178, no. 2, pp. 247–279, 2008.
- [30] C. G. Hoopes, R. A. M. Walterbos, and G. D. Bothun, "Far-ultraviolet and H α imaging of nearby spiral galaxies: the OB stellar population in the diffuse ionized gas," *The Astrophysical Journal Letters*, vol. 559, no. 2, pp. 878–891, 2001.
- [31] R. C. Kennicutt, "Star formation in galaxies along the hubble sequence," *Annual Review of Astronomy and Astrophysics*, vol. 36, pp. 189–231, 1998.
- [32] M. Pettini and B. E. J. Pagel, "[O III]/[N II] as an abundance indicator at high redshift," *Monthly Notices of the Royal Astronomical Society*, vol. 348, no. 3, pp. L59–L63, 2004.

- [33] L. J. Kewley and M. A. Dopita, “Using strong lines to estimate abundances in extragalactic H II regions and starburst galaxies,” *The Astrophysical Journal, Supplement Series*, vol. 142, no. 1, pp. 35–52, 2002.
- [34] G. A. Blanc, A. Heiderman, K. Gebhardt, N. J. Evans II, and J. Adams, “The spatially resolved star formation law from integral field spectroscopy: VIRUS-P observations of NGC 5194,” *The Astrophysical Journal*, vol. 704, no. 1, pp. 842–862, 2009.
- [35] L. M. Haffner, R. J. Reynolds, and S. L. Tufte, “WHAM observations of H α , [S II], and [N II] toward the Orion and perseus arms: probing the physical conditions of the warm ionized medium,” *The Astrophysical Journal*, vol. 523, no. 1, pp. 223–233, 1999.
- [36] B. Otte, R. J. Reynolds, J. S. Gallagher III, and A. M. N. Ferguson, “Searching for additional heating: [O II] emission in the diffuse ionized gas of NGC 891, NGC 4631, and NGC 3079,” *The Astrophysical Journal*, vol. 560, no. 1, pp. 207–221, 2001.
- [37] Y. Liu, X. Zhou, J. Ma, Y. Yang, J. Li, and J. Chen, “Deep surface photometry of M87 with 13 optical bands,” *The Astrophysical Journal*, vol. 129, no. 6, pp. 2628–2635, 2005.
- [38] G. Worthey and D. L. Ottaviani, “Hy and H δ absorption features in stars and stellar populations,” *The Astrophysical Journal, Supplement Series*, vol. 111, no. 2, pp. 377–386, 1997.
- [39] A. Vazdekis, P. Sanchez-Blazquez, J. Falcon-Barroso et al., “Evolutionary stellar population synthesis with MILES—I. The base models and a new line index system,” *Monthly Notices of the Royal Astronomical Society*, vol. 404, no. 4, pp. 1639–1671, 2010.
- [40] L. Drissen, A.-P. Bernier, L. Rousseau-Nepton et al., “SITELE: a wide-field imaging Fourier transform spectrometer for the Canada-France-Hawaii telescope,” in *3rd Ground-Based and Airborne Instrumentation for Astronomy*, vol. 7735 of *Proceedings of SPIE*, July 2010.
- [41] F. Grandmont, L. Drissen, J. Mandar, S. Thibault, and M. Baril, “Final design of SITELE: a wide-field imaging Fourier transform spectrometer for the Canada-France-Hawaii telescope,” in *4th Ground-Based and Airborne Instrumentation for Astronomy*, vol. 8446 of *Proceedings of SPIE*, October 2012.
- [42] T. Martin, L. Drissen, and G. Joncas, “ORBS: a data reduction software for the imaging Fourier transform spectrometers SpI-OMM and SITELE,” in *2nd Software and Cyberinfrastructure for Astronomy*, vol. 8451 of *Proceedings of the SPIE*, Amsterdam, The Netherlands, July 2012.
- [43] J. R. Graham, M. Abrams, C. Bennett et al., “The performance and scientific rationale for an infrared imaging Fourier transform spectrograph on a large space telescope,” *Publications of the Astronomical Society of the Pacific*, vol. 110, pp. 1205–1215, 1998.
- [44] R. Bacon, Y. Copin, G. Monnet et al., “The SAURON project—I. The panoramic integral-field spectrograph,” *Monthly Notices of the Royal Astronomical Society*, vol. 326, no. 1, pp. 23–35, 2001.
- [45] H. Kuntschner, E. Emsellem, R. Bacon et al., “The SAURON project—XVII. Stellar population analysis of the absorption line strength maps of 48 early-type galaxies,” *Monthly Notices of the Royal Astronomical Society*, vol. 408, no. 1, pp. 97–132, 2010.
- [46] E. Marmol-Queralto, S. F. Sánchez, R. A. Marino et al., “Integral field spectroscopy of a sample of nearby galaxies I. Sample, observations, and data reduction,” *Astronomy and Astrophysics*, vol. 534, article A8, 2011.
- [47] S. Sanchez, F. F. Rosales-Ortega, R. A. Marino et al., “Integral field spectroscopy of a sample of nearby galaxies II. Properties of the H II regions,” *Astronomy and Astrophysics*, vol. 546, article A2, 28 pages, 2012.
- [48] J. Iglesias-Paramo, J. M. Vílchez, L. Galbany et al., “Aperture corrections for disk galaxy properties derived from the CALIFA survey: balmer emission lines in spiral galaxies,” *Astronomy and Astrophysics*, vol. 553, article L7, 5 pages, 2013.
- [49] G. A. Blanc, A. Heiderman, K. Gebhardt, N. J. Evans II, and J. Adams, “The spatially resolved star formation law from integral field spectroscopy: VIRUS-P observations of NGC 5194,” *The Astrophysical Journal*, vol. 704, no. 1, p. 842, 2009.
- [50] G. A. Blanc, T. Weinzirl, M. Song et al., “The VIRUS-P exploration of nearby galaxies (VENGA): survey design, data processing, and spectral analysis methods,” *The Astrophysical Journal*, vol. 145, no. 5, p. 138, 2013.
- [51] F. Bresolin, “Clues on the rejuvenation of the S0 galaxy NGC 404 from the chemical abundance of its outer disk,” *The Astrophysical Journal*, vol. 772, no. 2, p. L23, 2013.
- [52] L. Kewley and H. J. Zahid, “Strong-line methods for oxygen abundance determinations in giant HII regions and emission line galaxies: methods and uncertainties,” Mapping Oxygen in the Universe, 2012, <http://www.iac.es/congreso/oxygenmap/pages/electronic-presentations.php>.

Review Article

The Integral Field View of the Orion Nebula

Adal Mesa-Delgado

Instituto de Astrofísica, Facultad de Física, Pontificia Universidad Católica de Chile, Avenida Vicuña Mackenna 4860, Macul, 782-0436, Santiago, Chile

Correspondence should be addressed to Adal Mesa-Delgado; amesad@astro.puc.cl

Received 18 October 2013; Accepted 12 December 2013; Published 23 February 2014

Academic Editor: Jorge Iglesias Páramo

Copyright © 2014 Adal Mesa-Delgado. This is an open access article distributed under the Creative Commons Attribution License, which permits unrestricted use, distribution, and reproduction in any medium, provided the original work is properly cited.

This paper reviews the major advances achieved in the Orion Nebula through the use of integral field spectroscopy (IFS). Since the early work of Vasconcelos and collaborators in 2005, this technique has facilitated the investigation of global properties of the nebula and its morphology, providing new clues to better constrain its 3D structure. IFS has led to the discovery of shock-heated zones at the leading working surfaces of prominent Herbig-Haro objects as well as the first attempt to determine the chemical composition of Orion protoplanetary disks, also known as *proplyds*. The analysis of these morphologies using IFS has given us new insights into the abundance discrepancy problem, a long-standing and unresolved issue that casts doubt on the reliability of current methods used for the determination of metallicities in the universe from the analysis of H II regions. Results imply that high-density clumps and high-velocity flows may play an active role in the production of such discrepancies. Future investigations based on the large-scale IFS mosaic of Orion will be very valuable for exploring how the integrated effect of small-scale structures may have impact at larger scales in the framework of star-forming regions.

1. Introduction

H II regions are huge volumes of gas associated with recent star formation. These gaseous clouds are mainly ionized and heated by the stellar ultraviolet (UV) radiation emitted by nearby OB-type stars. The study of the elemental abundances of H II regions is an essential tool for our knowledge of the chemical composition and evolution of the Universe, from the local interstellar medium (ISM) to high-redshift galaxies. We still naively tend to describe them as homogeneous Strömgren spheres, but this idealized picture is rarely observed. Instead, reality turns out to be much more complicated, and such regions are found to be highly structured at all scales with complex internal motions. Their morphology results from the structure of the parent molecular cloud, which is affected over time by the UV radiation, stellar winds, or high-velocity ejections associated with star-formation phenomena.

The Orion Nebula (M42, NGC1976) is one of the best studied objects in the sky and the best studied H II region of our Galaxy. The combination of being the nearest H II region, associated with a young stellar cluster containing massive OB-type stars, and having an apparent high surface

brightness makes this landmark object a fundamental reference of the solar neighborhood and the subject of multiple investigations by state-of-the-art instrumentation at both ground-based and space observatories. There are outstanding papers in the literature that review in great detail our present knowledge of this object. In particular, for a comprehensive view of the nebula and its associated stellar population, readers are referred to the compilation by O'Dell [1] and the references therein.

Although the Orion Nebula has a large extent of more than one-half degree diameter on the sky, most of the radiation comes from the inner part, the so-called Huygens region (Figure 1). This is an active and complex star-forming region, ionized by a group of four massive stars known as the Trapezium cluster. The main ionizing source of this cluster is named θ^1 Ori C (O7V [2]), which is responsible of the bulk of the nebular emission from the main ionization front (MIF). Physical, chemical, kinematical, and structural properties of the MIF have been studied by many authors making use of different observational techniques from X-rays to radio wavelengths (e.g., [3–13]) as well as by means of modeling (e.g., [14–19]).

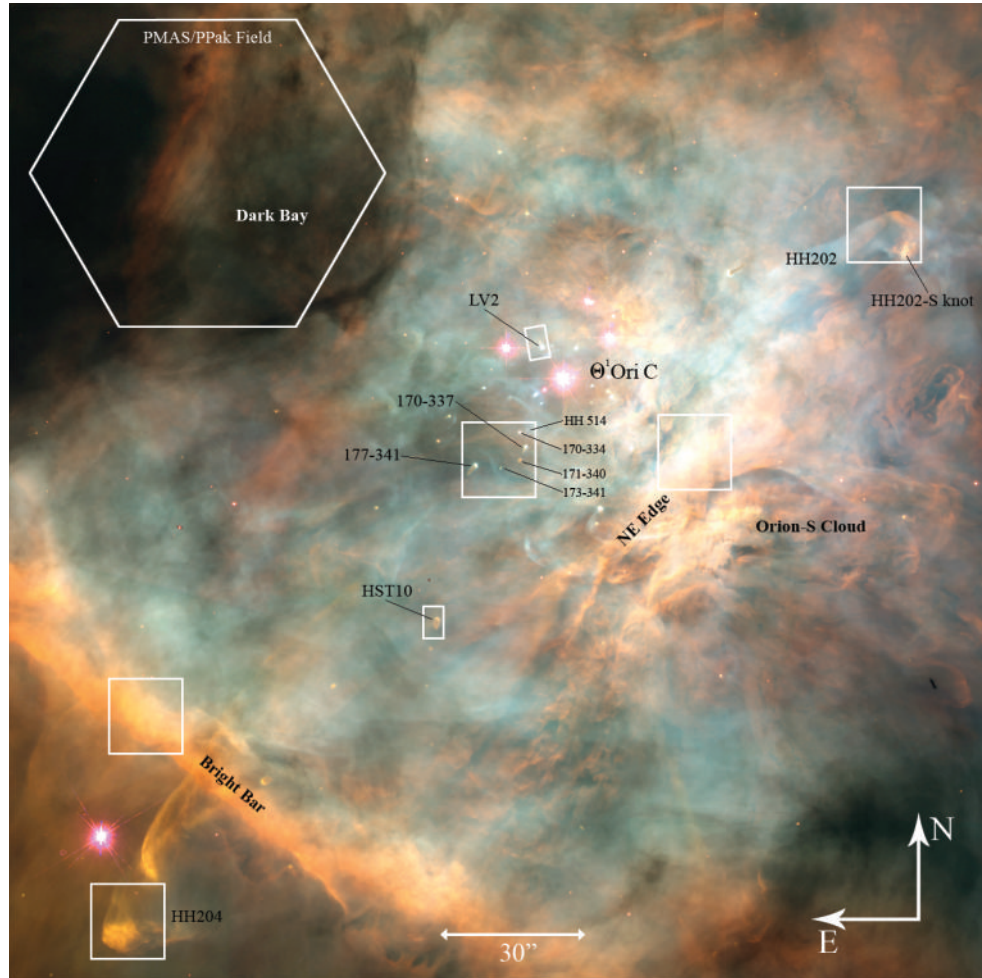


FIGURE 1: Color-composite image of the Huygens region observed with the Wide Field Planetary Camera 2 (WFPC2) on board the Hubble Space Telescope (HST) [6]. The fields of the different IFS studies carried out so far are shown on the image as well as the morphological structures that they contain. Additionally, the location of θ^1 Ori C, the Orion-S Cloud, and the Dark Bay are also marked. Squares represent the PMAS studies with the $16'' \times 16''$ integral field unit (IFU) that provides a spatial resolution of $1'' \times 1''$ [37, 53, 54, 65]. Rectangles show the FLAMES studies using the $6.8'' \times 4.3''$ Argus IFU with a spatial resolution of $0.13'' \times 0.31''$ [51, 66, 67]. The early work of Vasconcelos and collaborators [27] with GMOS on the LV2 proplyd had a slightly smaller field of view and spatial resolution than FLAMES. The field of view of the fiber-based PMAS/PPak mode of about 1 arcmin^2 is presented on the Dark Bay. As it is seen in Figure 8, this IFS mode was used to map the whole Huygens region with a spatial resolution of $2.7''$ [33, 36].

A major characteristic of the Orion Nebula and the Huygens region is that we actually see in great detail the processes related to the ongoing star-formation. The region is well populated with high-velocity outflows, produced by highly energetic ejections of material powered by young pre-main-sequence stars or their possible interactions. Examples of these phenomena are the Herbig-Haro (HH) objects detected in optical studies (e.g., [20–22]) or the molecular outflows observed in the BN/KL and Orion South (Orion-S) regions (e.g., [23, 24]). The Huygens region is also well known for containing hundreds of *proplyds* [25]. This term depicts a special class of protoplanetary disk, resulting from the evolution of a circumstellar disk in the presence of ionizing radiation from massive OB-type stars, and was coined by O’Dell and collaborators [26] to describe the silhouette and tear-drop shaped objects observed in the first imaging studies of the Orion Nebula using the Hubble Space Telescope (HST).

The aim of the present review is to summarize the recent advances that have been achieved in the Orion Nebula through the use of the integral field spectroscopy (IFS). The application of this technique is relatively new in the study of the Orion Nebula and its morphological structures. Indeed, the first work applying IFS in Orion goes back to 2005 [27], where the properties of the famous LV2 proplyd [28] and its associated outflow were studied. Since then, a total of 8 new studies have come out in the literature using this observational technique. Readers are referred to the original works for a detailed description of the reduction and analysis methods. The fields that have been mapped with IFS in these studies are shown in Figure 1. It is noted that up to today IFS has been used to investigate physical, chemical and structural properties of the MIF, HH objects, and proplyds. In the following sections, an extensive revision of these works is presented.

The Orion Nebula is also an excellent testing lab to investigate the abundance discrepancy (AD) problem, one of the major still unresolved issues in the physics of photoionized nebulae (see [29]). This problem arises from the observational fact that chemical abundances of heavy-element ions determined from the bright collisionally excited lines (CELs) are systematically lower than the abundances derived from the faint recombination lines (RLs) emitted by the same ions. IFS studies in the Orion Nebula have found new and interesting clues in the context of this problem, which are also reviewed here.

2. Resolving the Ionization Structure

One of the major capabilities of the IFS is the access to the bidimensional information, allowing us to spatially resolve the ionization structure of the ionized gas in Galactic and nearby extragalactic objects. Studying the ionization structure of the Orion MIF and its physical and chemical properties is a topic that has been addressed by several authors following different observational approaches: echelle and long-slit spectrophotometry (e.g., [9, 11, 15, 30]), Fabry-Perot imaging spectrophotometry [31], and CCD imaging (e.g., [5, 32]). However, it was not until 2007 that this topic was studied in Orion making use of IFS.

Sánchez and collaborators [33] were the first to conduct a global analysis of the Huygens region through IFS. Centered around the Trapezium cluster, a big mosaic was made by these authors from observations with the Potsdam Multi-Aperture Spectrograph (PMAS [34]) at the 3.5 m telescope of Calar Alto Observatory (Almería, Spain). The observations used the fiber-based integral field unit (IFU) of PMAS known as PPAk [35], which provides a hexagonal field of view of about 1 arcmin^2 on the sky and a spatial resolution of $2.7''$ (see Figure 1). Thanks to this dataset, it was possible to analyze the integrated properties of the whole nebula for the first time from spectroscopic observations. The physical conditions derived from this analysis were in general consistent with the results of previous spectroscopic works. An important amount of continuum emission in the blue was observed in the integrated spectra, which might be associated with diffuse continuum emission of scattered light (e.g., [35]). Unfortunately, the spectral and spatial resolution of this dataset were not high enough to address this topic. The spatial distribution maps of emission line fluxes, dust extinction, electron density and temperatures, and the He and O abundances were obtained by these authors and allowed them to detect the effects of well-known morphologies in Orion such as the Bright Bar, the Dark Bay, or prominent HH objects. A relation between the He abundance and the ionization structure that was interpreted as possible deviations of the case B recombination theory was also found. As it will be described in Section 6, this dataset presented certain limitations that have been recently considered, and an improved mosaic of Orion has been obtained with the aim of investigating the previous issues with the required accuracy (see Section 6 and preliminary results in [36]).

Analyzing the MIF is of special interest since it is the transition layer between the fully ionized gas and the neutral

surroundings, where density and temperature gradients are expected. Though the MIF is found in almost every direction towards the Huygens region, only certain geometries allow us to explore its ionization structure in depth. The author of this review and collaborators [37] presented the first dataset devoted to study the ionization structure of the MIF applying IFS on two conspicuous features of Orion: the Bright Bar (BB) and the northeast edge of the Orion-S cloud (NE-Orion-S). The observations were performed with PMAS and the $16'' \times 16''$ IFU. With this setup, emission line fluxes and ratios, physical conditions, and chemical abundances were mapped at spatial scales of $1'' \times 1''$. The location of the fields can be found in Figure 1.

The spatial distribution of the $[\text{O I}]/\text{H}\alpha$, $[\text{N II}]/\text{H}\alpha$, and $[\text{O III}]/\text{H}\beta$ line ratios in both BB and NE-Orion-S fields are plotted in Figure 2 for illustration. The maps clearly show the ionization stratification in the two morphological structures, which is the combined result of different inclination angles along the line of sight and different distances to $\theta^1 \text{ Ori C}$. On the one hand, the BB is located at about $111''$ to the southeast of $\theta^1 \text{ Ori C}$, seen as an elongated structure in both ionized gas (e.g., [20]) and molecular emission (e.g. [38]). In the current picture, the BB is viewed as an escarpment with an average inclination of 7° with respect to the line of sight, where the MIF changes from a face-on to an edge-on geometry [18, 39]. The fact that the MIF is almost edge-on allows us to nicely resolve the ionization structure of the BB as in Figure 2. On the other hand, the NE-Orion-S edge has the peculiarity of being the brightest zone of the Huygens region (see Figure 1), located about $30''$ to the southwest of $\theta^1 \text{ Ori C}$. Recently, the analysis of O'Dell and collaborators [12] suggested that Orion-S is a cloud suspended within the main body of the Orion Nebula in front of the MIF, more tilted than the BB, and ionized only on the side facing to $\theta^1 \text{ Ori C}$. Comparing the ionization structure resolved by PMAS of the BB and NE-Orion-S, it was possible to estimate that the main plane that may contain the NE-Orion-S edge is tilted in average about $48^\circ \pm 13^\circ$ with respect to the line of sight [37].

The PMAS results also showed that the NE-Orion-S is much denser than the BB in consistency with previous studies [31, 33]. Gradients in the electron density, n_e , were observed ranging from 3000 to 5000 cm^{-3} in the BB and from 8000 to $16,000 \text{ cm}^{-3}$ in the NE-Orion-S. The structure of the electron temperature, T_e , turned out rather featureless with relatively low gradients toward the direction of $\theta^1 \text{ Ori C}$. The $T_e([\text{N II}])$ maps presented variations from 9000 to 9600 K in the BB and from 9000 to $10,500 \text{ K}$ in the NE-Orion-S, while the $T_e([\text{O III}])$ ranges from 8200 to 8800 K in the BB and from 8300 to 8800 K in the NE-Orion-S. In the two fields, the maps of total O abundance—as derived from the sum of O^+ and O^{2+} CEL abundances—showed mean values consistent with previous determinations of the literature for the Orion Nebula ($\sim 8.50 \text{ dex}$ [9]). However, rather than being homogeneous as we would expect, they exhibit a structure very similar to the spatial distribution maps of the O^+/H^+ ratio and n_e ($[\text{S II}]$). The most plausible explanation is that collisional de-excitation would be affecting the $[\text{S II}]$ 6717, 6731 Å emission lines because the reported densities

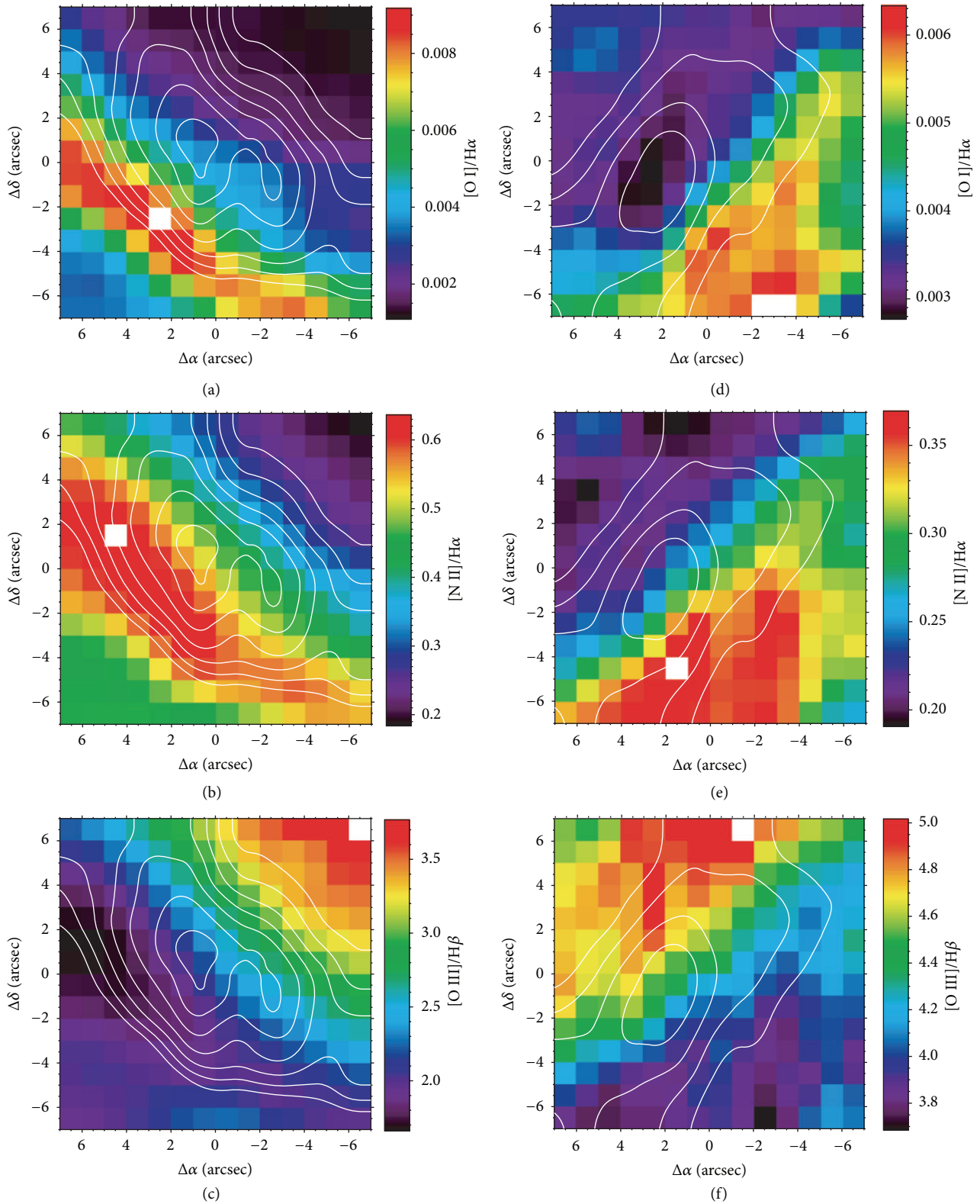


FIGURE 2: Spatial distribution maps of selected emission line ratios for the Bright Bar (left-hand side) and NE-Orion-S (right-hand side) taken from [37]. The sum of $[N II]$ 6548, 6584 Å and $[O III]$ 4959, 5007 Å nebular lines have been used to derive the $[N II]/H\alpha$ (middle) and $[O III]/H\beta$ (bottom) ratios, respectively. $H\alpha$ contours are overplotted in all maps.

are—especially in the case of the NE-Orion-S—close to their critical densities ($\sim 3000 \text{ cm}^{-3}$ for $\lambda 6717$ and $\sim 10,000 \text{ cm}^{-3}$ for $\lambda 6731$). This effect would lead to biased density estimates, which then would affect the chemical abundance calculations, in particular of those ions that are more dependent on the adopted physical conditions, as for instance O^+ (see [37]).

3. Effects of High-Velocity Outflows

In last decades, and especially after the launch of the HST, many outflows such as HH objects or collimated jets have been identified in the central part of the Orion Nebula (see e.g., [40–42]). CCD imaging observations (see e.g. [40]) revealed that several of these high-velocity flows are mainly dominated by photoionization from $\theta^1 \text{ Ori C}$, though the possibility cannot be completely discarded that a partial contribution of shocked gas might still exist. It is important to understand the relevance of this contribution and how it affects to the traditional methods used to determine physical and chemical properties in photoionized gas. In the literature, most spectroscopic studies of Orion HH flows have been focused on studying their gas kinematics (e.g., [21, 22]), while there is an important lack of detailed analysis of their physical and chemical properties as well as their effects on the surrounding media. Until today, this subject has been mainly addressed theoretically (e.g., [43, 44]); and sparsely investigated observationally only making use of high-resolution echelle spectroscopy in a few objects: HH529 [45], the south knot of HH202 (HH202-S [46]), HH888, and HH505 [47], and the microjet arising from the LV2 proplyd [48].

The incorporation of the IFS in the analysis of gas flows in Orion have been attempted since few years ago. Vasconcelos and collaborators [27] were the first using IFS in the Huygens region, focusing on the LV2 proplyd (see Figure 1) and, mainly, on its microjet. Intermediate-resolution ($R \approx 5500 \approx 55 \text{ km s}^{-1}$) observations were performed in the spectral range 5500–7500 Å with the Gemini Multiobject Spectrograph IFU (GMOS [49]) at the Gemini South Observatory. Though observations were limited by the seeing, the great spatial resolution of the GMOS IFU, $\sim 0.2''$, allowed the authors to spatially resolve the red-shifted jet from the proplyd. The authors also found traces that pointed out to the presence of a blue-shifted component of the jet, previously reported by Doi and collaborators [50]. From the $\text{H}\alpha$ flux in the jet, the mass-loss rate of the proplyd was estimated in this work, being consistent with previous estimations [48].

Recently, Tsamis and Walsh [51] have presented an improved IFS dataset with respect to those of Vasconcelos and collaborators. High-resolution ($R \approx 30,000 \approx 10 \text{ km s}^{-1}$) observations were accomplished with the Fibre Large Array Multi-Element Spectrograph (FLAMES; [52]) and the Argus 6.8'' \times 4.3'' IFU mode at the 8.2 m *Kueyen* Very Large Telescope. The high-quality of the dataset allowed these authors to characterize for the first time physical and chemical properties of the bipolar jet arising from LV2. Though the original spatial resolution provided by the selected Argus mode (0.31'' \times 0.31'') was limited by the seeing of the observing night ($\sim 0.8''$), both red- and blue-shifted lobes were marginally spatially detected in several emission

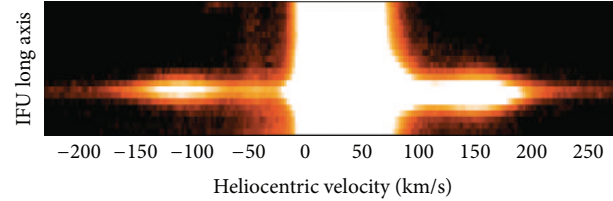


FIGURE 3: Image adapted from [51] showing the $\text{H}\alpha$ emission profile of the LV2 proplyd observed with FLAMES with an effective velocity resolution of about $2.3 \text{ km s}^{-1} \text{ pixel}^{-1}$ (FWHM velocity resolution of 7.7 km s^{-1}). The red- and blue-shifted components of the bipolar jet are clearly resolved, even without subtracting the bright background emission of the nebula. The intensity scale is logarithmic with a minimum of 5.4×10^{-17} (black) and a maximum of $1.1 \times 10^{-13} \text{ ergs}^{-1} \text{ cm}^{-2}$ (white). The length of the vertical axis is $6.6''$.

lines. Spectrally, the jet emission was well resolved as we can see in Figure 3.

In the work of Tsamis and Walsh, an accurate study of the surface brightness distributions of the red- and blue-shifted lobes in $\text{H}\alpha$, $\text{H}\gamma$, and $[\text{Fe III}] 4658 \text{ \AA}$ led the authors to conclude that the bipolar jet is being ejected in a projected axis almost perpendicular to the tail of the LV2 proplyd. From this result, it is clear that the use of IFS combined with high spectral resolution is a refined technique that can reveal unexpected properties that, on the other hand, would remain hidden—or would be more difficult to identify—under the view of the classical slit spectroscopy. Another interesting result is the drastic temperature variations observed in the velocity profile of the $T_e([\text{O III}])$, associated with the red-shifted emission of the jet, which might be produced by a shock discontinuity as the authors argued. Finally, a noteworthy result of this work is also the significantly enhanced Fe abundance in the jet emission, pointing to very efficient dust destruction mechanisms that might be operating in high-velocity irradiated jets as was also reported in the study of the HH202-S knot [46].

Models of photoionized HH flows [43] predict that the T_e along an HH object is of about the typical value of a gas in photoionization equilibrium—about 10^4 K —but shows a localized increase at the leading working surface of the bow shock due to shock heating. This zone is narrow and precedes the high-density shocked gas behind the working surface of the gas flow. Very recently, the discovery and localization of this structure have been possible thanks to the use of IFS. Making use of PMAS, its $16'' \times 16''$ IFU, and spatial scales of $1'' \times 1''$, the presence of this structure seems to have been found in the form of a high- T_e arc at the leading working surface of the prominent HH204 object of the Orion Nebula [53]. Though it was not reported, a similar narrow arc was also observed in the IFS study of HH202 using the same instrumentation and setup (see [54]). In Figure 4, the detection of these high- T_e arcs in the temperature distribution maps of HH204 and HH202 is illustrated. In both objects, the arcs were detected in the T_e derived from the nebular and auroral $[\text{N II}]$ line ratio. According to C. Morisset (private communication), the origin of these arcs should be

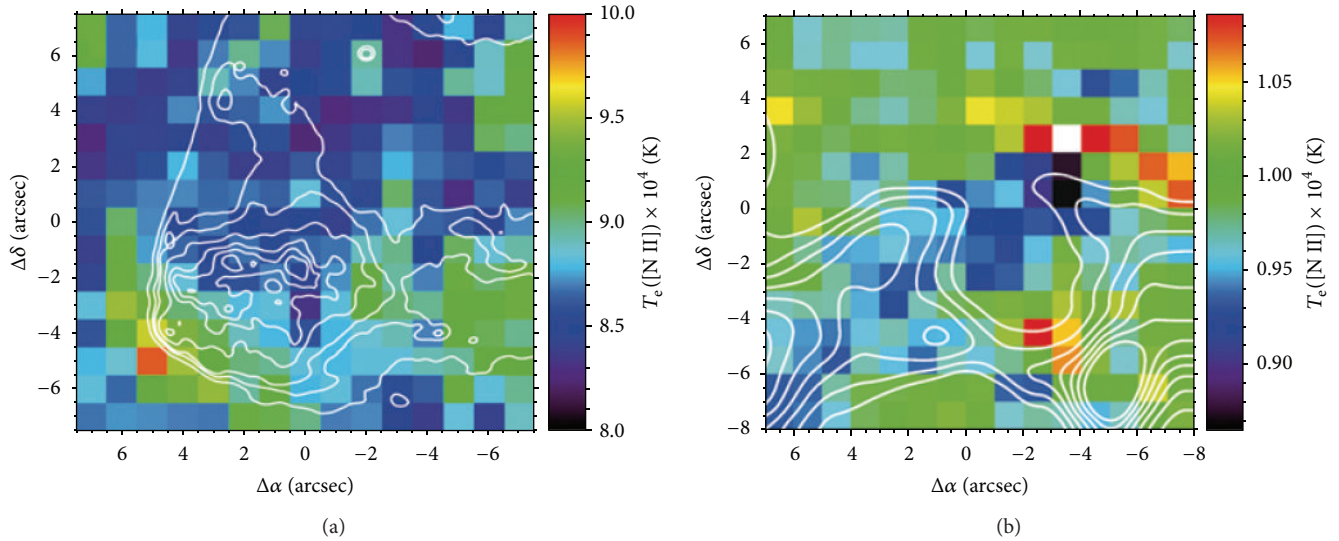


FIGURE 4: Spatial distribution maps of $T_e([\text{N II}])$ with $\text{H}\alpha$ contours overplotted for (a) HH204 and (b) HH202, adapted from [53, 54], respectively. High- T_e arcs are located along the narrow areas at the leading working surfaces of the gas flows: at the lower-left corner for HH204 and near the upper-right corner in HH202. An T_e enhancement that might be associated to a small high- T_e arc is also seen near the HH202-S knot.

regarded with caution because they may be artifacts produced by observations of two unresolved gaseous components with very different physical conditions. This clearly points out the need for confirming the true nature of the high- T_e arcs through high-resolution spectroscopy, resolving the kinematical component associated with the gas flow from the background emission. This kind of observations has been already done in the HH202-S knot [46], though unfortunately the slit did not cover the small high- T_e arc detected in this knot from the IFS study of HH202 (Figure 4).

Núñez-Díaz and collaborators [53] quantified the physical properties of the narrow shock-heated zone found in HH204, measuring a temperature enhancement of about 1000 K with respect to the ambient gas. From their analysis, it is concluded that the compression and heating of the gas due to the presence of high-velocity flows can directly affect the chemical abundance determinations due to: (a) an over-estimation of the collisional de-excitation effects on emission lines arising from levels with low critical densities; and (b) the use of too high T_e values for deriving abundances due to contamination from emission of the leading working surface. It is fundamental to investigate in depth the importance of these disturbing effects into the determination of chemical abundances in the Orion Nebula and, in general, H II regions, especially for those objects where these small-spatial scale phenomena cannot be resolved.

4. Chemical Composition of Orion Proplyds

Metallicity plays an important role in the evolution of circumstellar disks and in their associated potential to form planets (see [55]). The positive correlation found between the host star metallicity and the presence of giant planetary companions (see, e.g., [56]) has raised great interest in the

question of the chemical composition of planet formation circumstellar envelopes. Certainly, Orion proplyds are unique targets to investigate the metallicity content and its role in the evolution of circumstellar disks. The currently accepted model (e.g., [57–59]) is that far-ultraviolet photons heat the surface of the disk, forming a warm outflowing envelope of neutral gas that becomes photoionized after expanding to a few times the outer radius of the disc (see Figure 5). Though they are complex structures, the optical emission of the ionized photoevaporation flow provides an ample variety of emission line features, which can be used as robust diagnostics to determine physical and chemical properties of the gaseous phase. In particular, metallicity can be estimated through the usual proxy, the total O abundance, since O is the most abundant heavy element in the Universe.

The chemical composition of Orion proplyds has, however, remained unknown for a long time. Usually, it has been assumed to be roughly the same than the parent molecular cloud, given by the better known gaseous [9] and stellar [60] abundances of the Orion Nebula. Though spectroscopical studies have been carried out in several Orion proplyds (e.g. [27, 48, 61, 62]) and tentative evidence has been found about the evolution of dust properties in the thick molecular disk [63] and in the ionized photoevaporation flow [64], until very recently there was an important lack of comprehensive studies of the chemical abundances in any proplyd. In the last years, great advances have been done by few authors to correct this situation, where the use of IFS has turned out essential.

The spectroscopical analysis of proplyds is without any doubt a challenging task (see [62, 65]). The major difficulty lies in disentangling the intrinsic emission of the proplyd from possible sources of contamination, especially in low-resolution spectroscopical observations. In principle, the

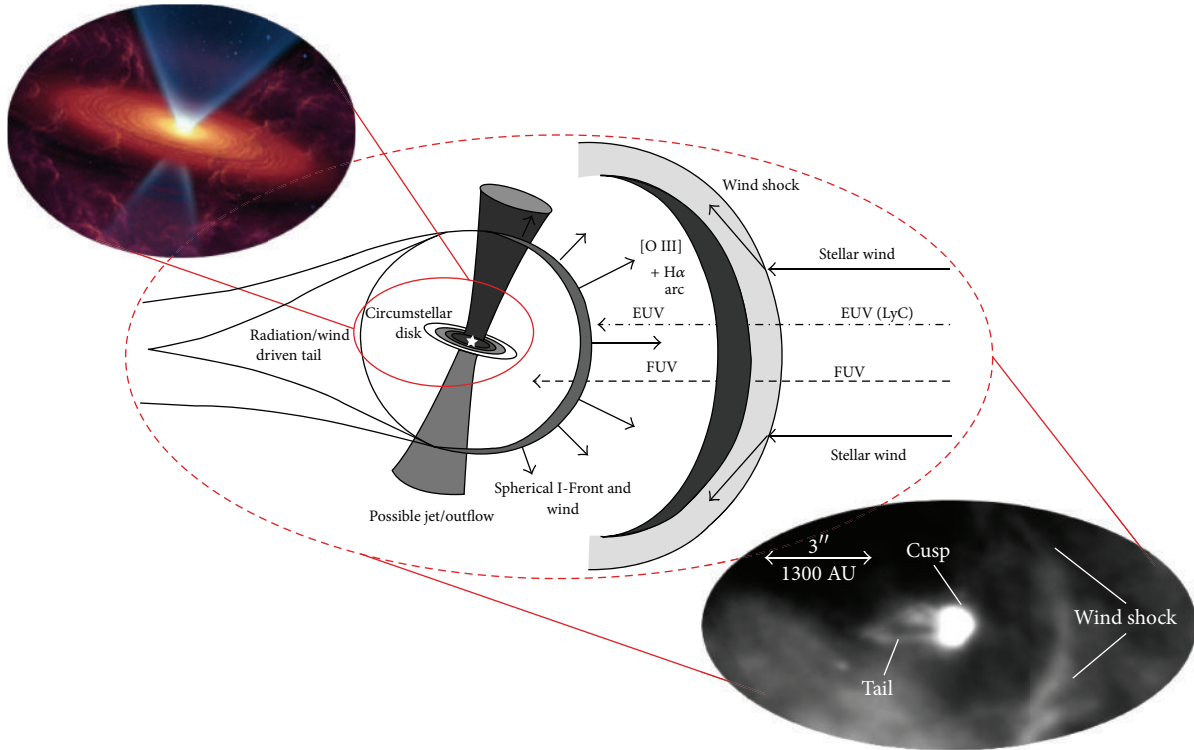


FIGURE 5: Schematic representation of a proplyd [61], where the young star has a circumstellar disk and a bipolar outflow. The scheme is accompanied by an artistic depiction of the circumstellar disk (upper left-hand side; Subaru Telescope Press Release on 31 August, 2005) and an $H\alpha$ image of the proplyd HST1 (lower right-hand side [6]). Stellar extreme-UV (EUV) and far-UV (FUV) photons enter from the right. The FUV photons penetrate the surface of the circumstellar disk around the star, driving a slow neutral flow ($\sim 3 \text{ km s}^{-1}$), which for most proplyds [57, 58] accelerates to mildly supersonic velocities before shocking and passing through an ionization front (I-Front) at a distance of a few disk radii. In the I-Front the gas is rapidly accelerated to about $10\text{--}20 \text{ km s}^{-1}$ and continues to accelerate as it expands away from the I-Front and reaches progressively higher stages of ionization due to the EUV photons. The interaction between the photoevaporation flow and the stellar wind can produce a wind shock in front of the proplyd. The neutral flow in the tail is fed by diffuse UV photons, which evaporate the back side of the disk, and possibly also by gas that left the front side of the disk but was redirected into the tail by pressure gradients in the shocked neutral layer. The ionized flow from the tail is induced by diffuse EUV photons, but stellar EUV photons entering from the side also play an important role in maintaining the ionization of the tail flow once it has left the I-Front, especially toward the front of the tail [59].

main source of contamination is the emission from the background of the nebula, which has to be properly subtracted. However, it is difficult to define an accurate background since the nebula shows significant brightness variations at small spatial scales. From an observational point of view, a background estimation can be obtained as the average of the nebular emission around the proplyd. In this sense, IFS can be more accurate and effective than slit spectroscopy, giving us more information of the nebular emission surrounding the proplyd. Depending on the particular design of the used spectrograph, IFS has also the advantages of ensuring a major collection of the total flux emitted by the proplyd and the capability of resolving spatially its structure. Instead, slit spectroscopy is more subjected to certain observational effects (selected slit width or seeing changes during the observing night) that could lead to flux losses as well as could complicate the background estimation and subtraction procedures. Independent of the observational strategy, the opacity due to the dust inside the proplyd is another unknown factor that may introduce systematic errors in the subtraction process of the nebular emission. At least an estimation of the

proplyd extinction could be provided; physical and chemical properties are limited to two extreme possibilities: (1) a fully opaque case or (2) a fully transparent case. Finally, another possible source of contamination is the presence of high-velocity emission from any jet associated with the proplyd, a problem that can be only solved by high-resolution spectroscopy or focusing on proplyds that do not present such jets (see [42]).

Currently, under the previous considerations, physical and chemical properties have been so far studied in three Orion proplyds: LV2 (167-317), HST1 (177-341), and HST10 (182-413). Out of this sample, the presence of high-velocity jets has been only reported in LV2 [42]. Intermediate-resolution ($R \approx 12,000$) spectroscopical observations of LV2 and HST10 were performed by Tsamis and collaborators [66, 67] with FLAMES and the setup already mentioned in the observation of the LV2 jet (see Section 3). The proplyd HST1 was observed at low spectral resolution ($R \approx 1500$) in the range $3500\text{--}7200 \text{ \AA}$ with PMAS by the author of this review and collaborators, as part of a larger IFS project in the Orion Nebula that included the PMAS observations already

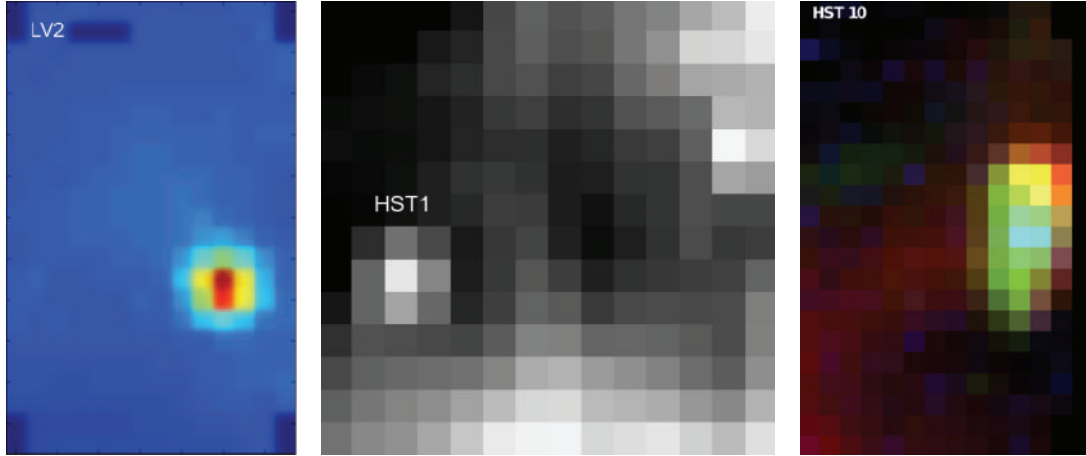


FIGURE 6: Spatial distributions maps of LV2 in $H\beta$ [66], HST1 in $H\alpha$ [65] and HST10 as a combination of $H\alpha$ (red), [O I] 6300 Å (green), and [O I] 5577 Å (blue) [67]. A comparison with Figure 1 is recommended.

presented in Section 2 and Section 3. As it is seen in Figure 1, the PMAS field containing HST1 (named 177–341 from its coordinates [68]) also includes other features. However, HST1 was the only proplyd with enough signal-to-noise to determine physical conditions and chemical abundances. In Figure 6, it is presented a sample of spatial distribution maps in different emission lines to illustrate how these proplyds are seen from IFS.

A global analysis of the results found in the three proplyds lead us to reach three conclusions that should be considered in future works in relation to the calculations of physical and chemical properties. Firstly, the structures associated with the proplyds and observed in the spatial distribution maps of several nebular properties (e.g., emission line fluxes, line ratios, or electron densities and temperatures) are dominated by collisional deexcitation effects due to the high densities of the proplyds. To properly account for this mechanism, a very detailed analysis of the proplyd spectra is mandatory in order to evaluate the reliability of the density diagnostics (see e.g., [65]). Assuming the full transparent case, electron density values of 2×10^6 , 4×10^5 , and 10^5 cm^{-3} were found at the cusp of the proplyds LV2, HST1, and HST10. Lower densities were found along the tails of LV2 and HST10. Though a large variation range is noted in the proplyd densities, temperatures derived from the [O III] line ratio turned out rather similar in three cases with values of about 8000–9000 K. Secondly, chemical abundances derived from CELs should preferentially use CELs with high critical densities to minimize collisional deexcitation effects because of the high densities in most proplyd cusps. Low-critical density CELs can be completely suppressed by such effects as it was shown in the analysis of HST1 and LV2. For instance, the O^+ abundance is crucial for the determination of the total oxygen abundance and, therefore, it should be calculated from observations of the high-critical density [O II] lines at $7320 + 30 \text{ Å}$ ($\sim 3 \times 10^6 \text{ cm}^{-3}$) rather than the low-critical density [O II] line at 3727 Å ($\sim 5000 \text{ cm}^{-3}$). Finally, the effects associated to the internal extinction by dust in the proplyd's neutral core are appreciable and may severely affect density

determinations and ionic abundances that are sensitive to the adopted density. As it was investigated in HST1, density determinations can range from $4 \times 10^5 \text{ cm}^{-3}$ in the full transparent case to $9 \times 10^4 \text{ cm}^{-3}$ in the full opaque case.

In order to investigate the chemical content of proplyds for a better understanding of their metallicity and evolution, intensive collaborations between modelers and observers are encouraged. As an alternative to the empirical analysis, the chemical compositions of proplyds can be also explored constructing physical models for the photoevaporation flows. These models combine simulations of radiative transfer, hydrodynamics, and atomic physics to predict fundamental parameters like the density, temperature, and ionization structure of the photoevaporation flows through the proplyd ionization front (see Figure 5 [65, 69]). For LV2, the modeling is still in progress (Flores-Fajardo et al. in prep.) and at the moment we count on the empirical abundances based on [O II] and [O III] CELs derived by Tsamis and collaborators [66]. For HST1, total O abundances were only determined from the photoevaporation model due to the absence of [O II] CELs in the intrinsic spectra of the proplyd. On the other hand, HST10 is the only case in which the total O abundance in the gaseous phase was estimated empirically and in the model from the analysis of [O II] and [O III] CELs. The comparison of the O abundances in the three proplyds is rather disparate, so it is difficult to see a consistent trend in their results. Although we find a roughly solar O abundance for HST10 from both empirical analysis and photoevaporation modeling, the O/H ratio was found to be almost twice solar in LV2 from the purely empirical analysis. In contrast, HST1 shows an O abundance of about $\sim 0.4 \times$ solar from the photoevaporation model fitting. Given the wide range of characteristic ionizations and densities found in the three proplyds, it is possible that systematic errors might be contributing to this abundance spread. To rule out any such effects, it is required to increase our knowledge on the chemical content of proplyds and perform similar analysis on a sample of proplyds with similar physical properties. Though IFS is a unique technique to investigate the metallicity in Orion proplyds, further work

is completely necessary before a definitive statement can be made about their gas-phase abundances.

5. The AD Problem from IFS

5.1. Consequences and Origin. The AD problem is far from negligible in the analysis of Galactic and extragalactic H II regions. A particular sensitive case is the O/H ratio, which is the most widely used proxy of the global metallicity Z . Observational studies have found that O abundances calculated from the O II 4630–4670 Å multiplet RLs are between 20% and 70% higher than those derived from the [O III] 4363, 4959, and 5007 Å CELs (e.g., [70–75]). Such discrepancies have direct effects on our current knowledge of the chemical composition and chemical evolution in the Universe, affecting (1) the calibration of the strong line methods as the R_{23} –O/H Pagel’s relation [76, 77], (2) the mass-metallicity and luminosity-metallicity relations [78], (3) the basic ingredients of chemical evolution models and predicted stellar yields [79], (4) the possible metallicity dependence of the Cepheid period-luminosity relation [80], (5) the metallicity dependence of the number ratios of the different types of W-R stars [81], and (6) the determination of the primordial helium [82].

What is the reason of this discrepancy? And which are the emission lines that we should trust? These are the two fundamental questions that after decades of intensive researching remain open and without a satisfactory answer. Traditionally, the AD has been associated with the presence of temperature fluctuations (of still unknown cause) as proposed by Peimbert more than 40 years ago [83–85]. According to this scenario, RLs should provide the correct abundances because their emissivities have a weaker temperature dependence than CELs—more affected by the presence of such fluctuations. From the proposal of Tsamis and Péquignot [86], Stasińska and collaborators explored the hypothesis of inhomogeneous abundances in the ISM (see [87]). They concluded that if this is the real scenario, then the chemical abundances derived from RLs and CELs should be upper and lower limits, respectively, to the true ones, though those from CELs should be more reliable. Very recently, [88] have proposed the possibility that electrons may depart from a Maxwell-Boltzmann equilibrium energy distribution, especially affecting the CEL emission. It is necessary to emphasize that the underlying assumptions of this theory are in contradiction with what has been established for half a century for the conditions in gaseous nebulae. Until the origin of this discrepancy is well understood, chemical abundances based on the standard CEL-method, which is used in the vast majority of cases, especially at extragalactic scales, should be regarded with caution.

5.2. Role of Small-Spatial Scale Structures. Given its proximity, the Orion Nebula is the perfect target to investigate the possible relation between the AD problem and the presence of morphological structures. Tackling this issue certainly requires reliable detections of RLs emitted by heavy-element ions to investigate the RL-CEL discrepancy. From optical long-slit spectroscopy with the Intermediate Dispersion Spectrograph and Imaging System (ISIS) at the

4.2 m William Herschel Telescope, the author of this review and collaborators addressed this topic for the first time in the Orion Nebula at spatial scales of $1.2''$ [11]. Very deep observations were performed in five slit positions of $3.7''$ long each. The slits were arranged on the Huygens region, covering different morphological structures such as proplyds, HH objects, and stratified bars. A total number of 730 one-dimensional spectra were extracted and reliable detections of the O II multiple 1 RLs were reported in 92% of them. Then, the authors could analyze the spatial distribution profiles of the RL-CEL discrepancy of O^{2+} abundance, which is usually quantified through the AD factor (ADF). In this review, we adopt the logarithmic form of the ADF, defined as the difference of abundances derived from RLs and CELs. One of the major results of this work was that the $ADF(O^{2+})$ remains rather constant along most of the observed areas of the nebula but showing localized enhancements at the positions of the prominent HH objects HH202, HH203, and HH204. On average, the $ADF(O^{2+})$ is about 0.15 dex, while in the HH areas, the discrepancy increases up to 0.3–0.5 dex.

Incorporating IFS has enormously improved our ability to spatially locate with much more precision areas on the nebula having high AD. This is well illustrated in the IFS analysis of the NE-Orion-S edge [37] and HH202 [54], where it was possible to map the emission of O II RLs in both structures. The $ADF(O^{2+})$ maps of these two fields are shown in Figure 7. In the case of NE-Orion-S, the $ADF(O^{2+})$ is slightly higher at the north-east corner of the field, though it does not seem to be related to the presence of any remarkable morphology when we compare it with the HST images of the Huygens region at that exact position (see Figure 1). On the contrary, the results found in the $ADF(O^{2+})$ map of HH202 are encouraging: the maximum $ADF(O^{2+})$ is located at the position where the gas flow reaches its maximum velocity, the HH202-S knot. The same research group carried out a subsequent study of HH202-S in which the emissions from the gas flow and the nebular background were spectrally resolved thanks to the high spectral resolution of the observations ($R \approx 30,000$). Interestingly, the $ADF(O^{2+})$ in the gas flow component turned out to be 0.35 ± 0.05 dex, a much higher discrepancy than the value of 0.11 ± 0.04 dex found in the ambient gas. These results also confirm what was found in the long-slit study and suggest a possible connection between high-velocity flows and high AD. To clearly establish the possible role of high-velocity flows in the AD problem, further investigation is still needed. The use of high-spectral resolution IFS would be the ideal observational approach.

The IFS studies of the proplyds HST1 and LV2 have also brought new clues into the AD problem (see [65, 66]). The possible role of proplyds was also attempted in the early ISIS work presented above, but those observations did not count on reliable diagnostics to properly determine the proplyd densities. A striking result found in HST1 and LV2 is that the $ADF(O^{2+})$ tends to zero when physical conditions of proplyds are well accounted as in both full opaque and transparent cases. It is observed that the high densities of proplyds produce a clear enhancement of the O^{2+} abundances derived from CELs with respect to the nebular background

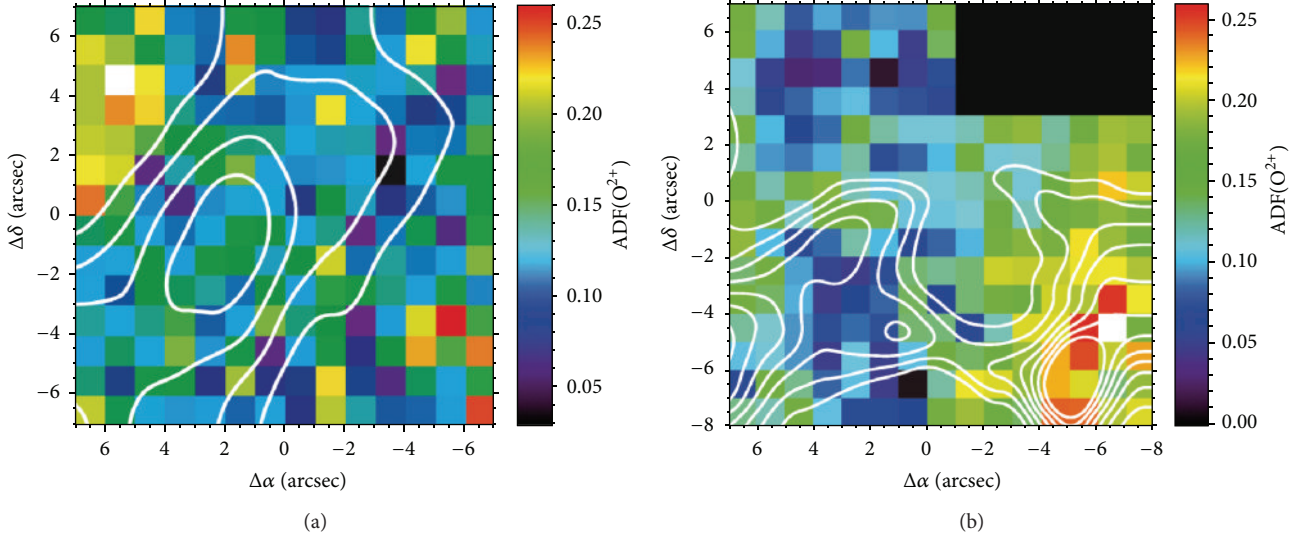


FIGURE 7: Spatial distribution maps of $\text{ADF}(\text{O}^{2+})$ with $\text{H}\alpha$ contours overplotted for (a) NE-Orion-S and (b) HH202, adapted from [37, 54], respectively. The black rectangle in the upper-right corner of HH202 corresponds to a masked area where O II RLs were marginally detected.

abundances, while those form RLs are basically similar in both cases. From these results, it is concluded that high-density gas (in the form of proplyds, globules, or unseen clumps/filaments acting at small spatial scales) may be playing a major role in the AD problem as Viegas and Clegg proposed in 1994 [89]. In a scenario where small, high-density, and semiionized clumps/filaments are mixed with diffuse gas in the observation aperture, the classical method based on CELs can be severely affected if collisional deexcitation of certain emission line diagnostics is not well accounted for. Instead, RLs would not be affected and, therefore, they should reliably yield the chemical abundances in the target field. Judging by the results of the proplyd IFS analyses thus far, these clumps do not need to be strongly hydrogen deficient, unlike those posited in previous scenarios to explain the AD problem in H II regions [86, 87].

6. A Deep Global View: The Big Mosaic of Orion

The big mosaic of the Huygens region constructed by Sánchez and collaborators [33] using IFS stands for a step ahead in the application of this technique. However, this dataset needed a significant improvement in at least three aspects. The dataset was poorly flux-calibrated, based on really short exposure time (2 s) and low spectral resolution. Today, these aspects have been improved and a new big mosaic has been observed with PMAS/PPak. Its analysis is still in progress (see preliminary results in [36]).

The much better quality of this new mosaic is definitively proven by the detection of the faint C II and O II RLs almost in the whole Huygens region (see Figure 8). Density and temperature maps have been obtained from different diagnostic ratios such as [S II] $\lambda 6717/\lambda 6731$, [Cl III] $\lambda 5517/\lambda 5537$, or [O III] $\lambda 5007/\lambda 4363$ (see [36]). The dataset is very valuable to investigate the AD problem as

an integrated property and compare the results with what is observed in extragalactic H II regions. It will also be possible to address a comparison with the previous IFU studies and investigate whether the AD problem is subject to dilution effects by using larger apertures. Other research interests such as the validity of the case B recombination theory, the effect of scattered light, the global ionization structure of the nebula, the effect of collisional deexcitation by the presence of high-density morphologies, the accuracy of the RL and CEL methods, or the correlation between physical conditions and chemical abundances with morphologies at large and intermediate scales will be explored thanks to this mosaic and the clear potential of IFS studies.

7. Final Remarks: A Bright Future for IFS Studies

The Orion Nebula is a landmark object of the solar neighborhood and serves as a paradigm for interpreting results throughout the Galaxy and beyond. It is a fundamental reference for our knowledge about formation and evolution processes of stars and planets and for evaluating the reliability of the methods used to ascertain the chemical composition in the universe. If H II regions like the Orion Nebula are more the rule rather than an exception, then this nebula is the only target that gives us the opportunity to investigate and understand underlying mechanisms that operate in the interior of these gaseous clouds at small spatial scales. Without any doubt, IFS plays an active role in this framework and exciting results have been, and will be surely, discovered by using this technique.

Applying IFS to unveil the intimate properties of the Orion Nebula is today in its rising stage. At the time that this review was written, a total of 9 IFS studies were found in the literature devoted to the Orion Nebula. As it has been

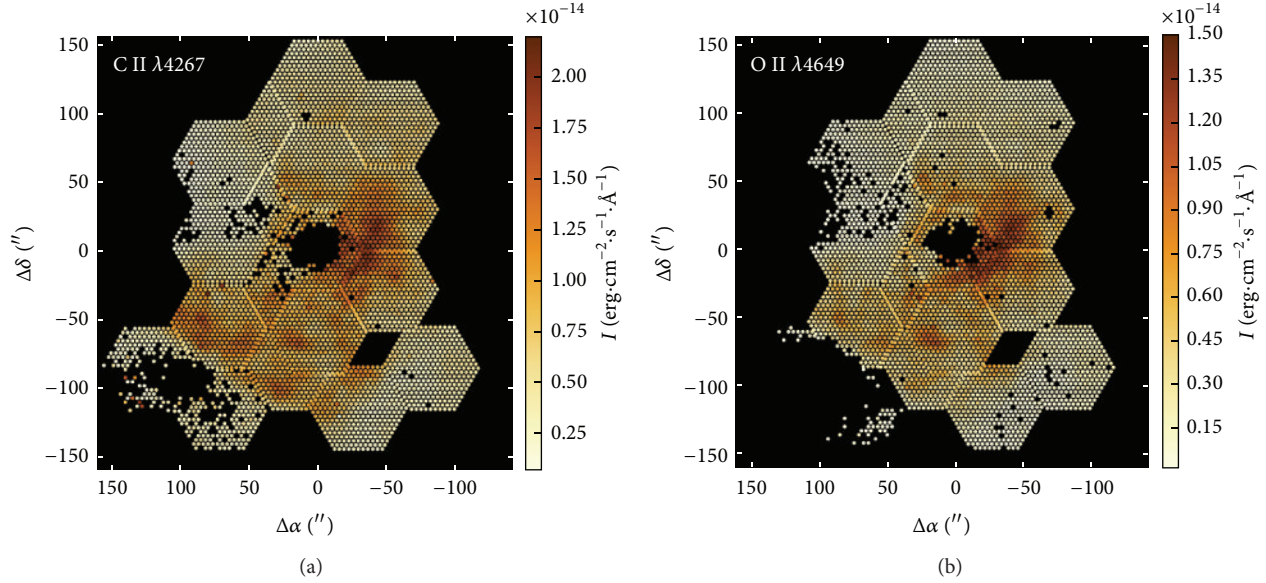


FIGURE 8: Spatial distribution maps of dereddened fluxes of RLs: (a) C II 4267 Å and (b) O II 4649 Å. The black areas in the center are contaminated by emission from the Trapezium stars. The coordinates are centered on θ^1 Ori C. The figure has been adapted from [36].

shown along the review, these studies have used the state-of-the-art optical spectrographs PMAS, GMOS, and FLAMES, currently working from ground-based observatories at the 3.5 m telescope of Calar Alto Observatory, the 8 m Gemini telescopes, and the 8.2 m VLT, respectively. The capabilities of IFS have allowed us to enhance our knowledge of physical, chemical, and structural properties of the Orion Nebula and its morphological substructures. For instance, the study of stratified bars has contributed to constrain with more detail the 3D picture of the Orion-S star-forming cloud. The IFS has allowed us to spatially locate and quantify the effects of high-velocity flows on their surrounding media as well as to investigate for the first time the chemical content of proplyds. Furthermore, it has been shown that small-spatial-scale morphologies may be playing an active role in the production of the AD problem. Results from the improved mosaic of Orion will be very useful to evaluate how the small-scale structure affects to the global properties of the nebula, which may give us new clues to understand the AD problem at larger scales.

Further investigation is still required in many of the achievements presented here. Second and third generations of integral field spectrographs with improved performances in the optical range will have much to say about it. Of these new generations, it should be highlighted: the simultaneous observation of the near-ultraviolet, optical and near-infrared spectral ranges offered by X-shooter, operating at intermediate resolutions [90]; the large fields of view that will be provided by MUSE [91] or VIRUS [92]; or the development of new IFS techniques as SAMI [93], which mixes the multiobject technique with spatial capability of the IFS. For the future 30 m telescopes, new advances in this area aims to combine the integral field technique with high spectral

resolution and adaptive optics systems (even in the optical range), auguring a bright future for the maturity of the IFS and, certainly, for expanding our current knowledge of the Orion Nebula.

Conflict of Interests

The authors declare that there is no conflict of interests regarding the publication of this paper.

Acknowledgments

The author is thankful to C. Esteban, W. J. Henney, C. R. O'Dell, T. H. Puzia, and the referee for the revision of the paper as well as for their suggestions, which have improved the readability of this work. The author deeply grateful for the inestimable dedication, support, and contribution of their coworkers: C. Esteban, N. Flores-Fajardo, J. García-Rojas, W. J. Henney, L. López-Martín, V. Luridiana, M. Núñez-Díaz, and Y. G. Tsamis. Without them, much of the reviewed work would not have been possible. The author thanks the organizers of the monographic “Metals in 3D: A Cosmic View from Integral Field Spectroscopy” for the opportunity of being part of it. Finally, the author acknowledges the funding support from Comité Mixto ESO-Chile, the Basal-CATA Grant no. PFB-06/2007 and the FONDECYT project no. 3140383.

References

- [1] C. R. O'Dell, “The Orion Nebula and its associated population,” *Annual Review of Astronomy and Astrophysics*, vol. 39, pp. 99–136, 2001.
- [2] S. Simón-Díaz, A. Herrero, C. Esteban, and F. Najarro, “Detailed spectroscopic analysis of the Trapezium cluster stars inside

- the Orion Nebula: rotational velocities, stellar parameters, and oxygen abundances," *Astronomy and Astrophysics*, vol. 448, no. 1, pp. 351–366, 2006.
- [3] J. J. Hester, R. Gilmozzi, C. R. O'Dell et al., "Ionization fronts and shocked flows: the structure of the Orion Nebula at 0.1 arcsec," *Astrophysical Journal Letters*, vol. 369, no. 2, pp. L75–L78, 1991.
- [4] M. Felli, E. Churchwell, T. L. Wilson, and G. B. Taylor, "The radio continuum morphology of the Orion Nebula—from 10 arcmin to 0.1 arcsec Resolution," *Astronomy and Astrophysics Supplement Series*, vol. 98, no. 1, pp. 137–164, 1993.
- [5] D. K. Walter, R. J. Dufour, and J. J. Hester, "The ionization structure of the Orion Nebula," *Revista Mexicana de Astronomia y Astrofisica*, vol. 27, pp. 207–211, 1993.
- [6] C. R. O'Dell and K. Wong, "Hubble space telescope mapping of the Orion Nebula. I. A survey of stars and compact objects," *Astronomical Journal*, vol. 111, p. 846, 1996.
- [7] C. R. O'Dell and F. Yusef-Zadeh, "High angular resolution determination of extinction in the Orion Nebula," *Astronomical Journal*, vol. 120, no. 1, p. 382, 2000.
- [8] C. M. Walmsley, A. Natta, E. Oliva, and L. Testi, "The structure of the Orion bar," *Astronomy and Astrophysics*, vol. 364, no. 1, pp. 301–317, 2000.
- [9] C. Esteban, M. Peimbert, J. García-Rojas, M. T. Ruiz, A. Peimbert, and M. Rodríguez, "A reappraisal of the chemical composition of the Orion Nebula based on very large Telescope echelle spectrophotometry," *Monthly Notices of the Royal Astronomical Society*, vol. 355, no. 1, pp. 229–247, 2004.
- [10] E. D. Feigelson, K. Getman, L. Townsley et al., "Global X-ray properties of the Orion Nebula region," *Astrophysical Journal*, vol. 160, no. 2, pp. 379–389, 2005.
- [11] A. Mesa-Delgado, C. Esteban, and J. García-Rojas, "Small-scale behavior of the physical conditions and the abundance discrepancy in the Orion Nebula," *The Astrophysical Journal*, vol. 675, no. 1, p. 389, 2008.
- [12] C. R. O'Dell, W. J. Henney, N. P. Abel, G. J. Ferland, and S. J. Arthur, "The three-dimensional dynamic structure of the inner Orion Nebula," *Astronomical Journal*, vol. 137, no. 1, pp. 367–382, 2009.
- [13] T. L. Wilson, S. Casassus, and K. M. Keating, "The structure of NGC 1976 in the radio range," *Astrophysical Journal*, vol. 744, no. 2, p. 161, 2012.
- [14] B. Zuckerman, "A model of the Orion Nebula," *Astrophysical Journal*, vol. 183, pp. 863–870, 1973.
- [15] J. A. Baldwin, G. J. Ferland, P. G. Martin et al., "Physical conditions in the Orion Nebula and an assessment of its helium abundance," *Astrophysical Journal Letters*, vol. 374, no. 2, pp. 580–609, 1991.
- [16] R. H. Rubin, J. P. Simpson, M. R. Haas, and E. F. Erickson, "Axisymmetric model of the ionized gas in the Orion Nebula," *Astrophysical Journal Letters*, vol. 374, no. 2, pp. 564–579, 1991.
- [17] Z. Wen and C. R. O'Dell, "A three-dimensional model of the Orion Nebula," *Astrophysical Journal*, vol. 438, no. 2, pp. 784–793, 1995.
- [18] E. W. Pellegrini, J. A. Baldwin, G. J. Ferland, G. Shaw, and S. Heathcote, "Orion's bar: physical conditions across the definitive $H^+/H^0/H_2$ interface," *Astrophysical Journal*, vol. 693, no. 1, p. 285, 2009.
- [19] S. J. Arthur, "What produces the diffuse X-ray emission from the Orion Nebula? I. Simple spherical models," *Mathematics & Physical Sciences*, vol. 421, no. 2, pp. 1283–1297, 2012.
- [20] M. T. Garía-Díaz and W. J. Henney, "Velocity structure in the Orion Nebula. I. Spectral mapping in low-ionization lines," *Astronomical Journal*, vol. 133, no. 3, p. 952, 2007.
- [21] W. J. Henney, C. R. O'Dell, L. A. Zapata, M. T. García-Díaz, L. F. Rodríguez, and M. Robberto, "Large-scale flows from Orion South," *Astronomical Journal*, vol. 133, no. 5, p. 2192, 2007.
- [22] C. R. O'Dell and W. J. Henney, "High spatial velocity features in the Orion Nebula," *Astronomical Journal*, vol. 136, no. 4, p. 1566, 2008.
- [23] L. A. Zapata, P. T. P. Ho, L. F. Rodríguez, C. R. O'Dell, Q. Zhang, and A. Muench, "Silicon monoxide observations reveal a cluster of hidden compact outflows in the OMC 1 South region," *Astronomical Journal*, vol. 653, no. 1, p. 398, 2006.
- [24] L. A. Zapata, J. Schmid-Burgk, P. T. P. Ho, L. F. Rodríguez, and K. M. Menten, "Explosive disintegration of a massive young stellar system in Orion," *Astrophysical Journal Letters*, vol. 704, no. 1, pp. L45–L48, 2009.
- [25] L. Ricci, M. Robberto, and D. R. Soderblom, "The Hubble Space Telescope/Advanced Camera for Surveys atlas of protoplanetary disks in the Great Orion Nebula," *Astronomical Journal*, vol. 136, no. 5, pp. 2136–2151, 2008.
- [26] C. R. O'Dell, Z. Wen, and X. Hu, "Discovery of new objects in the Orion Nebula on HST images—shocks, compact sources, and protoplanetary disks," *Astrophysical Journal*, vol. 410, no. 2, pp. 696–700, 1993.
- [27] M. J. Vasconcelos, A. H. Cerqueira, H. Plana, A. C. Raga, and C. Morisset, "Gemini multi-object spectrograph integral field unit spectroscopy of the 167–317 (LV2) proplyd in Orion," *Astronomical Journal*, vol. 130, no. 4, pp. 1707–1718, 2005.
- [28] P. Laques and J. L. Vidal, "Detection of a new type of condensations in the center of the Orion Nebula by means of S20 photocathode cells associated with a Lallemand electronic camera," *Astronomy and Astrophysics*, vol. 73, no. 1–2, pp. 97–106, 1979.
- [29] G. J. Ferland, "Quantitative spectroscopy of photoionized clouds," *Annual Review of Astronomy and Astrophysics*, vol. 41, pp. 517–554, 2003.
- [30] R. H. Rubin, P. G. Martin, R. J. Dufour et al., "Temperature variations from Hubble Space Telescope spectroscopy of the Orion Nebula," *Monthly Notices of the Royal Astronomical Society*, vol. 340, no. 2, pp. 362–374, 2003.
- [31] R. W. Pogge, J. Michael Owen, and B. Atwood, "Imaging spectrophotometry of the Orion Nebula core. I. Emission-line mapping and physical conditions," *Astrophysical Journal Letters*, vol. 399, no. 1, pp. 147–158, 1992.
- [32] C. R. O'Dell, M. Peimbert, and A. Peimbert, "Fine-scale temperature fluctuations in the Orion Nebula and the t_2 problem," *Astronomical Journal*, vol. 125, no. 5, pp. 2590–2608, 2003.
- [33] S. F. Sánchez, N. Cardiel, M. A. W. Verheijen, D. Martín-Gordón, J. M. Vilchez, and J. Alves, "PPAK integral field spectroscopy survey of the Orion Nebula data release," *Astronomy and Astrophysics*, vol. 465, no. 1, pp. 207–217, 2007.
- [34] M. M. Roth, A. Kelz, T. Fechner et al., "PMAS: the Potsdam multi-aperture spectrophotometer. I. Design, manufacture, and performance," *Publications of the Astronomical Society of the Pacific*, vol. 117, no. 832, pp. 620–642, 2005.
- [35] A. Kelz, M. A. W. Verheijen, M. M. Roth et al., "PMAS: the Potsdam multi-aperture spectrophotometer. II. The wide integral field unit PPAk," *Publications of the Astronomical Society of the Pacific*, vol. 118, no. 839, pp. 129–145, 2006.

- [36] M. Núñez-Díaz, C. Esteban, and A. Mesa-Delgado, “Highlights of Spanish astrophysics VII,” in *Proceedings of the 10th Scientific Meeting of the Spanish Astronomical Society (SEA '13)*, J. C. Guirado, L. M. Lara, V. Quilis, and J. Gorgas, Eds., pp. 594–599, Valencia, Spain, July 2013.
- [37] A. Mesa-Delgado, M. Núñez-Díaz, C. Esteban, L. Lopez-Martin, and J. Garcia-Rojas, “Integral field spectroscopy of selected areas of the Bright bar and Orion-S cloud in the Orion Nebula,” *Monthly Notices of the Royal Astronomical Society*, vol. 417, no. 1, pp. 420–433, 2011.
- [38] M. H. D. van der Wiel, F. F. S. van der Tak, V. Ossenkopf et al., “Chemical stratification in the orion bar: JCMT spectral legacy survey observations,” *Astronomy and Astrophysics*, vol. 498, no. 1, pp. 161–165, 2009.
- [39] B. Balick, R. H. Gammon, and R. M. Hjellming, “The structure of the Orion Nebula,” *Astronomical Society of the Pacific*, vol. 86, pp. 616–634, 1974.
- [40] C. R. O’Dell, P. Hartigan, W. M. Lane et al., “Herbig Haro objects in the Orion Nebula,” *Astronomical Journal*, vol. 114, no. 2, pp. 730–743, 1997.
- [41] J. Bally and B. Reipurth, “Irradiated Herbig-Haro jets in the Orion Nebula and near NGC 1333,” *Astrophysical Journal Letters*, vol. 546, no. 1, pp. 299–323, 2001.
- [42] J. Bally, J. O’Dell, and M. J. McCaughrean, “Disks, microjets, windblown bubbles, and outflows in the Orion Nebula,” *The Astronomical Journal*, vol. 119, no. 6, p. 2919, 2000.
- [43] A. C. Raga and B. Reipurth, “Herbig-haro jets emerging from a neutral cloud into a H \sim II region,” *Revista Mexicana de Astronomía y Astrofísica*, vol. 40, pp. 15–23, 2004.
- [44] A. C. Raga, J. Cantó, F. D. De Colle et al., “Radiative jets from variable sources,” in *Proceedings of the Revista Mexicana de Astronomía y Astrofísica Conference Series*, vol. 36, pp. 186–192, February 2008.
- [45] K. P. M. Blagrove, P. G. Martin, and J. A. Baldwin, “A photoionized Herbig-Haro object in the Orion Nebula,” *Astrophysical Journal Letters*, vol. 644, no. 2, pp. 1006–1027, 2006.
- [46] A. Mesa-Delgado, C. Esteban, J. García-Rojas et al., “Properties of the ionized gas in HH 202-II. Results from echelle spectrophotometry with ultraviolet visual Echelle spectrograph,” *Monthly Notices of the Royal Astronomical Society*, vol. 395, no. 2, pp. 855–876, 2009.
- [47] W. J. Henney, M. T. Garcia-Diaz, C. R. O’Dell, and R. H. Rubin, “Mapping the complex kinematics of LL objects in the Orion Nebula,” *Monthly Notices of the Royal Astronomical Society*, vol. 428, no. 1, pp. 691–711, 2013.
- [48] W. J. Henney, C. R. O’Dell, J. Meaburn, S. T. Garrington, and J. A. Lopez, “Mass loss and jet outflow in the Orion Nebula proplyd LV 2,” *Astrophysical Journal Letters*, vol. 566, no. 1, pp. 315–331, 2002.
- [49] J. Allington-Smith, G. Murray, R. Content et al., “Integral field spectroscopy with the Gemini multiobject spectrograph. I. Design, construction, and testing,” *Publications of the Astronomical Society of the Pacific*, vol. 114, no. 798, pp. 892–912, 2002.
- [50] T. Doi, C. R. O’Dell, and P. Hartigan, “Internal velocities in the Orion Nebula: large radial velocity features,” *The Astronomical Journal*, vol. 127, no. 6, p. 3456, 2004.
- [51] Y. G. Tsamis and J. R. Walsh, “Chemical abundances in the protoplanetary disc LV2 (Orion)-II. High-dispersion VLT observations and microjet properties,” *Monthly Notices of the Royal Astronomical Society*, vol. 417, no. 3, pp. 2072–2084, 2011.
- [52] L. Pasquini, G. Avila, A. Blecha et al., “Installation and commissioning of FLAMES, the VLT multifibre facility,” *The Messenger*, vol. 110, p. 1, 2002.
- [53] M. Núñez-Díaz, A. Mesa-Delgado, C. Esteban, L. Lopez-Martin, J. Garcia-Rojas, and V. Luridiana, “Exploring the effects of high-velocity flows in abundance determinations in H ii regions: bidimensional spectroscopy of HH 204 in the Orion Nebula,” *Monthly Notices of the Royal Astronomical Society*, vol. 421, no. 4, pp. 3399–3408, 2012.
- [54] A. Mesa-Delgado, L. Lopez-Martin, C. Esteban, J. Garcia-Rojas, and V. Luridiana, “Properties of the ionized gas in HH 202-I. Results from integral field spectroscopy with PMAS,” *Monthly Notices of the Royal Astronomical Society*, vol. 394, no. 2, pp. 693–703, 2009.
- [55] J. P. Williams and L. A. Cieza, “Protoplanetary disks and their evolution,” *Annual Review of Astronomy and Astrophysics*, vol. 49, pp. 67–117, 2011.
- [56] V. Neves, N. C. Santos, S. G. Sousa, A. C. M. Correia, and G. Israelian, “Chemical abundances of 451 stars from the HARPS GTO planet search program,” *Astronomy and Astrophysics*, vol. 497, no. 2, pp. 563–581, 2009.
- [57] W. J. Henney and S. J. Arthur, “Modeling the brightness profiles of the Orion proplyds,” *Astronomical Journal*, vol. 116, no. 1, pp. 322–335, 1998.
- [58] H. Störzer and D. Hollenbach, “Photodissociation region models of photoevaporating circumstellar disks and application to the proplyds in Orion,” *The Astrophysical Journal*, vol. 515, no. 2, p. 669, 1999.
- [59] W. J. Henney, “Ionized photoevaporation flows in H II regions and PNe,” in *Proceedings of the 7th Texas-Mexico Conference on Astrophysics: Flows, Blows and Glows*, vol. 10, pp. 57–60, April 2000.
- [60] M.-F. Nieva and N. Przybilla, “Present-day cosmic abundances: a comprehensive study of nearby early B-type stars and implications for stellar and Galactic evolution and interstellar dust models,” *Astronomy and Astrophysics*, vol. 539, p. A143, 2012.
- [61] J. Bally, R. S. Sutherland, D. Devine, and D. Johnstone, “Externally illuminated Young Stellar environments in the Orion Nebula: *HubbleSpaceTelescope* planetary camera and ultraviolet observations,” *The Astronomical Journal*, vol. 116, no. 1, p. 293, 1998.
- [62] W. J. Henney and C. R. O’Dell, “A keck high-resolution spectroscopic study of the Orion Nebula proplyds,” *The Astronomical Journal*, vol. 118, no. 5, p. 2350, 1999.
- [63] R. Y. Shuping, J. Bally, M. Morris, and H. Throop, “Evidence for grain growth in the protostellar disks of Orion,” *Astrophysical Journal Letters*, vol. 587, no. 2, pp. L109–L112, 2003.
- [64] F. García-Arredondo, W. J. Henney, and S. J. Arthur, “Hydrodynamic simulations of proplyd bow shocks,” *Astrophysical Journal Letters*, vol. 561, no. 2, pp. 830–842, 2001.
- [65] A. Mesa-Delgado, M. Núñez-Díaz, C. Esteban et al., “Ionized gas diagnostics from protoplanetary discs in the Orion Nebula and the abundance discrepancy problem,” *Monthly Notices of the Royal Astronomical Society*, vol. 426, no. 1, pp. 614–634, 2012.
- [66] Y. G. Tsamis, J. R. Walsh, J. M. Vilchez, and D. Pequignot, “Chemical abundances in the protoplanetary disc LV 2 (Orion): clues to the causes of the abundance anomaly in H II regions,” *Monthly Notices of the Royal Astronomical Society*, vol. 412, no. 2, pp. 1367–1380, 2011.
- [67] Y. G. Tsamis, N. Flores-Fajardo, W. J. Henney, J. R. Walsh, and A. Mesa-Delgado, “Chemical abundances in Orion protoplanetary

- discs: integral field spectroscopy and photoevaporation models of HST 10,” *Monthly Notices of the Royal Astronomical Society*, vol. 430, no. 4, pp. 3406–3421, 2013.
- [68] C. R. O’Dell and Z. Wen, “Postrefurbishment mission hubble space telescope images of the core of the Orion Nebula: *proplyds*, Herbig-Haro objects, and measurements of a circumstellar disk,” *The Astrophysical Journal*, vol. 436, no. 1, pp. 194–202, 1994.
- [69] W. J. Henney, S. J. Arthur, and M. T. Garcia-Diaz, “Photoevaporation flows in blister H II regions. I. Smooth ionization fronts and application to the Orion Nebula,” *The Astrophysical Journal*, vol. 627, no. 2, p. 813, 2005.
- [70] M. Peimbert, P. J. Storey, and S. Torres-Peimbert, “The O^{++}/H^{+} abundance ratio in gaseous nebulae derived from recombination lines,” *Astrophysical Journal Letters*, vol. 414, no. 2, pp. 626–631, 1993.
- [71] C. Esteban, M. Peimbert, S. Torres-Peimbert, and J. García-Rojas, “Chemical composition and temperature fluctuations in M17,” *Revista Mexicana de Astronomía y Astrofísica*, vol. 35, no. 1, pp. 65–83, 1999.
- [72] Y. G. Tsamis, M. J. Barlow, X.-W. Liu, I. J. Danziger, and P. J. Storey, “Heavy elements in galactic and magellanic cloud H II regions: recombination-line versus forbidden-line abundances,” *Monthly Notices of the Royal Astronomical Society*, vol. 338, no. 3, pp. 687–710, 2003.
- [73] J. García-Rojas and C. Esteban, “On the abundance discrepancy problem in H II regions,” *The Astrophysical Journal*, vol. 670, no. 1, p. 457, 2007.
- [74] A. R. López-Sánchez, C. Esteban, J. García-Rojas, M. Peimbert, and M. Rodríguez, “The localized chemical pollution in NGC 5253 revisited: results from deep Echelle spectrophotometry,” *The Astrophysical Journal*, vol. 656, no. 1, p. 168, 2007.
- [75] C. Esteban, F. Bresolin, M. Peimbert, J. García-Rojas, A. Peimbert, and A. Mesa-Delgado, “keck hires spectroscopy of extragalactic H II regions: C and O abundances from recombination lines,” *The Astrophysical Journal*, vol. 700, no. 1, p. 654, 2009.
- [76] B. E. J. Pagel, M. G. Edmunds, D. E. Blackwell, M. S. Chun, and G. Smith, “On the composition of H II regions in southern galaxies. I-NGC 300 and 1365,” *Monthly Notices of the Royal Astronomical Society*, vol. 189, pp. 95–113, 1979.
- [77] M. A. Peiña-Guerrero, A. Peimbert, and M. Peimbert, “recalibration of pagel’s method for H II regions considering the thermal structure, the ionization structure, and the depletion of O into dust grains,” *Astrophysical Journal Letters*, vol. 756, no. 1, p. L14, 2012.
- [78] C. A. Tremonti, T. M. Heckman, G. Kauffmann et al., “The origin of the mass-metallicity relation: insights from 53,000 star-forming galaxies in the sloan digital sky survey,” *Astrophysical Journal Letters*, vol. 613, no. 2, pp. 898–913, 2004.
- [79] L. Carigi, M. Peimbert, C. Esteban, and J. Uarcía-Rojas, “Carbon, nitrogen, and oxygen Galactic gradients: a solution to the carbon enrichment problem,” *Astrophysical Journal Letters*, vol. 623, no. 1, pp. 213–224, 2005.
- [80] S. Sakai, L. Ferrarese, R. C. Kennicutt Jr., and A. Saha, “The effect of metallicity on Cepheid-based distances,” *Astrophysical Journal Letters*, vol. 608, no. 1, pp. 42–61, 2004.
- [81] G. Meynet and A. Maeder, “Stellar evolution with rotation XI. Wolf-Rayet star populations at different metallicities,” *Astronomy and Astrophysics*, vol. 429, no. 2, pp. 581–598, 2005.
- [82] M. Peimbert, “The primordial helium abundance,” *Current Science*, vol. 95, no. 9, pp. 1165–1176, 2008.
- [83] M. Peimbert, “Temperature determinations of H II regions,” *The Astrophysical Journal*, vol. 150, p. 825, 1967.
- [84] M. Peimbert and R. Costero, “Chemical abundances in H II regions and their implications,” *Boletín de los Observatorios Tonantzintla y Tacubaya*, vol. 5, p. 3, 1969.
- [85] M. Peimbert and A. Peimbert, “Retrospective on “chemical abundances in H II regions and their implications” by Peimbert & Costero (1969),” in *Proceedings of the Revista Mexicana de Astronomía y Astrofísica Conference*, vol. 39, pp. 1–8, November 2009.
- [86] Y. G. Tsamis and D. Péquignot, “A photoionization-modelling study of 30 Doradus: the case for small-scale chemical inhomogeneity,” *Monthly Notices of the Royal Astronomical Society*, vol. 364, no. 2, pp. 687–704, 2005.
- [87] G. Stasińska, G. Tenorio-Tagle, M. Rodríguez, and W. J. Henney, “Enrichment of the interstellar medium by metal-rich droplets and the abundance bias in H II regions,” *Astronomy and Astrophysics*, vol. 471, no. 1, pp. 193–204, 2007.
- [88] D. C. Nicholls, M. A. Dopita, and R. S. Sutherland, “resolving the electron temperature discrepancies in H II regions and planetary nebulae: κ -distributed electrons,” *The Astrophysical Journal*, vol. 752, no. 2, p. 148, 2012.
- [89] S. M. Viegas and R. E. S. Clegg, “Density condensations in planetary nebulae and the electron temperature,” *Monthly Notices of the Royal Astronomical Society*, vol. 271, no. 4, p. 993, 1994.
- [90] J. Vernet, H. Dekker, S. D’Odorico et al., “X-shooter, the new wide band intermediate resolution spectrograph at the ESO very large telescope,” *Astronomy and Astrophysics*, vol. 536, p. A105, 2011.
- [91] R. M. McDermid, R. Bacon, S. Bauer et al., “MUSE: a second-generation integral-field spectrograph for the VLT,” in *Proceedings of the 2007 ESO Instrument Calibration 7 Workshop*, A. Kerber and F. Kaufer, Eds., p. 325, 2008.
- [92] G. J. Hill, S. E. Tuttle, H. Lee et al., “Initial results from VIRUS production spectrographs,” in *Proceedings of the SPIE 8446, Ground-based and Airborne Instrumentation for Astronomy IV*, vol. 8446 of *Society of Photo-Optical Instrumentation Engineers (SPIE) Conference Series*, 2012.
- [93] S. M. Croom, J. S. Lawrence, J. Bland-Hawthorn et al., “The Sydney-AAO Multi-object Integral field spectrograph,” *Monthly Notices of the Royal Astronomical Society*, vol. 421, no. 1, pp. 872–893, 2012.

Review Article

Chemodynamical Simulations of Dwarf Galaxy Evolution

Simone Recchi

Department of Astrophysics, Vienna University, Türkenschanzstrasse 17, 1180 Vienna, Austria

Correspondence should be addressed to Simone Recchi; simone.recchi@univie.ac.at

Received 18 October 2013; Accepted 13 December 2013; Published 17 February 2014

Academic Editor: José Manuel Vilchez Medina

Copyright © 2014 Simone Recchi. This is an open access article distributed under the Creative Commons Attribution License, which permits unrestricted use, distribution, and reproduction in any medium, provided the original work is properly cited.

In this review I give a summary of the state of the art for what concerns the chemo-dynamical numerical modelling of galaxies in general and of dwarf galaxies in particular. In particular, I focus my attention on (i) initial conditions, (ii) the equations to solve; (iii) the star formation process in galaxies, (iv) the initial mass function, (v) the chemical feedback, (vi) the mechanical feedback, (vii) the environmental effects. Moreover, some key results concerning the development of galactic winds in galaxies and the fate of heavy elements, freshly synthesised after an episode of star formation, have been reported. At the end of this review, I summarise the topics and physical processes, relevant to the evolution of galaxies, that in my opinion are not properly treated in modern computer simulations of galaxies and that deserve more attention in the future.

1. Introduction

Galaxies are extremely complex astrophysical objects. In order to study the evolution of galaxies, deep understanding of many physical processes, covering a broad range of spatial and temporal scales, is required. On the smallest scales, electromagnetic radiation and particle-particle and particle-radiation interactions determine the thermal and ionisation status of the interstellar medium (ISM). On the largest scales, galactic winds and environmental effects (interactions with neighbouring galaxies and with the intracluster medium) regulate the mass budget of the galaxy and strongly affect its metallicity. Many other key physical processes such as star formation, feedback, gas circulation, and stellar dynamics operate on intermediate spatial and temporal scales.

This review paper gives a summary of ingredients, methods, results, and challenges encountered in the study of the chemical and dynamical evolution of galaxies, with particular emphasis on the study of dwarf galaxies (DGs). The main focus of this review is the theoretical study of the chemodynamical evolution of galaxies by means of computer simulations. For a broader and more comprehensive summary of properties and physical processes in galaxies, the book *Dwarf Galaxies: Keys to Galaxy Formation and Evolution* (Springer) can be consulted.

The last three decades have seen an enormous surge of activity in the study of DGs, the most numerous galaxy

species in the Universe. Advanced ground-based and space-born observatories have allowed the observation of these faint objects in the local volume with incredible detail. From a theoretical perspective, the interest in the study of DGs is manifold. Their shallow potential well allows easier venting out of freshly produced metals than in more massive galaxies. Thus, DGs are perhaps significant polluters of the intracluster and intergalactic medium ([1], but see [2]). According to the hierarchical scenario for galaxy formation, dwarf galaxy-sized objects are the building blocks to form larger galaxies. DGs do not possess very prominent spiral structures or significant shear motions; hence the study of the star formation in these objects is somewhat easier than in spiral galaxies.

Besides providing key information about the kinematics of gas in galaxies, spectroscopy allows the determination of the metallicity and of the abundance ratios of specific elements. This is a very useful information because chemical abundance provide crucial clues to the evolution of galaxies. The increasing availability of large telescopes made the systematic study of extragalactic H II regions and other objects in external galaxies possible. In this way, variations of chemical composition between different galaxies and in different positions within a single galaxy could be studied. Integral field spectroscopy in this sense is a fundamental step forward. Detailed maps of the chemical abundance within a single galaxy can be obtained. In order to understand

the origin of such distributions of metals, one often has to resort to the work and models of theoreticians.

Although a few basic properties of galaxies can be understood with simple analytical and semianalytical considerations, the enormous complexity of galactic physics can only be handled (in part) with the help of numerical simulations. This is especially true for what concerns the chemical evolution of galaxies. Simple closed-box models [3] can provide a first-order explanation for the global metallicity in a galaxy, but the spatial distribution of metals cannot be addressed with these simplified tools. On the other hand, due to the large number of processes one has to take into account, numerical simulations generally make use of results taken from other research fields and combine them in such a way that a detailed description of the evolution of galaxies can emerge. The process of simulating galaxies is thus analogous to the process of cooking. To prepare a culinary dish, ingredients must be accurately chosen, the necessary equipment must be in place, a number of steps and operations must be performed to combine the ingredients, and sometimes a personal touch is added and standard cookbook recipes are modified in order to obtain a special effect.

For chemodynamical simulators of galaxy evolution, the main ingredients are

- (i) the initial conditions;
- (ii) the set of equations to solve;
- (iii) a description of the star formation process;
- (iv) the mass distribution of newly born stars (the initial mass function or IMF);
- (v) a description of the chemical feedback from stars to gas;
- (vi) a description of the energy interchange processes between stars and gas; there are many processes one might take into account but all of them are usually referred to as feedback; this includes also feedback processes related to the presence of supermassive black holes and active galactic nuclei (AGN); These kind of processes are usually dubbed AGN feedback;
- (vii) a description of the interactions between the galaxy and the surrounding environment (galaxy-galaxy interactions, ram-pressure stripping due to an external intergalactic medium, gas infall, and so on).

In this review, I will consider in some detail some of these ingredients and I will describe how they have been parametrised and implemented in numerical simulations of galaxies. Ingredients related to the chemical evolution of galaxies will be treated with particular care. In the description of these ingredients, some personal bias will be applied and higher priority will be given to the most relevant ingredients for the simulation of DGs. In particular, AGN feedback will be only very briefly mentioned.

In the process of preparing a dish, the necessary equipment (pans, pots, and stove) must be in place and the quality of the equipment affects the final outcome. This is also true for the numerical simulation of galaxies, where the main

equipment is a computer. More often, a cluster of computers equipped with fast processors is necessary. Besides having a fast computer, appropriate algorithms and sophisticated numerical methods must be in place in order to efficiently solve the complex equations describing the evolution of galaxies. Some of these methods will be summarised in this review too. Again, besides a very brief survey of most widely adopted methods, specific tools required for the study of the chemodynamical evolution of galaxies will be described with more care.

Numerical simulations always address specific issues in the evolution of galaxies, trying to give answers to open problems or trying to provide explanations to observed properties and characteristics of galaxies or groups of galaxies. In this review I will give a summary of the state of the art for what concerns some of these specific issues. In particular, I will focus on the conditions for the development of galactic winds and on the fate of heavy elements, freshly produced during an episode of star formation.

The organisation of this paper is thus quite simple: there is a section for each ingredient; initial conditions (Section 2), the equations (Section 3), the star formation (Section 4), the initial mass function (Section 5), the chemical feedback (Section 6), the mechanical feedback (Section 7), and the environmental effects (Section 8). In each section, commonly adopted methodologies and recipes will be introduced and some key results of past or ongoing studies will be summarised. In Section 9 I will summarise some relevant results of numerical investigations of DGs concerning galactic winds and their consequences. Finally, in Section 10 some conclusions will be drawn.

2. The Initial Conditions

Nowadays it is pretty common to find in the literature studies of the formation and evolution of galaxies in a cosmological context, meaning that initial conditions consist of a scale-free or nearly scale-free spectrum of Gaussian fluctuations as predicted by cosmic inflation, with cosmological parameters determined from observations of the cosmic microwave background radiation obtained by spacecrafts such as WMAP [4, 5]. However, the most detailed and sophisticated cosmological simulations to date, such as the Millennium-II simulation [6] and the Bolshoi simulation [7], have force resolutions of the order of 1 kpc. This is barely enough to resolve large galaxies, but it is clearly insufficient to resolve in detail DGs, whose optical radii are sometimes smaller than that. A much better spatial resolution can be achieved by zooming in and resimulating small chunks of a large cosmological box [8–10]. This method is gaining pace and has been applied by various groups to DGs [11–13]. Still, at the present time the best way to accurately simulate a DG is by numerically studying it as a single isolated entity [14–19].

Numerical studies of galaxies in isolation assume some initial configuration of gas density, temperature, and stellar distribution. This initial configuration is an equilibrium status of the system. Starting from an equilibrium condition is clearly necessary in order to pin down the effect of perturbing

phenomena (star formation, environmental effects, AGN feedback, etc.).

A common strategy is to consider a rotating, isothermal gas in equilibrium with the potential generated by a fixed distribution of stars and/or of dark matter [20–22]. Rotating gas configurations are usually better described by means of a cylindrical coordinate system (R, ϕ, z) . Often, axial symmetry is assumed. The relevant equation to solve in order to find the density distribution of gas $\rho(R, z)$ is thus the steady-state (time-independent) Euler equation

$$\frac{1}{\rho} \nabla P + (\mathbf{v} \cdot \nabla) \mathbf{v} = -\nabla \Phi, \quad (1)$$

where P is the pressure, \mathbf{v} is the bulk velocity of the gas, and Φ is the total gravitational potential. In this equation, only the component v_ϕ of the velocity must be considered because it gives centrifugal support against the gravity. Equation (1) in fact implies that the gravitational pull is counterbalanced by the combined effect of pressure gradient and centrifugal force.

Most of the authors assume Φ to be independent of ρ . this means that the self-gravity of the gas is not considered. A typical justification of this choice is as follows “the omission of self-gravity is reasonable, given that the baryonic-to-dark matter ratio of the systems is ~ 0.1 .” [23]. However, even if the total mass of a DG is dominated by a dark matter halo, within the Holmberg radius (the radius at which the surface brightness is $26.5 \text{ mag arcsec}^{-2}$), most of the galaxy is made of baryons [24, 25], so the inclusion of gas self-gravity in the central part of a DG appears to be important. I will come back to this point later in this section. For the moment it is enough to take note of the fact that the assumption that Φ is independent of ρ greatly simplifies the calculation of the steady-state density configuration. Furthermore, a barotropic equation of state $P = P(\rho)$ and dependence of the azimuthal velocity v_ϕ with known quantities is commonly assumed.

A widely used strategy is to assume that $v_\phi = e v_{\text{circ}}$, where $v_{\text{circ}} = \sqrt{R(d\Phi/dR)}$ is the circular velocity and e is the spin parameter that determines how much the galaxy is supported against gravity by rotation and how much it is supported by the pressure gradient. A typical value for e is 0.9, independent of the height z [26, 27]. Reference [28] assumes that $e = 0.9$ in the plane of the galaxy, but it drops exponentially with height in order to have nonrotating gas halos. It is however important to remark that, according to the Poincaré-Wavre theorem [29–31], the rotation velocity of any barotropic gas configuration (thus including also isothermal configurations) in rotating equilibrium must be independent of z . In other words, it is possible to construct a centrifugal potential to add to Φ in (1) only if the circular velocity is independent of z .

Other authors [32] solve instead the equilibrium equation in the plane

$$v_\phi^2 = v_{\text{circ}}^2 - \frac{R}{\rho} \left| \frac{dP}{dR} \right|_{z=0} \quad (2)$$

and assume the azimuthal velocity to be independent of z , in compliance with the Poincaré-Wavre theorem. The density

at any z is then found integrating the z -component of the hydrostatic equilibrium equation, for any R . Some authors then [19, 33, 34] set the gas in rotation around the z -axis, using the average angular momentum profile computed from cosmological simulations [35].

A different approach is followed by de Avillez and Breitschwerdt [36]. Initially, there is no balance between gravity and pressure and the gas collapses into the midplane. Supernovae (SNe) go off, principally along the disk and this drives the collapsed gas upwards again. Eventually, upward and downward flowing gas come into dynamical equilibrium. Some multiphase simulations [37, 38] adopt a similar approach of diffuse gas starts far from equilibrium. Then, it relaxes on a few dynamical time scales to a quasi-equilibrium state, which represents the initial conditions for the simulation.

One should be aware of the limitations of an equilibrium model without gas self-gravity. Most of the numerical simulations treat self-consistently the process of star formation. Since star formation occurs when the gas self-gravity prevails over pressure, neglecting the gas self-gravity in the setup of the model is clearly inconsistent. Moreover, without self-gravity, there is the risk of building gas configurations which would have never been realized if self-gravity was taken into account. In order to solve these problems, Vorobyov et al. [39] explicitly took into account gas self-gravity to build initial equilibrium configurations. The gravitational potential Φ is composed of two parts: one is due to a fixed component (dark matter and eventually also old stars), and one (Φ_g) is due to the gas self-gravity. The gas gravitational potential Φ_g is obtained by means of the Poisson equation

$$\nabla^2 \Phi_g = 4\pi G \rho. \quad (3)$$

The gas density distribution is thus used to calculate the potential, but this potential is then included in the Euler equation to find the gas distribution. Clearly, an iterative procedure, analogous to the classical self-consistent field method [40], is necessary to converge to an equilibrium solution.

For a given mass M_{DM} of the dark matter halo, many solutions are possible, according to the initial assumption about the density distribution of the gas. However, the self-gravitating equilibrium configurations always have a maximum allowed gas mass M_{max} , unlike the case of non-self-gravitating equilibria which can realize configurations with unphysically high gas masses. Moreover, only for some of the solutions, star formation was found to be permissible by Vorobyov et al. (two star formation criteria based on the surface gas density and on the Toomre parameter were assumed). The minimum gas mass M_g^{min} required to satisfy the star formation criteria was found to be mainly dependent on the gas temperature T_g , gas spin parameter e , and degree of nonthermal support. M_g^{min} was then compared with M_b , the amount of baryonic matter (for a given M_{DM}) predicted by the Λ CDM theory of structure formation. Galaxies with $M_{\text{DM}} \geq 10^9 M_\odot$ are characterised by $M_g^{\text{min}} \leq M_b$, implying that star formation in such objects is surely possible as the required gas mass is consistent with what is available

according to the Λ CDM theory. On the other hand, models with $M_{\text{DM}} \leq 10^9 M_{\odot}$ are often characterised by $M_g^{\text{min}} \gg M_b$, implying that they need much more gas than what is available to achieve a state in which star formation is allowed. In the framework of the Λ CDM theory, this implies the existence of a critical dark matter halo mass below which the likelihood of star formation drops significantly ([39]). It is observationally well established that the galactic stellar mass function for low-mass galaxies is quite shallow (i.e., $dn/dM_* \propto M_*^{\alpha}$, with $\alpha \sim -1.3$; see [41, 42]). This is at variance with the steeper ($\alpha \sim -1.8$) halo mass function predicted over the mass range of interest by the Λ CDM theory. It seems thus that the efficiency of forming stars within each dark matter halo decreases with the mass of the halo. The results of Vorobyov et al. illustrated above agree with this result (see also [42–44]).

3. The Equations

In order to follow the evolution of a galaxy, the basic equations to solve are of course the Euler equations, namely, the standard set of equations (conservation of mass, momentum, and energy) governing inviscid flows. Viscosity in astrophysical plasmas is in fact usually very small. It can be large in some localised system, for instance in accretion disks, but on a larger, galactic-wide scale the ISM can be considered inviscid and there is no need to invoke the Navier-Stokes equations. Conversely, astrophysical plasmas are usually very turbulent [45]. In spite of that, also the use of turbulence models in simulations of galaxies is still quite limited. The main reason for that is the lack of satisfying characterisation and modelling strategy for the compressible turbulence. Progress in this field is however constant and very sophisticated turbulence models have been applied recently to astrophysical problems [46–52]. Important first steps have been performed also in the simulation of turbulent gas in galaxies [16, 53–56].

Since a large volume fraction of the ISM of star forming galaxies is ionised, a description of the electromagnetic interactions is clearly required. This is most often realized by means of the so-called ideal magnetohydrodynamical equations, where various ions are treated as a single fluid, the conductivity of the ionised gas is assumed to be very large and the plasma is assumed to be frozen in the magnetic field. Many modern hydrodynamical codes, such as ZEUS [57], FLASH [58, 59], RAMSES [60, 61], and ATHENA [62], just to name a few, solve the ideal magnetohydrodynamical equations. The inclusion of magnetic fields affects the dynamics of gas in a galaxy in many ways. (i) Magnetic fields strongly reduce the transverse flow of charged particles and hence the thermal conduction in directions orthogonal to field lines [63]. Thermal conduction along field lines remains unaltered compared to nonmagnetised gases. (ii) Magnetic tension forces tend also to suppress dynamical instabilities parallel, but not perpendicular, to field lines [64]. Magnetic fields might also inhibit the break-out of hot bubbles and superbubbles [65]. Also the mixing between the hot bubble and the surrounding cold supershell can be reduced due to the presence of magnetic fields. (iii) The magnetic pressure

$B^2/8\pi$ plays an important role in the gas dynamics. It is in fact comparable with the thermal pressure and, if the magnetic field is not too weak, it is the dominant form of pressure for temperatures below ~ 200 K [66]. This is consistent with the fact that the estimated thermal pressure in the Milky Way is $\sim 5 \cdot 10^{-13}$ dyne cm^{-3} , whereas the estimated magnetic pressure is $\sim 10^{-12}$ dyne cm^{-3} (see [67]). Simulations of the formation of spiral galaxies [68] show indeed that the additional pressure due to magnetic fields can lead to lower star formation rates at late times compared to simulations without magnetic fields. Also the structure of the spiral arms is affected by the presence of magnetic fields.

It is less easy to assess the importance of magnetic fields in the simulations of DGs. In fact, not so much is known about magnetic fields in these objects. Starbursting DGs such as NGC1569 [69] or NGC4449 [70] are known to have magnetic fields with strengths as high as few tens of μG , whereas quiescent DGs have much weaker magnetic fields (a few μG , [1, 71]). Magnetic fields are probably not the main drivers of DG evolution, at least during periods of quiescent or weak star formation.

Since our knowledge of galaxies almost exclusively depends on their emitted (or absorbed) radiation, radiation hydrodynamics clearly allows a description of galaxies which is more complete and easier to compare with observations. The radiation hydrodynamical equations are more complex than the Euler equations. A few textbooks exist, in which these equations and related numerical methods are described in detail [72–74]. Many authors who attempted to solve them made simplifying assumptions about the matter-radiation coupling.

The simplest possible way to include the effects of radiation in hydrodynamical simulations is to assume that the gas is optically thin. The only effect of radiation is thus to reduce the available thermal energy of the gas; that is, radiation acts only as an energy sink. Many works in the literature are devoted to the calculation of the cooling function of an optically thin plasma [75–77] and these functions are used to calculate the rate of thermal energy loss as a function of density, temperature, and chemical composition. A further commonly adopted assumption is the on the spot approximation [78], according to which the photons produced in recombination processes do not propagate but are immediately absorbed locally. In this way, the transport of these photons must not be considered and that results in a considerable simplification of the problem at hand. The heat produced by the radiation is transported out according to a law similar to the thermal conduction. This approximation turns out to be valid as long as the particle density is sufficiently high, that is, when the optically thick limit applies. There are various examples of radiation hydrodynamical simulations which make use of the on-the-spot approximation [79–83]. A step forward is the so called flux limited diffusion, where the optically thin and optically thick limits are connected by appropriate flux limiter functions [84–86]. Radiation hydrodynamics is clearly very relevant and might quite substantially change our understanding of galaxy formation and evolution of galaxies [87–89].

In particular, the inclusion of radiation feedback (photoheating and radiation pressure) turns out to be very important and it helps reproducing the observed distribution of stellar masses in DGs, whereas simulations with only supernova feedback fail to reproduce the observed stellar masses ([90]; see also Section 7). In spite of significant recent progresses, the inherent complexity has so far limited the use of radiation hydrodynamical equations in galaxy simulations.

Of course, gas is not the only component of a galaxy. Stars and, very often, dark matter must be considered too. The gravitational potential they generate has been already considered in Section 2. However, their dynamics can be very important as well. The relevance of a live dark matter halo for the evolution of a galaxy is not clear and many authors still assume a fixed dark matter halo. Conversely, it is clear that the stellar dynamics plays an important role in the evolution of a galaxy, at least if one is interested in time spans larger than a few tens of Myr. This has been demonstrated for instance by Slyz [91] by means of a clear numerical experiment. According to this study, spurious results can be obtained if one does not allow stars to move from their natal sites. In particular, the energy of Type II Supernovae (SNeII) is, in this case, always released in regions of high densities (because in these regions it is more likely to form stars; see Section 4), where cooling rates are high. This leads to the so-called overcooling problem (see also Section 7). This problem can be simply avoided if one allows stars to move during their lifetimes and, hence, SNeII to explode in environments other than their natal ones (in particular, to explode in less dense environments).

A widely used strategy to follow the dynamics of stars (and of dark matter particles) is to consider individual stars, or more often, populations of stars, as point masses and to follow their orbits by means of standard N-body integration techniques. This approach is straightforward in SPH simulations of galaxies but it is widely used also in grid-based codes. However, in grid-based codes there is the problem that star particles must be mapped to the mesh in order for the global gravitational potential to be calculated. Once the gravitational potential is computed, it is then interpolated back to the particles. This process can lead to a loss of accuracy due to the required interpolations. It might also spuriously generate entropy if the particle resolution is too low to adequately sample the density field [92]. This might be the key to understand the differences seen in the central entropy profiles of galaxy clusters simulated with SPH and mesh-based Eulerian techniques [93]. Eventually, the interpolation processes increase the communication overhead in massively parallel simulations [94]. A possible remedy in grid-based codes is the stellar hydrodynamical approach [95, 96]. With this approach, the stars are treated as a collisionless fluid and their evolution is regulated by the moments of the Boltzmann equation. This approach has been used many times to simulate galaxies [97–100]. Recently, Mitchell et al. [94] implemented this method into the FLASH code. Numerical tests confirmed the validity of this approach and the advantages over the more conventional particle schemes.

Another very important aspect of the evolution of galaxies is the multifluid, multiphase treatment. Stars and gas

exchange mass, momentum, and energy during the whole life of the stars. Also dust and gas exchange mass and momentum (see Section 6 for more detail on dust-gas interactions). Moreover, various gaseous phases are known to exist in the ISM and phase transformations occur continuously during the life of a galaxy. Eventually, the gas in the ISM is composed of many different elements, with various ionisation states. A complete treatment of the galaxy evolution must take into account the various phases of a galaxy and all possible exchange processes among them. In the classical chemodynamical approach, put forward by Hensler and collaborators [95, 98, 101], stars and various gas phases (typically a cold and a warm-hot phase) coexist within a single grid and exchange mass, momentum, and energy according to physically based recipes. The dynamics of the various phases might or might not be the same. Typically, the various gas phases share the same velocity field whereas the dynamics of the stars are different. This approach has been refined over the years and many groups use it to simulate galaxies, with various degrees of sophistication [37, 102–107]. Nowadays, chemodynamics is a widely used term that generically refers to simulations in which some treatment of the chemical evolution is included [108–112]. Although these codes clearly represent a step forward with respect to more traditional single-fluid simulations, still they lack the complexity of the multiphase chemodynamical codes described above.

Unfortunately, not many works in the literature have been devoted to the direct comparison of single-phase and multiphase models. In simulations of the hot interstellar medium in elliptical galaxies [113], the treatment of SNe ejecta as a separate phase makes SN explosions less effective at heating the ISM because most of the explosion energy is released in a dense and metal rich medium and it is quickly radiated away. The SN energy is more efficiently transformed to thermal energy of the ISM in single-phase simulations. The multiphase description of the ISM in simulations of ram-pressure stripping (see Section 8) changes the distribution of gas compared to a single-phase model [114]. This is due to the fact that the ISM in multiphase simulations is more structured and with larger density variations. Steep density gradients are much better resolved in SPH multiphase implementations compared to classical single-phase ones [115]. The multiphase treatment can be the key to solve the so-called overcooling problem typically encountered in single-phase simulations (see Section 7 for more discussion on that aspect).

Also the metallicities and abundance ratios of simulated galaxies can be significantly affected by the multiphase treatment of the ISM. For instance, the presence of a cloudy phase dilutes the ISM, without preventing the formation of large-scale outflows, able to eject a fraction of the freshly produced heavy elements (see Section 9). The resulting final metallicity of model galaxies with a multiphase (cloud-intercloud) ISM treatment is therefore generally lower (by 0.2–0.4 dex) than the one attained by single-phase models [116]. A clear example of the effect of a cloudy medium is presented for instance in Figure 7 of [116]. Clouds (in particular infalling clouds) produce not only a decrease in the global metallicity but also a variation in the C/O, N/O,

and Fe/O abundance ratios. In particular, the observed N/O abundance in the galaxy I Zw 18 seems to require the presence of infalling clouds.

4. The Star Formation

In spite of many still open questions, enormous progresses have been made in the last decade in simulating the process of star formation [117–122]. However, the level of details and the resolution reached by these works cannot be matched by galactic simulations. Suitable parametrisations of the star formation need to be implemented. It is also worth mentioning that many papers dealing with simulations of galaxies do not self-consistently calculate the star formation but use prescribed star formation rates (SFRs) or star formation histories (SFHs). These are either based on the reconstructed SFH of specific galaxies [123, 124] or are simple functions of time such as instantaneous bursts or exponentially declining SFRs [20, 23, 125, 126]. This is a viable possibility if the star formation process itself is not the focus of the numerical study.

A star formation law scaling with some power of the gas volume or surface density is often assumed. This relation is based on the observation of star formation indicators in local galaxies [127] and is often called the Kennicutt-Schmidt law. To be more precise, the Kennicutt-Schmidt law implies that

$$\Sigma_{\text{SFR}} \propto \Sigma_g^n, \quad (4)$$

where Σ_{SFR} is the SFR surface density and Σ_g is the gas surface density. The value of n reported by Kennicutt [127] is 1.4 ± 0.15 . In many works, dependence on the total volume density [128–131] or on the molecular gas density [132–135] is also assumed. Dependence on the molecular gas density appears to be particularly relevant because there is a tight correlation between the H_2 and the SFR surface densities [136]. Moreover, in spiral galaxies, often the Toomre criterion is used to identify regions prone to star formation [39], or Σ_{SFR} is assumed to be $\propto \Omega \Sigma_g$, where Ω is the circular frequency [137, 138]. Eventually, the spatial distribution of a molecular cloud seems to play a critical role in determining its star formation activity [139], but the dependence of the SFR on the structure of a molecular cloud appear to be very difficult to implement in numerical simulations.

In hydrodynamical simulations, many authors still follow the star formation recipes of Katz [140], namely (see also Katz et al. [141])

- (i) the gas density must be larger than a certain threshold;
- (ii) the particle must reside in an overdense region;
- (iii) the gas flow must be converging ($\nabla \cdot \mathbf{v} < 0$);
- (iv) the gas particle must be Jeans unstable: $h/c_s > 1/\sqrt{4\pi G\rho}$, where h is the dimension of the gas particle (smoothing length for SPH simulations and the grid cell size for grid-based methods) and c_s is the local sound speed.

With small variants, this recipe has been applied in most of galaxy simulations [142–146]. The Jeans criterion appears

to be particularly relevant; otherwise artificial fragmentation and, hence, spurious star formation can arise [147, 148]. However, in some simulations the implementation of this criterion has led to unrealistic SFRs [144].

Often, a star formation law of the type

$$\psi(t) = c_* \frac{\rho}{t_{\text{dyn}}} \quad (5)$$

is assumed, where $\psi(t)$ is the SFR and c_* is the star formation efficiency [106, 144, 149]. Here t_{dyn} is a typical star formation timescale given by the free-fall timescale, the cooling timescale, or a combination of both. Notice that the free-fall time scale is proportional to $\rho^{-1/2}$; thus a star formation very similar to the Kennicutt-Schmidt law can be obtained in this way (see also [150]). Notice also that observed laws (such as the Kennicutt-Schmidt law (4)) involve surface densities, whereas theoretical models and simulations generally work with volume density laws such as (5) and these two formulations are not necessarily equivalent. Typically adopted values for c_* in (5) are quite low, ranging between 0.1 and 0.01 [144]. This is also the ratio between the gas consumption time scale and t_{dyn} . This assumption is in agreement with the conclusion, deduced from observations, that only a small fraction of gas in molecular clouds can be converted into stars [151, 152]. The star formation efficiencies are larger (of the order of 0.3) if one considers only the dense cores of molecular clouds [153]. Global star formation efficiencies tend to be even lower in DGs (see also Section 2 and below in this section).

As mentioned above, the fraction of molecular gas is taken into account in some star formation recipes. In particular, the right-hand side of (5) is often multiplied by f_{H_2} , that is, by the H_2 mass fraction [133, 134]. It has been shown [154, 155] that such a star formation law applied to cosmological simulations leads to a strong reduction of the star formation in low-mass halos compared to models without molecular fraction dependencies. This might help explain the mismatch between the observed mass distribution of DGs and the predictions of the Λ -CDM theories (see also Section 2).

Since the cooling timescale depends on the gas temperature, dependence of the star formation with the temperature is implicit in (5). It is of course very reasonable to assume that the SFR depends on the temperature, since star formation occurs in the very cold cores of molecular clouds. For this reason, some authors even assume a temperature threshold, above which star formation cannot occur [144, 156, 157]. However, one should be aware of the fact that simulations still do not have the capability to spatially resolve the cores of molecular clouds. The temperature of a star forming region is thus simply the average temperature of a region of gas, with size equal to a computational unit (gas particle in an SPH simulation or grid cell in grid-based codes), encompassing the star forming molecular cloud core. For this reason, typical temperature thresholds are of the order of 10^3 – 10^4 K, at least two orders of magnitude larger than typical molecular core temperatures.

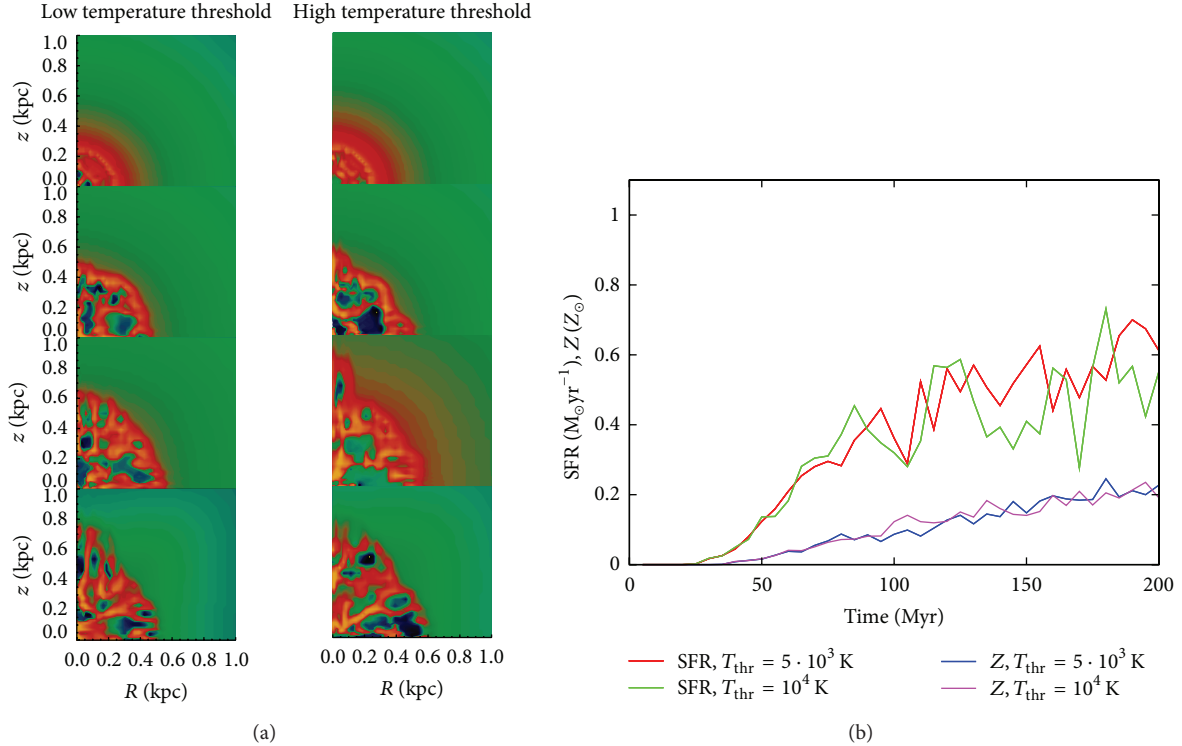


FIGURE 1: The effect of the temperature threshold T_{thr} above which star formation is not allowed. (a) The density distribution of gas in two runs with different T_{thr} : $T_{\text{thr}} = 5 \cdot 10^3 \text{ K}$ (left panels) and $T_{\text{thr}} = 10^4 \text{ K}$ (right panels). The four rows are snapshots of the evolution of the two models at four different moments in time: 50 Myr (uppermost panels), 100 Myr (second row of panels), 150 Myr (third row of panels), and 200 Myr (lowermost panels). Dense gas is in orange (upper densities are $10^{-23} \text{ g cm}^{-3}$); dilute gas is in blue (lower densities are $10^{-27} \text{ g cm}^{-3}$). (b) Star formation rates (in $M_{\odot} \text{yr}^{-1}$) and global metallicities (in Z_{\odot}) for the same models shown in the left panels, during the first 200 Myr of galactic evolution.

Some authors adopt more complex temperature dependence. For instance, Köppen et al. [158] derive

$$\psi(t) = c_* \rho^2 e^{-T/T_s}, \quad (6)$$

where the transition temperature $T_s = 1000 \text{ K}$ implies that the star formation is very low in regions with $T > T_s$. Notice that, in this case, c_* does not have the same dimensions (and the same meaning) of the c_* introduced in (5). This star formation recipe, coupled with the feedback from stellar winds and dying stars (see Section 7), nicely leads to self-regulation of the star formation process. In fact, a large SFR increases the feedback, which in turn strongly reduces further star formation whereas, if the feedback is low, the temperature does not increase and star formation is more efficient. Because of the self-regulation, the star formation process is not very dependent on the adopted parameters c_* and T_s .

Eventually, theoretical works [159] suggest that the star formation efficiency can depend on the external pressure, simply because gas collapse is favoured in environments with large pressures. This hypothesis is supported by the observational fact that the molecular fraction depends on the gas pressure [160, 161] and, as noticed above, the surface density of molecular gas strongly correlates with the SFR

[136]. DGs are usually characterised by lower pressures compared to larger galaxies, thus the predicted star formation efficiency is lower. This finding is in agreement with other lines of evidence, showing that DGs are quite inefficient in forming stars (see Skillman [162] for a review; see also Section 2). The pressure dependence on the star formation efficiency has been used in Harfst et al. [37].

Various works in the literature have been devoted to the comparison of different star formation schemes in simulations of galaxies. I will briefly summarise some of these works, but, before doing so, it is important to remark what written above: the star formation process (if adequately simulated) tends to self-regulate; therefore moderate variations of the involved parameters produce little changes in the final outcomes of the simulations. Figure 1 shows an example of this self-regulation. The outcomes of models simulating DGs without massive dark matter halos (modelled as in [157]) are shown. Two values of the temperature threshold T_{thr} , above which the star formation is not allowed, have been adopted. As one can see, the evolution of these two model galaxies (distribution of gas, SFR, and evolution of the global metallicity) is fairly insensitive to the chosen value of T_{thr} .

A thorough investigation of different prescriptions for turning cold gas into stars in SPH cosmological simulations [163] shows that the results are indeed fairly insensitive

to many parameters describing the star formation process (temperature and density thresholds, overdensity threshold). However, large differences in these parameters might indeed lead to completely different results (see, e.g., [142] for differences in DG models with density thresholds varying by up to four orders of magnitude). Also relaxing the criterion $\nabla \cdot \mathbf{v} < 0$ seems not to produce large differences in some simulations of galaxies [164]. Variations of the parameter c_* might instead lead to different results, at least in some implementations. The average SFR becomes larger for large values of c_* and a good fit with the observed Kennicutt-Schmidt law is obtained with $c_* = 0.05$ [144].

5. The Initial Mass Function

Once the stars are born, a mass distribution must be assumed. In fact, the chemical and mechanical feedback of massive stars substantially differ from the feedback of low- and intermediate-mass stars (see next sections); thus it is crucial to know how many stars are formed per each mass bin. Actually, the IMF is often combined with the SFR to obtain the so-called birthrate function $B(m, t)$ [3, 129], which gives the number of stars formed per unit stellar mass and per unit time. Usually, the time dependence is described by the SFR, whereas the mass dependence is determined by the IMF. However, one should already point out that, according to some lines of evidence, the IMF could depend on time too (see below).

The IMF $\xi(m)$ was originally defined by Salpeter [165] as the number of stars per unit logarithmic mass that have formed within a specific stellar system. Thus, the total mass of stars with masses between m and $m + dm$ is $\xi(m)dm$. A very useful concept is also the IMF in number $\varphi(m)$, giving the number of stars in the interval $[m, m + dm]$. Clearly, $\xi(m) = m\varphi(m)$. Salpeter found out that $\xi(m) \propto m^{-1.35}$ for $0.4M_\odot < m < 10M_\odot$. This estimate has been refined over the years [3, 166–168] and nowadays a commonly used parametrisation is the so-called Kroupa IMF [169], namely, a three-part power law $\xi(m) \propto m^{-\gamma}$ with $\gamma = -0.7$ in the interval $0.01M_\odot < m < 0.08M_\odot$ (i.e., in the brown dwarf domain), $\gamma = 0.3$ for $0.08M_\odot < m < 0.5M_\odot$, and finally $\gamma = 1.3$ (very similar to the Salpeter slope) for stellar masses larger than $0.5M_\odot$.

The paper of Romano et al. [170] clearly shows how different IMFs can change the fraction of stars in various mass bins (see their Table 1). IMFs predicting smaller fractions of massive stars produce less α -elements, because these elements are mainly synthesised by SNeII. This is evident in Figure 6 of [170], which shows the evolution of $[\alpha/\text{Fe}]$ versus $[\text{Fe}/\text{H}]$ for model galaxies characterised by different IMFs. Since more massive stars means more SNeII, clearly the IMF affects the energetics of a galaxy too. This has been shown in many simulations [112, 171–173]. In particular, flat IMFs tend to produce higher fractions of massive stars and, hence, larger SNeII luminosities. The energy supplied by SNeII could be enough to unbind a fraction of the ISM and produce a galactic wind (see also Section 9).

It is important to point out that, usually, numerical simulations adopt a fixed value for the IMF upper stellar mass m_{up} , irrespective of how much gas has been converted into stars. However, m_{up} should depend on the mass of the newly formed stellar particles, for the simple reason that only massive star clusters can host very massive stars. A correlation between the stellar cluster mass M_{cl} and the upper stellar mass is indeed observationally established and can be reproduced by simply assuming that m_{up} is the mass for which the IMF in number $\varphi(m)$ is equal to 1 [174]. Weidner and Kroupa [175] found that the theoretically derived $M_{\text{cl}}-m_{\text{up}}$ relation nicely reproduces the available observations (their Figures 7 and 8; see also [176]). Clearly, this assumption can greatly affect the outcomes of simulations, but, to the best of my knowledge, it has never been explored in detail in hydrodynamical simulations of galaxies.

Since a correlation between the most massive cluster in a galaxy and the SFR ψ is also observationally established [177], the logical consequence is that the galaxy-wide IMF in a galaxy must depend on the SFR too. In particular, the IMF is time dependent and is given by the integral of the IMFs of single star cluster, which are assumed to always be a Kroupa IMF, but with different upper masses m_{up} , depending on the star cluster mass. An upper cluster mass limit depending on ψ is then assumed. Given a mass distribution of embedded clusters $\varphi_{\text{cl}}(M_{\text{cl}})$ (giving the number of star clusters in the interval $[M_{\text{cl}}, M_{\text{cl}} + dM_{\text{cl}}]$), the global, galactic-scale IMF (integrated galactic IMF or IGIMF) is given by

$$\varphi_{\text{IGIMF}} = \int_{M_{\text{cl,inf}}}^{M_{\text{cl,sup}}(\psi)} \varphi(m < m_{\text{up}}(M_{\text{cl}})) \varphi_{\text{cl}}(M_{\text{cl}}) dM_{\text{cl}}, \quad (7)$$

(see [174, 178, 179] for details; notice also that in the original papers the IMF in number is designed with ξ instead of with φ). The IGIMF turns out to be steeper than the Kroupa IMF assumed in each star cluster and the difference is particularly significant for low values of the SFR. Notice however that the IMF tends to become top-heavy when the SFR is very high [180]. The effect of the IGIMF on the chemical evolution of galaxies has been already explored in a few papers [179, 181–183]. It turns out that the IGIMF is a viable explanation of the low metallicity [182] or of the low α/Fe ratios [179] observed in DGs. The main reason is that DGs have on average lower SFRs and this, in turn, implies steeper IMFs, characterised by a lower fraction of massive stars. The production of metals and, in particular, of α -elements is considerably reduced.

Chemodynamical simulations of galaxies can give a more complete picture of the evolution of DGs and of the effect of the IMF (and of the IGIMF, in particular). Figure 2 shows the comparison of the results of two chemodynamical simulations, with and without adopting the IGIMF. Methods, assumptions, and initial conditions are taken from [124]. In particular, the main structural properties of the shown model galaxies resemble the blue compact DG IZw 18 (see [184, 185] for a summary of observed properties of this galaxy). The SFH is shown in the upper left panel. This particular dependence of the SFR with time has been chosen again in agreement with the reconstructed SFH of IZw 18 as derived by Aloisi et al. [186]

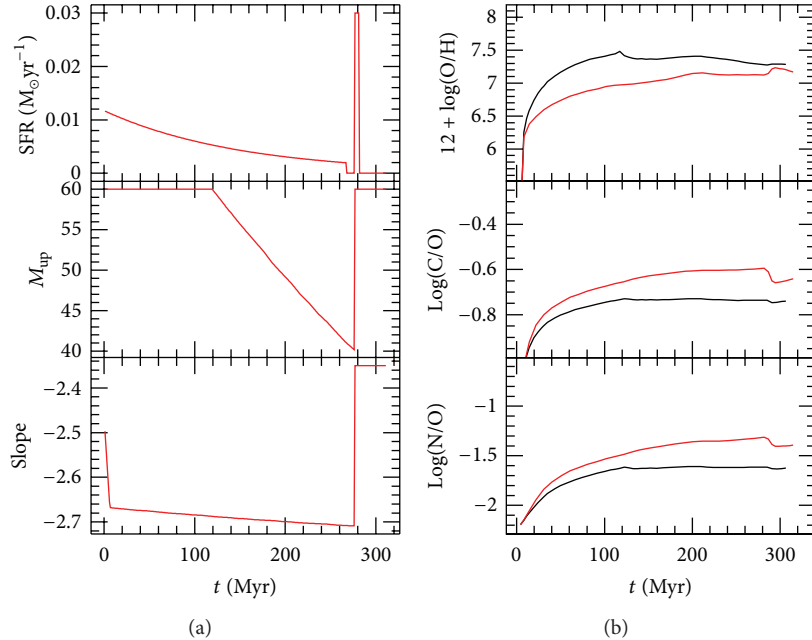


FIGURE 2: The effect of the IMF on the evolution of galaxies. (a) The adopted SFR (upper panel), together with the upper stellar mass M_{up} (in M_{\odot} , middle panel) and the average slope of the IMF (in number, lower panel) calculated for the IGIMF galactic model (red lines in the right panels). (b) Predicted evolution of abundance and abundance ratios for a IGIMF galactic model (red lines). Plotted are the evolution of oxygen (upper panel), carbon-to-oxygen ratio (middle panel), and nitrogen-to-oxygen ratio (lower panel). The black line represents the evolution of a model with a time-independent Salpeter IMF (i.e., with a slope of -2.35).

(but see [187] for a more recent determination of the SFH in IZw 18). According to this SFH, the IGIMF predicts variations of the upper stellar mass and of the average IMF slope as shown in the middle and lower panels, respectively.

The evolution of gas-phase abundance and abundance ratios in a simulation adopting these IGIMF prescriptions is shown in the right panels (red lines) and compared with the results obtained with a model adopting a standard, time-independent Salpeter IMF (black lines). Since the IGIMF is steeper (and poorer in massive stars) than the Salpeter IMF, the initial phases are characterised by lower production of oxygen and, consequently, higher values of C/O and N/O. However, due to the higher feedback, the model with Salpeter IMF experiences a galactic wind at $t \approx 120$ Myr. Since galactic winds tend to be metal enriched (see also Section 9), the onset of the galactic wind is characterised by a decrease in O/H. The galactic wind does not occur in the IGIMF run due to the reduced number of SNeII. At $t \approx 280$ Myr a burst of star formation occurs (see upper left panel). In the Salpeter IMF run, most of the freshly produced metals are channelled out of the galaxy and do not contribute to the chemical enrichment. In the IGIMF run instead, the metals newly synthesised during the burst do contribute to the chemical enrichment and this causes a sudden increase of the oxygen abundance (and a sudden decrease of C/O and N/O).

More detailed simulations, exploring wider parameter spaces, can show other effects of the IGIMF. In particular, the simulations shown in Figure 2 assume a predefined SFH, but it is clear that the adoption of the IGIMF can affect the onset of the star formation too, because it affects the energetics of the ISM. Numerical simulations of galaxies with IGIMF

and with star formation recipes as described in Section 4 would surely predict different SFHs as compared with models with SFR-independent IMFs. This has been shown already in chemical evolution models [181] but this effect can be even more dramatic in chemodynamical simulations.

An example of the effect of different IMF assumptions on the evolution of galaxies is provided by Ploekinger et al. [188]. In this paper, the star formation has been self-consistently modelled using (6). Stars organise themselves in clusters, whose masses depend on the local reservoir of gas. Within each cluster, it is assumed that the mass of the most massive star correlates with the total cluster mass, in compliance with the $M_{\text{cl}}-m_{\text{up}}$ relation described above (truncated IMF simulation). This truncated IMF model has been compared with a simulation in which the upper stellar mass in each cluster is always the same, irrespective of the cluster mass (filled IMF simulation). The assumption of a truncated IMF is particularly relevant for small clusters (with masses less than a few $10^2 M_{\odot}$): in these clusters, the most massive star is smaller than $10 M_{\odot}$; thus there are no (or very few) SNeII. Since SNeII dominate the energy feedback in DGs (see Section 7), the absence of these SNe leads to smaller temperatures compared to filled IMF simulation. This is shown in Figure 3: the gas density and temperature distributions of the truncated and filled IMF simulations are compared at an evolutionary time of 180 Myr (when the SFR reaches its peak). The temperature in the truncated IMF model is on average lower, thus the star formation can proceed for a longer time and at a higher rate compared to the filled IMF simulation (see also Figure 8 of [188]).

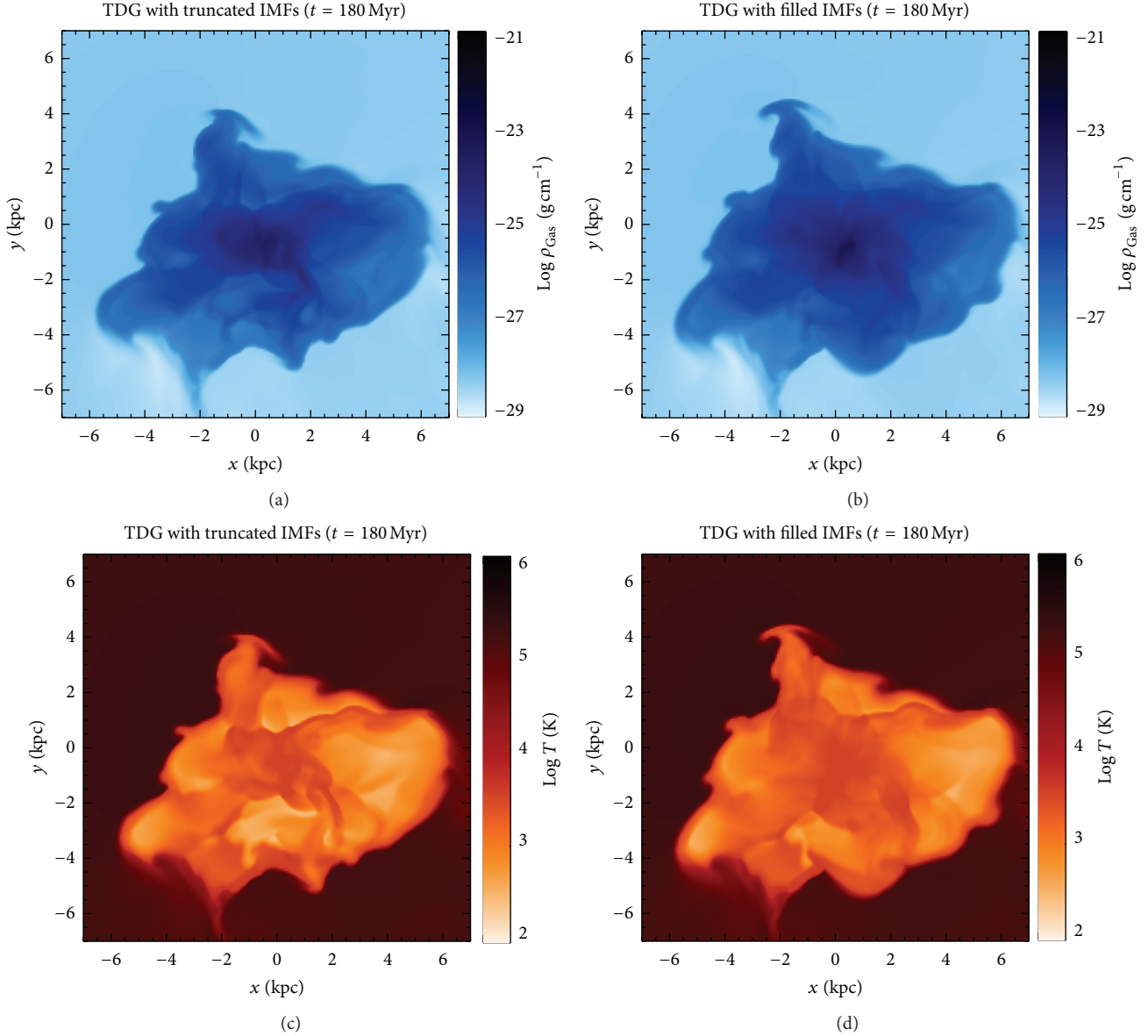


FIGURE 3: The density (a and b) and temperature (c and d) distributions after 180 Myr of evolution of two model galaxies. Strips on the right of each panel show the density and temperature scales. In one case (a and c), the upper mass in each formed star cluster depends on the total cluster mass (truncated IMF). In the other case (b and d), the upper IMF mass is always the same, irrespective of the mass of the star cluster. It is to notice that the temperature of the gas outside the galaxy has been set to 10^6 K. The temperature in the central region is hotter in the filled IMF model because of the larger amount of energy provided by SNeII.

It is also important to point out that, in (7), only the global, galactic-scale SFR is required to calculate the IGIMF. However, the star formation process is usually very inhomogeneous within a galaxy, with regions of very enhanced star formation. Clearly, the formation of massive stars is more likely in regions of high star formation density. It is reasonable thus to expect that the IMF varies not only with time but also with location within a galaxy. This approach has been used for instance by Pflamm-Altenburg and Kroupa [189] to explain the cut-off in $\text{H}\alpha$ radiation in the external regions of spiral galaxies (where the SFRs are milder). In [188] also this effect can be appreciated (see in particular their Figure 11). Observational evidence of the variation of

the IMF within galaxies is given by Dutton et al. [190]. To finish, several lines of evidence point towards dependence of the IMF on the metallicity too [191, 192], in the sense that the IMF appears to become top-heavy in metal poor environments. Clearly, the chemodynamical simulations of galaxies with spatially and temporally variable IMFs can give us new, different perspectives and insights to understand the evolution of galaxies.

6. The Chemical Feedback

In order to follow the chemical evolution of a galaxy, it is without any doubt important to know how stars with different

masses enrich the ISM with various chemical elements. The term stellar yields is commonly used to indicate the masses of fresh elements produced and ejected by a star of initial mass m and metallicity Z . However, the term yields was originally introduced to indicate the ratio between the mass of a specific chemical element newly created and ejected by a stellar generation and the mass locked up in remnants (brown dwarfs, white dwarfs, neutron stars, and black holes; see also Section 9).

Many groups in the past few decades calculated the stellar yields of both massive and intermediate-mass stars for different metallicities [193–201]. Unfortunately, except for a handful of elements whose nucleosynthesis in stars is well understood, yields of other elements calculated by different authors can vary by orders of magnitude. This is especially true not only for the majority of the iron-peak elements but also for much more abundant species such as carbon and nitrogen (see the review of Nomoto et al. [198]). Of course, model predictions are significantly affected by the choice of the set of yields. This has been shown by Romano et al. [202] by means of neat and clear numerical tests (see their Figures 3 and 15, for instance). One of the most significant sources of uncertainty in the calculation of stellar yields is the presence of stellar mass loss. Massive stars with solar metallicity might in fact lose a large amount of matter rich of He and C, thus subtracting those elements to further processing, which would eventually lead to the production of oxygen and other heavy elements. The models of Maeder [203] for instance predict that a $40M_{\odot}$ star ejects only $\sim 2M_{\odot}$ of O, whereas in most of nucleosynthetic calculations without winds [195, 201, 204] the production of oxygen is a factor of ~ 3 larger.

The yields from dying stars not only directly affect the chemical composition of the ISM in chemodynamical evolution of galaxies but can also affect the dynamics by means of chemical feedback. The main effect is due to cooling. In fact, it is known that the cooling function of an optically thin plasma has a strong dependence on metallicity, at least in the temperature range between $\sim 10^4$ and 10^5 K [75–77]. Moreover, different chemical elements contribute differently to the plasma radiative emission. Clearly, the assumption of different yields in chemodynamical models affects the chemical composition of the ISM, which in turn changes the cooling timescales. An example of the effect of different sets of yields on the dynamical evolution of galaxies is given in Figure 4. Two models of galaxy evolution (taken from the suite of simulations of Recchi et al. [157]) differ only in the adopted nucleosynthetic prescriptions for intermediate-mass stars: [197] (MM02) on the left panels and [193] (VG97) on the right panels. Yields of high-mass stars are in both cases taken from [201]. Feedback from SNeII and stellar winds creates a network of cavities and tunnels. The superbubble evolution is faster in the MM02 model. Indeed, MM02 produces on average more metals, therefore leading to larger cooling rates. On the one hand, it reduces the thermal energy content inside the superbubble, but on the other hand, this increased cooling favours the process of star formation, leading to more powerful feedback. The latter effect prevails, and a larger

energy is available in model MM02 to drive the expansion of the supershell. Within the time span of 100 Myr covered by these two simulations, the differences between the two models are not huge. They are, however, nonnegligible and they tend to increase with time. This simple test shows the effect of chemical feedback on the evolution of a galaxy, an aspect that has been often overlooked in the literature.

One should also be aware that other forms of chemical feedback operate in galaxies. The photoelectric emission from small dust grains and PAHs can substantially contribute to the heating of the ISM [205]. The amount of dust and PAH in a galaxy strongly correlates with its metallicity [206] and, consequently, the metallicity affects the photoelectric heating of the gas. It is commonly assumed that, for ISM metallicities below $Z_{\text{cr}} \sim 10^{-5}Z_{\odot}$, the star formation process is substantially different and leads to a top-heavy IMF producing, on average, very massive stars, the so-called PopIII stars [207]. As the ISM metallicity approaches Z_{cr} , the transition to a Salpeter-like IMF occurs.

Under some circumstances, chemical reactions can affect the chemical evolution as well. Astrochemistry is a vibrant and very active astrophysical discipline [67, 208] and nowadays the details of many important atomic and molecular reactions occurring in the ISM are known. Although the chemistry of the dense gas in clouds is very rich and variegated, less happens in the more dilute diffuse gas. Global, galactic-scale simulations usually do not require the implementation of complicated reaction networks. However, the presence of dust can significantly affect the chemical evolution. It is in fact well known that a large fraction of some chemical elements (particularly Fe, Co, Ni, Ca, C, and Si) are locked into dust grains [209]. Clearly, it is impossible to have a complete picture of the evolution of these chemical elements in the ISM without considering the dust. There have been several works about the chemical evolution of galaxies with dust [210–214]. It is more complicated to include dust into chemodynamical simulations of galaxies. On the one hand, still not much is known about the sources and composition of interstellar dust [67]. On the other hand, the physics of the dust-gas coupling is still poorly known and typically assumed drag forces lead to numerical problems [215]. In spite of these difficulties, progresses have been made and simulations of galaxies taking into account dust are becoming available [216, 217]. Clearly, this is a field where more needs to be done. Observations of dust in our own galaxy and in external galaxies are becoming extremely accurate and the astronomical community is in dire need of detailed chemodynamical simulations of dusty gases in order to help interpreting the observations.

7. The Mechanical Feedback

Explosions of SNe (of both Type Ia and II) and stellar winds are the main drivers of the ISM dynamics, at least in DGs (in larger galaxies, AGNs might play a fundamental role). Unfortunately, for the foreseeable future, galactic-scale simulations will not be able to solve individual SN remnants or the effect of the wind from individual stars. Hence, heuristic, subgrid recipes are needed to treat the mechanical

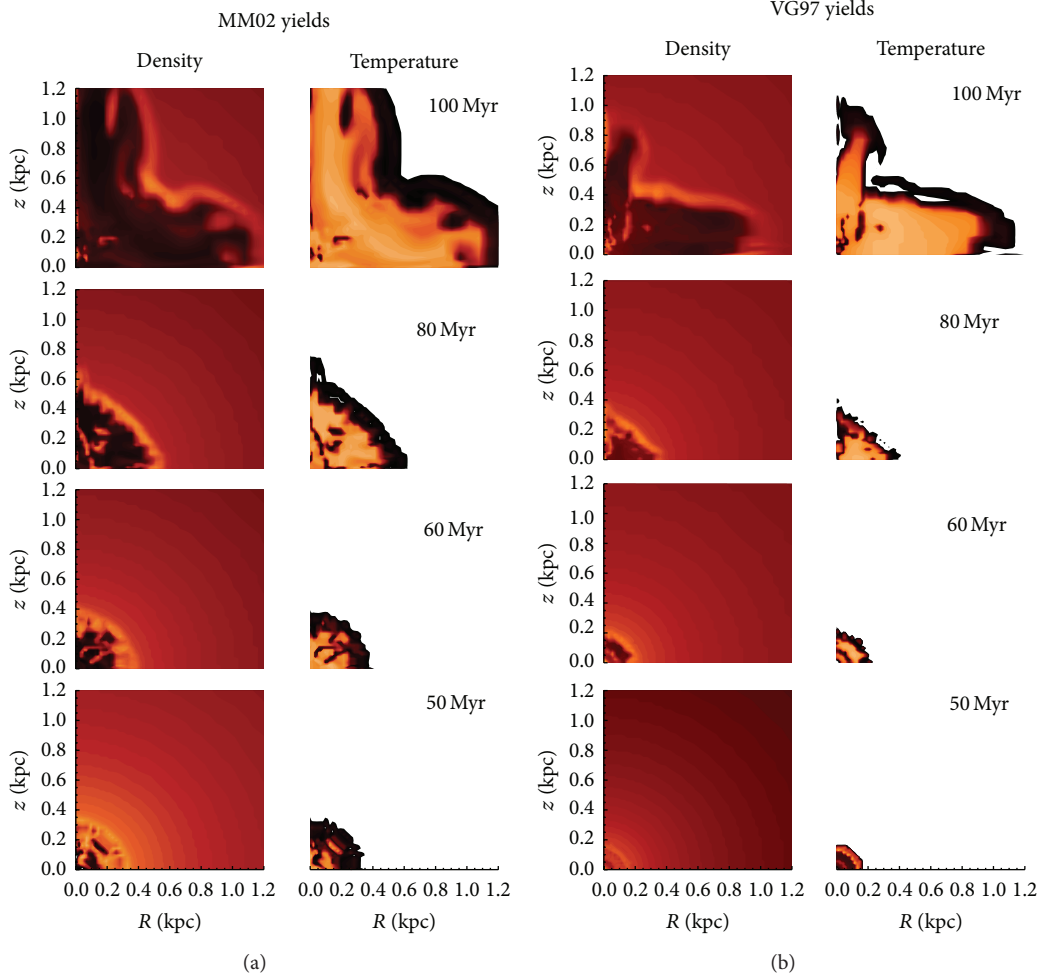


FIGURE 4: Density and temperature contours at 4 evolutionary times (labelled on each of the right panels) for a model adopting MM02 (a) and VG97 (b) yields, respectively. The (logarithmic) density scale (in g cm^{-3}) ranges between -27 (dark) and -23 (bright). The (logarithmic) temperature scale (in K) ranges between 3 (white) and 7 (orange).

feedback. This is a complex and still active research field. Although feedback prescriptions have been found to address specific issues [142, 218], no recipe appears to be widely applicable and physically justifiable. Comparison studies have been performed [88, 219, 220], and the overall conclusion (see in particular the Aquila comparison project, [219]) is that the outcomes of numerical simulations crucially depend on the feedback prescriptions and none of the considered codes is able to satisfactorily reproduce the observed properties of the baryonic component of galaxies.

Broadly speaking, feedback schemes can be divided into two categories: kinetic feedback [221–223] and thermal feedback [144, 157, 224, 225]. Kinetic feedback schemes are mostly used in SPH simulations (but see [33]). The SN explosion energy is transformed into kinetic energy of neighbouring particles. A kick is given to a few neighbouring particles, which move after the kick with a prescribed velocity, along a random direction. The problem with this scheme is that it is not physically justifiable and it is not easy to create galactic winds, unless kick velocities are chosen along prescribed directions.

In thermal feedback schemes instead, the SN energy is used up to heat the ISM. A well-known drawback of this scheme is that the cooling timescale of the particles affected by this thermal feedback is typically very short (often shorter than the timesteps of the simulation). The input energy is thus radiated away before it can be converted to kinetic energy. This leads to the so-called overcooling problem [141]. Various authors have tried to remedy this problem by simply switching off the cooling [144, 157, 226]. The inefficiency of thermal feedback is usually attributed to poor spatial resolution: the energy is deposited in gas that is too dense, because the hot, low-density, bubbles that fill much of the volume of the multiphase ISM are missing. In fact, in models in which the multiphase description of the ISM is taken into account a decoupling of the different thermal phases can be realized (sometimes arbitrarily) and the overcooling problem can be avoided [104, 106].

Another possibility to overcome the overcooling problem is the use of radiative feedback schemes [227]. Radiative feedback is very relevant because it has been recently suggested that photoheating and radiation pressure are the most

important sources of feedback in DGs [90]. Eventually, also cosmic rays have been suggested as an additional source of feedback [228–230]. Also a correct inclusion of stellar dynamics can be a way to avoid the overcooling problem (see Section 3). A much broader discussion would deserve the description of the feedback from the central AGN. This kind of feedback has gained popularity in the last decade. It appears in fact to be a useful recipe to use in semianalytical models of structure formation [231]. However, it is not clear how significant the AGN feedback can be for the evolution of low-mass galaxies. Scaling relations [232, 233] indicate that DGs possess very small central massive black holes. It is very likely that all these forms of feedback occur in real galaxies. However, before implementing them in simulations, one should be confident that the underlying physics is well understood and that reasonable parametrisations can be used.

Although feedback schemes are widely debated in the literature, the amount of energy a SN explosion deposits into the ISM appears to be less problematic. A value of 10^{51} erg is assumed as it represents the typical SN explosion energy E_{SN} [28, 234]. It is however worth reminding that SN kinetic explosion energies (theoretically calculated or deduced from observations) cover a very broad range, from a few 10^{48} ergs of the faintest SNe to the 10^{52} ergs or more of the hypernovae [235].

Some authors adopt a thermalization efficiency ϵ_{SN} , in order to account for the radiative energy losses during the early phases of the evolution of a SN remnant. A commonly adopted value of ϵ_{SN} is 0.1 [97]. Indeed, the simulations of Thornton et al. [236] suggest that only $\sim 10\%$ of the SN explosion energy can be used up to thermalize the ISM. However, detailed simulations of the impact of isolated stars on the ISM [79, 237, 238] show that the energy transfer efficiency can be even lower than 1%. A different approach, where the contribution of a whole population of stars is considered [239], clearly shows that ϵ_{SN} must be a function of time. During the early phases of galactic evolution, the SN remnants expand in a very dense and cold ISM. SN remnants evolve in isolation and radiative losses are very large. Only a small fraction of the SN explosion energy goes to increase the thermal budget of the ISM. When the ISM becomes hotter and more porous, radiative losses are less significant. Various SN remnants quickly coalesce and form a superbubble. Within this superbubble, the sound speed is large. If a SN explodes inside the superbubble, the time it takes for the SN shock velocity to become equal to the sound speed is very short. This is the time at which the shock loses its identity and the energy of the SN remnant can be transferred to the ISM. Clearly, in this situation the SN remnant does not have time to radiate away a large fraction of its energy, which can be thus efficiently converted into thermal energy of the ISM once the SN shock velocity becomes equal to the local sound speed.

Simple analytical estimates of the thermalization efficiency as a function of the ambient density and temperature are possible [111, 240–243]. Again, these formulae show that ϵ_{SN} is strongly reduced if the ambient density is large and

the temperature is low. A more quantitative evaluation of ϵ_{SN} for a single, isolated galaxy can be obtained as follows. The stalling radius R_s is defined as the radius at which the expansion velocity of the SN shock equals the local sound speed. At this radius, the material inside the SN shock can be causally connected with the external ISM and a transfer of energy can occur. R_s can be evaluated as [244]

$$R_s = 4.93 R_{\text{pds}} \left(\frac{E_{\text{SN}}^{1/14} n_0^{1/7} Z^{3/14}}{c_s} \right)^{3/7}. \quad (8)$$

Here, the SN explosion energy is expressed in units of 10^{51} ergs, the ambient density n_0 in cm^{-3} , the metallicity Z in units of the solar metallicity, and the sound speed c_s in units of 10^6 cm s^{-1} . R_{pds} is the radius of the SN shock at the moment in which cooling becomes important. Assuming that most of the SN energy at this stage is in the form of kinetic energy of the shell, the energy available to thermalize the ISM is

$$E_{\text{kin}} = \frac{2}{3} \pi R_s^3 \rho_0 c_s^2. \quad (9)$$

The thermalization efficiency is now simply the ratio between this residual energy and the initial explosion energy E_{SN} . Using the value of R_{pds} given by Cioffi et al. [244], one obtains

$$\epsilon_{\text{SN}} = 0.02 E_{\text{SN}}^{-5/98} n_0^{-54/49} Z^{-15/98} c_s^{5/7}. \quad (10)$$

This calculation is surely approximate. In particular, the ISM porosity and the possibility that various SN remnants merge have not been taken into account. However, additional corrections could be included and a more physically motivated description of the thermalization efficiency, depending on the local thermodynamical conditions, could be obtained.

Eventually, the expansion of ionisation fronts could be taken into account as well. Simple formulae could be devised to describe the variation of the Strömngren radius surrounding a single massive star or an association of stars [78, 245]. Within this radius the cooling is indeed strongly suppressed because Ly continuum photons are used up on the spot to ionise hydrogen atoms and only photons from the Balmer series onwards can leave the H II region. Combining these formulae with the ones describing the evolution of SN shocks and winds from massive stars seems to be theoretically possible. This method is perhaps a further viable solution of the overcooling problem. Of course, once radiative hydrodynamical codes will have enough resolution to solve individual H II regions and SNeII remnants, these analytical considerations will be superfluous. However, this seems not to be possible in the foreseeable future.

To finish this section, it is important to remind that the rate of energy release from SNe and stellar winds is as important in galaxy simulations as the way this energy is converted into ISM energy. It is commonly assumed that all the stars with masses larger than a certain threshold mass m_{thr} explode as SNeII at the end of their lifetimes. This assumption, together with prescribed stellar lifetime functions, makes the calculation of SNII rates quite straightforward. Two sources of uncertainty must be outlined. One is the stellar lifetime

function, which is still quite uncertain and model dependent. Romano et al. [170] demonstrated however that uncertainties in the lifetimes of massive stars are not so significant and do not crucially affect the results of galaxy evolution models. More critical is the choice of m_{thr} . A commonly adopted value is $8M_{\odot}$ but, since there is still not much known about the fate of stars in the mass interval $[8 : 12] M_{\odot}$, m_{thr} could be as high as $12M_{\odot}$. For a Salpeter IMF extending until $100M_{\odot}$, $\sim 78\%$ more SNeII go off if $m_{\text{thr}} = 8M_{\odot}$ instead of $m_{\text{thr}} = 12M_{\odot}$. Clearly, this is a nonnegligible fraction.

Even more uncertain and less standardised are the feedback recipes from stellar winds and Type Ia SNe (SNeIa). Many authors even neglect these energy contributions. However, the energetic input of stellar winds is very important to establish self-regulation in the star formation process (Köppen et al. [158]; see also Section 4). Many authors take into account stellar winds, either adopting suitable parametrisations based on observations [98] or adopting the results of models such as Starburst99 [246], which give the mechanical energy from stellar winds released by a single stellar population or due to a continuous episode of star formation. This approach has been followed, for instance, by [28, 157]. Since the stellar wind luminosity decreases with metallicity [247, 248], neglecting stellar winds is perhaps acceptable in simulations of very metal poor DGs.

Type Ia SNe play a very important role in the evolution of galaxies, as they are the major contributors of iron, a widely used metallicity proxy [129]. Since the lifetime of SNeIa progenitors can be as long as many Gyrs [249], they represent a source of energy more evenly distributed in time than SNeII. The relevance of SNeIa for the dynamical evolution of galaxies has been shown for instance by Recchi and Hensler [250]. Many papers neglect the contribution of SNeIa as they are interested in the early evolution of galaxies and SNeIa are not assumed to occur on short timescales [20]. However, evidence is mounting [251–254] that a significant fraction of SNeIa explode on timescales shorter than 100 Myr. Thus, SNeIa should be considered in chemodynamical models even if the time span of the simulation is of the order of 100 Myr.

A convenient parametrisation of the SNeIa rate is [255, 256]

$$R_{Ia}(t) = \int_{t_{\min}}^t A_{Ia}(t - \tau) D(t - \tau) \psi(\tau) d\tau, \quad (11)$$

where t_{\min} is a suitably chosen minimum timescale for the occurrence of SNeIa (typically 30 Myr), A_{Ia} is a normalisation constant, and D is the so-called delay time distribution (DTD), that is, the distribution of time intervals between the birth of the progenitor system (usually a binary system made of two intermediate-mass stars) and the SNIa explosion. According to (11), the DTD is thus proportional to the SNIa rate following an instantaneous burst of star formation. Unfortunately, the form of the DTD is still very uncertain, although some observations [257, 258] suggest the DTD to be inversely proportional to the elapsed time, that is, $D(t) \propto t^{-1}$. Studies of the chemical evolution of galaxies have been performed [253, 259, 260], showing that the adoption of different DTDs drastically changes the outcome of

the simulations. It is not difficult to imagine that even more drastic differences could be obtained in chemodynamical simulations of galaxies. The role of various DTDs on the evolution of galaxies is another aspect that has been barely considered so far in chemodynamical simulations and that, perhaps, deserves more attention.

8. Environmental Effects

Galaxies are sociable entities; galaxies out there on their own are quite rare. Most of them are found in galaxy clusters and groups. In order to fully understand the evolution of galaxies, the study of the galactic environment is thus paramount. The environment not only includes neighbouring galaxies, but also the tenuous gas between galaxies (the intergalactic medium, IGM, or intracluster medium, ICM, in cluster environments). There are many reasons why the study of galaxy interactions and mergers is very important for our understanding of the Universe as a whole. Perhaps one of the most important ones is that the largely accepted cosmological model, a Λ dominated cold dark matter based Universe, explicitly predicts that galaxies should form hierarchically in the merger process. However, the theoretical study of interactions and mergers is usually the realm of cosmological simulations and I refer the readers to the many books and review papers devoted to the argument [261–266].

One of the clearest evidence of the environmental effects is the morphology-density relation [267], according to which the fraction of early-type galaxies in clusters increases with the local density of the environment. Another key observational result is the star formation-density relation [268, 269], in the sense that star formation seems to be strongly reduced in dense environments. Moreover, cluster galaxies are H I deficient compared to their field counterparts. The deficiency increases towards the cluster centre. These and other observational facts (see also [270, 271] for reviews) clearly indicate that one or more processes in cluster and group environments remove gas from galaxies or make them consume their gas more quickly.

One possibility is that the dense environment promotes tidal interactions (galaxy-galaxy or galaxy-cluster). It has been shown that these interactions can remove matter from galactic halos quite efficiently [272–275]. Another possible physical mechanism able to remove gas in dense environment is the combined effect of multiple high-speed encounters with the interaction of the potential of the cluster as a whole, a process that has been named “harassment” [276, 277]. The first harassment simulations specifically targeting DGs have been performed by Mastropietro et al. [278]. In this paper, it is shown that the majority of galaxies undergo significant morphological transformation and move through the Hubble sequence from late-type discs to dwarf spheroidals. Less dramatic are the effects of harassment in computer simulations of late-type, disk DGs in the Virgo Cluster [279]. Strong tidal encounters, that can morphologically transform discs into spheroidals, are rare. They occur in $\sim 15\%$ of infalls for typical DG orbits in the potential of the Virgo Cluster. Harassment might have some impact on the globular cluster systems of DGs too [280].

By combining different processes, Boselli and Gavazzi [270] concluded that the most probable mechanism able to explain the observational differences between galaxies in clusters and in the field is ram pressure stripping, namely, the kinetic pressure that the ICM exerts on the moving galaxies. If the ram-pressure is larger than the restoring gravitational force (per unit surface) acting on a gas parcel of a galaxy moving through the ICM, this gas parcel is stripped off the galaxy [281]. There have been many simulations exploring the effect of ram-pressure stripping, with different settings and degrees of sophistication [14, 282–289]. There are many indications that ram-pressure stripping is a key process, able to radically modify the evolution of DGs. It is interesting to note that in dwarf irregulars, the removal of the gas by means of ram-pressure stripping can change the potential surrounding the stars enough to dynamically affect them, causing disk thickening by a factor of ~ 2 and disk distortion. Actually, even the dark matter can be dynamically affected by this [290]. Many authors even put forward the idea that ram-pressure stripping can convert gas-rich DGs into gas-poor ones. These ideas are comprehensively summarised in many excellent reviews [162, 291–293] and I refer the reader to these reviews for further details.

For the purposes of this review paper, it is more convenient to briefly summarise the results of the simulations of Marcolini and collaborators [294, 295]. These authors performed simulation of flattened, rotating DGs subject to ram-pressures typical of poor galaxy groups. Interestingly, despite the low values of the ram-pressure, some DGs can be completely stripped after 100–200 Myr. However, regions of very large surface density can be found at the front side of DGs experiencing ram-pressure stripping. This enhanced density can easily lead to a burst of star formation. If the DG experiences a galactic wind (see also Section 9), several parameters regulate the gas ejection process, such as the original distribution of the ISM and the geometry of the IGM-galaxy interaction. Contrary to the ISM content, the amount of the metal rich ejecta retained by the galaxy is more sensitive to the ram-pressure action. Part of the ejecta is first trapped in a low-density, extraplanar gas produced by the IGM-ISM interaction and then pushed back on to the galactic disc. Clearly, the interplay between galactic winds and environment is quite complex and very few studies address this issue in detail (see however [296]). This is another research field in which, in my opinion, more can be done. In particular, results of small-scale detailed simulations of individual galaxies could be used in large-scale simulations of galaxy clusters and groups, where the interaction processes between individual galaxies and the ICM cannot be appropriately resolved. This is for instance the approach followed by Creasey et al. [297], who simulate the feedback effect of SNe in a single galaxy in order to improve subgrid models of feedback in large-scale simulations. This approach should perhaps be further extended. Also simulations like the ones of Marcolini et al. (or similar “wind tunnel” experiments) could be used to better constrain the galactic wind-ICM interactions and improve galactic cluster-scale simulations.

9. Galactic Winds

Galactic winds are streams of high-speed particles often observed blowing out of galaxies. They are also thought to be the primary mechanism by which energy and metals are deposited into the intracluster and intergalactic medium (see also Section 8). Local examples of galactic winds are NGC1569 [298], NGC253 [299], NGC6810 [300], and, of course, the archetypal galactic wind in M82 [301]. There is clear evidence for galactic winds in the spectra of several $z > 1$ galaxies [302]. Probably, the fraction of galaxies experiencing galactic winds was larger at high redshifts [303–305]. A review of many observational (and theoretical) aspects of galactic winds is given in Veilleux et al. [306].

The mechanical feedback from SNe and stellar winds is the most probable driver of galactic winds in DGs, although other mechanisms, such as radiation pressure and cosmic rays, are possible and have been put forward [90, 229, 307–310]. There is a large (and ever growing) number of hydrodynamical simulations of galactic winds in the literature [227, 310–312]. Many of them, especially in the past, targeted specifically DG-sized objects [20, 21, 32, 313–315]. A quite common outcome of these simulations is that the energy deposited by SNe and stellar winds creates large bubbles of hot, highly pressurised gas. This gas pushes the surrounding ISM and, under favourable conditions, a large-scale outflow can emerge. If the outflow velocity is large enough, the gas entrained in it leaves the parent galaxy. A galactic wind has been created. If instead the wind velocity is not high enough, the gravitational pull eventually prevails and a galactic fountain is formed instead. Galactic fountains are more likely in large spiral galaxies like our own Milky Way and have been also extensively studied in the past [316–320]. Given the more reduced gravitational pull, galactic winds are more likely than galactic fountains in DGs. The threshold velocity for the formation of a galactic wind is typically set equal to the escape velocity. However, one should be aware that the motion of gas parcels in galactic winds is not ballistic and the escape velocity can give only an order-of-magnitude estimate of the velocity required to escape the galactic potential well.

Many authors [321–323] have speculated that, since the binding energy of typical DGs is equal to the explosion energy of just a few SNe, galactic winds can occur very early in DGs and can even lead to a quick transition from gas-rich to gas-poor DGs. However, there are three clear failings of this scenario: (i) it fails to explain the observed morphology-density correlation (see Section 8); (ii) it fails to explain the fact that all observed gas-poor DGs of the Local Group possess a large fraction of intermediate-mass stars (see [324, 325] for reviews on stellar populations of Local Group DGs); (iii) if the galactic wind occurs very early, Type Ia SNe do not have time to enrich the ISM (see Section 8). Since Type Ia SNe are the major sources of iron, one would expect very high $[\alpha/\text{Fe}]$ ratios in the stars of DGs. Exactly the contrary is observed: stellar populations in DGs are characterised by very low $[\alpha/\text{Fe}]$ ratios [325, 326]. Indeed, many simulations of the development of galactic winds in DGs cited above agree on the fact that the fraction of ISM ejected out of a galaxy as

a consequence of a galactic wind must be low. An excellent and still very relevant review about the effect of galactic winds in DGs is given by Skillman [327].

However, hydrodynamical simulations of DGs showed that the galactic winds are often able to expel a large fraction of metals, freshly produced during the star formation activity. This is mostly due to the fact that, if the initial DG gas distribution is flattened (as observed in gas-rich DGs), the galactic wind will preferentially expand along a direction perpendicular to the disk (the direction of the steepest pressure gradient; see also below). Most of the disk gas is not affected by the galactic wind. On the other hand, the freshly produced metals can be easily channelled along the funnel created by the galactic wind. Several papers in the literature have attempted to quantitatively address this point and study the effect of galactic winds on the circulation and redistribution of metals in DGs. The main results of the often-cited work Mac Low and Ferrara [20] are that, even in the presence of a strong galactic wind driven by SNeII, the ejection efficiency of unprocessed gas is almost always close to zero. It is different from zero only for the smallest considered galaxies (due to their very shallow potential well). On the other hand, the ejection efficiency of freshly produced heavy elements is almost always close to one. Silich and Tenorio-Tagle [21] found instead that galactic winds do not develop in most of the models, mainly due to the presence of a hot gaseous halo surrounding the galaxy. The effect of off-centred SN explosions and SN explosions distributed over a significant fraction of the disk's surface was also studied in the literature [23]. Metal ejection efficiencies are reduced in this case, due to more efficient cooling. Wind efficiencies are found to be low even if SN is injected directly into supersonic turbulence [16].

The ejection efficiency of individual chemical elements was investigated, too [111]. As a consequence of very short starbursts, metals with delayed production, like Fe and N, have large escape fractions (see also [328]). In fact, a significant fraction of α -elements, quickly produced by SNeII, mix locally before the development of a galactic wind (see also [329]). Metals produced by SNeIa and intermediate-mass stars can be instead easily channelled along the already-formed galactic wind and do not suffer much mixing with the walls of the wind. The situation is much less clear-cut in the presence of multiple bursts of star formation [125] or of complex SFHs [124]. One should be aware of the fact that turbulence can play a decisive role in the process of mixing metals, a mechanism usually called turbulent mixing [330]. However, it is a considerable experimental, theoretical, modelling, and computational challenge to capture and represent turbulent mixing and not much has been done in this direction for astrophysical flows (but see [331–333]).

An estimate of the probability of the development of a galactic wind can be obtained as follows (see [111, 334, 335]). Take for simplicity a source of energy producing a constant luminosity L . Assume also that the density and the metallicity of the ISM are uniform and that its vertical density distribution has a scale height H . The energy input creates a superbubble which is assumed to be spherical and characterised by a radius R . By means of standard, textbook

formulas for the evolution of a superbubble without radiative losses (i.e., $R \sim t^{-3/5}$), the time for the radius R of the superbubble to reach H is readily calculated:

$$t_D \sim H^{5/3} \left(\frac{\rho}{L} \right)^{1/3}. \quad (12)$$

However, radiative losses, in general, cannot be neglected. The radiative losses of the hot cavity can be more relevant for the dynamics of the superbubble than the radiative losses of the shocked material. The cooling timescale of the superbubble can be estimated as

$$t_c \sim 16(\beta Z)^{-35/22} L^{3/11} n^{-8/11} \text{ Myr}, \quad (13)$$

where L in this formula is in units of $10^{38} \text{ erg s}^{-1}$ and n in cm^{-3} . Here, β is a numerical factor (of the order of unity) that takes into account the fact that the cooling gas might be out of ionisation equilibrium. Clearly, if t_c is much shorter than t_D , the superbubble loses much of its pressure before the supershell can reach H and a large-scale outflow cannot occur. By combining (12) and (13) one obtains an approximate criterion for the occurrence of a galactic wind, namely,

$$L \gg 0.03n^{7/4} (\beta Z)^{21/8} H^{11/4}. \quad (14)$$

Although this derivation is quite approximate, the large dependence of the threshold luminosity on H is a solid result. The vertical distribution of gas strongly affects the development of a galactic wind (more than other factors). A galaxy characterised by a very thin disk experiences outflows much more easily than roundish galaxy. This result matches the physical intuition that in flat galaxies a large-scale outflows easily develop along the direction of steepest pressure gradient (i.e., perpendicularly to the disk), whereas in spherical galaxies the pressure gradient is isotropic and either the outflows occur along all directions, or the superbubble remains confined inside the galaxy. Indeed, simulations of spherical (or almost spherical) DGs have shown that it is not easy to create galactic winds, even if the energy input is significant [336] or the galaxy does not have a dark matter halo [103, 157]. Although the importance of the disk thickness for the development of outflows was soon recognised, this aspect has not been fully explored in the past in numerical investigation (but see [17, 28, 337–340]).

In Recchi and Hensler [341] we specifically addressed the role of gas distribution on the development of galactic winds and on the fate of freshly produced metals. We found that the gas distribution can change the fraction of lost metals through galactic winds by up to one order of magnitude. In particular, disk-like galaxies tend to lose metals more easily than roundish ones. In fact, the latter often do not develop galactic winds at all and, hence, they retain all the freshly produced metals. Consequently, the final metallicities attained by models with the same mass but with different gas distributions can also vary by up to one dex.

Confirming previous studies, we also show that the fate of gas and freshly produced metals strongly depends on the mass of the galaxy. Smaller galaxies (with shallower potential

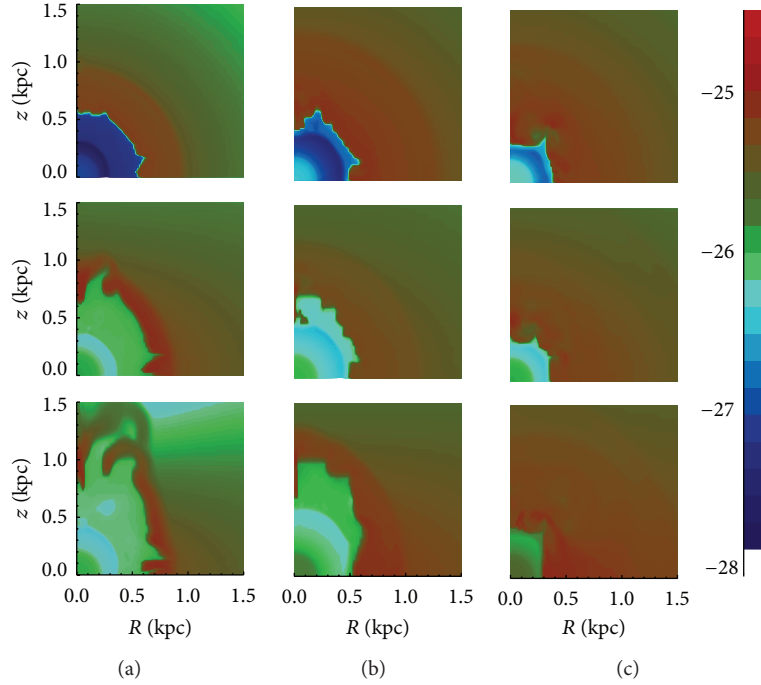


FIGURE 5: Gas density distribution for nine galaxy models differing on the degree of flattening and the initial baryonic mass, after 100 Myr of galactic evolution. The first column represents models with $10^7 M_{\odot}$ of initial baryonic mass, the middle column shows the gas distribution for models with mass $10^8 M_{\odot}$, and the right-hand column displays the models with $10^9 M_{\odot}$. The top rows of models are characterised by a roundish initial distribution. The middle rows show models with an intermediate degree of flattening, and the bottom rows are characterised by a flat initial distribution. The left-hand strip shows the (logarithmic) density scale (in g cm^{-3}).

wells) more easily develop large-scale outflows, so that the fraction of lost metals tends to be higher. An example of the results of these investigations is given in Figure 5. The gas density distribution for nine galaxy models differing on the degree of flattening and the initial baryonic mass, after 100 Myr of galactic evolution, is shown in this figure (see figure caption for more details). The effect of geometry on the development of galactic winds is clear from this figure: the density distribution in the models in the bottom row (flat models) is clearly elongated. In one case a galactic wind is already blowing. The models in the upper row are instead still roundish. Clearly, as described before, if a large-scale outflow is formed, freshly produced metals can be easily lost from the galaxy. Any time a galactic wind is formed, the ejection efficiency of metals is larger (sometimes much larger) than the ejection efficiency of the ISM, confirming that galactic winds must be metal enhanced. The fact that galactic winds are metal richer than the global ISM has been observationally verified [342, 343].

The fact that the galactic winds are metal-enriched is a commonly accepted result. It has been proposed as one of the main mechanisms leading to the so-called mass-metallicity relation, according to which the metallicity of a galaxy grows with its mass. Since galactic winds are metal-enhanced and since DGs experience more easily galactic winds, clearly one has to expect that DGs are metal poorer than larger galaxies [344, 345]. Although the effect of metal-enriched galactic winds on the chemical evolution of galaxies

might be already clear from the previous paragraphs, a more quantitative analysis can be performed, based on simple analytical considerations. Assuming linear flows, that is, assuming that infall rates and outflow rates in and out of galaxies are proportional to the SFR ψ , a set of differential equations can be found for the time evolution of the total baryonic mass M_t , total gas mass M_g , and total mass in metals M_Z within a galaxy (see [346, 347]):

$$\begin{aligned} \frac{dM_t}{dt} &= (\Lambda - \lambda)(1 - R)\psi(t), \\ \frac{dM_g}{dt} &= (\Lambda - \lambda - 1)(1 - R)\psi(t), \\ \frac{dM_Z}{dt} &= (1 - R)\psi(t)[\Lambda Z_A + \gamma_Z - (\lambda\alpha + 1)Z]. \end{aligned} \quad (15)$$

Here, Λ and λ are proportionality constants relating the SFR to the infall and outflow rate, respectively. Z_A is the metallicity of the infalling material and R is the fraction of the considered stellar populations locked into long-living stars and remnants. γ_Z is the stellar yield, in this case defined as the ratio between the mass of a specific chemical element ejected by a stellar generation and the mass locked up in remnants ([3]; see also Section 6). Finally, α is the parameter that takes into account metal-enriched galactic winds, that is, is the increase of metallicity of the wind compared to the ISM. Besides this last factor, the equations are standard, textbook

equations for the simple-model evolution of a galaxy [3, 129, 348] and analytical solutions can be found. An analytical solution can be found even including this further factor α (see Recchi et al. [347], (12)). If one assumes that the SFR ψ is proportional to the total gas mass M_g through a proportionality constant S (see Section 4), the final result is

$$\frac{Z(t)}{y_Z + \Lambda Z_A} = \frac{1 - [(\Lambda - \lambda + 1) - (\Lambda - \lambda)e^{h(t)}]^{(\Lambda + (\alpha - 1)\lambda)/(\Lambda - \lambda - 1)}}{\Lambda + (\alpha - 1)\lambda},$$

$$h(t) = (\lambda + 1 - \Lambda)(1 - R)St. \quad (16)$$

This solution has been plotted in Figure 6 for $\Lambda = 0$, $\lambda = 2$, $S = 1 \text{ Gyr}^{-1}$, and $R = 0.26$ (from [201]). The strong effect of α (a factor of ~ 20) on the final metallicity of the galaxy is evident from this figure. Clearly, this kind of modelling can only give an approximate idea about the chemical evolution of galaxies and that full chemodynamical simulations are required for a deeper insight and understanding of the metal enrichment process. However, this kind of analytical calculations is nowadays quite popular, as it enlightens in a simple way complex correlations among galaxies [344, 349, 350].

10. Conclusions and Outlook

In this review I presented a summary of the state of the art for what concerns the chemodynamical modelling of galaxies in general and of dwarf galaxies in particular. I have devoted one section for each of the main ingredients of a realistic simulation of a galaxy, namely, (i) initial conditions (Section 2), (ii) the equations to solve (Section 3), (iii) the star formation process (Section 4), (iv) the initial mass function (Section 5), (v) the chemical feedback (Section 6), (vi) the mechanical feedback (Section 7) and (vii) the environmental effects (Section 8). In each section, commonly adopted methodologies and recipes have been introduced and some key results of past or ongoing studies have been summarised. Moreover, some key results concerning the development of galactic winds and the fate of heavy elements, freshly synthesised after an episode of star formation, have been summarised in Section 9.

Throughout this review, I outlined topics, physical processes, and ingredients that in my opinion are not properly or adequately treated in modern simulations of galaxy evolution. I summarise below the topics that in my opinion deserve more attention.

(i) *Inclusion of Self-Gravity in Building Initial Equilibrium Configurations.* This is clearly an important step towards building more realistic initial configurations and, as described in Section 2, the difference between models with and without self-gravity can be extremely large. Of course, taking self-gravity into account in building initial equilibrium configurations is computationally demanding. However, it

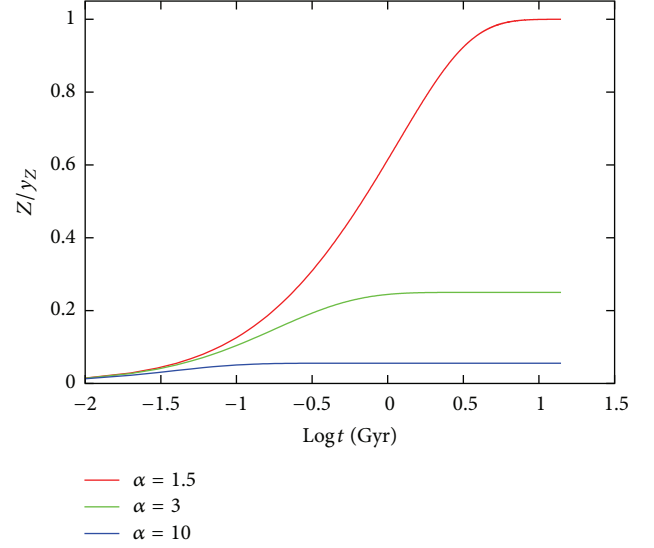


FIGURE 6: The metallicity of a galaxy, as a function of time, for models with metal-enriched galactic winds. This plot shows the solution of (16) for three different values for the enrichment parameter α .

is clearly a necessary step in simulations in which the star formation process is treated in detail, as the gas self-gravity is the main driver of the star formation process. Of course, galactic simulations in a cosmological context do not need any special recipe to build initial configurations.

(ii) *Inclusion of Turbulence in Galactic Simulations.* There is no doubt that the gas in galaxies is turbulent; therefore it is necessary to devote more efforts to a proper modelling of (compressive) turbulence in galaxies. As mentioned in Section 7, turbulence is also a key ingredient to study the process of circulation and mixing of heavy elements in galaxies; it thus helps to interpret more properly observational data, such as the ones obtained by means of integral field spectroscopy. As reported in Section 3, some galactic simulations with a proper treatment of turbulence have been already performed. However, in these simulations chemistry is usually treated in a very crude and approximate way. The inclusion in these simulations of methods and recipes about the production and circulation of heavy metals, adopted in other chemodynamical simulations, appears to be feasible. Moreover, some of the assumptions and equations used to simulate turbulence in the ISM are based on experimental results on incompressible turbulence. A more focused study of physical processes and modelling of compressible turbulence in the ISM is arguable and I am sure that in the next years we will experience great progresses in this field.

(iii) *A Multiphase, Multifluid Treatment of the ISM in Galaxy Simulations.* Realistic simulations of galaxies should take into account the multiphase nature of the ISM in galaxies and the complex network of reactions between stars and various gas phases. This has been done in some simulations, particularly thanks to the work of Hensler and collaborators (see, e.g.,

[37, 97, 98, 101, 107]). These works unveiled the complexity of true multiphase simulations of galaxies. Yet, these complex simulations are necessary in order to reproduce more faithfully the ISM. Thanks to enormous progresses in the field of multiphase simulations in other branches of physics (see, e.g., the monographs [351–353]) I hope that we can witness a boost of true multiphase, multi-fluid galactic simulations in the next years.

(iv) *Inclusion of Dust.* As already mentioned in Section 6, many works about the chemical evolution of galaxies [210–214] include dust and show how important this component is to interpret data about the chemical composition of galaxies. It is very likely that the inclusion of dust can drastically change also the results of chemodynamical evolution of galaxies and can dramatically improve our knowledge about the physics of the dust-gas interaction and about the circulation of metals in galaxies. In spite of useful attempts, current state-of-the-art numerical simulations of galaxies do not take dust into account (but see [354, 355]). A proper inclusion of dust is difficult and can also lead to numerical problems. However, in other branches of astrophysics some of these numerical issues have been solved and sophisticated simulations of gas-dust mixtures have been performed [356–359]. It would be extremely beneficial for the astronomers working on simulations of galaxies to learn from these works and improve the treatment of dust physics and dust-gas interactions in galactic simulations. It is also worth noticing that the publicly available Pencil Code [46, 47, 360] already includes relevant dust physics. A wider use of this code for simulating ISM in galaxies is certainly arguable.

(v) *A More Self-Consistent Treatment of the IMF.* Recent, detailed simulation of the ISM with a proper treatment of the star formation process [117, 361, 362] is able to recover the main shape and features of the IMF. In these simulations, thus, the IMF is not assumed a priori but is self-consistently reproduced. Galaxy-wide simulations do not have an adequate spatial resolution; therefore some simplifying assumptions about the IMF need to be made. Yet, it appears to me that a lot is known about physical properties and mass distribution of stellar clusters in galaxies, and these can be used to constrain the formation mechanisms of star clusters in galactic simulations. Within each cluster, the observationally based maximum-mass versus cluster-mass (m_{\max} - M_{cl} , [175, 176, 191]) relation can be used to link the upper stellar mass within each cluster to the cluster mass. This appears to be a simple and physically motivated exercise, that can significantly change the outcome of a galactic simulation. Finally, the full IGIMF theory as developed by Kroupa and collaborators (see Section 5 and [191] for a review) can be implemented in numerical simulations. As shown in Section 5 with two simple examples, the results can drastically change compared to simulations adopting a universal IMF. In spite of some attempts [188, 355, 363], almost nothing has been done in this field.

(vi) *Feedback Recipes.* This is a very vibrant and active field of research, with new methods and implementations appearing

weekly in the preprint archives. However, it seems to me that some ingredients and topics are receiving less attention than they deserve. In particular, before concentrating on methods and algorithms to inject energy into the ISM (the kinetic, thermal, and radiative feedback schemes described in Section 7) I think one should be sure that all relevant sources of energy are included and properly treated. In particular (i) Type II SNe are always included but it is usually not appreciated how much the total energy coming from SNeII can change if the threshold mass m_{thr} above which SNeII can explode is changed. As shown in Section 7, a change in m_{thr} can lead to a change in total SNII energy by a factor of almost 2. It is also not always appreciated how uncertain is the fraction of the SNII explosion energy that can effectively thermalize the ISM. Some analytical estimates of this fraction are available in the literature (see also Section 7) and I think it could be very useful to use more often and more consistently these kinds of analytical estimates. (ii) Type Ia SNe are often neglected and, if they are considered, no systematic study of the dependence of the results of the simulations on the Type Ia SN rates is available in the literature. This appears to be a simple and yet quite useful exercise. (iii) Stellar winds from massive and intermediate-mass stars can also contribute very significantly to the energy budget of a galaxy, in particular if the metallicity is not extremely low. This ingredient, also is often neglected or not properly considered in galactic simulations. The availability of softwares like Starburst99 [246] makes the inclusion of stellar winds in numerical simulations quite simple.

(vii) *Synergy between Galactic-Scale and Cluster-Scale or Cosmological Simulations.* As mentioned in Section 8, results of detailed simulations of individual galaxies could be used in simulations of galaxy clusters or groups or even in cosmological simulations, in order to improve the subgrid recipes of these large-scale simulations. In particular, details of the formation of galactic winds and their impact on the external intergalactic or intracluster medium (see Section 9) can be extremely beneficial in large-scale simulations where these effects are usually treated very crudely.

Conflict of Interests

The author declares that there is no conflict of interests regarding the publication of this paper.

Acknowledgments

The author would like to thank Annibale D’Ercole and Gerhard Hensler for careful reading of the paper and for very useful suggestions and corrections; Sylvia Plöckinger for having produced Figure 3; Francesco Calura, Pavel Kroupa, Nigel Mitchell, Sylvia Plöckinger, Donatella Romano, Rory Smith, Eduard Vorobyov, and Svitlana Zhukovska for having read sections of this review and for having provided very useful comments; and an anonymous referee, whose comments improved the quality of the paper. Finally his wife, Sonja Recchi, is warmly thanked for careful English proofreading.

References

- [1] U. Klein, “The ISM of dwarf galaxies,” in *Dwarf Galaxies: Keys to Galaxy Formation and Evolution*, P. Papaderos, S. Recchi, and G. Hensler, Eds., pp. 23–36, Springer, 2012.
- [2] B. K. Gibson and F. Matteucci, “On dwarf galaxies as the source of intracluster gas,” *The Astrophysical Journal*, vol. 475, no. 1, pp. 47–56, 1997.
- [3] B. M. Tinsley, “Evolution of the stars and gas in galaxies,” *Fundamentals of Cosmic Physics*, vol. 5, p. 287, 1980.
- [4] E. Komatsu, K. M. Smith, J. Dunkley et al., “Seven-year Wilkinson Microwave Anisotropy Probe (WMAP) observations: cosmological interpretation,” *The Astrophysical Journal Supplement Series*, vol. 192, no. 2, p. 18, 2011.
- [5] D. N. Spergel, L. Verde, H. V. Peiris et al., “First-year Wilkinson Microwave Anisotropy Probe (WMAP) observations: determination of cosmological parameters,” *The Astrophysical Journal Supplement Series*, vol. 148, no. 1, pp. 175–194, 2003.
- [6] M. Boylan-Kolchin, V. Springel, S. D. M. White, A. Jenkins, and G. Lemson, “Resolving cosmic structure formation with the Millennium-II Simulation,” *Monthly Notices of the Royal Astronomical Society*, vol. 398, no. 3, pp. 1150–1164, 2009.
- [7] A. A. Klypin, S. Trujillo-Gomez, and J. Primack, “Dark matter halos in the standard cosmological model: results from the Bolshoi simulation,” *The Astrophysical Journal*, vol. 740, no. 2, article 102, 2011.
- [8] J. Diemand, M. Kuhlen, P. Madau et al., “Clumps and streams in the local dark matter distribution,” *Nature*, vol. 454, no. 7205, pp. 735–738, 2008.
- [9] V. Springel, J. Wang, M. Vogelsberger et al., “The Aquarius Project: the subhaloes of galactic haloes,” *Monthly Notices of the Royal Astronomical Society*, vol. 391, no. 4, pp. 1685–1711, 2008.
- [10] G. S. Stinson, C. Brook, A. V. Macciò, J. Wadsley, T. R. Quinn, and H. M. P. Couchman, “Making galaxies in a cosmological context: the need for early stellar feedback,” *Monthly Notices of the Royal Astronomical Society*, vol. 428, no. 1, pp. 129–140, 2013.
- [11] M. Martig, F. Bournaud, R. Teyssier, and A. Dekel, “Morphological quenching of star formation: making early-type galaxies red,” *The Astrophysical Journal*, vol. 707, no. 1, pp. 250–267, 2009.
- [12] K. Pilkington, C. G. Few, B. K. Gibson et al., “Metallicity gradients in disks: do galaxies form inside-out?” *Astronomy & Astrophysics*, vol. 540, article A56, 2012.
- [13] T. Sawala, Q. Guo, C. Scannapieco, A. Jenkins, and S. White, “What is the (dark) matter with dwarf galaxies?” *Monthly Notices of the Royal Astronomical Society*, vol. 413, no. 1, pp. 659–668, 2011.
- [14] L. Mayer, C. Mastropietro, J. Wadsley, J. Stadel, and B. Moore, “Simultaneous ram pressure and tidal stripping: How dwarf spheroidals lost their gas,” *Monthly Notices of the Royal Astronomical Society*, vol. 369, no. 3, pp. 1021–1038, 2006.
- [15] Y. Revaz, P. Jablonka, T. Sawala et al., “The dynamical and chemical evolution of dwarf spheroidal galaxies,” *Astronomy & Astrophysics*, vol. 501, no. 1, pp. 189–206, 2009.
- [16] E. Scannapieco and M. Brüggen, “Simulating supersonic turbulence in galaxy outflows,” *Monthly Notices of the Royal Astronomical Society*, vol. 405, no. 3, pp. 1634–1653, 2010.
- [17] J. Schroyen, S. de Rijcke, S. Valcke, A. Cloet-Osselaer, and H. Dejonghe, “Simulations of the formation and evolution of isolated dwarf galaxies—II. Angular momentum as a second parameter,” *Monthly Notices of the Royal Astronomical Society*, vol. 416, no. 1, pp. 601–617, 2011.
- [18] G. S. Stinson, J. J. Dalcanton, T. Quinn, T. Kaufmann, and J. Wadsley, “Breathing in low-mass galaxies: a study of episodic star formation,” *The Astrophysical Journal*, vol. 667, no. 1, pp. 170–175, 2007.
- [19] R. Teyssier, A. Pontzen, Y. Dubois, and J. I. Read, “Cusp-core transformations in dwarf galaxies: observational predictions,” *Monthly Notices of the Royal Astronomical Society*, vol. 429, no. 4, pp. 3068–3078, 2013.
- [20] M.-M. Mac Low and A. Ferrara, “Starburst-driven mass loss from dwarf galaxies: efficiency and metal ejection,” *The Astrophysical Journal*, vol. 513, no. 1, pp. 142–155, 1999.
- [21] S. A. Silich and G. Tenorio-Tagle, “On the fate of processed matter in dwarf galaxies,” *Monthly Notices of the Royal Astronomical Society*, vol. 299, no. 1, pp. 249–266, 1998.
- [22] K. Tomisaka and S. Ikeuchi, “Starburst nucleus: galactic-scale bipolar flow,” *The Astrophysical Journal*, vol. 330, pp. 695–717, 1988.
- [23] P. C. Fragile, S. D. Murray, and D. N. C. Lin, “Ejection of supernova-enriched gas from dwarf disk galaxies,” *The Astrophysical Journal*, vol. 617, no. 2, pp. 1077–1090, 2004.
- [24] P. Papaderos, H.-H. Loose, K. J. Fricke, and T. X. Thuan, “Optical structure and star formation in blue compact dwarf galaxies: II. Relations between photometric components and evolutionary implications,” *Astronomy & Astrophysics*, vol. 314, no. 3, pp. 59–72, 1996.
- [25] R. A. Swaters, R. Sancisi, T. S. van Albada, and J. M. van der Hulst, “Are dwarf galaxies dominated by dark matter?” *The Astrophysical Journal*, vol. 729, no. 2, article 118, 2011.
- [26] A. A. Suchkov, D. S. Balsara, T. M. Heckman, and C. Leitherer, “Dynamics and X-ray emission of a galactic superwind interacting with disk and halo gas,” *The Astrophysical Journal*, vol. 430, no. 2, pp. 511–532, 1994.
- [27] K. Tomisaka and J. N. Bregman, “Extended hot gas halos around starburst galaxies,” *Publications of the Astronomical Society of Japan*, vol. 45, pp. 513–528, 1993.
- [28] D. K. Strickland and I. R. Stevens, “Starburst-driven galactic winds—I. Energetics and intrinsic X-ray emission,” *Monthly Notices of the Royal Astronomical Society*, vol. 314, no. 3, pp. 511–545, 2000.
- [29] M. Barnabè, L. Ciotti, F. Fraternali, and R. Sancisi, “Hydrostatic models for the rotation of extra-planar gas in disk galaxies,” *Astronomy & Astrophysics*, vol. 446, no. 1, pp. 61–69, 2006.
- [30] N. R. Lebovitz, “Rotating fluid masses,” *Annual Review of Astronomy and Astrophysics*, vol. 5, pp. 465–480, 1967.
- [31] J. L. Tassoul, *Theory of Rotating Stars*, Princeton University Press, Princeton, NJ, USA, 1980.
- [32] A. D’Ercole and F. Brighenti, “Galactic winds and circulation of the interstellar medium in dwarf galaxies,” *Monthly Notices of the Royal Astronomical Society*, vol. 309, no. 4, pp. 941–954, 1999.
- [33] Y. Dubois and R. Teyssier, “On the onset of galactic winds in quiescent star forming galaxies,” *Astronomy & Astrophysics*, vol. 477, no. 1, pp. 79–94, 2008.
- [34] T. Kaufmann, L. Mayer, J. Wadsley, J. Stadel, and B. Moore, “Angular momentum transport and disc morphology in smoothed particle hydrodynamics simulations of galaxy formation,” *Monthly Notices of the Royal Astronomical Society*, vol. 375, no. 1, pp. 53–67, 2007.
- [35] J. S. Bullock, A. Dekel, T. S. Kolatt et al., “A universal angular momentum profile for galactic halos,” *The Astrophysical Journal*, vol. 555, no. 1, pp. 240–257, 2001.

- [36] M. A. de Avillez and D. Breitschwerdt, "Volume filling factors of the ISM phases in star forming galaxies I. The role of the disk-halo interaction," *Astronomy & Astrophysics*, vol. 425, no. 3, pp. 899–911, 2004.
- [37] S. Harfst, C. Theis, and G. Hensler, "Modelling galaxies with a 3d multi-phase ISM," *Astronomy & Astrophysics*, vol. 449, no. 2, pp. 509–518, 2006.
- [38] L. Liu, M. Petrov, P. Berczik et al., *Astronomy & Astrophysics*. In press.
- [39] E. I. Vorobyov, S. Recchi, and G. Hensler, "Self-gravitating equilibrium models of dwarf galaxies and the minimum mass for star formation," *Astronomy & Astrophysics*, vol. 543, article A129, 2012.
- [40] J. P. Ostriker and J. W. K. Mark, "Rapidly rotating stars. I. The self-consistent-field method," *The Astrophysical Journal*, vol. 151, pp. 1075–1088, 1968.
- [41] S. Cole, P. Norberg, C. M. Baugh et al., "The 2dF galaxy redshift survey: near-infrared galaxy luminosity functions," *Monthly Notices of the Royal Astronomical Society*, vol. 326, no. 1, pp. 255–273, 2001.
- [42] X. Yang, H. J. Mo, and F. C. van den Bosch, "Galaxy Groups in the SDSS DR4: III. the luminosity and stellar mass functions," *The Astrophysical Journal*, vol. 695, no. 2, p. 900, 2009.
- [43] E. Papastergis, A. Cattaneo, S. Huang, R. Giovanelli, and M. P. Haynes, "A direct measurement of the Baryonic mass function of galaxies and implications for the galactic Baryon fraction," *The Astrophysical Journal*, vol. 759, no. 2, p. 138, 2012.
- [44] J. Silk and G. A. Mamon, "The current status of galaxy formation," *Research in Astronomy and Astrophysics*, vol. 12, no. 8, p. 917, 2012.
- [45] B. G. Elmegreen and J. Scalo, "Interstellar turbulence I: observations and processes," *Annual Review of Astronomy and Astrophysics*, vol. 42, pp. 211–273, 2004.
- [46] A. Brandenburg, "Computational aspects of astrophysical MHD and turbulence," in *Advances in Nonlinear Dynamics*, p. 269, Taylor and Francis, London, UK, 2003.
- [47] A. Brandenburg and W. Dobler, "Hydromagnetic turbulence in computer simulations," *Computer Physics Communications*, vol. 147, no. 1-2, pp. 471–475, 2002.
- [48] S. C. O. Glover, C. Federrath, M.-M. Mac Low, and R. S. Klessen, "Modelling CO formation in the turbulent interstellar medium," *Monthly Notices of the Royal Astronomical Society*, vol. 404, no. 1, pp. 2–29, 2010.
- [49] L. Iapichino, J. Adamek, W. Schmidt, and J. C. Niemeyer, "Hydrodynamical adaptive mesh refinement simulations of turbulent flows—I. Substructure in a wind," *Monthly Notices of the Royal Astronomical Society*, vol. 388, no. 3, pp. 1079–1088, 2008.
- [50] L. Iapichino, M. Viel, and S. Borgani, "Turbulence driven by structure formation in the circumgalactic medium," *Monthly Notices of the Royal Astronomical Society*, vol. 432, no. 3, pp. 2529–2540, 2013.
- [51] M. Micić, S. C. O. Glover, C. Federrath, and R. S. Klessen, "Modelling H₂ formation in the turbulent interstellar medium: solenoidal versus compressive turbulent forcing," *Monthly Notices of the Royal Astronomical Society*, vol. 421, no. 3, pp. 2531–2542, 2012.
- [52] E. Scannapieco and M. Brüggen, "Subgrid modeling of AGN-driven turbulence in galaxy clusters," *The Astrophysical Journal*, vol. 686, no. 2, p. 927, 2008.
- [53] F. Bournaud, B. G. Elmegreen, R. Teyssier, D. L. Block, and I. Puerari, "ISM properties in hydrodynamic galaxy simulations: turbulence cascades, cloud formation, role of gravity and feedback," *Monthly Notices of the Royal Astronomical Society*, vol. 409, no. 3, pp. 1088–1099, 2010.
- [54] H. Koyama and E. C. Ostriker, "Gas properties and implications for galactic star formation in numerical models of the turbulent, multiphase interstellar medium," *The Astrophysical Journal*, vol. 693, no. 2, p. 1316, 2009.
- [55] M.-M. Mac Low and S. C. O. Glover, "The abundance of molecular hydrogen and its correlation with midplane pressure in galaxies: non-equilibrium, turbulent, chemical models," *The Astrophysical Journal*, vol. 746, no. 2, article 135, 2012.
- [56] F. Renaud, F. Bournaud, E. Emsellem et al., "A sub-parsec resolution simulation of the Milky Way: global structure of the ISM and properties of molecular clouds," *Monthly Notices of the Royal Astronomical Society*, vol. 436, no. 2, pp. 1836–1851, 2013.
- [57] J. M. Stone and M. L. Norman, "ZEUS-2D: a radiation magnetohydrodynamics code for astrophysical flows in two space dimensions. I—the hydrodynamic algorithms and tests," *The Astrophysical Journal Supplement Series*, vol. 80, pp. 791–818, 1992.
- [58] B. Fryxell, K. Olson, P. Ricker et al., "Flash: an adaptive mesh hydrodynamics code for modeling astrophysical thermonuclear flashes," *The Astrophysical Journal Supplement Series*, vol. 131, no. 1, pp. 273–334, 2000.
- [59] T. Linde, "MHD simulations with the FLASH code," in *Proceedings of the APS Meeting*, 2002, abstract no. 3005.
- [60] S. Fromang, P. Hennebelle, and R. Teyssier, "RAMSES-MHD: an AMR Godunov code for astrophysical applications," in *SF2A-2005: Semaine de l'Astrophysique Francaise*, p. 743, 2005.
- [61] R. Teyssier, "Cosmological hydrodynamics with adaptive mesh refinement: a new high resolution code called RAMSES," *Astronomy & Astrophysics*, vol. 385, no. 1, pp. 337–364, 2002.
- [62] J. M. Stone, T. A. Gardiner, P. Teuben, J. F. Hawley, and J. B. Simon, "Athena: a new code for astrophysical MHD," *The Astrophysical Journal Supplement Series*, vol. 178, no. 1, pp. 137–177, 2008.
- [63] L. Spitzer, *Physics of Fully Ionized Gases*, Interscience, New York, NY, USA, 2nd edition, 1962.
- [64] R. Dong and J. M. Stone, "Buoyant bubbles in intracluster gas: effects of magnetic fields and anisotropic viscosity," *The Astrophysical Journal*, vol. 704, no. 2, pp. 1309–1320, 2009.
- [65] H. Kamaya, "Final size of a magnetized superbubble," *The Astrophysical Journal*, vol. 493, no. 2, pp. L95–L96, 1998.
- [66] M. A. de Avillez and D. Breitschwerdt, "Global dynamical evolution of the ISM in star forming galaxies I. High resolution 3D simulations: effect of the magnetic field," *Astronomy & Astrophysics*, vol. 436, no. 2, pp. 585–600, 2005.
- [67] A. G. G. M. Tielens, *The Physics and Chemistry of the Interstellar Medium*, Cambridge University Press, Cambridge, UK, 2005.
- [68] R. Pakmor and V. Springel, "Simulations of magnetic fields in isolated disc galaxies," *Monthly Notices of the Royal Astronomical Society*, vol. 432, no. 1, pp. 176–193, 2013.
- [69] A. A. Kepley, S. Mühle, J. Everett, E. G. Zweibel, E. M. Wilcots, and U. Klein, "The role of the magnetic field in the interstellar medium of the post-starburst dwarf irregular galaxy NGC 1569," *The Astrophysical Journal*, vol. 712, no. 1, p. 536, 2010.
- [70] K. T. Chyży, R. Beck, S. Kohle, U. Klein, and M. Urbanik, "Regular magnetic fields in the dwarf irregular galaxy NGC 4449," *Astronomy & Astrophysics*, vol. 355, no. 1, pp. 128–137, 2000.

- [71] U. Klein, “Dwarf galaxies and the magnetisation of the IGM,” in *Low-Metallicity Star Formation: From the First Stars to Dwarf Galaxies*, Proceedings of the IAU Symposium, no. 255, p. 167, 2008.
- [72] J. I. Castor, *Radiation Hydrodynamics*, Cambridge University Press, Cambridge, UK, 2004.
- [73] W. Kalkofen, *Numerical Radiative Transfer*, Cambridge University Press, Cambridge, UK, 1988.
- [74] D. Mihalas and B. W. Mihalas, *Foundations of Radiation Hydrodynamics*, Oxford University Press, New York, NY, USA, 1984.
- [75] H. Boehringer and G. Hensler, “Metallicity-dependence of radiative cooling in optically thin, hot plasmas,” *Astronomy & Astrophysics*, vol. 215, no. 1, pp. 147–149, 1989.
- [76] K. M. Schure, D. Kosenko, J. S. Kaastra, R. Keppens, and J. Vink, “A new radiative cooling curve based on an up-to-date plasma emission code,” *Astronomy & Astrophysics*, vol. 508, no. 2, pp. 751–757, 2009.
- [77] R. S. Sutherland and M. A. Dopita, “Cooling functions for low-density astrophysical plasmas,” *The Astrophysical Journal Supplement Series*, vol. 88, no. 1, pp. 253–327, 1993.
- [78] L. Spitzer, *Physical Processes in the Interstellar Medium*, Wiley-Interscience, New York, NY, USA, 1978.
- [79] T. Freyer, G. Hensler, and H. W. Yorke, “Massive stars and the energy balance of the interstellar medium. I. The impact of an isolated $60 M_{\odot}$ star,” *The Astrophysical Journal*, vol. 594, no. 2, pp. 888–910, 2003.
- [80] T. Freyer, G. Hensler, and H. W. Yorke, “Massive stars and the energy balance of the interstellar medium. II. The $35 M_{\odot}$ star and a solution to the ‘missing wind problem,’” *The Astrophysical Journal*, vol. 638, no. 1, pp. 262–280, 2006.
- [81] M. Gritschneider, T. Naab, A. Burkert, S. Walch, F. Heitsch, and M. Wetzstein, “IVINE—ionization in the parallel tree/sph code VINE: first results on the observed age-spread around O-stars,” *Monthly Notices of the Royal Astronomical Society*, vol. 393, no. 1, pp. 21–31, 2009.
- [82] L. B. Lucy, “A numerical approach to the testing of the fission hypothesis,” *The Astronomical Journal*, vol. 82, no. 12, pp. 1013–1024, 1977.
- [83] S. Viau, P. Bastien, and S.-H. Cha, “An implicit method for radiative transfer with the diffusion approximation in smooth particle hydrodynamics,” *The Astrophysical Journal*, vol. 639, no. 1, pp. 559–570, 2006.
- [84] C. L. Fryer, G. Rockefeller, and M. S. Warren, “SNSPH: a parallel three-dimensional smoothed particle radiation hydrodynamics code,” *The Astrophysical Journal*, vol. 643, no. 1, pp. 292–305, 2006.
- [85] M. R. Krumholz and T. A. Thompson, “Direct numerical simulation of radiation pressure-driven turbulence and winds in star clusters and galactic disks,” *The Astrophysical Journal*, vol. 760, no. 2, p. 155, 2012.
- [86] S. C. Whitehouse and M. R. Bate, “The thermodynamics of collapsing molecular cloud cores using smoothed particle hydrodynamics with radiative transfer,” *Monthly Notices of the Royal Astronomical Society*, vol. 367, no. 1, pp. 32–38, 2006.
- [87] R. Cen and J. P. Ostriker, “Cold dark matter cosmology with hydrodynamics and galaxy formation: the evolution of the intergalactic medium and background radiation fields,” *The Astrophysical Journal*, vol. 417, no. 2, pp. 404–414, 1993.
- [88] J. Kim, M. R. Krumholz, J. H. Wise, M. J. Turk, N. J. Goldbaum, and T. Abel, “Dwarf galaxies with ionizing radiation feedback. I: escape of ionizing photons,” *The Astrophysical Journal*, vol. 775, no. 2, p. 109, 2013.
- [89] J. H. Wise, T. Abel, M. J. Turk, M. L. Norman, and B. D. Smith, “The birth of a galaxy—II. The role of radiation pressure,” *Monthly Notices of the Royal Astronomical Society*, vol. 427, no. 1, pp. 311–326, 2012.
- [90] P. F. Hopkins, D. Keres, and J. Onorbe, “Galaxies on FIRE (Feedback In Realistic Environments): Stellar feedback explains cosmologically inefficient star formation,” <http://arxiv.org/abs/1311.2073>.
- [91] A. D. Slyz, “Simulating star formation and feedback on a galaxy scale,” *EAS Publications Series*, vol. 24, pp. 89–94, 2007.
- [92] V. Springel, “Smoothed particle hydrodynamics in astrophysics,” *Annual Review of Astronomy and Astrophysics*, vol. 48, pp. 391–430, 2010.
- [93] N. L. Mitchell, I. G. McCarthy, R. G. Bower, T. Theuns, and R. A. Crain, “On the origin of cores in simulated galaxy clusters,” *Monthly Notices of the Royal Astronomical Society*, vol. 395, no. 1, pp. 180–196, 2009.
- [94] N. L. Mitchell, E. I. Vorobyov, and G. Hensler, “Collisionless stellar hydrodynamics as an efficient alternative to N-body methods,” *Monthly Notices of the Royal Astronomical Society*, vol. 428, no. 3, pp. 2674–2687, 2013.
- [95] G. Hensler and A. Burkert, “Chemo-dynamical evolution of galaxies,” in *Windows on Galaxies*, vol. 160 of *Astrophysics and Space Science Library*, pp. 321–331, 1990.
- [96] R. B. Larson, “A method for computing the evolution of star clusters,” *Monthly Notices of the Royal Astronomical Society*, vol. 147, pp. 323–337, 1970.
- [97] M. Samland, G. Hensler, and C. Theis, “Modeling the evolution of disk galaxies. I. The chemodynamical method and the galaxy model,” *The Astrophysical Journal*, vol. 476, no. 2, pp. 544–549, 1997.
- [98] C. Theis, A. Burkert, and G. Hensler, “Chemo-dynamical evolution of massive spherical galaxies,” *Astronomy & Astrophysics*, vol. 265, no. 2, pp. 465–477, 1992.
- [99] E. I. Vorobyov and C. Theis, “Boltzmann moment equation approach for the numerical study of anisotropic stellar discs,” *Monthly Notices of the Royal Astronomical Society*, vol. 373, no. 1, pp. 197–208, 2006.
- [100] E. I. Vorobyov and C. Theis, “Shape and orientation of stellar velocity ellipsoids in spiral galaxies,” *Monthly Notices of the Royal Astronomical Society*, vol. 383, no. 3, pp. 817–830, 2008.
- [101] G. Hensler and A. Burkert, “Chemo-dynamical evolution of galaxies,” *Astrophysics and Space Science*, vol. 170, no. 1-2, pp. 231–238, 1990.
- [102] C. Chiosi and G. Carraro, “Formation and evolution of elliptical galaxies,” *Monthly Notices of the Royal Astronomical Society*, vol. 335, no. 2, pp. 335–357, 2002.
- [103] G. Hensler, C. Theis, and J. S. Gallagher III, “Evolution of dwarf-elliptical galaxies,” *Astronomy & Astrophysics*, vol. 426, no. 1, pp. 25–36, 2004.
- [104] G. Murante, P. Monaco, M. Giovalli, S. Borgani, and A. Diaferio, “A subresolution multiphase interstellar medium model of star formation and supernova energy feedback,” *Monthly Notices of the Royal Astronomical Society*, vol. 405, no. 3, pp. 1491–1512, 2010.
- [105] M. Petrov and G. Hensler, “Evolution of the Milky Way halo by accretion of dwarf satellite galaxies,” *EAS Publications Series*, vol. 48, pp. 415–417, 2011.

- [106] C. Scannapieco, P. B. Tissera, S. D. M. White, and V. Springel, "Feedback and metal enrichment in cosmological SPH simulations—II. A multiphase model with supernova energy feedback," *Monthly Notices of the Royal Astronomical Society*, vol. 371, no. 3, pp. 1125–1139, 2006.
- [107] B. Semelin and F. Combes, "Formation and evolution of galactic disks with a multiphase numerical model," *Astronomy & Astrophysics*, vol. 388, no. 3, pp. 826–841, 2002.
- [108] C. G. Few, S. Courty, B. K. Gibson, D. Kawata, F. Calura, and R. Teyssier, "RAMSES-CH: a new chemodynamical code for cosmological simulations," *Monthly Notices of the Royal Astronomical Society*, vol. 424, no. 1, pp. L11–L15, 2012.
- [109] D. Kawata and B. K. Gibson, "GCD+: a new chemodynamical approach to modelling Supernovae and chemical enrichment in elliptical galaxies," *Monthly Notices of the Royal Astronomical Society*, vol. 340, no. 3, pp. 908–922, 2003.
- [110] C. Kobayashi, "GRAPE-SPH chemodynamical simulation of elliptical galaxies—I. Evolution of metallicity gradients," *Monthly Notices of the Royal Astronomical Society*, vol. 347, no. 3, pp. 740–758, 2004.
- [111] S. Recchi, F. Matteucci, and A. D'Ercole, "Dynamical and chemical evolution of gas-rich dwarf galaxies," *Monthly Notices of the Royal Astronomical Society*, vol. 322, no. 4, pp. 800–820, 2001.
- [112] L. Tornatore, S. Borgani, F. Matteucci, S. Recchi, and P. Tozzi, "Simulating the metal enrichment of the intracluster medium," *Monthly Notices of the Royal Astronomical Society*, vol. 349, no. 1, pp. L19–L24, 2004.
- [113] Y. Fujita, J. Fukumoto, and K. Okoshi, "Evolution of the multiphase hot interstellar medium in elliptical galaxies," *The Astrophysical Journal*, vol. 488, no. 2, pp. 585–594, 1997.
- [114] S. Tonnesen and G. L. Bryan, "Gas stripping in simulated galaxies with a multiphase interstellar medium," *The Astrophysical Journal*, vol. 694, no. 2, pp. 789–804, 2009.
- [115] B. W. Ritchie and P. A. Thomas, "Multiphase smoothed-particle hydrodynamics," *Monthly Notices of the Royal Astronomical Society*, vol. 323, no. 3, pp. 743–756, 2001.
- [116] S. Recchi and G. Hensler, "The effect of clouds in a galactic wind on the evolution of gas-rich dwarf galaxies," *Astronomy & Astrophysics*, vol. 476, no. 2, pp. 841–852, 2007.
- [117] M. R. Bate, "Stellar, brown dwarf and multiple star properties from a radiation hydrodynamical simulation of star cluster formation," *Monthly Notices of the Royal Astronomical Society*, vol. 419, no. 4, pp. 3115–3146, 2012.
- [118] M. R. Bate, I. A. Bonnell, and V. Bromm, "The formation of a star cluster: predicting the properties of stars and brown dwarfs," *Monthly Notices of the Royal Astronomical Society*, vol. 339, no. 3, pp. 577–599, 2003.
- [119] I. A. Bonnell and M. R. Bate, "Star formation through gravitational collapse and competitive accretion," *Monthly Notices of the Royal Astronomical Society*, vol. 370, no. 1, pp. 488–494, 2006.
- [120] T. H. Greif, V. Springel, S. D. M. White et al., "Simulations on a moving mesh: the clustered formation of population III protostars," *The Astrophysical Journal*, vol. 737, no. 2, article 75, 2011.
- [121] M. R. Krumholz, R. I. Klein, C. F. McKee, S. S. R. Offner, and A. J. Cunningham, "The formation of massive star systems by accretion," *Science*, vol. 323, no. 5915, pp. 754–757, 2009.
- [122] M. R. Krumholz and C. F. McKee, "A general theory of turbulence-regulated star formation, from spirals to ultraluminous infrared galaxies," *The Astrophysical Journal*, vol. 630, no. 1, pp. 250–268, 2005.
- [123] S. Recchi, G. Hensler, L. Angeretti, and F. Matteucci, "Dynamical and chemical evolution of NGC 1569," *Astronomy & Astrophysics*, vol. 445, no. 3, pp. 875–888, 2006.
- [124] S. Recchi, F. Matteucci, A. D'Ercole, and M. Tosi, "Continuous star formation in IZw18," *Astronomy & Astrophysics*, vol. 426, no. 1, pp. 37–51, 2004.
- [125] S. Recchi, F. Matteucci, A. D'Ercole, and M. Tosi, "Multiple starbursts in blue compact galaxies," *Astronomy & Astrophysics*, vol. 384, no. 3, pp. 799–811, 2002.
- [126] M. Tosi, "Models of galactic chemical evolution—the problem of uniqueness," *Astronomy & Astrophysics*, vol. 197, no. 1-2, pp. 33–46, 1988.
- [127] R. C. Kennicutt Jr., "The global schmidt law in star-forming galaxies," *The Astrophysical Journal*, vol. 498, no. 2, pp. 541–552, 1998.
- [128] M. A. Dopita and S. D. Ryder, "On the law of star formation in disk galaxies," *The Astrophysical Journal*, vol. 430, no. 1, pp. 163–178, 1994.
- [129] F. Matteucci, *Chemical Evolution of Galaxies*, Astronomy and Astrophysics Library, Springer, Berlin, Germany, 2012.
- [130] F. Matteucci and L. Greggio, "Relative roles of type I and II supernovae in the chemical enrichment of the interstellar gas," *Astronomy & Astrophysics*, vol. 154, no. 1-2, pp. 279–287, 1986.
- [131] R. J. Talbot Jr. and W. D. Arnett, "The evolution of galaxies. IV—highly flattened disks," *The Astrophysical Journal*, vol. 197, pp. 551–570, 1975.
- [132] P. F. Hopkins, D. Narayanan, and N. Murray, "The meaning and consequences of star formation criteria in galaxy models with resolved stellar feedback," *Monthly Notices of the Royal Astronomical Society*, vol. 432, no. 4, pp. 2647–2653, 2013.
- [133] M. R. Krumholz, "The star formation law in molecule-poor galaxies," *Monthly Notices of the Royal Astronomical Society*, vol. 436, no. 3, pp. 2747–2762, 2013.
- [134] M. R. Krumholz, C. F. McKee, and J. Tumlinson, "The star formation law in atomic and molecular gas," *The Astrophysical Journal*, vol. 699, no. 1, pp. 850–856, 2009.
- [135] N. C. Rana and D. A. Wilkinson, "Star formation and some aspects of the chemical evolution of the galaxy," *Monthly Notices of the Royal Astronomical Society*, vol. 218, no. 3, pp. 497–532, 1986.
- [136] F. Bigiel, A. Leroy, F. Walter et al., "The star formation law in nearby galaxies on SUB-KPC scales," *The Astronomical Journal*, vol. 136, no. 6, pp. 2846–2871, 2008.
- [137] L. Portinari and C. Chiosi, "On star formation and chemical evolution in the Galactic disc," *Astronomy & Astrophysics*, vol. 350, no. 3, pp. 827–839, 1999.
- [138] R. F. G. Wyse and J. Silk, "Star formation rates and abundance gradients in disk galaxies," *The Astrophysical Journal*, vol. 339, pp. 700–711, 1989.
- [139] C. Lada, M. Lombardi, C. Roman-Zuniga, J. Forbrich, and J. Alves, "Schmidt's conjecture and star formation in molecular clouds," *The Astrophysical Journal*, vol. 778, no. 2, p. 133, 2013.
- [140] N. Katz, "Dissipational galaxy formation. II. Effects of star formation," *The Astrophysical Journal*, vol. 391, no. 2, pp. 502–517, 1992.
- [141] N. Katz, D. H. Weinberg, and L. Hernquist, "Cosmological simulations with TreeSPH," *The Astrophysical Journal Supplement Series*, vol. 105, no. 1, pp. 19–35, 1996.

- [142] F. Governato, C. Brook, L. Mayer et al., “Bulgeless dwarf galaxies and dark matter cores from supernova-driven outflows,” *Nature*, vol. 463, no. 7278, pp. 203–206, 2010.
- [143] A. D. Slyz, J. E. G. Devriendt, G. Bryan, and J. Silk, “Towards simulating star formation in the interstellar medium,” *Monthly Notices of the Royal Astronomical Society*, vol. 356, no. 2, pp. 737–752, 2005.
- [144] G. Stinson, A. Seth, N. Katz, J. Wadsley, F. Governato, and T. Quinn, “Star formation and feedback in smoothed particle hydrodynamic simulations—I. Isolated galaxies,” *Monthly Notices of the Royal Astronomical Society*, vol. 373, no. 3, pp. 1074–1090, 2006.
- [145] E. J. Tasker and G. L. Bryan, “The effect of the interstellar model on star formation properties in galactic disks,” *The Astrophysical Journal*, vol. 673, no. 2, pp. 810–831, 2008.
- [146] K. Wada and C. A. Norman, “The global structure and evolution of a self-gravitating multiphase interstellar medium in a galactic disk,” *The Astrophysical Journal*, vol. 516, no. 1, pp. L13–L16, 1999.
- [147] A. Burkert, M. R. Bate, and P. Bodenheimer, “Protostellar fragmentation in a power-law density distribution,” *Monthly Notices of the Royal Astronomical Society*, vol. 289, no. 3, pp. 497–504, 1997.
- [148] J. K. Truelove, R. I. Klein, C. F. Mckee, J. H. Holliman II, L. H. Howell, and J. A. Greenough, “The jeans condition: a new constraint on spatial resolution in simulations of isothermal self-gravitational hydrodynamics,” *The Astrophysical Journal*, vol. 489, no. 2, pp. L179–L183, 1997.
- [149] G. de Lucia, V. Springel, S. D. M. White, D. Croton, and G. Kauffmann, “The formation history of elliptical galaxies,” *Monthly Notices of the Royal Astronomical Society*, vol. 366, no. 2, pp. 499–509, 2006.
- [150] B. G. Elmegreen, “Star formation from galaxies to globules,” *The Astrophysical Journal*, vol. 577, no. 1, pp. 206–220, 2002.
- [151] N. J. Evans II, M. M. Dunham, J. K. Jørgensen et al., “The Spitzer c2d legacy results: star-formation rates and efficiencies; evolution and lifetimes,” *The Astrophysical Journal Supplement Series*, vol. 181, no. 2, p. 321, 2009.
- [152] N. Murray, “Star formation efficiencies and lifetimes of giant molecular clouds in the Milky Way,” *The Astrophysical Journal*, vol. 729, no. 2, p. 133, 2011.
- [153] J. Alves, M. Lombardi, and C. J. Lada, “The mass function of dense molecular cores and the origin of the IMF,” *Astronomy & Astrophysics*, vol. 462, no. 1, pp. L17–L21, 2007.
- [154] M. Kuhlen, M. R. Krumholz, P. Madau, B. D. Smith, and J. Wise, “Dwarf galaxy formation with H_2 -regulated star formation,” *The Astrophysical Journal*, vol. 749, no. 1, article 36, 2012.
- [155] M. Kuhlen, P. Madau, and M. R. Krumholz, “Dwarf galaxy formation with H_2 -regulated star formation: II. Gas-rich dark galaxies at redshift 2.5,” *The Astrophysical Journal*, vol. 776, no. 1, p. 34, 2013.
- [156] O. Agertz, A. V. Kravtsov, S. N. Leitner, and N. Y. Gnedin, “Toward a complete accounting of energy and momentum from stellar feedback in galaxy formation simulations,” *The Astrophysical Journal*, vol. 770, no. 1, article 25, 2013.
- [157] S. Recchi, C. Theis, P. Kroupa, and G. Hensler, “The early evolution of tidal dwarf galaxies,” *Astronomy & Astrophysics*, vol. 470, no. 1, pp. L5–L8, 2007.
- [158] J. Köppen, C. Theis, and G. Hensler, “The self-regulated star formation in chemodynamical models of galaxies,” *Astronomy & Astrophysics*, vol. 296, p. 99, 1995.
- [159] B. G. Elmegreen and Y. N. Efremov, “A universal formation mechanism for open and globular clusters in turbulent gas,” *The Astrophysical Journal*, vol. 480, no. 1, pp. 235–245, 1997.
- [160] L. Blitz and E. Rosolowsky, “The role of pressure in GMC formation II: the H_2 -pressure relation,” *The Astrophysical Journal*, vol. 650, no. 2, pp. 933–944, 2006.
- [161] A. K. Leroy, F. Walter, E. Brinks et al., “The star formation efficiency in nearby galaxies: measuring where gas forms stars effectively,” *The Astronomical Journal*, vol. 136, no. 6, pp. 2782–2845, 2008.
- [162] E. D. Skillman, “Outstanding questions in dwarf galaxy research,” in *Dwarf Galaxies: Keys to Galaxy Formation and Evolution*, P. Papaderos, S. Recchi, and G. Hensler, Eds., pp. 3–21, Springer, Berlin, Germany, 2012.
- [163] S. T. Kay, F. R. Pearce, C. S. Frenk, and A. Jenkins, “Including star formation and supernova feedback within cosmological simulations of galaxy formation,” *Monthly Notices of the Royal Astronomical Society*, vol. 330, no. 1, pp. 113–128, 2002.
- [164] F. Buonomo, G. Carraro, C. Chiosi, and C. Lia, “Galaxy formation and evolution—II. Energy balance, star formation and feedback,” *Monthly Notices of the Royal Astronomical Society*, vol. 312, no. 2, pp. 371–379, 2000.
- [165] E. E. Salpeter, “The luminosity function and stellar evolution,” *The Astrophysical Journal*, vol. 121, pp. 161–167, 1955.
- [166] G. Chabrier, “The galactic disk mass function: reconciliation of the Hubble space telescope and nearby determinations,” *The Astrophysical Journal*, vol. 586, no. 2, pp. L133–L136, 2003.
- [167] P. Kroupa, C. A. Tout, and G. Gilmore, “The distribution of low-mass stars in the Galactic disc,” *Monthly Notices of the Royal Astronomical Society*, vol. 262, pp. 545–587, 1993.
- [168] J. M. Scalo, “The stellar initial mass function,” *Fundamentals of Cosmic Physics*, vol. 11, pp. 1–278, 1986.
- [169] P. Kroupa, “On the variation of the initial mass function,” *Monthly Notices of the Royal Astronomical Society*, vol. 322, no. 2, pp. 231–246, 2001.
- [170] D. Romano, C. Chiappini, F. Matteucci, and M. Tosi, “Quantifying the uncertainties of chemical evolution studies I. Stellar lifetimes and initial mass function,” *Astronomy & Astrophysics*, vol. 430, no. 2, pp. 491–505, 2005.
- [171] J. Schaye, C. Dalla Vecchia, C. M. Booth et al., “The physics driving the cosmic star formation history,” *Monthly Notices of the Royal Astronomical Society*, vol. 402, no. 3, pp. 1536–1560, 2010.
- [172] E. Tescari, M. Viel, V. D’Odorico et al., “Cosmic evolution of the CIV in high-resolution hydrodynamic simulations,” *Monthly Notices of the Royal Astronomical Society*, vol. 411, no. 2, pp. 826–848, 2011.
- [173] R. P. C. Wiersma, J. Schaye, and T. Theuns, “The effect of variations in the input physics on the cosmic distribution of metals predicted by simulations,” *Monthly Notices of the Royal Astronomical Society*, vol. 415, no. 1, pp. 353–371, 2011.
- [174] P. Kroupa and C. Weidner, “Galactic-field initial mass functions of massive stars,” *The Astrophysical Journal*, vol. 598, no. 2, pp. 1076–1078, 2003.
- [175] C. Weidner and P. Kroupa, “The maximum stellar mass, star-cluster formation and composite stellar populations,” *Monthly Notices of the Royal Astronomical Society*, vol. 365, no. 4, pp. 1333–1347, 2006.
- [176] C. Weidner, P. Kroupa, and J. Pflamm-Altenburg, “The m_{\max} - M_{cd} relation, the IMF and IGIMF: probabilistically sampled functions,” *Monthly Notices of the Royal Astronomical Society*, vol. 434, no. 1, pp. 84–101, 2013.

- [177] C. Weidner, P. Kroupa, and S. S. Larsen, "Implications for the formation of star clusters from extragalactic star formation rates," *Monthly Notices of the Royal Astronomical Society*, vol. 350, no. 4, pp. 1503–1510, 2004.
- [178] C. Weidner and P. Kroupa, "The variation of integrated star initial mass functions among galaxies," *The Astrophysical Journal*, vol. 625, no. 2, pp. 754–762, 2005.
- [179] S. Recchi, F. Calura, and P. Kroupa, "The chemical evolution of galaxies within the IGIMF theory: the $[\alpha/\text{Fe}]$ ratios and downsizing," *Astronomy & Astrophysics*, vol. 499, no. 3, pp. 711–722, 2009.
- [180] C. Weidner, P. Kroupa, and J. Pflamm-Altenburg, "Top-heavy integrated galactic stellar initial mass functions in starbursts," *Monthly Notices of the Royal Astronomical Society*, vol. 412, no. 2, pp. 979–986, 2011.
- [181] F. Calura, S. Recchi, F. Matteucci, and P. Kroupa, "Effects of the integrated galactic IMF on the chemical evolution of the solar neighbourhood," *Monthly Notices of the Royal Astronomical Society*, vol. 406, no. 3, pp. 1985–1999, 2010.
- [182] J. Köppen, C. Weidner, and P. Kroupa, "A possible origin of the mass-metallicity relation of galaxies," *Monthly Notices of the Royal Astronomical Society*, vol. 375, no. 2, pp. 673–684, 2007.
- [183] S. Recchi, F. Calura, B. K. Gibson, and P. Kroupa, "The $[\alpha/\text{Fe}]$ ratios of very metal-poor stars within the integrated galactic initial mass function theory," *Monthly Notices of the Royal Astronomical Society*, vol. 437, no. 1, pp. 994–1008, 2014.
- [184] P. Papaderos and G. Östlin, "I Zw 18 as morphological paradigm for rapidly assembling high- z galaxies," *Astronomy & Astrophysics*, vol. 537, article A126, 2012.
- [185] J. M. Vílchez and J. Iglesias-Páramo, "Bidimensional spectroscopic mapping and chemical abundances of the star-forming dwarf galaxy I Zw 18," *The Astrophysical Journal*, vol. 508, no. 1, p. 248, 1998.
- [186] A. Aloisi, M. Tosi, and L. Greggio, "The star formation history of I Zw 18," *The Astronomical Journal*, vol. 118, no. 1, pp. 302–322, 1999.
- [187] F. Annibali, M. Cignoni, M. Tosi et al., "The star formation history of the very metal-poor blue compact dwarf I Zw 18 from HST/ACS data," *The Astronomical Journal*, vol. 146, no. 6, p. 144, 2013.
- [188] S. Ploeckinger, G. Hensler, S. Recchi, N. Mitchell, and P. Kroupa, "Chemo-dynamical evolution of tidal dwarf galaxies. I. Method and IMF dependence," *Monthly Notices of the Royal Astronomical Society*, vol. 437, no. 4, pp. 3980–3993, 2014.
- [189] J. Pflamm-Altenburg and P. Kroupa, "Clustered star formation as a natural explanation for the $\text{H}\alpha$ cut-off in disk galaxies," *Nature*, vol. 455, no. 7213, pp. 641–643, 2008.
- [190] A. A. Dutton, T. Treu, B. J. Brewer et al., "The SWELLS survey—V. A Salpeter stellar initial mass function in the bulges of massive spiral galaxies," *Monthly Notices of the Royal Astronomical Society*, vol. 428, no. 4, pp. 3183–3195, 2013.
- [191] P. Kroupa, C. Weidner, J. Pflamm-Altenburg et al., "The stellar and sub-stellar initial mass function of simple and composite populations," in *Planets, Stars and Stellar Systems*, pp. 115–242, Springer, 2013.
- [192] M. Marks, P. Kroupa, J. Dabringhausen, and M. S. Pawlowski, "Evidence for top-heavy stellar initial mass functions with increasing density and decreasing metallicity," *Monthly Notices of the Royal Astronomical Society*, vol. 422, no. 3, pp. 2246–2254, 2012.
- [193] L. B. van den Hoek and M. A. T. Groenewegen, "New theoretical yields of intermediate mass stars," *Astronomy and Astrophysics Supplement Series*, vol. 123, no. 2, pp. 305–328, 1997.
- [194] C. Kobayashi, H. Umeda, K. Nomoto, N. Tominaga, and T. Ohkubo, "Galactic chemical evolution: carbon through zinc," *The Astrophysical Journal*, vol. 653, no. 2, pp. 1145–1171, 2006.
- [195] M. Limongi and A. Chieffi, "Evolution, explosion, and nucleosynthesis of core-collapse supernovae," *The Astrophysical Journal*, vol. 592, no. 1, pp. 404–433, 2003.
- [196] M. Limongi and A. Chieffi, "The nucleosynthesis of ^{26}Al and ^{60}Fe in solar metallicity stars extending in mass from 11 to $120 M_{\odot}$: the hydrostatic and explosive contributions," *The Astrophysical Journal*, vol. 647, no. 1, pp. 483–500, 2006.
- [197] G. Meynet and A. Maeder, "Stellar evolution with rotation: VIII. Models at $Z = 10^{-5}$ and CNO yields for early galactic evolution," *Astronomy & Astrophysics*, vol. 390, no. 2, pp. 561–583, 2002.
- [198] K. Nomoto, C. Kobayashi, and N. Tominaga, "Nucleosynthesis in stars and the chemical enrichment of galaxies," *Annual Review of Astronomy and Astrophysics*, vol. 51, pp. 457–509, 2013.
- [199] L. Portinari, C. Chiosi, and A. Bressan, "Galactic chemical enrichment with new metallicity dependent stellar yields," *Astronomy & Astrophysics*, vol. 334, no. 2, pp. 505–539, 1998.
- [200] A. Renzini and M. Voli, "Welcoming new players to the stage," *Astronomy & Astrophysics*, vol. 94, pp. 175–193, 1981.
- [201] S. E. Woosley and T. A. Weaver, "The evolution and explosion of massive stars. II. Explosive hydrodynamics and nucleosynthesis," *The Astrophysical Journal Supplement Series*, vol. 101, no. 1, pp. 181–235, 1995.
- [202] D. Romano, A. I. Karakas, M. Tosi, and F. Matteucci, "Quantifying the uncertainties of chemical evolution studies: II. Stellar yields," *Astronomy & Astrophysics*, vol. 522, no. 2, article A32, 2010.
- [203] A. Maeder, "Stellar yields as a function of initial metallicity and mass limit for black hole formation," *Astronomy & Astrophysics*, vol. 264, no. 1, pp. 105–120, 1992.
- [204] T. Rauscher, A. Heger, R. D. Huffman, and S. E. Woosley, "Nucleosynthesis in massive stars with improved nuclear and stellar physics," *The Astrophysical Journal*, vol. 576, no. 1, pp. 323–348, 2002.
- [205] E. L. O. Bakes and A. G. G. M. Tielens, "The photoelectric heating mechanism for very small graphitic grains and polycyclic aromatic hydrocarbons," *The Astrophysical Journal*, vol. 427, no. 2, pp. 822–838, 1994.
- [206] U. Lisenfeld and A. Ferrara, "Dust-to-gas ratio and metal abundance in dwarf galaxies," *The Astrophysical Journal*, vol. 496, no. 1, p. 145, 1998.
- [207] R. Schneider, A. Ferrara, P. Natarajan, and K. Omukai, "First stars, very massive black holes, and metals," *The Astrophysical Journal*, vol. 571, no. 1, p. 30, 2002.
- [208] W. W. Duley and D. A. Williams, *Interstellar Chemistry*, Academic Press, London, UK, 1984.
- [209] B. D. Savage and K. R. Sembach, "Interstellar abundances from absorption-line observations with the hubble space telescope," *Annual Review of Astronomy and Astrophysics*, vol. 34, no. 1, pp. 279–329, 1996.
- [210] F. Calura, A. Pipino, and F. Matteucci, "The cycle of interstellar dust in galaxies of different morphological types," *Astronomy & Astrophysics*, vol. 479, no. 3, pp. 669–685, 2008.
- [211] E. Dwek, "The evolution of the elemental abundances in the gas and dust phases of the galaxy," *The Astrophysical Journal*, vol. 501, no. 2, pp. 643–665, 1998.

- [212] A. Pipino, X. L. Fan, F. Matteucci et al., “The chemical evolution of elliptical galaxies with stellar and QSO dust production,” *Astronomy & Astrophysics*, vol. 525, no. 19, article A61, 2011.
- [213] S. Zhukovska, H.-P. Gail, and M. Tieloff, “Evolution of interstellar dust and stardust in the solar neighbourhood,” *Astronomy & Astrophysics*, vol. 479, no. 2, pp. 453–480, 2008.
- [214] S. Zhukovska and T. Henning, “Dust input from AGB stars in the large magellanic cloud,” *Astronomy & Astrophysics*, vol. 555, article A99, p. 15, 2013.
- [215] F. Miniati, “A hybrid scheme for gas-dust systems stiffly coupled via viscous drag,” *Journal of Computational Physics*, vol. 229, no. 10, pp. 3916–3937, 2010.
- [216] G. Laibe and D. J. Price, “Dusty gas with smoothed particle hydrodynamics—II. Implicit timestepping and astrophysical drag regimes,” *Monthly Notices of the Royal Astronomical Society*, vol. 420, no. 3, pp. 2365–2376, 2012.
- [217] C. Theis and N. Orlova, “Are galactic disks dynamically influenced by dust?” *Astronomy & Astrophysics*, vol. 418, no. 3, pp. 959–978, 2004.
- [218] R. Davé, K. Finlator, B. D. Oppenheimer et al., “The nature of submillimetre galaxies in cosmological hydrodynamic simulations,” *Monthly Notices of the Royal Astronomical Society*, vol. 404, no. 3, pp. 1355–1368, 2010.
- [219] C. Scannapieco, M. Wadepuhl, O. H. Parry et al., “The Aquila comparison project: the effects of feedback and numerical methods on simulations of galaxy formation,” *Monthly Notices of the Royal Astronomical Society*, vol. 423, no. 2, pp. 1726–1749, 2012.
- [220] E. J. Tasker, R. Brunino, N. L. Mitchell et al., “A test suite for quantitative comparison of hydrodynamic codes in astrophysics,” *Monthly Notices of the Royal Astronomical Society*, vol. 390, no. 3, pp. 1267–1281, 2008.
- [221] A. Aguirre, L. Hernquist, J. Schaye, N. Katz, D. H. Weinberg, and J. Gardner, “Metal enrichment of the intergalactic medium in cosmological simulations,” *The Astrophysical Journal*, vol. 561, no. 2, pp. 521–549, 2001.
- [222] C. D. Vecchia and J. Schaye, “Simulating galactic outflows with kinetic supernova feedback,” *Monthly Notices of the Royal Astronomical Society*, vol. 387, no. 4, pp. 1431–1444, 2008.
- [223] V. Springel and L. Hernquist, “Cosmological smoothed particle hydrodynamics simulations: a hybrid multiphase model for star formation,” *Monthly Notices of the Royal Astronomical Society*, vol. 339, no. 2, pp. 289–311, 2003.
- [224] P. Monaco, G. Murante, S. Borgani, and K. Dolag, “Schmidt-Kennicutt relations in SPH simulations of disc galaxies with effective thermal feedback from supernovae,” *Monthly Notices of the Royal Astronomical Society*, vol. 421, no. 3, pp. 2485–2497, 2012.
- [225] S. Skory, E. Hallman, J. O. Burns, S. W. Skillman, B. W. O’Shea, and B. D. Smith, “On the road to more realistic galaxy cluster simulations: the effects of radiative cooling and thermal feedback prescriptions on the observational properties of simulated galaxy clusters,” *The Astrophysical Journal*, vol. 763, no. 1, p. 38, 2013.
- [226] J. Sommer-Larsen, M. Götz, and L. Portinari, “Galaxy formation: cold dark matter, feedback, and the hubble sequence,” *The Astrophysical Journal*, vol. 596, no. 1, p. 47, 2003.
- [227] P. F. Hopkins, E. Quataert, and N. Murray, “Stellar feedback in galaxies and the origin of galaxy-scale winds,” *Monthly Notices of the Royal Astronomical Society*, vol. 421, no. 4, pp. 3522–3537, 2012.
- [228] C. M. Booth, O. Agertz, A. V. Kravtsov, and N. Y. Gnedin, “Simulations of disk galaxies with cosmic ray driven galactic winds,” *The Astrophysical Journal*, vol. 777, no. 1, article L16, 2013.
- [229] E. A. Dorfi and D. Breitschwerdt, “Time-dependent galactic winds: I. Structure and evolution of galactic outflows accompanied by cosmic ray acceleration,” *Astronomy & Astrophysics*, vol. 540, article A77, 2012.
- [230] M. Jubelgas, V. Springel, T. Enßlin, and C. Pfrommer, “Cosmic ray feedback in hydrodynamical simulations of galaxy formation,” *Astronomy & Astrophysics*, vol. 481, no. 1, pp. 33–63, 2008.
- [231] D. J. Croton, V. Springel, S. D. M. White et al., “The many lives of active galactic nuclei: cooling flows, black holes and the luminosities and colours of galaxies,” *Monthly Notices of the Royal Astronomical Society*, vol. 365, no. 1, pp. 11–28, 2006.
- [232] L. Ferrarese and D. Merritt, “A fundamental relation between supermassive black holes and their host galaxies,” *The Astrophysical Journal*, vol. 539, no. 1, pp. L9–L12, 2000.
- [233] N. J. McConnell, C. P. Ma, K. Gebhardt et al., “Two ten-billion-solar-mass black holes at the centres of giant elliptical galaxies,” *Nature*, vol. 480, pp. 215–218, 2011.
- [234] C. Dalla Vecchia and J. Schaye, “Simulating galactic outflows with thermal supernova feedback,” *Monthly Notices of the Royal Astronomical Society*, vol. 426, no. 1, pp. 140–158, 2012.
- [235] K. Nomoto, S. Wanajo, Y. Kamiya, N. Tominaga, and H. Umeda, “Chemical yields from supernovae and hypernovae,” in *The Galaxy Disk in Cosmological Context*, vol. 4 of *Proceedings of the IAU Symposium*, no. 254, p. 355, 2009.
- [236] K. Thornton, M. Gaudlitz, H.-T. H. Janka, and M. Steinmetz, “Energy input and mass redistribution by supernovae in the interstellar medium,” *The Astrophysical Journal*, vol. 500, no. 1, pp. 95–119, 1998.
- [237] G. Hensler, “Massive stars: their contribution to energy and element budget in chemo-dynamical galaxy evolution,” *EAS Publications Series*, vol. 24, pp. 113–118, 2007.
- [238] D. Kröger, G. Hensler, and T. Freyer, “Chemical self-enrichment of HII regions by the Wolf-Rayet phase of an 85 M_{\odot} star,” *Astronomy & Astrophysics*, vol. 450, no. 1, pp. L5–L8, 2006.
- [239] C. Melioli and E. M. de Gouveia Dal Pino, “Evolution of the ISM of starburst galaxies: the SN heating efficiency,” *Astronomy & Astrophysics*, vol. 424, no. 3, pp. 817–831, 2004.
- [240] F. Bradamante, F. Matteucci, and A. D’Ercole, “The influence of stellar energetics and dark matter on the chemical evolution of dwarf irregulars,” *Astronomy & Astrophysics*, vol. 337, no. 2, pp. 338–348, 1998.
- [241] B. M. Lasker, “The energization of the interstellar medium by ionization-limited H II regions,” *The Astrophysical Journal*, vol. 149, p. 23, 1967.
- [242] L. Spitzer, *Diffuse Matter in Space*, Interscience, New York, NY, USA, 1968.
- [243] D. K. Strickland, T. M. Heckman, E. J. M. Colbert, C. G. Hoopes, and K. A. Weaver, “A high spatial resolution X-ray and H α study of hot gas in the halos of star-forming disk galaxies. II. Quantifying supernova feedback,” *The Astrophysical Journal*, vol. 606, no. 2, pp. 829–852, 2004.
- [244] D. F. Cioffi, C. F. McKee, and E. Bertschinger, “Dynamics of radiative supernova remnants,” *The Astrophysical Journal*, vol. 334, pp. 252–265, 1988.
- [245] T. I. Larsen, J. Sommer-Larsen, and B. E. J. Pagel, “The chemical evolution of gas-rich dwarf galaxies,” *Monthly Notices of the Royal Astronomical Society*, vol. 323, no. 3, pp. 555–576, 2001.

- [246] C. Leitherer, D. Schaerer, J. D. Goldader et al., “Starburst99: synthesis models for galaxies with active star formation,” *The Astrophysical Journal Supplement Series*, vol. 123, no. 1, p. 3, 1999.
- [247] R.-P. Kudritzki and J. Puls, “Winds from hot stars,” *Annual Review of Astronomy and Astrophysics*, vol. 38, no. 1, pp. 613–666, 2000.
- [248] H. J. G. L. M. Lamers and J. P. Cassinelli, *Introduction to Stellar Winds*, Cambridge University Press, Cambridge, UK, 1999.
- [249] B. Wang and Z. Han, “Progenitors of Type Ia supernovae,” *New Astronomy Reviews*, vol. 56, no. 4, pp. 122–141, 2012.
- [250] S. Recchi and G. Hensler, “The refill of superbubble cavities,” *Astronomy & Astrophysics*, vol. 445, no. 3, pp. L39–L42, 2006.
- [251] F. Mannucci, M. Della Valle, and N. Panagia, “Two populations of progenitors for Type Ia supernovae?” *Monthly Notices of the Royal Astronomical Society*, vol. 370, no. 2, pp. 773–783, 2006.
- [252] F. Matteucci and S. Recchi, “On the typical timescale for the chemical enrichment from Type Ia supernovae in galaxies,” *The Astrophysical Journal*, vol. 558, no. 1, pp. 351–358, 2001.
- [253] F. Matteucci, E. Spitoni, S. Recchi, and R. Valiante, “The effect of different Type Ia supernova progenitors on galactic chemical evolution,” *Astronomy & Astrophysics*, vol. 501, no. 2, pp. 531–538, 2009.
- [254] E. Scannapieco and L. Bildsten, “The Type Ia supernova rate,” *The Astrophysical Journal*, vol. 629, no. 2, pp. L85–L88, 2005.
- [255] L. Greggio, “The rates of type Ia supernovae I. Analytical formulations,” *Astronomy & Astrophysics*, vol. 441, no. 3, pp. 1055–1078, 2005.
- [256] P. Ruiz-Lapuente and R. Canal, “Type Ia Supernova counts at high z : signatures of Cosmological models and progenitors,” *The Astrophysical Journal*, vol. 497, no. 2, pp. L57–L60, 1998.
- [257] D. Maoz, F. Mannucci, and T. D. Brandt, “The delay-time distribution of Type Ia supernovae from Sloan II,” *Monthly Notices of the Royal Astronomical Society*, vol. 426, no. 4, pp. 3282–3294, 2012.
- [258] T. Totani, T. Morokuma, T. Oda, M. Doi, and N. Yasuda, “Delay time distribution measurement of Type Ia supernovae by the Subaru/XMM-Newton deep survey and implications for the progenitor,” *Publications of the Astronomical Society of Japan*, vol. 60, no. 6, pp. 1327–1346, 2008.
- [259] I. Bonaparte, F. Matteucci, S. Recchi, E. Spitoni, A. Pipino, and V. Grieco, “Galactic and cosmic Type Ia supernova (SNIa) rates: is it possible to impose constraints on SNIa progenitors?” *Monthly Notices of the Royal Astronomical Society*, vol. 435, no. 3, pp. 2460–2473, 2013.
- [260] F. Matteucci, N. Panagia, A. Pipino, F. Mannucci, S. Recchi, and M. Della Valle, “A new formulation of the Type Ia supernova rate and its consequences on galactic chemical evolution,” *Monthly Notices of the Royal Astronomical Society*, vol. 372, no. 1, pp. 265–275, 2006.
- [261] J. E. Barnes and D. B. Sanders, *Galaxy Interactions at Low and High Redshift*, vol. 186 of *International Astronomical Union Symposia*, Springer, 1999.
- [262] F. Bournaud, “Star formation in galaxy interactions and mergers,” in *Star Formation in the Local Universe—EES2010*, vol. 51 of *EAS Publications Series*, pp. 107–131, Cambridge University Press, Cambridge, UK, 2011.
- [263] C. J. Conselice, “Galaxy mergers and interactions at high redshift,” in *Galaxy Evolution across the Hubble Time*, Proceedings of the IAU Symposium, no. 235, pp. 381–384, 2007.
- [264] C. S. Frenk and S. D. M. White, “Dark matter and cosmic structure,” *Annalen der Physik*, vol. 524, no. 9-10, pp. 507–534, 2012.
- [265] B. Smith, J. Higdon, S. Higdon, and N. Bastian, *Galaxy Wars: Stellar Populations and Star Formation in Interacting Galaxies*, vol. 423 of *ASP Conference Series*, 2010.
- [266] C. Struck, “Galaxy collisions—dawn of a new era,” *Astrophysics Update 2*, Springer, Berlin, Germany, vol. 2, pp. 115–158, 2006.
- [267] A. Dressler, “Galaxy morphology in rich clusters—implications for the formation and evolution of galaxies,” *The Astrophysical Journal*, vol. 236, pp. 351–365, 1980.
- [268] M. Balogh, V. Eke, C. Miller et al., “Galaxy ecology: groups and low-density environments in the SDSS and 2dFGRS,” *Monthly Notices of the Royal Astronomical Society*, vol. 348, no. 4, pp. 1355–1372, 2004.
- [269] M. Tanaka, T. Goto, S. Okamura, K. Shimasaku, and J. Brinkmann, “The environmental dependence of galaxy properties in the local universe: dependences on luminosity, local density, and system richness,” *The Astronomical Journal*, vol. 128, no. 6, pp. 2677–2695, 2004.
- [270] A. Boselli and G. Gavazzi, “Environmental effects on late-type galaxies in nearby clusters,” *Publications of the Astronomical Society of the Pacific*, vol. 118, no. 842, pp. 517–559, 2006.
- [271] J. Iglesias-Páramo, “Properties of H α emitting dwarf galaxies in nearby clusters,” in *Dwarf Galaxies: Keys to Galaxy Formation and Evolution*, P. Papaderos, S. Recchi, and G. Hensler, Eds., Astrophysics and Space Science Proceedings, pp. 277–284, Springer, 2012.
- [272] G. Byrd and M. Valtonen, “Tidal generation of active spirals and S0 galaxies by rich clusters,” *The Astrophysical Journal*, vol. 350, no. 1, pp. 89–94, 1990.
- [273] D. Merritt, “Relaxation and tidal stripping in rich clusters of galaxies. I. Evolution of the mass distribution,” *The Astrophysical Journal*, vol. 264, pp. 24–48, 1983.
- [274] L. Spitzer Jr. and W. Baade, “Stellar populations and collisions of galaxies,” *The Astrophysical Journal*, vol. 113, pp. 413–418, 1951.
- [275] M. Valluri and C. J. Jog, “Collisional removal of H I from the inner disks of virgo cluster galaxies,” *The Astrophysical Journal*, vol. 357, no. 2, pp. 367–372, 1990.
- [276] B. Moore, N. Katz, G. Lake, A. Dressler, and A. Oemler Jr., “Galaxy harassment and the evolution of clusters of galaxies,” *Nature*, vol. 379, no. 6566, pp. 613–616, 1996.
- [277] B. Moore, G. Lake, and N. Katz, “Morphological transformation from galaxy harassment,” *The Astrophysical Journal*, vol. 495, no. 1, pp. 139–151, 1998.
- [278] C. Mastropietro, B. Moore, L. Mayer, V. P. Debattista, R. Piffaretti, and J. Stadel, “Morphological evolution of discs in clusters,” *Monthly Notices of the Royal Astronomical Society*, vol. 364, no. 2, pp. 607–619, 2005.
- [279] R. Smith, J. I. Davies, and A. H. Nelson, “How effective is harassment on infalling late-type dwarfs?” *Monthly Notices of the Royal Astronomical Society*, vol. 405, no. 3, pp. 1723–1735, 2010.
- [280] R. Smith, R. Sánchez-Janssen, M. Fellhauer, T. H. Puzia, J. A. L. Aguerri, and J. P. Farias, “The impact of galaxy harassment on the globular cluster systems of early-type cluster dwarf galaxies,” *Monthly Notices of the Royal Astronomical Society*, vol. 429, no. 2, pp. 1066–1079, 2013.
- [281] J. E. Gunn and J. R. Gott III, “On the infall of matter into clusters of galaxies and some effects on their evolution,” *The Astrophysical Journal*, vol. 176, pp. 1–19, 1972.
- [282] M. G. Abadi, B. Moore, and R. G. Bower, “Ram pressure stripping of spiral galaxies in clusters,” *Monthly Notices of the Royal Astronomical Society*, vol. 308, no. 4, pp. 947–954, 1999.

- [283] R. Farouki and S. L. Shapiro, "Computer simulations of environmental influences on galaxy evolution in dense clusters. I. Ram-pressure stripping," *The Astrophysical Journal*, vol. 241, pp. 928–945, 1980.
- [284] T. Kronberger, W. Kapferer, S. Unterguggenberger, S. Schindler, and B. L. Ziegler, "The effects of ram-pressure stripping on the internal kinematics of simulated spiral galaxies," *Astronomy & Astrophysics*, vol. 483, no. 3, pp. 783–791, 2008.
- [285] S. Plöckinger and G. Hensler, "Do high-velocity clouds trace the dark matter subhalo population?" *Astronomy & Astrophysics*, vol. 547, article A43, 2012.
- [286] E. Roediger and M. Brüggen, "Ram pressure stripping of disc galaxies: the role of the inclination angle," *Monthly Notices of the Royal Astronomical Society*, vol. 369, no. 2, pp. 567–580, 2006.
- [287] E. Roediger and G. Hensler, "Ram pressure stripping of disk galaxies from high to low density environments," *Astronomy & Astrophysics*, vol. 433, no. 3, pp. 875–895, 2005.
- [288] S. Schulz and C. Struck, "Multi stage three-dimensional sweeping and annealing of disc galaxies in clusters," *Monthly Notices of the Royal Astronomical Society*, vol. 328, no. 1, pp. 185–202, 2001.
- [289] R. Smith, P. A. Duc, G. N. Candlish, M. Fellhauer, Y.-K. Sheen, and B. K. Gibson, "The influence of ram pressure on the evolution of tidal dwarf galaxies," *Monthly Notices of the Royal Astronomical Society*, vol. 436, no. 1, pp. 839–853, 2013.
- [290] R. Smith, M. Fellhauer, and P. Assmann, "Ram pressure drag—the effects of ram pressure on dark matter and stellar disc dynamics," *Monthly Notices of the Royal Astronomical Society*, vol. 420, no. 3, pp. 1990–2005, 2012.
- [291] G. Hensler, "Morphological mutations of dwarf galaxies," in *Dwarf Galaxies: Keys to Galaxy Formation and Evolution*, P. Papaderos, S. Recchi, and G. Hensler, Eds., pp. 75–91, Springer, Berlin, Germany, 2012.
- [292] L. Mayer, "Environmental mechanisms shaping the nature of dwarf spheroidal galaxies: the view of computer simulations," *Advances in Astronomy*, vol. 2010, Article ID 278434, 21 pages, 2010.
- [293] E. D. Skillman and R. Bender, "The dwarf galaxy star formation crisis," *Revista Mexicana de Astronomia y Astrofisica Conference Series*, vol. 3, p. 25, 1995.
- [294] A. Marcolini, F. Brighenti, and A. D'Ercole, "Three-dimensional simulations of the interstellar medium in dwarf galaxies—I. Ram pressure stripping," *Monthly Notices of the Royal Astronomical Society*, vol. 345, no. 4, pp. 1329–1339, 2003.
- [295] A. Marcolini, F. Brighenti, and A. D'Ercole, "Three-dimensional simulations of the interstellar medium in dwarf galaxies—II. Galactic winds," *Monthly Notices of the Royal Astronomical Society*, vol. 352, no. 2, pp. 363–375, 2004.
- [296] S. Schindler, W. Kapferer, W. Domainko et al., "Metal enrichment processes in the intra-cluster medium," *Astronomy & Astrophysics*, vol. 435, no. 2, pp. L25–L28, 2005.
- [297] P. Creasey, T. Theuns, and R. G. Bower, "How supernova explosions power galactic winds," *Monthly Notices of the Royal Astronomical Society*, vol. 429, no. 3, pp. 1922–1948, 2013.
- [298] M. S. Westmoquette, L. J. Smith, J. S. Gallagher III, and K. M. Exter, "Gemini GMOS/integral field unit spectroscopy of NGC 1569—II. Mapping the roots of the galactic outflow," *Monthly Notices of the Royal Astronomical Society*, vol. 381, no. 3, pp. 913–931, 2007.
- [299] K. Matsubayashi, H. Sugai, T. Hattori et al., "Galactic wind in the nearby starburst galaxy NGC 253 observed with the kyoto3dii fabry-perot mode," *The Astrophysical Journal*, vol. 701, no. 2, pp. 1636–1643, 2009.
- [300] D. K. Strickland, "A new superwind galaxy: XMM-Newton observations of NGC 6810," *Monthly Notices of the Royal Astronomical Society*, vol. 376, no. 2, pp. 523–533, 2007.
- [301] A. Contursi, A. Poglitsch, J. Grácia Carpio et al., "Spectroscopic FIR mapping of the disk and galactic wind of M 82 with Herschel-PACS," *Astronomy & Astrophysics*, vol. 549, article A118, pp. 1–26, 2013.
- [302] J. D. Lowenthal, D. C. Koo, R. Guzmán et al., "Keck spectroscopy of redshift $z \sim 3$ galaxies in the Hubble deep field," *The Astrophysical Journal*, vol. 481, no. 2, pp. 673–688, 1997.
- [303] B. F. Lundgren, G. Brammer, P. van Dokkum et al., "Large-scale star-formation-driven outflows at $1 < z < 2$ in the 3D-HST survey," *The Astrophysical Journal*, vol. 760, no. 1, p. 49, 2012.
- [304] M. Pettini, S. L. Ellison, J. Bergeron, and P. Petitjean, "The abundances of nitrogen and oxygen in damped Lyman α systems," *Astronomy & Astrophysics*, vol. 391, no. 1, pp. 21–34, 2002.
- [305] M. Pettini, A. E. Shapley, C. C. Steidel et al., "The rest-frame optical spectra of Lyman break galaxies: star formation, extinction, abundances, and kinematics," *The Astrophysical Journal*, vol. 554, no. 2, pp. 981–1000, 2001.
- [306] S. Veilleux, G. Cecil, and J. Bland-Hawthorn, "Galactic winds," *Annual Review of Astronomy and Astrophysics*, vol. 43, pp. 769–826, 2005.
- [307] D. Breitschwerdt, J. F. McKenzie, and H. J. Voelk, "Galactic winds: I. Cosmic ray and wave-driven winds from the galaxy," *Astronomy & Astrophysics*, vol. 245, pp. 79–97, 1991.
- [308] N. Murray, B. Ménard, and T. A. Thompson, "Radiation pressure from massive star clusters as a launching mechanism for super-galactic winds," *The Astrophysical Journal*, vol. 735, no. 1, p. 66, 2011.
- [309] M. Sharma, B. B. Nath, and Y. Shchekinov, "Dust-driven wind from disk galaxies," *The Astrophysical Journal*, vol. 736, no. 2, article L27, 2011.
- [310] M. Uhlig, C. Pfrommer, M. Sharma, B. B. Nath, T. A. Enßlin, and V. Springel, "Galactic winds driven by cosmic ray streaming," *Monthly Notices of the Royal Astronomical Society*, vol. 423, no. 3, pp. 2374–2396, 2012.
- [311] P. Barai, M. Viel, S. Borgani et al., "Galactic winds in cosmological simulations of the circumgalactic medium," *Monthly Notices of the Royal Astronomical Society*, vol. 430, no. 4, pp. 3213–3234, 2013.
- [312] D. S. N. Rupke and S. Veilleux, "The multiphase structure and power sources of galactic winds in major mergers," *The Astrophysical Journal*, vol. 768, no. 1, p. 75, 2013.
- [313] D. S. de Young and J. S. Gallagher III, "Selective loss of metals from low-mass galaxies," *The Astrophysical Journal*, vol. 356, no. 1, pp. L15–L19, 1990.
- [314] D. S. de Young and T. M. Heckman, "The effect of central starbursts on the interstellar medium of dwarf galaxies," *The Astrophysical Journal*, vol. 431, no. 2, pp. 598–603, 1994.
- [315] M. Mori, A. Ferrara, and P. Madau, "Early metal enrichment by pregalactic outflows. II. Three-dimensional simulations of blow-away," *The Astrophysical Journal*, vol. 571, no. 1, pp. 40–55, 2002.
- [316] V. Baumgartner and D. Breitschwerdt, "Superbubble evolution in disk galaxies. I. Study of blow-out by analytical models," *Astronomy & Astrophysics*, vol. 557, article A140, 2013.

- [317] J. N. Bregman, “The galactic fountain of high-velocity clouds,” *The Astrophysical Journal*, vol. 236, pp. 577–591, 1980.
- [318] C. Melioli, F. Brighenti, A. D’Ercole, and E. M. de Gouveia Dal Pino, “Hydrodynamical simulations of Galactic fountains—I. Evolution of single fountains,” *Monthly Notices of the Royal Astronomical Society*, vol. 388, no. 2, pp. 573–586, 2008.
- [319] E. Spitoni, S. Recchi, and F. Matteucci, “Galactic fountains and their connection with high and intermediate velocity clouds,” *Astronomy & Astrophysics*, vol. 484, no. 3, pp. 743–753, 2008.
- [320] G. Tenorio-Tagle, “The gas dynamics of H II regions. I—the champagne model,” *Astronomy & Astrophysics*, vol. 71, no. 1-2, pp. 59–65, 1979.
- [321] A. Dekel and J. Silk, “The origin of dwarf galaxies, cold dark matter, and biased galaxy formation,” *The Astrophysical Journal*, vol. 303, pp. 39–55, 1986.
- [322] R. B. Larson, “Effects of supernovae on the early evolution of galaxies,” *Monthly Notices of the Royal Astronomical Society*, vol. 169, pp. 229–246, 1974.
- [323] J. P. Vader, “Metal-enhanced galactic winds. I,” *The Astrophysical Journal*, vol. 305, pp. 669–678, 1986.
- [324] M. L. Mateo, “Dwarf galaxies of the local group,” *Annual Review of Astronomy and Astrophysics*, vol. 36, pp. 435–506, 1998.
- [325] E. Tolstoy, V. Hill, and M. Tosi, “Star-formation histories, abundances, and kinematics of dwarf galaxies in the local group,” *Annual Review of Astronomy and Astrophysics*, vol. 47, pp. 371–425, 2009.
- [326] D. Thomas, C. Maraston, R. Bender, and C. Mendes de Oliveira, “The epochs of early-type galaxy formation as a function of environment,” *The Astrophysical Journal*, vol. 621, no. 2, pp. 673–694, 2005.
- [327] E. D. Skillman, “Evidence for and against galactic wind dominated evolution of dwarf irregular galaxies,” *Revista Mexicana de Astronomia y Astrofisica Conference Series*, vol. 6, p. 36, 1997.
- [328] T. Tsujimoto and K. Bekki, “Stripping of nitrogen-rich AGB ejecta from interacting dwarf irregular galaxies,” *Monthly Notices of the Royal Astronomical Society*, vol. 436, no. 2, pp. 1191–1200, 2013.
- [329] A. Rieschick and G. Hensler, “Chemodynamical gas flow cycles and their influence on the chemical evolution of dwarf irregular galaxies,” *Astrophysics and Space Science*, vol. 284, no. 2, pp. 861–864, 2003.
- [330] P. E. Dimotakis, “Turbulent mixing,” *Annual Review of Fluid Mechanics*, vol. 37, pp. 329–356, 2005.
- [331] D. S. Balsara and J. Kim, “Amplification of interstellar magnetic fields and turbulent mixing by supernova-driven turbulence. II. The role of dynamical chaos,” *The Astrophysical Journal*, vol. 634, no. 1, pp. 390–406, 2005.
- [332] L. Pan, *Turbulent mixing of chemical elements in galaxies [Ph.D. thesis]*, The University of Texas at Austin, 2008.
- [333] L. Pan and E. Scannapieco, “Mixing in supersonic turbulence,” *The Astrophysical Journal*, vol. 721, no. 2, pp. 1765–1782, 2010.
- [334] A. Ferrara and E. Tolstoy, “The role of stellar feedback and dark matter in the evolution of dwarf galaxies,” *Monthly Notices of the Royal Astronomical Society*, vol. 313, no. 2, pp. 291–309, 2000.
- [335] M. M. Mac Low and R. McCray, “Superbubbles in disk galaxies,” *The Astrophysical Journal*, vol. 324, pp. 776–785, 1988.
- [336] A. Marcolini, A. D’Ercole, F. Brighenti, and S. Recchi, “Star formation feedback and metal enrichment by Types Ia and II Supernovae in dwarf spheroidal galaxies: the case of Draco,” *Monthly Notices of the Royal Astronomical Society*, vol. 371, no. 2, pp. 643–658, 2006.
- [337] D. Michielsen, S. Valcke, and S. de Rijcke, “Simulating the flattening—metallicity relation of dwarf elliptical galaxies,” *EAS Publications Series*, vol. 24, pp. 287–288, 2007.
- [338] S. Recchi, G. Hensler, and D. Anelli, “Galactic outflows and the chemical evolution of dwarf galaxies,” <http://arxiv.org/abs/0901.1976>.
- [339] S. Silich and G. Tenorio-Tagle, “On the energy required to eject processed matter from galaxies,” *The Astrophysical Journal*, vol. 552, no. 1, pp. 91–98, 2001.
- [340] E. O. Vasiliev, E. I. Vorobyov, and Y. A. Shchekinov, “First supernovae in dwarf protogalaxies,” *Astronomy & Astrophysics*, vol. 489, no. 2, pp. 505–515, 2008.
- [341] S. Recchi and G. Hensler, “The fate of heavy elements in dwarf galaxies—the role of mass and geometry,” *Astronomy & Astrophysics*, vol. 551, article A41, 12 pages, 2013.
- [342] C. L. Martin, H. A. Kobulnicky, and T. M. Heckman, “The metal content of dwarf starburst winds: results from Chandra observations of NGC 1569,” *The Astrophysical Journal*, vol. 574, no. 2, pp. 663–692, 2002.
- [343] J. Ott, F. Walter, and E. Brinks, “A Chandra X-ray survey of nearby dwarf starburst galaxies—I. Data reduction and results,” *Monthly Notices of the Royal Astronomical Society*, vol. 358, no. 4, pp. 1423–1452, 2005.
- [344] E. Spitoni, F. Calura, F. Matteucci, and S. Recchi, “The origin of the mass-metallicity relation: an analytical approach,” *Astronomy & Astrophysics*, vol. 514, no. 10, article A73, 2010.
- [345] C. A. Tremonti, T. M. Heckman, G. Kauffmann et al., “The origin of the mass-metallicity relation: insights from 53,000 star-forming galaxies in the sloan digital sky survey,” *The Astrophysical Journal*, vol. 613, no. 2, pp. 898–913, 2004.
- [346] F. Matteucci, *The Chemical Evolution of the Galaxy*, Astrophysics and Space Science Library, Kluwer Academic Publishers, Dordrecht, The Netherlands, 2001.
- [347] S. Recchi, E. Spitoni, F. Matteucci, and G. A. Lanfranchi, “The effect of differential galactic winds on the chemical evolution of galaxies,” *Astronomy & Astrophysics*, vol. 489, no. 2, pp. 555–565, 2008.
- [348] B. E. J. Pagel, *Nucleosynthesis and Chemical Evolution of Galaxies*, Cambridge University Press, Cambridge, UK, 1997.
- [349] P. Dayal, A. Ferrara, and J. S. Dunlop, “The physics of the fundamental metallicity relation,” *Monthly Notices of the Royal Astronomical Society*, vol. 430, no. 4, pp. 2891–2895, 2013.
- [350] S. J. Lilly, C. M. Carollo, A. Pipino, A. Renzini, and Y. Peng, “Gas regulation of galaxies: the evolution of the cosmic specific star formation rate, the metallicity-mass-star-formation rate relation, and the stellar content of halos,” *The Astrophysical Journal*, vol. 772, no. 2, p. 119, 2013.
- [351] C. E. Brennen, *Fundamentals of Multiphase Flow*, Cambridge University Press, Cambridge, UK, 2009.
- [352] N. I. Kolev, *Multiphase Flow Dynamics I: Fundamentals*, Springer, Berlin, Germany, 2007.
- [353] H. Staedtke, *Gasdynamic Aspects of Two-Phase Flow: Hyperbolicity, Wave Propagation Phenomena and Related Numerical Methods*, John Wiley & Sons, New York, NY, USA, 2006.
- [354] K. Bekki, “Coevolution of dust, gas and stars in galaxies—I. Spatial distributions and scaling-relations of dust and molecular hydrogen,” *Monthly Notices of the Royal Astronomical Society*, vol. 432, no. 3, pp. 2298–2323, 2013.
- [355] K. Bekki, “Simulating galaxy evolution with a non-universal stellar initial mass function,” *Monthly Notices of the Royal Astronomical Society*, vol. 436, no. 3, pp. 2254–2275, 2013.

- [356] S.-J. Paardekooper and G. Mellema, "Dust flow in gas disks in the presence of embedded planets," *Astronomy & Astrophysics*, vol. 453, no. 3, pp. 1129–1140, 2006.
- [357] D. W. Silvia, B. D. Smith, and J. M. Shull, "Numerical simulations of supernova dust destruction. I. Cloud-crushing and post-processed grain sputtering," *The Astrophysical Journal*, vol. 715, no. 2, pp. 1575–1590, 2010.
- [358] D. W. Silvia, B. D. Smith, and J. M. Shull, "Numerical simulations of supernova dust destruction. II. Metal-enriched ejecta knots," *The Astrophysical Journal*, vol. 748, no. 1, article 12, 2012.
- [359] A. J. van Marle, Z. Meliani, R. Keppens, and L. Decin, "Computing the dust distribution in the bow shock of a fast-moving, evolved star," *The Astrophysical Journal*, vol. 734, no. 2, article L26, 2011.
- [360] N. E. L. Haugen, A. Brandenburg, and W. Dobler, "Simulations of nonhelical hydromagnetic turbulence," *Physical Review E*, vol. 70, no. 1, Article ID 016308, 2004.
- [361] M. R. Bate, "The importance of radiative feedback for the stellar initial mass function," *Monthly Notices of the Royal Astronomical Society*, vol. 392, no. 4, pp. 1363–1380, 2009.
- [362] M. R. Krumholz, R. I. Klein, and C. F. McKee, "Radiation-hydrodynamic simulations of the formation of orion-like star clusters II. The initial mass function from winds, turbulence, and radiation," *The Astrophysical Journal*, vol. 754, no. 1, p. 71, 2012.
- [363] K. Bekki, "Origin of a bottom-heavy stellar initial mass function in elliptical galaxies," *The Astrophysical Journal*, vol. 779, no. 1, p. 9, 2013.

Research Article

Observing and Reducing IFUs: INTEGRAL and PMAS—Properties of the Ionized Gas in HH 202

Luis López-Martín^{1,2}

¹ Instituto de Astrofísica de Canarias, La Laguna, 38205 Tenerife, Spain

² Departamento de Astrofísica, Universidad de La Laguna, La Laguna, 38206 Tenerife, Spain

Correspondence should be addressed to Luis López-Martín; luislm@iac.es

Received 18 October 2013; Accepted 6 December 2013; Published 5 February 2014

Academic Editor: José Manuel Vilchez Medina

Copyright © 2014 Luis López-Martín. This is an open access article distributed under the Creative Commons Attribution License, which permits unrestricted use, distribution, and reproduction in any medium, provided the original work is properly cited.

The reduction of integral field spectroscopy (IFS) data requires several stages and many repetitive operations to convert raw data into, typically, a large number of spectra. Instead there are several semiautomatic data reduction tools and here we present this data reduction process using some of the Image Reduction and Analysis Facility (IRAF) tasks devoted to reduce spectroscopic data. After explaining the whole process, we illustrate the power of this instrumental technique with some results obtained for the object HH202 in the Orion Nebula (Mesa-Delgado et al., 2009).

1. Introduction

Simultaneously storing both spectral and spatial information, 3D spectroscopy (known also as 2D spectroscopy, spectral imaging, or integral field spectroscopy) guarantees the homogeneity of the data, offers a perfect way to address astrophysical problems, and opens up new lines of research. Since its inception in the eighties (Vanderriest [1] on the CFHT) and early nineties, research in this field has grown enormously. Three-dimensional spectrographs, or integral field units, (IFUs) provide spectra for a large number of spatial elements (“spaxel”) within a two-dimensional field of view, rather than only along a traditional one-dimensional spectrograph slit. Figure 1 shows how this spectroscopical information is collected into a data cube. Most of the advantages of the IFS technique are direct consequences of the simultaneity when recording spatial and spectral information, which guarantees a great homogeneity in the data. The complexity of these data makes it a little more difficult to reduce them than in long slit spectroscopy; in next sections we will briefly describe how it is possible to do this reduction using IRAK tasks. To finish, we will show a scientific application of this observational technique: 3D spectroscopy of photoionized HH objects in the Orion nebula—the case of HH 202—[2]. Part of this work was contributed in the meeting “Metals in 3D: New insights

from Integral Field Spectroscopy,” held in Granada in 18–20/04/2012.

2. Observing with INTEGRAL (WHT) and PMAS (CAHA)

We will describe the process of reduction of 3D spectroscopic data through spectra obtained with two different instruments located at WHT 4.2 m (Observatorio del Roque de los Muchachos) and CAHA 3.5 m (Observatorio de Calar Alto) telescopes: INTEGRAL and PMAS.

INTEGRAL [3], is mounted on the Nasmyth focus of the WHT at the Roque de los Muchachos Observatory on La Palma. In its standard configuration, it has three fiber bundles that simultaneously feed the entrance of the WYFFOS fibre spectrograph. The three bundles are located in the focal plane on a revolving wheel (see Figure 2).

But currently four bundles are mounted in the INTEGRAL Swinging Plate: SB1, SB2, SB3, and equalized. At the focal plane the fibers are arranged in two groups, one forming a rectangle, while the other forms a ring (except for the equalized bundle) which is intended for collecting background light (for small-sized objects). Table 1 shows the main characteristics of the four bundles.

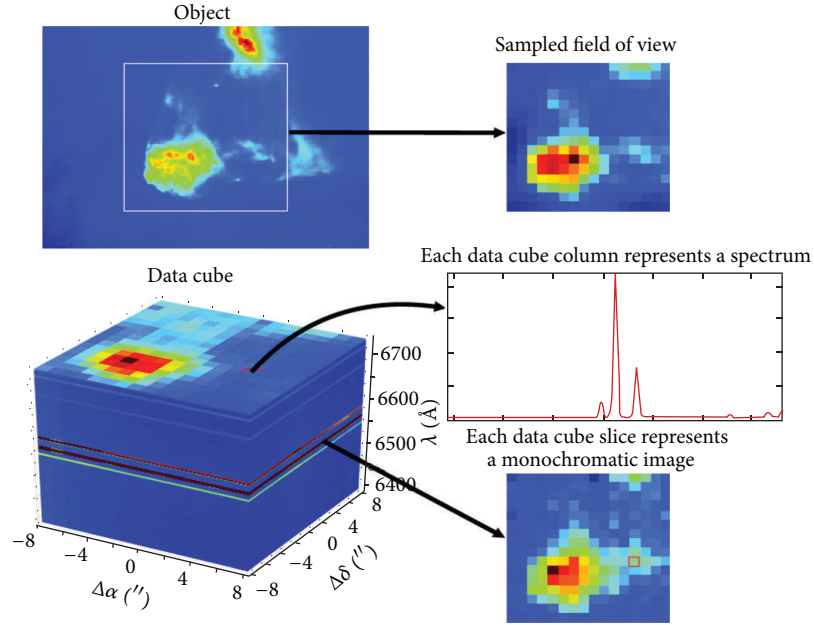


FIGURE 1: Section of a $H\alpha$ *HST* image of Orion [4] with a sampling of 1 arcsec (top left, white box indicates the FoV of a typical 2D PMAS observation). A result of this PMAS observation with spaxels of 1×1 arcsec is shown on the top right. Bottom left shows a section of the data cube observed where we can see a monochromatic image at the upper slice. Bottom right shows an integrated spectrum of a group of spaxels and a flux map integrated over an emission line (figure extracted from the Ph.D. thesis of M. Núñez-Díaz).

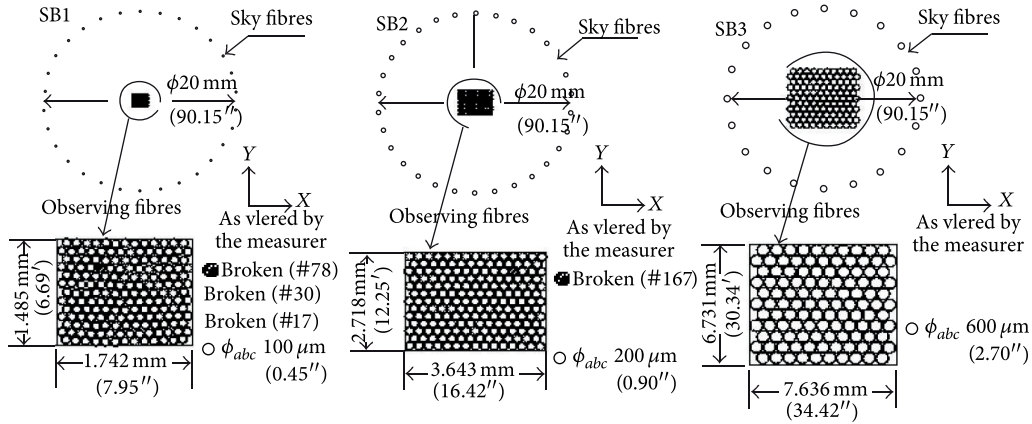


FIGURE 2: Sketch of the geometrical characteristics of the bundles of fibres in INTEGRAL. Extracted from Arribas et al. [3].

Their tilt angles can be varied in order to select a specific wavelength region. For any particular grating the spectral resolution depends on the fibre bundle as a consequence of the different fibre sizes. Table 2 shows the spectral resolution achieved with the INTEGRAL bundles for the available gratings.

PMAS [5], the Potsdam Multi-Aperture Spectrophotometer, is an integral field instrument developed at the AIP. It is currently installed at the Calar Alto Observatory 3.5 m Telescope in Spain. Actually, it is an integral field spectroscopy with fiber-coupled lens array or fiber bundle IFU and fiber spectrograph.

PMAS employs an all-refractive fiber spectrograph, built with CaF_2 optics, to provide good transmission and high image quality over the entire nominal wavelength range. A set of user-selectable reflective gratings provides low to medium spectral resolution in first order of approximately 1.5, 3.2, and 7 \AA , depending on the groove density (1200, 600, 300 gr/mm).

The instrument was specifically designed to address the science case of 3D spectrophotometry of spatially resolved, individual objects, with an emphasis on broad wavelength coverage in the optical wavelength regime. Table 3 lists the main properties of the PMAS spectrograph. In addition,

TABLE 1: Characteristics of the fiber bundles of INTEGRAL (see <http://www.iac.es/proyecto/integral/>).

	Fiber size (")	Number (field + sky)	Spatial covering (")	Fiber size (pixeles)	External ring (")
SB1	0.45	205 (175 + 30)	7.8×6.4	1.9–2.2	90
SB2	0.90	219 (189 + 30)	16.0×12.3	3.5–4	90
SB3	2.70	135 (115 + 20)	33.6×29.4	13–14	90
“Equalized”	0.45	115 (115 + 0)	6.3×5.4	1.9–2.2	NO

TABLE 2: Mean spectral resolution, linear dispersions, and spectral coverage for different gratings and bundles (see <http://www.iac.es/proyecto/integral/>).

	1200 L/mm	600 L/mm	300/316 L/mm
Resolution (SB1) (Å)	0.7	1.3	2.6
Resolution (SB2) (Å)	1.3	2.6	5.2
Resolution (SB3) (Å)	5.5	11	22
Dispersion (Å/pix)	0.4	0.8	1.6
Covering (Å)	1620	3240	6480

TABLE 3: Characteristics of PMAS lens array (see http://www.caha.es/pmas/PMAS_OVERVIEW/pmas_overview.html).

Standard-IFU	
Principle of operation	Square lens array with fore optics
Lens array	16×16 square elements, 1 mm pitch (32×32 array upgrade in preparation)
3 magnifications	0.5 arcsec sampling, 8×8 arcsec ² FOV 0.75 arcsec sampling, 12×12 arcsec ² FOV 1.0 arcsec sampling, 16×16 arcsec ² FOV
Fiber configuration	256 OH-doped fibers, 150 um core diameter

the properties of the gratings available for PMAS are listed in Table 4, together with the achievable spectral resolutions.

3. Reducing IFUs with IRAF

3.1. Reduction Steps versus IRAF Tasks. Although there are some 3D reduction packages (R3D [6, 7], P3D [8], etc.), we will describe the data reduction using IRAF reduction package SPECRED. Specific reduction packages probably are faster ways to reach reduced data (once the user knows how it works). Reducing using individual IRAF tasks probably takes a lot of time, mainly because for each reduction stage a different task must be used, and the output of each of these stages must be verified; but on the other hand it can be checked that every task is producing satisfying results.

The data reduction process has several steps that we can summarize in this way: after bias subtraction, spectra are traced on the continuum lamp exposure obtained before each science exposure and wavelength calibrated using a Hg-Ne arc lamp. The continuum lamp and sky flats are used to determine the response of the instrument for each fibre and wavelength. Finally, for the standard stars we coadded the spectra of the central fibres and compared them with the tabulated one-dimensional spectra. Due to the complexity of these data we are going to describe with more detail step

by step the process. In Figure 3 we present a scheme of this process in which we can see the products after each step.

3.2. Bias Subtraction. The subtraction of the bias level is the first step in the data reduction. This bias level is introduced onto the CCD chip for ensuring that the chip is working in a linear regime.

This pedestal level (bias) can be removed from images according to one of the following proceedings: get the mean value on the overscan region of each frame and subtract this constant off the whole rest of the frame, or average a sample (around 10) of bias frames pixel by pixel in order to get a mean bias frame, and subtract this frame from each image.

In these data we have bias subtracted following the second way using *imcombine* and *imarith* tasks of IRAF.

3.3. Spectra Extraction. The extraction of one-dimension spectra from the two-dimensional image is a multistage process. First, we must find the spectra from the image using the continuum lamp as reference. This continuum lamp traces spectra over the CCD image. The task *apall* just looks over this image and extracts the place where spectra will be found (see Figure 4). This task produces a final multispectra image (with *a.ms* extension file).

3.4. Wavelength Calibration. Now, we would like to see the wavelength calibrated spectra. For this, we need to determine the dispersion solution in order to transform the pixel to the wavelength scale. This can be done interactively for the first time in one calibration lamp reference spectrum (identify task), and this solution is used as a starting point to determine the dispersion solution for the rest of the spectra (*reidentify* task).

In Figure 5(a) we can see a wavelength calibrated spectrum identifying lamp lines using a database. This identification gives an initial dispersion solution able to be applied to the rest of spectra (Figure 5(b)). In Figure 6 we can see the image resulting to apply the wavelength calibration.

3.5. Instrumental Response. Once spectra have been wavelength-calibrated, it is necessary to correct from the instrumental response. This response varies from pixel to pixel not only for a different sensitivity to the intensity of the incoming light but also to the response at a different wavelength.

For both responses we must use continuum lamp and sky spectra, obtained before each object exposure. Using *msresp1d* IRAF task we can obtain that function (see Figure 7).

TABLE 4: Linear dispersions and spectral coverage for different gratings used in PMAS (see http://www.caha.es/pmas/PMAS_OVERVIEW/pmas_gratings.html).

Grating design.	Cartr. ID number	Grooves per mm	Dispersion (Å/pix)	Blaze angle	Lambda (nm)	dLambda (Å)
U1200	1	1200	0.39	10.4	300	794
V1200	2	1200	0.35	17.5	500	725
R1200	3	1200	0.30	26.7	750	609
I1200	4	1200	0.22	36.8	1000	460
J1200	5	1200	0.22	46.0	1200	341
J1200	5	1200	0.17	46.0	600	450
U600	6	600	0.81	5.2	300	1656
V600	7	600	0.80	8.6	500	1630
R600	8	600	0.75	13.9	800	1533
U300	9	300	1.67	2.5	300	3404
V300	10	300	1.67	4.3	500	3404

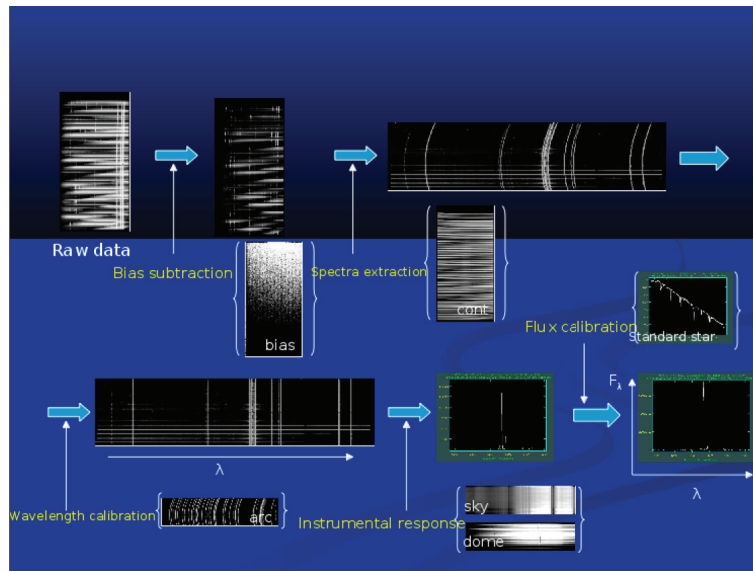


FIGURE 3: Sketch of the 3D data reduction process. Data taken from INTEGRAL observations.

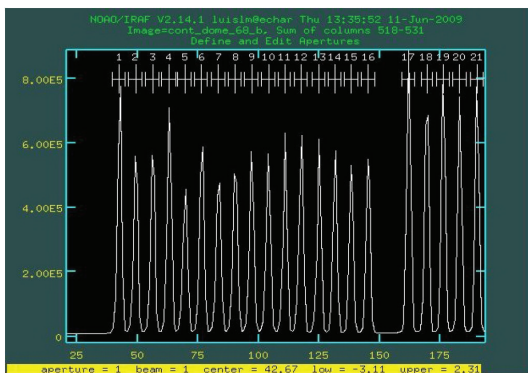


FIGURE 4: Spectra extraction of INTEGRAL data using continuum lamp.

3.6. *Flux Calibration.* For some users, leaving the wavelength calibrated spectra in terms of integrated numbers of counts is sufficient. For the rest, it is necessary to observe suitable

spectrophotometric standard stars, in order to transform the data in flux units.

First, we must find the sensitivity function using the spectrophotometric star spectra with *standard* and *sensfunc* tasks. Then, we need to apply this function to the object spectra (*calibrate* task). This way, we obtain spectra in counts units. At this point, it is necessary to know how much flux units correspond to one count; to do this, we coadd all the spectrophotometric spectra and we compare them with tabulated flux values. In Figure 8(a) we can see how the response function varies with wavelength; once this function is applied we obtain a nonflux calibrated spectrum (Figure 8(b)), and finally if we compare it with tabulated flux values, we obtain the flux calibrated spectra (Figure 8(c)).

4. Application of 3D Spectroscopy to HH 202

Perhaps the most interesting feature of 3D spectroscopy is the possibility of having a spectrum for each spaxel in

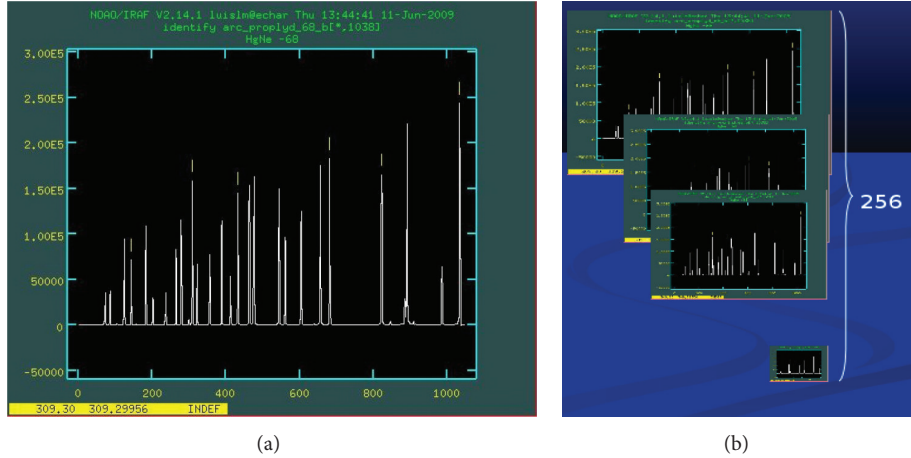


FIGURE 5: Wavelength calibration using Cu-Ne-Ar calibration lamp spectra ((a) using *identify*), and application of this wavelength calibration solution to the rest of the spectra ((b) using *reidentify*).

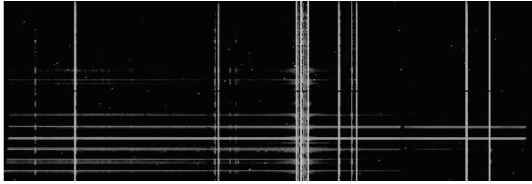


FIGURE 6: Example of wavelength calibrated spectra image of INTEGRAL data.

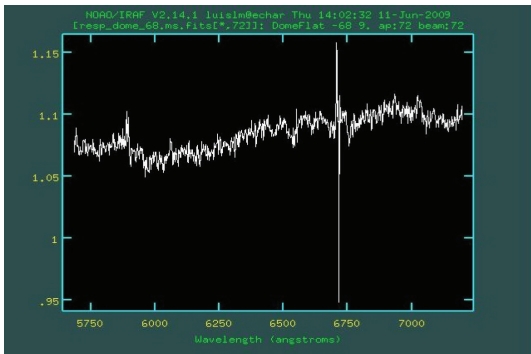


FIGURE 7: Example of instrumental response for one of the spectra of INTEGRAL data.

the observed field (typically the fiber in the case of fiber-fed spectrographs as INTEGRAL and PMAS). This means that the spectral features of interest contained in our spectra can be measured throughout the observed field of view and, thus, bidimensional images of these features can be reconstructed by just arranging properly the spectra in the 2D space.

This capability is an important improvement compared to the classical long-slit spectroscopy that allowed only performing one-dimensional analysis. We mention here two examples showing that bidimensional spectroscopy is also possible with a long-slit spectrograph, by using a complicated observing setup consisting of taking several long-slit spectra

at adjacent positions, shifting the pointing of the telescope by small distances (of the order of the required spatial resolution) with the position angle of the slit perpendicular to the spatial shift of the telescope [9, 10]. The results of this technique were found to be satisfactory although they were not comparable to those of real 3D spectroscopy and the main differences were found in the morphological details of the bidimensional reconstructed images.

In this section we apply the results of the data reduction and calibration process to a particular scientific case: the study of the Herbig-Haro object HH202 in the Orion nebula (see Figure 9). A detailed study on this object and the complete results of this work can be found in Mesa-Delgado et al. [2].

Herbig-Haro objects are nebulosities associated to high-velocity clouds of ionized gas. Several of them have been detected in the Orion nebula (e.g., HH202, HH203, and HH204, among others). The origin of these objects is still uncertain but some authors associate them with infrared objects [11].

In particular, HH202 was observed at Calar Alto Observatory with the fiber-fed spectrograph PMAS [5] at the 3.5 m telescope using lens array configuration, giving a field of view of $16'' \times 16''$, with a spectral resolution of 3.6 \AA and a spatial sampling of $1''$ (see Figure 9). The total spectral coverage ranged from 3500 \AA in the blue end to 7200 \AA in the red end, in two different setups overlapping in the range 5100 \AA – 5700 \AA . This choice of the spectral range ensures the observation of the emission lines of interest.

In this work, two sets of emission lines were selected with different purposes.

Balmer lines ($H\alpha$, $H\beta$, \dots , HII) were used to estimate the correction for dust extinction (following the theoretical line ratios from [12], and using the reddening function by [13]). These lines were used in addition to correct for differential atmospheric refraction (DAR [14]).

Atmospheric refraction is the deviation of the light as it passes through the atmosphere due to the variation in air density as a function of altitude. Bluer wavelengths are

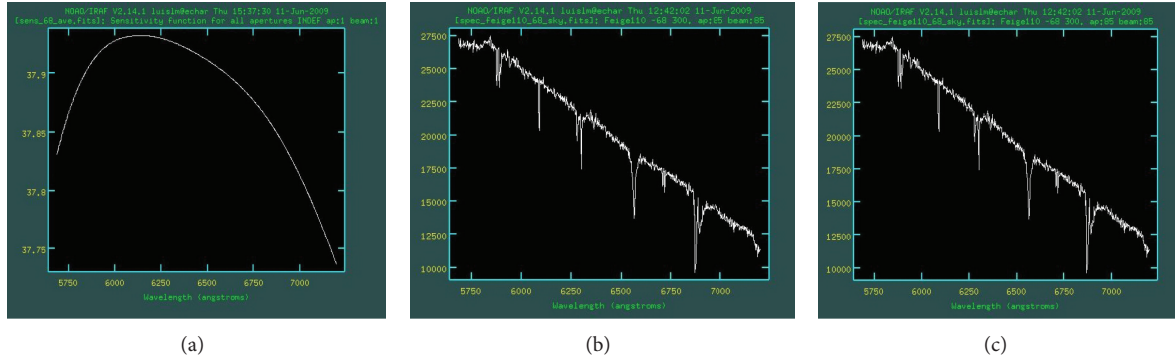


FIGURE 8: (a) Response function of INTEGRAL data to the different wavelength. (b) Nonflux calibrated spectrum (counts units). (c) Flux calibrated spectrum (flux units).

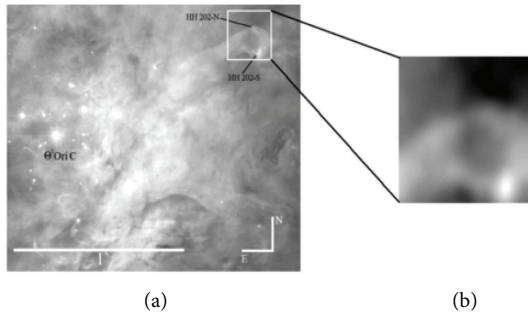


FIGURE 9: *HST* image of the central part of the Orion Nebula, which combines Wide-Field Planetary Camera 2 (WFPC2) images taken in different filters [4]. The white square corresponds to the FOV of PMAS IFU used, covering the head of HH 202. The separate close-up image on the right shows the $H\alpha$ map obtained with PMAS. The original map is 16×16 pixel of 1×1 arcsec² size and has been rebinned to 160×160 pixel. Note the remarkable similarity between the *HST* image and our rebinned PMAS $H\alpha$ map. Extracted from Mesa-Delgado et al. [2].

refracted more strongly than redder wavelengths, which means that a white point source is spread out into a little spectrum along the elevation angle producing the called differential atmospheric refraction. In the absence of DAR the images of a star at all the wavelengths are coincident, and the spectra obtained from any aperture are basically the same, but when DAR is present the images of a star at different wavelengths are not in positional agreement. One of the most interesting aspects of IFS is that it is possible to determine and to correct in the spectra the effects of this DAR using a posteriori procedure (e.g., [15]). For this, we use the lines of the Balmer series. The Balmer series is a set of recombination lines corresponding to H^+ and spanning a wide range of wavelength (although always in the optical). In the absence of dust, the relative intensities of these lines are fixed, but this is never observed in real nebula. In addition, all these lines should be spatially coincident. But, as mentioned above, the effect of the atmosphere shifts the emission of the different Balmer lines depending on their wavelength. This disadvantage can be sorted out since IFS provides bidimensional maps of any spectral feature of

interest. Thus, a simple spatial matching of the observed Balmer emission line maps solves this problem.

The first step for the correction of the DAR effects is to determine the shifts among images generated at different wavelengths. In our case, we have noticed the effect of the differential atmospheric refraction in the monochromatic images of HH 202 obtained for Balmer lines at different wavelengths reaching the value of ~ 1.3 arcsec between $H\alpha$ and $H11$. We have measured offsets between all Balmer line images and shifted with respect to $H\alpha$.

A second set of emission lines was used to estimate abundances and can be split into two categories: (a) collisionally excited lines ([OIII]4363, 4959, 5007 Å, [SII]6717, 6731 Å, [NII]5755, 6548, 6583 Å) to estimate physical properties, like electronic density and temperature and ionic abundances; and (b) recombination lines of CII and OII (and others) to estimate ionic abundances.

To illustrate the power of the 3D spectroscopy technique we focus on an open astrophysical problem discussed in Mesa-Delgado et al. [2]. Figure 10 shows the spatial distribution of the abundances of several ions using different methods: the collisionally excited lines (CELs) and the recombination lines (RLs). Figure 10 stresses the relevance of the abundance discrepancy factor (ADF) which is defined as the difference between abundances determined from CELs and RLs. In particular, Figures 10(a) and 10(b) show clear differences of the same quantity ($12 + \log O^{2+}/H^+$) depending on the method used to compute it, which in some cases are larger than 0.2dex. Interestingly, these differences are not constant but vary from point to point, suggesting a complexity that probably involves several physical variables. The ADF problem has been largely studied in the literature for HII regions and for planetary nebulae [16–20] with no clear concluding results about its origin.

The most relevant aspect that 3D spectroscopy can provide to this fundamental astrophysical problem is the fact that all the physical information relevant to tackle on this problem is available for each spatial element: electronic density and temperature, reddening, underlying stellar population, and so forth. This means that a complete analysis can be performed, which will likely result in a particular solution for each spaxel. But even more, the whole set of solutions

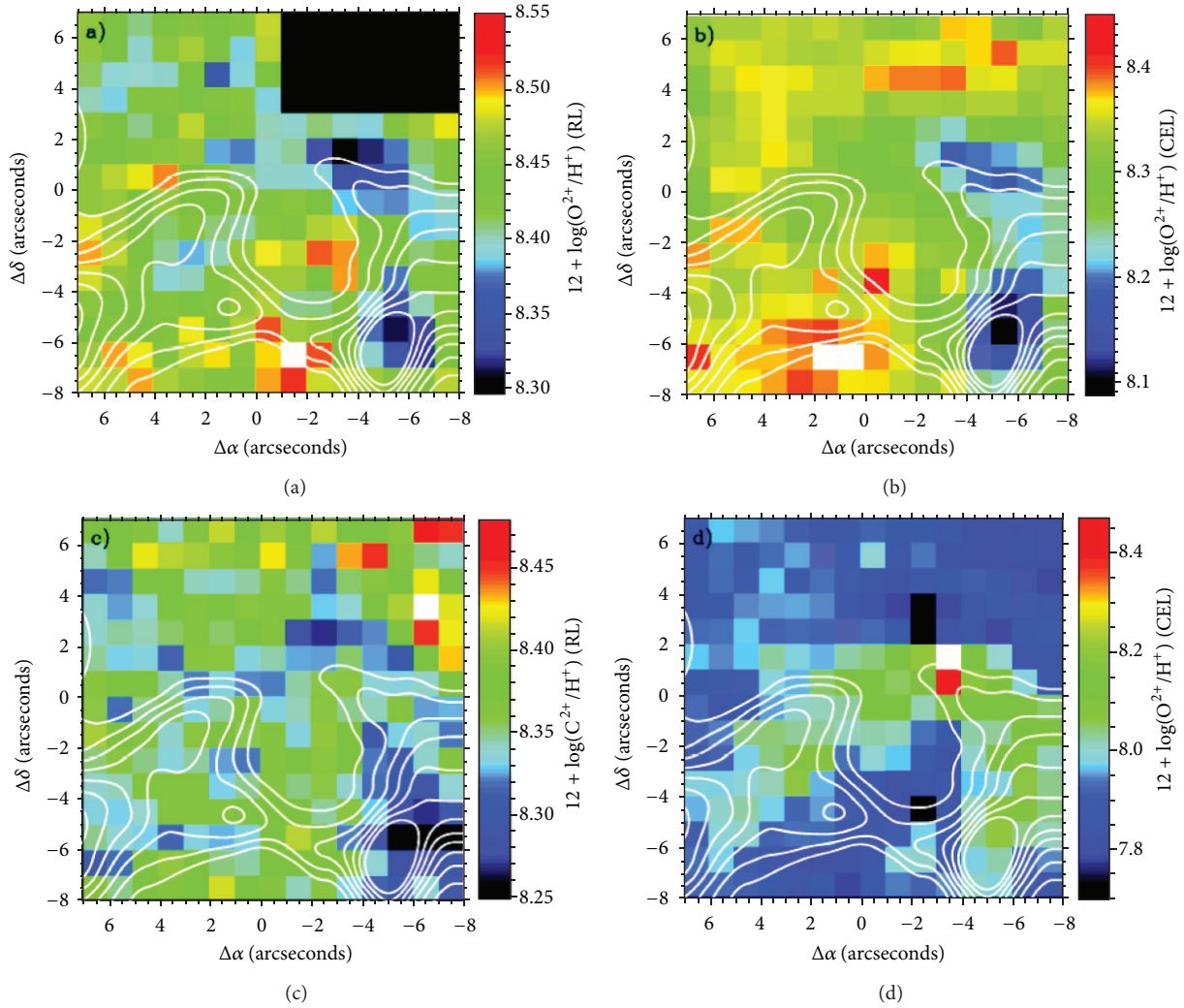


FIGURE 10: Ionic abundance maps with H α contours overplotted: (a) $12 + \log O^{2+}/H^+$ from RLs, (b) $12 + \log O^{2+}/H^+$ from CELs, (c) $12 + \log C^{2+}/H^+$ from RLs, and (d) $12 + \log O^+/H^+$ from CELs. Extracted from Mesa-Delgado et al. [2].

must keep an internal coherence that must be consistent with the physical assumptions adopted. Moreover, the bidimensional results obtained from 3D spectroscopy must also put constraints to the physically motivated theoretical models of radiation transfer in ionized media.

Conflict of Interests

The author declares that there is no conflict of interests regarding the publication of this paper.

References

- [1] C. Vanderriest, "Fiber optics in astronomy II," in *Proceedings of the 2nd Fibre Optics in Astronomy Conference*, P. M. Gray, Ed., vol. 37, Sydney, Australia, November 1991, Astronomical Society of the Pacific (ASP), San Francisco, Calif, USA, p.338, 1993.
- [2] A. Mesa-Delgado, L. López-Martín, C. Esteban, J. García-Rojas, and V. Luridiana, "Properties of the ionized gas in HH 202. I: results from integral field spectroscopy with PMAS," *Monthly Notices of the Royal Astronomical Society*, vol. 394, no. 2, pp. 693–703, 2009.
- [3] S. Arribas, E. Mediavilla, and F. Watson, *Fiber Optics in Astronomy III*, vol. 152 of *ASP Conference Series*, 1998.
- [4] C. R. O'Dell and S. K. Wong, "Hubble space telescope mapping of the Orion Nebula. I: a survey of stars and compact objects," *Astronomical Journal*, vol. 111, no. 2, pp. 846–855, 1996.
- [5] M. M. Roth, A. Kelz, T. Fechner et al., "The potsdam multi-aperture spectrophotometer. I: design, manufacture, and performance," *Publications of the Astronomical Society of the Pacific*, vol. 117, no. 832, p. 620, 2005.
- [6] J. R. Walsh and M. M. Roth, "Developing 3D spectroscopy in Europe," *The Messenger*, no. 109, pp. 54–56, 2002.
- [7] S. F. Sánchez, "E3D, the Euro3D visualization tool. I: description of the program and its capabilities," *Astronomische Nachrichten*, vol. 325, no. 2, pp. 167–170, 2004.
- [8] C. Sandin, T. Becker, M. M. Roth et al., "P3D: a general data-reduction tool for fiber-fed integral-field spectrographs," *Astronomy and Astrophysics*, vol. 515, no. 5, Article ID 14022, 2010.

- [9] J. M. Vílchez and J. Iglesias-Páramo, “Bidimensional spectroscopic mapping and chemical abundances of the star-forming Dwarf Galaxy I Zw 18,” *Astrophysical Journal*, vol. 508, article 248, 1998.
- [10] J. Maíz-Apellániz, J. M. Mas-Hesse, C. Muñoz-Tuñón, J. M. Vílchez, and H. O. Castañeda, “Bidimensional spectroscopy of NGC, 4214: evolutionary state and interstellar extinction,” *Astronomy and Astrophysics*, vol. 329, p. 409, 1998.
- [11] C. R. O’Dell and W. J. Henney, “High spatial velocity features in the Orion Nebula,” *Astronomical Journal*, vol. 136, no. 4, pp. 1566–1586, 2008.
- [12] P. J. Storey and D. G. Hummer, “Recombination line intensities for hydrogenic ions. IV. Total recombination coefficients and machine-readable tables for $Z=1$ to 8,” *Monthly Notices of the Royal Astronomical Society*, vol. 272, pp. 41–48, 1995.
- [13] K. P. M. Blagrove, P. G. Martin, R. H. Rubin et al., “Deviations from He I Case B recombination theory and extinction corrections in the Orion Nebula,” *Astrophysical Journal*, vol. 655, no. 1, article 299.
- [14] A. V. Filippenko, “The importance of atmospheric differential refraction in spectrophotometry,” *Publications of the Astronomical Society of the Pacific*, vol. 94, pp. 715–721, 1982.
- [15] S. Arribas, E. Mediavilla, B. García-Lorenzo, C. del Burgo, and J. J. Fuensalida, “Differential atmospheric refraction in integral-field spectroscopy: effects and correction. Atmospheric refraction in IFS,” *Astronomy and Astrophysics*, vol. 136, pp. 189–192.
- [16] Y. G. Tsamis, M. J. Barlow, X. W. Liu, I. J. Danziger, and P. J. Storey, “A deep survey of heavy element lines in planetary nebulae. I: observations and forbidden-line densities, temperatures and abundances,” *Monthly Notices of the Royal Astronomical Society*, vol. 345, no. 1, pp. 186–220, 2003.
- [17] J. García-Rojas and C. Esteban, “On the abundance discrepancy problem in H II regions,” *Astrophysical Journal*, vol. 670, pp. 457–470, 2007.
- [18] G. Stasinska, G. Tenorio-Tagle, M. Rodríguez, and W. J. Henney, “Enrichment of the interstellar medium by metal-rich droplets and the abundance bias in H II regions,” *Astronomy and Astrophysics*, vol. 471, pp. 193–204, 2007.
- [19] Y. G. Tsamis, M. J. Barlow, X. W. Liu, P. J. Storey, and I. J. Danziger, “A deep survey of heavy element lines in planetary nebulae. II: recombination-line abundances and evidence for cold plasma,” *Monthly Notices of the Royal Astronomical Society*, vol. 353, no. 3, pp. 953–979, 2004.
- [20] Y. G. Tsamis and D. Péquignot, “A photoionization-modelling study of 30 Doradus: the case for small-scale chemical inhomogeneity,” *Monthly Notices of the Royal Astronomical Society*, vol. 364, no. 2, p. 687, 2005.

Review Article

Properties of the HII Regions Derived Using Integral Field Spectroscopy

Sebastian F. Sánchez^{1,2,3}

¹ Instituto de Astrofísica de Andalucía (CSIC), Glorieta de la Astronomía s/n, Apartado 3004, 18080 Granada, Spain

² Centro Astronómico Hispano Alemán, Calar Alto (CSIC-MPG), C/Jesús Durbán Remón 2-2, 04004 Almería, Spain

³ Astronomical Institute, Academy of Sciences of the Czech Republic, Boční II 1401/1a, 141 00 Prague, Czech Republic

Correspondence should be addressed to Sebastian F. Sánchez; sanchez@caha.es

Received 15 August 2013; Accepted 4 November 2013

Academic Editor: Polychronis Papaderos

Copyright © 2013 Sebastian F. Sánchez. This is an open access article distributed under the Creative Commons Attribution License, which permits unrestricted use, distribution, and reproduction in any medium, provided the original work is properly cited.

Here we review some of our more recent results on the observed properties of HII regions using Integral Field Spectroscopy. In particular, we illustrate the use of this technique to study in detail the ionization conditions across the nebulae for galactic HII regions (focused on the Orion Nebula) and the statistical study of large samples of extragalactic HII regions. We review the reported new scaling relation between the local mass density and the oxygen abundance across the disk galaxies and the recently discovered universal gradient for oxygen abundances. We update our previous results the lack of a dependence of the Mass-Metallicity relation with the starformation rate, including new unpublished data. Finally we discuss on the relation between the ionization conditions in the nebulae and the underlying stellar population. All together our results indicate that disk galaxies present a chemical enrichment dominated by an inside-out growth scenario, with a less evident effect of radial migrations and/or outflows.

1. Introduction

Nebular emission lines from bright-individual HII regions have been, historically, the main tool at our disposal for the direct measurement of the gas-phase abundance at discrete spatial positions in galaxies. A good observational understanding of the distribution of element abundances across the surface of nearby galaxies is necessary to place constraints on theories of galactic chemical evolution. The same information is crucial to derive accurate star formation histories of and obtain information on the stellar nucleosynthesis in normal spiral galaxies.

Several factors dictate the chemical evolution in a galaxy, including the primordial composition, the content and distribution of molecular and neutral gas, the star formation history (SFH), feedback, the transport and mixing of gas, the initial mass function (IMF), (e.g., [1, 2] and references therein). All these ingredients contribute through a complex process to the evolutionary histories of the stars and the galaxies in general. Accurate measurements of the present

chemical abundance constrain the different possible evolutionary scenarios, and therefore it is important to determine the elemental composition using a common approach, among different galaxy types.

Previous spectroscopic studies have unveiled some aspects of the complex processes at play between the chemical abundances of galaxies and their physical properties. Although these studies have been successful in determining important relationships, scaling laws and systematic patterns (e.g., luminosity-metallicity, mass-metallicity, and surface brightness versus metallicity relations [3–7]; effective yield versus luminosity and circular velocity relations [8]; abundance gradients and the effective radius of disks [9]; systematic differences in the gas-phase abundance gradients between normal and barred spirals [6, 10]; characteristic versus integrated abundances [11], etc.), they have been limited by statistics, either in the number of observed HII regions or in the coverage of these regions across the galaxy surface.

The advent of Multiobject Spectrometers and Integral Field Spectroscopy (IFS) instruments with large fields of view

now offers us the opportunity to undertake a new generation of emission-line surveys, based on samples of hundreds of HII regions and full two-dimensional (2D) coverage of the discs of nearby spiral galaxies (e.g., [12–14]). On the other hand, these new techniques allow us to study with unprecedented detail the ionization conditions and chemical enrichment processes within the individual nebulae in the Galaxy and provide with unique links between those local processes and the global ones that govern the evolution of galaxies (e.g., [15, 16]).

In the last few years we started a major observational program to understand the statistical and individual properties of HII regions and to unveil the nature of the reported physical relations, using IFS. Here we present a summary of our main results, including the analysis of the spatially resolved ionization condition in the Orion Nebula (Section 2), the connection between the ionization conditions in the HII regions and the properties of the underlying stellar population (Section 3), some of the highlights of our current IFS studies (Section 4), and the evidence of an inside-out growth in disk galaxies on the basis that we have found (Section 5).

2. The Orion Nebula

The Orion Nebula is the brightest and best studied HII region in the sky. It has been used for decades as a fundamental laboratory in the study of the star formation regions, the ionization processes, and the helium and heavy elements enrichment. However, despite the large number of studies on this target, there is still a lot to know about it, even from optical studies. The more we know the more complex it seems to be.

Several spectroscopic surveys have tried to characterize its spectroscopic properties, taken spectra at different “representative” locations (e.g., [17, 18]). In particular, Osterbrock [19] show a compilation of high and low dispersion deep spectra of the central bright region in the optical-NIR region (3000–11000 Å). They measured 225 emission lines, 88 at the wavelength range of our IFS data. Using the relative intensities of these lines they derived the relative abundances of several elements, the electronic temperature ($T = 9000$ K) and density ($N_e = 4 \times 10^3 \text{ cm}^{-3}$), and the extinction ($A_V \sim 1.08$ mag, derived from the $H\alpha/H\beta$ ratio). Such properties are frequently compared with those of distant HII regions in our Galaxy and extragalactic ones (e.g., [20]). However, due to their distance most of these regions are poorly resolved, and their integrated properties are compared with those of particular areas in the Orion Nebula.

Very little effort has been done to study the distribution of the physical properties across the Nebula, apart from some peculiar areas (e.g., [18]), or their integrated values in large aperture areas. Pogge et al. [21] performed Fabry-Perot (FP) imaging spectrophotometry on an area of $\sim 6' \times 6'$ centered in the Trapezium area. Their FP data covered the brightest emission lines in the Nebula $H\beta$, $[OIII] \lambda 5007$, $H\alpha$, $[NII] \lambda 6548$, 6583 , $[SII] \lambda 6716$, 6731 , and $[HeI] \lambda 6678$. They derived some of the average spectroscopic parameters of the core of the Nebula, including the integrated $H\alpha$ flux, the average extinction, the average ionization line ratios ($[OIII]/H\beta$,

$[NII]/H\alpha$ and $[SII]/H\alpha$), the He^+ / H^+ ionic abundance ratio, and the average electron density. Evenmore, they derived the first reliable maps of the distribution of these properties across the Nebula, which show a considerable degree of structure. They found significant differences with some of the previously reported values that correspond to particular regions in the Nebula (e.g., [19]). However, due to the reduced spectroscopic coverage of their dataset, it was not possible to fully characterize the ionization conditions in the Nebula.

In [15], we presented a low-resolution Integral Field Spectroscopy (IFS) survey of an almost similar field of view of the FP observations presented by Pogge et al. [21] but covering the entire optical wavelength range ($\sim 3700\text{--}7100$ Å). The data, comprising 8121 individual spectra sampling circular areas of $2.7''$ each one, were reduced to be released publicly for the community (<http://www.caha.es/sanchez/orion/>). This is the largest spectroscopic survey ever performed for a single HII region.

Line intensity maps for different emission lines were obtained to study the complex structure of the ionized gas in the Nebula. The derived $H\alpha$ intensity map, shown in Figure 1(a), a tracer of the ionized hydrogen, was found to be similar to that one found using Fabry-Perot and narrow-band imaging. The electron density and temperature maps were derived using the $[SII]$ line ratios and $[OIII]$ and $[NII]$ line ratios, respectively, as described in [15]. A considerable amount of structure was found in both distributions. We used them to create a map of the expected $H\alpha/H\beta$ line ratio, based on case B recombination. A comparison between this expected line ratio and the observed one, that we show in Figure 1(b), was used to obtain a dust extinction map, that was used to correct all the derived emission lines for reddening.

The ionized structure was studied based on the classical diagnostic line ratios $[NII]/H\alpha$ and $[OIII]/H\beta$, shown in Figures 1(c) and 1(d). The distribution of helium and oxygen abundances was derived based on the $[HeI]\lambda 6678/H\alpha$ line ratio and the temperature metallicity indicator (based on the $[OII]/H\beta$ and $[OIII]/H\beta$ line ratios). No clear relation was found between both abundance distributions, contrary to expected from the study of the integrated properties of known HII regions. There is a relation between the helium abundance and the ionization structure, in the sense that partially ionized areas are less abundant in helium and more abundant in heavy elements. Two possible deviations from case B recombination theory in the Orion Nebula were proposed by [15] to explain this trend and the lack of relation between the Helium and Oxygen abundances: (i) the fact that the Nebula is not fully ionized, which could lead to a systematic underestimation the helium mass fraction due to the nonnegligible contribution of neutral helium, and (ii) the suspicion that there are dust grains mixed with the emitting gas which absorbs the ionizing Lyman-continuum photons and not a simple dust screen.

The oxygen abundance presents a rich structure that it is not clearly related to the ionization structure. At a first order it has positive gradient, with a minimum near the trapezium (the ionizing source), of the order of $12 + \log(O/H) \sim 8.2$, increasing towards the outer parts, where it reaches a level of $12 + \log(O/H) \sim 8.8$. This is a good example of how

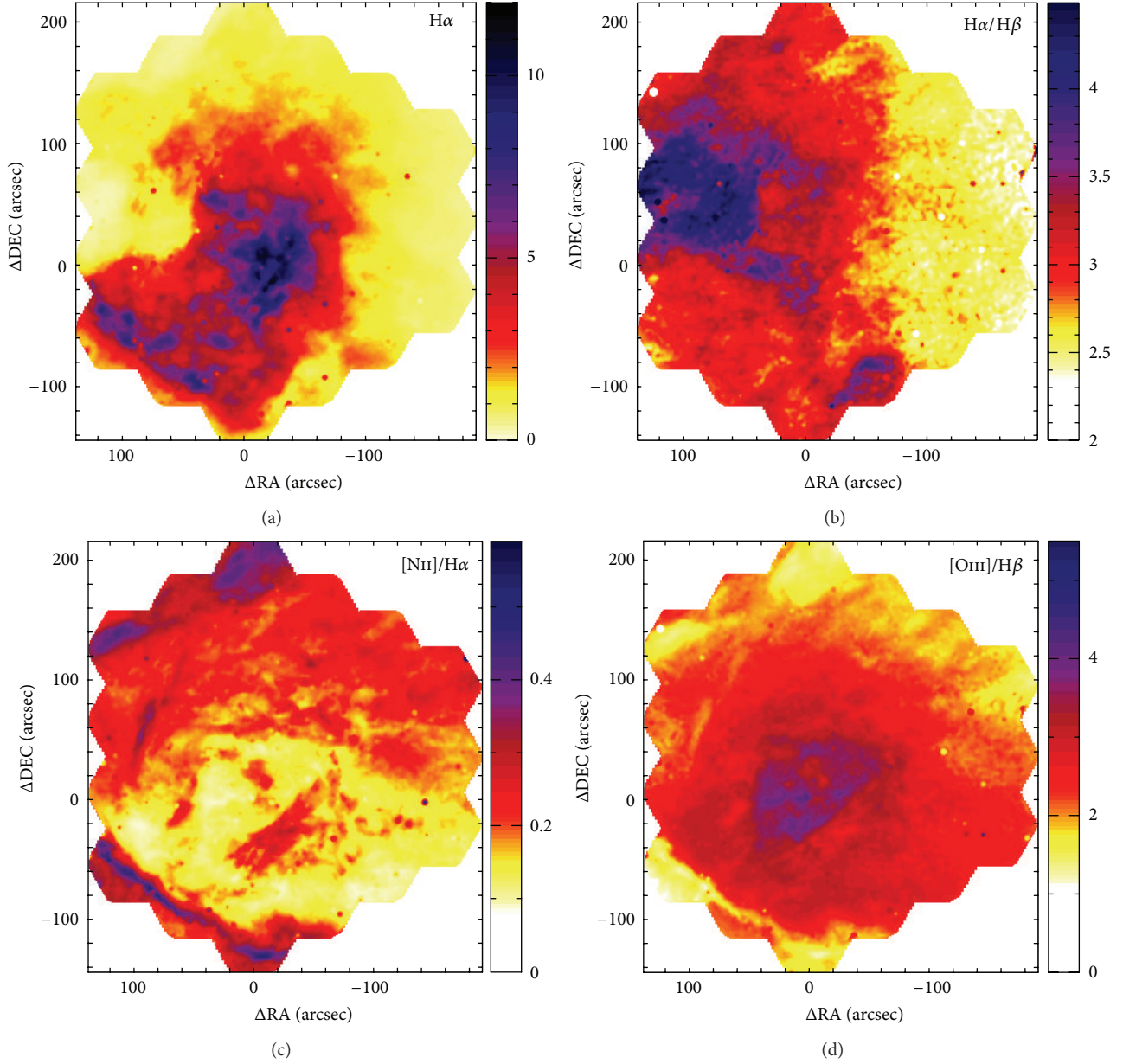


FIGURE 1: (a) Observed $H\alpha$ Line intensity map in units of $10^{-12} \text{ erg s}^{-1} \text{ cm}^2 \text{ arcsec}^{-2}$ obtained by fitting a single Gaussian function to the $H\alpha$ emission line for each single spectrum in the dataset. The intensity map is then reconstructed by interpolating the recovered flux at the location of each spectrum, as described in the text. (b) Observed $H\alpha/H\beta$ line ratio map. ((c) and (d)) Classical diagnostic line ratio maps. (c) $[NII]\lambda 6583/H\alpha$ line ratio map. (d) $[OIII]\lambda 5007/H\beta$ line ratio map.

the abundance and ionizing condition can change across an HII region, and, therefore, to be very precise, it is not correct to assign a particular abundance and defined ionizing conditions to the whole Nebula, as frequently done in study of extragalactic HII regions. The comparison of the distribution of ionized conditions across the Orion Nebula with the ones derived for the integrated spectrum (coadding the ~ 8000 individual spectra) indicates that the *integrated* properties seem to be representative of the *average* ones across the Nebulae. However, it is still unclear how representative these average properties may be for different HII regions.

3. HII Regions and the Underlying Stellar Population

Classical HII regions are gas clouds ionized by short lived hot OB stars, associated with star formation. They are frequently selected on the basis of demarcation lines defined in the so-called diagnostic diagrams (e.g., [18, 22]), which compare different line ratios, like $[OIII]/H\beta$ versus $[NII]/H\alpha$, $[OIII]/H\beta$ versus $[OII]/H\alpha$, $[NII]/H\alpha$ versus $[SII]/H\alpha$, and/or $[NII]/H\alpha$ versus $[SII]_{6717,6731}/H\alpha$. In most of the cases these ratios discriminate well between strong ionization sources,

like classical HII regions and powerful AGNs (e.g., [23]). However, they are less accurate in distinguishing between low-ionization sources, like weak AGNs, shocks, and/or post-AGBs stars (e.g., [24, 25]). Alternative methods based on a combination of the classical line ratios with additional information regarding the underlying stellar population have been proposed. For example, Cid Fernandes et al. [24] proposed the use of the $EW(H\alpha)$, to distinguish between retired (non-star-forming) galaxies, weak AGNs, and star-forming galaxies.

Among the classical diagnostic diagrams, the most widely used is the diagram that uses the ratio between the strongest emission lines that are, at the same time, less affected by dust attenuation: $[OIII]/H\beta$ versus $[NII]/H\alpha$ [23]. We will refer hereafter to this diagnostic diagram as the BPT diagram along this study. Different demarcation lines have been proposed for this diagram. The most popular ones are the Kauffmann et al. [26] and Kewley et al. [27] curves. They are usually invoked to distinguish between star-forming regions (below the Kauffmann et al. [26] curve), and AGNs (above the Kewley et al. [27] curve) The location between both curves is normally assigned to a mixture of different sources of ionization. Additional demarcation lines have been proposed for the region above the Kewley et al. [27] curve to segregate between Seyfers and LINERs (e.g., [28]).

Despite the benefits of this *clean* segregation for classification purposes, it may introduce biases when trying to select HII regions. The Kewley et al. [27] curve was derived on the basis of photoionization models. It corresponds to the maximum envelope in the considered plane for ionization produced by hot stars. Therefore, to the extent that these photoionization models are realistic, any combination of line ratios below this curve can be produced entirely by OB star photoionization. Finally it defines all the area above it as *unreachable* by ionization associated with photoionization by OB-stars directly associated with starformation. Other sources of ionization that may be related somehow with starformation at larger time scales, like shocks, ionization by X-ray binaries are not contemplated in their photoionization models. However, the derived line ratios and/or morphological structure of this ionization are clearly different and in most cases above the considered demarcation line. The Kauffmann et al. [26] curve has a completely different origin. It is an empirical envelope defined to segregate between starforming galaxies and the *so-called* AGN branch in the BPT diagram based on the analysis of the emission lines for the SDSS galaxies. It describes well the envelope of classical HII regions found in the disks of spiral galaxies. However, it is known that certain HII regions can be found above this demarcation line as we will show below.

Kennicutt et al. [29] first recognized that HII regions in the center of galaxies distinguish themselves spectroscopically from disk ones by their stronger low-ionization forbidden emission. The nature of this difference was not clear. It may be due to contamination by an extra source of ionization, like diffuse emission or the presence of an AGN. However, other stellar processes like nitrogen enhancement due to a natural aging process of HII regions and the surrounding ISM can produce the same effect. These early

results were confirmed by Ho et al. [30], who demonstrate that inner starforming regions may populate the right branch of the BPT diagram, at a location above the demarcation line defined latter by Kauffmann et al. [26]. However, we have found that HII regions with similar ionisation characteristics are not restricted to the central regions and can be found at any galactocentric distances, even at more than 2 effective radii (r_e), which excludes a possible contamination by the ionization of an AGN the origin of the detected line ratios. The nature of these HII regions will be addressed in detail elsewhere. For the purpose of the current study it is important to define a selection criterion that does not exclude them. However, we would like to clarify that we do not find a correlation between the presence of these HII regions and other possible contaminating sources of ionization, like shocks and/or Active Galactic Nuclei (AGN).

Therefore, selecting HII regions based on the Kauffmann et al. [26] curve may bias any sample towards classical disk regions, excluding an interesting population of these objects. On the other hand, it does not guarantee the exclusion of other sources of nonstellar ionizations that can populate this area, like shocks (e.g., [31, 32]), post-AGB stars (e.g., [25]), and dusty AGNs (e.g., [33]). Following Cid Fernandes et al. [34] and Cid Fernandes et al. [24], we consider that an alternative method to distinguish between different sources of ionization is to compare the properties of the ionized gas with those of the underlying stellar population. Cid Fernandes et al. [34] used the $EW(H\alpha)$ in combination with the $[NII]/H\alpha$ line ratio to distinguish between strong and weak ionization sources and between starformation and AGNs.

In Sanchez et al. ([35], submitted) we adopted a different selection criteria, using the fraction of young stars (f_y), provided by the multi-Simple Stellar Population (SSP) analysis of the underlying stellar population, as a proxy of the starformation activity. For starforming regions this parameter provides a similar information as the $EW(H\alpha)$. Figure 2(a) shows the distribution of $EW(H\alpha)$ against the fraction of young stars for the ~ 7000 clumpy ionized regions selected by HIIEXPLORER. For those regions with $EW(H\alpha) > 6 \text{ \AA}$, and/or with a fraction of young stars larger than 20%, both parameters present a strong log-linear correlation ($r_{\text{corr}} = 0.95$).

The threshold imposed by HIIEXPLORER on the surface brightness of $H\alpha$ and the requirement that the distribution of emission is clumpy remove efficiently most of the ionization corresponding to weak-emission lines described. This is mostly diffuse emission that peaks in the described diagram at $EW(H\alpha) \sim 1\text{-}2 \text{ \AA}$ and $f_y \sim 5\text{-}10\%$. This weak $EW(H\alpha)$ is dominated mostly by post-AGB stars (e.g., [25, 36]), and, therefore, no correlation is expected between its intensity and the fraction of young stars. On the other hand, high $EW(H\alpha)$ could be produced by other mechanisms, like AGNs and shocks, that do not require to be correlated with the properties of the underlying stellar population. A cut in the $EW(H\alpha)$ cannot remove those regions. Therefore, we consider that the fraction of young stars provides an indicator of recent star-formation activity.

Figure 3(a) shows the distribution of the ionized regions across the BPT diagram, indicating with contours the density

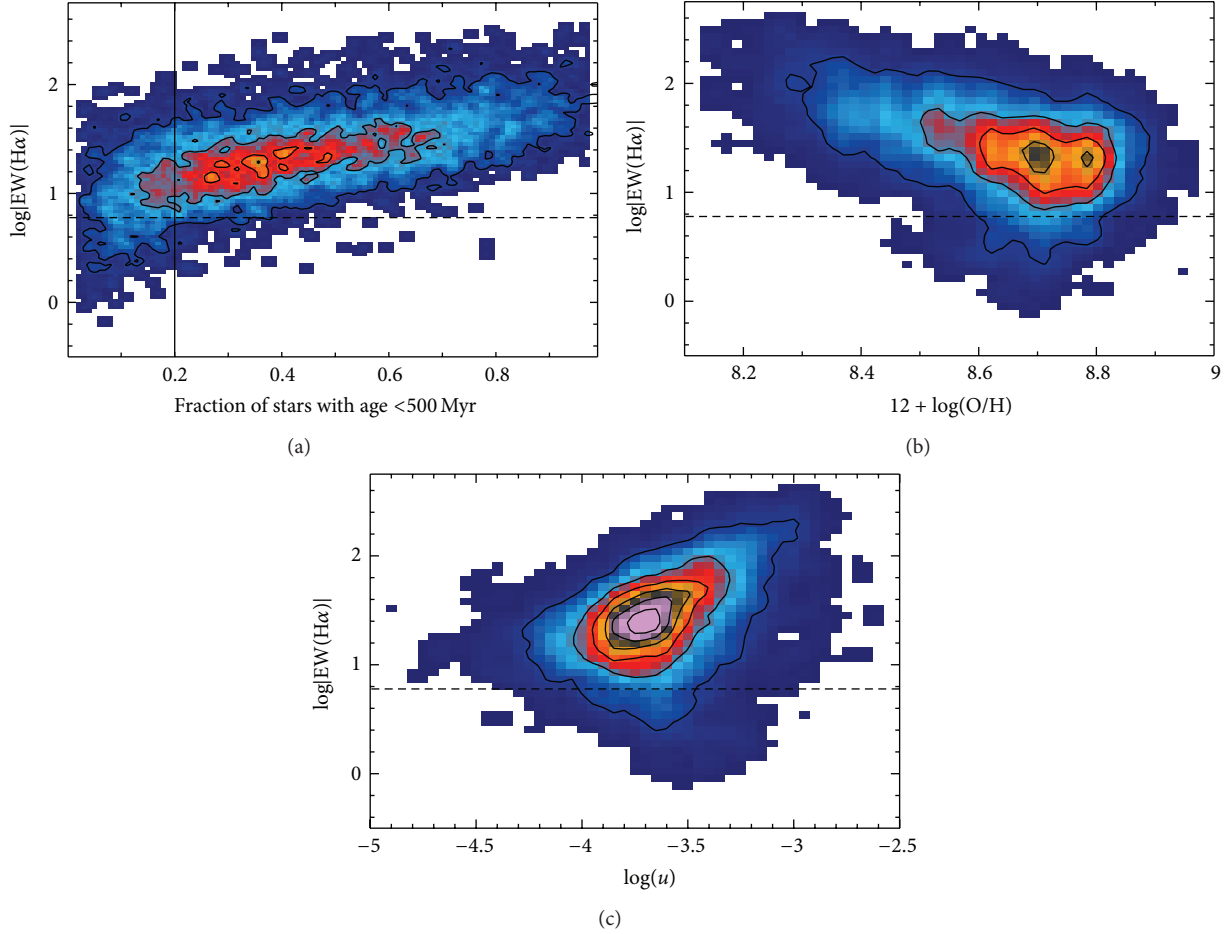


FIGURE 2: (a) Absolute value of the equivalent width of $H\alpha$, in logarithmic scale, plotted against the luminosity fraction of young stars in the V -band, in the underlying stellar population (according to the SSP modelling by FIT3D) for the clumpy ionized regions selected with HIIEXPLORER. (b) Absolute value of the equivalent width of $H\alpha$, in logarithmic scale, plotted against the oxygen abundance for the same ionized regions. (c) Absolute value of the equivalent width of $H\alpha$, in logarithmic scale, plotted against the ionization strength for the same ionized regions.

of regions at each location. The outermost of those contours encloses 95% of the detected regions, with each consecutive one encircling less regions. This contour is located below the Kewley et al. [27] demarcation curve, which indicates that the ionization of our selected clumpy regions is already dominated by star formation. Indeed, only $\sim 2\%$ of all regions are located above the Kewley et al. [27] line, and $\sim 80\%$ are below the Kauffmann et al. [26] line (i.e., where classical disk HII regions are located). If we had adopted this latter demarcation curve as our selection criteria, we would have missed a significant number of regions.

The color code in Figure 3 indicates the average luminosity fraction of young stars in the V -band at each location (i.e., the x -axis in Figure 2), ranging from nearly 100% for the regions at the top-left area of the diagram to nearly 0% for regions at the top-right location.

Based on these results, we classified as HII regions those clumpy ionized regions for which young stars (<500 Myr) contribute at least a 20% to the flux in the V -band. This particular fraction is the lowest for which the correlation

coefficient between f_y and the $EW(H\alpha)$ is still higher than $r_{\text{corr}} > 0.95$ and for which the fraction of excluded regions is not higher than the one that would be excluded by adopting the more common Kauffmann et al. [26] curve. We would like to stress that we are not considering that any star younger than 500 Myr may produce photoionization. The actual age of the ionizing population should be much younger (<20 Myr), in order to supply enough ionizing photons. However, the derived age of the underlying population does not depend only on the physical properties of that population but also on our ability to distinguish between different ages. This in turn depends on the S/N of the continuum, its spectral resolution, the covered wavelength range, and the selected SSP-template. For many HII regions, the continuum has a poor S/N, and therefore we prefer to adopt a very crude SSP library with just 4 ages (and 3 metallicities). Of them, a 50% are younger than 500 Myrs and the other ones older than this age. Our spectral fit assigns all the blue component to ages younger than this limit, which, obviously, should not be interpreted as the true age of the ionizing population at all.

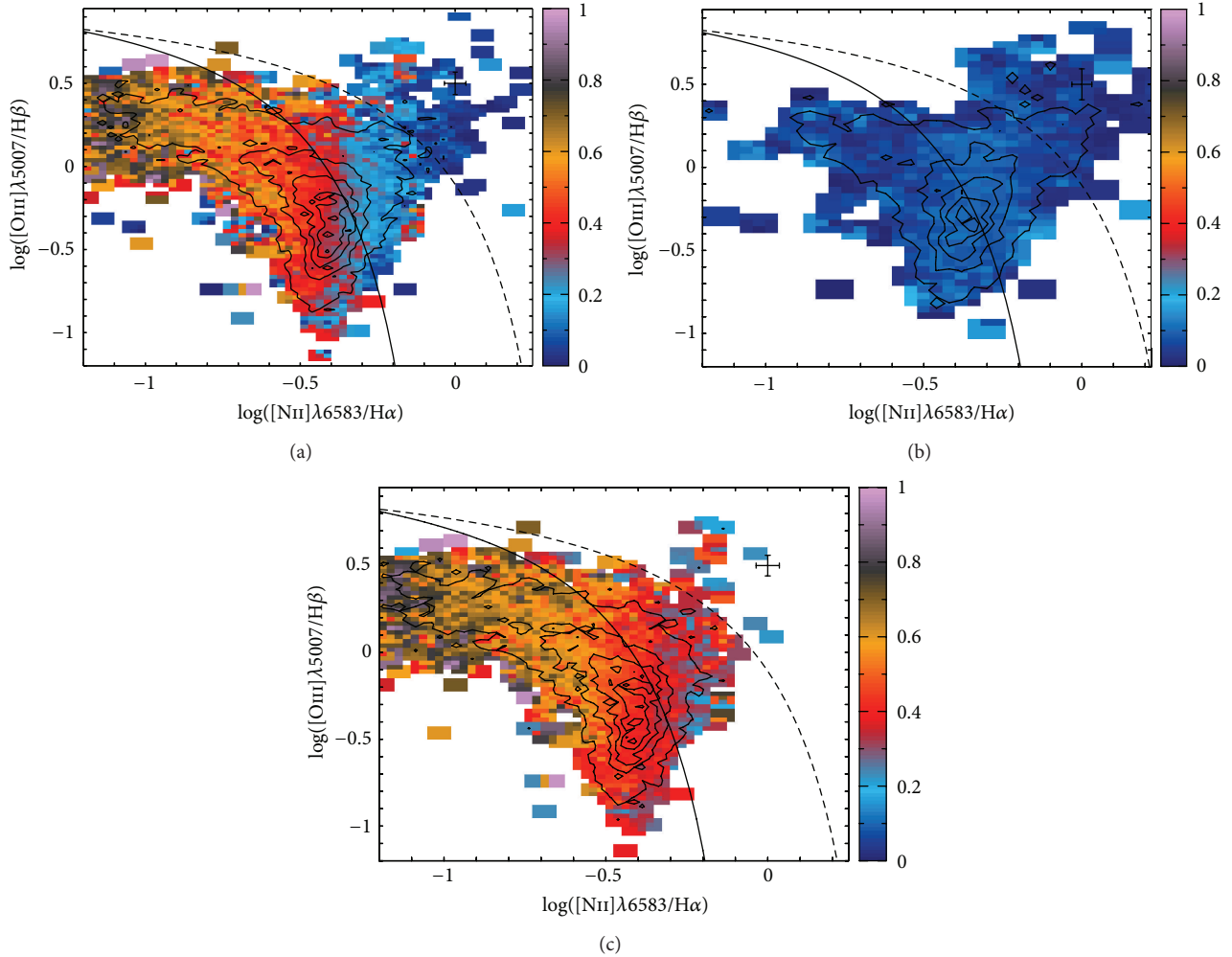


FIGURE 3: (a) $[\text{OIII}]\lambda 5007/\text{H}\beta$ versus $[\text{NII}]\lambda 6583/\text{H}\alpha$ diagnostic diagram for the ~ 7000 ionized regions described in the text. The contours show the density distribution of these regions with the diagram plane, with the outermost contour enclosing 95% of the regions, and each consecutive one enclosing 20% less regions. The color indicates the fraction of young stellar population in the underlying continuum. (b) The same diagnostic diagram restricted to those ionized regions with less than a 20% of young stellar population (~ 1800 regions). (c) The same diagnostic diagram restricted to those ionized regions with more than a 20% of young stellar population (~ 5800 regions). In all the panels, the solid- and dashed-line represent, respectively, the Kauffmann et al. [26] and Kewley et al. [27] demarcation curves. They are usually invoked to distinguish between classical star-forming objects (below the solid line) and AGN powered sources (above the dashed line). Regions between both lines are considered intermediate ones.

Figure 3(b) shows the same distribution as the one shown in Figure 3(a) but restricted to the 1787 regions for which the fraction of young stars is lower than 20%. The fraction of regions above the Kewley et al. [27] curve is significantly larger ($\sim 7\%$), with more than a 40% above the Kauffmann et al. [26] one. Although there are still 1043 regions below this latter curve, they comprise just $\sim 15\%$ of the original sample. We consider this fraction as the incompleteness limit of detected HII regions.

Figure 3(c) shows the same distribution, but for the 5229 regions with a fraction of young stars larger than 20%, that is, our final sample of HII regions. Of them, only 23 are above the Kewley et al. [27] curve ($\sim 99.5\%$ are below it). On the other hand, there are 713 regions in the so-called intermediate region, with a significant fraction of young stars ($\sim 40\%$ on average). These regions would have been excluded if we had

adopted the Kauffmann et al. [26] curve as our selection criteria, losing HII at any galactocentric distance.

Figures 3 and 2(a) indicate that the location of an HII region in the BPT diagram is strongly correlated with the properties of the underlying stellar population. It is important to recall here that the $\text{EW}(\text{H}\alpha)$ is a proxy of the specific star-formation rate (sSFR) or the current star-formation rate compared to the total stellar mass (e.g., [37]). Evenmore, the fraction of young stars is a direct measurement of the most recent star-forming activity. Therefore, the $\text{EW}(\text{H}\alpha)$ and f_y are tracers of the composition of the underlying stellar population and the recent star-formation history of the galaxy at the location of the HII region. We must mention also that both parameters are measured including the line-of-sight underlying stellar population, since the extraction of the spectra is performed on simple apertures

(segmented regions) and therefore these spectra comprise both young and old stars (although only the young ones are responsible of the gas ionization).

Under the assumption of a particular IMF, a particular burst (instantaneous or continuous), a particular dust model, and a fixed evolutionary track for the stars and the prescriptions for the stellar atmosphere (which are model dependent), the location in the BPT diagram is well defined by two parameters: (i) the ionization strength, u (directly related to the ionization parameter), and (ii) the metallicity (e.g., [27]). This is clearly illustrated in Figure 3, where the distribution of the same ionized regions is shown as in Figure 3, without discriminating between different sources of ionization, together with the expected location for two ionization models produced with MAPPINGS-III [27, 38], under certain reasonable assumptions for the dust attenuation and adopting the evolutionary tracks for the ionizing population derived from the PEGASE code [39]. The models assume a fixed electron density of $n_e = 350 \text{ cm}^{-3}$ (near the average value reported for our HII regions) and a set of ionization strengths and metallicities. Two model grids are considered, one assuming an instant starburst at a zero age (left panel) and the other assume a continuous starformation process, which is represented at 4 Myr (right panel). The ionized regions located within the BPT diagram in the area described by the classical HII regions in the disk of galaxies are characterized well by models comprising a single instantaneous starburst, with different ionization strengths and metallicities. However, those ionized regions located above the Kauffmann et al. [26] demarcation line can be reproduced only if a continuous starformation is assumed. A similar behavior was reported by Terlevich et al. [40], when analyzing the age of HII galaxies, that corresponds much better with a sequence of star-formation events rather than with a single burst. It seems that the HII regions located in the inner-most areas and in the older galaxies present a similar behavior.

In any case, it is clear that the location in the BPT diagram is directly related to the ionization strength and metallicity. On the other hand, in Figure 3 this location is directly related with the properties of the underlying stellar population, weighted by the $\text{EW}(\text{H}\alpha)$ or the fraction of young stars, parameters that are strongly correlated (Figure 2). Taking both results together, a strong correlation is expected between the properties of the underlying stellar population and both the ionization strength and the gas abundance. Indeed, this is the case. Figures 2(a) and 2(b), shows the clear correlation between the $\text{EW}(\text{H}\alpha)$ and both the gas abundance and the ionization strength, directly derived from different emission line ratios (see [14], for details on the calculations). Similar correlations are found with the fraction of young stars, f_y , defined before. Thus, although HII regions are short-lived events, its ionization conditions appear to be strongly related to the preexisting underlying stellar population and therefore to the overall star-formation history at their location.

4. Highlights on Our Previous Results

Our program to understand the star-formation processes and chemical evolution of galaxies based on the study of

ionized gas in HII regions has two approaches. In the first one we focused on the study of the ionization processes within individual HII regions in our Galaxy, like Orion Nebula [15] or M1-67 [16]. In the second one we focused on the study of the statistical properties of large samples of extragalactic HII regions, the main highlights of which we summarize here.

This statistical program was initiated with the PINGS survey [12], which acquired IFS mosaic data for a number of medium size nearby galaxies. In Sánchez et al. [41] and Rosales-Ortega et al. [42] we studied in detail the ionized gas and HII regions of the largest galaxy in the sample (NGC 628). The main results of these studies are included in the contribution by Rosales-Ortega in the current edition. We then continued the acquisition of IFS data for a larger sample of visually classified face-on spiral galaxies [43], as part of the feasibility studies for the CALIFA survey [13]. The spatially resolved properties of a typical galaxy in this sample, UGC9837, were presented by [44].

In Sánchez et al. [14] we presented a new method to detect, segregate, and extract the main spectroscopic properties of HII regions from IFS data (HIIEXPLORER (http://www.caha.es/sanchez/HII_explorer/)). In this paper a catalog of ~ 2600 HII regions and aggregations extracted from 38 face-on spiral galaxies compiled from the PINGS and CALIFA feasibility studies was presented. Using this catalog we found a new local scaling relation between the stellar mass density and oxygen abundance, the so-called Σ -Z relation, that can naturally explain the well-known mass-metallicity relation [45]. This relation is consistent with an inside-out growth scenario for disk-dominated galaxies, supported by different observational results based on photometric studies (e.g., [46–49]), classical slit spectroscopy (e.g., [50, 51]), and recent IFS results (e.g., [52, 53]).

The same catalog allows us to explore the galactocentric radial gradient of the oxygen abundance [14]. Models based on the standard inside-out scenario of disk formation predict a relatively quick self-enrichment with oxygen abundances and an almost universal negative metallicity gradient once this is normalized to the galaxy optical size Boissier and Prantzos [54, 55]. In Sánchez et al. [14], we confirmed that up to ~ 2 disk effective radii there is a negative gradient of the oxygen abundance in all the analyzed spiral galaxies. The gradient presents a very similar slope for all the galaxies ($\sim -0.12 \text{ dex}/r_e$), when the radial distances are measured in units of the disk effective radii. We found no difference in the slope for galaxies of different morphological types: early/late spirals, barred/nonbarred, and grand-design/flocculent.

Beyond ~ 2 disk effective radii our data show evidence of a flattening in the abundance, consistent with several other spectroscopic explorations, based mostly on single objects (e.g., [42, 56–59]). The same pattern in the abundance has been described in the case of the extended UV disks discovered by GALEX [60, 61], which show oxygen abundances that are rarely below one-tenth of the solar value. Additional results, based on the metallicity gradient of the outer disk of NGC 300 from single-star CMD analysis [62], or spectroscopic analysis of the HII region NGC 2579 in the outer regions of the Milky-Way [63], support the presence of a flatter gradient towards the outer disk. Despite all these

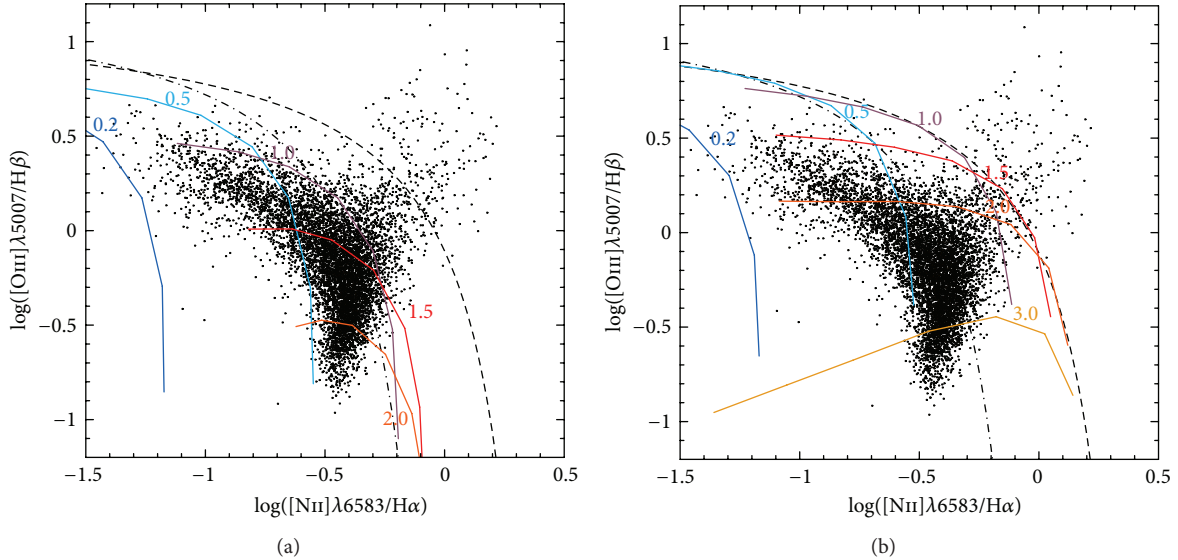


FIGURE 4: (a) $[\text{OIII}]\lambda 5007/\text{H}\beta$ versus $[\text{NII}]\lambda 6583/\text{H}\alpha$ diagnostic diagram for the ~ 7000 ionized regions shown in Figure 3(a). The color solid-lines represent the expected line ratios derived from the MAPPINGS-III ionization models, based on an instantaneous zero-age starburst model based on the PEGASE spectral energy distribution. Each solid-line corresponds to a different metallicity, which is indicated with the corresponding label in units of solar abundance, with a different ionization strength that varies from strong to weak ionizations from left to right in each line. (b) Identical diagram to that in (a), with the only difference that in this particular case the color solid-lines represents the expected line ratios for a continuous starburst model after 4 Myr of its ignition. In ((a), (b)), the dot-dashed and dashed-line represent, respectively, the Kauffmann et al. [26] and Kewley et al. [27] demarcation curves. They are usually invoked to distinguish between classical star-forming objects (below the solid line) and AGN powered sources (above the dashed line). Regions between both lines are considered intermediate ones.

results, the outermost parts of the disk have not been explored properly, either due to the limited number of objects explored by the previous studies or due to the limited spatial coverage (e.g., [14]).

To further explore these issues, we applied the same procedure to the IFS data provided by the CALIFA survey [13] (<http://califa.caha.es/>). CALIFA is an ongoing exploration of the spatially resolved spectroscopic properties of galaxies in the Local Universe ($z < 0.03$) using wide-field IFS to cover the full optical extent (up to $\sim 3-4r_e$) of ~ 600 galaxies of any morphological type, distributed across the entire color-magnitude diagram (Walcher et al., in prep.), and sampling the wavelength range 3650–7500 Å. So far, the survey has completed $\sim 1/2$ of its observations, with 306 galaxies observed (May 2013), and the first data release, comprising 100 galaxies, was already delivered in November 2012 by Husemann et al. [64].

In Sánchez et al. [35] we presented the first results based on the catalog of HII regions extracted from these galaxies. In Here, we studied the dependence of the \mathcal{M} -Z relation with the star-formation rate, for the 113 galaxies with enough HII regions to derive the characteristic oxygen abundance. We found no secondary relation different than the one induced by the well-known relation between the star formation and the mass, contrary to what was claimed by other authors [65, 66], based on single aperture spectroscopic data (SDSS). Although the reason for the discrepancy is still not clear, we postulate that simple aperture bias, like the one present in previous datasets, may induce the reported secondary relation.

Figure 6 presents an updated version of these results, including the last list of analyzed galaxies (193 galaxies from the CALIFA sample together with 31 galaxies from the CALIFA-pilot studies). Figure 4(a) shows the \mathcal{M} -Z relation found for these galaxies, with color code indicating the integrated SFR for each galaxy. It is appreciated that the stronger gradient in SFR be along the stellar mass, as expected for star-forming galaxies. Once the best fitted function to the \mathcal{M} -Z relation subtracted, the residual of the abundance does not present any evident secondary relation with the SFR (as it is seen in Figure 4(b)). That is, the results presented in [35] are confirmed with a sample of galaxies enlarged by almost a factor two.

We also confirmed the local Σ -Z relation unveiled by [42], with a larger statistical sample of HII regions (~ 5000). Both the Σ -Z relation, the evidence for a common slope in the gradient of the oxygen abundance, and the lack of dependence of the \mathcal{M} -Z relation with the star-formation rate are consistent with chemical evolution dominated by an inside-out growth with little/limited influence of processes that redistribute metals, like out flows and/or radial migrations.

In Sanchez et al. [67] we used the updated CALIFA catalog of ~ 5000 HII regions, extracted from 193 individual galaxies shown in Figure 6, to study the radial oxygen abundance gradient up to 3-4 disk effective radii. We confirmed that the abundance gradients present a common slope up to ~ 2 effective radii, with a distribution compatible with that being produced by random fluctuations, for all galaxies when normalized to the disk effective radius of $\alpha_{\text{O/H}} = -0.1 \text{ dex}/r_e$.

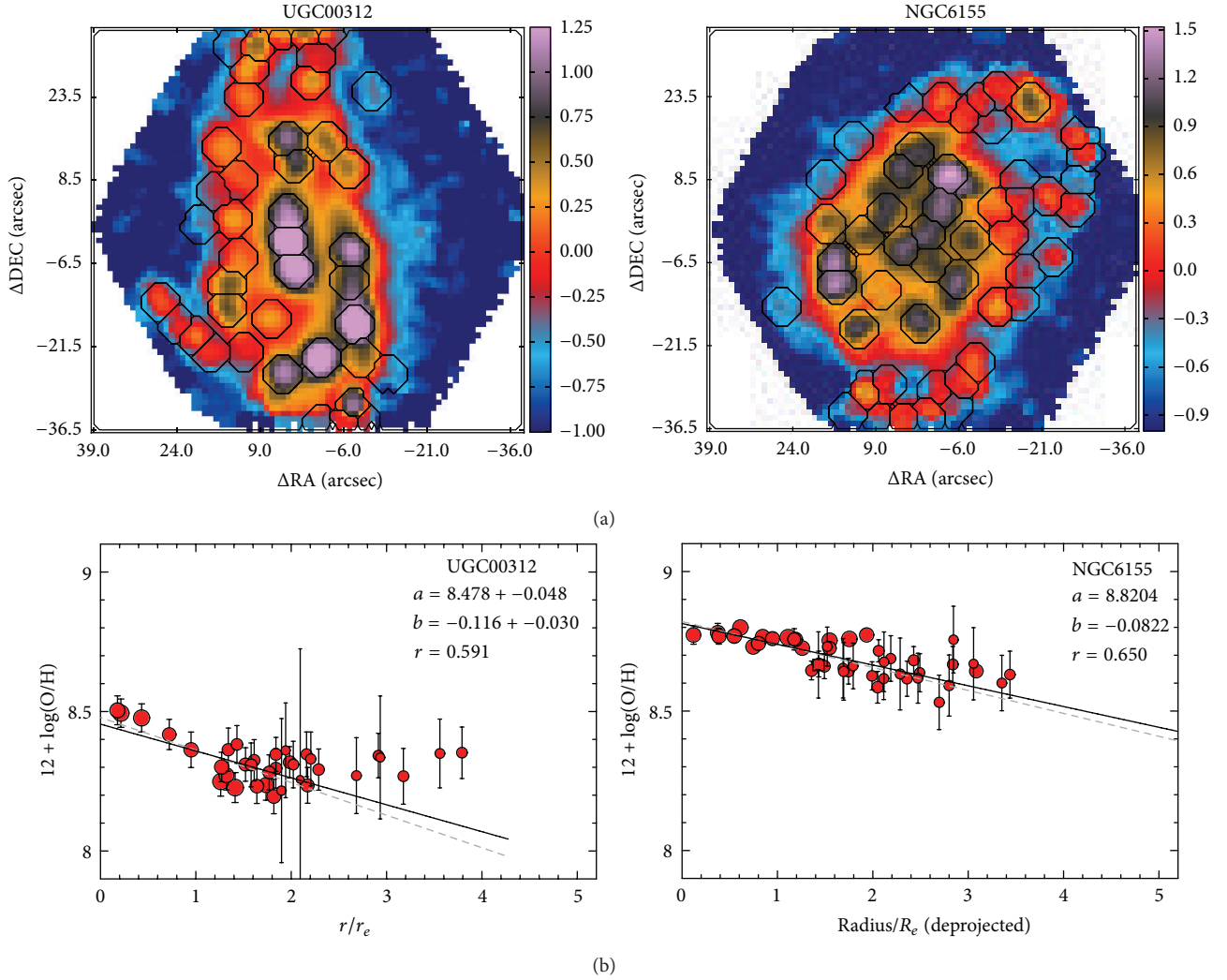


FIGURE 5: (a) IFS-based $H\alpha$ maps, in units of $10^{-16} \text{ erg s}^{-1} \text{ cm}^{-2} \text{ arcsec}^{-2}$, derived for two representative galaxies of the sample (color images), together with the detected HII regions shown as black segmented contours. (b) Radial distribution of the oxygen abundance derived for the individual HII regions with abundance errors below 0.15 dex, as a function of the deprojected distance (i.e., corrected for inclination), normalized to the effective radius, for the same galaxies. The size of the circles is proportional to the $H\alpha$ intensity.

Figure 5 shows the segregation map based on $H\alpha$ intensity to define the HII regions, and the radial gradient in the oxygen abundance two galaxies in our sample (a poor metal and a rich one). No significant differences are found on the basis of the morphological type, presence or absence of bars, absolute magnitude and/or stellar mass. The only clear deviation from the common slope is seen in galaxies with evidence of interaction or undergoing a merging process. For these galaxies the gradient is significantly flatter. These results agree with the main conclusion of our previous study [14], where a limited sample of 38 face-on spiral galaxies was analysed, using similar methods as the ones described here. In a companion article (Sánchez-Blazquez [51] in prep.), we analyse the radial gradient of stellar metallicity, where we have found consistent results.

Beyond $\sim 2r_e$ our data reveal clear evidence of a flattening in the abundance in most of the galaxies with detected HII

regions at this radial distances. A change in the slope of the radial gradient of oxygen abundance has been reported by several authors (e.g., [14, 56, 58, 59]), although with less significant numbers. We cannot provide a conclusive answer regarding the origin of this flattening.

5. Evidence for an Inside-Out Growth

Along this paper we described the different results we have obtained in our studies of HII regions using IFS. Our main results can be summarized as follows.

- (i) HII regions present a large variety of properties across their optical extent, both with regard to the ionization strength and gas abundances, and they do not seem to be fully ionized everywhere across their entire optical extent (as seen in the IFU data of the Orion Nebula).

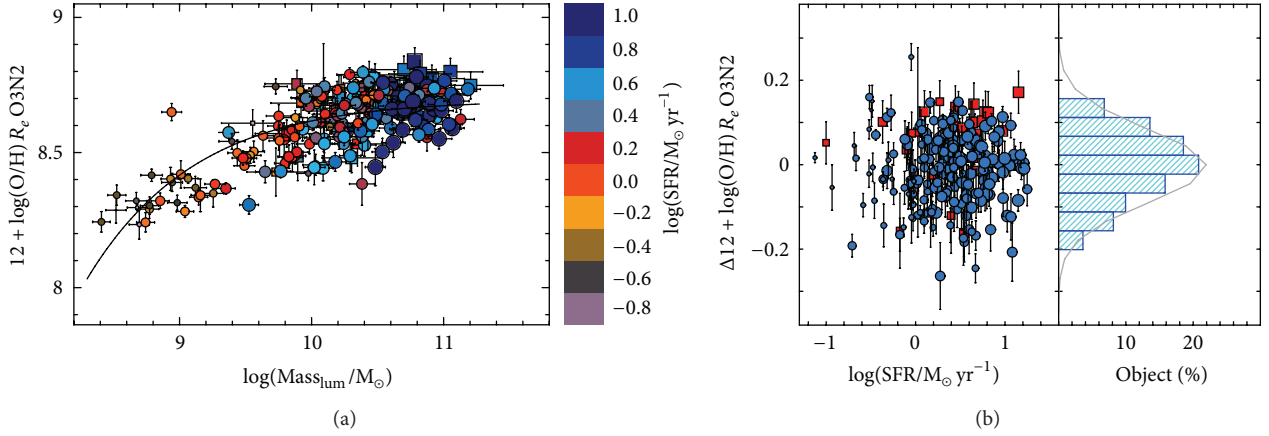


FIGURE 6: (a) Distribution of the oxygen abundances at the effective radii as a function of the integrated stellar masses for the CALIFA galaxies (193, circles). For comparison purposes, we show similar values for the galaxies observed in the CALIFA feasibility studies (31, squares) included in the HII regions catalog described in Sánchez et al. [14]. The size of the symbols is proportional to the integrated SFR. The solid line represents the best-fitting curve, as described in Sanchez et al. [35]. The colors represent the logarithm of the integrated SFR for each galaxy. (b) Distribution of the differential oxygen abundances with respect to the solid-line shown in (a) (i.e., the dependence on the stellar mass), as a function of the integrated SFR for the CALIFA galaxies (113, blue solid circles). The size of the symbols is proportional to the oxygen abundances shown in Figure 6. The histogram shows the same distribution of differential oxygen abundances. The solid line represents a Gaussian function with the same central value (0.01 dex) and standard deviation (0.07 dex) as the represented distribution, scaled to match the histogram.

- (ii) The spectroscopic properties derived using integrated spectra over large areas of HII regions seem to be representative of the average properties derived when analysing individual spectra across their optical extent.
- (iii) The ionization strength and gas abundance and therefore the location of the HII regions in the different diagnostic diagrams correlate with the properties of their underlying stellar population and thus reflect the local star-formation history.
- (iv) The gas abundance presents a negative radial gradient, with more metal rich HII regions in the inner areas and more metal poor ones in the outer ones. Independently of the galaxy properties all galaxies present a common slope for this gradient up to 2 effective radii of $\alpha_{\text{O}/\text{H}} = -0.1 \text{ dex}/r_{\text{e}}$, when the galactocentric distance is normalized to the effective radius of the disk.
- (v) The gas abundance is strongly correlated with the stellar surface mass density (Σ -Z relation), following a correlation similar to the \mathcal{M} -Z relation.
- (vi) Our high-quality data do not reveal any evidence for a secondary relation between the \mathcal{M} -Z relation (or the Σ -Z relation) with the star-formation rate (or the SFR density), different than the well-known relation between the SFR and the stellar mass for star-forming galaxies.

The existence of a universal radial decrease in the oxygen abundance has been already reported in many previous studies (e.g., [5, 9, 14, 42, 56–59]). This observational property is compatible with our current understanding of the formation and evolution of spiral galaxies (e.g., [68] and the references

therein). Gas accretion brings gas into the galactic center, where it first reaches the required density to ignite star formation. Thus the inner regions are populated by older stars, and they have undergone a faster gas reprocessing, and galaxies experience an inside-out mass growth (e.g., [54, 69]). Both the extinction-corrected color gradients in nearby galaxies, [49] and weak dependence of the mass-size relation with redshift [46–48] support an inside-out scenario for the evolution of disks. Recent results, based on analysis of the star-formation history of CALIFA data, found undisputed evidence of the inside-out growth of the stellar mass in galaxies [52], at least for galaxies more massive than $7 \times 10^{10} M_{\odot}$. These results are also supported by the radial distribution of the stellar ages found for the same dataset [53].

However, the described characteristic slope for the abundance gradient, independent of many of the properties of the galaxies, was only recently proposed [14]. This result imposes a more severe restriction to our current understanding of how disk galaxies grow. In essence, it agrees with the recently proposed Σ -Z relation [45] that links the gas abundance with the mass density of the underlying stellar population. It describes how the stellar mass and the gas abundance, both fundamental products of the star formation history, grow consistently in disk galaxies, from the center to the outer-parts. Together with the \mathcal{M} -Z relation, they indicate that more massive galaxies (that trace the strongest potential wells) are formed before and faster, accumulating more stellar mass and more metals. The presence of a common gradient in the abundance indicates that all disk dominated galaxies of the same disk effective radius (hence, the same disk mass) build up their metal content at a given normalized radius with a similar efficiency.

The common slope suggests that the chemical evolution of galaxies is very similar in all disk galaxies, being compatible with a closed-box model. The classical closed-box model considers that each radial bin of a galaxy comprises primordial gas from the which stars which are born, live all their life time, and die *in-situ*, according to a given SFR and IMF prescriptions [70]. Therefore, if the amount of primordial gas is proportional to the depth of the potential well and the efficiency of the SFR is the same for all the galaxies, both the stellar mass and the enrichment would be just proportional to the time, for a given halo mass. The lack of dependence of the \mathcal{M} - Z and Σ - Z relations with the SFR (or the SFR surface density) supports also this scenario. Under this assumption all galaxies should have a universal gradient of their oxygen abundance with its zero point being proportional to the total mass.

However, it is well known that the closed-box model cannot predict the right fraction of metal-poor stars with respect to the observed metallicity distribution of nearby long-lived stars in the Milky Way (e.g., [71]). A more realistic model overcomes this problem by allowing the disk of galaxies to form via continuous accretion gas, driven by the gravitational force. This accretion can be compensated or even overcome for certain galaxies and certain periods by supernova explosions (e.g., [72]). However, the outflow of gas is not expected to feature in the history of most spiral galaxies and is usually neglected in the models [71]. This modified model is consistent with the described common radial gradient if the local gas recycling is faster than other timescales involved [73], and if the radial inflow is similar for those radial bins with the same stellar mass.

Despite these evidences, other authors consider that galactic winds play a fundamental role in the shaping of spiral galaxies (e.g., [74]) and may be an essential ingredient in their formation. Galactic winds are normally associated with strong star-formation events, but there is also evidence for such winds at more moderate SFR. They seem to be a ubiquitous event in high redshift galaxies (e.g., [75, 76]), and some theoretical work emphasizes that they are a fundamental ingredient in the evolution of galaxies (e.g., [77, 78]). In particular, they may play a role in the enrichment of the intergalactic medium, although in most of the cases they do not seem to escape the dark matter halo around the considered galaxy. However, our results indicate that gas flows seem to have a less relevant effect in the shape of the chemical gradient in galaxies than anticipated, that is, their net effect is not clearly evident.

Our results do not rule out the existence of radial gas motions and metal mixing, and they, however, add new constraints on their net effect on the chemical abundance patterns of disk galaxies. Contrary to the isolated disk galaxies, interacting/merging galaxies show a clearly flatter metallicity distribution, in agreement with Kewley et al. [79] and Rich et al. [80]. This indicates that galaxy interactions can result in an effective mixing of metals. The absence of a clear difference in the radial abundance slopes of barred and unbarred galaxies suggests that bars (i) do not significantly enhance the efficiency of metal mixing in galaxies or (ii) produce a roughly proportional change in the gas abundance

and stellar mass distribution that compensates each other when normalized to the disk effective radius, or (iii) are of temporary nature and their lifetime is shorter than the timescale for chemical abundance mixing in galaxies.

In general, the properties of the ionized gas in late-type galaxies are consistent with a quiescent evolution, where gas recycling is faster than other times scales involved [73]. This would imply that the galaxies seem to behave more locally in a similar manner than globally dominated by a radial mass distribution following the potential well of the matter, with an inside-out growth that is regulated by gas inflow and local downsizing star formation. Therefore, the dominant parameter that defines the amount of metals is the stellar mass, since both parameters are the consequence of a (almost) closed-box star-formation process. However, we should remark that our results are only valid for galaxies with stellar masses higher than $\sim 10^{9.5} M_{\odot}$, where the CALIFA sample becomes complete.

Acknowledgments

Sebastian F. Sánchez thanks the director of CEFCA, M. Moles, for his sincere support of this project. This study makes use of the data provided by the Calar Alto Legacy Integral Field Area (CALIFA) survey (<http://califa.caha.es/>). CALIFA is the first legacy survey being performed at Calar Alto. The CALIFA collaboration would like to thank the IAA-CSIC and MPIA-MPG as major partners of the observatory and CAHA itself, for the unique access to telescope time and support in manpower and infrastructures. The CALIFA collaboration also thanks the CAHA staff for the dedication to this project. Based on observations collected at the Centro Astronómico Hispano Alemán (CAHA) at Calar Alto, operated jointly by the Max-Planck-Institut für Astronomie and the Instituto de Astrofísica de Andalucía (CSIC). The author thanks the anonymous referee for the many useful and detailed comments. The author also thanks P. Papaderos for the useful comments and the suggestions to clean and clarify the text. We thank the *Viabilidad, Diseño, Acceso y Mejora* funding program, ICTS-2009-10, for supporting the initial development of this project. He thanks the *Plan Nacional de Investigación y Desarrollo* funding programs, AYA2010-22111-C03-03 and AYA2010-10904E, of the Spanish *Ministerio de Ciencia e Innovación*, for the support given to this project. He thanks the the *Ramón y Cajal* project RyC-2011-07590 of the Spanish *Ministerio de Economía y Competitividad*, for the support give to this project. He acknowledges support by the Grants nos. MI00031241 and MI00031201 of the Academy of Sciences of the Czech Republic (ASCR internal support program of international cooperation projects—PIPPMS) and by the Czech Republic program for the long-term development of the research institution no. RVO67985815.

References

- [1] Á. R. López-Sánchez, “Massive star formation in Wolf-Rayet galaxies: V. Star-formation rates, masses and the importance of galaxy interactions,” *Astronomy & Astrophysics*, vol. 521, article A63, 31 pages, 2010.

- [2] Á. R. López-Sánchez and C. Esteban, “Massive star formation in Wolf-Rayet galaxies: IV. Colours, chemical-composition analysis and metallicity—luminosity relations,” *Astronomy & Astrophysics*, vol. 517, article A85, 28 pages, 2010.
- [3] J. Lequeux, M. Peimbert, J. F. Rayo, A. Serrano, and S. Torres-Peimbert, “Chemical composition and evolution of irregular and blue compact galaxies,” *Astronomy & Astrophysics*, vol. 80, pp. 155–166, 1979.
- [4] E. D. Skillman, “Empirical oxygen abundances and physical conditions for relatively low abundance HII regions,” *Astrophysical Journal*, vol. 347, pp. 883–893, 1989.
- [5] M. B. Vila-Costas and M. G. Edmunds, “The relation between abundance gradients and the physical properties of spiral galaxies,” *Monthly Notices of the Royal Astronomical Society*, vol. 259, no. 1, pp. 121–145, 1992.
- [6] D. Zaritsky, R. C. Kennicutt Jr., and J. P. Huchra, “HII regions and the abundance properties of spiral galaxies,” *Astrophysical Journal Letters*, vol. 420, no. 1, pp. 87–109, 1994.
- [7] C. A. Tremonti, T. M. Heckman, G. Kauffmann et al., “The origin of the mass-metallicity relation: insights from 53,000 star-forming galaxies in the sloan digital sky survey,” *Astrophysical Journal Letters*, vol. 613, no. 2, pp. 898–913, 2004.
- [8] D. R. Garnett, “The luminosity-metallicity relation, effective yields, and metal loss in spiral and irregular galaxies,” *Astrophysical Journal Letters*, vol. 581, no. 2, pp. 1019–1031, 2002.
- [9] A. I. Diaz, “Abundance gradients in disc galaxies and chemical evolution models,” in *Evolutionary Phenomena in Galaxies*, J. E. Beckman and B. E. J. Pagel, Eds., pp. 377–397, 1989.
- [10] P. Martin and J.-R. Roy, “The influence of bars on the chemical composition of spiral galaxies,” *Astrophysical Journal Letters*, vol. 424, no. 2, pp. 599–614, 1994.
- [11] J. Moustakas and R. C. Kennicutt Jr., “An integrated spectrophotometric survey of nearby star-forming galaxies,” *Astrophysical Journal Supplement Series*, vol. 164, no. 1, pp. 81–98, 2006.
- [12] F. F. Rosales-Ortega, R. C. Kennicutt Jr., S. F. Sánchez et al., “PINGS: the PPAK IFS nearby galaxies survey,” *Monthly Notices of the Royal Astronomical Society*, vol. 405, pp. 735–758, 2010.
- [13] S. F. Sánchez, R. C. Kennicutt Jr., A. Gil de Paz et al., “CALIFA, the Calar Alto Legacy Integral Field Area survey: I. Survey presentation,” *Astronomy & Astrophysics*, vol. 538, article A8, 2012.
- [14] S. F. Sánchez, F. F. Rosales-Ortega, R. A. Marino et al., “Integral field spectroscopy of a sample of nearby galaxies: II. Properties of the H II regions,” *Astronomy & Astrophysics*, vol. 546, article A2, 28 pages, 2012.
- [15] S. F. Sánchez, N. Cardiel, M. A. W. Verheijen et al., “PPAK integral field spectroscopy survey of the Orion nebula,” *Astronomy & Astrophysics*, vol. 465, no. 1, pp. 207–217, 2007.
- [16] A. Fernández-Martín, J. M. Vilchez, E. Pérez-Montero et al., “Integral field spectroscopy of M1-67. A Wolf-Rayet nebula with luminous blue variable nebula appearance,” *Astronomy & Astrophysics*, vol. 554, article A104, 15 pages, 2013.
- [17] J. B. Kaler, “A catalog of relative emission line intensities observed in planetary and diffuse nebulae,” *Astrophysical Journal Supplement Series*, vol. 31, no. 688, p. 517, 1976.
- [18] J. A. Baldwin, G. J. Ferland, P. G. Martin et al., “Physical conditions in the orion nebula and an assessment of its helium abundance,” *Astrophysical Journal Letters*, vol. 374, no. 2, pp. 580–609, 1991.
- [19] D. E. Osterbrock, *Astrophysics of Gaseous Nebulae and Active Galactic Nuclei*, University Science Books, Mill Valley, Calif, USA, 1989, Research supported by the University of California, John Simon Guggenheim Memorial Foundation, University of Minnesota, et al.
- [20] B. E. J. Pagel, M. G. Edmunds, D. E. Blackwell, M. S. Chun, and G. Smith, “On the composition of H II regions in southern galaxies. I—NGC 300 and 1365,” *Monthly Notices of the Royal Astronomical Society*, vol. 189, pp. 95–113, 1979.
- [21] R. W. Pogge, J. M. Owen, and B. Atwood, “Imaging spectrophotometry of the Orion Nebula core. I—emission-line mapping and physical conditions,” *Astrophysical Journal*, vol. 399, no. 1, pp. 147–158, 1992, Erratum in “imaging spectrophotometry of the Orion Nebula core. I—emission-line mapping and physical conditions,” *Astrophysical Journal*, vol. 408, p. 758, 1993.
- [22] S. Veilleux and D. E. Osterbrock, “Spectral classification of emission-line galaxies,” *Astrophysical Journal Supplement Series*, vol. 63, pp. 295–310, 1987.
- [23] J. A. Baldwin, M. M. Phillips, and R. Terlevich, “Classification parameters for the emission-line spectra of extragalactic objects,” *Publications of the Astronomical Society of the Pacific*, vol. 93, pp. 5–19, 1981.
- [24] R. Cid Fernandes, G. Stasińska, A. Mateus, and N. Vale Asari, “A comprehensive classification of galaxies in the Sloan Digital Sky Survey: how to tell true from fake AGN?” *Monthly Notices of the Royal Astronomical Society*, vol. 413, no. 3, pp. 1687–1699, 2011.
- [25] C. Kehrig, A. Monreal-Ibero, P. Papaderos et al., “The ionized gas in the CALIFA early-type galaxies: I. Mapping two representative cases: NGC 6762 and NGC 5966,” *Astronomy & Astrophysics*, vol. 540, article A11, 2012.
- [26] G. Kauffmann, T. M. Heckman, C. Tremonti et al., “The host galaxies of active galactic nuclei,” *Monthly Notices of the Royal Astronomical Society*, vol. 346, no. 4, pp. 1055–1077, 2003.
- [27] L. J. Kewley, M. A. Dopita, R. S. Sutherland, C. A. Heisler, and J. Trevena, “Theoretical modeling of starburst galaxies,” *Astrophysical Journal Letters*, vol. 556, no. 1, pp. 121–140, 2001.
- [28] L. J. Kewley, B. Groves, G. Kauffmann, and T. Heckman, “The host galaxies and classification of active galactic nuclei,” *Monthly Notices of the Royal Astronomical Society*, vol. 372, no. 3, pp. 961–976, 2006.
- [29] R. C. Kennicutt Jr., W. C. Keel, and C. A. Blaha, “A comparison of the physical conditions in nuclear, hotspot, and disk H II regions,” *Astronomical Journal*, vol. 97, pp. 1022–1035, 1989.
- [30] L. C. Ho, A. V. Filippenko, and W. L. W. Sargent, “Properties of H I regions in the centers of nearby galaxies,” *Astrophysical Journal Letters*, vol. 487, no. 2, pp. 579–590, 1997.
- [31] M. G. Allen, B. A. Groves, M. A. Dopita, R. S. Sutherland, and L. J. Kewley, “The mappings III library of fast radiative shock models,” *The Astrophysical Journal Supplement Series*, vol. 178, no. 1, pp. 20–55, 2008.
- [32] E. M. Levesque, L. J. Kewley, and K. L. Larson, “Theoretical modeling of star-forming galaxies. I. Emission-line diagnostic grids for local and low-metallicity galaxies,” *Astronomical Journal*, vol. 139, no. 2, pp. 712–727, 2010.
- [33] B. A. Groves, M. A. Dopita, and R. S. Sutherland, “Dusty, radiation pressure-dominated photoionization. II multiwavelength emission line diagnostics for narrow-line regions,” *Astrophysical Journal Supplement Series*, vol. 153, no. 1, pp. 75–91, 2004.
- [34] R. Cid Fernandes, G. Stasińska, M. S. Schlickmann et al., “Alternative diagnostic diagrams and the “forgotten” population of weak line galaxies in the SDSS,” *Monthly Notices of the Royal Astronomical Society*, vol. 403, no. 2, pp. 1036–1053, 2010.

- [35] S. F. Sanchez, F. F. Rosales-Ortega, B. Jungwiert et al., “Mass-metallicity relation explored with CALIFA. I. Is there a dependence on the star-formation rate?” *Astronomy & Astrophysics*, vol. 554, article A58, 8 pages, 2013.
- [36] P. Papaderos, J. M. Gomes, J. M. Vilchez et al., “Nebular emission and the Lyman continuum photon escape fraction in CALIFA early-type galaxies,” *Astronomy & Astrophysics*, vol. 555, article L1, 5 pages, 2013.
- [37] R. C. Kennicutt Jr., “The global schmidt law in star-forming galaxies,” *Astrophysical Journal Letters*, vol. 498, no. 2, pp. 541–552, 1998.
- [38] M. A. Dopita, L. J. Kewley, C. A. Heisler, and R. S. Sutherland, “A theoretical recalibration of the extragalactic H II region sequence,” *Astrophysical Journal Letters*, vol. 542, no. 1, pp. 224–234, 2000.
- [39] M. Fioc and B. Rocca-Volmerange, “PEGASE: a UV to NIR spectral evolution model of galaxies: application to the calibration of bright galaxy counts,” *Astronomy & Astrophysics*, vol. 326, no. 3, pp. 950–962, 1997.
- [40] R. Terlevich, S. Silich, D. Rosa-González, and E. Terlevich, “How old are H II galaxies?” *Monthly Notices of the Royal Astronomical Society*, vol. 348, no. 4, pp. 1191–1196, 2004.
- [41] S. F. Sánchez, F. F. Rosales-Ortega, R. C. Kennicutt Jr. et al., “PPAK wide-field integral field spectroscopy of NGC 628—I. The largest spectroscopic mosaic on a single galaxy,” *Monthly Notices of the Royal Astronomical Society*, vol. 410, no. 1, pp. 313–340, 2011.
- [42] F. F. Rosales-Ortega, A. I. Díaz, R. C. Kennicutt Jr., and S. F. Sánchez, “PPAK wide-field Integral field spectroscopy of NGC 628—II. Emission line abundance analysis,” *Monthly Notices of the Royal Astronomical Society*, vol. 415, no. 3, pp. 2439–2474, 2011.
- [43] E. Mármol-Queraltó, S. F. Sánchez, R. A. Marino et al., “Integral field spectroscopy of a sample of nearby galaxies,” *Astronomy & Astrophysics*, vol. 534, article A8, 17 pages, 2011.
- [44] K. Viironen, S. F. Sánchez, E. Marmol-Queraltó et al., “Spatially resolved properties of the grand-design spiral galaxy UGC 9837: a case for high-redshift 2-D observations,” *Astronomy & Astrophysics*, vol. 538, article A144, 2012.
- [45] F. F. Rosales-Ortega, S. F. Sánchez, J. Iglesias-Páramo et al., “A new scaling relation for H II regions in spiral galaxies: unveiling the true nature of the mass-metallicity relation,” *Astrophysical Journal*, vol. 756, no. 2, p. L31, 2012.
- [46] I. Trujillo, G. Rudnick, H.-W. Rix et al., “The luminosity-size and mass-size relations of galaxies out to $z \sim 31$,” *Astrophysical Journal Letters*, vol. 604, no. 2, pp. 521–533, 2004.
- [47] M. Barden, H. W. Rix, R. S. Somerville et al., “GEMS: the surface brightness and surface mass density evolution of disk galaxies,” *Astrophysical Journal*, vol. 635, no. 2, pp. 959–981, 2005.
- [48] I. Trujillo, N. M. Förster Schreiber, G. Rudnick et al., “The size evolution of galaxies since $z \sim 3$: combining SDSS, GEMS, and FIRES,” *Astrophysical Journal Letters*, vol. 650, no. 1, pp. 18–41, 2006.
- [49] J. C. Muñoz-Mateos, A. G. de Paz, S. Boissier et al., “Specific star formation rate profiles in nearby spiral galaxies: quantifying the inside-out formation of disks,” *Astrophysical Journal Letters*, vol. 658, no. 2, pp. 1006–1026, 2007.
- [50] L. A. MacArthur, J. J. González, and S. Courteau, “Stellar population and kinematic profiles in spiral bulges and discs: population synthesis of integrated spectra,” *Monthly Notices of the Royal Astronomical Society*, vol. 395, no. 1, pp. 28–63, 2009.
- [51] P. Sánchez-Blázquez, P. Ocvirk, B. K. Gibson, I. Pérez, and R. F. Peletier, “Star formation history of barred disc galaxies,” *Monthly Notices of the Royal Astronomical Society*, vol. 415, no. 1, pp. 709–731, 2011.
- [52] E. Pérez, R. Cid Fernandes, R. M. González Delgado et al., “The evolution of galaxies resolved in space and time: a view of inside-out growth from the califa survey,” *Astrophysical Journal*, vol. 764, no. 1, p. L1, 2013.
- [53] R. M. González Delgado, E. Pérez, R. Cid Fernandes et al., “The evolution of galaxies resolved in space and time: a view of inside-out growth from the CALIFA survey,” *Astrophysical Journal Letters*, vol. 764, no. 1, article L1, 6 pages, 2013.
- [54] S. Boissier and N. Prantzos, “Chemo-spectrophotometric evolution of spiral galaxies—I. The model and the Milky Way,” *Monthly Notices of the Royal Astronomical Society*, vol. 307, no. 4, pp. 857–876, 1999.
- [55] S. Boissier and N. Prantzos, “Chemo-spectrophotometric evolution of spiral galaxies—II. Main properties of present-day disc galaxies,” *Monthly Notices of the Royal Astronomical Society*, vol. 312, no. 2, pp. 398–416, 2000.
- [56] F. Bresolin, E. Ryan-Weber, R. C. Kennicutt Jr., and Q. Goddard, “The flat oxygen abundance gradient in the extended disk of M83,” *Astrophysical Journal*, vol. 695, no. 1, pp. 580–595, 2009.
- [57] P. Yoachim, R. Roškar, and V. P. Debattista, “Integral field unit spectroscopy of the stellar disk truncation region of NGC 6155,” *Astrophysical Journal Letters*, vol. 716, no. 1, pp. L4–L8, 2010.
- [58] R. A. Marino, A. Gil de Paz, A. Castillo-Morales et al., “Integral field spectroscopy and multi-wavelength imaging of the nearby spiral galaxy NGC 5668*: an unusual flattening in metallicity gradient,” *Astrophysical Journal*, vol. 754, no. 1, p. 61, 2012.
- [59] F. Bresolin, R. C. Kennicutt Jr., and E. Ryan-Weber, “Gas metallicities in the extended disks of NGC 1512 and NGC 3621. Chemical signatures of metal mixing or enriched gas accretion?” *Astrophysical Journal*, vol. 750, no. 2, article 122, 2012.
- [60] A. Gil de Paz, B. F. Madore, S. Boissier et al., “Discovery of an extended ultraviolet disk in the nearby galaxy NGC 4625,” *Astrophysical Journal*, vol. 627, no. 1, pp. L29–L32, 2005.
- [61] D. A. Thilker, L. Bianchi, G. Meurer et al., “A search for extended ultraviolet disk (XUV-disk) galaxies in the local universe,” *Astrophysical Journal Supplement Series*, vol. 173, no. 2, pp. 538–571, 2007.
- [62] M. Vlajić, J. Bland-Hawthorn, and K. C. Freeman, “The abundance gradient in the extremely faint outer disk of NGC 300,” *Astrophysical Journal*, vol. 697, no. 1, p. 361, 2009.
- [63] C. Esteban, L. Carigi, M. V. F. Copetti et al., “NGC 2579 and the carbon and oxygen abundance gradients beyond the solar circle,” *Monthly Notices of the Royal Astronomical Society*, vol. 433, no. 1, pp. 382–393, 2013.
- [64] B. Husemann, K. Jahnke, S. F. Sánchez et al., “CALIFA, the Calar Alto Legacy Integral Field Area survey. II. First public data release,” *Astronomy & Astrophysics*, vol. 549, article A87, 25 pages, 2013.
- [65] M. A. Lara-López, J. Cepa, A. Bongiovanni et al., “A fundamental plane for field star-forming galaxies,” *Astronomy & Astrophysics*, vol. 521, article L53, 5 pages, 2010.
- [66] F. Mannucci, G. Cresci, R. Maiolino, A. Marconi, and A. Gnerucci, “A fundamental relation between mass, star formation rate and metallicity in local and high-redshift galaxies,” *Monthly Notices of the Royal Astronomical Society*, vol. 408, no. 4, pp. 2115–2127, 2010.

- [67] S. F. Sanchez, F. F. Rosales-Ortega, J. Iglesias-Paramo et al., "A characteristic oxygen abundance gradient in galaxy disks unveiled with CALIFA," <http://arxiv.org/abs/1311.7052>.
- [68] T. Tsujimoto, J. Bland-Hawthorn, and K. C. Freeman, "Evidence of early enrichment of the galactic disk by large-scale winds," *Publications of the Astronomical Society of Japan*, vol. 62, no. 2, pp. 447–456, 2010.
- [69] F. Matteucci and P. Francois, "Galactic chemical evolution—abundance gradients of individual elements," *Monthly Notices of the Royal Astronomical Society*, vol. 239, pp. 885–904, 1989.
- [70] B. E. J. Pagel and B. E. Patchett, "Metal abundances in nearby stars and the chemical history of the solar neighborhood," *Monthly Notices of the Royal Astronomical Society*, vol. 172, pp. 13–40, 1975.
- [71] B. K. Gibson, Y. Fenner, A. Renda, D. Kawata, and H.-C. Lee, "Galactic chemical evolution," *Publications of the Astronomical Society of Australia*, vol. 20, no. 4, pp. 401–415, 2003.
- [72] R. B. Larson, "Effects of supernovae on the early evolution of galaxies," *Monthly Notices of the Royal Astronomical Society*, vol. 169, pp. 229–246, 1974.
- [73] J. Silk, "Dissipative processes in galaxy formation," *Proceedings of the National Academy of Sciences of the United States of America*, vol. 90, no. 11, pp. 4835–4839, 1993.
- [74] S. Veilleux, G. Cecil, and J. Bland-Hawthorn, "Galactic winds," *Annual Review of Astronomy and Astrophysics*, vol. 43, pp. 769–826, 2005.
- [75] A. E. Shapley, C. C. Steidel, M. Pettini, and K. L. Adelberger, "Rest-frame ultraviolet spectra of $z \sim 3$ Lyman break galaxies," *Astrophysical Journal Letters*, vol. 588, no. 1, pp. 65–89, 2003.
- [76] B. J. Weiner, A. L. Coil, J. X. Prochaska et al., "Ubiquitous outflows in deep2 spectra of star-forming galaxies at $z = 1.4$," *Astrophysical Journal*, vol. 692, no. 1, p. 187, 2009.
- [77] A. Dekel, A. Zolotov, D. Tweed, M. Cacciato, D. Ceverino, and J. R. Primack, "Toy models for galaxy formation versus simulations," *Monthly Notices of the Royal Astronomical Society*, vol. 435, pp. 999–1019, 2013.
- [78] S. J. Lilly, C. M. Carollo, A. Pipino, A. Renzini, and Y. Peng, "Gas regulation of galaxies: the evolution of the cosmic specific star formation rate, the metallicity-mass-star-formation rate relation, and the stellar content of halos," *Astrophysical Journal*, vol. 772, no. 2, p. 119, 2013.
- [79] L. J. Kewley, D. Rupke, H. Jabran Zahid, M. J. Geller, and E. J. Barton, "Metallicity gradients and gas flows in galaxy pairs," *Astrophysical Journal Letters*, vol. 721, no. 1, pp. L48–L52, 2010.
- [80] J. A. Rich, P. Torrey, L. J. Kewley, M. A. Dopita, and D. S. N. Rupke, "An integral field study of abundance gradients in nearby luminous infrared galaxies," *Astrophysical Journal*, vol. 753, no. 1, p. 5, 2012.

Review Article

The Mitchell Spectrograph: Studying Nearby Galaxies with the VIRUS Prototype

Guillermo A. Blanc

Observatories of the Carnegie Institution for Science, 813 Santa Barbara Street, Pasadena, CA 91101, USA

Correspondence should be addressed to Guillermo A. Blanc; gblancm@obs.carnegiescience.edu

Received 7 August 2013; Accepted 2 October 2013

Academic Editor: Jorge Iglesias Páramo

Copyright © 2013 Guillermo A. Blanc. This is an open access article distributed under the Creative Commons Attribution License, which permits unrestricted use, distribution, and reproduction in any medium, provided the original work is properly cited.

The Mitchell Spectrograph (a.k.a. VIRUS-P) on the 2.7 m Harlan J. Smith telescope at McDonald Observatory is currently the largest field of view (FOV) integral field unit (IFU) spectrograph in the world ($1.7' \times 1.7'$). It was designed as a prototype for the highly replicable VIRUS spectrograph which consists of a mosaic of IFUs spread over a $16'$ diameter FOV feeding 150 spectrographs similar to the Mitchell. VIRUS will be deployed on the 9.2 meter Hobby-Eberly Telescope (HET) and will be used to conduct the HET Dark Energy Experiment (HETDEX). Since seeing first light in 2007 the Mitchell Spectrograph has been widely used, among other things, to study nearby galaxies in the local universe where their internal structure and the spatial distribution of different physical parameters can be studied in great detail. These observations have provided important insight into many aspects of the physics behind the formation and evolution of galaxies and have boosted the scientific impact of the 2.7 meter telescope enormously. Here I review the contributions of the Mitchell Spectrograph to the study of nearby galaxies, from the investigation the spatial distribution of dark matter and the properties of supermassive black holes, to the studies of the process of star formation and the chemical composition of stars and gas in the ISM, which provide important information regarding the formation and evolution of these systems. I highlight the fact that wide field integral field spectrographs on small and medium size telescopes can be powerful cost effective tools to study the astrophysics of galaxies. Finally I briefly discuss the potential of HETDEX for conducting studies on nearby galaxies. The survey parameters make it complimentary and competitive to ongoing and future surveys like SAMI and MANGA.

1. Introduction

The Mitchell Spectrograph (a.k.a. VIRUS-P) was commissioned in early 2007 on the 2.7 m Harlan J. Smith telescope at McDonald Observatory. It is owned and operated by the University of Texas at Austin and was designed as a prototype for the Visible Integral Field Replicable Unit Spectrograph (VIRUS; [1]), a massively replicated fiber-fed IFU spectrograph for the 9.2 m Hobby-Eberly Telescope (HET). VIRUS consists of a mosaic of $75 50'' \times 50''$ IFUs spread regularly with a 1/4 filling factor over a $16'$ diameter field of view. The IFUs themselves have a 1/3 filling factor and feed 150 spectrographs similar to the Mitchell Spectrograph. VIRUS will be used to conduct the HET Dark Energy Experiment (HETDEX; [2–4]), a large ($\sim 90 \text{ deg}^2$) blind integral field spectroscopic survey aimed at studying the properties of dark energy at high redshift by measuring the power spectrum of $\sim 8 \times 10^5 \text{ Ly}\alpha$

emitting galaxies (LAEs) at $1.9 < z < 3.5$. VIRUS is currently under construction and first light is expected to occur in mid-2014.

In its 6-year lifetime the Mitchell Spectrograph has provided a test bench for the technology and the components involved in the construction of VIRUS and a proof of concept for the observing strategy, data processing, and analysis algorithms that will be used in HETDEX [3]. Although these were the main goals behind the design and construction of the Mitchell Spectrograph, the prototype has proved to be a unique and powerful instrument for the study of galaxies not only in the nearby universe but also at high redshift (e.g., [3–7]).

In this paper I review the impact that the Mitchell Spectrograph has had on the field of galaxy astrophysics. Numerous studies that use Mitchell Spectrograph data have been published during the last few years. These studies are

focused on a large range of astrophysical processes that are important for galaxy evolution, including the physics of super massive black holes (SMBHs) in the centers of galaxies [8–11]; the spatial structure of the dark matter (DM) halos in which galaxies live [12, 13]; the chemical composition, dynamics, and physical conditions of gas in the interstellar medium (ISM) and the circumgalactic medium (CGM) of galaxies [14–16]; the process of star formation on galactic scales [17, 18]; and the physical properties of the stellar populations present in different regions of nearby star forming and early-type systems [19–21].

During the last decade a new generation of wide field integral field spectrographs, like SAURON on the 4.2 m William Herschel Telescope [22], PPAK on the 3.5 m at Calar Alto Observatory [23], SparsePak on the WIYN 3.5 m telescope [24], and the Mitchell Spectrograph on the 2.7 m, have demonstrated the power of integral field spectroscopy as a tool that is extremely well suited for small and medium aperture telescopes. These instruments have been systematically used to study nearby galaxies. Surveys like SAURON [25], ATLAS3D [26], PINGS [27], CALIFA [28], VENGA [29], and VIXENS [18] either have or are in the process of building revolutionary spectroscopic datasets on these systems.

The large fields of view and large plate scales that typically characterize these instruments allow for an efficient mapping of large areas on the sky and make these instruments extremely sensitive to low surface brightness emission. At a fixed focal ratio, the plate scale is inversely proportional to the telescope aperture size. Therefore, modulo differences in transmission between different telescopes, the surface brightness sensitivity of an IFU with a fixed spatial resolution element size in physical units is independent of the size of the telescope in which it is installed. This fact, combined with moderate instrument building costs and the relative facility with which large amounts of time can be scheduled for an observing program in smaller facilities, makes wide field IFU spectrographs extremely cost effective and scientifically competitive instruments for small and medium size telescopes. I hope this review helps spread this idea by presenting the Mitchell Spectrograph as an example of what can be achieved with this type of instruments.

In Section 2 I provide a brief description of the instrument and its various components. I present a showcase of scientific results on nearby galaxies and discuss ongoing surveys being conducted with the Mitchell Spectrograph in Section 3. I discuss the prospects for studying nearby galaxies with VIRUS in the context of the HETDEX survey in Section 4 and present some final conclusions in Section 5.

2. The Mitchell Spectrograph (a.k.a. VIRUS-P)

The Mitchell Spectrograph (<http://www.as.utexas.edu/mcdonald/facilities/2.7m/virus-p.html>) design and construction are described in detail in Hill et al. [30]. The instrument is shown in Figure 1. The IFU uses a densepak-type 246 fiber bundle. Fibers are arranged following an hexagonal pattern with a 1/3 filling factor across a square $1.7' \times 1.7'$ FOV, requiring three dithered observations to ensure an almost

complete coverage of the field. The IFU is fed at $f/3.65$ through a telecentric, two-group dioptric focal reducer. At the plate scale of the 2.7 m telescope fibers subtend a $4.2''$ diameter on sky.

The spectrograph has a double-Schmidt optical design. It uses a volume phase holographic (VPH) grating at the pupil between the articulating $f/3.32$ folded collimator and the $f/1.33$ cryogenic prime focus camera. Gratings are interchangeable and can be blazed at different angles. A set of four VPH gratings are available which can be used in different modes to provide spectral resolutions in the $800 < R < 4000$ range and sample different bandpasses across the 3600–6900 Å range. High on-sky throughput is achieved by the use of high reflectivity dielectric coatings. The Mitchell Spectrograph is gimbal-mounted on the telescope to allow short fibers for high UV throughput, while maintaining high mechanical stability. This translates in good instrument stability and observing efficiency as it eliminates the need for calibration frames at the position of the science targets. The instrument software and the $4.5' \times 4.5'$ field, fixed-offset guider provide rapid acquisition, guiding, and precision dithering. A custom data reduction pipeline called VACCINE [3] yields Poisson noise limited sky subtracted spectra.

3. Nearby Galaxies Studies

Thanks to the fact that we can resolve nearby galaxies down to small physical scales, they offer unique laboratories in which we can test our understanding of the critical processes involved in galaxy formation and evolution. Integral field spectroscopy allows one to study important processes affecting baryons in galaxies like star formation, chemical enrichment, and feedback, in a spatially resolved manner. Furthermore, wide field stellar and gas kinematics can be used to constrain the shape of the dark matter gravitational potential in which all these processes take place. Being able to map the kinematics and physical properties of stars and gas across the different environments and morphological structures present in galaxies allows one to study in detail the fossil record of the processes by which these objects have formed and evolved.

In this section I provide an overview of the contributions of the Mitchell Spectrograph to the study of nearby galaxies. This might not be a complete compilation of papers in the literature that use Mitchell data but rather a selection of the most relevant works to the field of nearby galaxy astrophysics that I am aware of and that are based on Mitchell Spectrograph data.

3.1. Stellar Populations: The Assembly of Nearby Spheroids and Disks. By modeling the relative strength of different absorption features in the integrated stellar spectrum of galaxies or regions within galaxies we can estimate relevant physical properties of the stellar populations that are present (e.g., [31, 32]). Integral field spectroscopy provides two important advantages at the time of conducting this type of measurement in nearby galaxies. First, the two-dimensional nature of the data allows one to study stellar populations as

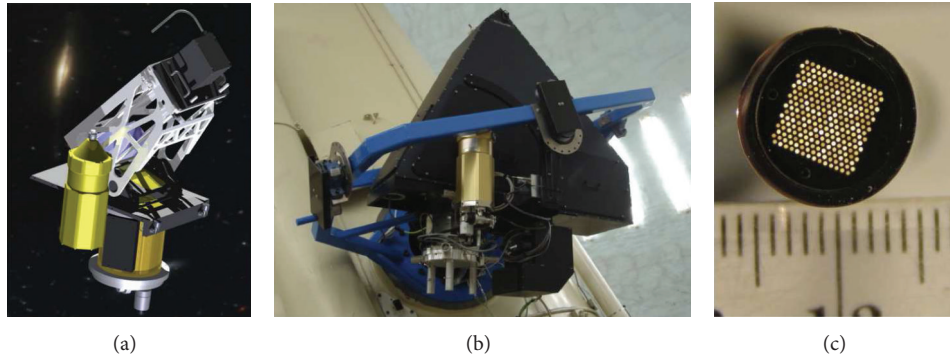


FIGURE 1: The Mitchell Spectrograph. (a) Diagram showing the interior of the instrument. The casing of the fiber output pseudoslit can be seen in black at the top right, from there light is reflected onto the collimator mirror (purple), back onto a flat mirror at the position of the pseudo-slit, and down through the VPH grating (yellow) and into the Schmidt camera at the bottom of the spectrograph (gold). Dispersed light is reimaged onto a Fairchild Instruments 2048 × 2048 backside illuminated, antireflection coated CCD. The liquid N₂ dewar is also shown in the foreground. (b) The Mitchell Spectrograph installed on the broken Cassegrain focus of the 2.7 m telescope. The gimbal mount can be seen in blue. (c) A zoom into the input head of the 246 fiber IFU.

a function of position or environment within galaxies in a way that is challenging for slit spectroscopy. Second, integral field spectroscopy allows the observer to integrate the spectra over large arbitrarily shaped regions across nearby galaxies. Smart binning schemes can be used to boost the signal to noise (S/N) of the spectra allowing the measurement of stellar population parameters in low surface brightness regions. The latter, combined with the good low surface brightness sensitivity at the native spatial resolution of IFUs with large spaxels like the Mitchell Spectrograph (4.2'' diameter fibers), has opened a new avenue in the study of stellar populations in nearby galaxies by permitting measurements at large galactocentric radii. This is important as, in a hierarchical universe like the one we live in, the outskirts of galaxies can provide valuable information regarding their merging and gas accretion history.

Almost all aspects of galaxy formation and evolution are encoded in the physical properties of the stellar populations present in galaxies. The metallicities, abundance ratios, and ages of different generations of stars across a galaxy are set by the history of gas accretion, star formation, and feedback induced outflows within the galaxy itself and its accreted satellites. The Mitchell Spectrograph has been used to study stellar populations in both nearby early-type (E, S0) and spiral galaxies.

Elliptical galaxies have long been known to show color gradients with bluer colors towards their outer regions (e.g., [33]). Spectroscopic stellar population studies have shown that these color gradients are mainly driven by gradients in metallicity with the abundance of metals decreasing towards larger radii (e.g., [34, 35]). In view of the recent discovery of a population of massive compact passively evolving galaxies at $z = 1 - 2$ [36, 37] and the dramatic size evolution implied if one attempts to link these objects as progenitors of present day elliptical galaxies, studying the stellar populations present in the halos of nearby massive ellipticals can shed light on the processes that drive this evolution. The most likely scenario currently invoked to explain the growth of the outer halo

of early type galaxies is late time minor merging at $z < 1$ ([38, 39]).

In Greene et al. [21] the authors use the Mitchell Spectrograph to observe a sample of eight nearby (~ 85 Mpc) early type galaxies (six ellipticals and two S0s) with the goal of conducting a spatially resolved stellar population analysis out to large radii ($2.5 R_e$). In only 40 minutes of effective exposure time per fiber (i.e., per dither) and after coadding the spectra in elliptical annuli with a width of $0.5 R_e$ ($\sim 4''$ or one fiber at the typical distance of the targets) they are able to reach S/Ns ~ 40 in continuum for the outermost radial bins at $2.5 R_e$. Figure 2 shows an example of the azimuthally binned spectra for NGC 7509. Using these high S/N spectra the authors can make quality measurements of the EWs of the H β , Mgb, and $\langle \text{Fe} \rangle$ absorption features out to large galactocentric radii (see Figure 2). These spectral indexes are used to derive gradients in age, metallicity [Fe/H], and α -abundance [α/Fe].

A common trend in all the galaxies observed in Greene et al. [21] is the presence of a steep gradient in the Mgb EW which drops towards the outer regions while the $\langle \text{Fe} \rangle$ and H β indexes remain roughly flat out to $2.5 R_e$. Modeling the observed EWs the authors find that this average behavior is driven by significant [Fe/H] gradients in the majority of the galaxies accompanied by a subtler gradient in [α/Fe] which decreases slightly towards large radii. This is the first detection of an [α/Fe] gradient in elliptical galaxies.

One interesting result of this study is the observed change in behavior of the well established Mgb- σ_* relation [40, 41] when considering regions at larger distance from the galaxy nucleus. Within R_e elliptical galaxies show a tight correlation between the Mgb index and the effective stellar velocity dispersion. Greene et al. [21] find that if one measures Mgb in regions outside R_e the normalization of the Mgb- σ_* relation decreases, the scatter increases significantly, and there are indications of a steepening. These effects are stronger towards larger radii. They reflect a clear change in the stellar populations of the outskirts of early type galaxies with respect to their centers and are consistent with a scenario

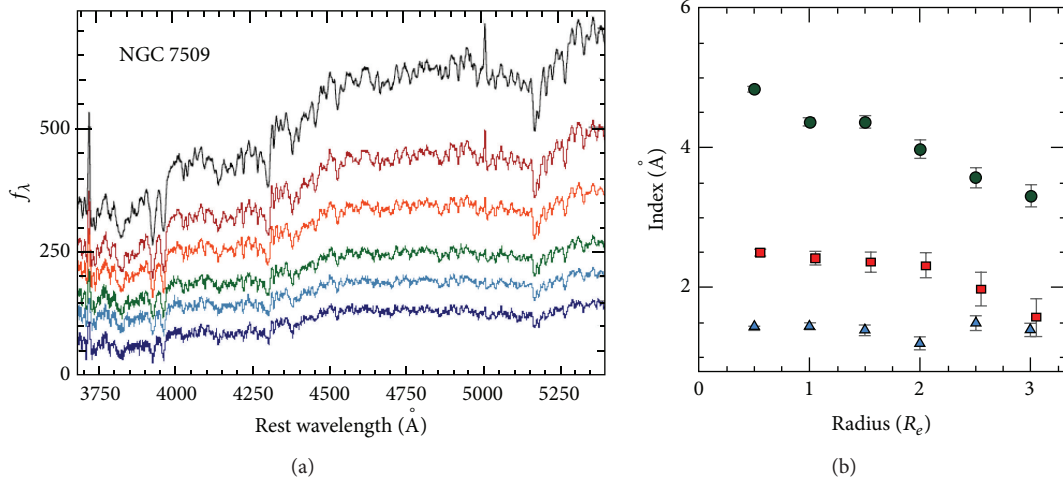


FIGURE 2: (a) Coadded spectra in elliptical annuli at $0 - 0.5 R_e$, $0.5 - 1 R_e$, $1.5 - 2 R_e$, and $2 - 2.5 R_e$ (from top to bottom) for NGC 7509. (b) Index EW radial profiles for Mg b (green), $\langle Fe \rangle$ (red), and H β (blue). Taken from Greene et al. [21].

in which the stellar halos of elliptical galaxies are formed by the accretion of objects formed at earlier times in small halos that have truncated star formation histories.

By matching the observed Mg b EW at $>2 R_e$ to galaxy mass using the relations of Graves et al. [42] the authors find that the stellar halo of present day ellipticals was most likely formed by the accretion of satellites with stellar masses which are typically a factor of ~ 10 smaller than the central object. The data also implies that the progenitors of the stellar halo had lower metallicities and higher α -abundance than present day ellipticals of similar masses. This is in contrast with predictions from the “monolithic collapse” scenario in which α -abundances are lower than expected in the stellar halo as winds can eject metals more easily than from the central regions where the potential is deeper [43]. The authors conclude that “*the outer parts of these galaxies [massive ellipticals] are built up via minor merging with a ratio of $\sim 10 : 1$, but that the accreted galaxies did not have sufficient time to lower their α -abundance ratios to those seen in $\sim L_*$ elliptical galaxies today.*”

The Mitchell Spectrograph has also been used to study the stellar populations in the outskirts of late-type star forming disk galaxies by Yoachim et al. [19, 20]. These two papers are aimed at studying the nature of breaks in the exponential surface brightness profiles of disk galaxies at large radii. Pohlen and Trujillo [44] used the Sloan Digital Sky Survey (SDSS) to show that the majority (60%) of late-type disk galaxies in the local universe show truncated exponential profiles which transition to a steeper exponential at some break radius typically found at 1.5–4.5 times the scale length of the inner component. Of the rest of their sample, 30% show shallower exponential profiles outside the break radius, and 10% can be best fit by a single component.

The classical explanation for the existence of a truncation in the edge of disk galaxies is the presence of a star formation threshold [45] or more likely a significant drop in the star formation efficiency in the low gas surface density environments typical of the outskirts of galaxies [46]. Work by Schrub

et al. [47] has shown that this low star formation efficiency at large radii is caused by a low-molecular-to-atomic gas fraction and not by an actual drop in the star formation efficiency of molecular gas. On top of in situ star formation, another process that could be important at populating the outskirts of disk galaxies is secular stellar migration caused by gravitational interactions with disk structure (e.g., [48, 49]). Since stellar migration is a random walk stars require longer times to venture further out in the disk. Therefore if the stellar populations beyond the edges of disks are dominated by this process we expect to observe significant changes in stellar population parameters beyond the break radius, where the contrast between migrated and formed in situ stars is the greatest and the ages of migrated stars are the oldest.

In Yoachim et al. [20] the authors observe a sample of twelve nearby spiral galaxies chosen to match the Mitchell Spectrograph field of view. The bulk of the sample (9/12) shows truncated photometric profiles, one object shows an upbending profile, and the remaining two galaxies are best fit by single exponentials. In only 20–45 minutes of effective exposure time and after binning the spectra in $4''$ wide elliptical annuli they obtain spectra deep enough ($S/N \sim 40$) to measure stellar population parameters down to a V -band surface brightness 23–24 mag arcsec $^{-2}$. This allows them to successfully measure ages outside the break radius for six galaxies in the sample (all of them with downbending profiles).

An interesting contribution from this work comes from the detailed study that the authors do of the systematics associated measuring stellar population parameters in late-type systems. While individual absorption features (e.g., Lick indices) have been successfully used to study the stellar populations of old passively evolving early-type galaxies (as in the Greene et al. [21] study described above), they are not reliable tools to use for studying star forming objects. The multiple generations of stars present in the disks of spiral galaxies due to their extended star formation histories (SFH) and the presence of significant dust extinction complicate

the interpretation of Lick indices as degeneracies between different populations are introduced (e.g., [50]). The two approaches that are typically used to overcome this problem are the fitting of linear combinations of single stellar populations (SSP, e.g., [51, 52]) and the use of parametrized SFHs to construct composite stellar populations (e.g., constant and exponentially declining or increasing SFHs, a.k.a. $\pm\tau$ models). After conducting detailed simulations the authors recommend and adopt the latter approach as linear combinations of SSPs are found to perform poorly in the young age and low metallicity regimes. It is worth noting though that these problems, which arise from degeneracies among the large number of parameters inherit to the linear combination of many SSP templates, can be overcome to some extent by using regularization schemes that limit the solutions to conform with certain imposed conditions (e.g., smoothness of the SFH, [52]).

Three of the six disks for which age measurements could be conducted beyond the profile break in Yoachim et al. [20] show evidence for a significant contribution from stellar migration to the stellar populations beyond the truncation radius. This is seen as an upbend in the stellar age radial profile at a position close to the surface brightness profile break and a transition from increasing SFHs to decreasing SFHs towards large radii. In these three objects the changes in stellar population parameters are also clearly seen in the radial profiles of the D4000 and Balmer absorption indices. Two of these objects also show a decrease in stellar metallicity which is correlated with the increase in age at large radii. No significant change in metallicity is seen for the third system. The authors warn that their metallicity measurements are “rather crude” as their SFHs do not include a chemical enrichment model.

For the other three objects with good stellar population measurements at large radii the authors find “*little or no sign of the outer disk being formed through stellar migration despite having some of the strongest profile breaks*”. Although these objects do not show up bending age profiles at large radii like the ones discussed above, they do show a flattening in the stellar age profile towards large radii. An interesting result, although based on low number statistics, is that the objects with the weakest profile breaks show the strongest evidence for radial migration and the objects with the strongest profile breaks show young stars most likely formed in situ in the outer disk. This is consistent with stellar migration as objects which have experienced the most migration should have the weakest profile breaks. Given the wide range of stellar population behaviors found beyond the profile breaks of these galaxies the authors conclude that “*while radial migration can contribute to the stellar populations beyond the break, it appears that more than one mechanism is required to explain all of our observed stellar profile breaks*”.

3.2. Galaxy Dynamics: Dark Matter Haloes and Super Massive Black Holes. Dark matter is a fundamental mass component in galaxies and drives both the dynamics and evolution of these systems. Similarly SMBHs, which appear to live in the center of all massive galaxies in the universe, seem to be closely linked to the evolution of the central stellar component of galaxies as are evidenced by the tight correlations

seen between black hole (BH) mass (M_{BH}) and the stellar velocity dispersion, stellar mass, and luminosity of central stellar spheroids ([53–55] and references therein). It is not well established if this link is caused by the effects of AGN feedback following gas accretion or simply by the averaging effects of subsequent mergers (e.g., [56, 57]). Both dark matter and SMBHs affect the dynamics of stars and gas in galaxies in a way that can be significantly detected using modern spectroscopic techniques. The Mitchell Spectrograph has been systematically used to measure the stellar and gaseous dynamics of nearby galaxies in order to put constraints on the shape of the DM halos in that they inhabit and the masses of their central SMBHs.

A problem that has received a lot of attention in the last decade is the apparent discrepancy between the cuspy DM halo profiles predicted by cosmological N-body simulations (e.g., NFW, [58]) and observations of low surface brightness and late-type dwarf galaxies which suggest the presence of cored DM halos (e.g., [59–61]). In Adams et al. [13] the authors use the 2400 lines mm^{-1} grating in the Mitchell Spectrograph which provides a velocity resolution of 40–60 km s^{-1} to measure the stellar and ionized gas kinematics of the late-type dwarf galaxy NGC 2976. This galaxy was one of the cleanest examples of a cored DM halo based on ionized gas kinematics [59]. The goal of Adams et al. [13] study is to constrain the shape of the DM halo in NGC 2976 by using a noncollisional dynamical tracer of the potential (i.e., the stellar component) and compare the results to those obtained using gas kinematics.

Using a mass model based on a multi-Gaussian expansion fit to the R -band and HI 21 cm maps to account for the stellar and atomic gas components and conducting an anisotropic Jeans modeling of the second moment velocity field $V_{\text{rms}} = \sqrt{V_{\text{los}}^2 + \sigma^2}$, [62] the authors put simultaneous constraints on the inner slope of the DM halo profile α and the R -band stellar mass-to-light ratio $Y_{*,R}$. The results from this fitting are shown in Figure 3. The authors find that if both the profile slope and the mass-to-light ratio are fitted freely, both parameters are highly correlated and no significant statistical distinction can be made between the cusp and core scenarios (Figure 3(a)). In this case the best-fit value for $Y_{*,R}$ is 3.49 which is largely inconsistent with the $Y_{*,R} = 1.1 \pm 0.8$ value derived from synthetic stellar population fits to both the integrated spectrum and the optical through near-IR photometric SED of the galaxy. Repeating the fit adopting the value and uncertainty of the mass-to-light ratio derived from stellar populations yields the constraints shown in Figure 3(b). If a realistic value of the stellar mass-to-light ratio is adopted, a cuspy DM halo ($\alpha = 1$) profile is consistent with the observed stellar dynamics while a cored profile ($\alpha = 0$) is rejected at 2.2σ significance. This is at odds with the results of Simon et al. [59] where the ionized gas velocity field measured from H α is better fit by a cored model.

In Adams et al. [13] the authors also measure the ionized gas velocity field using the [OII] λ 3727 doublet. Modeling the gas dynamics with a harmonic decomposition method [63] similar to the one used by Simon et al. [59] yields results that are consistent with that study. That is, a cored DM halo is preferred. On the other hand using a tilted-ring model

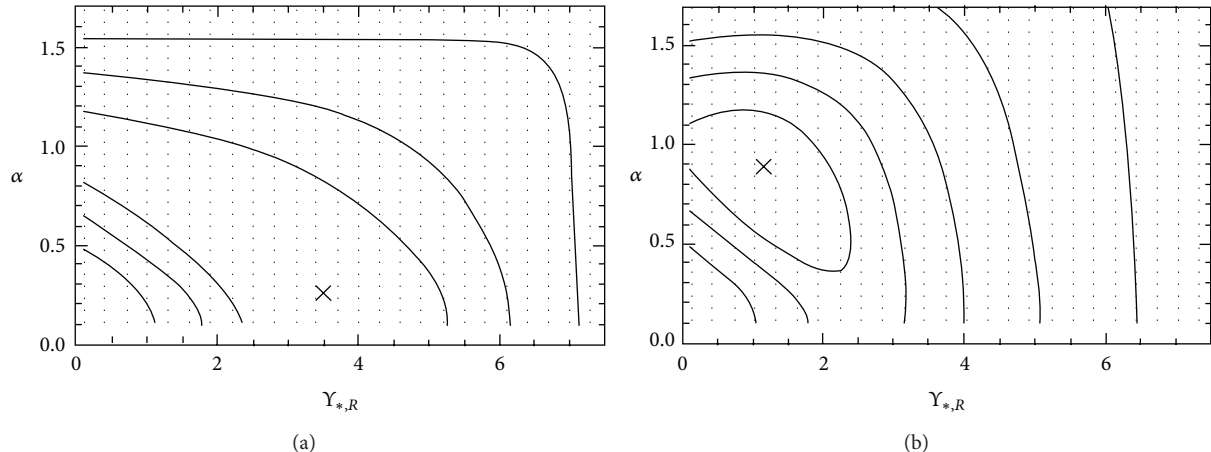


FIGURE 3: Confidence intervals for the inner slope of the DM halo (α) and the R -band mass-to-light ratio ($Y_{*,R}$) for NGC 2976. The left panel shows the result of leaving both parameters free while fitting. The right panel shows the same fit but constraining $Y_{*,R}$ to lie within the limits allowed by a synthetic stellar population fit to the integrated optical spectra and SED of the galaxy. Taken from Adams et al. [13].

with a variable position angle to fit the velocity field [64] excludes a cored model and is compatible with the results from the stellar kinematics analysis. These discrepancies highlight the challenges faced by measurements of the radial mass profile of DM halos, where results can depend on both the adopted dynamical tracer of the gravitational potential and the methodology used to model the observed dynamics. The authors conclude that *“the analysis of this first galaxy shows promising evidence that dark matter halos in late-type dwarfs may in fact be more consistent with cuspy dark matter distributions than earlier work has claimed”*.

The Mitchell Spectrograph has also been used to study the properties of DM halos in massive early type galaxies. Murphy et al. [12] measures stellar kinematics in the second-rank galaxy of the Virgo cluster M87 out to $238''$ ($\sim 2 R_e$) by tiling five IFU pointing. The authors complement the dataset with higher spatial resolution IFU spectroscopy from SAURON [65] in the inner $13''$ of the galaxy and globular cluster (GC) kinematics out to $540''$ ($\sim 5 R_e$). By fitting this extended kinematical information with axisymmetric orbit-based dynamical models [66, 67] the authors constrain the mass and shape of the dark matter halo in M87 as well as the V -band stellar mass-to-light ratio ($Y_{*,V}$) and the behavior of the stellar velocity ellipsoid (SVE) as a function of radius for this system. A central SMBH with a mass of $6.6 \times 10^9 M_\odot$ is included in the dynamical models ([8]; see below).

The authors find that the dynamics of M87 are best described by a logarithmic DM halo (i.e., a flat core in the center that transitions to a $\rho \propto r^{-2}$ profile at radius r_c), which is statistically preferred over a classical cuspy NFW profile. Models without a DM halo are excluded at high significance. Out to $5 R_e$ the best-fit logarithmic halo implies a total enclosed mass in the system of $5.7_{-0.9}^{+1.3} \times 10^{12} M_\odot$ making M87 one of the most massive galaxies in the local universe, with dark matter accounting for 17%, 49%, and 85% of the total mass at 1, 2, and $5 R_e$, respectively. The stellar mass-to-light ratio is constrained to be $Y_{*,V} = 9.1 \pm 0.2$. Interestingly the inclusion of the GC kinematics reaching out to large radii

has a significant impact on the derived value of $Y_{*,V}$ yielding much higher values if this data is ignored. This is because the kinematics at large radii strongly influence the measurement of the total enclosed mass in the DM halo so any mass not assigned to the dark matter component artificially boosts the mass-to-light ratio of the stars.

The addition of the Mitchell Spectrograph data extends the stellar kinematics in M87 to larger radii by about an order of magnitude compared to what had been achieved with previous IFU and long-slit datasets (e.g., [68]). This has a significant impact on the derived values of the circular velocity and core radius of the DM halo and highly reduces the covariance between these two parameters seen in previous datasets covering only the central parts of the galaxy. This, together with the impact of the GC kinematics on the derived mass-to-light ratio discussed above, highlights the importance of measuring kinematics out to large radii when studying the dynamics of nearby galaxies. This is an area in which wide field of view IFU spectroscopy is having a tremendous impact.

Finally, in Murphy et al. [12] the orbital structure in the best-fit dynamical model implies a drastic change in the anisotropy of the SVE at around $0.5 R_e$. Within this radius stars show a significant amount of radial-to-tangential anisotropy ($\sigma_r/\sigma_t \sim 1.1$) while outside this radius the orbits become mildly tangentially anisotropic ($\sigma_r/\sigma_t \lesssim 1$). Although the authors do not explore the origin of this behavior they state that it can be related to the formation mechanism that gave rise to this system.

An accompanying paper to Murphy et al. [12] is that by Gebhardt et al. [8] which discusses the mass of the SMBH in the center of M87. Here the authors add adaptive optics (AO) corrected Gemini NIFS integral field spectroscopy to the SAURON+Mitchell Spectrograph dataset discussed above. The AO data provides spatially resolved kinematics for the central $2''$ (170 pc) of the galaxy at $0.08''$ (7 pc) FWHM spatial resolution and therefore resolves the region where the kinematic influence of the SMBH is important.

The degeneracy discussed above between the DM halo mass and the stellar mass-to-light ratio has an impact on the determination of SMBH masses when the sphere of influence of the BH is not resolved. Neglecting or underestimating the dark halo artificially increases the mass-to-light ratio in the stellar component which translates into underestimated BH masses in the best-fit dynamical models (factors of two are common, e.g., [68]). Therefore if the relatively expensive high spatial resolution data (HST or AO) is not available, one can only expect to be able to measure unbiased BH masses if the DM halo is well constrained by kinematic measurements at large radii.

After removing any contamination from the AGN and the jet in the nucleus of M87 and doing a detailed modeling of the AO PSF in the NIFS data Gebhardt et al. [8] measure a SMBH mass of $6.6 \pm 0.4 \times 10^9$. The previously reported covariance between BH mass, mass-to-light ratio, and dark halo parameters seen in Gebhardt and Thomas [68] disappears once the AO data is included. That is, directly resolving the sphere of influence of the BH yields unbiased BH masses that are independent of the inclusion of the dark halo. The authors further test this by excluding the large radii kinematics ($>100''$) from their modeling finding a modest 2% (0.5σ) drop in the BH mass. The similarity between the measured BH mass and its uncertainty in this study and the $6.4 \pm 0.5 \times 10^9 M_\odot$ BH mass measured by Gebhardt and Thomas [68] support the idea that unbiased BH masses can be accurately measured if the DM halo is properly modeled and constrained by large scale kinematic measurements which wide field integral field spectrographs like the Mitchell Spectrograph provide. The authors conclude that *“if one has sufficient signal to noise and two-dimensional coverage (e.g., SAURON or VIRUS-P), then it should be possible to measure a BH mass robustly. Thus, it is not necessarily required to resolve the region influenced by the BH. Being able to use data that do not resolve well the BHs influence on the kinematics allows us to study BHs that are either distant or of low mass. Both of these regimes are important for understanding the physical nature of the BH correlations with the host galaxy”*.

A similar study is that by McConnell et al. [10] who also use AO corrected IFU spectroscopy from Gemini+NIFS and Keck+OSIRIS in combination with Mitchell Spectrograph data at large radii to measure the SMBH mass in four brightest cluster galaxies (BCGs) in nearby clusters. Using the same dynamical modeling techniques as Gebhardt et al. [8] they measure SMBH masses of $2.1_{-1.6}^{+1.6} \times 10^{10} M_\odot$ for NGC 4889, $9.7_{-2.5}^{+3.0} \times 10^9 M_\odot$ for NGC 3842, and $1.3_{-0.4}^{+0.5} \times 10^9 M_\odot$ for NGC 7768, while putting an upper limit of $<9.0 \times 10^9 M_\odot$ on the central BH mass in NGC 2832. The results for two of these objects (NGC3842 in Abell 1367 and NGC 4889 in the Coma Cluster) were previously reported in McConnell et al. [9] as the two highest BH masses ever measured in the local universe.

Interestingly the measured BH masses in all these objects are systematically higher than those predicted by even the steepest versions of the $M_{\text{BH}} - \sigma$ relation found in the literature. For NGC 4889 and NGC 3842 the deviations are in excess of the intrinsic scatter in the relation. A similar trend

is seen when comparing the measured values to predictions from the $M_{\text{BH}} - L$ (i.e., black hole versus bulge luminosity) relation and from less well established relations between BH mass and DM halo mass or circular velocity. The authors state that the data suggests a steepening in the $M_{\text{BH}} - \sigma$ relation at the high mass end. Such a steepening is expected if the most massive elliptical galaxies form by means of “dry” (i.e., gas poor) mergers of early-type systems. Furthermore, both McConnell et al. [10] and Gebhardt et al. [8] observe significant tangential anisotropy in the orbital structure in the centers of these galaxies over spatial scales comparable to their photometric cores. A depletion of radial orbits in the centers of these systems is consistent with a scenario in which following a merger a binary BH preferentially ejects stars on radial orbits from the central regions.

In McConnell et al. [11] the authors extend the dynamical modeling on NGC 4889, NGC 3842, and NGC 7768 to allow the inclusion of a spatial gradient in the stellar mass-to-light ratio Y in order to study the systematic effects that this quantity has on the derived BH masses. It is standard practice in this type of dynamical modeling to assume a constant Y across the galaxy therefore equating the stellar surface density to the surface brightness in a given band. On the other hand, as we mentioned above when discussing the stellar population work of Greene et al. [21], many of these systems show gradients in broad-band colors and absorption line indexes which are caused by underlying changes in the metallicity and star formation history of the stellar populations. McConnell et al. [11] modify the code by Gebhardt et al. [53] in order to include a radial gradient in Y which they parameterize as $\alpha = d \log(Y)/d \log(r)$ and rerun the fitting for a grid of values in the $-0.2 < \alpha < 0.1$ range. This range covers the values allowed by current constraints on the broad-band color and stellar population gradients of these objects which support a slightly negative value for α . For example, stellar population modeling of the Mitchell Spectrograph data in NGC 3842 implies $\alpha = -0.13 \pm 0.30$.

The authors find a $\sim 25\%$ decrease in the BH mass as α is decreased from 0 to -0.2 . For two of the three galaxies this difference is comparable to the statistical uncertainties in the measured BH mass so the effect is significant. Models with positive α are mildly disfavored by the data, which is consistent with the negative color gradients of the three objects, and yield higher BH masses. It is seen that introducing a gradient with a negative value moves more stellar mass in the dynamical models to smaller radii, therefore requiring lower BH masses to explain the kinematics. This also translates into slightly more massive DM halos necessary to compensate for the lower stellar mass at large radii. This effect might prove important not only for individual BH mass determinations in systems with strong stellar population gradients but also for determining the slope of BH mass scaling relations. The authors state that *“A systematic variation in α with galaxy stellar mass or velocity dispersion can have an impact on the slopes of the $M_{\text{BH}} - M_{\text{bulge}}$ and $M_{\text{BH}} - \sigma$ scaling relations, which are currently determined assuming $\alpha = 0$ ”*.

3.3. *The ISM of Nearby Star Forming Galaxies.* Nebular emission lines at optical wavelengths are important coolants for

ionized gas in HII regions and are therefore typically bright in star forming galaxies. The observed brightness and line ratios of these transitions have been used extensively in the literature to determine important quantities like metallicity, ionization parameter, electron density, dust extinction, and the SFR ([69] and references therein). Furthermore, AGN activity, shocks, and diffuse ionized gas in the ISM can also contribute significantly to the nebulae emission line spectrum of galaxies. The Mitchell Spectrograph has been widely used to study the star formation activity and the properties of ionized gas in nearby star forming galaxies.

A fundamental aspect of galaxy evolution is the formation of stars from cold gas in the ISM. Star formation gives rise to galaxies and drives their evolution by building up their stellar mass, injecting energy and metals into the ISM, and consuming their gas reservoirs. Understanding what sets the SFR in the different environments present within galaxies is therefore of great importance. In Blanc et al. [17] the authors use data gathered as part of the VIRUS-P Exploration of Nearby Galaxies (VENGA, Blanc et al. [29], Section 3.4.1) to study the spatially resolved star formation law (SFL, a.k.a. the Schmidt-Kennicutt Law) in the inner disk of the nearby spiral galaxy NGC 5194 (a.k.a. M 51a). The SFL is the relation between either the atomic, molecular, or total gas surface densities (Σ_{HI} , Σ_{H_2} , $\Sigma_{\text{HI}+\text{H}_2}$) and the SFR surface density (Σ_{SFR}). It has been long known that when integrated measurements of these quantities are made over disk galaxies and starburst nuclear regions in nearby galaxies the total gas surface density correlates with the SFR surface density with relatively small scatter and a slope $N \approx 1.5$ over several orders of magnitude in both quantities [70]. Spatially resolved measurements of the SFL at sub-kpc scales have shown that it is the molecular gas component of the ISM that drives this correlation while the atomic gas surface density and the SFR surface density are largely uncorrelated on small scales (10^{2-3} kpc, e.g. [71, 72]).

Different authors measure different slopes for the spatially resolved molecular SFL with some favoring a value close to $N \sim 1.5$ (similar to that of the integrated SFL, e.g., [71, 73]) while others find slopes closer to unity or slightly lower (e.g., [17, 72, 74, 75]). Determining the slope of this correlation is important as different theoretical models attempting to explain the process of star formation on galactic scales make different predictions regarding its value (e.g., [76–78]). In Blanc et al. [17] the authors combine the Mitchell Spectrograph data with CO (1-0) and HI 21 cm maps from the literature to study the atomic and molecular SFL at ~ 200 pc scales across the inner disk of the galaxy. They use the Balmer decrement to calculate nebular dust extinctions and correct the observed $\text{H}\alpha$ fluxes in order to measure Σ_{SFR} . A major advantage of using integral field spectroscopy comes from the ability to use different emission line ratio diagnostics to identify regions contaminated by AGN photoionization and shocks and to separate the contribution to the $\text{H}\alpha$ flux from extraplanar diffuse ionized gas and localized star formation in the disk of the galaxy (i.e., HII regions).

The authors find that the level of discrepancy seen in the slope of the molecular SFL in the literature can be partly

attributed to systematic biases associated with the different linear regression methods used to fit the correlation. They propose a new Monte Carlo based method for fitting SFL which includes the intrinsic scatter in the relation as a free parameter and is unbiased. This method has been used latter by Leroy et al. [79] who provide a detailed analysis of its robustness. Using this new fitting method Blanc et al. [17] find no correlation between Σ_{SFR} and Σ_{HI} , in agreement with previous studies, a clear correlations between Σ_{SFR} and Σ_{H_2} with a slope $N = 0.82$, and a typical gas depletion timescale $\tau = \Sigma_{\text{HI}+\text{H}_2}/\Sigma_{\text{SFR}} \approx 2$ Gyr (see Figure 4). At ~ 200 pc resolution the molecular SFL shows an intrinsic scatter $\epsilon = 0.43 \pm 0.02$ dex in good agreement with the measurements by Schrubba et al. [80] and Leroy et al. [79]. These results reject a superlinear molecular gas SFL in NGC 5194 at high significance in agreement with the work of Bigiel et al. [46]. This has been latter confirmed using Bayesian inference by Shetty and Ostriker [81]. In Blanc et al. [82] the authors fit the data of Kennicutt et al. [71] using the method proposed by Blanc et al. [17] and derive a best-fit slope of $N = 1.0$, in contrast with the $N = 1.56$ value derived by the original study. It is currently thought that the steeper slope seen for the integrated SFL arises from a combination of two effects. First, a drop of the molecular-to-atomic gas fraction at low densities which steepens the correlation between the SFR and the total gas surface densities and a true steepening of the small scale molecular SFL in the high surface density regime of starbursts caused by a physical transition in the properties of GMCs in an overpressurized ISM (e.g., [76]). Under the normal conditions typical of the disks of spiral galaxies the relation between Σ_{H_2} and Σ_{SFR} on 10^{2-3} pc scales is roughly linear. Studies such as Blanc et al. [17] showcase the power of combining optical IFU spectroscopy with observations at other wavelengths (e.g., radio, mm) to obtain a complete picture of the ionized, atomic, and molecular ISM and its relation to the stellar component of galaxies.

A major observational challenge faced by star formation and ISM studies in general is the proper characterization of molecular gas. Measuring and studying molecular gas in galaxies are fundamental to understand star formation and the physical processes setting the balance between the different phases of the ISM. Molecular hydrogen (H_2) amounts for the bulk of the mass in molecules in the universe, but its transitions are rarely excited at the typically cold temperatures (~ 10 K) of gas inside giant molecular clouds (GMCs). To overcome this observational difficulty, the second most abundant molecule in GMCs, the carbon monoxide (CO) molecule, is typically used as a proxy for estimating the total mass in H_2 . Rotational transitions of CO observed at millimeter (mm) wavelengths can be easily excited under the typical density and temperature conditions in GMCs and are therefore bright enough to be detectable. Using CO emission to estimate the H_2 mass requires knowledge of the CO intensity to H_2 column density conversion factor X_{CO} and, while evidence exists that this factor changes in different environments, it is common usage in the literature to assume it has a constant value ([85], and references within).

Blanc et al. [16] use Mitchell Spectrograph observations of the nearby face-on grand design spiral NGC 628 (also

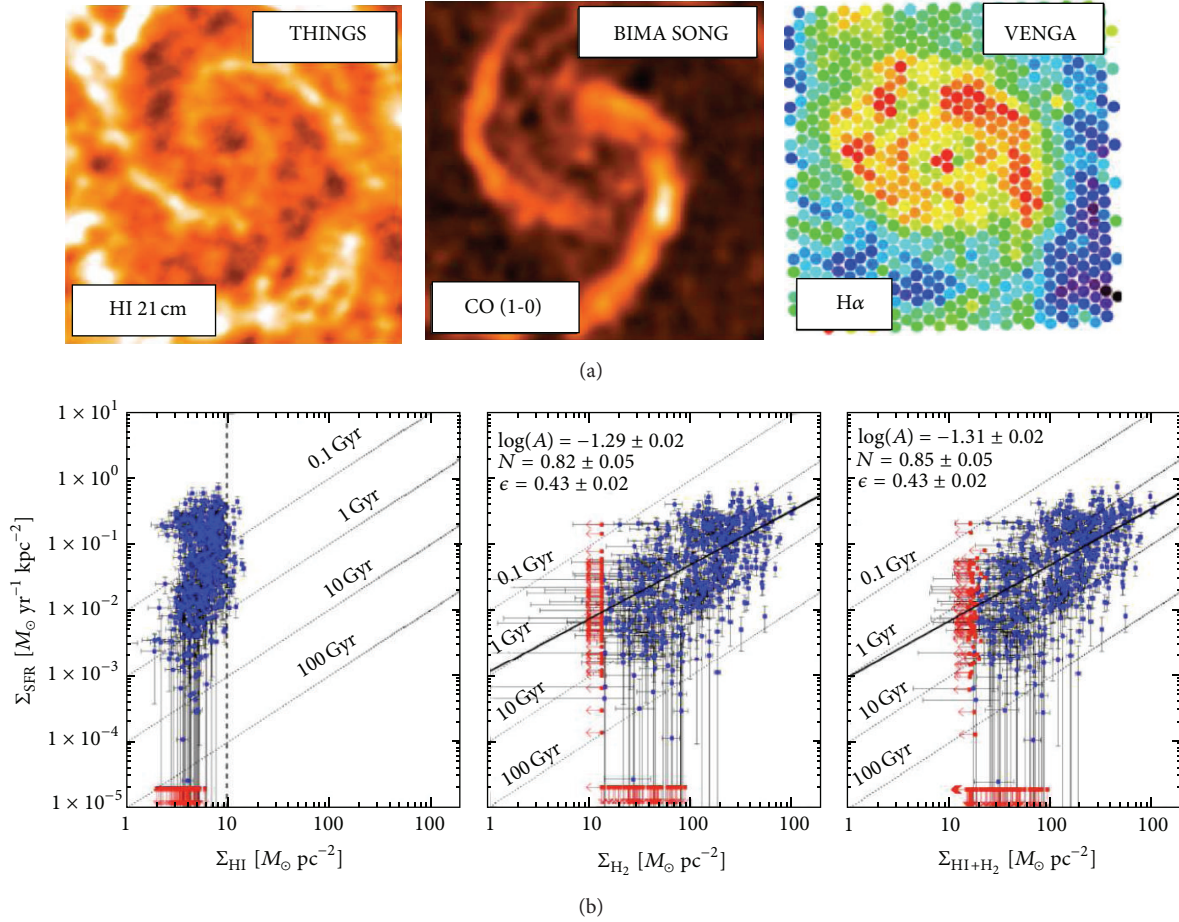


FIGURE 4: (a) Maps of the HI 21 cm, CO (1-0), and H α emission (from left to right) from the THINGS [83], BIMA-SONG [84], and VENGA [29] surveys used in Blanc et al. [17] to study the spatially resolved SFL in the central 4 kpc of NGC 5194. (b) The HI, H $_2$, and total SFL as measured by Blanc et al. [17]. Each blue dot corresponds to a single Mitchell Spectrograph fiber. Upper limits are shown in red and dotted lines show lines of constant depletion time. The best-fit relations are also shown as well as the corresponding best-fit parameters.

taken as part of VENGA; see Section 3.4.1) in combination with CO (1-0) and CO (2-1) maps from different sources as well as *Spitzer* 24 μ and *GALEX* far-UV data to look for changes in the CO-to-H $_2$ conversion factor X_{CO} across the disk of this galaxy. Their method consists in inverting the molecular gas SFL to estimate the H $_2$ surface density from the SFR surface density. By comparing this estimate to the observed CO surface brightness they measure the radial X_{CO} profile in NGC 628.

This study finds a drop by a factor of 2 in X_{CO} from $R \sim 7$ kpc to the center of the galaxy, implying brighter CO emission at a given H $_2$ surface density in the central regions. Using line ratio diagnostics from the Mitchell Spectrograph data they can measure how the metallicity and the ionization parameter change across the disk of the galaxy and study how changes in X_{CO} follow changes in these quantities. By comparing to theoretical models for CO radiative transfer in the ISM [86, 87] they show that the observed gradient in X_{CO} can be explained by a combination of decreasing metallicity, and decreasing Σ_{H_2} with radius. Photoelectric heating from the local UV radiation field appears to contribute to the decrease

X_{CO} in higher density regions. The authors state that “Our results show that galactic environment plays an important role at setting the physical conditions in star forming regions, in particular the chemistry of carbon in molecular complexes, and the radiative transfer of CO emission. We caution against adopting a single X_{CO} value when large changes in gas surface density or metallicity are present”.

The Mitchell Spectrograph has also been used to study nebular chemical abundances in nearby galaxies. Integral field spectroscopy allows one to measure gas-phase metallicity gradients in spiral galaxies in an efficient manner, as spectra for multiple HII regions can be obtained in a single IFU pointing. Robertson et al. [88] take advantage of this fact and use the Mitchell Spectrograph to study how the gas-phase metallicity of cluster spiral galaxies depends on HI deficiency. As infall into the intra-cluster medium can remove gas from galaxies by means of ram pressure and tidal stripping and cutoff of the accretion of low metallicity IGM gas into these systems (strangulation), one can expect the environment to affect the chemical enrichment of galaxies by regulating the amount of gas available for star formation and mixing enriched and pristine gas in the ISM.

In Robertson et al. [88] the authors observe six spiral galaxies in the Perseus I cluster with the Mitchell Spectrograph and measure their metallicity gradients using the R23 strong line method of Zaritsky et al. [89]. In about 1 hr of effective exposure time per dither the authors obtain reliable measurements of $H\beta$ and the [OII] and [OIII] doublets for about a dozen HII regions in each galaxy. At the distance of Pegasus I the targets easily fit in the Mitchell Spectrograph field of view. They estimate a characteristic metallicity for each galaxy from the radial metallicity profile and compare this to the HI deficiency parameter (DEF) measured by Levy et al. [90] which quantifies the deviation in HI content with respect to the average expectation value given a galaxy luminosity and Hubble type. A clear correlation between metallicity and DEF is observed with more HI deficient systems showing higher chemical abundances. This is consistent with previous results based on Virgo cluster spirals by Skillman et al. [91].

Robertson et al. [88] test the possibility that the observed correlation is driven by a dependence of DEF with stellar mass combined via the well established mass-metallicity relation of galaxies [92]. They find that for the Pegasus I and Virgo samples DEF is uncorrelated with stellar mass and that using a differential in metallicity with respect to the expectation from the mass-metallicity relation instead of the metallicity absolute value makes the correlation with DEF even stronger. Therefore they conclude that HI deficiency (either by gas removal or strangulation) has a significant effect on the level of chemical enrichment in cluster galaxies in a way that is independent of the stellar mass. The authors compare their results for cluster spirals to a small sample of field galaxies from Zaritsky et al. [89] finding lack of correlation between metallicity and DEF for the latter. This leads them to interpret the observed effect as something particular of dense environments, although a recent extension of their work to a larger and better selected sample of field galaxies shows that the relation between HI deficiency and metallicity is also present in the field and shows a similar slope as that seen in clusters [93].

The Mitchell Spectrograph has also been used recently to study the properties of blue compact galaxies by Cairós et al. [15]. Understanding these type of objects is of great interest as the most massive galaxies in this class are the closest local universe analogs to the high redshift star forming galaxies typically selected using the Lyman break and $Ly\alpha$ techniques. Therefore they offer a window to the conditions under which star formation occurs at high redshift but at a distance at which physical processes can be studied in a spatially resolved manner. Cairós et al. [15] observed the five massive blue compact galaxies II Zw 33, Haro I, NGC 4670, Mrk 314, and III Zw 102 with the Mitchell Spectrograph as part of a long term campaign to obtain integral field spectroscopy of blue compact galaxies. The goal of this study is to characterize the morphology and kinematics of both the stellar and ionized gas components in these objects and to use emission line ratio diagnostics to investigate the spatial distribution of gas ionization and dust extinction. The authors also measure the global gas phase metallicity of these objects from integrated spectra.

While all the objects analyzed in this study show a relatively smooth and regular morphology in the stellar continuum, a large morphological diversity is seen in the ionized gas which displays more complex patterns with some objects revealing filamentary emission and the presence of bubbles and holes. The galaxies display a variety of different ionization patterns as revealed by maps of the [OIII] λ 5007/ $H\beta$ ratio. While in II Zw 33 and Mrk 314 high ionization regions follow star forming regions, as expected from ionization from hot OB stars, NGC 4670 also shows peaks in [OIII]/ $H\beta$ over two filaments seen in ionized gas emission above and below the plane of the galaxy, likely caused by shock excitation. Haro I and III Zw 102 on the other hand simply show a positive radial gradient in the line ratio consistent with the metallicity gradients typically seen in spiral galaxies and with the fact that they are the two most massive objects in the sample. All systems show significant amounts of dust extinction and a variety of kinematical behaviors are present in the sample from rotating disks to complex velocity fields consistent with the presence of multiple kinematic components.

Finally, an extremely interesting application that takes advantage of the superb sensitivity to low surface brightness emission of the Mitchell Spectrograph is the study of Adams et al. [14]. In this work the authors attempt to detect $H\alpha$ emission arising from the rim of the outer HI disk of two edge-on late type disk galaxies (UGC 1281 and UGC 7321) as it becomes ionized by the metagalactic ultraviolet background (UVB). If the atomic gas spatial distribution is known at the edge of the HI disk, then a direct measurement of the $H\alpha$ flux can be directly linked to the strength of the UVB. The authors use deep HI 21 cm VLA data on these objects to fit an exponential HI distribution in both the radial and vertical directions. This profile is then extrapolated to the expected position of the disk rim given by the UVB induced photoionization front. This extrapolation seems reasonable since both of the systems analyzed by Adams et al. [14] show extremely thin disks with minimal warping and no signs of flaring at large radii, as well as no massive nearby neighbors which could disturb their HI disks. Despite this, the authors also attempt a measurement that is independent of the above extrapolation and which yields very similar results.

After obtaining extremely deep exposures (~ 15 hours) using two different gratings providing $R = 1288$ for UGC 1281 and $R = 3860$ for UGC 7321 and trying different binning strategies to coadd the spectra of different fibers, the authors do not detect $H\alpha$ to a 5σ limit in surface brightness of $6.4 \times 10^{-19} \text{ erg s}^{-1} \text{ cm}^{-1} \text{ arcsec}^{-1}$ in UGC 7321 and $25 \times 10^{-19} \text{ erg s}^{-1} \text{ cm}^{-1} \text{ arcsec}^{-1}$ in UGC 1281. The difference in depth between the two galaxies is mainly driven by the higher spectral resolution grating used to observe UGC 7321 and exemplify how the combination of large fiber size and high spectral resolution is ideal to achieve good low surface brightness sensitivity. These limits translate in upper limits for the UVB induced HI photoionization rate of $\Gamma(z=0) < 1.7 \times 10^{-14} \text{ s}^{-1}$ for UGC 7321 and $\Gamma(z=0) < 14 \times 10^{-14} \text{ s}^{-1}$ for UGC 1281. The UGC 7321 is currently the most stringent limit on the strength of the UVB at $z=0$ and falls below the predictions of current theoretical models.

3.4. Nearby Galaxies Surveys. The Mitchell Spectrograph has been used to conduct two surveys of galaxies in the nearby universe. The first of these surveys, the VIRUS-P Exploration of Nearby Galaxies (VENGA, [29]), is focused on the study of normal star forming disk galaxies while the second one, the VIRUS-P Investigation of the eXtreme ENvironments of Starbursts (VIXENS, [18]), is focused on the study of starburst/interacting systems. Here we describe these observing campaigns, their goals, and some recent scientific results that have come out of them.

3.4.1. VENGA: The VIRUS-P Exploration of Nearby Galaxies. VENGA uses the Mitchell Spectrograph to map the disks of 30 nearby spiral galaxies which span a wide range in Hubble type, star formation activity, morphology, and inclination. The Mitchell Spectrograph data can be used to produce 2D maps of the star formation rate, dust extinction, electron density, stellar population parameters, the kinematics and chemical abundances of both stars and ionized gas, and other physical quantities derived from the fitting of the stellar spectrum and the measurement of nebular emission lines. The goal of VENGA is to measure relevant physical parameters across different environments within these galaxies, allowing a series of studies on star formation, structure assembly, stellar populations, chemical evolution, galactic feedback, nuclear activity, and the properties of the interstellar medium in massive disk galaxies.

The survey strategy and data processing methods are thoroughly described in Blanc et al. [29]. The VENGA datacubes have $5.6''$ FWHM spatial resolution and $\sim 5 \text{ \AA}$ FWHM spectral resolution, sample the 3600 \AA – 6800 \AA range, and cover large areas typically sampling galaxies out to $\sim 0.7 R_{25}$. The VENGA sample together with the fields covered by the Mitchell Spectrograph is shown in Figure 5.

VENGA has produced a series of scientific results regarding the properties of the ISM and the process of star formation in nearby spirals. These include the studies on the SFL in NGC 5194 and the X_{CO} gradient in NGC 628 discussed in Section 3.3 [16, 17]. In the near future a series of studies addressing the chemical composition and the kinematics of the ionized gas in nearby spirals are expected to be published.

3.4.2. VIXENS: VIRUS-P Investigation of the Extreme Environments of Starbursts. The VIXENS survey [18] uses the Mitchell Spectrograph to map 15 nearby infrared bright ($L_{\text{IR}} > 3 \times 10^{10} L_{\odot}$) starburst/interacting galaxies. The sample covers a wide range of interaction stages, from early (close pairs) to late phases (coalesced systems with multiple nuclei) with mass ratios in the $1/3 < M_1/M_2 < 1/1$ range. All the objects possess a wealth of ancillary data including *Spitzer* $24 \mu\text{m}$, GALEX far-UV, and existing $^{12}\text{CO}(1-0)$ and HI maps. The VIXENS sample is shown in Figure 6. A parallel campaign to map high density molecular gas tracers (e.g., HCN(1-0), HCO⁺(1-0), and HNC(1-0)) for the VIXENS sample is being conducted with the Nobeyama 45 m and IRAM 30 m telescopes as well as with the CARMA array. VIXENS will explore the relation between the star formation rate and gas content on spatially resolved scales of ~ 0.2 – 1 kpc

in starburst/interacting galaxies as a function of interaction phase [18, 97].

4. VIRUS and HETDEX: A Look into the Future

As mentioned in Section 1 the Hobby-Eberly Telescope Dark Energy Experiment (HETDEX) will use the VIRUS instrument to conduct a blind spectroscopic survey covering an effective area of ~ 90 degrees². While the main goal of HETDEX is to detect Ly α emitters at high redshift ($2 < z < 3.5$), large numbers of lower redshift objects, including nearby galaxies and MW stars, will fall in the survey footprint. HETDEX will reach a depth in continuum of $m_{\text{AB}} = 22.6$ (21.5, 20.7) at S/N = 3 (5, 10) per fiber per resolution element. VIRUS observes in the 3500 – 5500 \AA range, has a resolving power of $R = 700$, and a spatial resolution given by the $1.5''$ diameter fiber size. Given these parameters, $g < 17$ spiral galaxies will typically have S/N > 3 continuum detections per resolution element per fiber out to 2 effective radii and emission line spectra out to at least their optical radius. HETDEX will spatially resolve ~ 4500 local galaxies down to that limit without any photometric preselection, and an additional ~ 10000 local galaxies will have spatially resolved (i.e., $D_{25} > 5''$) spectroscopy below that limit $17 < g < 19$ (Niv Drory private communication). At $g = 19$ HETDEX will still obtain integrated galaxy spectra at S/N = 10 per resolution element in the continuum. These parameters and the lack of photometric pre-selection make HETDEX very competitive and complimentary with ongoing and future surveys like SAMI [98] and MANGA (<http://www.sdss3.org/future/manga.php>), although science applications will be constrained to the restricted blue wavelength range of VIRUS.

The spatially resolved absorption and emission spectra will provide information on star formation and dust extinction, the ISM chemical abundance and ionization state, and the properties of stellar populations, as well as rotation curves for an unbiased galaxy sample unprecedented in size. A wealth of information regarding a galaxy's formation history is encoded in the spatial distribution (mostly gradients) of these properties within galaxies, so moving beyond single-fiber (SDSS-like) spectra for large samples of spatially resolved galaxies opens a new parameter space for future studies of galaxy formation and evolution.

5. Conclusions

The Mitchell Spectrograph has proven to be a unique instrument for studying nearby galaxies. It is characterized by its large FOV and its high sensitivity to low surface brightness emission which make it an extremely efficient tool to observe extended sources. As I have reviewed throughout this article, the instrument has produced a large number of scientific results regarding the properties of nearby galaxies and the physical processes involved in the formation and evolution of their components, including their stars, ISM, dark matter halos, and central SMBHs.

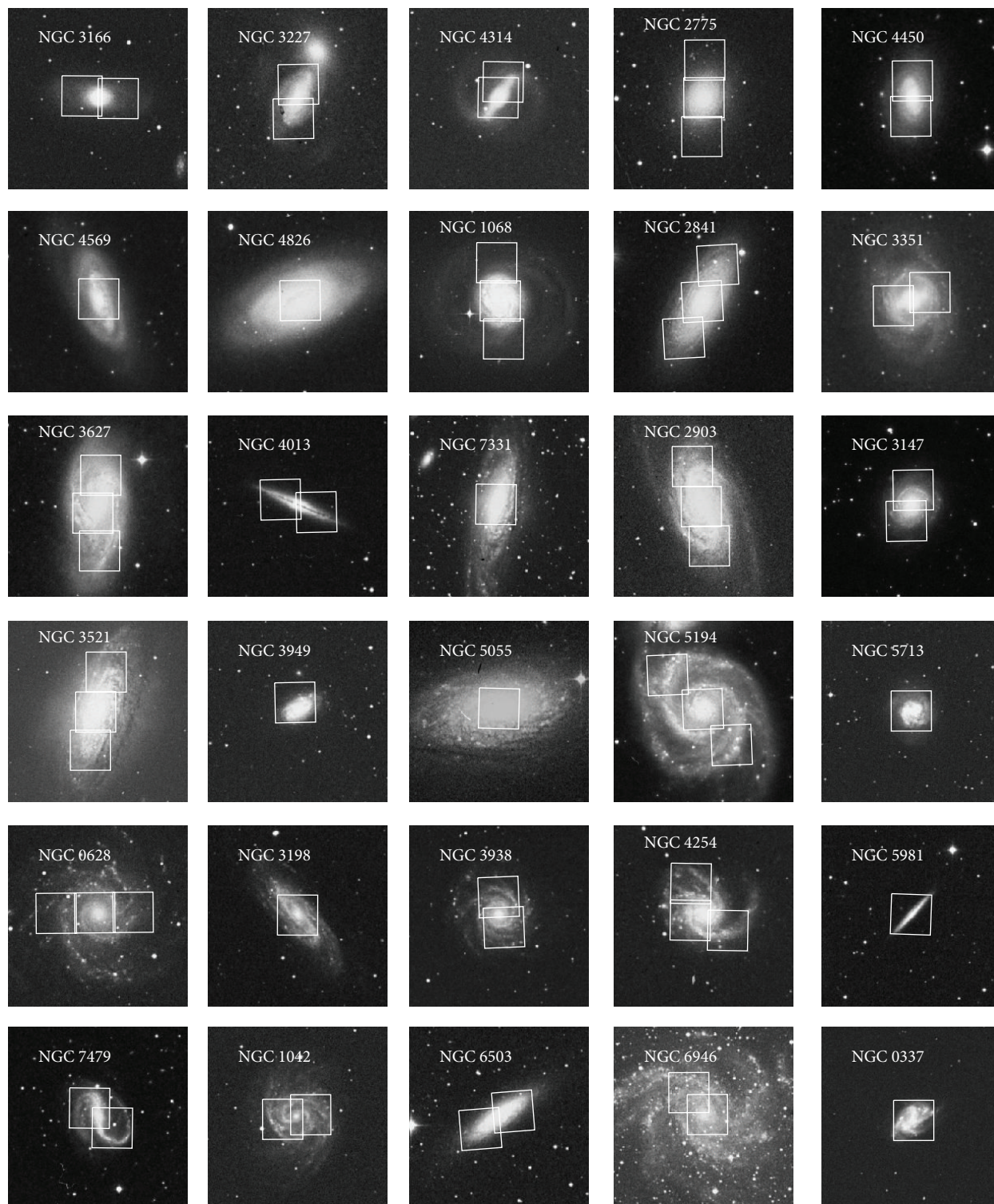


FIGURE 5: Digital Sky Survey cutouts of the 30 galaxies in the VENGAsample. The targets are ordered by Hubble type (taken from RC3, de Vaucouleurs et al. [94–96]) from earlier to later. White boxes show the VIRUS-P $1.7' \times 1.7'$ pointing observed on each galaxy. Taken from Blanc et al. [29].

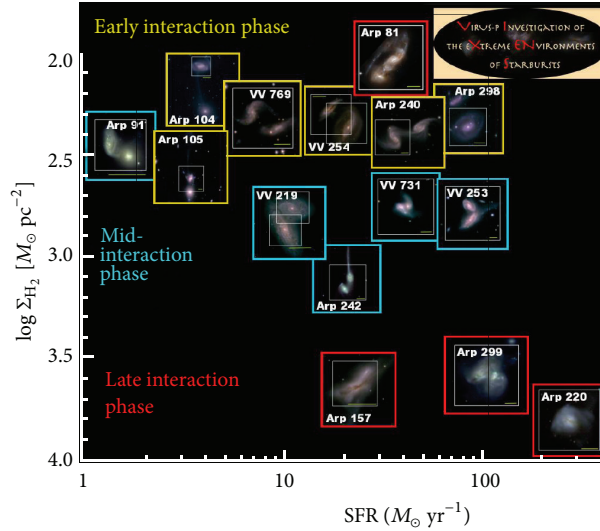


FIGURE 6: SDSS RGB (i,r,g) images of the VIXENS interacting galaxy sample. White boxes show the Mitchell Spectrograph field of view and the yellow lines indicate a scale of 10 kpc. Taken from Heiderman et al. [18].

The commissioning of the Mitchell Spectrograph on the McDonald 2.7 m telescope has boosted the scientific output of this facility enormously. Wide field integral field spectrographs are extremely powerful scientific instruments for small and medium sized telescopes. The Mitchell Spectrograph and similar instruments in its category have shown during the last decade that relatively modest investments in advanced instrumentation can turn a relatively small telescope into a competitive forefront facility with unique capabilities. Given the difficulties being faced by scientific funding agencies across the world and the current prospects for small optical facilities in the US, this is a very important concept to keep in mind.

Beyond single IFU spectrographs, more ambitious projects like HETDEX and MANGA will soon begin to move the IFU business into the “large data” era. Spatially resolved spectroscopy for tens of thousands of galaxies will soon be available to us. An enormous effort is currently underway to develop the tools necessary to digest and analyze these enormous datasets. While these projects will undoubtedly have an enormous impact on our understanding of galaxies, more detailed studies on smaller numbers of sources for which high spatial resolution, high S/N, full multiwavelength datasets are available will continue to provide a reference point to interpret the statistical results coming out of big surveys. On all fronts integral field spectroscopy is becoming a widely used technique and it is providing an invaluable contribution to the field of galaxy astrophysics.

Acknowledgments

The construction of the Mitchell Spectrograph (formerly VIRUS-P) was possible thanks to the generous support of the Cynthia & George Mitchell Foundation. Gary Hill and Phillip McQueen at McDonald Observatory lead the design and construction of the spectrograph. The IFU and optical fiber bundle were built by the Leibniz Institute for Astrophysics

(AIP). The author acknowledges David Doss and the staff at McDonald Observatory for their invaluable help supporting observations. HETDEX is led by the University of Texas at Austin, McDonald Observatory, and Department of Astronomy with participation from the Universitäts-Sternwarte of the Ludwig-Maximilians-Universität Munchen, the Max-Planck-Institut für Extraterrestrische-Physik (MPE), Astrophysikalisches Institut Potsdam (AIP), Texas A&M University, Pennsylvania State University, and the HET consortium. In addition to Institutional support, HETDEX is funded in part by gifts from Harold C. Simmons, Robert and Annie Graham, The Cynthia and George Mitchell Foundation, Louis and Julia Beecherl, Jim and Charlotte Finley, Bill and Bettye Nowlin, Robert and Fallon Vaughn, Eric Stumberg, and many others and by AFRL under Agreement no. FA9451-04-2-0355, the Texas Norman Hackerman Advanced Research Program under Grants 003658-0005-2006 and 003658-0295-2007, and the National Science Foundation under Grant AST-0926815.

References

- [1] G. J. Hill, S. E. Tuttle, H. Lee et al., “VIRUS: production of a massively replicated 33k fiber integral field spectrograph for the upgraded Hobby-Eberly telescope,” in *Ground-Based and Airborne Instrumentation for Astronomy IV*, vol. 8446 of *Proceedings of SPIE*, September 2012.
- [2] G. J. Hill, K. Gebhardt, E. Komatsu et al., “The Hobby-Eberly Telescope Dark Energy Experiment (HETDEX): description and early pilot survey results,” in *Panoramic Views of Galaxy Formation and Evolution*, T. Kodama, T. Yamada, and K. Aoki, Eds., vol. 399 of *ASP Conference Series*, pp. 115–118, Astronomical Society of the Pacific, San Francisco, Calif, USA, 2008.
- [3] J. J. Adams, G. A. Blanc, G. J. Hill, K. Gebhardt, N. Drory, and L. Hao, “The HETDEX pilot survey—I. Survey design, performance, and catalog of emission-line galaxies,” *The Astrophysical Journal Supplement Series*, vol. 192, no. 1, p. 5, 2011.

- [4] G. A. Blanc, J. J. Adams, K. Gebhardt et al., “The hetdex pilot survey. II. the evolution of the Ly α escape fraction from the ultraviolet slope and luminosity function of $1.9 < z < 3.8$ LAEs,” *The Astrophysical Journal*, vol. 736, no. 1, article 31, 21 pages, 2011.
- [5] J. J. Adams, G. J. Hill, and P. J. MacQueen, “B2 0902+34: a collapsing protogiant elliptical galaxy at $z = 3.4$,” *The Astrophysical Journal*, vol. 694, no. 1, pp. 314–326, 2009.
- [6] R. Ciardullo, C. Gronwall, J. J. Adams et al., “The Hetdex Pilot Survey. IV. The evolution of [O II] emitting galaxies from $z \sim 0.5$ to $z \sim 0$,” *The Astrophysical Journal*, vol. 769, no. 1, article 83, 2013.
- [7] T. Chonis, G. Blanc, G. Hill et al., 2013, arxiv???????
- [8] K. Gebhardt, J. Adams, D. Richstone et al., “The black hole mass in M87 from Gemini/NIFS adaptive optics observations,” *The Astrophysical Journal*, vol. 729, no. 2, article 119, 2011.
- [9] N. J. McConnell, C. P. Ma, K. Gebhardt et al., “Two ten-billion-solar-mass black holes at the centres of giant elliptical galaxies,” *Nature*, vol. 480, pp. 215–218, 2011.
- [10] N. J. McConnell, C. P. Ma, J. D. Murphy et al., “Dynamical measurements of black hole masses in four brightest cluster galaxies at 100 Mpc,” *The Astrophysical Journal*, vol. 756, no. 2, article 179, 2012.
- [11] N. J. McConnell, S. F. S. Chen, C. P. Ma, J. E. Greene, T. R. Lauer, and K. Gebhardt, “The effect of spatial gradients in Stellar mass-to-light ratio on black hole mass measurements,” *The Astrophysical Journal*, vol. 768, no. 1, article L21, 2013.
- [12] J. D. Murphy, K. Gebhardt, and J. J. Adams, “Galaxy kinematics with VIRUS-P: the dark matter halo of M87,” *The Astrophysical Journal*, vol. 729, no. 2, article 129, 2011.
- [13] J. J. Adams, K. Gebhardt, G. A. Blanc et al., “The central dark matter distribution of NGC2976,” *The Astrophysical Journal*, vol. 745, no. 1, article 92, 17 pages, 2012.
- [14] J. J. Adams, J. M. Uson, G. J. Hill, and P. J. MacQueen, “A new $z = 0$ metagalactic ultraviolet background limit,” *The Astrophysical Journal*, vol. 728, no. 2, article 107, 15 pages, 2011.
- [15] L. M. Cairós, N. Caon, B. G. Lorenzo et al., “Mapping luminous blue compact galaxies with VIRUS-P,” *Astronomy & Astrophysics*, vol. 547, article A24, 15 pages, 2012.
- [16] G. A. Blanc, A. Schruha, N. J. Evans II et al., “The VIRUS-P exploration of nearby galaxies (VENGA): the X_{CO} gradient in NGC 628,” *The Astrophysical Journal*, vol. 764, no. 2, article 117, 2013.
- [17] G. A. Blanc, A. Heiderman, K. Gebhardt, N. J. Evans, and J. Adams, “The spatially resolved star formation law from integral field spectroscopy: VIRUS-P observations of NGC 5194,” *The Astrophysical Journal*, vol. 704, no. 1, pp. 842–862, 2009.
- [18] A. L. Heiderman, N. J. Evans, N. J. II, K. Gebhardt et al., “New horizons in astronomy,” in *Proceedings of the Frank N. Bash Symposium on New Horizons in Astronomy (BASH '11)*, S. Salviander, J. Green, and A. Pawlik, Eds., Austin, Tex, USA, October 2011.
- [19] P. Yoachim, R. Roskar, and V. P. Debattista, “Integral field unit spectroscopy of the stellar disk truncation region of NGC 6155,” *The Astrophysical Journal*, vol. 716, no. 1, pp. L4–L8, 2010.
- [20] P. Yoachim, R. Roškar, and V. P. Debattista, “Spatially resolved spectroscopic star formation histories of nearby disks: hints of stellar migration,” *The Astrophysical Journal*, vol. 752, no. 2, article 97, 2012.
- [21] J. E. Greene, J. D. Murphy, J. M. Comerford, K. Gebhardt, and J. J. Adams, “The stellar halos of massive elliptical galaxies,” *The Astrophysical Journal*, vol. 750, no. 1, p. 32, 2012.
- [22] R. Bacon, Y. Copin, G. Monnet et al., “The SAURON project—I. The panoramic integral-field spectrograph,” *Monthly Notices of the Royal Astronomical Society*, vol. 326, no. 1, pp. 23–35, 2001.
- [23] A. Kelz, M. A. W. Verheijen, M. M. Roth et al., “PMAS: the potsdam multi-aperture spectrophotometer. II. The wide integral field unit PPak,” *Publications of the Astronomical Society of the Pacific*, vol. 118, no. 839, pp. 129–145, 2006.
- [24] M. A. Bershad, D. R. Andersen, J. Harker, L. W. Ramsey, and M. A. W. Verheijen, “Sparsepak: a formatted fiber field unit for the WIYN telescope bench spectrograph. I. Design, construction, and calibration,” *Publications of the Astronomical Society of the Pacific*, vol. 116, no. 820, pp. 565–590, 2004.
- [25] P. T. de Zeeuw, M. Bureau, E. Emsellem et al., “The SAURON project—II. Sample and early results,” *Monthly Notices of the Royal Astronomical Society*, vol. 329, no. 3, pp. 513–530, 2002.
- [26] M. Cappellari, E. Emsellem, D. Krajnović et al., “The ATLAS3D project—I. A volume-limited sample of 260 nearby early-type galaxies: science goals and selection criteria,” *Monthly Notices of the Royal Astronomical Society*, vol. 413, pp. 813–836, 2011.
- [27] F. F. Rosales-Ortega, R. C. Kennicutt Jr., S. F. Sánchez et al., “PINGS: the PPAK IFS nearby galaxies survey,” *Monthly Notices of the Royal Astronomical Society*, vol. 405, no. 12, pp. 735–758, 2010.
- [28] S. F. Sánchez, R. C. Kennicutt Jr., A. G. de Paz et al., “CALIFA, The Calar Alto Legacy Integral Field Area Survey,” *Astronomy & Astrophysics*, vol. 538, article A8, 31 pages, 2012.
- [29] G. A. Blanc, T. Weinzirl, M. Song et al., “The VIRUS-P Exploration of Nearby Galaxies (VENGA): survey design, data processing, and spectral analysis methods,” *The Astronomical Journal*, vol. 145, no. 5, p. 138, 2013.
- [30] G. J. Hill, P. J. MacQueen, M. P. Smith et al., “Design, construction, and performance of VIRUS-P: the prototype of a highly replicated integral-field spectrograph for HET,” in *Ground-Based and Airborne Instrumentation for Astronomy II*, vol. 7014 of *Proceedings of the SPIE*, Marseille, France, June 2008.
- [31] D. Thomas, C. Maraston, and R. Bender, “Stellar population models of Lick indices with variable element abundance ratios,” *Monthly Notices of the Royal Astronomical Society*, vol. 339, no. 3, pp. 897–911, 2003.
- [32] G. J. Graves and R. P. Schiavon, “Measuring ages and elemental abundances from unresolved stellar populations: Fe, Mg, C, N, and Ca,” *The Astrophysical Journal Supplement Series*, vol. 177, no. 2, pp. 446–464, 2008.
- [33] S. E. Strom, K. M. Strom, J. W. Goad, F. J. Vrba, and W. Rice, “Color and metallicity gradients in E and S0 galaxies,” *The Astrophysical Journal*, vol. 204, part 1, pp. 684–693, 1976.
- [34] P. Sánchez-Blázquez, D. A. Forbes, J. Strader, J. Brodie, and R. Proctor, “Spatially resolved spectroscopy of early-type galaxies over a range in mass,” *Monthly Notices of the Royal Astronomical Society*, vol. 377, no. 2, pp. 759–786, 2007.
- [35] A.-M. Weijmans, M. Cappellari, R. Bacon et al., “Stellar velocity profiles and line strengths out to four effective radii in the early-type galaxies NGC 3379 and 821,” *Monthly Notices of the Royal Astronomical Society*, vol. 398, no. 2, pp. 561–574, 2009.
- [36] I. Trujillo, G. Feulner, Y. Goranova et al., “Extremely compact massive galaxies at $z \sim 1.4$,” *Monthly Notices of the Royal Astronomical Society*, vol. 373, no. 1, pp. L36–L40, 2006.
- [37] P. G. van Dokkum, M. Franx, M. Kriek et al., “Confirmation of the remarkable compactness of massive quiescent galaxies at $z \sim 2.3$: early-type galaxies did not form in a simple monolithic collapse,” *The Astrophysical Journal*, vol. 677, no. 1, pp. L5–L8, 2008.

- [38] T. Naab, P. H. Johansson, and J. P. Ostriker, “Minor mergers and the size evolution of elliptical galaxies,” *The Astrophysical Journal*, vol. 699, no. 2, pp. L178–L182, 2009.
- [39] S. Huang, L. C. Ho, C. Y. Peng, Z.-Y. Li, and A. J. Barth, “Fossil evidence for the two-phase formation of elliptical galaxies,” *The Astrophysical Journal*, vol. 768, no. 2, article L28, 2013.
- [40] R. Bender, D. Burstein, and S. M. Faber, “Dynamically hot galaxies. II. Global stellar populations,” *The Astrophysical Journal*, vol. 411, no. 1, pp. 153–169, 1993.
- [41] S. C. Trager, S. M. Faber, G. Worthey, and J. J. González, “The stellar population histories of early-type galaxies. II. Controlling parameters of the stellar populations,” *Astronomical Journal*, vol. 120, no. 1, pp. 165–188, 2000.
- [42] G. J. Graves, S. M. Faber, R. P. Schiavon, and R. Yan, “Ages and abundances of red sequence galaxies as a function of liner emission-line strength,” *The Astrophysical Journal*, vol. 671, no. 1, pp. 243–271, 2007.
- [43] C. Kobayashi, “GRAPE-SPH chemodynamical simulation of elliptical galaxies—I. Evolution of metallicity gradients,” *Monthly Notices of the Royal Astronomical Society*, vol. 347, pp. 740–758, 2004.
- [44] M. Pohlen and I. Trujillo, “The structure of galactic disks: studying late-type spiral galaxies using SDSS,” *Astronomy and Astrophysics*, vol. 454, no. 3, pp. 759–772, 2006.
- [45] C. L. Martin and R. C. Kennicutt Jr., “Star formation thresholds in galactic disks,” *The Astrophysical Journal*, vol. 555, no. 1, pp. 301–321, 2001.
- [46] F. Bigiel, A. Leroy, F. Walter et al., “Extremely inefficient star formation in the outer disks of nearby galaxies,” *Astronomical Journal*, vol. 140, no. 5, pp. 1194–1213, 2010.
- [47] A. Schrubba, A. K. Leroy, F. Walter et al., “A molecular star formation law in the atomic-gas-dominated regime in nearby galaxies,” *Astronomical Journal*, vol. 142, no. 2, p. 37, 2011.
- [48] J. A. Sellwood and J. J. Binney, “Radial mixing in galactic discs,” *Monthly Notices of the Royal Astronomical Society*, vol. 336, no. 3, pp. 785–796, 2002.
- [49] R. Roškar, V. P. Debattista, G. S. Stinson, T. R. Quinn, T. Kaufmann, and J. Wadsley, “Beyond inside-out growth: formation and evolution of disk outskirts,” *The Astrophysical Journal*, vol. 675, no. 2, article L65, 2008.
- [50] P. Serra and S. C. Trager, “On the interpretation of the age and chemical composition of composite stellar populations determined with line-strength indices,” *Monthly Notices of the Royal Astronomical Society*, vol. 374, no. 3, pp. 769–774, 2007.
- [51] C. R. Fernandes, A. Mateus, L. Sodré Jr., G. Stasińska, and J. M. Gomes, “Semi-empirical analysis of sloan digital sky survey galaxies—I. Spectral synthesis method,” *Monthly Notices of the Royal Astronomical Society*, vol. 358, no. 2, pp. 363–378, 2005.
- [52] P. Ocvirk, C. Pichon, A. Lançon, and E. Thiebaud, “STECKMAP: Stellar content and Kinematics from high resolution galactic spectra via Maximum A Posteriori,” *Monthly Notices of the Royal Astronomical Society*, vol. 365, no. 1, pp. 74–84, 2006.
- [53] K. Gebhardt, R. Bender, G. Bower et al., “A relationship between nuclear black hole mass and galaxy velocity dispersion,” *The Astrophysical Journal*, vol. 539, no. 1, pp. L13–L16, 2000.
- [54] L. Ferrarese and D. Merritt, “A fundamental relation between supermassive black holes and their host galaxies,” *The Astrophysical Journal*, vol. 539, no. 1, pp. L9–L12, 2000.
- [55] J. Kormendy and L. C. Ho, “Coevolution (or not) of supermassive black holes and host galaxies,” *Annual Review of Astronomy and Astrophysics*, vol. 51, pp. 511–653, 2013.
- [56] B. Robertson, L. Hernquist, T. J. Cox et al., “The evolution of the MBH- σ relation,” *The Astrophysical Journal*, vol. 641, no. 1, pp. 90–102, 2006.
- [57] C. Y. Peng, “What do statistics reveal about the $M \sim B \sim H-M \sim b \sim u \sim l \sim g \sim e$ correlation and co-evolution?” in *Proceedings of the 267th International Astronomical Union Symposium*, pp. 161–171, 2010.
- [58] J. F. Navarro, C. S. Frenk, and S. D. M. White, “The structure of cold dark matter halos,” *The Astrophysical Journal*, vol. 462, no. 2, pp. 563–575, 1996.
- [59] J. D. Simon, A. D. Bolatto, A. Leroy, and L. Blitz, “High-resolution measurements of the dark matter halo of NGC 2976: evidence for a shallow density profile,” *The Astrophysical Journal*, vol. 596, no. 2, pp. 957–981, 2003.
- [60] W. J. G. de Blok, F. Walter, E. Brinks, C. Trachternach, S.-H. Oh, and R. C. Kennicutt Jr., “High-resolution rotation curves and galaxy mass models from things,” *Astronomical Journal*, vol. 136, no. 6, pp. 2648–2719, 2008.
- [61] R. C. Kennicutt Jr., S.-H. Oh, W. J. G. de Blok, E. Brinks, and F. Walter, “Dark and luminous matter in things dwarf galaxies,” *Astronomical Journal*, vol. 141, no. 6, p. 193, 2011.
- [62] M. Cappellari, “Measuring the inclination and mass-to-light ratio of axisymmetric galaxies via anisotropic Jeans models of stellar kinematics,” *Monthly Notices of the Royal Astronomical Society*, vol. 390, no. 1, pp. 71–86, 2008.
- [63] D. Krajnovic, M. Cappellari, P. T. de Zeeuw, and Y. Copin, “Kinemetry: a generalization of photometry to the higher moments of the line-of-sight velocity distribution,” *Monthly Notices of the Royal Astronomical Society*, vol. 366, no. 3, pp. 787–802, 2006.
- [64] D. H. Rogstad, I. A. Lockhart, and M. C. H. Wright, “Aperture-synthesis observations of H I in the galaxy M83,” *The Astrophysical Journal*, vol. 193, pp. 309–319, 1974.
- [65] E. Emsellem, M. Cappellari, R. F. Peletier et al., “The SAURON project—III. Integral-field absorption-line kinematics of 48 elliptical and lenticular galaxies,” *Monthly Notices of the Royal Astronomical Society*, vol. 352, no. 3, pp. 721–743, 2004.
- [66] M. Schwarzschild, “A numerical model for a triaxial stellar system in dynamical equilibrium,” *The Astrophysical Journal*, vol. 232, pp. 236–247, 1979.
- [67] K. Gebhardt, D. Richstone, S. Tremaine et al., “Axisymmetric dynamical models of the central regions of galaxies,” *The Astrophysical Journal*, vol. 583, no. 1, pp. 92–115, 2003.
- [68] K. Gebhardt and J. Thomas, “The black hole mass, stellar mass-to-light ratio, and Dark Halo in m87,” *The Astrophysical Journal*, vol. 700, no. 2, pp. 1690–1701, 2009.
- [69] D. E. Osterbrock and G. J. Ferland, *Astrophysics of Gaseous Nebulae and Active Galactic Nuclei*, University Science Books, Sausalito, Calif, USA, 2nd edition, 2006.
- [70] R. C. Kennicutt Jr., “The global schmidt law in star-forming galaxies,” *The Astrophysical Journal*, vol. 498, no. 2, pp. 541–552, 1998.
- [71] R. C. Kennicutt Jr., D. Calzetti, F. Walter et al., “Star formation in NGC 5194 (M51a). II. The spatially resolved star formation law,” *The Astrophysical Journal*, vol. 671, no. 1, article 333, 2007.
- [72] F. Bigiel, A. Leroy, F. Walter et al., “The star formation law in nearby galaxies on SUB-KPC scales,” *Astronomical Journal*, vol. 136, no. 6, pp. 2846–2871, 2008.
- [73] G. Liu, J. Koda, D. Calzetti, M. Fukuhara, and R. Momose, “The super-linear slope of the spatially resolved star formation law in NGC 3521 and NGC 5194 (M51a),” *The Astrophysical Journal*, vol. 735, no. 1, article 63, 2011.

- [74] N. Rahman, A. D. Bolatto, R. Xue et al., “Carma Survey Toward Infrared-Bright Nearby Galaxies (STING). II. Molecular gas star formation law and depletion time across the blue sequence,” *The Astrophysical Journal*, vol. 745, no. 2, article 183, 2012.
- [75] R. Shetty, B. C. Kelly, and F. Bigiel, “Evidence for a non-universal Kennicutt-Schmidt relationship using hierarchical Bayesian linear regression,” *Monthly Notices of the Royal Astronomical Society*, vol. 430, no. 1, pp. 288–304, 2013.
- [76] M. R. Krumholz, C. F. McKee, and J. Tumlinson, “The star formation law in atomic and molecular gas,” *The Astrophysical Journal*, vol. 699, no. 1, pp. 850–856, 2009.
- [77] F. Renaud, K. Kraljic, and F. Bournaud, “Star formation laws and thresholds from ISM structure and turbulence,” *The Astrophysical Journal*, vol. 760, no. 1, article L16, 2012.
- [78] I. A. Bonnell, C. L. Dobbs, and R. J. Smith, “Shocks, cooling and the origin of star formation rates in spiral galaxies,” *Monthly Notices of the Royal Astronomical Society*, vol. 430, no. 3, pp. 1790–1800, 2013.
- [79] A. K. Leroy, F. Walter, K. Sandstrom et al., “Molecular gas and star formation in nearby disk galaxies,” *The Astronomical Journal*, vol. 146, no. 2, p. 19, 2013.
- [80] A. Schruba, A. K. Leroy, F. Walter, K. Sandstrom, and E. Rosolowsky, “The scale dependence of the molecular gas depletion time in M33,” *The Astrophysical Journal*, vol. 722, no. 2, pp. 1699–1706, 2010.
- [81] R. Shetty and E. C. Ostriker, “Maximally star-forming galactic disks. II. Vertically resolved hydrodynamic simulations of starburst regulation,” *The Astrophysical Journal*, vol. 754, no. 1, article 2, 2012.
- [82] G. A. Blanc, K. Gebhardt, A. L. Heiderman et al., “The VIRUS-P Exploration of Nearby Galaxies (VENGA): survey design and first results,” in *Proceedings of the 3rd Biennial Frank N. Bash Symposium on New Horizons in Astronomy (BASH '09)*, vol. 432, pp. 180–186, Austin, Tex, USA, October 2009.
- [83] F. Walter, E. Brinks, W. J. G. de Blok et al., “Things: the HI nearby galaxy survey,” *Astronomical Journal*, vol. 136, no. 6, pp. 2563–2647, 2008.
- [84] T. T. Helfer, M. D. Thornley, M. W. Regan et al., “The BIMA survey of nearby galaxies (BIMA song). II. The CO data,” *The Astrophysical Journal Supplement Series*, vol. 145, no. 2, pp. 259–327, 2003.
- [85] A. D. Bolatto, M. Wolfire, and A. K. Leroy, “The CO-to-H₂ conversion factor,” *Annual Review of Astronomy and Astrophysics*, vol. 51, pp. 207–268, 2013.
- [86] D. Narayanan, M. R. Krumholz, E. C. Ostriker, and L. Hernquist, “A general model for the CO-H₂ conversion factor in galaxies with applications to the star formation law,” *Monthly Notices of the Royal Astronomical Society*, vol. 421, no. 4, pp. 3127–3146, 2012.
- [87] R. Feldmann, N. Y. Gnedin, and A. V. Kravtsov, “The x-factor in galaxies. I. Dependence on environment and scale,” *The Astrophysical Journal*, vol. 747, no. 2, article 124, 2012.
- [88] P. Robertson, G. A. Shields, and G. A. Blanc, “Enhanced abundances in spiral galaxies of the Pegasus I Cluster,” *The Astrophysical Journal*, vol. 748, no. 1, article 48, 2012.
- [89] D. Zaritsky, R. C. Kennicutt Jr., and J. P. Huchra, “H II regions and the abundance properties of spiral galaxies,” *The Astrophysical Journal*, vol. 420, no. 1, pp. 87–109, 1994.
- [90] L. Levy, J. A. Rose, J. H. van Gorkom, and B. Chaboyer, “The effect of cluster environment on galaxy evolution in the Pegasus I Cluster,” *Astronomical Journal*, vol. 133, no. 3, pp. 1104–1124, 2007.
- [91] E. D. Skillman, R. C. Kennicutt Jr., G. A. Shields, and D. Zaritsky, “Chemical abundances in virgo spiral galaxies. II. Effects of cluster environment,” *The Astrophysical Journal*, vol. 462, no. 1, pp. 147–162, 1996.
- [92] C. A. Tremonti, T. M. Heckman, G. Kauffmann et al., “The origin of the mass-metallicity relation: insights from 53,000 star-forming galaxies in the sloan digital sky survey,” *The Astrophysical Journal*, vol. 613, no. 2, pp. 898–913, 2004.
- [93] P. Robertson, G. A. Shields, R. Davé, G. A. Blanc, and A. Wright, “Dependence of nebular heavy-element abundance on H I content for spiral galaxies,” *The Astrophysical Journal*, vol. 773, no. 1, article 4, 2013.
- [94] G. de Vaucouleurs, A. de Vaucouleurs, H. G. Corwin Jr., R. J. Buta, G. Paturel, and P. Fouqué, *Third Reference Catalogue of Bright Galaxies. Volume I: Explanations and References*, Springer, New York, NY, USA, 1991.
- [95] G. de Vaucouleurs, A. de Vaucouleurs, H. G. Corwin Jr., R. J. Buta, G. Paturel, and P. Fouqué, *Third Reference Catalogue of Bright Galaxies. Volume II: Data for galaxies between 0^h and 12^h*, Springer, New York, NY, USA, 1991.
- [96] G. de Vaucouleurs, A. de Vaucouleurs, H. G. Corwin Jr., R. J. Buta, G. Paturel, and P. Fouqué, *Third Reference Catalogue of Bright Galaxies. Volume III: Data for galaxies between 12^h and 24^h*, Springer, New York, NY, USA, 1991.
- [97] A. L. Heiderman et al., in preparation.
- [98] S. M. Croom, J. S. Lawrence, J. Bland-Hawthorn et al., “The Sydney-AAO multi-object integral field spectrograph,” *Monthly Notices of the Royal Astronomical Society*, vol. 421, no. 1, pp. 872–893, 2012.

Research Article

Studying the Interstellar Medium of H II/BCD Galaxies Using IFU Spectroscopy

Patricio Lagos and Polychronis Papaderos

Centro de Astrofísica da Universidade do Porto, Rua das Estrelas, 4150-762 Porto, Portugal

Correspondence should be addressed to Patricio Lagos; plagos@astro.up.pt

Received 19 April 2013; Accepted 23 July 2013

Academic Editor: Jorge Iglesias Páramo

Copyright © 2013 P. Lagos and P. Papaderos. This is an open access article distributed under the Creative Commons Attribution License, which permits unrestricted use, distribution, and reproduction in any medium, provided the original work is properly cited.

We review the results from our studies, and previous published work, on the spatially resolved physical properties of a sample of H II/BCD galaxies, as obtained mainly from integral-field unit spectroscopy with Gemini/GMOS and VLT/VIMOS. We confirm that, within observational uncertainties, our sample galaxies show nearly spatially constant chemical abundances similar to other low-mass starburst galaxies. They also show He II $\lambda 4686$ emission with the properties being suggestive of a mix of excitation sources and with Wolf-Rayet stars being excluded as the primary ones. Finally, in this contribution, we include a list of all H II/BCD galaxies studied thus far with integral-field unit spectroscopy.

1. Introduction

The concept of *compact galaxies* was introduced by Zwicky [1], who has described them as “galaxies barely distinguishable from stars” on the Palomar Sky Survey plates. The term blue compact dwarf (BCD) galaxies [2] identify those objects that show low luminosity, small linear dimensions, strong emission lines superposed on a blue continuum, and spectral properties that indicate low chemical abundances. BCDs form a subset of H II galaxies, a large number of which have been identified on objective prism surveys by [3–6] by the presence of strong emission lines, similar to Giant H II regions (GH IIRs) in our galaxy. Here, we will refer to H II/BCD galaxies as objects with a metallicity $7.0 \leq 12 + \log(\text{O}/\text{H}) \leq 8.4$ (e.g., [7]), low luminosity ($M_B \geq -18$), and gas-rich objects (e.g., [8]) undergoing vigorous starburst activity in a relatively small physical size (≤ 1 Kpc). The star forming component, in these objects, typically contains multiple knots of star-formation with unresolved ensembles of young star clusters (e.g., [9, 10]). The hypothesis of these systems being young, forming their first generation of stars, has been discarded by the detection of an evolved underlying stellar host with an age > 1 Gyr, in the majority of the nearby H II/BCD population (e.g., [11, 12]). Figure 1 shows the optical

spectrum of the galaxy Tol 2146-391 obtained using integral field unit (IFU) observations with Gemini/GMOS. In this figure, we label the most important emission lines used in our studies, in particular, the strong Balmer hydrogen recombination lines and collisionally excited emission lines, such as [O II] $\lambda\lambda 3726, 3729$, [O III] $\lambda 4363$, [O III] $\lambda 5007$, [S II] $\lambda\lambda 6717, 6731$, and [N II] $\lambda 6584$, which have been used for the determination of physical conditions (e.g., electron temperature and density) and chemical abundances (e.g., oxygen, nitrogen, etc.). We also detect in some of our galaxies the high-ionization emission line He II $\lambda 4686$.

Although progress has been made in this field, important unsolved questions remain with regard to the mode of star formation (e.g., quasicontinuous versus fluctuating), and the triggering mechanism of ongoing starburst activity in H II/BCDs. It has been suggested [10] that the cluster formation efficiency is lower in compact H II/BCD galaxies than the one found in more luminous galaxies. These luminous systems generally show an irregular outer shape and kinematical signatures of merging in their interstellar medium (ISM). In some cases, the formation of star cluster complexes occurs coevally [10], whereas in others star formation occurs in a propagating manner [13, 14]. In any case, the mechanism which may trigger the current star formation in these galaxies

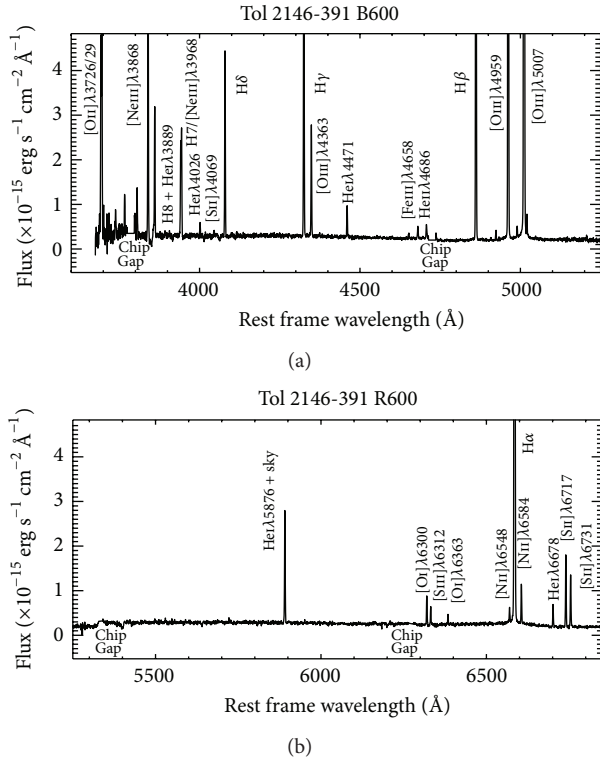


FIGURE 1: Integrated spectra of the H II/BCD galaxy Tol 2146-391. Top panel: blue spectrum (grating B600). Bottom panel: red spectrum (grating R600).

is not well understood; in particular the relative importance of intrinsic and environmental properties remains a subject of investigation.

Another important issue is the chemical and kinematical imprints of star cluster formation and evolution on the spatially resolved properties of the ISM in H II/BCD galaxies. As a natural consequence of star formation driven feedback, the newly synthesized elements will be dispersed and mixed across the ISM via hydrodynamic mechanisms (e.g., [15]), leading to *chemical homogeneity in the oxygen abundance* [16, 17] of H II/BCD galaxies (e.g., [18] and references therein). The nitrogen-to-oxygen ratio N/O has also been found to be rather constant ($\log(\text{N/O}) \approx -1.6$; [19–21]) at low metallicity ($12 + \log(\text{O/H}) \leq 7.6$), suggesting primary production by massive stars [21] as the main contribution to nitrogen enrichment at those very low metallicities. A small fraction of H II/BCD galaxies fall in this very low metallicity regime [22] and are commonly referred to as extremely metal-poor (XMP) galaxies or XMP BCDs. These galaxies are the best nearby candidates for cosmologically young objects, as various arguments imply that they have formed most of their stellar mass in the past 1–3 Gyr [14, 23]. At intermediate metallicity ($7.6 \leq 12 + \log(\text{O/H}) \leq 8.3$), the large observed spread in N/O has been attributed mainly to the loss of heavy elements via galactic winds [24], and/or to the delayed release of nitrogen by intermediate and/or massive stars and oxygen by massive stars [19, 25]. However, the delayed-release scenario cannot explain the presence of some H II/BCD

galaxies with a high N/O ratio at low metallicities. The most plausible explanation for the high N/O ratio observed in these objects is the chemical pollution of the ISM by nitrogen released by massive Wolf-Rayet (WR) stars as is, apparently, the case of the well-studied BCD NGC 5253 [26–29]. Finally, at higher metallicities ($12 + \log(\text{O/H}) \geq 8.3$), the N/O ratio clearly increases with increasing oxygen abundance and the nitrogen content is mainly due to secondary production by intermediate-mass stars.

So far, an increasing number of H II/BCD galaxies has been studied with IFU spectroscopy (see Table 1 where we provide an overview of the literature) with the main focus on the spatial properties of the ISM. Recently, we have started a program investigating with IFU spectroscopy the physical conditions in the ISM of the most compact H II/BCD galaxies, laying special emphasis on the extinction patterns, emission line ratios, oxygen and nitrogen abundances, kinematics and the relation to the intrinsic properties of star formation as well as possible evolutionary effects [18, 33]. To this end, we observed a sample of H II/BCD galaxies using the GMOS-IFU on Gemini South and North and, more recently, with VLT/VIMOS. The GMOS-IFU observations were performed using the gratings B600 and R600 in one slit mode, covering a total spectral range from ~ 3000 to ~ 7230 Å. This observational setup provides a pattern of 500 hexagonal elements with a projected diameter of $0''.2$, covering a total $3''.5 \times 5''$ field of view (FoV). The VIMOS-IFU observations were obtained using the gratings HR_blue and HR_orange covering a spectral range from ~ 3710 to ~ 7700 Å. Our data yield a scale on the sky of $0''.33$ per fiber and cover a FoV of $13'' \times 13''$. In Figure 2, we show the g-band acquisition image of the XMP BCD galaxy HS2236+1344, in which we indicated the total field of view of $4'' \times 8''$ and the H α map of the galaxy obtained from the composition of two different pointings with GMOS-IFU. In Figure 3, we show the H α emission line map of the galaxies UM 461 and Tol 65 obtained using VIMOS-IFU. Table 2 lists the general parameters of our sample of galaxies.

This contribution is organized as follows: the metallicity content and the spatial distribution of the ISM in our sample galaxies are described in Section 2, and in Section 3, we discuss the high-ionization emission line He II $\lambda 4686$ and its relationship to the properties of the ISM. Finally, in Section 4, we summarize our results and conclusions.

2. The Metal Content in the ISM of H II/BCD Galaxies

Using the reddening corrected emission line intensities of the spectra of each one of the spaxels, we can derive the physical conditions (electron temperature and density) and the chemical abundances (O and N) across the ISM of the galaxies. We calculate oxygen abundances in regions where the [OIII] $\lambda 4363$ emission line has been detected assuming $\text{O/H} = \text{O}^+/\text{H}^+ + \text{O}^{++}/\text{H}^+$, while nitrogen abundances are obtained assuming $\text{N/H} = \text{ICF(N)} \times \text{N}^+/\text{H}^+$, with ICF(N) denoting the ionization correction factor $(\text{O}^+ + \text{O}^{++})/\text{O}^+$. For the sake of illustration, in Figure 4, we show the spatial

TABLE 1: H II/BCD galaxies with published IFU observations. The list could be incomplete and does not include Fabry-Perot observations. Redshift distances obtained from NED assuming $H_0 = 73 \text{ km s}^{-1} \text{ Mpc}^{-1}$. M_B computed from the tabulated values of m_B obtained from HyperLeda.

Name	Coordinates (J2000)		Distance (Mpc)	M_B (mag)	Reference	Instrument
IC 10	00:20:17.3	+59:18:14	0.8	-12.73	[30]	PMAS
Haro 11	00:36:52.7	-33:33:17	84.6	-20.30	[31]	FLAMES
Tol 0104-388	01:07:02.2	-38:31:51	91.6	—	[32, 33]	GMOS-IFU
Mrk 996	01:27:35.5	-06:19:36	22.2	-16.56	[34]	VIMOS-IFU
HS0128+2832	01:31:21.3	+28:48:12	66.3	—	[35]	PMAS
UM 408	02:11:23.4	+02:20:30	49.3	-15.76	[18, 36]	GMOS-IFU
UM 420	02:20:54.5	+00:33:24	240.1	-21.19	[37]	VIMOS-IFU
Mrk 370	02:40:29.0	+19:17:50	10.8	-16.40	[38]	INTEGRAL
SBS 0335-052	03:37:44.0	-05:02:40	55.6	-16.77	[39, 40]	SINFONI, FLAMES
IIZw 33	05:10:48.1	-02:40:54	38.81	-18.45	[41]	VIRUS-P
IIZw 40	05:55:42.6	+03:23:32	10.8	-16.69	[42, 43]	SINFONI, GMOS-IFU
Haro 1	07:36:56.7	+35:14:31	51.9	-21.02	[41]	VIRUS-P
He 2-10	08:36:15.1	-26:24:34	12.0	-17.93	[44, 45]	FLAMES, SINFONI
HS0837+4717	08:40:29.9	+47:07:10	172.4	-18.15	[35]	PMAS
Mrk 1418	09:40:27.0	+48:20:15	10.6	-16.27	[46]	PMAS
Mrk 407	09:47:47.6	+39:05:03	21.8	-16.50	[47]	PMAS
Mrk 409	09:49:41.2	+32:13:16	21.2	-17.11	[48]	PMAS
Tol 1004-296	10:06:33.4	-29:56:05	15.3	-17.56	[39]	SINFONI
Mrk 32	10:27:02.0	+56:16:14	11.4	-14.20	[47]	PMAS
Mrk 35	10:45:22.4	+55:57:37	12.9	-17.33	[38]	INTEGRAL
Mrk 178	11:33:28.9	+49:14:14	3.4	-13.25	[49]	INTEGRAL
UM 448	11:42:12.4	+00:20:03	76.3	-19.93	[50]	FLAMES
Mrk 750	11:50:02.7	+15:01:23	10.3	-14.30	[47]	PMAS
UM 462	11:52:37.2	-02:28:10	14.5	-16.20	[37]	VIMOS-IFU
Mrk 206	12:24:17.0	+67:26:24	18.0	-15.90	[47]	PMAS
NGC 4670	12:45:17.1	+27:07:31	14.7	-17.68	[41]	VIRUS-P
NGC 5253	13:39:55.9	-31:38:24	5.6	-17.68	[29, 45, 51, 52]	SINFONI, FLAMES, GMOS-IFU
Tol 1434+032	14:37:08.9	+03:02:50	23.4	-14.94	[47]	PMAS
Mrk 475	14:39:05.4	+36:48:22	8.0	-13.10	[47]	PMAS
IIZw 70	14:50:56.5	+35:34:18	16.2	-16.28	[53]	PMAS
I Zw 123	15:37:04.2	+55:15:48	9.1	-14.35	[47]	PMAS
Mrk 297	16:05:13.0	+20:32:32	65.0	-20.60	[38]	INTEGRAL
I Zw 159	16:35:21.0	+52:12:52	37.0	-17.19	[47]	PMAS
Tol 2146-391	21:49:48.2	-38:54:09	120.7	—	[32, 33]	GMOS-IFU
HS2236+1344	22:38:31.1	+14:00:30	84.5	—	[54]	GMOS-IFU
Mrk 314	23:02:59.2	+16:36:19	28.5	-18.20	[38, 41]	INTEGRAL, VIRUS-P
III Zw 102	23:20:30.1	+17:13:32	22.4	-18.81	[38, 41]	INTEGRAL, VIRUS-P
Mrk 930	3:31:58.3	+28:56:50	75.2	—	[35]	PMAS

distribution of $12 + \log(\text{O}/\text{H})$ in the GMOS-IFU FoV of the galaxy Tol 2146-391. We can see in this figure that, despite a slight depression in the inner part of the galaxy, the oxygen abundance appears to be uniform across the galaxy (see Figure 18 in [33]). In [36], we compare the spatial distribution of $12 + \log(\text{O}/\text{H})$, found in [18], with the position of the star cluster/complexes detected in the galaxy UM 408 by [10] using high resolution near-IR K_s -band images. We found that the variation of the observed data points (see Figure 9 in [18] and Figure 1 in [36]) may not be statistically significant, indicating that these regions have identical chemical

properties within the errors. It is interesting to note that we observed a marginal gradient of decreasing abundance from the center outward in UM 408, indicating that the highest abundance values are found near the peak of $\text{H}\alpha$ emission and extinction $c(\text{H}\beta)$, and coincident with the position of the brightest star cluster/complex [10]. In any case, the absence of chemical overabundances in the ISM of UM 408, Tol 2146-391, Tol 0104-388, and HS2236+1344 and in the dwarf galaxies studied in the literature (e.g., [16, 17, 57-60]) indicates that the population of young star clusters is not producing localized oxygen overabundances. The most likely explanation for this

TABLE 2: General parameters of our studied galaxies.

Name	Coordinates ^a (J2000)		D (Mpc) ^a	M_B ^b (mag)	$12 + \log(\text{O}/\text{H})$	Instrument
Tol 0104–388	01:07:02.2	−38:31:51	91.6	—	8.02 [33]	GMOS-IFU
UM 408	02:11:23.4	+02:20:30	49.3	−15.76	7.87 [18]	GMOS-IFU
Mrk 600	02:51:04.6	+04:27:14	13.8	−15.38	7.88 [55]	VIMOS-IFU
UM 461	11:51:33.3	−02:22:22	14.2	−14.36	7.72 [56]	VIMOS-IFU
Tol 65	12:25:46.9	−36:14:01	38.5	−15.44	7.53–7.56 [55]	VIMOS-IFU
Tol 2146–391	21:49:48.2	−38:54:09	120.7	—	7.82 [33]	GMOS-IFU
HS2236+1344	22:38:31.1	+14:00:30	84.5	—	7.55 [54]	GMOS-IFU

^aObtained from NED.

^bObtained from HyperLeda.

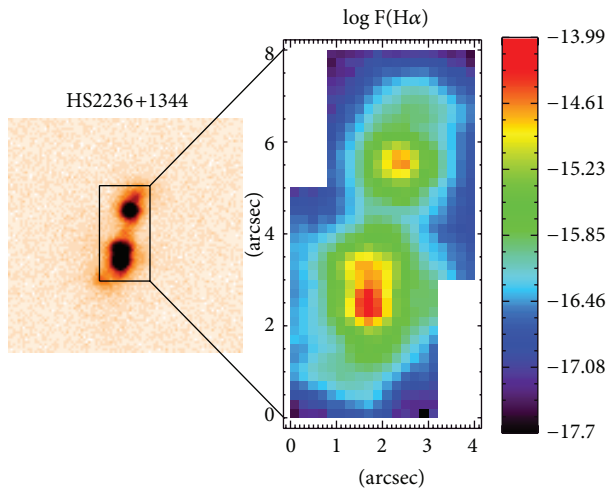


FIGURE 2: GMOS-IFU observation of the XMP galaxy HS2236+1344. Left: g-band acquisition image of the galaxy. The rectangle indicates the total field of view of $4'' \times 8''$ obtained from the composition of two different pointings with GMOS-IFU. Right: $\text{H}\alpha$ map of the galaxy. $\log F(\text{H}\alpha)$ in units of $\text{ergs cm}^{-2} \text{s}^{-1}$. Further details will be presented in a forthcoming paper [54].

is that metals formed in the current star-formation episode reside in a hot gas phase ($T \sim 10^7 \text{ K}$; [15]); thus, they are not observable in optical wavelengths, whereas metals from previous star formation events are well mixed and homogeneously distributed through the whole galaxy. In Tol 2146-391, the $12 + \log(\text{N}/\text{H})$ radial distribution shows a slight decrease with radius. This would argue in favor of heavy elements being produced in a previous burst of star formation and dispersed within the ISM by starburst-driven supershells [33], while the depressed central region could be attributed to radial inflow of relatively low metallicity gas from large radii to the center, thus diluting the abundance of the gas in the nuclear region.

Regarding the integrated properties of the galaxies, [61–63] suggest that there is a dependence between N/O and the $\text{EW}(\text{H}\beta)$, in the sense of an increasing N/O ratio with decreasing $\text{EW}(\text{H}\beta)$. Izotov et al. [61] argues that this trend is naturally explained by nitrogen ejection from WR stars. In the following analysis, we mainly concentrate on the spatially resolved physical properties of the ISM in individual galaxies

and their possible relation to the star formation process (e.g., the star formation history, burst parameter, and WR star content). In Figure 5 (see [33]), we show the $\log(\text{N}/\text{O})$ versus $\text{EW}(\text{H}\beta)$ and $12 + \log(\text{O}/\text{H})$ versus $\log(\text{N}/\text{O})$ for all spaxels of the galaxies Tol 0104-388 and Tol 2146-391. From that figure, it can be seen that the $\text{EW}(\text{H}\beta)$ values are rather constant, with a very small variation of equivalent widths as the N/O ratio increases. A comparison of $\log(\text{N}/\text{O})$ versus $12 + \log(\text{O}/\text{H})$ in Tol 2146-391 (Figure 3(b)) reveals that the $\log(\text{N}/\text{O})$ values increase with the $12 + \log(\text{O}/\text{H})$. This data point distribution has similar patterns to those found in $\text{H II}/\text{BCD}$ galaxies by [21] of increasing N/O ratios with respect to the oxygen abundance. The inner region of Tol 2146-391 (near the peak of $\text{H}\alpha$) presents N/O ratios which are larger than those expected by pure primary production of nitrogen. This might be a signature of time delay between the release of oxygen and nitrogen [17], or gas infall or outflow. In any case, for the metallicity of Tol 2146-391 purely secondary nitrogen enrichment appears implausible. In the case of HS2236+1343, we reported in [54] evidence for a high N/O ratio in one of the three GH II/Rs of the galaxy. But again, the spatial distribution of these abundances, at large scales, leads us to consider that oxygen and hydrogen are well mixed and homogeneously distributed over the ISM of the galaxy.

In summary, the results obtained in our studies suggest that the chemical properties (O, N and N/O) across $\text{H II}/\text{BCD}$ galaxies are fairly uniform, although a slight gradient of O and N is observed in the ISM of UM 408 and Tol 2146-391, respectively. We suggest that global hydrodynamical processes, such as starburst-driven supershells or/and inflow of gas might be governing the transport and mixing of metals across these galaxies, keeping the N/O ratio constant through the ISM at large scales [33, 35].

3. The High Ionization Emission Line $\text{He II } \lambda 4686$

The origin of high-ionization emission lines, such as $[\text{Ne V}] \lambda 3426$, $[\text{Fe V}] \lambda 4227$, and $\text{He II } \lambda 4686$, in starburst and $\text{H II}/\text{BCD}$ galaxies has been a subject of study in the last years, given that photoionization models of H II regions generally fail to reproduce the observed intensities of these lines (see, e.g., [64]). Several mechanisms for producing hard ionizing radiation have been proposed in the literature, such as WR

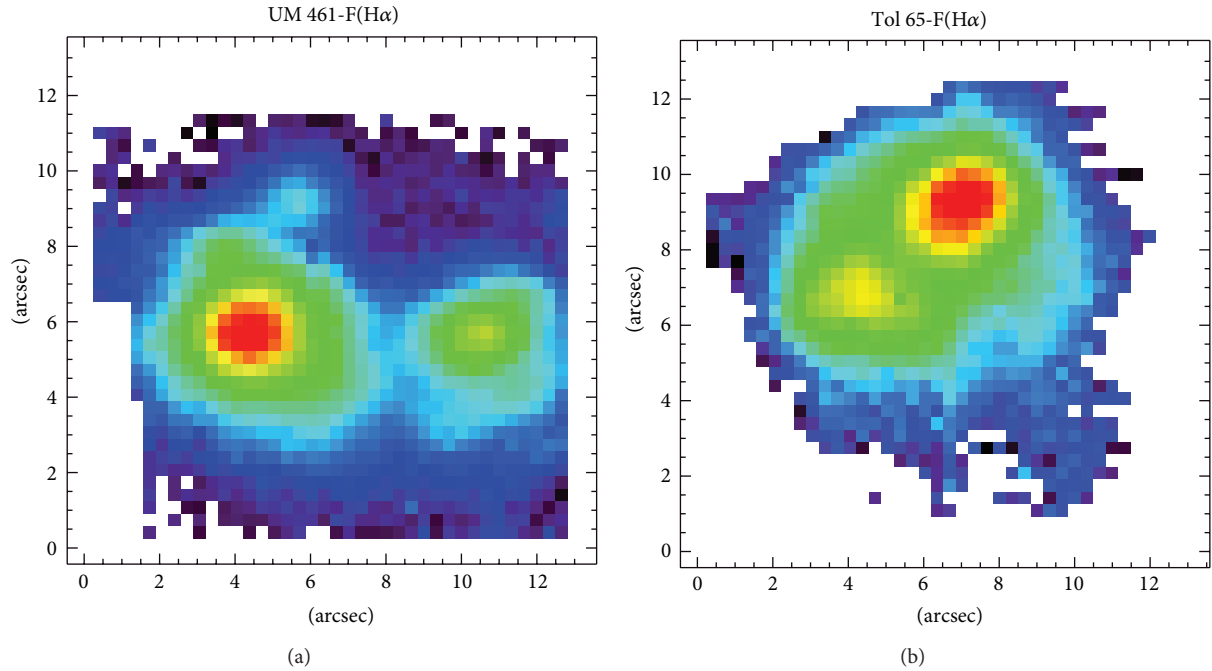


FIGURE 3: VIMOS-IFU $H\alpha$ emission line map of the XMP BCD galaxies UM 461 (a) and Tol 65 (b). North is to the top and east to the left. Further details will be presented in a forthcoming paper.

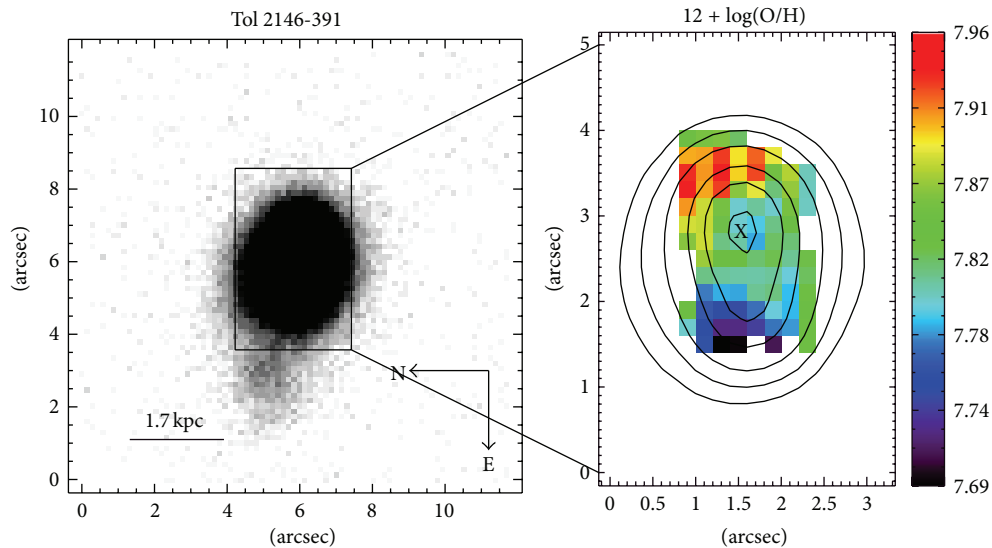


FIGURE 4: Spatial distribution of oxygen abundances in the galaxy Tol 2146-391. Left: g-band acquisition image of the galaxy. The rectangle indicates the FoV of $3''.5 \times 5''$ covered by our GMOS-IFU observation. Right: $12 + \log(O/H)$ spatial distribution. The isocontours display the $H\alpha$ emission. The maximum $H\alpha$ emission is indicated in the maps by an X symbol. We considered spaxels with signal-to-noise ratio (S/N) > 3 in the [OIII] $\lambda 4363$ line. More details in [33].

stars [65], primordial (zero-metallicity) stars, high-mass X-ray binaries (HMXB; [66]), radiative shocks [67], and O stars at low metallicity [62]. In [33, 54], we studied with GMOS-IFU the spatial distribution of He II $\lambda 4686$ in the compact H II galaxies Tol 0104-388 and Tol 2146-391 and in the XMP BCD galaxy HS2236+1344, respectively, in order to gain insights into the nature of their hard ionization radiation and its possible dependence on the properties of the ISM [64, 66].

Based on a spaxel-by-spaxel analysis, instead of the integrated properties of the galaxies (see Figure 15 in [33]), our results indicate that the spatial distribution of He II $\lambda 4686$ relative to $H\beta$ does not depend on the $EW(H\beta)$, oxygen abundance, or $\log(N/O)$. In particular, the oxygen abundance appears to be constant through the whole extent of our sample galaxies, as already is observed in other H II/BCD galaxies (e.g., [18]; and references therein).

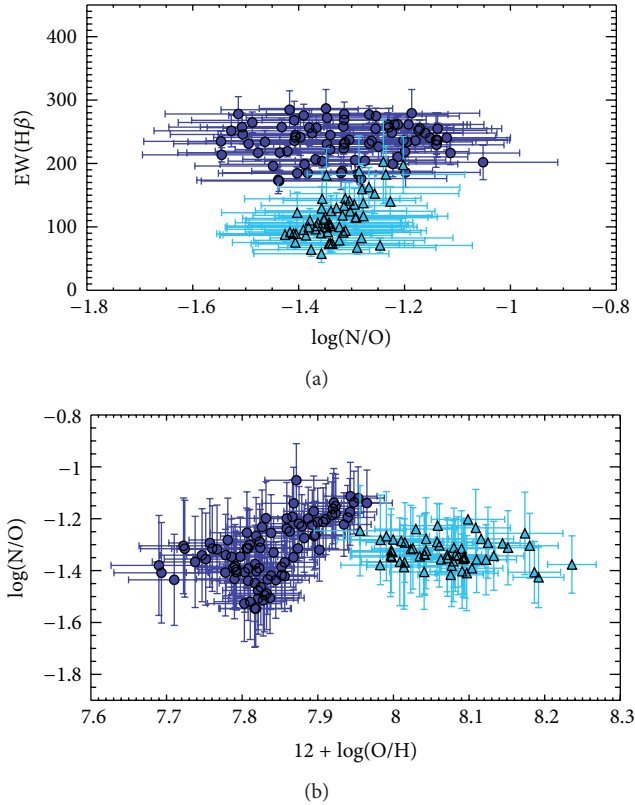


FIGURE 5: (a) Log (N/O) ratio versus $EW(H\beta)$. (b) $12 + \log(O/H)$ ratio versus $\log(N/O)$. Triangles correspond to the data points of Tol 0104-388 and circles correspond with the data points of Tol 2146-391. More details in [33].

The opposite trend is found if we consider the integrated spectra of galaxies, in the sense that this emission line is stronger in galaxies at low metallicity [61]. The lack of a relationship between the hardness of the ionizing radiation and the $EW(H\beta)$, or age, [68] suggests that the presence of high-ionization lines, in particular He II $\lambda 4686$, is not due to a single excitation mechanism. For instance, in [69], it was found for a sample of galaxies, with detected and non-detected WR features, the same dependence of $I(He II \lambda 4686)/I(H\beta)$ on the $EW(H\beta)$. This indicates that WR stars are not the sole origin of He II $\lambda 4686$ in star-forming regions (see also [70]). In galaxies with detected WR stars, the He II $\lambda 4686$ commonly appears to not be coincident with the location of the WR bumps (e.g., Mrk 178) and these stellar features are not always seen when nebular He II is observed (e.g., Tol 2146-391, HS2236+1344, Tol 65). The spatial offset between WR stars and He II $\lambda 4686$, in Mrk 178, is interpreted by [49] as an effect of the mechanical energy injected by WR star winds, so WR stars are not ruled out as the main source of the observed He II $\lambda 4686$ in that galaxy. An examination of individual spaxels in our data cubes, and also in the integrated spectra of our sample galaxies (e.g., Figure 1 in this contribution), does not reveal any clear stellar WR features. In the case of the XMP BCD galaxy HS2236+1344, we detected the He II $\lambda 4686$ emission line in only one of

the GH IIRs of the galaxy (the brightest one). In this galaxy, the He II $\lambda 4686$ line appears to be excited through point sources within a compact volume which, interestingly, does not coincide with the position where a high N/O abundance ratio has been observed. We discuss, in [54], the possibility that the He II $\lambda 4686$ emission line, in HS2236+1344, is associated with WR stars, high-mass X-ray binaries (HMXBs), O stars at low metallicities, and/or a low-luminosity Active Galactic Nucleus. However, since clear WR features have not been detected in that galaxy, WR stars are excluded as the primary excitation source of He II $\lambda 4686$ emission.

4. Conclusions

As far as the spatial distribution of oxygen abundances is concerned, we did not detect localized overabundances in any of our sample galaxies. However, we found evidence for a marginal negative radial abundance gradient, with the highest abundances seen at the position of the brightest star cluster complexes (peak of $H\alpha$ emission), in the H II/BCD galaxy UM 408 at least. If real, the slight trend for an increasing $12 + \log(N/H)$ abundance, in the galaxy Tol 2146-391, suggests rapid self-enrichment by the freshly produced heavy elements in the present starburst on scales of hundreds of pc, or, alternatively, metal pollution by a previous star formation episode. In any case, the oxygen and nitrogen appear to be well mixed across the ISM of H II/BCD galaxies, suggesting efficient transport by expanding starburst-driven supershells and/or gas infall from the halo.

Our spectroscopic IFU studies suggest a mixture of compact sources as the main excitation source for localized He II $\lambda 4686$ emission in H II/BCD galaxies, without clear WR signatures, with WR stars probably being of secondary importance. In the galaxy Tol 2146-391, we favor the idea of extended He II $\lambda 4686$ emission being primarily due to radiative shocks in the ISM.

Acknowledgments

Patricio Lagos is supported by a PostDoctoral Grant SFRH/BPD/72308/2010, funded by FCT (Portugal) and Polychronis Papaderos by Ciencia 2008 Contract, funded by FCT/MCTES (Portugal) and POPH/FSE (EC). We are very thankful to Andrew Humphrey for his very useful suggestions which have improved the paper. We would like to thank the anonymous referee for his/her comments and suggestions which substantially improved the paper. The authors acknowledge the support by the Fundação para a Ciência e a Tecnologia (FCT) under project FCOMP-01-0124-FEDER-029170 (Reference FCT PTDC/FIS-AST/3214/2012), funded by the FEDER program. This research has made use of the NASA/IPAC Extragalactic Database (NED) which is operated by the Jet Propulsion Laboratory, California Institute of Technology, under contract with the National Aeronautics and Space Administration. We acknowledge the usage of the HyperLeda database (<http://leda.univ-lyon1.fr>). The data presented in this paper have been obtained through the Gemini programs

GS-2004B-Q-59, GS-2005B-Q-19, and GN-2010B-Q-69 and the ESO-VLT program 090.B-0242.

References

- [1] I. F. Zwicky, "Compact galaxies and compact parts of galaxies. I," *The Astrophysical Journal*, vol. 140, p. 1467, 1964.
- [2] T. X. Thuan and G. E. Martin, "Blue compact dwarf galaxies. I. Neutral hydrogen observations of 115 galaxies," *The Astrophysical Journal*, vol. 247, pp. 823–848, 1981.
- [3] G. Haro, "Preliminary note on blue emission-line galaxies," *BOTT*, vol. 2, no. 14, pp. 8–18, 1956.
- [4] I. F. Zwicky, "Compact galaxies and compact parts of galaxies. II," *The Astrophysical Journal*, vol. 143, p. 192, 1966.
- [5] B. E. Markarian, "Galaxies with an ultraviolet continuum," *Astrofizika*, vol. 3, pp. 24–38, 1967.
- [6] W. L. W. Sargent and L. Searle, "Isolated extragalactic H II regions," *The Astrophysical Journal*, vol. 162, pp. L155–L160, 1970.
- [7] D. Kunth and W. L. W. Sargent, "Spectrophotometry of 12 metal-poor galaxies—implications for the primordial helium abundance," *The Astrophysical Journal*, vol. 273, pp. 81–98, 1983.
- [8] M. E. Filho, B. Winkel, J. S. Almeida et al., "Extremely metal-poor galaxies: the HI content," *Astronomy & Astrophysics*, vol. 558, article A18, 30 pages, 2013.
- [9] P. Lagos, E. Telles, and J. Melnick, "Narrow-band H β images of star-formation regions in H II galaxies," *Astronomy & Astrophysics*, vol. 476, no. 1, pp. 89–96, 2007.
- [10] P. Lagos, E. Telles, A. Nigoche-Netro, and E. R. Carrasco, "Star cluster complexes and the host galaxy in three H II galaxies: Mrk 36, UM 408, and UM 461," *Astronomical Journal*, vol. 142, no. 5, article 162, 2011.
- [11] P. Papaderos, H.-H. Loose, T. X. Thuan, and K. J. Fricke, "Optical structure and star formation in blue compact dwarf galaxies I. Observations and profile decomposition," *Astronomy and Astrophysics Supplement Series*, vol. 120, no. 2, pp. 207–228, 1996.
- [12] E. Telles and R. Terlevich, "The VRI colours of H II galaxies," *Monthly Notices of the Royal Astronomical Society*, vol. 286, no. 1, pp. 183–208, 1997.
- [13] P. Papaderos, Y. I. Izotov, K. J. Fricke, T. X. Thuan, and N. G. Guseva, "On the age of the nearby blue compact dwarf galaxy SBS 0335-052," *Astronomy & Astrophysics*, vol. 338, no. 1, pp. 43–55, 1998.
- [14] P. Papaderos, N. G. Guseva, Y. I. Izotov, and K. J. Fricke, "Extremely metal-poor star-forming galaxies," *Astronomy & Astrophysics*, vol. 491, no. 1, pp. 113–129, 2008.
- [15] G. Tenorio-Tagle, "Interstellar matter hydrodynamics and the dispersal and mixing of heavy elements," *Astronomical Journal*, vol. 111, no. 4, pp. 1641–1650, 1996.
- [16] H. A. Kobulnicky and E. D. Skillman, "Elemental abundance variations and chemical enrichment from massive stars in starbursts. II. NGC 1569," *Astrophysical Journal Letters*, vol. 489, no. 2, pp. 636–655, 1997.
- [17] H. A. Kobulnicky and E. D. Skillman, "Testing CNO enrichment scenarios in metal-poor galaxies with hubble space telescope spectroscopy," *Astrophysical Journal Letters*, vol. 497, no. 2, pp. 601–617, 1998.
- [18] P. Lagos, E. Telles, C. Muñoz-Tuñán, E. R. Carrasco, F. Cuisinier, and G. and Tenorio-Tagle, "On the compact H II galaxy UM 408 as seen by GMOS-IFU: physical conditions," *The Astronomical Journal*, vol. 137, no. 6, pp. 5068–5079, 2009.
- [19] M. G. Edmunds and B. E. J. Pagel, "Nitrogen synthesis and the "age" of galaxies," *Monthly Notices of the Royal Astronomical Society*, vol. 185, pp. 77–80, 1978.
- [20] D. Alloin, S. Collin-Souffrin, M. Joly, and L. Vigroux, "Nitrogen and oxygen abundances in galaxies," *Astronomy & Astrophysics*, vol. 78, pp. 200–216, 1979.
- [21] Y. I. Izotov and T. X. Thuan, "Heavy-element abundances in blue compact galaxies," *Astrophysical Journal Letters*, vol. 511, no. 2, pp. 639–659, 1999.
- [22] D. Kunth and G. Östlin, "The most metal-poor galaxies," *The Astronomy and Astrophysics Review*, vol. 10, no. 1-2, pp. 1–79, 2000.
- [23] P. Papaderos, Y. I. Izotov, T. X. Thuan et al., "The blue compact dwarf galaxy I Zw 18: a comparative study of its low-surface-brightness component," *Astronomy & Astrophysics*, vol. 393, no. 2, pp. 461–483, 2002.
- [24] L. van Zee, J. J. Salzer, and M. P. Haynes, "Abundances in spiral galaxies: evidence for primary nitrogen production," *Astrophysical Journal Letters*, vol. 497, no. 1, pp. L1–L4, 1998.
- [25] D. R. Garnett, "Nitrogen in irregular galaxies," *The Astrophysical Journal*, vol. 363, pp. 142–153, 1990.
- [26] J. R. Walsh and J.-R. Roy, "Optical spectroscopic and abundance mapping of the amorphous galaxy NGC 5253," *Monthly Notices of the Royal Astronomical Society*, vol. 239, pp. 297–324, 1989.
- [27] H. A. Kobulnicky, E. D. Skillman, J.-R. Roy, J. R. Walsh, and M. R. Rosa, "Hubble space telescope faint object spectrograph spectroscopy of localized chemical enrichment from massive stars in NGC 5253," *Astrophysical Journal Letters*, vol. 477, no. 2, pp. 679–692, 1997.
- [28] A. R. López-Sánchez, C. Esteban, J. Garcia-Rojas, M. Peimbert, and M. and Rodriguez, "The localized chemical pollution in NGC 5253 revisited: results from deep Echelle spectrophotometry," *The Astrophysical Journal*, vol. 656, no. 1, pp. 168–185, 2007.
- [29] M. S. Westmoquette, B. James, A. Monreal-Ibero, and J. R. Walsh, "Piecing together the puzzle of NGC 5253: abundances, kinematics and WR stars," *Astronomy & Astrophysics*, vol. 550, article A88, 16 pages, 2013.
- [30] A. R. López-Sánchez, A. Mesa-Delgado, L. López-Martín, and C. Esteban, "The ionized gas at the centre of IC10: a possible localized chemical pollution by Wolf-Rayet stars," *Monthly Notices of the Royal Astronomical Society*, vol. 411, no. 3, pp. 2076–2092, 2011.
- [31] B. L. James, Y. G. Tsamis, J. R. Walsh, M. J. Barlow, and M. S. Westmoquette, "The Lyman break analogue Haro 11: spatially resolved chemodynamics with VLT FLAMES," *Monthly Notices of the Royal Astronomical Society*, vol. 430, pp. 2097–2112, 2013.
- [32] P. Lagos and C. Muñoz-Tuñán, "The spatial distribution of the He II λ 4686 emission line in compact H II galaxies," *European Astronomical Society*, vol. 48, pp. 165–166, 2011.
- [33] P. Lagos, E. Telles, A. Nigoche-Netro, and E. R. Carrasco, "GMOS-IFU spectroscopy of the compact H II galaxies Tol 0104–388 and Tol 2146–391: the dependence on the properties of the interstellar medium," *Monthly Notices of the Royal Astronomical Society*, vol. 427, pp. 740–754, 2012.
- [34] B. L. James, Y. G. Tsamis, M. J. Barlow et al., "A VLT VIMOS study of the anomalous BCD Mrk 996: mapping the ionized gas kinematics and abundances," *Monthly Notices of the Royal Astronomical Society*, vol. 398, no. 1, pp. 2–22, 2009.
- [35] E. Pérez-Montero, J. M. Vilchez, B. Cedrés et al., "Integral field spectroscopy of nitrogen overabundant blue compact dwarf galaxies," *Astronomy & Astrophysics*, vol. 532, article A141, 2011.

- [36] P. Lagos, E. Telles, and E. R. Carrasco, "Super star clusters in H II galaxies," in *Proceedings of the International Astronomical Union (IAUS '10)*, vol. 5, symposium S266, pp. 447–450, 2010.
- [37] B. L. James, Y. G. Tsamis, and M. J. Barlow, "A VLT VIMOS integral-field spectroscopic study of perturbed blue compact galaxies: UM 420 and UM 462," *Monthly Notices of the Royal Astronomical Society*, vol. 401, no. 2, pp. 759–774, 2010.
- [38] B. García-Lorenzo, L. M. Cairós, N. Caon, A. Monreal-Ibero, and C. Kehrig, "Integral field spectroscopy of blue compact dwarf galaxies," *Astrophysical Journal Letters*, vol. 677, no. 1, pp. 201–218, 2008.
- [39] L. Vanzi, G. Cresci, M. Sauvage, and R. Thompson, "Integral field spectroscopy in the near infrared of NGC 3125-A and SBS 0335-052," *Astronomy & Astrophysics*, vol. 534, article A70, 9 pages, 2011.
- [40] Y. I. Izotov, D. Schaerer, A. Blecha, F. Royer, N. G. Guseva, and P. North, "VLT/GIRAFFE spectroscopic observations of the metal-poor blue compact dwarf galaxy SBS 0335-052E," *Astronomy & Astrophysics*, vol. 459, no. 1, pp. 71–84, 2006.
- [41] L. M. Cairós, N. Caon, B. García-Lorenzo et al., "Mapping luminous blue compact galaxies with VIRUS-P: morphology, line ratios and kinematics," *Astronomy & Astrophysics*, vol. 547, article A24, 15 pages, 2012.
- [42] L. Vanzi, G. Cresci, E. Telles, and J. Melnick, "Integral field near-infrared spectroscopy of II Zw 40," *Astronomy & Astrophysics*, vol. 486, no. 2, pp. 393–403, 2008.
- [43] V. Bordalo, H. Plana, and E. Telles, "The internal kinematics of the H II galaxy II Zw 40," *Astrophysical Journal*, vol. 696, no. 2, pp. 1668–1682, 2009.
- [44] T. Marquart, K. Fathi, G. Östlin, N. Bergvall, R. J. Cumming, and P. Amram, "Star-gas decoupling and a non-rotating stellar core in He 2-10 Integral field spectroscopy with FLAMES/ARGUS," *Astronomy & Astrophysics*, vol. 474, no. 1, pp. L9–L12, 2007.
- [45] G. Cresci, L. Vanzi, M. Sauvage, G. Santangelo, and P. van Der Werf, "Integral-field near-infrared spectroscopy of two blue dwarf galaxies: NGC 5253 and He 2-10," *Astronomy & Astrophysics*, vol. 520, no. 11, article A82, 10 pages, 2010.
- [46] L. M. Cairós, N. Caon, C. Zurita, C. Kehrig, P. Weilbacher, and M. Roth, "Mapping the starburst in blue compact dwarf galaxies. PMA5 integral field spectroscopy of Mrk 1418," *Astronomy & Astrophysics*, vol. 507, no. 3, pp. 1291–1301, 2009.
- [47] L. M. Cairós, N. Caon, C. Zurita, C. Kehrig, M. Roth, and P. Weilbacher, "Mapping the properties of blue compact dwarf galaxies: integral field spectroscopy with PMA5," *Astronomy & Astrophysics*, vol. 520, no. 14, article A90, 26 pages, 2010.
- [48] L. M. Cairós, N. Caon, P. Papaderos et al., "New light in star-forming dwarf galaxies: the PMA5 integral field view of the blue compact dwarf galaxy mrk 409," *Astrophysical Journal Letters*, vol. 707, no. 2, pp. 1676–1690, 2009.
- [49] C. Kehrig, E. Perez-Montero, J. M. Vichez et al., "Uncovering multiple Wolf-Rayet star clusters and the ionized ISM in Mrk 178: the closest metal-poor Wolf-Rayet H 00 galaxy," *Monthly Notices of the Royal Astronomical Society*, vol. 432, no. 4, pp. 2731–2745, 2013.
- [50] B. L. James, Y. G. Tsamis, M. J. Barlow, J. R. Walsh, and M. S. Westmoquette, "The merging dwarf galaxy UM 448: chemodynamics of the ionized gas from VLT integral field spectroscopy," *Monthly Notices of the Royal Astronomical Society*, vol. 428, no. 1, pp. 86–102, 2013.
- [51] A. Monreal-Ibero, J. M. Vílchez, J. R. Walsh, and C. Muñoz-Tunón, "A study of the interplay between ionized gas and star clusters in the central region of NGC 5253 with 2D spectroscopy," *Astronomy & Astrophysics*, vol. 517, article A27, 19 pages, 2010.
- [52] A. Monreal-Ibero, J. R. Walsh, and J. M. Vílchez, "The ionized gas in the central region of NGC 5253. 2D mapping of the physical and chemical properties," *Astronomy & Astrophysics*, vol. 544, article A60, 2012.
- [53] C. Kehrig, J. M. Vílchez, S. F. Sánchez, E. Telles, E. Pérez-Montero, and D. Martín-Gordón, "The interplay between ionized gas and massive stars in the H II galaxy IIZw70: integral field spectroscopy with PMA5," *Astronomy & Astrophysics*, vol. 477, no. 3, pp. 813–822, 2008.
- [54] P. Lagos, P. Papaderos, J. M. Gomes, L. R. Vega, and A. V. Smith, "On the properties of the interstellar medium in extremely metal-poor blue compact dwarf galaxies: GMOS-IFU spectroscopy of the double-knot galaxy HS2236+1344," *Astronomy & Astrophysics*. In preparation.
- [55] N. G. Guseva, Y. I. Izotov, G. Stasińska, K. J. Fricke, C. Henkel, and P. Papaderos, "VLT spectroscopy of low-metallicity emission-line galaxies: abundance patterns and abundance discrepancies," *Astronomy & Astrophysics*, vol. 529, article A149, 62 pages, 2011.
- [56] A. Nava, D. Casebeer, R. B. C. Henry, and D. Jevremovic, "On the determination of N and O abundances in low-metallicity systems," *Astrophysical Journal Letters*, vol. 645, no. 2, pp. 1076–1091, 2006.
- [57] E. D. Skillman, R. C. Kennicutt, and P. W. Hodge, "Oxygen abundances in nearby dwarf irregular galaxies," *The Astrophysical Journal*, vol. 347, pp. 875–882, 1989.
- [58] H. Lee, E. D. Skillman, and K. A. Venn, "The spatial homogeneity of nebular and stellar oxygen abundances in the Local Group dwarf irregular galaxy NGC 6822," *Astrophysical Journal Letters*, vol. 642, no. 2, pp. 813–833, 2006.
- [59] K. V. Croxall, L. van Zee, H. Lee et al., "Chemical abundances of seven irregular and three tidal dwarf galaxies in the M81 group," *The Astrophysical Journal*, vol. 705, no. 1, pp. 723–738, 2009.
- [60] D. A. Berg, E. D. Skillman, A. R. Marble et al., "Direct oxygen abundances for low-luminosity LVL galaxies," *The Astrophysical Journal*, vol. 754, no. 2, article 98, 33 pages, 2012.
- [61] Y. I. Izotov, G. Stasińska, G. Meynet, N. G. Guseva, and T. X. Thuan, "The chemical composition of metal-poor emission-line galaxies in the data release 3 of the Sloan Digital Sky Survey," *Astronomy & Astrophysics*, vol. 448, no. 3, pp. 955–970, 2006.
- [62] J. Brinchmann, D. Kunth, and F. Durret, "Galaxies with Wolf-Rayet signatures in the low-redshift Universe. A survey using the Sloan Digital Sky Survey," *Astronomy & Astrophysics*, vol. 485, pp. 657–677, 2008.
- [63] A. R. López-Sánchez and C. Esteban, "Massive star formation in Wolf-Rayet galaxies. IV. Colours, chemical-composition analysis and metallicity-luminosity relations," *Astronomy & Astrophysics*, vol. 517, article A85, 28 pages, 2010.
- [64] Y. I. Izotov, K. G. Noeske, N. G. Guseva, P. Papaderos, T. X. Thuan, and K. J. Fricke, "Discovery of the high-ionization emission line [Ne V] λ 3426 in the blue compact dwarf galaxy Tol 1214-277," *Astronomy & Astrophysics*, vol. 415, no. 2, pp. L27–L30, 2004.
- [65] D. Schaerer, "About the initial mass function and He II emission in young starbursts," *The Astrophysical Journal*, vol. 467, pp. L17–L20, 1996.
- [66] D. R. Garnett, R. C. Kennicutt Jr., Y.-H. Chu, and E. D. Skillman, "He II emission in extragalactic H II regions," *Astrophysical Journal Letters*, vol. 373, no. 2, pp. 458–464, 1991.

- [67] M. A. Dopita and R. S. Sutherland, "Spectral signatures of fast shocks. I. Low-density model grid," *Astrophysical Journal Supplement*, vol. 102, pp. 161–188, 1996.
- [68] T. X. Thuan and Y. I. Izotov, "High-ionization emission in metal-deficient blue compact dwarf galaxies," *The Astrophysical Journal Supplement Series*, vol. 161, no. 2, pp. 240–270, 2005.
- [69] N. G. Guseva, Y. I. Izotov, and T. X. Thuan, "A spectroscopic study of a large sample of Wolf-Rayet galaxies," *Astrophysical Journal Letters*, vol. 531, no. 2, pp. 776–803, 2000.
- [70] M. Shirazi and J. Brinchmann, "Strongly star forming galaxies in the local Universe with nebular He II $\lambda 4686$ emission," *Monthly Notices of the Royal Astronomical Society*, vol. 421, pp. 1043–1063, 2012.

Review Article

The Study of Nebular Emission on Nearby Spiral Galaxies in the IFU Era

Fernando Fabián Rosales-Ortega

Instituto Nacional de Astrofísica, Óptica y Electrónica, Luis E. Erro 1, 72840 Tonantzintla, PUE, Mexico

Correspondence should be addressed to Fernando Fabián Rosales-Ortega; frosales@inaoep.mx

Received 7 August 2013; Accepted 27 September 2013

Academic Editor: José Manuel Vílchez Medina

Copyright © 2013 Fernando Fabián Rosales-Ortega. This is an open access article distributed under the Creative Commons Attribution License, which permits unrestricted use, distribution, and reproduction in any medium, provided the original work is properly cited.

A new generation of wide-field emission-line surveys based on integral field units (IFU) is allowing us to obtain spatially resolved information of the gas-phase emission in nearby late-type galaxies, based on large samples of HII regions and full two-dimensional coverage. These observations are allowing us to discover and characterise abundance differentials between galactic substructures and new scaling relations with global physical properties. Here I review some highlights of our current studies employing this technique: (1) the case study of NGC 628, the largest galaxy ever sampled with an IFU; (2) a statistical approach to the abundance gradients of spiral galaxies, which indicates a *universal* radial gradient for oxygen abundance; and (3) the discovery of a new scaling relation of HII regions in spiral galaxies, the *local* mass-metallicity relation of star-forming galaxies. The observational properties and constrains found in local galaxies using this new technique will allow us to interpret the gas-phase abundance of analogue high-*z* systems.

1. Introduction

The study of the interstellar medium (ISM), like many other areas of astrophysics, has undergone a remarkable acceleration in the flow of data over the last few years. Large surveys such as the 2dFGRS [1], SDSS [2], GEMS [3], or COSMOS [4], to name a few, have revolutionised our understanding of the Universe and its constituents as they have enabled us to study the global properties of a large number of objects, allowing for meaningful statistical analysis to be performed, together with a broad coverage of galaxy subtypes and environmental conditions.

The nebular emission arising from extragalactic objects has played an important role in this new understanding. Nebular emission lines have been, historically, the main tool at our disposal for the direct measurement of the gas-phase abundance at discrete spatial positions in low redshift galaxies. They trace the young, massive star component in galaxies, illuminating and ionizing cubic kiloparsec-sized volumes of ISM. Metals are a fundamental parameter for cooling mechanisms in the intergalactic and interstellar medium, star-formation, stellar physics, and planet formation. Measuring

the chemical abundance in individual galaxies and galactic substructures, over a wide range of redshifts, is a crucial step to understanding the chemical evolution and nucleosynthesis at different epochs, since the heavy atomic nuclei trace the evolution of past and current stellar generations. This evolution is dictated by a complex array of parameters, including the local initial gas composition, star-formation history (SFH), gas infall and outflows, radial transport and mixing of gas within discs, stellar yields, and the initial mass function. Although it is difficult to disentangle the effects of the various contributors, determinations of current elemental abundance constrain the possible evolutionary histories of the existing stars and galaxies, and the interaction of galaxies with the intergalactic medium. The details of such a complex mechanism are still observationally not well established and theoretically not well developed and threaten our understanding of galaxy evolution from the early Universe to the present day.

The relevance of the study of the ISM in the local Universe cannot be underestimated, since it actually constitutes the bases of the methods and calibrations employed to derive

abundance and their relations with global galaxy parameters in high redshift galaxies (e.g., [5, 6]), objects that are typically solely identifiable by their emission line spectra. Nearby galaxies offer a unique opportunity to study the SFH-ISM coupling on a spatially resolved basis, over large dynamic ranges in gas density and pressure, metallicity, dust content, and other physically relevant parameters of gas and dust. However, most of the observations targeting nebular emission in nearby galaxies have been made with multiband and narrow-band imaging in the optical and near-infrared, or single-aperture or long-slit spectrographs, resulting in samples of typically a dozen or fewer HII regions per galaxy. These observations have been used to derive the properties of their dominant stellar populations, gas content, and kinematics (e.g., [7–9]). Nevertheless, despite many efforts, it has been difficult to obtain a complete picture of the main properties of these galaxies, especially those ones that can only be revealed by spectroscopic studies (like the nature of the ionization and/or the metal content of the gas). This is because previous spectroscopic studies only sampled a very few discrete regions in these complex targets (e.g., [10, 11]), or used narrow-band imaging of specific fields to obtain information of star-forming regions and the ionized gas (e.g., [9]), and in many cases they were sampling very particular types of regions [12–15]. Integrated spectra over large apertures were required to derive these properties in a more complete way (e.g., *drift-scanning*, [16]), but even in these cases, only a single integrated spectrum is derived, and the spatial information is lost.

On the other hand, although large spectroscopic surveys like the 2dFGRS or the SDSS do provide a large number of objects sampled and vast statistical information, they are generally limited to one spectrum per galaxy, thus missing all the radial information and spatially resolved properties of the galaxy. These surveys have been successful to describe the integrated properties and relations of a large number of galaxies along a wide redshift range. But galaxies are complex systems not fully represented by a single spectrum or just broad band colours. Disc and spheroidal components are structurally and dynamically different entities with different SFH and chemical evolution. A main drawback of this technique is that it leads to aperture bias that is difficult to control, as the area covered to integrate the spectra corresponds to different physical scales at different redshifts (e.g., SDSS), and also the physical mechanisms involved in ionizing the gas may be very different within the sampled area, as this would include regions with emission due to diffuse ionized gas (DIG), shocks, or AGN/LINER activity.

The advent of Multi-Object Spectrometers (MOS) and Integral Field Spectroscopy (IFS) instruments with large fields of view (FoV) now offers us the opportunity to undertake a new generation of surveys, based on a full two-dimensional (2D) coverage of the optical extent of nearby galaxies. The first application of IFS to obtain spatially resolved, continuously sampled spectroscopy of certain portions of nearby galaxies was due to the SAURON project [17, 18]. SAURON was specifically designed to study the kinematics and stellar populations of a sample of nearby elliptical and lenticular galaxies. The application of SAURON

to spiral galaxies was restricted to the study of spiral bulges [19]. However, IFS was rarely used in a “survey mode” to investigate sizeable samples. There were several reasons for the lack of a systematic study targeting galaxies in the local Universe using IFS that could cover a substantial fraction of their optical sizes. The reasons included small wavelength coverage, fibre-optic calibration problems, but mainly the limited FoV of the instruments available worldwide. Most IFUs have a FoV of the order of arcsec, preventing a good coverage of the target galaxies on the sky in a reasonable time, even with a mosaicking technique. Furthermore, in some cases the emission lines used in chemical abundance studies were not covered by the restricted wavelength range of the instruments. Moreover, the complex data reduction and visualisation imposed a further obstacle.

In order to fill this gap, in the last few years we started a major observational programme aimed at studying the 2D properties of the ionized gas and HII regions in a representative sample of nearby face-on spiral galaxies using IFS. The spatially resolved information provided by these observations is allowing us to test and extend the previous body of results from small-sample studies, while at the same time it opens up a new frontier of studying the 2D gas abundance on discs and the intrinsic dispersion in metallicity, progressing from a one-dimensional study (radial abundance gradients) to a 2D understanding (distributions), allowing us at the same time to strengthen the diagnostic methods that are used to measure HII region abundance in galaxies.

Here we present the highlights of our current studies employing this large spectroscopic database: (1) the case of NGC 628, the largest galaxy ever sampled with IFS; (2) an IFS-based statistical approach to the abundance gradients of spiral galaxies; and (3) the discovery of a new scaling relation of HII regions in spiral galaxies and how we use it to reproduce—with remarkable agreement—the mass-metallicity relation of star-forming galaxies.

2. A IFS Sample of Nearby Disc Galaxies

The studies here described were performed using IFS data of a sample of nearby disc galaxies. The observations were designed to obtain continuous coverage spectra of the whole surface of the galaxies. They include observations from the PPAK IFS Nearby Galaxies Survey: PINGS [20], and a sample of face-on spiral galaxies from Mármol-Queraltó et al. [21], as part of the feasibility studies for the CALIFA survey [22, 23], a legacy project which aims to observe a statistically complete sample of ~600 galaxies in the local Universe; all projects are carried out at the Centro Astronómico Hispano-Alemán of Calar Alto, Spain.

PINGS represented the first attempt to obtain continuous coverage spectra of the whole surface of a representative sample of late-type galaxies in the nearby Universe. This first sample includes normal, lopsided, interacting and barred spirals with a good range of galactic properties and star-forming environments with available multiwavelength public data (e.g., see Figure 1). The second sample consists of visually classified face-on spirals from Mármol-Queraltó et al. [21]

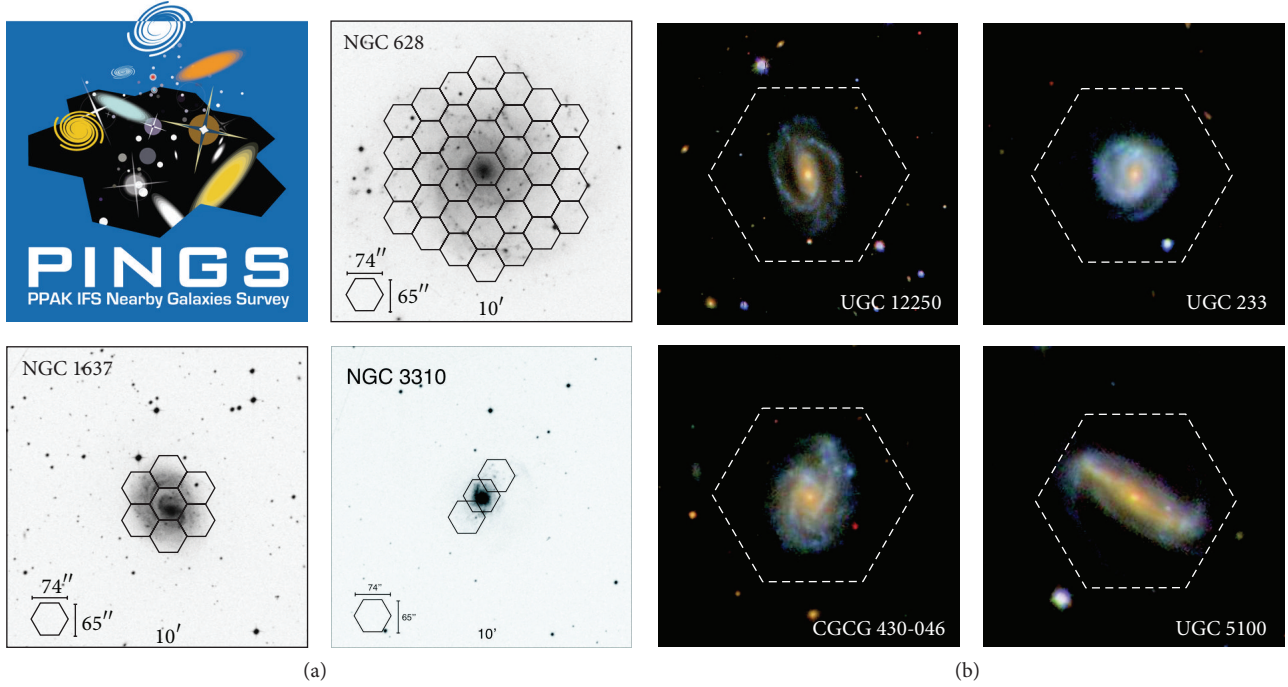


FIGURE 1: (a) Examples of the PINGS IFS mosaics, each panel shows a B -band Digital Sky Survey image of the galaxy with the PPAK mosaic pointings as overlaid hexagons indicating the FoV of the central fibre bundle. (b) Examples of the face-on spirals drawn from the Mármol-Queralto et al. [21] sample of IFS galaxies, each panel shows a colour-composite SDSS image of the galaxy with the PPAK FoV footprint overlaid.

extracted from the SDSS DR4 imaging sample selecting galaxies brighter than $r < 15.75$ mag with redshifts in the range $0.005 < z < 0.025$ (selection in volume and limiting magnitude) and from face-on disc galaxies included in the DiskMass Survey [24] with appropriate sizes to fill the FoV of the PPAK instrument (angular isophotal-diameter selection, see below).

Both samples were observed with the PMAS spectrograph [25] in the PPAK mode [26, 27] on the 3.5 m telescope in Calar Alto with similar setup, resolutions, and integration times, covering their optical extension up to ~ 2.4 effective radii within a wavelength range $\sim 3700\text{--}7000$ Å. The PPAK fiber bundle consists of 382 fibers of 2.7 arcsec diameter each. Of these 382 fibers, 331 (the science fibers) are concentrated in a single hexagonal bundle covering a field-of-view of 74×64 arcsec², with a filling factor of $\sim 60\%$. The sky background is sampled by 36 additional fibers, distributed in 6 bundles of 6 fibers each, along a circle ~ 72 arcsec from the center of the instrument FoV.

In the case of PINGS, the observations consisted of IFU spectroscopic mosaics for 17 spiral galaxies within a maximum distance of 100 Mpc; the average distance of the sample is 28 Mpc (for $H_0 = 73$ km s⁻¹ Mpc⁻¹). Most of the objects in PINGS could not be covered in a single pointing with IFS instruments, so a new observing-reduction technique had to be developed to perform accurate mosaicking of the targets. The spectroscopic mosaicking was acquired during a period of three years and the final data set comprises more than 50 000 individual spectra, covering in total an

observed area of nearly 80 arcmin², and an observed surface without precedents by a IFS study up to that point (the case study of NGC 628 presented in Section 3 is based in the data of this survey). For the second sample, the galaxies were observed over fifteen nights in several observing runs. The main difference is that, for the latter sample, a single pointing strategy using a dithering scheme was applied, while, for the largest galaxies of the PINGS survey, a mosaic comprising different pointings was required. This is due to the differences in projected size, considering the different redshift range of both samples: the PINGS galaxies correspond to $z \sim 0.001\text{--}0.003$, while, for the face-on spirals, it is $z \sim 0.01\text{--}0.025$. Therefore, in both survey samples, the data extent corresponds to about ~ 2 effective radii for all galaxies (The effective radius is classically defined as the radius at which one half of the total light of the system is emitted). So the final sample comprises 38 objects, with a redshift range between ~ 0.001 and 0.025. Although this sample is by no means a statistical subset of the galaxies in the local Universe, it is a representative sample of face-on, mostly quiescent, and spiral galaxies at the considered redshift range (see Figure 1).

Data reduction was performed using R3D [31], obtaining as an output a data cube for each galaxy, with a final spatial sampling between 1-2 arcsec/pixel, which translates to a linear physical size between a few hundreds of parsecs to ~ 1 kpc. Using this database we catalogued more than ≈ 2500 HII regions with good spectroscopic quality in all 38 galaxies, representing one of the largest and more homogeneous 2D spectroscopic HII region surveys ever accomplished.

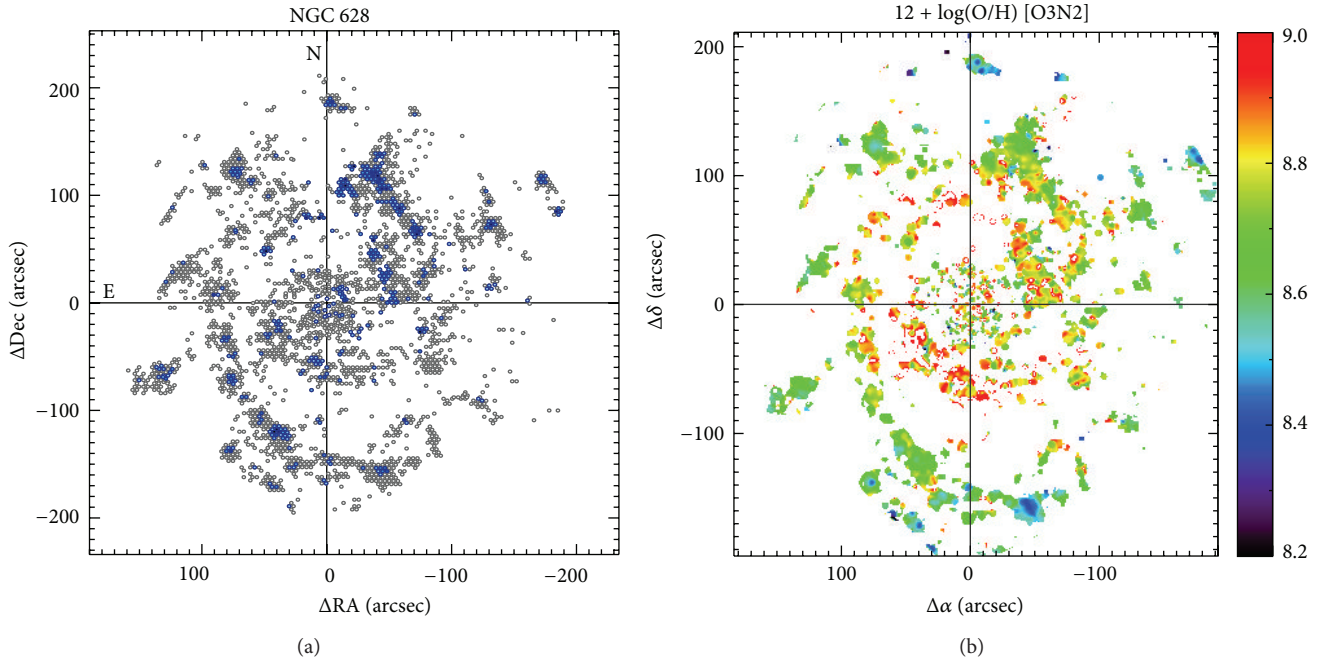


FIGURE 2: (a) Spatial map of the fibres within the IFS mosaic of NGC 628 where nebular emission was detected. Blue fibres indicate regions above a S/N threshold for a proper abundance analysis, and grey fibres correspond to a *diffuse* emission. The size and position of the fibres (at real scale) are displayed in the standard NE-positive orientation. The crosshairs mark the central reference point of the IFS mosaic. The colour intensity of each fibre in the blue sample has been scaled to the flux intensity of $H\alpha$ for that particular spectrum. (b) Oxygen abundance map of NGC 628 derived by applying the O3N2 calibrator [28] to the emission line maps of the galaxy. The figure shows a clear gradient in metallicity, with more abundant regions in the inner part of the galaxy. Figure adapted from Sánchez et al. [29] and Rosales-Ortega et al. [30].

The discussion presented in Sections 4 and 5 is based on these databases. The primary scientific objectives of these surveys were to use the 2D IFS observations to study the small and intermediate scale variation in the line emission and stellar continuum by means of pixel-resolved maps across the discs of nearby galaxies, as described in the following sections.

3. NGC 628: A Case Study of IFS-Based Nebular Emission Studies

NGC 628 (or M 74) is the largest galaxy in projected angular size ($\sim 10.5 \times 9.5 \text{ arcmin}^2$, $z \sim 0.00219 \sim 9 \text{ Mpc}$) of the PINGS sample. Due to the large size of NGC 628 compared to the FoV of the PPAK instrument ($72 \times 64 \text{ arcsec}^2$) a mosaicking scheme was adopted, employing 34 different pointings. The initial pointing was centered on the bulge of the galaxy. Consecutive pointings followed a concentric ring-shaped pattern, adjusted to the shape of the PPAK bundle (see Figure 1). The observations of this galaxy spanned a period of three years. The area covered by all the observed positions accounts approximately for 34 arcmin^2 , making this galaxy the widest spectroscopic survey ever made on a single nearby galaxy. The spectroscopic mosaic contains 11094 individual spectra.

With such dimensions, this galaxy allows us to study the 2D metallicity structure of the disc, the second order properties of its abundance distribution, and—as a very important

byproduct—a complete 2D picture of the underlying stellar populations of the galaxy. Note that the linear physical scale that a single PPAK fibre samples at the assumed distance of the galaxy is $\sim 120 \text{ pc}$. This scale can be compared to the physical diameter of a well-known HII region in our Galaxy, that is, the Orion nebula ($D \sim 8 \text{ pc}$), or to the extent of what is considered prototypes of extragalactic giant HII regions, such as 30 Doradus ($D \sim 200 \text{ pc}$) or NGC 604 ($D \sim 460 \text{ pc}$). The area sampled by an individual fibre in the mosaic would subtend a fraction of a typical giant HII region in NGC 628, but the same area would fully encompass a number of small and medium size HII regions of the galaxy (see Figure 2).

The IFS analysis of NGC 628 was taken as a case study in order to explore different spectra extraction and analysis methodologies, taking into account the signal-to-noise of the data, the 2D spatial coverage, the physical meaning of the derived results, and the final number of analysed spectra. The analysis performed on this object represents an example of the potential and extent of studies based on IFS on nearby galaxies. In the first paper of the series ([29], hereafter Paper I), we present a study of the line emission and stellar continuum of NGC 628 by means of pixel-resolved maps across the disc of the galaxy. This study includes a qualitative description of the 2D distribution of the physical properties inferred from the line intensity maps and a comparison of these properties with both the integrated spectrum of the galaxy and the spatially resolved spectra. In the second article ([30], hereafter Paper II), we present a detailed, spatially

resolved spectroscopic abundance analysis, based on different spectral samples extracted from the area covered by the IFS observations of NGC 628, and we define a spectra selection methodology specially conceived for the study of the nebular emission in IFU-based spectroscopic observations. This allows us to derive the gas chemistry distribution across the surface of the galaxy with unprecedented detail. In the third paper of the series (Sánchez-Blázquez et al., submitted; hereafter Paper III), we present a stellar population analysis of the galaxy, after applying spectral inversion methods to derive 2-dimensional maps of star-formation histories and chemical enrichment.

In Paper I, spatially resolved maps of the emission line intensities and physical properties were derived for NGC 628. Contrary to previous attempts to perform a 2D wide-field analysis based on narrow-band (or Fabry-Perot) imaging, which only allowed a basic analysis of the physical parameters and/or required assumptions on the line ratios included within individual filters (e.g., $H\alpha$), the emission line maps presented in this paper were constructed from individual (deblended) emission lines at any discrete spatial location of the galaxy, where enough signal-to-noise was found. This fact allowed investigating the point-to-point variation of the physical properties over a considerable area on the galaxy. Extinction, ionization, and metallicity-sensitive indicator maps were derived from reddening corrected emission line maps. In general, they show that the ionized gas in these spiral galaxies exhibits a complex structure, morphologically associated with the star-forming regions located along the spiral arms. The (thermal) ionization is stronger along the spiral arms, associated with the HII regions, and more intense in the outer than in the inner ones. Indeed, the surface SFR is an order of magnitude stronger in the outer HII regions, at distance larger than ~ 100 arcsec (4.5 kpc), than in the inner ones. Considering that in these outer regions there is a lower mass density, the growing rate of stellar mass is considerably larger there than in the inner ones. Therefore, the growth of the galaxy is dominated by the inside-out process.

The spatially resolved distribution of the abundance shows a clear gradient of higher oxygen metallicity values from the inner part to the outer part of the galaxy, and along the spiral arms (see right-panel of Figure 2). However, in some instances, the value of the oxygen abundance (and other physical properties like extinction and the ionization parameter) varies within what would be considered a classical well-defined HII region (or HII complex), showing some level of structure. Indeed, the 2D character of the data allows us to study the small-scale variation of the spectra within a given emitting area. The values of the emission line ratios measured using different extraction apertures vary considerably as a function of the aperture size, and the scatter of the central value is larger than the statistical error in the measurements, reflecting that this might in fact be a physical effect. By constructing 2D maps of the oxygen abundance distributions, we found that the 2D metallicity structure of the galaxy varies depending on the metallicity calibrator employed in order to derive the oxygen abundance. Different calibrators find regions of enhanced $\log(O/H)$ at spatial positions which are not coincident among them. This implies that the use of

different empirical calibrations does not only reflect in a linear scale offset but may introduce spurious inhomogeneities. This information is usually lost in a simple radial abundance gradient, and that might be relevant when constructing a chemical evolution model based on a particular abundance determination (see Figure 3).

The emission line maps presented in Paper I proved to be useful in describing the general 2D properties of the galaxy. More robust conclusions were presented in Paper II, where we analysed specific individual regions across the disc of the galaxy, either by taking individual spectra above a certain S/N threshold, or by coadding spectra with the same physical properties and comparing the results in the 2D context. With the first method we were able to identify regions of interstellar *diffuse* emission (see left panel of Figure 3), while with the second we created a *classic* catalogue of HII regions from a purely geometrical principle, that is, by coadding fibres considered to belong to the same morphological region.

Some highlights of this study (which also apply to the rest of the PINGS galaxies analysed so far) are the following.

- (1) Despite the large number of spectra contained in the original observed mosaic, the final number of fibres containing analysable spectra of enough signal-to-noise for a spectroscopic study of the ionized gas represents only a reduced percentage of the total number of fibres contained in the full IFS mosaic. For the particular case of NGC 628, less than 10% of the total area sampled by the IFU observations is considered of sufficient quality.
- (2) Independently of the abundance calibrator used, the metallicity distribution of NGC 628 is consistent with a nearly flat distribution in the innermost regions of the galaxy ($\rho/\rho_{25} < 0.2$), a steep negative gradient for $0.2 \leq \rho/\rho_{25} < 1$, and a shallow or nearly constant distribution beyond the optical edge of the galaxy, that is, implying a multimodality of the abundance gradient of NGC 628. The same feature is observed for the N/O versus ρ distribution. The existence of this feature may be related to the differences in the 2D gas surface density and star-formation rate between the inner and outer disc which inhibits the formation of massive stars in the outer regions, causing a lack of chemical evolution in the outer disc compared with the inner regions.
- (3) The observed dispersion in the metallicity at a given radius is neither a function of spatial position, nor due to low S/N of the spectra, and shows no systematic dependence on the ionization conditions of the gas, implying that the dispersion is real and is reflecting a true spatial physical variation of the oxygen content (see Figure 3).
- (4) The values of the oxygen abundance derived from the integrated spectrum for each calibrator equal the abundance derived from the radial gradient at a radius $\rho \sim 0.4\rho_{25}$, confirming for this galaxy the previous results obtained for other objects, that is, that the integrated abundance of a normal disc

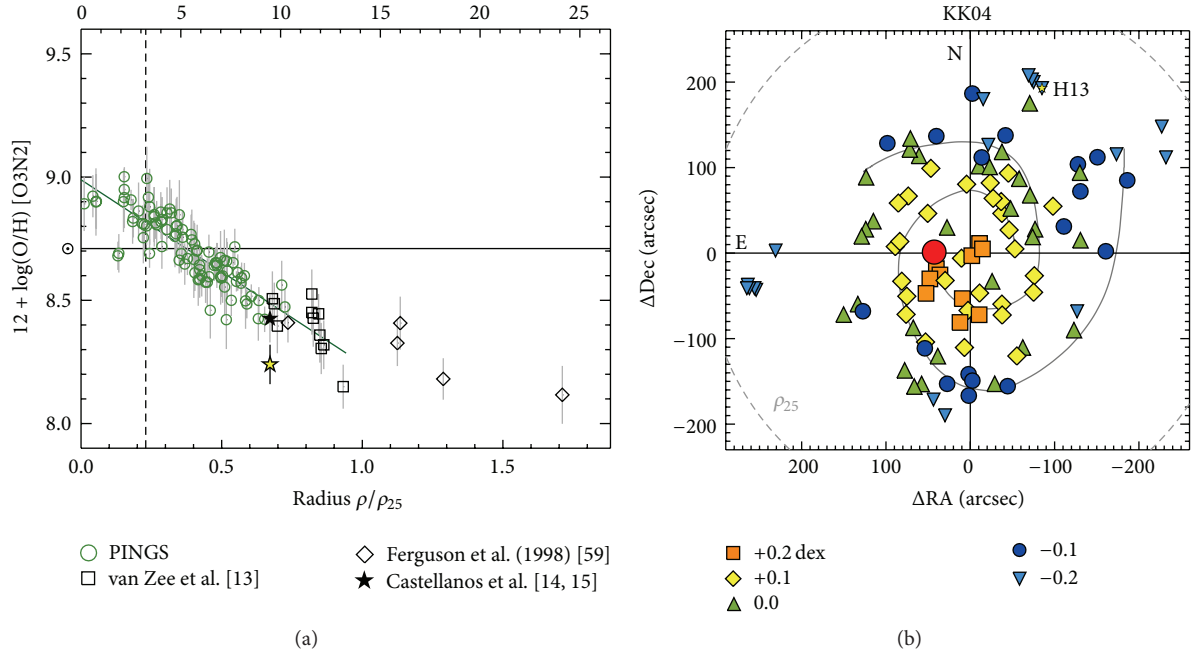


FIGURE 3: (a) Radial abundance gradient derived for NGC 628 based on the PINGS HII region catalogue (green symbols), and HII regions from the literature (black symbols) using the O3N2 calibrator. The horizontal grey lines correspond to the abundance derived using the integrated spectrum as reported in Paper I. The top X-axis values correspond to the projected radii in arcsec for the radial average data. Note the flattening of the gradient for innermost regions of the galaxy and for radii $> \rho_{25}$, that is, a multimodality of the abundance gradient. (b) 2D distribution of the oxygen abundance derived from the IFS H II regions catalogue of NGC 628 (plus selected HII regions from the literature), for the KK04 (top-left) metallicity calibrators. The shape and colours of the symbols correspond to the difference $\Delta [12 + \log(\text{O}/\text{H})] \equiv \Delta \log(\text{O}/\text{H})$ between the abundance obtained on each HII region with respect to the characteristic abundance $12 + \log(\text{O}/\text{H})_{\rho=0.4\rho_{25}}$ of the same calibrator, grouped into bins of 0.0, ± 0.1 , 0.2 dex (e.g., +0.1 dex = $0.05 \leq \Delta \log(\text{O}/\text{H}) < 0.15$). The large symbol in red colour stands for the location of the HII region with the maximum amount of $12 + \log(\text{O}/\text{H})$ measured for that calibrator. The grey thick lines define the operational spiral arms of the galaxy. The dotted circle corresponds to the size of the optical radius ρ_{25} . Figure adapted from Rosales-Ortega et al. [30].

galaxy correlates with the characteristic gas-phase abundance measured at $\rho \sim 0.4\rho_{25}$.

- (5) While trying to find axisymmetric variations of the metallicity content in the galaxy, we found slight variations between the central oxygen abundance and slopes for both the geometrical (quadrants) and morphological (arms) regions of the galaxy. However, these small variations fall within the expected errors involved in strong-line empirical calibrations (see Figure 4). If the radial trends in the ionization parameter and metallicity abundance were somewhat distinct, this would indicate that, to a certain extent, the physical conditions and the star-formation history of different-symmetric regions of the galaxy would have evolved in a different manner. Likewise, [32] found no evidence for significant large-scale azimuthal variations of the oxygen abundance across the whole disk of M 101 and marginal evidence for the existence of moderate deviations from chemical abundance homogeneity in the interstellar medium of this galaxy.

In the case of the stellar populations, in Paper III we derive maps of the mean (luminosity and mass weighted) age and metallicity that reveal a negative age gradient and the presence of structures such as a nuclear ring, previously

seen in molecular gas (see Figure 5). The disc is dominated in mass by an old stellar component at all radii sampled by the IFS data, while the percentage of young stars increases with radius, as predicted in an inside-out formation scenario, where outer parts of the disc formed later due to the increasing timescales for gas infall with radius. We also detect an inversion of the metallicity gradient at the very centre of the galaxy (~ 1 kpc), where apparently there exists a ring of old stars at this distance, with a trend to younger ones at the very center. Similar results are found in the Milky Way (MW) using Open Clusters and Cepheids, that is, a clear bimodal gradient for the older population, with a flat outer plateau, and a more continuous gradient for the younger population (e.g., [33–36]). This behaviour has also been reported in other galaxies, mostly Sa/S0, where the inner regions of their bulges present bluer colors, consistent with younger stellar populations (e.g., [37]).

The relevance of this study regarding the nebular emission is that the young component shows a metallicity gradient that is very similar to that of the gas, and that is flatter than that of the old stars. Although the metallicity gradients for the young stars and the gas also show a break, this is much less prominent than for the old stars. The position of the break is more coincident with the corotation radius of the oval distortion than that of the spiral pattern, which is

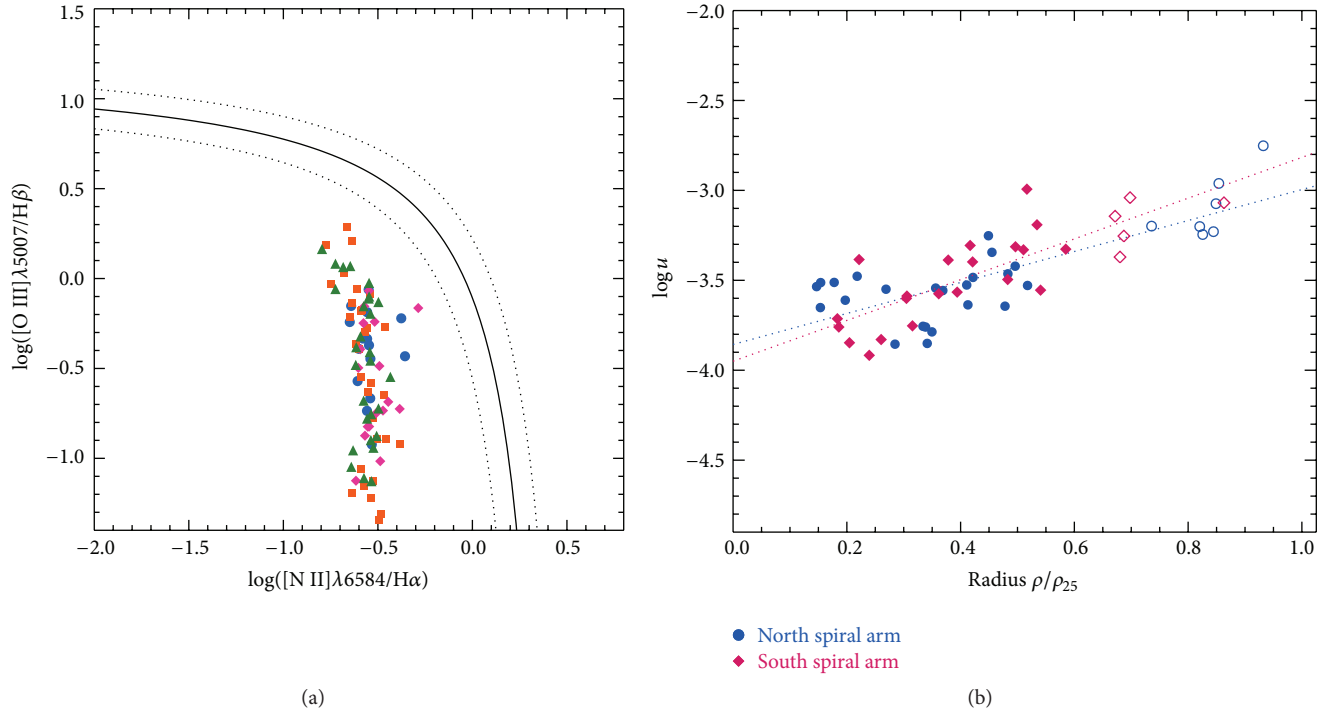


FIGURE 4: (a) BPT diagnostic diagram for HII regions coded according to the geometric position (quadrants) with respect to the an arbitrary axis drawn across the galaxy surface. The locus of different sectors does not show a clear trend or do not populate a clearly visible region on any diagram, compared to the rest of the quadrants. Points from all the regions are equally distributed within the cloud of points on each diagnostic diagram, indicating that the emission line ratios of the HII regions are not a function of azimuthal angle across the disc. (b) Radial gradients of the ionization parameter $\log u$ for morphologically selected HII regions of NGC 628. The panel shows the $\log u$ versus ρ relation for the regions belonging to the north and south spiral arms of the galaxy. The difference between the two spiral arms resides in the slope of the gradient of $\log u$, for the north arm, and the values of $\log u$ increase moderately with galactocentric distance, while, for the south arm, the ionization parameter increases with a steeper slope, although within the errors of the linear fittings. Figure adapted from Rosales-Ortega et al. [30].

beyond the radius sampled by our data. We speculate about the possible origin of this break, the possibilities being due to star-formation variation with the spiral pattern speed or that is due to radial mixing produced by either the spiral arms, the oval distortion, or a coupling of both. We argue that NGC 628 could represent a good example of secular evolution due to the presence of a dissolving bar. In this scenario, the strong bar has funneled large amounts of gas into the central regions while radial flows induced in the disc have flattened the O/H gradient. Nuclear starbursts resulting from the gas sinking into the center contributed to the bulge's growth until enough mass was accreted to dissolve the bar by dynamical instabilities. The oval distortion observed in the central region could be the remains of the bar. Forthcoming studies analysing a sample of galaxies with different masses and showing different morphological features (e.g., bars of different strength, spiral arms with different morphologies, etc.) using, for example, the CALIFA survey that will help to elucidate the importance of the different mechanisms producing radial mixing in the galaxy discs.

4. Hints of a Universal Abundance Gradient

IFS offers the possibility to analyse and study a single object in great detail, such as the case of NGC 628 described

above. However, it also offers the unique chance of studying the spectroscopic properties of thousands of HII regions in a homogeneous way. We used our catalogue of HII regions introduced in Section 2 to characterize the radial trends and the physical properties of the HII regions of the galaxy sample. However, contrary to the case of NGC 628 where the HII regions on the disc of the galaxy were basically selected and extracted by-hand, the HII regions in these galaxies were detected, spatially segregated, and spectrally extracted using HIIexplorer [39], a new automatic procedure to detect HII regions, based on the contrast of the $H\alpha$ intensity maps extracted from the data cubes. Once detected, the algorithm provides with the integrated spectra of each individual segmented region. This change of paradigm is totally necessary when working with thousands of HII regions, contrary to the case of a handful of targets in classic long-slit spectroscopy. We detected a total of 2573 HII regions with good spectroscopic quality. This is by far the *largest* spatially resolved, nearby spectroscopic HII region survey ever accomplished. The emission lines were decoupled from the underlying stellar population using FIT3D [40], following a robust and well-tested methodology [20, 29]. Extinction-corrected, flux intensities of the stronger emission lines were obtained and used to select only star-forming regions based on typical BPT diagnostic diagrams. The final

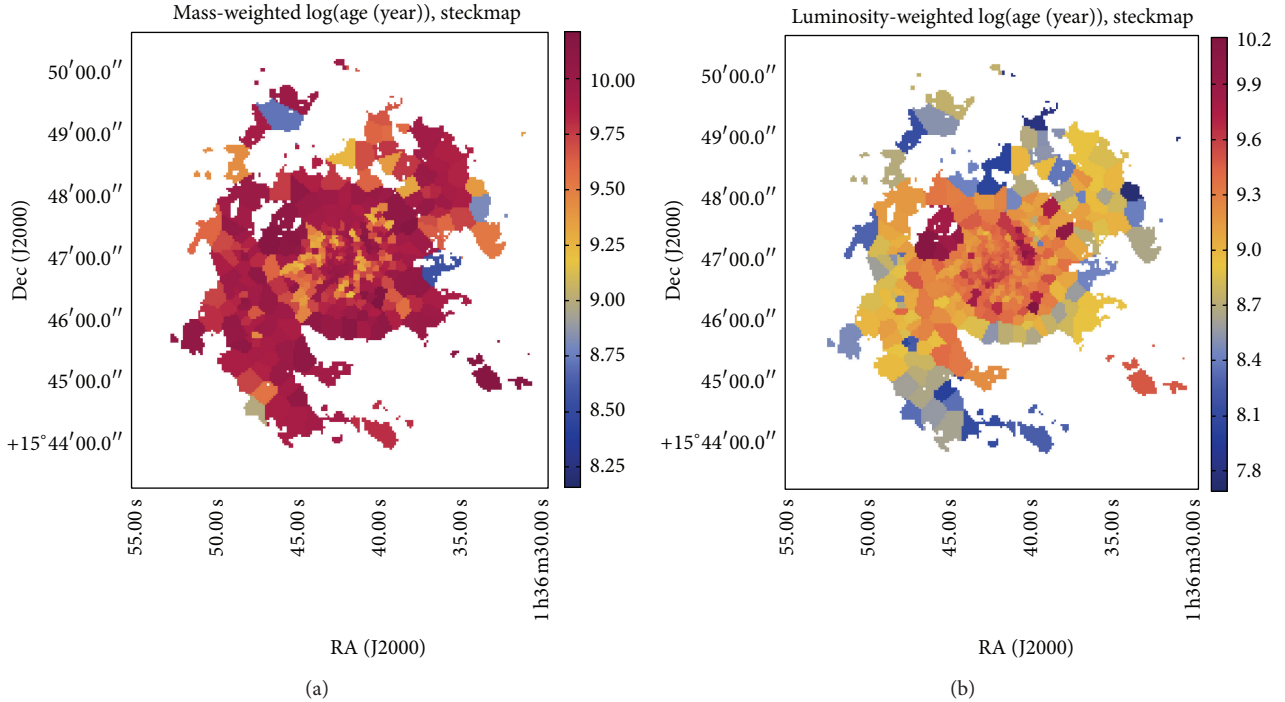


FIGURE 5: Mean age 2-D maps weighted by the mass (a) and by the light (b) of the stars. The different regions correspond to a Voronoi-tessellation binning scheme performed to the IFS mosaic of NGC 628. Figure adapted from Sánchez-Blázquez et al. (submitted).

sample comprises 1896 high-quality, spatially resolved HII regions/aggregations of disc galaxies in the local Universe [39].

It is well known that different spectroscopic properties of HII regions show strong variations across the area of disc galaxies. In particular, some of these parameters (e.g., oxygen abundance, $EW[H\alpha]$, etc.), show a strong radial gradient, that in average indicates that more evolved, metal rich, stellar populations are located in the center of galaxies, and less evolved, metal poor ones are in the outer ones. Despite the several different studies describing these observational events, there is a large degree of discrepancy between the actual derived parameters describing the gradients: (i) slope of the gradient, (ii) average value and dispersion of the zero-point, and (iii) scale length of the truncation. In general, this is mostly due to different observational biases and the lack of a proper statistical number of analysed HII regions per galaxy.

For each galaxy of our sample we derived the correlation coefficient, the slope, and the zero point of a linear regression for a number of parameters showing radial distributions across the discs of the galaxies. For those properties showing a strong correlation, we investigated if the gradient was universal within our range of explored parameters. We found that, for the equivalent width of $H\alpha$ and the oxygen abundance, the slopes of the gradients are consistent with a Gaussian distribution; that is, the dispersion of values found for each individual galaxy is compatible with the average one, not showing strong statistical deviations. This implies that we can define a characteristic value for the slope and that we do not find a population of galaxies with slopes inconsistent with

this normal distribution. The right panel of Figure 6 shows the radial density distribution for the oxygen abundance derived using the $O3N2$ indicator [28], once scaled to the average value at the effective radius for each galaxy. The radial distance was normalised to the effective radius of each galaxy. The solid line shows the average linear regression found for each individual galaxy. The red-dashed line shows the actual regression found for all the HII regions detected for all the galaxies.

Our results seem to indicate that there is a *universal* radial gradient for oxygen abundance and the equivalent width of $H\alpha$ when normalized with the *effective radii* of the galaxies; that is, they present a radial gradient that, statistically, has the same slope for all the galaxies in our sample. The derived slopes for each galaxy are compatible with a Gaussian random distribution and are independent of the morphology of the analysed galaxies (barred/nonbarred, grand-design/flocculent). This is one of the most important results in the abundance gradients of spiral galaxies, obtained thanks to the use of IFS.

5. The Local Mass-Metallicity Relation

The existence of a strong correlation between stellar mass and gas-phase metallicity in galaxies is a well-known fact. The mass-metallicity ($M-Z$) relation is consistent with more massive galaxies being more metal-enriched; after the seminal work on this relationship by Lequeux et al. [41], it was firmly established observationally by Tremonti et al. ([42], hereafter T04) using the SDSS. However, there has been no

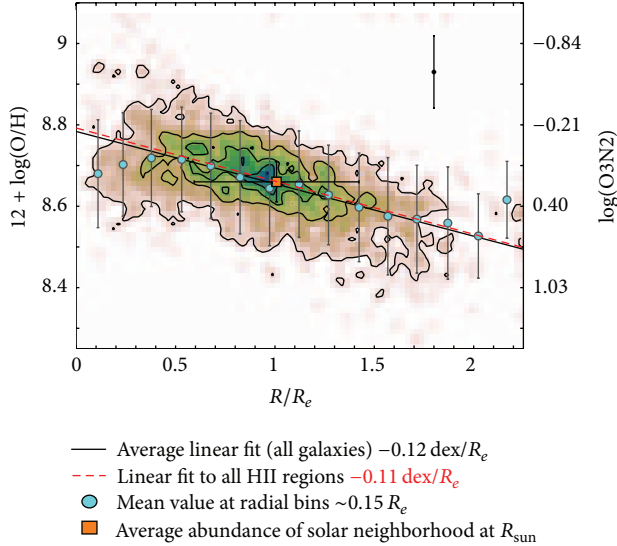


FIGURE 6: Radial oxygen abundance density distribution for the whole HII region spectroscopic sample discussed in the text. The first contour indicates the mean density, with a regular spacing of four times this value for each consecutive contour. The light-blue solid circles indicate the mean value (plus $1 - \sigma$ errors) for each consecutive radial bin of $\sim 0.15 R_e$. The average error of the derived oxygen abundance is shown by a single error bar located at the top-right side of the panel. The solid-orange square indicates the average abundance of the solar neighbourhood, at the distance of the Sun to the Milky-Way galactic center. The lines represent linear fits to all galaxies (black) and all HII regions (dotted red) independently, showing a *universal* slope $\sim -0.1 \text{ dex}/R_e$. Figure is adapted from Rosales-Ortega et al. [38].

major effort to test the \mathcal{M} -Z relation using *spatially resolved* information. We used our IFS observations in order to test the distribution of mass and metals *within* the discs of the galaxies. We derived the (luminosity) surface mass density (Σ_{Lum} , $M_{\odot} \text{ pc}^{-2}$) within the area encompassed by our IFS-segmented HII regions, using the prescriptions given by Bell and de Jong [43] to convert $B-V$ colors into a B -band mass-to-light ratio (M/L).

The left panel of Figure 7 shows the striking correlation between the local surface mass density and gas metallicity for our sample of nearby HII regions, that is, the *local* \mathcal{M} -Z relation, extending over ~ 3 orders of magnitude in Σ_{Lum} and a factor ~ 8 in metallicity [38]. The notable similarity with the global \mathcal{M} -Z relation can be visually recognised with the aid of the blue lines which stand for the [42] fit ($\pm 0.2 \text{ dex}$) to the global \mathcal{M} -Z relation, shifted arbitrarily both in mass and metallicity to coincide with the peak of the HII region \mathcal{M} -Z distribution. Other abundance calibrations were tested obtaining the same shape (and similar fit) of the relation.

In addition, we find the existence of a more general relation between mass surface density, metallicity, and the equivalent width of $\text{H}\alpha$, defined as the emission-line luminosity normalized to the adjacent continuum flux, that is, a measure of the SFR per unit luminosity [44]. This functional relation is evident in a 3D space with orthogonal coordinate axes defined by these parameters, consistent with $|\text{EW}(\text{H}\alpha)|$ being

inversely proportional to both Σ_{Lum} and metallicity, as shown in Figure 8. As discussed in Rosales-Ortega et al. [38], we interpret the local \mathcal{M} -Z-EW($\text{H}\alpha$) relation as the combination of (i) the well-known relationships between both the mass and metallicity with respect to the differential distributions of these parameters found in typical disc galaxies, that is, the *inside-out* growth, and (ii) the fact that more massive regions form stars faster (i.e., at higher SFRs), thus earlier in cosmological times.

In order to test whether the global \mathcal{M} -Z relation observed by [42] using SDSS data is a reflection (aperture effect) of the local HII region mass-density versus metallicity relation, we perform the following exercise. We simulate a galaxy with typical M_B and $B-V$ values drawn from flat distributions in magnitude (-15 to -23) and colour ($\sim 0.4-1$). A redshift is assumed for the mock galaxy, drawn from a Gaussian distribution with mean ~ 0.1 and $\sigma = 0.05$, with a redshift cut $0.02 < z < 0.3$ in order to resemble the SDSS [42] distribution. The mass of the galaxy is derived using the integrated B -band magnitudes, $B-V$ colours, and the average M/L ratio following Bell and de Jong [43]. The metallicity of the mock galaxy is derived using the local \mathcal{M} -Z relation within an aperture equal to the SDSS fiber (3 arcsec), that is, the metallicity that corresponds to the mass density surface at this radius. The process is repeated over 10,000 times in order to obtain a reliable distribution in the mass and metallicity of the mock galaxies.

The right panel of Figure 8 shows the result of the simulation, that is, the distribution of the mock galaxies in the \mathcal{M} -Z parameter space. We reproduce—with a *remarkable* agreement—the overall shape of the global \mathcal{M} -Z relation assuming a local \mathcal{M} -Z relation and considering the aperture effect of the SDSS fiber. The overlaid lines correspond to the [42] fit (black) and the Kewley and Ellison [45] $\pm 0.2 \text{ dex}$ relation (blue), for which the agreement is extremely good over a wide range of masses. The result is remarkable considering that we are able to reproduce the global \mathcal{M} -Z relation over a huge dynamical range, using a local \mathcal{M} -Z relation derived from a galaxy sample with a restricted range in mass ($9.2 < \log M_{\text{Lum}} < 11.2$) and metallicity ($8.3 < 12 + \log(\text{O}/\text{H}) < 8.9$), indicated by the rectangle shown in the right panel of Figure 8.

Therefore, by using the power of IFS applied to a sample of nearby galaxies we demonstrate the existence of a *local* relation between the surface mass density, gas-phase oxygen abundance, and $|\text{EW}(\text{H}\alpha)|$ in ~ 2000 spatially resolved HII regions of the Local Universe. The projection of this distribution in the metallicity versus Σ_{Lum} plane—the *local* \mathcal{M} -Z relation—shows a tight correlation expanding over a wide range in this parameter space. We use the local \mathcal{M} -Z relation to reproduce the global \mathcal{M} -Z relation by means of a simple simulation which considers the aperture effects of the SDSS fiber at different redshifts.

Note that the “local” \mathcal{M} -Z- $|\text{EW}(\text{H}\alpha)|$ relation is conceptually different from the “global” \mathcal{M} -Z-SFR relation proposed by Lara-López et al. ([46], dubbed FP), Mannucci et al. ([47], dubbed FMR), or Hunt et al. [48], based on the integrated spectra of galaxies (the basic difference between these relations is the proposed *shape* in the 3D distribution, that is, a

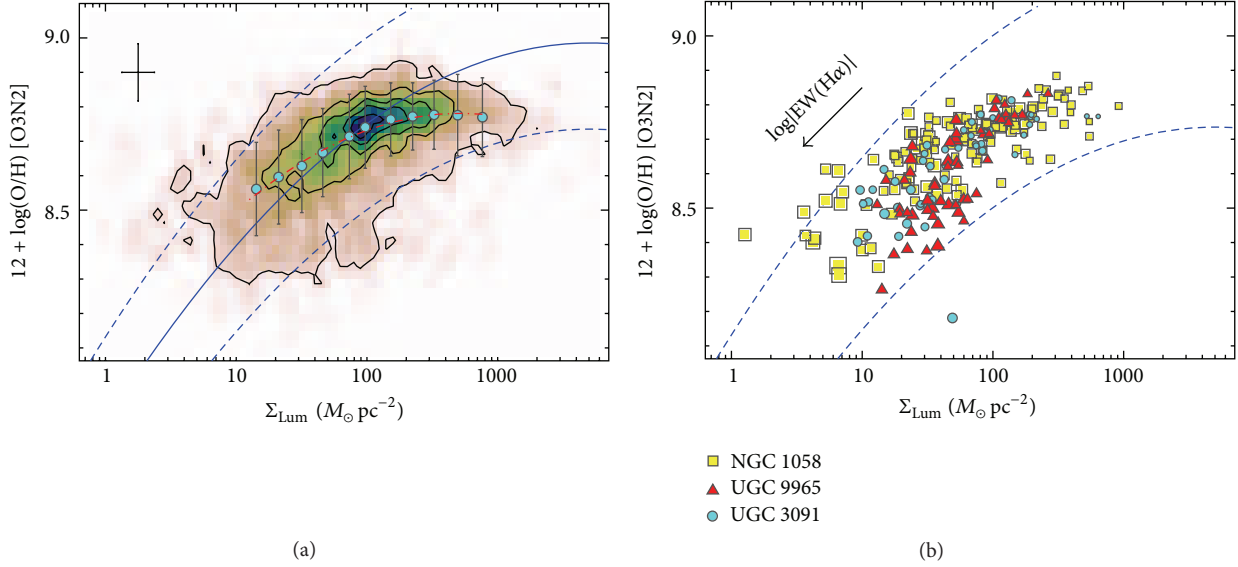


FIGURE 7: (a) The relation between surface mass density and gas-phase oxygen metallicity for ~ 2000 HII regions in nearby galaxies, the *local* \mathcal{M} -Z relation. The first contour stands for the mean density value, with a regular spacing of four times this value for each consecutive contour. The blue circles represent the mean (plus 1σ error bars) in bins of 0.15 dex. The red dashed-dotted line is a polynomial fit to the data. The blue lines correspond to the [42] relation (± 0.2 dex) scaled to the relevant units. Typical errors for Σ_{Lum} and metallicity are represented. (b) Distribution of HII regions along the local \mathcal{M} -Z relation for three galaxies of the sample at different redshifts. The size of the symbols is linked to the value of $|\text{EW}(\text{H}\alpha)|$, being inversely proportional to Σ_{Lum} and metallicity as shown. Figure is adapted from Rosales-Ortega et al. [38].

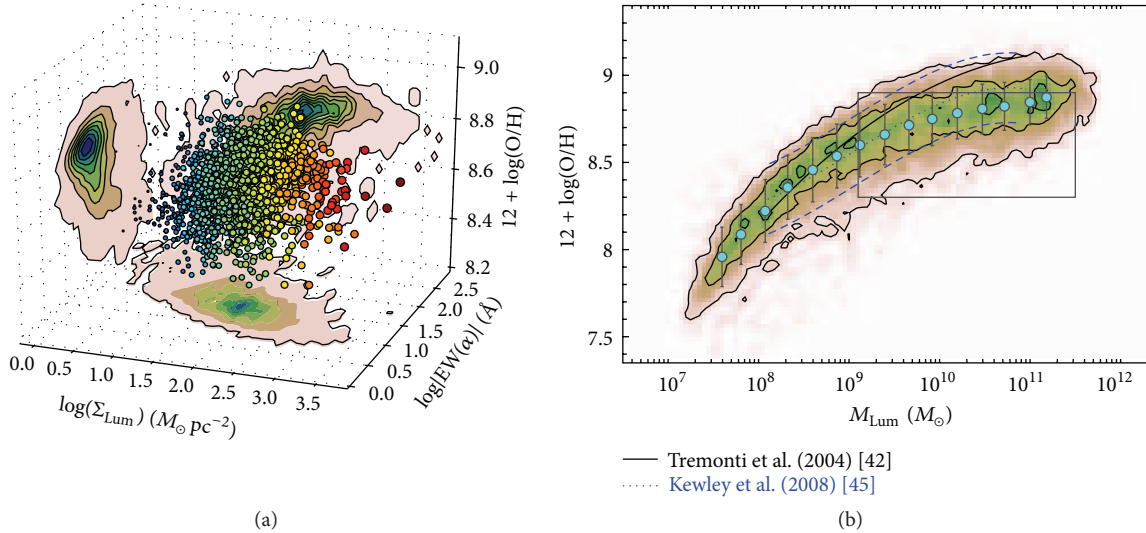


FIGURE 8: (a) 3D representation of the local \mathcal{M} -Z-EW(H α) relation. The size and color scaling of the data points are linked to the value of $\log \Sigma_{\text{Lum}}$ (i.e. low-blue to high-red values). The projection of the data over any pair of axes reduces to the local \mathcal{M} -Z, \mathcal{M} -EW(H α), and metallicity-EW(H α) relations. An online 3D animated version is available at <http://tinyurl.com/local-mass-metallicity>. (b) Distribution of simulated galaxies in the \mathcal{M} -Z plane assuming a *local* \mathcal{M} -Z relation and considering the aperture effect of the SDSS fiber, as explained in the text. The contours correspond to the density of points, while the circles represent the mean value (plus 1σ error bars) in bins of 0.15 dex. The black line stands for the [42] fitting, while the blue lines correspond to the Kewley and Ellison [45] ± 0.2 dex relation. The rectangle encompasses the range in mass and metallicity of the galaxy sample. Figure is adapted from Rosales-Ortega et al. [38].

surface or a plane). However, the obvious parallelism between these two scaling relations deserves a discussion. While the “local” \mathcal{M} -Z- $|\text{EW}(\text{H}\alpha)|$ relation is related to the intrinsic physics involved in the growth of the galaxy disc in an *inside-out* scenario, the existence of the “global” \mathcal{M} -Z-SFR relation is explained, according to Mannucci et al. [47], by the interplay

of infall of pristine gas and outflow of enriched material at different redshifts epochs, supporting the smooth accretion scenario, where galaxy growth is dominated by continuous accretion of cold gas in the local Universe. However, Sánchez et al. [49], using CALIFA data, found no secondary relation of the mass and metallicity with the SFR other than the one

induced by the primary relation of this quantity with the stellar mass. The same was found with respect to the specific SFR rate. The results by Sánchez et al. [49] agree with a scenario in which gas recycling in galaxies, both locally and globally, is much faster than other typical timescales, such like that of gas accretion by inflow and/or metal loss due to outflows. In essence, late-type/disc-dominated galaxies seem to be in a quasi-steady situation, with a behavior similar to the one expected from an instantaneous recycling/closed-box model.

In this scenario, the inner regions of the galaxy form first and faster, increasing the gas metallicity of the surrounding interstellar medium. As the galaxy evolves and grows with time, the star-formation progresses radially creating a radial metallicity gradients in the disk of spirals. Mass is progressively accumulated at the inner regions of the galaxy, raising the surface mass density and creating a bulge, with corresponding high metallicity values but low SSFR (low $|EW(H\alpha)|$), that is, an “inside-out” galaxy disk growth. In such a case, the local \mathcal{M} -Z relation would reflect a more fundamental relation between mass, metallicity, and star-formation efficiency as a function of radius, equivalent to a local *downsizing* effect, similar to the one observed in individual galaxies. Following this reasoning, the origin of the global \mathcal{M} -Z relation can be explained as the combined effect of the existence of the local \mathcal{M} -Z relation, an aperture bias due to the different fibers covering factors of the spectroscopic surveys from which the FMR and FP were derived (as second-order effect), and a possible selection of a bias of the galaxy populations which are most common at a particular redshift, and may not reflect the physics of how galaxies evolve. Supporting evidence in favour of the *inside-out* scenario of galaxy growth comes from the recent analysis of the spatially resolved history of the stellar mass assembly in galaxies of the local Universe [50]. In summary, the existence of the M-Z-SFR relation could also be interpreted as a scaled-up version of the local M-Z-sSFR relation in the distribution of star-forming regions across the discs of galaxies as described in Rosales-Ortega et al. [38] and confirmed by Sánchez et al. [49]; that is, the relationship is not primary, but obtained from the sum of a number of local linear relations (and their deviations) with respect to the galaxy radius.

6. Conclusions

The emergence of a new generation of instrumentation, that is, multiobject and integral field spectrometers with large fields of view, capable of performing emission-line surveys based on samples of hundreds of spectra in a 2D context, are revolutionising the methods and techniques used to study the gas-phase component of star-forming galaxies in the nearby Universe (objects which were typically studied with small samples based on long-slit spectroscopy). A new body of results is coming out from these studies, opening up a new frontier of studying the 2D structure and intrinsic dispersion of the physical and chemical properties of the discs of nearby spiral galaxies. In this paper we review some of the projects that in the last years tackled for the first time

the problem of obtaining spatially resolved spectroscopic information of the gas in nearby galaxies. PINGS represented the first endeavour to obtain full 2D coverage of the discs of a sample of spiral galaxies in the nearby Universe. The PINGS sample covered different galaxy types, including normal, lopsided, interacting, and barred spirals with a good range of galactic properties and star-forming environments, with multiwavelength public data. The spectroscopic data set comprises more than 50 000 individual spectra, covering an observed area of nearly 80 arcmin², an observed surface without precedents by an IFS study by the time.

The IFS analysis of NGC 628, the largest spectroscopic mosaic on a single galaxy, was taken as an example of the new methodology and analysis that could be performed with a large spectroscopic database for a single object. The contribution of PINGS also resides in defining a self-consistent methodology in terms of observation, data reduction and analysis for present and future IFS surveys of the kind, as well as a whole new set of visualization and analysis software that has been made public to the community (e.g., [51, 52]). Despite all the complexities involved in the observations, data reduction, and analysis, PINGS proved to be feasible. In less than a three-year period, it was possible to build a comprehensive sample of galaxies with a good range of galactic properties and available multiwavelength ancillary data, maximising both the original science goals of the project and the possible archival value of the survey. In fact, the science case of the PINGS project was the inspiration for the ongoing CALIFA survey. The face-on spirals from Mármol-Queraltó et al. [21] were part of the feasibility studies for the CALIFA survey. On completion, CALIFA will be the largest and the most comprehensive wide-field IFU survey of galaxies carried out to date. It will thus provide an invaluable bridge between large single aperture surveys and more detailed studies of individual galaxies.

6.1. Results from Other IFU Projects on Star-Forming Galaxies.

Other projects have followed this initiative; for example, the Mitchell spectrograph instrument at McDonald Observatory (a.k.a VIRUS-P) is currently used to carry out two small IFS surveys, namely, VENGA [53] and VIXENS [54]. VENGA (VIRUS-P Exploration of Nearby Galaxies) is an integral field spectroscopic survey, which maps the disks of 30 nearby spiral galaxies, in a very similar manner to PINGS in terms of spectral coverage, resolution, and area sampled (3600 Å–6800 Å, ~ 5 Å FWHM, $\sim 0.7R_{25}$) although with a different spatial resolution (5.6 arcsec FWHM). Their targets span a wide range in Hubble type, star-formation activity, morphology, and inclination. Likewise PINGS, the VENGA group used the data cubes of their observations to produce 2D maps of the star-formation rate, dust extinction, electron density, stellar population parameters, the kinematics and chemical abundance of both stars and ionized gas, and other physical quantities derived from the fitting of the stellar spectrum and the measurement of nebular emission lines. Their first results focus on (1) the spatially resolved star-formation law of NGC 5194 where they give support to the evidence for a low, and close to constant, star-formation

efficiency ($SFE = \tau^{-1}$) in the molecular component of the interstellar medium [55] and (2) using IFS observations of NGC 628, they measure the radial profile of the $^{12}\text{CO}(1-0)$ to H_2 conversion factor (X_{CO}) in this galaxy and study how changes in X_{CO} follow changes in metallicity, gas density, and ionization parameter [56], and also they use the IFS data to propose a new method to measure the inclination of nearly face-on systems based on the matching of the stellar and gas rotation curves using asymmetric drift corrections [53]. In the case of VIXENS (VIRUS-P Investigation of the eXtreme ENvironments of Starburst), their goal of our survey is to investigate the relation between star-formation and gas content in the extreme environments of interacting galaxy pairs and mergers on spatially resolved scales of 0.2–0.8 kpc, by using IFS of 15 interacting/starburst galaxies. VIXENS will make extensive use of multiwavelength data in order to investigate the star-formation in this object, including data from Spitzer, GALEX, IRAM, CARMA archival CO, and Hi maps. These projects and datasets are clearly focused on specific science questions, adopting correspondingly optimized sample selection criteria and also observing strategies.

Other surveys in the local Universe using the power of IFS for a detailed study of nearby galaxies include the next generation surveys like Sydney university AAO MOS IFU [57] (SAMI) and Mapping Nearby Galaxies at APO, PI: Kevin Bundy, IPMU (MaNGA), or the new generation instrumentation for Very Large Telescope (VLT, ESO) like Multi Unit Spectroscopic Explorer [58] (MUSE), which aim at studying the the chemical and dynamical evolution history and dark matter contents of galaxies, the physical role of environment in galaxy evolution, when, where, and why does star-formation occur, and so forth, based on spatially resolved spectroscopic surveys of 10^4 – 10^5 galaxies. The continuous coverage spectra provided by the imaging spectroscopy technique employed in these projects are already allowing us to study the small and intermediate linear scale variation in line emission and the gas chemistry for a statistically representative number of galaxies of the nearby Universe. The primary motivation common to all of these observational efforts is to use this information to link the properties of high redshift galaxies with those we see around us today and thereby understand the physical processes at play in the formation and evolution of galaxies. The power and importance of all these projects resides in the fact that they will provide an observational anchor of the spatially resolved properties of the galaxies in the local Universe, which will have a potential impact in the interpretation of observed properties at high redshift from new generation facilities, such as the James Webb Space Telescope (JWST), the Giant Magellan Telescope (GMT), or the European Extremely Large Telescope (E-ELT), projects that will hopefully revolutionise the understanding of our Universe in future years.

Acknowledgments

Based on observations collected at the Centro Astronómico Hispano-Alemán (CAHA) at Calar Alto, operated jointly by the Max-Planck Institut für Astronomie and the Instituto de

Astrofísica de Andalucía (CSIC) Fernando Fabián Rosales-Ortega acknowledges the Mexican National Council for Science and Technology (CONACYT) for financial support under the Programme Estancias Posdoctorales y Sabáticas al Extranjero para la Consolidación de Grupos de Investigación, 2010–2012. The author also acknowledges financial support for the ESTALLIDOS collaboration by the Spanish Ministerio de Ciencia e Innovación under Grant AYA2010-21887-C04-03.

References

- [1] S. Folkes, S. Ronen, I. Price et al., “The 2dF galaxy redshift survey: spectral types and luminosity functions,” *Monthly Notices of the Royal Astronomical Society*, vol. 308, no. 2, pp. 459–472, 1999.
- [2] D. G. York, J. Adelman, J. E. Anderson et al. et al., “The sloan digital sky survey: technical summary,” *The Astronomical Journal*, vol. 120, no. 3, article 1579, 2000.
- [3] H.-W. Rix, M. Barden, S. V. W. Beckwith et al., “GEMS: galaxy evolution from morphologies and SEDs,” *Astrophysical Journal*, vol. 152, no. 2, pp. 163–173, 2004.
- [4] N. Scoville, H. Aussel, M. Brusa et al., “The cosmic evolution survey (COSMOS): overview,” *Astrophysical Journal, Supplement Series*, vol. 172, no. 1, pp. 1–8, 2007.
- [5] T. Nagao, R. Maiolino, and A. Marconi, “Gas metallicity diagnostics in star-forming galaxies,” *Astronomy and Astrophysics*, vol. 459, no. 1, pp. 85–101, 2006.
- [6] R. Maiolino, T. Nagao, A. Grazian et al., “AMAZE: I. The evolution of the mass metallicity relation at $z > 3$,” *Astronomy and Astrophysics*, vol. 488, no. 2, pp. 463–479, 2008.
- [7] R. C. Kennicutt and P. W. Hodge, “H II regions in NGC 628. III. H-alpha luminosities and the luminosity function,” *The Astrophysical Journal*, vol. 241, article 573, 1980.
- [8] J. Belley and J.-R. Roy, “The abundance gradients across the spiral galaxies NGC 628 and NGC 6946,” *Astrophysical Journal*, vol. 78, no. 1, pp. 61–85, 1992.
- [9] P. A. Scowen, J. J. Hester, J. S. Gallagher, E. Wilcots, and T. W. Idt, “HST WFPC-2 observations of typical star formation in M101,” in *Proceedings of the 189th AAS Meeting*, vol. 28, p. 1360, Bulletin of the American Astronomical Society, 1996.
- [10] J. R. Roy and J.-R. Walsh, “Imaging spectroscopy of H II regions in the barred Spiral galaxy NGC,” *Monthly Notices of the Royal Astronomical Society*, vol. 234, article 977, 1988.
- [11] R. C. Kennicutt Jr. and D. R. Garnett, “The composition gradient in M101 revisited. I. H II region spectra and excitation properties,” *Astrophysical Journal Letters*, vol. 456, no. 2, pp. 504–518, 1996.
- [12] M. L. McCall, P. M. Rybski, and G. A. Shields, “The chemistry of galaxies. I: the nature of giant extragalactic HII regions,” *The Astrophysical Journal*, vol. 57, no. 1, 1985.
- [13] L. Van Zee, J. J. Salzer, M. P. Haynes, A. A. O’Donoghue, and T. J. Balonek, “Spectroscopy of outlying HII regions in spiral galaxies: abundances and radial gradients,” *Astronomical Journal*, vol. 116, no. 6, pp. 2805–2833, 1998.
- [14] M. Castellanos, A. I. Díaz, and E. Terlevich, “A comprehensive study of reported high-metallicity giant HII regions. I: detailed abundance analysis,” *Monthly Notices of the Royal Astronomical Society*, vol. 329, no. 2, pp. 315–335, 2002.
- [15] M. Castellanos, Á. I. Díaz, and G. Tenorio-Tagle, “On the large escape of ionizing radiation from giant extragalactic HII

- regions,” *Astrophysical Journal Letters*, vol. 565, no. 2, pp. L79–L82, 2002.
- [16] J. Moustakas and R. C. Kennicutt Jr., “An integrated spectrophotometric survey of nearby star-forming galaxies,” *Astrophysical Journal*, vol. 164, no. 1, pp. 81–98, 2006.
- [17] R. Bacon, Y. Copin, G. Monnet et al., “The SAURON project. I: the panoramic integral-field spectrograph,” *Monthly Notices of the Royal Astronomical Society*, vol. 326, no. 1, pp. 23–35, 2001.
- [18] P. T. de Zeeuw, M. Bureau, E. Emsellem et al., “The SAURON project. II: sample and early results,” *Monthly Notices of the Royal Astronomical Society*, vol. 329, no. 3, pp. 513–530, 2002.
- [19] K. Ganda, J. Falcón-Barroso, R. F. Peletier et al., “Late-type galaxies observed with SAURON: two-dimensional stellar and emission-line kinematics of 18 spirals,” *Monthly Notices of the Royal Astronomical Society*, vol. 367, no. 1, pp. 46–78, 2006.
- [20] F. F. Rosales-Ortega, R. C. Kennicutt, S. F. Sánchez et al., “PINGS: the PPAK IFS nearby galaxies survey,” *Monthly Notices of the Royal Astronomical Society*, vol. 405, pp. 735–758, 2010.
- [21] E. Mármol-Queraltó, S. F. Mármol, R. A. Marino et al., “Integral field spectroscopy of a sample of nearby galaxies: I. sample, observations, and data reduction,” *Astronomy and Astrophysics*, vol. 534, article A8, 2011.
- [22] S. F. Sanchez, R. C. Kennicutt, A. Gil de Paz et al. et al., “CALIFA, the calar alto legacy integral field area survey,” *Astronomy and Astrophysics*, vol. 538, article 8, 2012.
- [23] B. Husemann, K. Jahnke, S. F. Sanchez et al. et al., “CALIFA, the calar alto legacy integral field area survey,” *Astronomy & Astrophysics*, vol. 549, article 87, 25 pages, 2013.
- [24] M. A. Bershad, M. A. W. Verheijen, R. A. Swaters, D. R. Andersen, K. B. Westfall, and T. Martinsson, “The disk mass survey. I: overview,” *Astrophysical Journal Letters*, vol. 716, no. 1, pp. 198–233, 2010.
- [25] M. M. Roth, A. Kelz, T. Fechner et al., “PMAS: the Potsdam multi-aperture spectrophotometer. I: design, manufacture, and performance,” *Publications of the Astronomical Society of the Pacific*, vol. 117, no. 832, pp. 620–642, 2005.
- [26] M. A. W. Verheijen, M. A. Bershad, D. R. Andersen et al., “The Disk Mass project; science case for a new PMAS IFU module,” *Astronomische Nachrichten*, vol. 325, no. 2, pp. 151–154, 2004.
- [27] A. Kelz, M. A. W. Verheijen, M. M. Roth et al., “PMAS: the potsdam multi-aperture spectrophotometer. II: the wide integral field unit PPAK,” *Publications of the Astronomical Society of the Pacific*, vol. 118, no. 839, pp. 129–145, 2006.
- [28] M. Pettini and B. E. J. Pagel, “[O III]/[N II] as an abundance indicator at high redshift,” *Monthly Notices of the Royal Astronomical Society*, vol. 348, no. 3, pp. L59–L63, 2004.
- [29] S. F. Sánchez, F. F. Rosales-Ortega, R. C. Kennicutt et al., “PPAK Wide-field integral field spectroscopy of NGC 628. I: the largest spectroscopic mosaic on a single galaxy,” *Monthly Notices of the Royal Astronomical Society*, vol. 410, no. 1, pp. 313–340, 2011.
- [30] F. F. Rosales-Ortega, A. I. Díaz, R. C. Kennicutt, and S. F. Sánchez, “PPAK wide-field integral field spectroscopy of NGC628. II: emission line abundance analysis,” *Monthly Notices of the Royal Astronomical Society*, vol. 415, no. 3, pp. 2439–2474, 2011.
- [31] S. F. Sánchez, “Techniques for reducing fiber-fed and integral-field spectroscopy data: an implementation on R3D,” *Astronomische Nachrichten*, vol. 327, p. 850, 2006.
- [32] Y. Li, F. Bresolin, and R. C. J. Kennicutt, “Testing for azimuthal abundance gradients in M101,” *The Astrophysical Journal*, vol. 766, article 17, 2013.
- [33] Andrievsky, S. M. Bersier, D. Kovtyukh et al., “Using Cepheids to determine the galactic abundance gradient. II: towards the galactic center,” *Astronomy and Astrophysics*, vol. 384, pp. 140–144, 2002.
- [34] S. Pedicelli, G. Bono, B. Lemasle et al., “On the metallicity gradient of the Galactic disk,” *Astronomy and Astrophysics*, vol. 504, no. 1, pp. 81–86, 2009.
- [35] J. R. D. Lépine, P. Cruz, J. Scarano et al., “Overlapping abundance gradients and azimuthal gradients related to the spiral structure of the Galaxy,” *Monthly Notices of the Royal Astronomical Society*, vol. 417, no. 1, pp. 698–708, 2011.
- [36] B. Lemasle, P. Francois, K. Genovali et al. et al., “Galactic abundance gradients from Cepheids: alpha and heavy elements in the outer disk,” In Press. <http://xxx.tau.ac.il/abs/1308.3249>.
- [37] J.-M. Deharveng, R. Jedrzejewski, P. Crane, M. J. Disney, and B. Rocca-Volmerange, “Blue stars in the center of the S0 galaxy NGC 5102,” *Astronomy and Astrophysics*, vol. 326, no. 2, pp. 528–536, 1997.
- [38] F. F. Rosales-Ortega, S. F. Sanchez, J. Iglesias-Paramo et al., “A new scaling relation for HII regions in spiral galaxies: unveiling the true nature of the mass-metallicity relation,” *The Astrophysical Journal*, vol. 756, article L31, 2012.
- [39] S. F. Sánchez, F. F. Rosales-Ortega, R. A. Marino et al. et al., “Integral field spectroscopy of a sample of nearby galaxies,” *Astronomy and Astrophysics*, vol. 546, article A2, 2012.
- [40] S. F. Sánchez, N. Cardiel, M. A. W. Verheijen, S. Pedraz, and G. Covone, “Morphologies and stellar populations of galaxies in the core of Abell 2218,” *Monthly Notices of the Royal Astronomical Society*, vol. 376, no. 1, pp. 125–150, 2007.
- [41] J. Lequeux, M. Peimbert, J. F. Rayo, A. Serrano, and S. Torres-Peimbert, “Chemical composition and evolution of irregular and blue compact galaxies,” *Astronomy and Astrophysics*, vol. 80, pp. 155–166, 1979.
- [42] C. A. Tremonti, T. M. Heckman, G. Kauffmann et al., “The origin of the mass-metallicity relation: insights from 53,000 star-forming galaxies in the sloan digital sky survey,” *Astrophysical Journal Letters*, vol. 613, no. 2, pp. 898–913, 2004.
- [43] E. F. Bell and R. S. de Jong, “Stellar mass-to-light ratios and the Tully-Fisher relation,” *Astrophysical Journal Letters*, vol. 550, no. 1, pp. 212–229, 2001.
- [44] R. C. Kennicutt, “Star formation in galaxies along the Hubble sequence,” *ARA Stronomy and Astrophysics*, vol. 36, article 189, 1998.
- [45] L. J. Kewley and S. L. Ellison, “Metallicity calibrations and the mass-metallicity relation for star-forming galaxies,” *Astrophysical Journal Letters*, vol. 681, no. 2, pp. 1183–1204, 2008.
- [46] M. A. Lara-López, J. Cepa, A. Bongiovanni et al., “A fundamental plane for field star-forming galaxies,” *Astronomy and Astrophysics*, vol. 521, no. 2, article L53, 2010.
- [47] F. Mannucci, G. Cresci, R. Maiolino, A. Marconi, and A. Gnerucci, “A fundamental relation between mass, star formation rate and metallicity in local and high-redshift galaxies,” *Monthly Notices of the Royal Astronomical Society*, vol. 408, no. 4, pp. 2115–2127, 2010.
- [48] L. Hunt, L. Magrini, D. Galli et al. et al., “Scaling relations of metallicity, stellar mass and star formation rate in metal-poor starbursts. I: a fundamental plane,” *Monthly Notices of the Royal Astronomical Society*, vol. 427, no. 2, pp. 906–918, 2012.
- [49] S. F. Sánchez, F. F. Rosales-Ortega, B. Jungwiert et al. et al., “Mass-metallicity relation explored with CALIFA,” *Astronomy and Astrophysics*, vol. 554, article 58, 2013.

- [50] E. Perez, R. Cid Fernandes, R. M. Gonzalez Delgado et al. et al., “The evolution of galaxies resolved in space and time: an inside-out growth view from the CALIFA survey,” *The Astrophysical Journal Letters*, vol. 764, no. 1, 2013.
- [51] F. F. Rosales-Ortega, “PINGSoft: an IDL visualisation and manipulation tool for integral field spectroscopic data,” *New Astronomy*, vol. 16, pp. 220–228, 2011.
- [52] F. F. Rosales-Ortega, S. Arribas, and L. Colina, “Integrated spectra extraction based on signal-to-noise optimization using integral field spectroscopy,” *Astronomy and Astrophysics*, vol. 539, article A73, 2012.
- [53] G. A. Blanc, T. Weinzirl, M. Song et al. et al., “The virus-P exploration of nearby galaxies (venga): survey design, data processing, and spectral analysis methods,” *The Astronomical Journal*, vol. 145, article 138, 2013.
- [54] A. L. Heiderman, N. J. I. Evans, K. Gebhardt et al., “The VIRUS-P Investigation of the extreme environments of starbursts (VIXENS): survey and first results,” in *Proceedings of the Frank N. Bash Symposium on New Horizons in Astronomy*, 2011.
- [55] G. A. Blanc, A. Heiderman, K. Gebhardt, N. J. I. Evans, and J. Adams, “The spatially resolved star formation law from integral field spectroscopy: virus-p observations of NGC 5194,” *Astrophysical Journal Letters*, vol. 704, no. 1, pp. 842–862, 2009.
- [56] G. A. Blanc, A. Schrubba, N. J. I. Evans et al. et al., “The virus-P exploration of nearby galaxies (venga): the X co gradient in NGC 628,” *The Astrophysical Journal*, vol. 764, article 117, 2013.
- [57] S. M. Croom, J. S. Lawrence, J. Bland-Hawthorn et al., “The Sydney-AAO Multi-object Integral field spectrograph,” *Monthly Notices of the Royal Astronomical Society*, vol. 421, no. 1, pp. 872–893, 2012.
- [58] R. Bacon, S. M. Bauer, R. Bower et al. et al., “The second generation VLT instrument MUSE: science drivers and instrument design,” in *Groundbased Instrumentation for Astronomy*, A. F. M. Moorwood and I. Masanori, Eds., Proceedings of the SPIE, pp. 1145–1149, Observatoire de Lyon, Lyon, France, 2004.
- [59] A. M. N. Ferguson, J. S. Gallagher, and R. F. G. Wyse, “The Extreme Outer Regions of Disk Galaxies. I. Chemical Abundances of HII Regions,” *Astronomical Journal*, vol. 116, article 673, 1998.

Research Article

Are Wolf-Rayet Stars Able to Pollute the Interstellar Medium of Galaxies? Results from Integral Field Spectroscopy

Enrique Pérez-Montero,¹ Carolina Kehrig,¹ Jarle Brinchmann,²
José M. Vilchez,¹ Daniel Kunth,³ and Florence Durret³

¹ Instituto de Astrofísica de Andalucía-CSIC, Apartado. 3004, 18008 Granada, Spain

² Leiden Observatory, Leiden University, P.O. Box 9513, 2300 RA Leiden, The Netherlands

³ Institut d'Astrophysique de Paris, UMR 7095 CNRS, Université Pierre & Marie Curie, 98 bis boulevard Arago, 75014 Paris, France

Correspondence should be addressed to Enrique Pérez-Montero; epm@iaa.es

Received 17 May 2013; Accepted 30 August 2013

Academic Editor: Polychronis Papaderos

Copyright © 2013 Enrique Pérez-Montero et al. This is an open access article distributed under the Creative Commons Attribution License, which permits unrestricted use, distribution, and reproduction in any medium, provided the original work is properly cited.

We investigate the spatial distribution of chemical abundances in a sample of low metallicity Wolf-Rayet (WR) galaxies selected from the SDSS. We used the integral field spectroscopy technique in the optical spectral range (3700 Å–6850 Å) with PMAS attached to the CAHA 3.5 m telescope. Our statistical analysis of the spatial distributions of O/H and N/O, as derived using the direct method or strong-line parameters consistent with it, indicates that metallicity is homogeneous in five out of the six analysed objects in scales of the order of several kpc. Only in the object WR404 is a gradient of metallicity found in the direction of the low surface brightness tail. In contrast, we found an overabundance of N/O in spatial scales of the order of hundreds of pc associated with or close to the positions of the WR stars in 4 out of the 6 galaxies. We exclude possible hydrodynamical causes, such as the metal-poor gas inflow, for this local pollution by means of the analysis of the mass-metallicity relation (MZR) and mass-nitrogen-to-oxygen relation (MNOR) for the WR galaxies catalogued in the SDSS.

1. Introduction

Wolf-Rayet (WR) galaxies host very bright episodes of star formation characterized by the emission of broad WR bumps in their optical spectrum [1]. The two main bumps in the optical range are the blue bump, centered at a wavelength of 4650 Å, produced by the emission from N v, N III, C III/C IV, and He II, and associated with WC and WN stars, and the red bump which is fainter, centered at ~5800 Å, produced mainly by C III and C IV, and associated with WC stars. The lines making up these bumps originate in the dense stellar winds from WR stars ejecting metals into the interstellar medium (ISM).

The number of known WR galaxies has tremendously increased from the discovery of the first one (He 2–10: [2]), with different published catalogs [3–6], until the list of WR galaxies in the Sloan Digital Sky Survey (SDSS) by Brinchmann et al. [7] with around 570 objects with the identification of the WR bumps in their integrated spectra.

There is increasing evidence that the most challenging problems for this kind of objects appear in the low metallicity galaxies. Although it is well documented that the number of WR stars and the intensity of the WR bumps are higher for higher metallicities [8], the values found in some low metallicity H II galaxies, such as IZw18 [9], are claimed to be much higher than those predicted by synthesis population models (e.g., [10]).

Among the other important open issues regarding WR galaxies is the chemical enrichment of the ISM surrounding the stellar clusters where the WR stars are located. It is well known that there is an overabundance of the N/O ratio found in some WR nebulae (e.g., [11–13]) and also in the ISM of some WR galaxies, where the WR features are diluted (e.g., HS0837 + 4717, [14], NGC5253, [15], other H II galaxies in [16, 17], and *green pea* galaxies, [18]). Brinchmann et al. [7] also showed that the median N/O ratio in WR galaxies with $EW(H\beta) < 100 \text{ \AA}$ has an excess of ~25% in relation to the other star-forming galaxies in the SDSS. Chemical evolution

TABLE 1: The sample of observed Wolf-Rayet galaxies with different properties, including names, redshifts, positions, WR index, and date of observations with PMAS.

Name	Redshift	R.A (2000)	δ (2000)	WR class	Other designation	Observing date
WR 038	0.0158	17 h 29 m 06.55 s	+56 d 53 m 19.23 s	2	SHOC 575	22-23 Jun 2009
WR 039	0.0472	17 h 35 m 01.24 s	+57 d 03 m 08.55 s	2	SHOC 579	25 Jun 2009
WR 057	0.0179	00 h 32 m 18.59 s	+15 d 00 m 14.16 s	3	SHOC 022	11 Oct 2009
WR 266	0.0213	15 h 38 m 22.00 s	+45 d 48 m 07.02 s	2		24-25 Jun 2009
WR 404	0.0220	21 h 34 m 37.80 s	+11 d 25 m 10.19 s	2	CGCG 427-004	24-25 Jun 2009
WR 505	0.0164	16 h 27 m 51.17 s	+13 d 35 m 13.73 s	2		22-23 Jun 2009

models do not predict high N/O values in these low-metallicity galaxies [19], as for $12 + \log(\text{O}/\text{H}) < 8.2$ most of the N in the ISM has a primary origin, and therefore, its chemical abundance does not depend on the metallicity of the gas, and the expected N/O ratio for closed-box models has a constant value around $\log(\text{N}/\text{O}) \approx -1.5$. However, many of these integrated observations do not allow us to properly relate the excess in some chemical species with their WR content.

To investigate the issue, among others, of the possible connection between the presence of WR stars and the chemical pollution of the surrounding ISM, we have carried out a program to study metal-poor WR galaxies by means of integral field spectroscopy (IFS; [20–22]). Integrated observations, such as long slit or fibers, may fail to correlate the spatial location and distribution of WR features with respect to the physical conditions and the chemical abundances of the ISM as derived from the optical emission lines. Thus, a two-dimensional analysis of the ionized material in galaxies helps us to better understand the interplay between the massive stellar population and the ISM. For instance, whether WR stars are a significant contributor to abundance fluctuations on timescales of $t \sim 10^7$ yr and to the formation of high-ionization lines (e.g., He II 4686 Å) is still an unsolved issue (e.g., [23, 24]) that can be probed more precisely when applying IFS to nearby galaxies (see [22]).

Thus far, the results coming from WR galaxies studied IFS point to different scenarios, depending on the relative position between the local or extended N and/or He enrichment and the location(s) of the WR stars. López-Sánchez et al. [25] claimed to find a local N overabundance associated with WR emission in IC-10. A similar result is found by James et al. [26] for the blue compact dwarf galaxy Haro 11. Monreal-Ibero et al. [27] also find in NGC5253 local peaks of high N/O (see also [28]), but only some of them are associated with WR emission; so this could be indicative of a different timescale between the formation of the WRs and the mixing of the ejected material with the surrounding ISM. A similar scenario is found by Kehrig et al. [22] in Mrk178, where only one out of three detected WR clusters can be associated with an overabundance of N and He. Finally, in Pérez-Montero et al. [21], the IFS study of N overabundant objects HS0837 + 4717 and Mrk930, also identified as WR galaxies, leads to high values of N/O in scales of more than 1 kpc, much beyond the power of the observed WR stars to pollute the ISM in these scales and thus pointing to other hydrodynamical processes affecting the chemistry of the gas in these galaxies, such as the

infall of metal-poor gas [29]. James et al. [30] also propose a similar scenario for their results of IFS observations of the merging galaxy UM448.

In this work, we extend the sample of low-metallicity WR galaxies studied by means of IFS by six objects selected from the WR galaxy catalog by Brinchmann et al. [7]. The paper is organized as follows. In Section 2, we describe the observed WR galaxies, and we report the IFS observations and data reduction. In Section 3, we present our results, including emission-line maps and derivation of oxygen and nitrogen chemical abundances and their distributions in the observed fields of view. We also describe the measurement of the WR bumps in the observed galaxies. In Section 4, we discuss our results about the chemical pollution of the ISM in the context of WR stars the surrounding ISM. Finally, we summarize our results and present our conclusions in Section 5.

2. Data Acquisition and Reduction

2.1. Object Selection and Observations. We obtained IFS data of a sample of six objects selected from the SDSS WR galaxy catalog by Brinchmann et al. [7] following three criteria: (i) galaxies should be associated with a WR index of 2 (convincing WR features in the SDSS spectrum) or 3 (very clear features) in the catalog, (ii) the main ionization source should be dominated by star formation as derived using diagnostic diagrams based on strong emission lines [31], and (iii) galaxies should have oxygen abundances lower than half the solar value [$12 + \log(\text{O}/\text{H}) \approx 8.4$] as derived from the direct method. These criteria were completed with two other observational conditions: (i) to have sizes smaller than the field of view (FoV) of PMAS in lens array mode $16'' \times 16''$ in order to cover the entire galaxy in one single pointing, (ii) all objects were visible from the CAHA observatory in the assigned dates at an air mass lower than 1.2. The six target WR galaxies are listed in Table 1. Column (1) quotes the names of the objects from the catalog of Brinchmann et al. [7]. Column (2) shows the redshift of each galaxy. Columns (3) and (4) give the object coordinates. Column (5) gives the WR index as done by Brinchmann et al. [7], column (6) gives other names, and finally column (7) shows the observing date.

The data were acquired with the Integral Field Unit (IFU) Potsdam Multi-Aperture Spectrophotometer (PMAS), developed at the Astrophysikalisches Institut Potsdam [32]. PMAS is attached to the 3.5 m Telescope at the CAHA Observatory (Spain). The PMAS spectrograph is equipped with 256 fibers coupled to a 16×16 lens array. Each fiber has a spatial

sampling of $1'' \times 1''$ on the sky resulting in a FoV of $16'' \times 16''$ collecting square areas known as spaxels.

We were awarded a service mode run on the nights of June 22–25, 2009 (program F09-3.5-27). In addition, we continued our program with additional time on October 11th, 2009 as part of the commissioning run for the new PMAS CCD.

During observations taken in June, 2009 with the old PMAS $2K \times 2K$ CCD, we used the V600 grating in two separate spectral ranges: the blue side, covering a spectral range $\sim 3700\text{--}5200 \text{ \AA}$ (centered at 4500 \AA), and the red one (centered at 6325 \AA), providing a spectral range from ~ 5350 to 6850 \AA . For the galaxy WR057, taken with the new $4K \times 4K$ PMAS CCD but with the same resolution, we were able to cover the whole optical spectral range ($\sim 3700\text{--}6850 \text{ \AA}$) in one shot using the same V600 grating. The data were binned by a factor of 2 in the spectral direction, yielding a spectral resolution of $\sim 1.6 \text{ \AA/pixel}$. The data were acquired under nonphotometric conditions and with a seeing varying between $1''$ and $1''.5$. To avoid major differential atmospheric refraction (DAR) effects, all expositions were taken at air mass < 1.2 . We used one single pointing for each galaxy, covering in all cases the most intense burst of star formation and its surroundings. Observations of the spectrophotometric standard stars BD + 253941 and PG1633 in the first run and BD + 284211 for the calibration of WR057 in the second one were obtained during the observing nights for flux calibration. Bias frames, arc exposures (HgNe), and spectra of a continuum lamp were taken following the science exposures as part of the PMAS baseline calibrations.

2.2. Data Reduction. For all objects observed with the PMAS $2K \times 2K$ CCD, the first steps of the data reduction were done through the R3D package [33]. We used the P3d tool [34] to perform the basic data reduction of WR057, taken with the new PMAS $2K \times 4K$ CCD. This CCD is read out in four quadrants which have slightly different gains [35]. At the time we observed WR057, P3d was the only software capable to handle the characteristics of the new CCD.

After trimming, combining the four quadrants for WR057 and bias subtraction, the expected locations of the spectra were traced on a continuum-lamp exposure obtained before each target exposure. We extracted the target spectra by adding the signal from the 5 pixels around the central traced pixel (that is, the total object spectrum width). With exposures of HgNe arc lamps obtained immediately after the science exposures, the spectra were wavelength calibrated.

Fibers have different transmissions that may depend on the wavelength. The continuum-lamp exposures were used to determine the differences in the transmission fiber-to-fiber and to obtain a normalized fiber-flat image, including the wavelength dependence. This step was carried out by running the FIBER-FLAT.PL script from the R3D package. In order to homogenize the response of all the fibers, we divided our wavelength calibrated science images by the normalized fiber flat [33]. Then, to remove cosmic rays, different exposures taken at the same pointing were combined using the IMCOMBINE routine in IRAF (IRAF is distributed by the National Optical Astronomical Observatories, which are operated by

the Association of Universities for Research in Astronomy, Inc., under cooperative agreement with the National Science Foundation). Flux calibration was performed using the IRAF tasks STANDARD, SENSFUNC, and CALIBRATE. We coadded the spectra of the central fibers of the standard star to create a one-dimensional spectrum that was used to obtain the sensitivity function.

The reduced spectra were contained in a data cube for each object.

3. Results

3.1. Line Measurements. The emission-line fluxes on the extracted one-dimensional spectra were measured for each spaxel using a Gaussian fitting over the local position of the continuum. This procedure was done using an automatic routine based on the IRAF task SPLOT. In the case of those lines with a lower signal-to-noise (S/N) (e.g., [O III] 4363 \AA and [N II] 6584 \AA), the results from this routine were revised by eye inspection and, if necessary, repeated using a manual measurement.

The adjacent continuum to each line can be affected by the underlying stellar population which can depress the intensity of the Balmer emission lines with stellar absorption wings (e.g., [36]). This stellar absorption was studied for the brightest spaxels by fitting a combination of synthesis spectra of single stellar populations (SSP) libraries by Bruzual and Charlot [37] and the code STARLIGHT (the STARLIGHT project is supported by the Brazilian agencies CNPq, CAPES, and FAPESP and by the France-Brazil CAPES/Cofecub program) [38, 39]. The fitted spectra were later subtracted from the observed ones and the emission-line intensities of the residuals were compared with the corresponding noncorrected values. For those objects of our sample with very high $H\beta$ equivalent widths (more than 200 \AA for WR039 and around 100 \AA for WR038, WR057, WR404, and WR505), the correction at $H\beta$ wavelength is negligible (less than 1 \AA). Only in the case of WR266, with $EW(H\beta)$ of 54 \AA , we found a correction around 4 \AA for $EW(H\beta)$. For this object, appropriate corrections for each Balmer line were taken into account according to the SSP fitting in the brightest spaxels.

We calculated the statistical errors of the line fluxes, σ_l , using the expression $\sigma_l = \sigma_c N^{1/2} [1 + EW/N\Delta]^{1/2}$ (as in [40]), where σ_c represents a standard deviation of the noise in a range centred close to the measured emission line, N is the number of pixels used in the measurement of the line flux, EW is the equivalent width of the line, and Δ is the wavelength dispersion in \AA/pixel . This expression takes into account the error in the continuum and the photon count statistics of the emission line. The error measurements were performed on the extracted one-dimensional spectra. In order to minimize errors in the ratios between a certain emission line and $H\beta$, we always took first its ratio in relation to the closest hydrogen emission line (i.e., $H\alpha$ in the case of [N II]), and then, we renormalized using the corresponding theoretical ratio (i.e., at the electron temperature derived in the integrated SDSS observations for each object) from Storey and Hummer [41]. We checked that the variation of this temperature across the FoV of the instrument does not introduce errors in the

TABLE 2: Total oxygen abundances and N/O derived for the six studied WR galaxies using different methods as described in the text. The confidence level from the Lilliefors test for those spaxels where all involved emission lines were measured is the P value. Column (3) lists the mean value and standard deviation (σ) from the Gaussian fit as long as P value > 0.05 ; otherwise, the mean value and σ of the data distribution are shown. Column (4) and (5) show the O/H, N/O, and their corresponding errors derived from the brightest spaxel and from the SDSS spectrum for each galaxy, respectively. The number in parenthesis indicates the method used to derive the chemical abundances: (1) from direct method with [O II] 3727 Å, (2) from direct method with [O II] 7319, 7330 Å, (3) from N2, (4) from O3N2, and (5) from N2O2.

	P value	Mean \pm st. deviation	Brightest	SDSS
$12 + \log(\text{O}/\text{H})$				
WR038	0.51	8.14 ± 0.06 (3)	8.09 ± 0.07 (1)	8.16 ± 0.11 (2)
WR039	0.07	8.06 ± 0.09 (1)	7.96 ± 0.05 (1)	8.13 ± 0.05 (1)
WR057	0.10	7.94 ± 0.06 (3)	8.14 ± 0.10 (1)	8.06 ± 0.06 (2)
WR266	0.23	8.23 ± 0.05 (3)	8.26 ± 0.30 (1)	8.18 ± 0.14 (1)
WR404	0.02	8.26 ± 0.02 (4)	8.23 ± 0.30 (4)	8.23 ± 0.05 (1)
WR505	0.30	8.31 ± 0.06 (4)	8.16 ± 0.16 (4)	8.09 ± 0.08 (2)
$\log(\text{N}/\text{O})$				
WR038	0.01	-1.14 ± 0.14 (5)	-0.87 ± 0.27 (1)	-1.06 ± 0.24 (2)
WR039	0.04	-1.09 ± 0.09 (1)	-0.80 ± 0.20 (1)	-1.17 ± 0.14 (1)
WR057	0.39	-1.42 ± 0.07 (5)	-1.48 ± 0.26 (1)	-1.32 ± 0.15 (2)
WR266	0.04	-1.29 ± 0.10 (5)	-1.13 ± 0.30 (1)	-1.18 ± 0.24 (1)
WR404	0.00	-1.37 ± 0.07 (5)	-1.39 ± 0.30 (5)	-1.40 ± 0.06 (1)
WR505	0.00	-1.21 ± 0.15 (5)	-1.15 ± 0.38 (5)	-1.27 ± 0.16 (2)

theoretical ratio larger than those associated with the flux of the emission lines.

3.2. Extinction Correction and $H\alpha$ Maps. For each fiber spectrum, we derived its corresponding reddening coefficient, $c(H\beta)$, using a weighted fit to the values of the Balmer decrement derived from $H\alpha/H\beta$ and $H\gamma/H\beta$ as compared to the theoretical values expected for recombination case B from Storey and Hummer [41] at the electron density and temperature obtained from the integrated SDSS DR-7 spectra and applying the extinction law given by Cardelli et al. [42] with $R_V = 3.1$. In all cases, homogeneous low values of the reddening constant were derived in agreement with the same values derived from the analysis of the corresponding SDSS one-dimensional spectra.

The fluxes of the emission lines for each spaxel were corrected for extinction using its corresponding $c(H\beta)$ value. $H\alpha$ emission line maps (continuum subtracted and extinction corrected) are shown in Figure 1. As can be seen, the observed FoV encompasses the whole optical extent of our galaxies, which are mostly very compact, with the exception of WR404, which presents a cometary aspect with a low brightness tail towards the NE direction, and WR505, which presents several knots of star formation other than the brightest one at west of the FoV.

3.3. Oxygen and Nitrogen Chemical Abundances. The chemical abundances of oxygen and nitrogen were studied in a representative sample of the observed spaxels in the six WR galaxies using different methods as explained below.

The most accurate method to derive oxygen abundances in emission-line objects, as those in our sample, is the so-called direct method which depends on the relative intensity

of both nebular oxygen emission lines to a hydrogen recombination emission line, such as $H\beta$ (i.e., $[\text{O II}]/H\beta$ for O^+/H^+ and $[\text{O III}]/H\beta$ for O^{2+}/H^+), and the previous determination of the electron temperature, via the quotient between auroral-to-nebular emission lines, such as $[\text{O III}] 4363 \text{ \AA}$ and $[\text{O III}] 5007 \text{ \AA}$. See, for instance, Pérez-Montero et al. [21] or Kehrig et al. [22] for additional details of this procedure and how to calculate the low-excitation electron temperature to derive low-excitation ionic abundances. This method was applied to the SDSS DR7 spectra of the brightest regions of the six observed galaxies leading to values of the total oxygen abundances compatible with the low metallicity regime. Owing to the spectral coverage in the SDSS spectra (3800–9100 Å), the $[\text{O II}] 3727 \text{ \AA}$ emission line was not detected in WR038, WR057, and WR505, and the $[\text{O II}] 7319, 7330 \text{ \AA}$ were used instead, as described in Kniazev et al. [43]. The total abundances derived in the SDSS spectra using this method are listed in Table 2.

Regarding the PMAS IFS observations, the direct method was applied in a representative number of spaxels only in WR039, where the $[\text{O III}] 4363 \text{ \AA}$ emission line was detected with acceptable S/N (> 2.5). In the other galaxies of our sample, the direct method could only be applied in the brightest spaxels in WR038, WR057, and WR505 and in none of them in WR266 and WR404.

Therefore, the spatial analysis of the chemical properties in these galaxies was done by means of strong-line methods. We first resorted to the N2 parameter (e.g., [44]), defined as the ratio between $[\text{N II}] 6584 \text{ \AA}$ and $H\alpha$. This parameter has the advantage that it does not depend on reddening nor flux calibration uncertainties and is linearly well correlated with oxygen abundance up to solar metallicities. On the contrary, it has an important drawback when it is used for extended

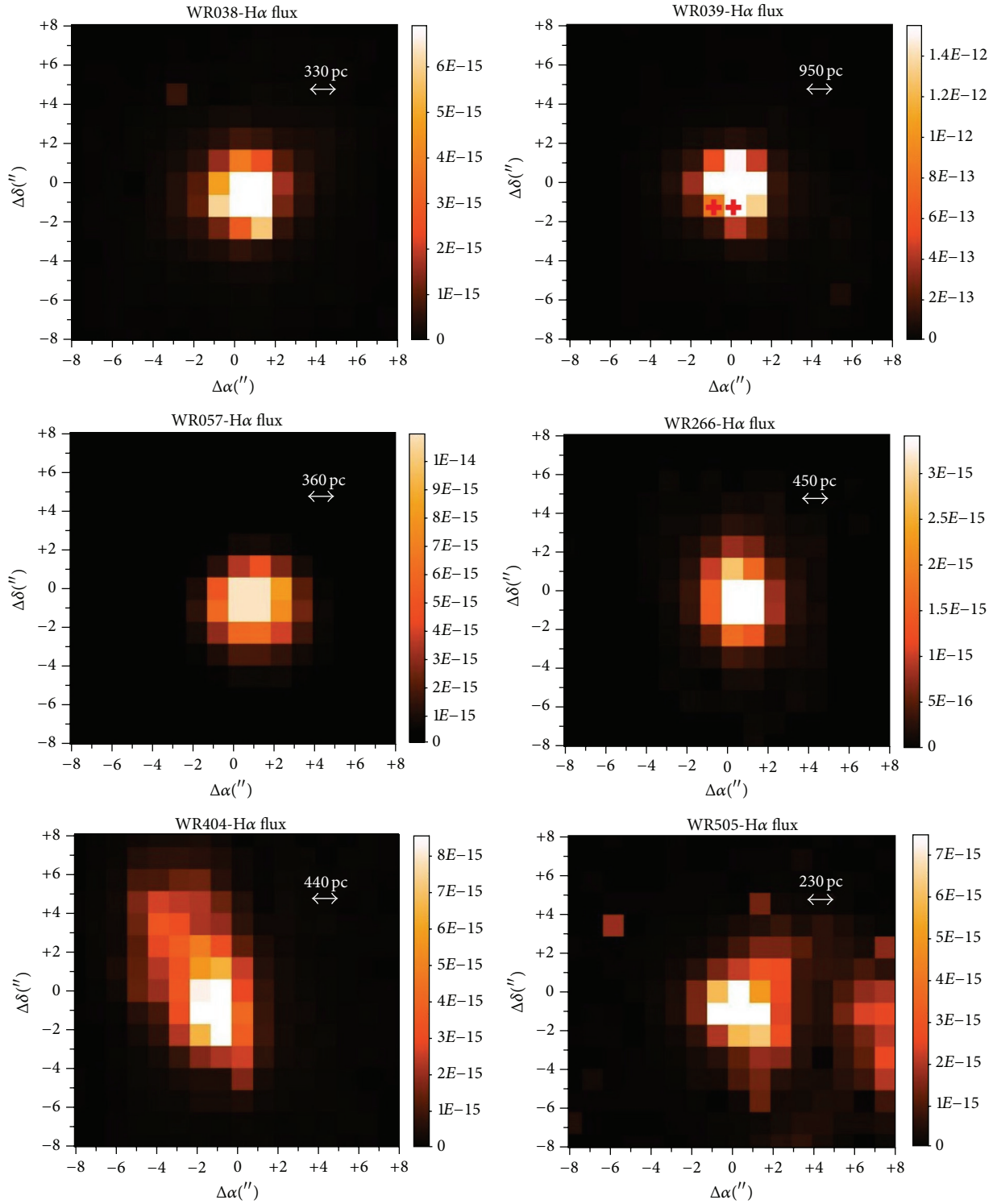


FIGURE 1: Extinction corrected H α maps of the six observed WR galaxies. In all images, each spaxel has $1''$ of resolution. North is up, and east is to the left. Fluxes are in units of erg/s/cm^2 . The relative size in parsecs, at the adopted distance of each object, is indicated. For WR038, the spaxels where the WR bump was detected from our PMAS data are marked with red crosses.

objects, as those studied in this work by means of IFS, as it also varies as a function of the excitation conditions [45]. We verified in what objects this method could be applied to derive reliably the spatial distribution of the oxygen abundance, by plotting in Figure 2 the relation between the N2 parameter and the $[\text{O II}]/[\text{O III}]$ ratio, which traces the nebular excitation. As can be seen, in the most extended objects of our sample, WR404 and WR505, there is a clear correlation between these two emission-line ratios. In the other objects, there is no clear relation between them, with the possible exception of WR057, but in this object, the spatial variation of N2 is lower than the observational errors. Hence, in the case of WR404 and WR505 galaxies, we used the strong-line parameter O3N2, firstly introduced as a metallicity calibrator by Alloin et al. [46] and which is defined as the emission-line ratio between $[\text{O III}] 5007 \text{ \AA}$ and $[\text{N II}] 6584 \text{ \AA}$. According to several authors, such as Pettini and Pagel [47] or Pérez-Montero and Contini [48], this parameter is not valid for very low metallicity objects ($12 + \log(\text{O}/\text{H}) < 8.0$), but, on the contrary, its dependence on excitation is much lower than in the case of N2. According to the values derived from the SDSS spectra for WR404 and WR505, their mean oxygen abundances are higher than the lower limit for O3N2, so this parameter was used for these two objects instead.

For the sake of consistency between the three employed methods (direct method in the case of WR039, N2 parameter for WR038, WR057, and WR266, and O3N2 for WR404 and WR505), we used the calibrations presented in Pérez-Montero and Contini [48] for N2 and O3N2, which are consistent with the direct method. The resulting oxygen abundance maps of the six observed galaxies are plotted in Figure 3 along with the histogram distributions of the abundances in those spaxels with enough S/N in all the involved emission lines ($S/N > 2.5$).

In the case of the nitrogen-to-oxygen ratio (N/O), the direct method can also be used to derive the N^+/H^+ ratio and then deriving N/O using the approximation $\text{N}^+/\text{O}^+ \approx \text{N}/\text{O}$ [as before, see further details in [21, 22]], but this method could only be used in a representative number of spaxels in WR039. For the other five galaxies, we resorted to the N2O2 parameter, defined as the ratio of $[\text{N II}] 6584 \text{ \AA}$ and $[\text{O II}] 3727 \text{ \AA}$. This ratio has the advantage that it has a monotonic linear relation with N/O and, contrary to N2, it does not have any dependence on excitation as it only depends on low-excitation emission lines. As in the case of oxygen abundances, we used the empirical calibration of N2O2 with N/O from Pérez-Montero and Contini [48], which is consistent with the direct method derivations of this chemical abundance ratio. The resulting N/O maps of the six observed galaxies are plotted in Figure 4 along with the histogram distributions of the abundances in those spaxels with enough S/N in all the involved emission lines.

3.4. Spatial Chemical Homogeneity. To study to what extent the chemical content of the gas can be considered as homogeneous and to give the statistical significance of the O/H and N/O distributions, we used the procedure presented in Pérez-Montero et al. [21] and refined in Kehrig et al. [22]. This method is based on the assumption that a certain

property can be considered as spatially homogeneous across the observed FoV if two conditions are satisfied: for the corresponding dataset (i) the null hypothesis (i.e., the data come from a normally distributed population) of the Lilliefors test [49] cannot be rejected at the 5% significance level and (ii) the observed variations of the data distribution around the single mean value can be explained by random errors; that is, the corresponding Gaussian sigma should be lower or of the order of the typical uncertainty of the considered property; we take as typical uncertainty the square root of the weighted sample variance. In Table 2, we show the results from our statistical analysis for both total O/H and N/O.

The Lilliefors test for each of the distributions was performed on the linear values of the chemical abundances. The corresponding confidence levels (P values) are listed in Table 2 with the resulting means and Gaussian sigma in case that the P value is higher than 0.05. Otherwise, the means and standard deviations are those of the distributions. In those cases where the P value is larger than 0.05, the second condition imposed to consider a homogeneous distribution is also satisfied in all cases. In all distributions where a strong-line method was used to derive both O/H and N/O, the sigma of the Gaussian is much lower than the intrinsic uncertainty associated with these methods (~ 0.3 dex). For WR039, where the direct method was used, the weighted sigma for both oxygen abundance and N/O is 0.2 dex, which also is larger than the usual sigmas in the Gaussian fittings.

4. Discussion: Are WR Stars Able to Pollute the ISM of Galaxies?

The use of IFS is fundamental to study the spatial extent of the chemical properties of the ISM in extended objects. In this context, this technique along with the use of appropriate statistical tools allows us to explore the presence of chemical inhomogeneities in both O/H and N/O and to relate this local pollution with the position of WR stars, whose stellar winds enrich the surrounding ISM with the products of the main sequence nuclear burning of massive stars.

Our statistical method points to a high degree of homogeneity in O/H across the FoV of the studied galaxies, implying scales of several kpc, with the only exception of WR404, where a possible gradient of metallicity is found. This spatial variation of the metallicity goes from lower values in the brightest region of the galaxy at the SE to slightly higher values in the low surface brightness tail towards the NW.

Our spatial analysis of N/O reveals that only WR057 presents values for which the homogeneity of this abundance ratio cannot be ruled out. In contrast, for all the other cases, the conditions assumed to consider a homogeneous distribution of N/O are not fulfilled, as very high values of this ratio in certain positions of the FoV were measured.

Although the WR blue bump is detectable in the SDSS spectra of the six selected galaxies, we only found it in our PMAS observations in two spaxels of the WR039 galaxy. These are marked with red crosses in Figure 1. A thorough analysis of the causes of the missing detection of the bump in the other objects will be performed in a forthcoming paper. Figure 5 shows a portion of the spectrum obtained

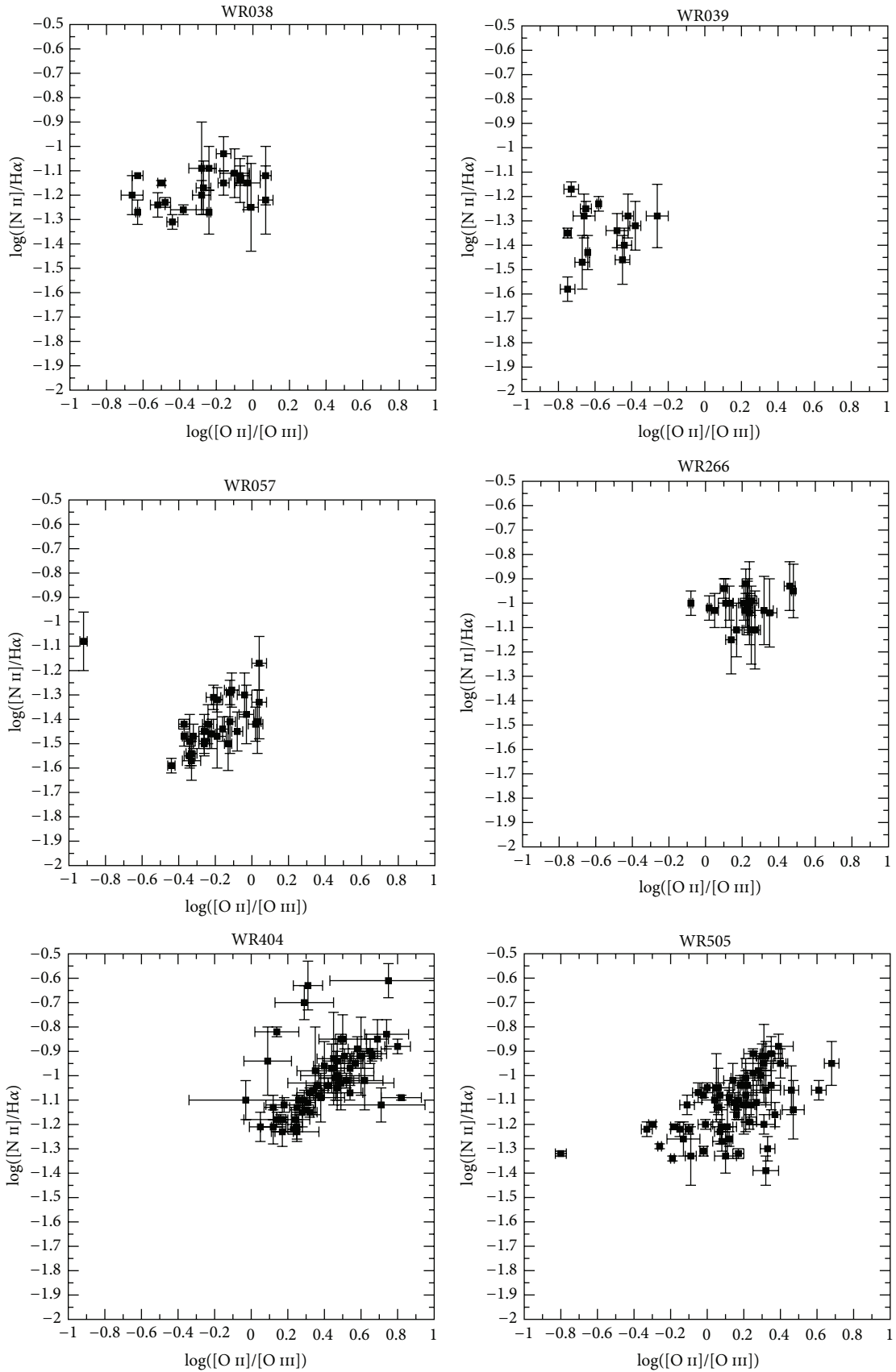


FIGURE 2: Relation between the $[\text{O II}]/[\text{O III}]$ and $[\text{N II}]/\text{H}\alpha$ emission line ratios for those spaxels with sufficient S/N in the four involved lines of the six observed galaxies.

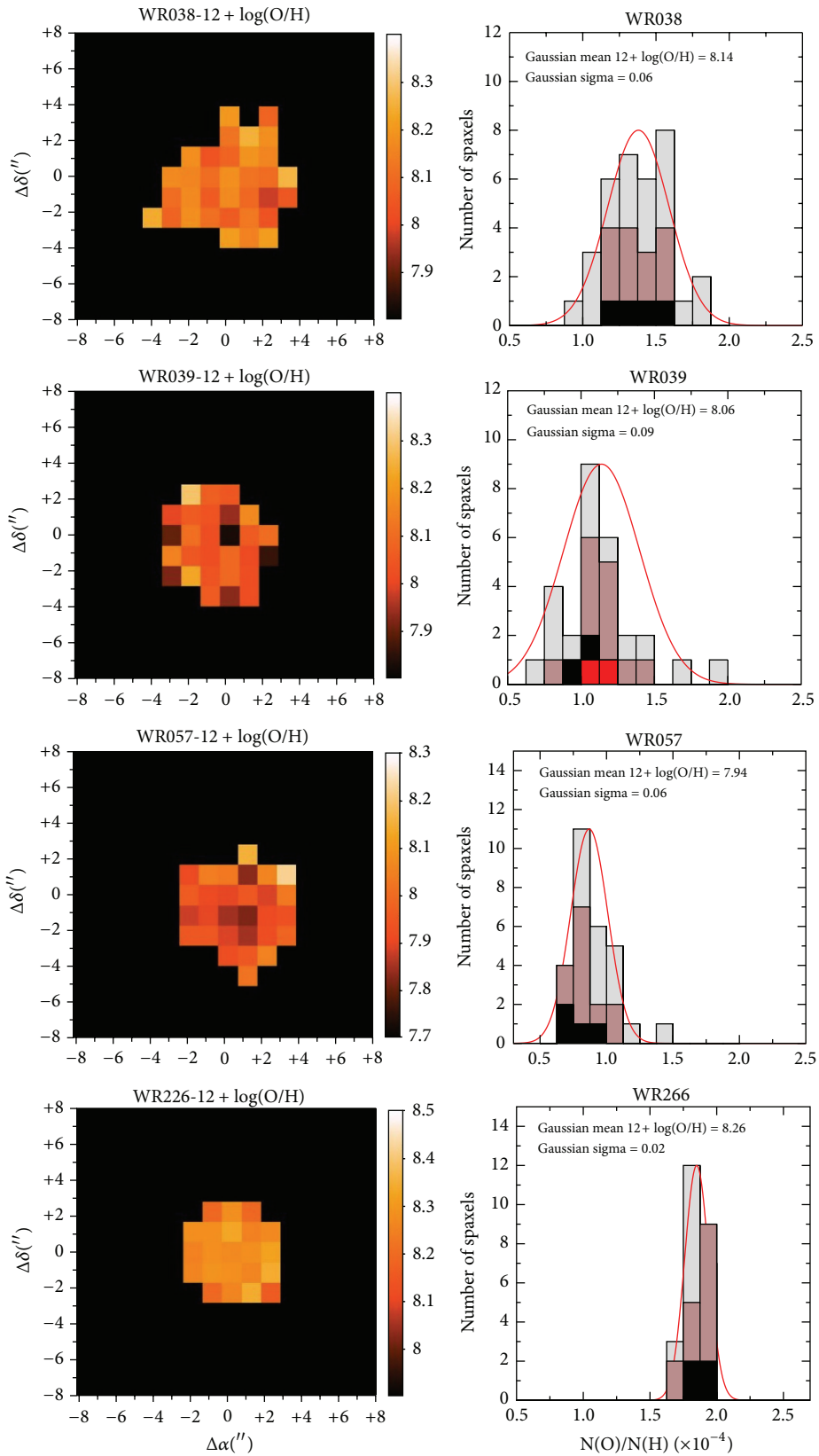


FIGURE 3: Continued.

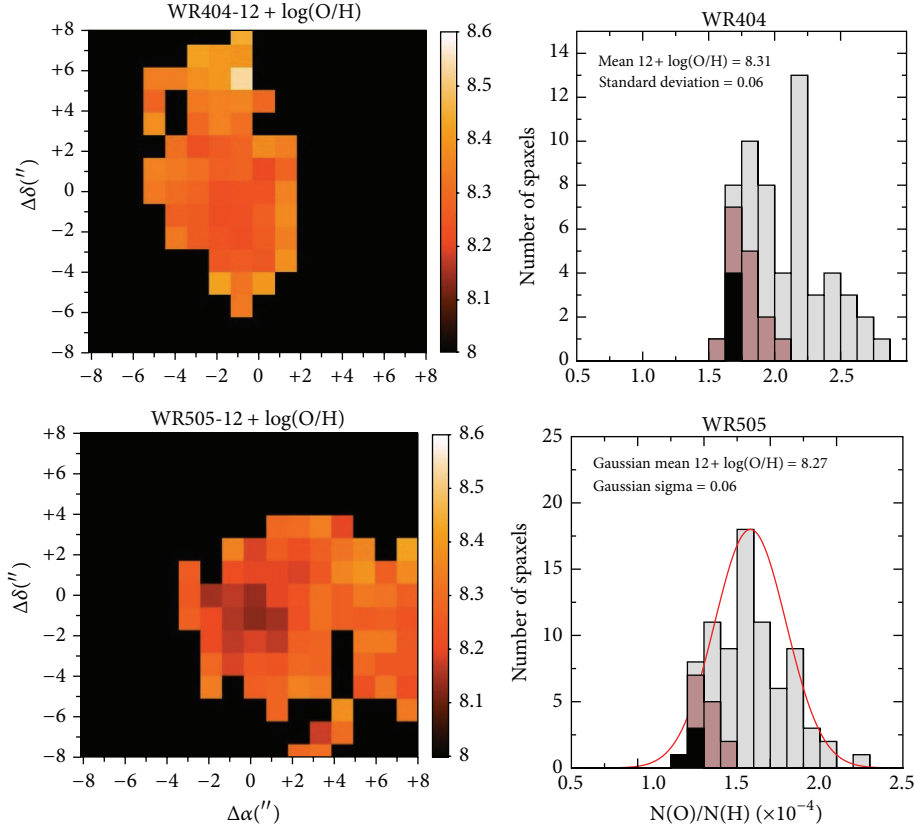


FIGURE 3: Oxygen abundance maps derived as described in the text and histogram distributions in linear scale for WR038, WR039, and WR057. In all images, each spaxel has $1''$ resolution, north is up and east is left. The bars in the histogram represent spaxels with detected WR emission (red), spaxels in the same positions as the SDSS pointing (black), spaxels adjacent to this position (brown), and the other spaxels (grey). Same figure for WR266, WR404, and WR505.

by coadding the emission from the 2 spaxels with the WR bump detection. The measured luminosity of the bump at the adopted distance, once the emission lines over the bump were removed, [$L_{\text{WR}} = 10^{40.08 \pm 0.08}$ erg/s], is consistent with the value measured in the integrated SDSS spectrum [$L_{\text{WR}} = 10^{39.97 \pm 0.15}$ erg/s]. In contrast, the equivalent width of the bump in these two spaxels ($20 \pm 4 \text{ \AA}$) is much higher than in the SDSS spectrum ($8 \pm 4 \text{ \AA}$), as expected, taking into account the fact that the collected stellar continuum in the area of the two $1''$ PMAS spaxels is fainter than in the $3''$ SDSS fiber.

To investigate the possible connection between the detected nitrogen overabundance and the location of the WR stars, we identified in the histograms shown in Figures 3 and 4 the probable positions of the WR stars. In the case of WR039, where the WR bump was detected in our IFS data, the corresponding spaxels with WR emission are plotted as red bars. In the rest of the objects, we selected the four spaxels probably encompassed by the SDSS fiber and which are thought to host the WR population, and we plotted them in the histograms as black bars. This subset of spaxels always includes the brightest $\text{H}\alpha$ position in the observed galaxies. Finally, to study the possible extent of the N pollution, we also identified the 12 spaxels around these 4 positions of the SDSS fiber as brown bars in the histograms. As can be seen in the histograms

and can also be confirmed by visual inspection of the N/O maps, the nitrogen overabundance is tightly related to the position of the WRs in WR038, WR039, WR266, and WR505, although there is not a perfect match between them. This is well illustrated in the unique case where we identified the WR emission, WR039, where the N overabundance is slightly displaced in relation to the position of the WR bumps. The other galaxy whose N/O is not homogeneous is WR404, but in this case, this is probably related to the gradient of metallicity across its tail detected in the O/H analysis, as no direct relation between the N overabundance and the positions of the WRs is detected.

The results obtained in this work, in which we find evidence for a local nitrogen overabundance (in zones of the order of 100 pc around the position of the WR bumps) in four out of the six observed galaxies by means of IFS have the following implications

- (i) WR stars are possibly the main cause of the overabundance of nitrogen observed in 4 out of 6 observed galaxies at spatial scales of the order of several hundreds of parsecs detected around the position of these stars, differing from the objects studied in Pérez-Montero et al. [21], where this overabundance was detected at scales of several kpc.

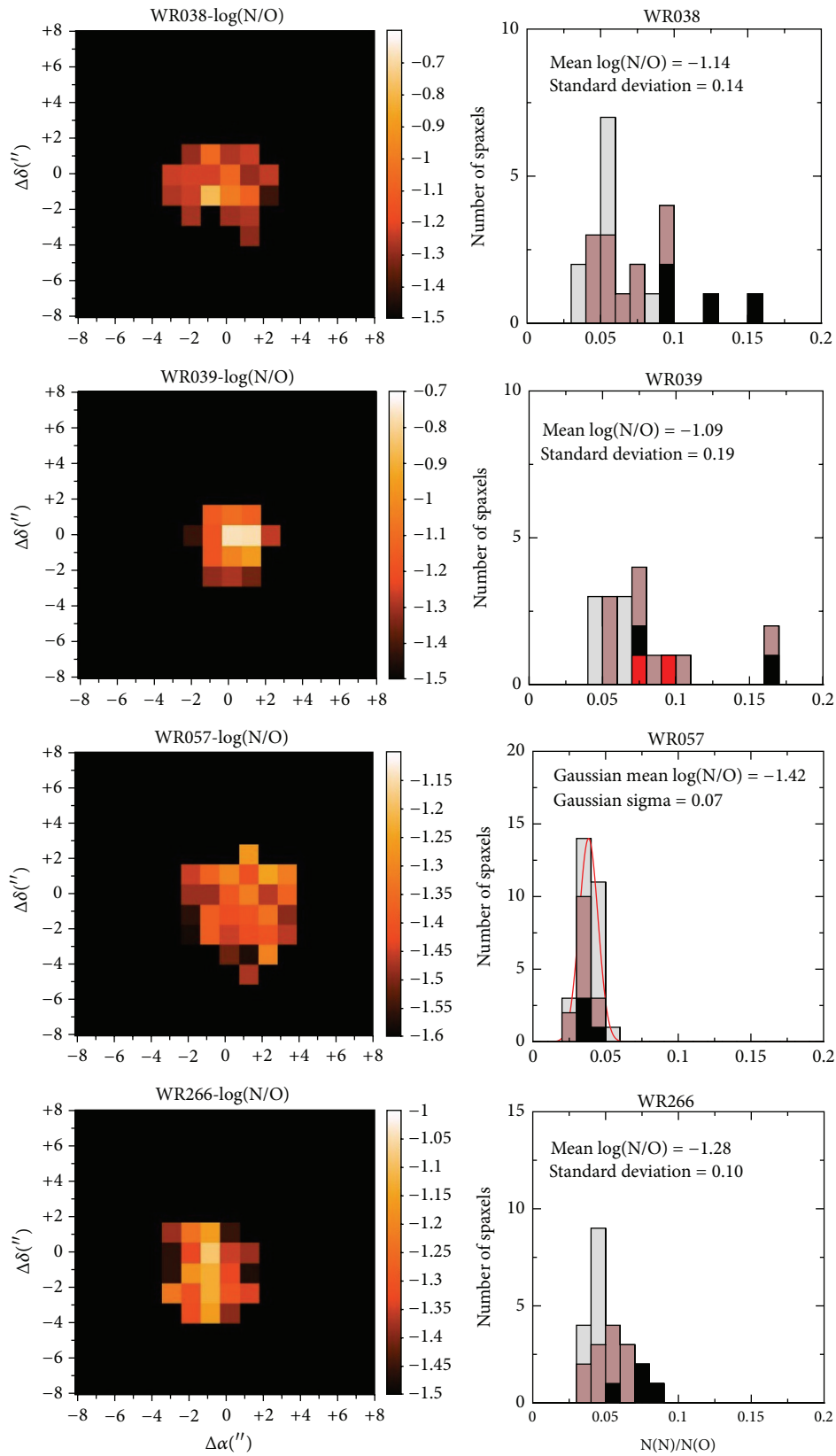


FIGURE 4: Continued.

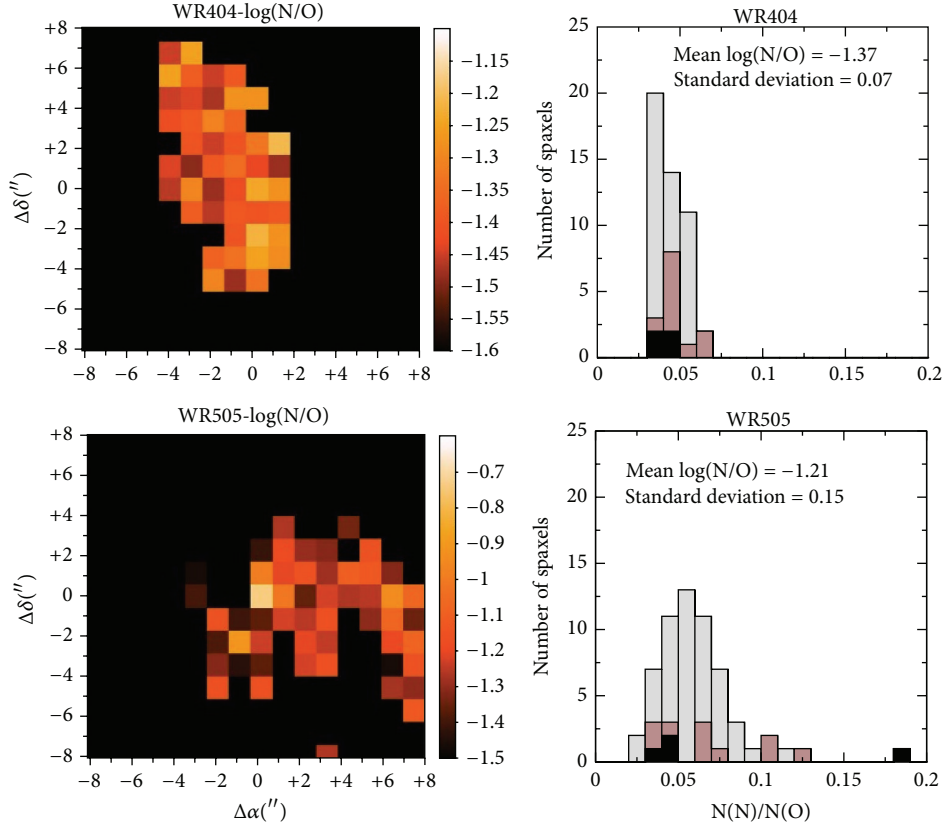


FIGURE 4: N/O ratio maps derived as described in the text and histogram distributions in linear scale for WR038, WR039, and WR057. In all images, each spaxel has $1''$ resolution, north is up, and east is left. The colors in the bars have the same meaning as in Figure 3. Same figure for WR266, WR404, and WR505.

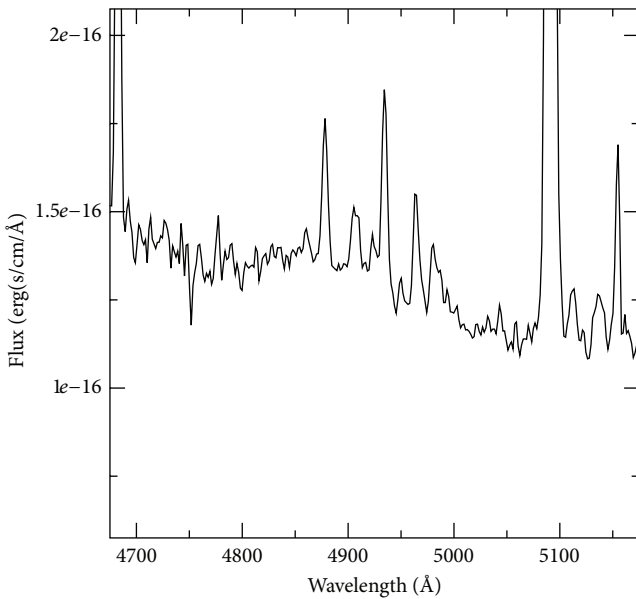


FIGURE 5: Optical spectrum obtained by coadding the two spaxels in WR038 where the Wolf-Rayet blue bump is detected.

According to the chemical yields of massive stars from Mollá and Terlevich [50] presented in Figure 14 of

Pérez-Montero et al. [21], the stellar masses of the ionizing clusters in the sample of WR galaxies studied here (all of them around $10^7 M_{\odot}$) can produce a N/O excess at distances compatible with the scales at which the N pollution has been detected by means of IFS in this work.

- (ii) As the local N pollution has not been observed in all the studied objects in this work and in those where it was observed, it does not show a perfect match with the positions of the WR bump. Although it is necessary to take the limited spatial resolution of our observations into account, this mismatch could be possibly due to a timescale offset between the lifetime of the WR stars and the mixing of the ejected material with the ISM. Possibly, the positions with relatively high N/O trace regions where the WR stars were present. In contrast, the positions where the bumps are detected are tracing the ongoing star formation regions. This spatial mismatch between N excess and WR positions has also been observed in other nearby star-forming objects studied by means of optical IFS (e.g., NGC5253, [27]). This timescale offset between WR lifetimes and N mixing is supported by the results from other previous works based on IFS data where WR stars were reported, but not the excess

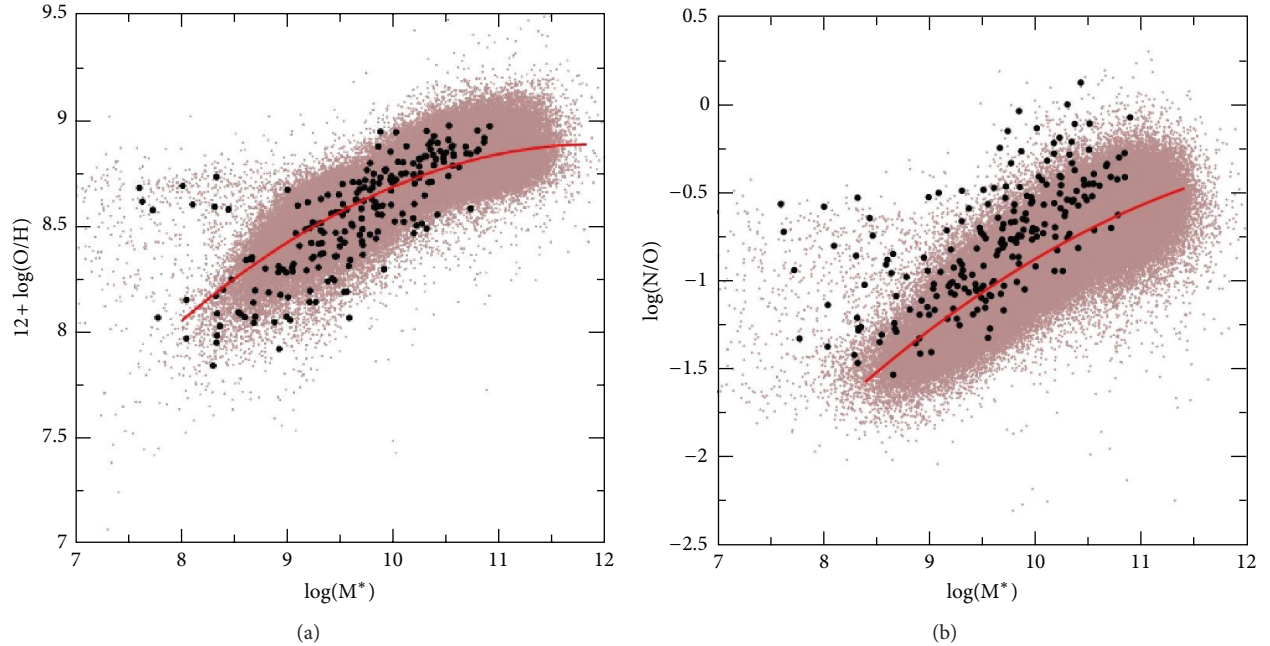


FIGURE 6: MZR (a) and MNOR (b) relations for the star-forming galaxies selected from the SDSS DR7. The solid red lines, calculated by Pérez-Montero et al. [55], are quadratic fits to the medians in stellar mass bins of 0.2 dex. The black points are the galaxies matching the catalog of WR galaxies by Brinchmann et al. [7].

- in N/O (e.g., in this work, WR057 and WR404, in HS0837 + 4717 and Mrk930 in [21], or in two out of the three WR clusters detected in Mrk178 [22]).
- (iii) The local nitrogen pollution happens while homogeneous values of the oxygen abundance are found, which could be indicative that oxygen is not noticeably present in the winds ejected by the WR stars at this stage. Apparently, the properties of these winds (density, velocity, etc.) favour the mixing of their components with the surrounding warm ISM. However, the mixing expected later of the oxygen ejected during the last stages of the WR phase and the subsequent O-rich SNe explosions have a timescale much longer than that of early WR winds (e.g., [51]).
 - (iv) Additional mechanisms other than the enrichment due to WR winds are thought to be responsible for the nitrogen overabundance in star-forming galaxies. This is the case of collisional deexcitation of O^+ in strong shocks associated with mergers [52] or other hydrodynamical processes, such as the infall of pristine gas [29], which can at same time reduce the overall metallicity of galaxies and boost the star formation. These processes could be behind the relation between metallicity and star-formation rate in galaxies. On the contrary, such a mechanism will not have any influence on the abundance ratio of metals as N and O [53]. A very suitable tool to identify these processes and to distinguish them from local pollution, as in the case of N ejection by WR stars, is the simultaneous analysis of the relations between stellar mass and metallicity (MZR) and with N/O (MNOR). This

was already used by Amorín et al. [54] to understand the low metallicity combined with N/O ratio much higher than the values in the plateau of the diagram O/H versus N/O measured in *green pea* galaxies. In that work the analysis of these galaxies shows that these objects have the expected N/O for their masses, while they have systematically lower metallicities, even though WR stars have been detected in deep GTC spectra of some of them [18].

Hence, for WR galaxies, we try to understand their average observed N/O excess, as reported by Brinchmann et al. [7], doing the same analysis. In Figure 6 the MZR is shown for the star-forming galaxies of the SDSS, with their stellar masses compiled from the Max Planck Institute for Astrophysics-Johns Hopkins University (MPA-JHU) catalog (available at <http://www.mpa-garching.mpg.de/SDSS/>) and oxygen abundances calculated using the N2 parameter for emission lines with S/N larger than 2. The solid red line, as explained in Pérez-Montero et al. [55], is a quadratic fit to the medians for stellar mass bins of 0.2 dex. The black points are the matches between the WR galaxy catalog by Brinchmann et al. [7] and all the other star-forming SDSS galaxies selected from the MPA/JHU list. The number of matches obeying the S/N criterion and having a minimum redshift ($z > 0.02$) to avoid serious aperture effects in the determination of the stellar mass, as described in Pérez-Montero et al. [55], is 254. In the right panel of the same figure, the MNOR is shown, as calculated using the N2S2 parameter with the calibration by Pérez-Montero and Contini [48]. As can be appreciated and contrary to *green pea* galaxies, the WR galaxies are in average in agreement with the metallicities expected for their stellar

mass but, in contrast, have larger N/O ratios, which could be just local pollution values in the same region covered by the SDSS fiber and possibly due to the enrichment by WR stars.

5. Summary

In this work, we presented 3.5 m CAHA-PMAS IFS observations of six metal-poor compact WR galaxies selected from the catalog published by Brinchmann et al. [7] in the optical spectral range 3700–6850 Å. Our aim is to study the connection between the presence of WR stars and N/O excess as compared with the values predicted by chemical evolution models at this metallicity regime.

We derived O/H and N/O abundances ratios using the direct method (i.e., with the determination of the electron temperature) or strong-line methods based on [N II] 6584 Å emission line, such as N2, O3N2 (for O/H), and N2O2 (for N/O) with the calibrations provided by Pérez-Montero and Contini [48], which are consistent with the direct method. We studied the homogeneity of the spatial distributions of both O/H and N/O using the same statistical procedure introduced by Pérez-Montero et al. [21] and improved by Kehrig et al. [22].

Our results indicate that in all the studied objects O/H can be considered as uniform in scales of the order of several kpc, with the exception of WR404, for which a gradient of O/H is found in the same direction of a low surface brightness tail. In contrast, N/O can only be considered as homogeneous in WR057. In four of the six studied galaxies (WR038, WR039, WR266, and WR505), we found positions associated with or close to the WR stars with N excess in spatial scales of the order of several hundreds of pc. We discussed that, according to the models presented by Pérez-Montero et al. [21] based on massive star yields of Mollá and Terlevich [50], the N excess length scale is consistent with the distances at which the stellar clusters in these galaxies can enhance the gas-phase abundance of N. On the other hand, our analysis of both the MZR and the MNOR of the WR galaxies of the SDSS WR catalog of Brinchmann et al. [7] excludes hydrodynamical effects, such as metal-poor gas inflows, as the more frequent cause of the N excess detected in the SDSS galaxies with a detection of the WR bump.

Based on observations collected at the Centro Astronómico Hispano Alemán (CAHA) at Calar Alto, operated jointly by the Max-Planck Institut für Astronomie and the Instituto de Astrofísica de Andalucía (CSIC).

Acknowledgment

This work has been partially supported by projects AYA2007-67965-C03-02 and AYA2010-21887-C04-01 of the Spanish National Plan for Astronomy and Astrophysics. The authors thank an anonymous referee for his/her very thorough revision of this paper that has helped to improve it.

References

- [1] D. E. Osterbrock and R. D. Cohen, “Two galaxies with Wolf-Rayet features in their spectra,” *Astrophysical Journal*, vol. 261, pp. 64–69, 1982.
- [2] D. A. Allen, A. E. Wright, and W. M. Goss, “The dwarf emission galaxy He 2.10,” *Monthly Notices of the Royal Astronomical Society*, vol. 177, p. 91, 1976.
- [3] P. S. Conti, C. D. Garmany, and P. Massey, “Spectroscopic studies of Wolf-Rayet stars. V-Optical spectrophotometry of the emission lines in Small Magellanic Cloud stars,” *The Astrophysical Journal*, vol. 341, pp. 113–119, 1989.
- [4] D. Schaerer, T. Contini, and M. Pindao, “New catalogue of Wolf-Rayet galaxies and high-excitation extra-galactic HII regions,” *Astronomy & Astrophysics*, vol. 136, no. 1, pp. 35–52, 1999.
- [5] N. G. Guseva, Y. I. Izotov, and T. X. Thuan, “A spectroscopic study of a large sample of Wolf-Rayet galaxies,” *Astrophysical Journal Letters*, vol. 531, no. 2, pp. 776–803, 2000.
- [6] W. Zhang, X. Kong, C. Li, H.-Y. Zhou, and F.-Z. Cheng, “Wolf-Rayet galaxies in the Sloan Digital Sky Survey: the metallicity dependence of the initial mass function,” *Astrophysical Journal Letters*, vol. 655, no. 2 I, pp. 851–862, 2007.
- [7] J. Brinchmann, D. Kunth, and F. Durret, “Galaxies with Wolf-Rayet signatures in the low-redshift Universe,” *Astronomy & Astrophysics*, vol. 485, pp. 657–677, 2008.
- [8] P. A. Crowther, “Physical properties of Wolf-Rayet stars,” *Annual Review of Astronomy & Astrophysics*, vol. 45, pp. 177–219, 2007.
- [9] F. Legrand, D. Kunth, J.-R. Roy, J. M. Mas-Hesse, and J. R. Walsh, “Detection of WR stars in the metal-poor starburst galaxy IZw 18,” *Astronomy & Astrophysics*, vol. 326, no. 3, pp. L17–L20, 1997.
- [10] R. M. G. Delgado, M. Cerviño, L. P. Martins, C. Leitherer, and P. H. Hauschildt, “Evolutionary stellar population synthesis at high spectral resolution: optical wavelengths,” *Monthly Notices of the Royal Astronomical Society*, vol. 357, no. 3, pp. 945–960, 2005.
- [11] J. M. Vílchez and C. Esteban, “Wolf Rayet stars and interrelations with other massive stars in galaxies,” in *Proceedings of the IAU Symposium*, vol. 143, Bali, Indonesia, 1991.
- [12] C. Esteban and J. M. Vílchez, “On the chemodynamics of Wolf-Rayet ring nebulae—NGC 6888,” *The Astrophysical Journal*, vol. 390, pp. 536–540, 1992.
- [13] A. Fernández-Martín, D. Martín-Gordón, J. M. Vílchez et al., “Ionization structure and chemical abundances of the Wolf-Rayet nebula NGC 6888 with integral field spectroscopy,” *Astronomy & Astrophysics*, vol. 541, article A119, 2012.
- [14] S. Pustilnik, A. Kniazev, A. Pramskij et al., “HS 0837 + 4717—a metal-deficient blue compact galaxy with large nitrogen excess,” *Astronomy & Astrophysics*, vol. 419, no. 2, pp. 469–484, 2004.
- [15] A. R. López-Sánchez, C. Esteban, J. García-Rojas, M. Peimbert, and M. Rodríguez, “The localized chemical pollution in NGC 5253 revisited: results from deep echelle spectrophotometry,” *The Astrophysical Journal*, vol. 656, p. 168, 2007.
- [16] G. F. Hägele, E. Pérez-Montero, Á. I. Díaz, E. Terlevich, and R. Terlevich, “The temperature and ionization structure of the emitting gas in H II galaxies: implications for the accuracy of abundance determinations,” *Monthly Notices of the Royal Astronomical Society*, vol. 372, no. 1, pp. 293–312, 2006.
- [17] G. F. Hägele, Á. I. Díaz, E. Terlevich, R. Terlevich, E. Pérez-Montero, and M. V. Cardaci, “Precision abundance analysis of bright H II galaxies,” *Monthly Notices of the Royal Astronomical Society*, vol. 383, pp. 209–229, 2008.
- [18] R. Amorín, E. Pérez-Montero, J. M. Vílchez, and P. Papaderos, “The star formation history and metal content of the green peas. New detailed gtc-osiris spectrophotometry of three galaxies,” *The Astrophysical Journal*, vol. 749, article 185, 2012.

- [19] M. Mollá, J. M. Vílchez, M. Gavilán, and A. I. Díaz, “The nitrogen-to-oxygen evolution in galaxies: the role of the star formation rate,” *Monthly Notices of the Royal Astronomical Society*, vol. 372, pp. 1069–1080, 2006.
- [20] C. Kehrig, J. M. Vílchez, and S. F. Sánchez, “The interplay between ionized gas and massive stars in the HII galaxy IIZw70: integral field spectroscopy with PMAS,” *Astronomy & Astrophysics*, vol. 477, pp. 813–822, 2008.
- [21] E. Pérez-Montero, J. M. Vílchez, B. Cedrés et al., “Integral field spectroscopy of nitrogen overabundant blue compact dwarf galaxies,” *Astronomy & Astrophysics*, vol. 532, article A141, 2011.
- [22] C. Kehrig, E. Perez-Montero, J. M. Vílchez et al., “Uncovering multiple Wolf-Rayet star clusters and the ionized ISM in Mrk 178: the closest metal-poor Wolf-Rayet H ii galaxy,” *Monthly Notices of the Royal Astronomical Society*, vol. 432, pp. 2731–2745, 2013.
- [23] C. Kehrig, M. S. Oey, P. A. Crowther et al., “Gemini GMOS spectroscopy of HeII nebulae in M 33,” *Astronomy & Astrophysics*, vol. 526, no. 16, article A128, 2011.
- [24] M. Shirazi and J. Brinchmann, “Strongly star forming galaxies in the local Universe with nebular HeII λ 4686 emission,” *Monthly Notices of the Royal Astronomical Society*, vol. 421, no. 2, pp. 1043–1063, 2012.
- [25] Á. R. López-Sánchez, A. Mesa-Delgado, L. López-Martín, and C. Esteban, “The ionized gas at the centre of IC10: a possible localized chemical pollution by Wolf-Rayet stars,” *Monthly Notices of the Royal Astronomical Society*, vol. 411, no. 3, pp. 2076–2092, 2011.
- [26] B. L. James, Y. G. Tsamis, J. R. Walsh, M. J. Barlow, and M. S. Westmoquette, “The Lyman break analogue Haro 11: spatially resolved chemodynamics with VLT FLAMES,” *Monthly Notices of the Royal Astronomical Society*, vol. 430, pp. 2097–2112, 2013.
- [27] A. Monreal-Ibero, J. R. Walsh, and J. M. Vílchez, “The ionized gas in the central region of NGC 5253. 2D mapping of the physical and chemical properties,” *Astronomy & Astrophysics*, vol. 544, article A60, 2012.
- [28] M. S. Westmoquette, B. James, A. Monreal-Ibero, and J. R. Walsh, “Piecing together the puzzle of NGC 5253: abundances, kinematics and WR stars,” *Astronomy & Astrophysics*, vol. 550, article A88, 2013.
- [29] J. Köppen and G. Hensler, “Effects of episodic gas infall on the chemical abundances in galaxies,” *Astronomy & Astrophysics*, vol. 434, no. 2, pp. 531–541, 2005.
- [30] B. L. James, Y. G. Tsamis, M. J. Barlow, J. R. Walsh, and M. S. Westmoquette, “The merging dwarf galaxy UM 448: chemodynamics of the ionized gas from VLT integral field spectroscopy,” *Monthly Notices of the Royal Astronomical Society*, vol. 428, no. 1, pp. 86–102, 2013.
- [31] J. A. Baldwin, M. M. Phillips, and R. Terlevich, “Classification parameters for the emission-line spectra of extragalactic objects,” *Publications of the Astronomical Society of the Pacific*, vol. 93, pp. 5–19, 1981.
- [32] M. M. Roth, T. Fechner, D. Wolter et al., “Commissioning of the CCD231 4K \times 4K detector for PMAS,” in *High Energy, Optical, and Infrared Detectors for Astronomy IV*, vol. 7742 of *Proceedings of SPIE*, June 2010.
- [33] S. F. Sánchez, “Techniques for reducing fiber-fed and integral-field spectroscopy data: An implementation on R3D,” *Astronomische Nachrichten*, vol. 327, pp. 850–861, 2006.
- [34] C. Sandin, T. Becker, M. M. Roth et al., “P3D: a general data-reduction tool for fiber-fed integral-field spectrographs,” *Astronomy & Astrophysics*, vol. 515, article A35, 2010.
- [35] A. Kelz, M. A. W. Verheijen, M. M. Roth et al., “PMAS: the potsdam multi-aperture spectrophotometer—II. The wide integral field unit PPak,” *Publications of the Astronomical Society of the Pacific*, vol. 118, no. 839, pp. 129–145, 2006.
- [36] A. I. Diaz, “Hydrogen absorption line profiles of ionizing star clusters,” *Monthly Notices of the Royal Astronomical Society*, vol. 231, pp. 57–67, 1988.
- [37] G. Bruzual and S. Charlot, “Stellar population synthesis at the resolution of 2003,” *Monthly Notices of the Royal Astronomical Society*, vol. 344, no. 4, pp. 1000–1028, 2003.
- [38] R. Cid Fernandes, Q. Gu, J. Melnick et al., “The star formation history of Seyfert 2 nuclei,” *Monthly Notices of the Royal Astronomical Society*, vol. 355, no. 1, pp. 273–296, 2004.
- [39] A. Mateus, L. Sodré Jr., R. C. Fernandes, G. Stasińska, W. Schoenell, and J. M. Gomes, “Semi-empirical analysis of Sloan Digital Sky Survey galaxies—II. The bimodality of the galaxy population revisited,” *Monthly Notices of the Royal Astronomical Society*, vol. 370, no. 2, pp. 721–737, 2006.
- [40] E. Pérez-Montero and A. I. Díaz, “Line temperatures and elemental abundances in H II galaxies,” *Monthly Notices of the Royal Astronomical Society*, vol. 346, no. 1, pp. 105–118, 2003.
- [41] P. J. Storey and D. G. Hummer, “Recombination line intensities for hydrogenic ions-IV. Total recombination coefficients and machine-readable tables for $Z=1$ to 8,” *Monthly Notices of the Royal Astronomical Society*, vol. 272, pp. 41–48, 1995.
- [42] J. A. Cardelli, G. C. Clayton, and J. S. Mathis, “The relationship between infrared, optical, and ultraviolet extinction,” *The Astrophysical Journal*, vol. 345, pp. 245–256, 1989.
- [43] A. Y. Kniazev, E. K. Grebel, L. Hao, M. A. Strauss, J. Brinkmann, and M. Fukugita, “Discovery of eight new extremely metal-poor galaxies in the sloan digital sky survey,” *Astrophysical Journal Letters*, vol. 593, no. 2, pp. L73–L76, 2003.
- [44] G. Denicoló, R. Terlevich, and E. Terlevich, “New light on the search for low-metallicity galaxies—I. The N2 calibrator,” *Monthly Notices of the Royal Astronomical Society*, vol. 330, no. 1, pp. 69–74, 2002.
- [45] E. Pérez-Montero and A. I. Díaz, “A comparative analysis of empirical calibrators for nebular metallicity,” *Monthly Notices of the Royal Astronomical Society*, vol. 361, no. 3, pp. 1063–1076, 2005.
- [46] D. Alloin, S. Collin-Souffrin, M. Joly, and L. Vigroux, “Nitrogen and oxygen abundances in galaxies,” *Astronomy & Astrophysics*, vol. 78, pp. 200–216, 1979.
- [47] M. Pettini and B. E. J. Pagel, “[O III]/[N II] as an abundance indicator at high redshift,” *Monthly Notices of the Royal Astronomical Society*, vol. 348, no. 3, pp. L59–L63, 2004.
- [48] E. Pérez-Montero and T. Contini, “The impact of the nitrogen-to-oxygen ratio on ionized nebula diagnostics based on [N ii] emission lines,” *Monthly Notices of the Royal Astronomical Society*, vol. 398, no. 2, pp. 949–960, 2009.
- [49] H. W. Lilliefors, “On the Kolmogorov-Smirnov test for normality with mean and variance unknown,” *Journal of the American Statistical Association*, vol. 62, pp. 399–402, 1967.
- [50] M. Mollá and R. Terlevich, “Modelling the composition of a young star cluster ejecta,” *Monthly Notices of the Royal Astronomical Society*, vol. 425, pp. 1696–1708, 2012.
- [51] G. Tenorio-Tagle, “Interstellar matter hydrodynamics and the dispersal and mixing of heavy elements,” *Astronomical Journal*, vol. 111, no. 4, pp. 1641–1650, 1996.
- [52] J. C. Raymond, “Shock waves in the interstellar medium,” *Astrophysical Journal*, vol. 39, pp. 1–27, 1979.

- [53] M. G. Edmunds, "General constraints on the effect of gas flows in the chemical evolution of galaxies," *Monthly Notices of the Royal Astronomical Society*, vol. 246, p. 678, 1990.
- [54] R. O. Amorín, E. Pérez-Montero, and J. M. Vílchez, "On the oxygen and nitrogen chemical abundances and the evolution of the "green pea" galaxies," *The Astrophysical Journal Letters*, vol. 715, article L128, 2010.
- [55] E. Pérez-Montero, T. Contini, F. Lamareille et al., "The cosmic evolution of oxygen and nitrogen abundances in star-forming galaxies over the past 10 Gyr," *Astronomy & Astrophysics*, vol. 549, article A25, 2013.